Imperial College of Science, Technology and Medicine
Royal School of Mines
Department of Earth Science & Engineering

Geomechanical modelling of subsurface storage of hydrogen in depleted natural gas reservoirs

James Edward John Burtonshaw

A thesis submitted in partial fulfilment of the requirements for the degree of
Doctor of Philosophy (PhD) in Energy Storage Engineering
March 2025

Abstract

Underground Hydrogen Storage (UHS) in depleted gas fields is a novel energy transition technology that is the most efficient solution for satisfying periods of renewable energy deficit in low carbon energy economies. The cyclical injection, storage and withdrawal of an ultra-low density, ultra-low viscosity fluid such as hydrogen may exacerbate geomechanical phenomena that compromise the integrity of the storage, damage surface equipment and infrastructure, risk the loss of a social license to operate, invoke large economic losses due to loss of stored product, and in the worst case scenario, lead to the loss of human life.

In this work, key geomechanical phenomena including induced seismicity, caprock integrity, and surface uplift and subsidence, are examined during the multi-year storage of gaseous hydrogen into various versions of a generalised North sea depleted gas field model. Three-dimensional, linear elastic, monolithically-coupled, hydromechanical, finite element simulations are performed using the Imperial College Geomechanics Toolkit (ICGT) to evaluate these phenomena. A comprehensive literature review of rock mechanical and lithological properties was performed to design the model. Processes such as fault slip, fracture growth, damage, fracture nucleation and poroelastic rock expansion and compaction are considered. The ICGT is validated against a published numerical CO2 storage study, and the classical analytical solutions of Geertsma, to enhance confidence in the fault slip and uplift/subsidence computations herein, respectively.

Declaration of Authorship

I, James Edward John BURTONSHAW, declare that this doctoral thesis titled

Geomechanical modelling of subsurface storage of hydrogen in depleted natural gas reservoirs

and the work presented within is entirely my own work. I confirm that:

- This work was done wholly while in candidature for a doctoral research degree at Imperial College.
- Where I have consulted the published work of others, this is always appropriately acknowledged. Where I have cited or quoted from the work of others, or where material could be construed as the work of others, the source is always fully cited and referenced.
- I have acknowledged all sources of help.

The copyright of this thesis rests with the author. Unless otherwise indicated, its contents are licensed under a Creative Commons Attribution-NonCommercial 4.0 International Licence (CC BY-NC). Under this licence, you may copy and redistribute the material in any medium or format. You may also create and distribute modified versions of the work. This is on the condition that: you credit the author and do not use it, or any derivative works, for a commercial purpose. When reusing or sharing this work, ensure you make the licence terms clear to others by naming the licence and linking to the licence text. Where a work has been adapted, you should indicate that the work has been changed and describe those changes. Please seek permission from the copyright holder for uses of this work that are not included in this licence or permitted under UK Copyright Law.

Signature:.....

Name of Student: James Edward John Burtonshaw

Name of Supervisor(s): Dr Adriana Paluszny and Professor Robert W. Zimmerman

'What we usually consider as impossible are simply engineering problems. There's no law of physics preventing them.'

Dr. Michio Kaku

Acknowledgements

This PhD project was funded by the Janet Watson Scholarship, which is awarded to a student demonstrating exceptional academic merit in engineering, geology, geophysics and/or earth science (or closely related subject)' within the Department of Earth Science & Engineering at Imperial College.

This thesis is the product and culmination of nine years of study and work in the Department of Earth Science & Engineering at Imperial College, which has included a BSc in Geophysics, MSc in Petroleum Engineering, one year as a Research Associate in the Rock Mechanics Research Group, and this four year PhD. I have thoroughly enjoyed this time and greatly benefited from the fantastic teaching, mentorship, and seminars of the many elite academics that work at this institution. In particular, during my undergraduate degree I enjoyed lectures from Prof. Joanna Morgan, Prof. Jan Cilliers, Dr Rebecca Bell, and Prof. Richard Herrington encompassing petrophysics, minerals processing, ore deposits, and seismic techniques for exploration, which first initiated my interest in harnessing geoscience and engineering within the realm of energy and resources. During my masters degree, lectures from Prof. Martin Blunt, Prof. Sam Krevor, Prof. Robert Zimmerman, and Dr Peter Fitch, introduced me to the concepts of reservoir engineering, enhanced oil recovery, fluid flow in porous media, and advanced petrophysics, and gave me clear direction to want to pursue this PhD and a career in Petroleum or Geo-Storage Engineering. Special mention must also go to Dr Robin Thomas, who supervised my masters thesis on hydraulic fracturing of unconventional shales and whom introduced me to the art of academic writing and whose mentorship greatly developed my research skills.

Over the past five years, I have had the pleasure of working closely with Dr Adriana Paluszny and Professor Robert W. Zimmerman, world experts in the fields of rock and fracture mechanics. I can say with certainty that both of them are the hardest workers I have met and their dedication to their work has always been truly inspiring. The wealth of knowledge they both possess never ceases to amaze me. It has been a privilege to have the chance to have learnt from them both over the years. Adriana has dedicated somewhere in close proximity to 100 hours of time to me in the past few years in specialized coding sessions helping me to understand and develop my coding skills but also conceiving a truly infinite supply of thoughtful new directions

where I could take my research if I lived for a millenium! Prof. Zimmerman has provided similar amounts of time in reviewing my written work in meticulous detail and seems to always be awake, regularly replying rapidly to my emails even at 2 to 4 am in the morning! I am greatly appreciative to them for everything they have done for me over the years.

The greatest thanks must go to my family. Firstly, the financial and moral support over this past decade has been critical to my success. My mother (Laura) and father (Alan) have worked tirelessly over the years and sacrificed greatly to pay for my degree tuition and living expenses. They have always offered great support to my ambitions, whether that was to get a place at St Olave's Grammar School in London, to get an undergraduate place at Imperial, or to pursue this PhD. I hope that I will be able to pay this back in the future. The moral support and light-hearted, humorous spirit of my brother (Jonathan) has kept me sane over these last few years during the periods of elevated stress that are routine in any PhD. I would not have accomplished this without them.

Both sets of my grandparents - John/Patricia and Edward(Ted)/Shirley - have over the years also generously provided me with financial and moral support that have enabled me to reach this level. Both of my grandfathers inspired me at a young age to find a fascination in mathematics and in engineering. John would spend hours with me as a child between the age of 5 and 8 whilst my parents were at work, teaching me relatively advanced concepts of mathematics such as trigonometry and algebra which certainly gave me a pivotal mathematical advantage when I was younger. Ted engineered components of the Hubble Telescope - which in 2022 imaged the furthest star ever seen (Earendel) at 12.9 billion light years from Earth. His house, full of weird and bygone engineering and design apparatus, got me curious about engineering and building things from an early age.

Finally, I must thank my colleagues in the Rock Mechanics Research Group - Ellya Kanimova, John Walding, Aslan Mohammadpour, Navid Hosseini, and Cristina Saceanu, whose comments during group meetings have greatly enhanced my work. Emily Simeons - an undergraduate student in the Department of Earth Science & Engineering, who undertook her UROP under my supervision - contributed some of the entries in the subsidence literature review tables in this thesis during her time with me, for which I am greatly appreciative.

Contents

Abstract **i**

Declaration of Authorship **ii**

Acknowledgements **iv**

Nomenclature **1**

Abbreviations **6**

1 Introduction **9**

1.1 Background 9

1.2 Motivation 12

1.2.1 Caprock Integrity 12

1.2.2 Subsidence and Uplift 13

1.2.3 Induced Seismicity 14

1.2.4 Objective 15

1.3 Thesis Overview 17

1.4 Publications 19

1.5 Awards 22

2 Review: Hydrogen as a Resource, Storage Methods, and Challenges of Geological Hydrogen Storage 24

2.1 Types of Hydrogen . . . 24

2.1.1 Green Hydrogen . . . 25

2.1.2 Blue Hydrogen . . . 28

2.1.3 Grey Hydrogen . . . 29

2.1.4 Black Hydrogen . . . 30

2.1.5 Brown Hydrogen . . . 31

2.1.6 Pink, Purple and Red Hydrogen . . . 31

2.1.7 Yellow Hydrogen . . . 34

2.1.8 White Hydrogen . . . 35

2.1.9 Turquoise Hydrogen . . . 40

2.1.10 Orange Hydrogen . . . 41

2.1.11 Summary . . . 42

2.2 Methods of Surface and Subsurface Hydrogen Storage . . . 42

2.2.1 Surface Storages . . . 43

2.2.1.1 Physical Storages . . . 43

2.2.1.1.1 CGH_2 Tanks . . . 43

2.2.1.1.2 LH_2 Tanks . . . 44

2.2.1.1.3 CcH_2Tanks . . . 45

2.2.1.2 Material/Chemical Storages . . . 45

2.2.1.2.1 Adsorbents . . . 45

2.2.1.2.2 Liquid Organics . . . 46

2.2.1.2.3 Interstitial Hydrides 47
2.2.1.2.4 Complex Hydrides 48
2.2.1.2.5 Chemical Hydrogen 49
2.2.2 Subsurface Storages 50
2.2.2.1 History of Geological Hydrogen Storage 50
2.2.2.2 Salt Caverns 53
2.2.2.3 Depleted Gas Fields 56
2.2.2.4 Depleted Oil Fields 56
2.2.2.5 Aquifers 58
2.2.2.6 Other Storages 58
2.2.2.6.1 Lined Rock Caverns 59
2.2.2.6.2 Refrigerated Mine Caverns 59
2.2.2.6.3 Abandoned Coal Mines 60
2.3 Challenges of Hydrogen Storage in Porous Media 61
2.3.1 Fluid Flow 61
2.3.1.1 Viscous Fingering 61
2.3.1.2 Gravitational Override 63
2.3.1.3 Capillary Fingering 65
2.3.1.4 Diffusion and Mixing 67
2.3.1.5 Straining 68
2.3.1.6 Wettability and Pore-scale Trapping 69
2.3.2 Chemical 72

2.3.2.1 Mineral Dissolution 72
2.3.2.2 Mineral Precipitation 74
2.3.2.3 Gas Production 74
2.3.3 Biological 75
2.3.3.1 Microbial Hydrogen Consumption 75
2.3.3.2 Microbial Clogging 77
2.3.3.3 Microbe-induced Corrosion 78
2.3.4 Operational 80
2.3.4.1 Hydrogen Embrittlement of Surface and Downhole Infrastructure 80
2.3.4.2 Irrecoverable Pore Space with Each Injection 82
2.3.4.3 Wellbore Scales 83
2.3.5 Mechanical 84
2.3.6 Summary 84
2.4 Fluid Properties of Hydrogen 86
2.4.1 Density 86
2.4.2 Viscosity 86
2.4.3 Compressibility 87

3 Methodology of the ICGT **88**

3.1 Stress and Strain 88
3.2 Matrix Flow, Fault Flow and Rock Deformation 89
3.3 Friction, Contact and Slip 90
3.4 Moment Release and Moment Magnitude 91

3.5 Fracture Nucleation and Damage . . . 92
3.6 Fracture Growth . . . 93
3.7 Fracture Extension . . . 95
3.8 Permeability . . . 96

4 Effect of Mechanical, Fluid, Crack and Operational Properties on Mechanical and Hydraulic Caprock Integrity during UHS 100

4.1 Introduction . . . 100
4.2 Literature Review . . . 106
4.2.1 Mechanical Caprock Integrity during Hydrogen Storage . . . 107
4.2.2 Chemical Caprock Integrity during Hydrogen Storage . . . 110
4.2.3 Hydraulic Caprock Integrity during Hydrogen Storage . . . 111
4.2.4 Caprock Integrity during CO_2 Storage . . . 114
4.3 Methodology . . . 118
4.4 Mesh Effects . . . 123
4.5 Results . . . 125
4.5.1 Effect of Initial Fracture Array . . . 126
4.5.1.1 Initial Fracture Size . . . 126
4.5.1.2 Initial Fracture Spacing . . . 128
4.5.1.3 Initial Fracture Orientation . . . 135
4.5.1.4 Crack Propagation Velocity . . . 138
4.5.1.5 Vertical Fracture Spacing . . . 141
4.5.2 Effect of Caprock Mechanical Properties . . . 143

4.5.2.1 Fracture Toughness . . . 143
4.5.2.2 Young's Modulus . . . 145
4.5.2.3 Poisson's Ratio . . . 147
4.5.2.4 Initial Matrix Permeability . . . 148
4.5.2.5 Biot Coefficient . . . 151
4.5.3 Stresses . . . 152
4.5.4 Fracture Nucleation: Tensile Strength . . . 157
4.6 Discussion . . . 162
4.6.1 Initial Fracture Size . . . 164
4.6.1.1 Initial Fracture Spacing . . . 165
4.6.1.2 Initial Fracture Orientation . . . 166
4.6.1.3 Crack Propagation Velocity . . . 168
4.6.1.4 Vertical Fracture Spacing . . . 170
4.6.1.5 Fracture Toughness . . . 172
4.6.1.6 Young's Modulus . . . 173
4.6.1.7 Poisson's Ratio . . . 175
4.6.1.8 Initial Matrix Permeability . . . 176
4.6.1.9 Biot Coefficient . . . 178
4.6.1.10 Stresses . . . 179
4.6.1.11 Fracture Nucleation: Tensile Strength . . . 185
4.7 Conclusion . . . 187

5 Effect of Mechanical and Operational Properties on Surface Uplift and Subsidence during UHS 191

5.1 Introduction . . . 191

5.2 Literature Review of Numerical and Experimental Studies of Subsidence and Uplift 195

5.2.1 Surface Subsidence and Uplift from Hydrogen Storage . . . 195

5.2.2 Surface Uplift from CO_2 Storage . . . 196

5.2.3 Surface Subsidence from Natural Gas/Oil Production . . . 197

5.2.4 Surface Uplift from Water Injection . . . 198

5.3 Methodology . . . 199

5.4 Validation against Geertsma's Solutions . . . 203

5.4.1 Nucleus of Strain . . . 203

5.4.2 Extended Nucleus of Strain with Effect of Free Surface . . . 209

5.5 Mesh Effects . . . 211

5.6 Results . . . 213

5.6.1 Base Case . . . 213

5.6.2 Injection Rate . . . 220

5.6.3 Young's Modulus . . . 221

5.6.3.1 Reservoir . . . 221

5.6.3.2 Caprock . . . 222

5.6.3.3 Overburden . . . 225

5.6.4 Biot Coefficient . . . 226

5.6.4.1 Reservoir . . . 226

5.6.4.2 Caprock . . . 228

5.6.4.3 Overburden . . . 230
5.6.5 Poisson's Ratio . . . 231
5.6.5.1 Reservoir . . . 231
5.6.5.2 Caprock . . . 232
5.6.5.3 Overburden . . . 233
5.6.6 Permeability . . . 234
5.6.6.1 Reservoir . . . 234
5.6.6.2 Caprock . . . 236
5.6.6.3 Overburden . . . 236
5.7 Discussion . . . 237
5.8 Conclusions . . . 241

6 Effect of Mechanical, Fluid, Operational and Fault Properties on Fault Slip and Induced Seismicity along Reservoir Faults during UHS 243

6.1 Introduction . . . 243
6.2 Literature Review . . . 245
6.2.1 Mechanical Properties . . . 247
6.2.1.1 Poisson's ratio . . . 247
6.2.1.2 Young's modulus . . . 247
6.2.1.3 Biot coefficient . . . 248
6.2.1.4 Intrinsic permeability and porosity . . . 249
6.2.2 Fault Properties . . . 251
6.2.2.1 Friction Coefficient . . . 251

6.2.2.2 Fault Permeability . . . 252
6.2.2.3 Fault Length . . . 253
6.2.2.4 Fault Roughness and Orientation . . . 253
6.2.3 Operational Properties . . . 254
6.2.3.1 Injection Rate . . . 254
6.2.3.2 Withdrawal Rate . . . 255
6.2.4 Fluid Properties . . . 256
6.2.4.1 Fluid Viscosity . . . 256
6.2.4.2 Fluid Compressibility . . . 257
6.2.5 Stresses . . . 258
6.2.6 Summary . . . 258
6.3 Comparison of Slip against CO_2 Storage Study . . . 260
6.4 Methodology . . . 261
6.5 Mesh Effects . . . 263
6.5.1 Domain Mesh Refinement . . . 263
6.5.2 Fault Mesh Refinement . . . 267
6.6 Numerical Experiments . . . 269
6.7 Results . . . 270
6.7.1 Effect of Mechanical Properties . . . 270
6.7.1.1 Young's Modulus . . . 270
6.7.1.2 Poisson's ratio . . . 273
6.7.1.3 Biot Coefficient . . . 275

6.7.1.4 Permeability 281
6.7.2 Effect of Fault Properties 282
6.7.2.1 Friction Coefficient 282
6.7.2.2 Fault Permeability 285
6.7.2.3 Fault Length 285
6.7.2.4 Fault Dip 286
6.7.2.5 Fault Strike 287
6.7.3 Effect of Operational Properties 289
6.7.3.1 Injection Rate 289
6.7.3.2 Withdrawal Rate 293
6.7.3.3 Horizontal Well Length 295
6.7.3.4 Vertical Well Perforation Length 297
6.7.3.5 Well-Fault Spacing 300
6.7.4 Effect of Fluid Properties 301
6.7.4.1 Hydrogen Viscosity 301
6.7.4.2 Hydrogen Density 303
6.7.4.3 Hydrogen Compressibility 305
6.7.5 Effect of Stresses 306
6.8 Discussion 310
6.8.1 Young's Modulus 311
6.8.2 Poisson's Ratio 311
6.8.3 Biot Coefficient 312

6.8.3.1 Permeability . . . 312
6.8.4 Friction Coefficient . . . 313
6.8.5 Fault Permeability . . . 314
6.8.6 Fault Length . . . 315
6.8.7 Fault Dip . . . 316
6.8.8 Injection Rate . . . 317
6.8.9 Withdrawal Rate . . . 318
6.8.10 Horizontal Well Length . . . 319
6.8.11 Hydrogen Viscosity . . . 319
6.8.12 Hydrogen Compressibility . . . 320
6.8.13 *In Situ* Stresses . . . 321
6.8.14 Limitations of Modelling Procedure . . . 322
6.9 Conclusion . . . 325

7 Effect of Mechanical, Fluid, Operational and Fault Properties on Fault Slip and Induced Seismicity along Basement Faults during UHS 328

7.1 Introduction . . . 328
7.2 Methodology . . . 332
7.3 Mesh and Time Step Effects . . . 335
7.3.1 Domain Mesh Refinement . . . 336
7.3.2 Fault Mesh Refinement . . . 336
7.3.3 Time Step . . . 338
7.4 Results . . . 339

7.4.1 Effect of Mechanical Properties . . . 340
7.4.1.1 Young's modulus . . . 340
7.4.1.2 Poisson's ratio . . . 342
7.4.1.3 Biot coefficient . . . 344
7.4.1.4 Matrix permeability . . . 346
7.4.2 Effect of Operational Properties . . . 348
7.4.2.1 Injection Rate . . . 348
7.4.2.2 Withdrawal Rate . . . 349
7.4.3 Effect of Fault Properties . . . 351
7.4.3.1 Fault Permeability . . . 351
7.4.3.2 Friction Coefficient . . . 354
7.4.4 Stresses . . . 356
7.5 Discussion . . . 357
7.5.1 Young's Modulus . . . 359
7.5.2 Poisson's Ratio . . . 360
7.5.3 Biot Coefficient . . . 360
7.5.4 Permeability . . . 361
7.5.5 Further Discussion . . . 362
7.5.6 Advantages and Limitations of the Modelling Procedure . . . 364
7.5.6.1 1-D vs. 2-D Fault Representations . . . 364
7.5.6.2 Rock Homogeneity, Isotropy and Linear Elasticity . . . 364
7.5.6.3 Thermal Effects . . . 365

7.5.6.4 Static Coulomb Friction vs. Rate-and-State Friction 366

7.5.6.5 Fault Geometry Simplifications 368

7.5.6.6 Seismic vs. Aseismic Slip 368

7.5.6.7 Single Phase Flow vs. Multiphase Flow 369

7.6 Conclusion 370

8 Conclusion **371**

8.1 Summary of Geomechanical Risks 371

8.2 Summary of Thesis 375

8.3 Future Work 379

Bibliography **381**

List of Tables

2.1 Lithological, geospatial and operational information about white hydrogen deposits around the world. E denotes 'exploration' and P denotes 'production.' M denotes 'main,' S denotes 'secondary' and 'O' denotes 'other'. The references are as follows: [a]Maiga et al. [2023], [b]Frery et al. [2022], [c]Elkhateeb et al. [2019],[d]Apak et al. [2000], [e]Bourdet et al. [2023], [f]Izart et al. [2016], [g]Hemelsdael et al. [2023], [h]Guélard et al. [2017], [i]Zgonnik et al. [2019], [j]Nivin [2019], [k]McMahon et al. [2023], [l]Wood [1972], [m]Gregory et al. [2019], [n]Mathur et al. [2024], and [o]Donze et al. [2020]. 38

2.2 Different types of hydrogen, the chemical or physical route by which they were produced, their cost, their percentage of the current global hydrogen mix and their cleanliness in terms of their CO_2 emissions. 39

2.3 All known current and past geological hydrogen storage projects. The four minor salt cavern hydrogen storages in Germany (Engelbostel, Bad Lauchstädt, Hähnlein and Eschenfelden) are excluded from this table. [a][DBI GUT, 2017], [b][Pérez et al., 2016], [c][Kruck et al., 2013], [d][Wolf, 2015], [e][Würdemann et al., 2004], [f][Barbir, 2021], [g][Hévin, 2019], [h][Brugier et al., 2017], [i][Pichler, 2019], [j][Cihlar et al., 2021], [k][Basniev et al., 2010], [l][Andiappan et al., 2023]. 53

4.1 Studies examining the mechanical, chemical or hydraulic integrity of the caprock during hydrogen storage and the mechanical integrity of the caprock during carbon dioxide storage. Some studies involving other fluids such as natural gas are included. The following acronyms are used: a_f = fracture aperture, ΔB_I = brittleness index, BIB-SEM = broad ion beam-scanning electron microscopy, cap-res = caprock-reservoir interface, CBM = captive bubble method, CH_4 = methane or represents natural gas, D_c = diffusion coefficient, DF = diamond foil, DGVS = dynamic gravimetric vapor/gas sorption system, DIC = digital image correlation, FDM = finite difference method, FEM = finite element method, FVM = finite volume method, HC = hydrocarbon field, HRA = heterogeneous rock analysis, KBM = kinetic batch modelling, KGD = Khristianovich-Geertsma-de Klerk fracture, M = mechanical model, MC = Mohr-Coulomb, M/HPTA = medium and high pressure triaxial apparatuses, OB = overburden, OC = oedometric cell, P = pressure, p = pore pressure, p_f = fracture pressure, PCT = plastic centrifugal tubes, SDM = sessile drop method, SGS = sequential gaussian simulation, T = temperature, THM = thermohydromechanical, TMNS = triple-mean-normal-stress, TOC = total organic carbon, TPM = tilted plate method, VT = Voronoi tessellation technique, w/o = 'without', XRD = x-ray diffraction, XRF = x-ray fluorescence, Δ = 'change in', σ = stress, $\sigma^{'}$ = effective stress, ϵ = strain. 117

4.2 The mechanical, fluid, geometrical, and lithological properties and the *in situ* stresses of the four different lithologies within the model. The properties of the fractures in the caprock unit are also provided. The symbology in the table is as follows: k = permeability, ϕ = porosity, h = thickness, E = Young's modulus, ν = Poisson's ratio, α = Biot coefficient, ρ_b = rock density, σ_t = tensile strength, K_{IC} = fracture toughness, ρ_f = fluid density, μ = fluid viscosity, c = fluid compressibility, σ_h = minimum horizontal *in situ* stress at base, σ_H = maximum horizontal *in situ* stress at base, σ_V = *vertical *in situ* stress at top (i.e. just the overlying vertical stress due to the sea water not the overlying rock), Δa_v = maximum extension length at any node on any fracture, β_f = fracture growth rate exponent, β_n = tip growth rate exponent and r_i = initial radius of fractures. The table is adapted from Burtonshaw et al. [2024a] and Burtonshaw et al. [2024b]. 119

4.3 Fracture and mechanical properties of the different growth and nucleation simulations performed. The nomenclature is: ψ = normal fracture orientation vector, r_i = initial fracture radius at time t=0, Δa_v = maximum extension length at any node on any fracture per step, s_{xy} = fracture spacing for simulations with fractures in the x-y plane, s_{xz} = fracture spacing for simulations with fractures in the x-z plane, K_{IC} = caprock mode I fracture toughness, E = caprock Young's modulus, ν = caprock Poisson's ratio, α = caprock Biot coefficient, k = caprock permeability, k_{fN} = caprock normal fracture leak-off permeability, and σ_t = caprock ultimate tensile strength. 122

5.1 Known field cases of induced subsidence or uplift resultant from subsurface injection, storage and withdrawal technologies. 'Subs.', 'Up.' and 'Aq.' denotes the words 'Subsidence', 'Uplift' and 'Acquisition' respectively. Subsidence is denoted by negative values in the 'Total Subs./Up. (cm)' column and uplift is denoted by positive values. References are as follows: [a]Maghsoudi et al. [2018], [b]Wang et al. [2020],[c]Motagh et al. [2017], [d]Rutqvist et al. [2009], [e]Liu et al. [2017], [f]Bawden et al. [2001],[g]Barba-Sevilla et al. [2018], [h]Heimlich et al. [2015], [i]Zheng et al. [2023], [j]Shi et al. [2019], [k]van Thienen-Visser and Breunese [2015], [l]Erban et al. [2014], [m]Feng et al. [2008],[n]Wösten et al. [1997], [o]Herrera et al. [2010],[p]Aobpaet et al. [2013], [q]Teatini et al. [2011], [r]Shirzaei et al. [2016], [s]Ji et al. [2016], [t]Yang et al. [2015], and [u]Staniewicz et al. [2020]. 200

5.2 Literature review of studies examining surface subsidence and uplift from various geo-energy technologies such as hydrogen storage, CO_2 sequestration, wastewater disposal, natural gas production, EOR, coal mine dewatering and geothermal. . 201

5.3 The four simulation cases run for each mechanical property (Young's modulus, Biot coefficient, Poisson's ratio and permeability) of each unit to examine the effect of such properties on surface subsidence/uplift. 204

5.4 Properties of the sphere and the surrounding rock used in the ICGT replication model of Geertsma's 'nucleus of strain' model. 206

6.1 Key cases of induced seismicity occurring along faults in direct hydraulic communication with the injection/production well from a variety of geo-energy technologies. [a]Kaven et al. [2015]; [b]Verdon et al. [2015]; [c]Gan and Frohlich [2013]; [d]Brown et al. [2004]; [e]Verdon [2016]; [f]Paap et al. [2014]; [g]White et al. [2017]; [h]White et al. [2014a]; [i]Rodríguez-Pradilla and Verdon [2024]; [j]Clarke et al. [2014]; [k]Esmaeilzadeh and Eaton [2021]; [l]Farahbod et al. [2015]; [m]Fasola et al. [2019]; [o]Cheng et al. [2023]; [p]Majer and Peterson [2007]; [q]Zhou et al. [2022]; [r]Baisch et al. [2010]; [s]Hjörleifsdóttir et al. [2020]; [t]Baisch et al. [2006]; [u]Flóvenz et al. [2015]; [v]Urban and Lermo [2013]; [w]Richter et al. [2020]; [x]Rutledge et al. [1994]. 246

6.2 Summary of the Literature Review. The 'Effect on Slip/Seismicity' column refers to the subsequent effect on slip/seismicity as that parameter increases in value.[a]Meng et al. [2020], [b]Hui et al. [2021b],[c]Zbinden et al. [2017], [d]Dal Zilio et al. [2022], [e]Fan et al. [2019], [f]Mortezaei and Vahedifard [2015], [g]Alghannam and Juanes [2020], [h]Ji et al. [2022b], [i]Nepveu et al. [2016], [j]Sijacic et al. [2017], [k]Deng et al. [2021], [l]Chang and Segall [2016b], [m]Mazzoldi et al. [2012], [n]Anyim and Gan [2020], [o]Rutqvist et al. [2013] 250

6.3 The mechanical, geometrical, geological, fluid dynamic, and fault properties and the *in situ* stresses of the four different rock layers within the models. The symbology in the table is as follows: k = Permeability, ϕ = Porosity, h = Thickness, E = Young's modulus, ν = Poisson's ratio, α = Biot coefficient, ρ_b = Rock Density, K = Bulk Modulus, σ^* - Uniaxial Tensile Strength, ρ_f = Fluid Density, μ = Fluid Viscosity, c = Fluid Compressibility, σ_h = minimum horizontal *in situ* stress at base, σ_H = maximum horizontal *in situ* stress at base, σ_V = vertical *in situ* stress at top, L = fault length, w = fault width, θ = fault dip, ψ = fault orientation to North and x = fault centroid location (x,y,z). The properties herein are derived from the 'Overall Range' column of Table 4. 264

6.4 Literature review of values of reservoir, underburden/caprock and overburden properties and their sources or the sources from which data was taken to compute a value for that field. The range for each property is given in the 'overall range' column, from which the values in Table 3 were chosen. The subscripts R, A, E, W, T, B, A-s, B-s, C-s denote range, average, east, west, top, bottom, A-sand, B-sand and C-sand respectively. KC, CM and NSC refer to Kimmeridge Clay, Coal Measures Rocks and North Sea Chalk respectively. KC is the underburden rock for the Britannia and Goldeneye Fields, whereas CM is the underburden for the Leman Field. North Sea Chalk is the overburden rock for the Britannia and Goldeneye Fields. References from which each property was extracted were: E_{res} - Monsees et al. [2021], Camm et al. [2020], Shell [2014]; K_{res} - Hillier [2003], Camm et al. [2020], Shell [2015a]; $\rho_{b,res}$ - Hillier [2003], Camm et al. [2020], Shell [2015b]; ν_{res} - Ji et al. [2018], Dvorkin and Nur [1996], Shell [2014]; $c_{r,res}$ - Noy et al. [2012], Camm et al. [2020], Shell [2014]; ϕ_{res} - Hillier [2003], Camm et al. [2020], Shell [2015a]; E_{und} - Khandelwal and Singh [2009], Sayers [2013], Kumar et al. [2012]; K_{und} - Karacan [2009], Huang et al. [2022], Gaus et al. [2019], Hawthorn [2004]; $\rho_{b,und}$ - Khandelwal and Singh [2009], Bell et al. [1997], Hornby [1998]; ν_{und} - Khandelwal and Singh [2009], Sayers [2013]; ϕ_{und} - Curtis et al. [2012], Hawthorn [2004], Huang et al. [2022], Hornby [1998]. The sources for the property values of the overburden and the caprock, assuming a chalk overburden and shale caprock as in the Britannia and Goldeneye fields are as follows: E_{over} - Descamps et al. [2017], Olsen [2007]; K_{over} - Keszthelyi et al. [2016]; $\rho_{b,over}$ - Japsen [1998]; α_{over} - Olsen et al. [2008], Gommesen et al. [2007]; ν_{over} - Gommesen et al. [2007]; $c_{r,over}$ - Alam et al. [2012]; ϕ_{over} - Keszthelyi et al. [2016], Gommesen et al. [2007]; α_{cap} - Thompson et al. [2021]. The remaining caprock properties: E_{cap}, K_{cap}, $\rho_{b,cap}$, ν_{cap}, $c_{r,cap}$ and ϕ_{cap} are set to be equal to the underburden properties.* denotes that the value is not specifically for that field but is the value for the equivalent lithological unit in another geographical location or outcrop or if that was not available, the value of a similar rock type. The properties used in Table 6.3 are derived from the 'Overall Range' column herein. 265

6.5 Five simulation cases run to examine the effect of domain refinement on the slip solution. 267

6.6 Five simulation cases run to examine the effect of fracture refinement on the slip solution. 269

6.7 Mechanical properties of the different simulation cases. E = Young's modulus, k = Permeability, α = Biot coefficient, and ν = Poisson's ratio. The subscript 'res' refers to the reservoir unit. 269

7.1 Cases of induced seismicity occurring along underburden/basement faults below the injection/extraction unit for a variety of geo-energy technologies. [a]Kaven et al. [2015]; [b]Yeck et al. [2016]; [c]Horton [2012]; [d]Keranen et al. [2013]; [e]Goebel et al. [2016]; [f]Lee et al. [2019]; [g]Seeber et al. [2004]; [h]Schultz et al. [2017]; [i]Kim [2013]; [j]Glasgow et al. [2021]. 331

7.2 The geological, mechanical, geometrical, fluid dynamic, and fault properties and the *in situ* stresses of the four different rock layers within the models. The symbology in the table is as follows: k = permeability, ϕ = porosity, h = thickness, E = Young's modulus, ν = Poisson's ratio, α = Biot coefficient, ρ_b = rock density, K = bulk modulus, σ^* - uniaxial tensile strength, ρ_f = fluid density, μ = fluid viscosity, c = fluid compressibility, σ_h = minimum horizontal *in situ* stress at base, σ_H = maximum horizontal *in situ* stress at base, L = fault length, w = fault width, $a_{f,r}$ = residual aperture, θ = fault dip, ψ = fault orientation to North and x = fault centroid location (x,y,z). 334

7.3 Four simulation cases run to examine the effect of domain refinement on the slip solution. 336

7.4 Five simulation cases run to examine the effect of fault refinement on the slip solution. 338

8.1 Risk table for different geomechanical properties of the key geological units. Red indicates high risk and green indicates low risk. The arrows indicate an increasing or decreasing risk with higher values of that property. 373

8.2 Total variance in the chosen parameter used to assess failure or loss of integrity for each simulation set and maximal value of the chosen failure parameter in that simulation set. 'H', 'V' and 'A' denote horizontal, vertical and angled (non-horizontal or vertical) fractures, respectively. M_w refers to the moment magnitude. The quantities with units of mm and mD/nD are net surface uplifts and effective permeabilities, respectively. The dimensionless numbers are the logarithmic differences in the highest and lowest effective permeabilities: $\log_{10} k_{eff,max}$ - $\log_{10} k_{eff,min}$. 374

List of Figures

1.1 Schematic of hydrogen storage underground in a depleted gas reservoir, an aquifer and a salt cavern. Key mechanical and flow risks are highlighted. 13

4.1 (a) A 3-D perspective view of the model displaying the four distinct lithological units: a chalk overburden in cream, a shale caprock in grey, a sandstone reservoir in orange and a shale/coal underburden in light grey. (b) The same as (a) with the sandstone reservoir unit removed so that the location of the injection (amber) and withdrawal (pink) wellbores can be seen. The dashes display the trace of the wellbores within the reservoir unit if the caprock and overburden units were removed. (c) The caprock unit showing the dimensions and location of the naturally fractured region of the caprock. For clarity, the box is diagrammatically exaggerated in size relative to the 4000×4000 m x-y dimensions of the caprock. (d) The initial fracture array that is located within the blue region in (c). In the default simulation case, the fractures are oriented vertical and all exist in the same x-y plane such that all fractures are centred at the same depth of 2350 m, which is the mid-depth of the caprock. The caprock region outside of the blue box in (c) is unfractured. 120

4.2 (a-d) Plane views (x-y) of the mesh along the top surface of the caprock in four simulations of different caprock refinement. The number of nodes in the model is denoted by 'n' and the number of elements is denoted by 'e'. The refinement increases in ascending order of figure lettering: (a) is the coarsest case and (d) is the most refined case. (e) Effective permeability of the 150×150×100 m caprock region versus time for one cycle of hydrogen injection, storage and withdrawal. 124

4.3 The final state of the fracture network after three years of hydrogen storage for four cases of (a-d) initial natural fracture radius, (e-h) initial horizontal natural fracture spacing, (i-l) crack propagation velocity, and (m-p) caprock fracture toughness. 129

4.4 P_{21} versus time for four cases of varying (a-d) initial natural fracture radius, (e-h) initial horizontal natural fracture spacing, (i-l) crack propagation velocity and (m-p) caprock fracture toughness. Note that the y-axes are not the same in each case. Marker size has no physical meaning. 130

4.5 Dimensionless P_{32}, $P_{32,D}$, versus time for four cases of varying (a) initial natural fracture radius, (b) initial horizontal natural fracture spacing, (c) crack propagation velocity, (d) caprock fracture toughness, (e) caprock Poisson's ratio, (f) caprock matrix permeability, (g) caprock Biot coefficient, (h) caprock Young's modulus, (i) initial vertical natural fracture spacing, and (j) initial natural fracture orientation. The y-axis is logarithmic. 131

4.6 Total average aperture of all fractures versus time for four cases of varying (a) initial natural fracture radius, (b) initial horizontal natural fracture spacing, (c) crack propagation velocity, (d) caprock fracture toughness, (e) caprock Poisson's ratio, (f) caprock matrix permeability, (g) caprock Biot coefficient, (h) caprock Young's modulus, (i) initial vertical natural fracture spacing, and (j) initial natural fracture orientation. 132

4.7 Effective permeability of the fractured caprock region versus time for four cases of varying (a) initial natural fracture radius, (b) initial horizontal natural fracture spacing, (c) crack propagation velocity, (d) caprock fracture toughness, (e) caprock Poisson's ratio, (f) caprock matrix permeability, (g) caprock Biot coefficient, (h) caprock Young's modulus, (i) initial vertical natural fracture spacing, and (j) initial natural fracture orientation. 133

4.8 The final state of the fracture network after three years of hydrogen storage for four cases of (a-d) caprock Poisson's ratio, (e-h) caprock matrix permeability, and (i-l) caprock Biot coefficient 136

4.9 The final state of the fracture network after three years of hydrogen storage for four cases of (a-d) caprock Young's modulus, (e-h) initial natural fracture vertical spacing, and (i-n) initial natural fracture orientation. Note that for the vertical spacing and orientation cases, the diagrams have been re-oriented to fit in the same shape boxes as the Young's modulus cases. 139

4.10 P_{21} versus time for four cases of varying (a-d) caprock Poisson's ratio, (e-h), caprock matrix permeability, and (i-l) caprock Biot coefficient. Note that the y-axes are not the same in each case. Marker size has no physical meaning. . . . 150

4.11 P_{21} versus time for four cases of varying (a-d) caprock Young's modulus, (e-h) initial vertical natural fracture spacing, and (i-n) initial natural fracture orientation. The y-axes are not the same in each case. Marker size has no physical meaning. 153

4.12 The final state of the fracture network after three years of hydrogen storage for eight cases of varying *in situ* horizontal stresses (σ_x, σ_y). (a-d) Homogeneous stress cases and (e-h) heterogeneous stress cases. 157

4.13 (a) The dimensionless P_{32} and (b) the total average aperture of the fractured caprock region. The total average aperture is the average of the average aperture of all fractures. 158

4.14 P_{21} versus time for eight cases of varying horizontal *in situ* stresses. (a-d) Homogeneous stress cases and (e-h) heterogeneous stress cases. 159

4.15 Comparison of equivalent and effective permeabilities. (a) Lang et al. [2014] geomechanical equivalent permeability versus time and (b) Snow [1969] effective permeability versus time for eight cases of varying horizontal *in situ* stresses. . 160

4.16 Lang et al. [2014] geomechanical equivalent permeability versus time for eight cases of varying horizontal *in situ* stresses. (a) in the x-direction, (b) y-direction and (c) z-direction, respectively. 161

4.17 The state of the induced fracture networks within the caprock unit at the end of three years of hydrogen storage in four simulations with varying caprock tensile strength. 163

5.1 Depleted gas field model containing chalk overburden (beige), shale caprock (light grey), sandstone reservoir (orange) and shale underburden (darker grey). A horizontal wellbore of 100 m length is located at the centre of the model and strikes parallel to the right boundary that is visible. Its depth is denoted by the blue circle. 202

5.2 Comparison of Geertsma's nucleus of strain model to the ICGT computation of displacements. 207

5.3 The 120 × 120 × 120 m^3 model used within the ICGT to replicate Geertsma's 'nucleus of strain' scenario. The purple box highlights the location of the 1 m radius sphere at the model centre. (b) The depleting sphere enlarged from (a). . 208

5.4 Comparison of Geertsma's nucleus of strain model with free surface to the ICGT computation for the displacement along the line on the model surface, passing through the surface center, and starting and terminating from the left and right boundaries. 210

5.5 Zoomed view of the pressure field at and around the depleting sphere at the very small scale. 211

5.6 Four different meshes used to examine the effect of mesh refinement on the net uplift versus time solution. 212

5.7 Net uplift versus time for four cases of varying mesh refinement. 213

5.8 Reservoir pressure with radial distance from the well after five months of injection (end of first injection period). 214

5.9 Base case. (a) The vertical uplift along the top surface of the caprock and reservoir units after five months of injection. (b) Uplift versus time at the centre point of the model top surface. 218

5.10 The net uplift across the base case model surface at selected key times. 219

5.11 The net uplift versus time at the centre point on the surface for four cases of varying injection rate. 221

5.12 The net uplift versus time at the centre point on the surface for three cases of varying (a) reservoir, (b) caprock, and (c) overburden Young's modulus. 223

5.13 The net uplift versus time at the centre point on the surface for three cases of varying (a) reservoir, (b) caprock, and (c) overburden Biot coefficient. 229

5.14 The net uplift versus time at the centre point on the surface for three cases of varying (a) reservoir, (b) caprock, and (c) overburden Poisson's ratio. 232

5.15 The net uplift versus time at the centre point on the surface for three cases of varying (a) reservoir, (b) caprock, and (c) overburden permeability. 235

6.1 Model depth versus slip along the fault for different reservoir permeabilities. The results are presented after injection times of approximately 110 days, 280 days and 1400 days in the 10^{-12}, 10^{-13} and 10^{-14} m^2 cases respectively, as in the numerical comparison paper. The fault exists with vertical coordinates between 1000 and 2000 m. The solid black line represents the numerical solution of Mortezaei and Vahedifard [2015] and e denotes elements. The dashed lines represent results generated from the ICGT. 261

6.2 (a) A solid and wireframe view of the model showing the four rock layers (overburden is cream, caprock is light grey, reservoir is orange, underburden is dark grey). b) A perspective front-right solid and wireframe view of the fault (cyan) contained with the reservoir unit and the injection well on the left of the domain (orange) and the withdrawal well on the right of the domain (red). The reservoir unit is removed in order to observe these. c) A top view of the rectangular fracture surface. 263

6.3 (Top) Wireframe views of the five versions of the model for each refinement case in Table 6.5. The dashed boxes denote the zones of increased refinement. (Bottom) Zoomed views of the mesh at the centre of the reservoir unit. 266

6.4 Mesh of the fault surface for the five versions of the fault in the model for each refinement case in Table 6.6, for varying amount of fracture elements E_{frac}. . . . 267

6.5 Plots of average slip as a function of operation time for (a) five cases of different bulk rock/domain refinements represented by different numbers of nodes and (b) five cases of different fault refinements represented by different numbers of fault elements showing two distinct slip events. A zoomed view of the two slip periods for both (a) and (b) are shown below. 268

6.6 Average slip as a function of operation time for four cases of varying reservoir (a) Young's modulus, (b) Poisson's ratio, (c) Biot coefficient and (d) permeability. Zoomed views of the slip peaks can be found in Figure 6.7. 271

6.7 Zoomed views of the two distinct slip periods as a function of operation time from Figure 6.6 for four cases of varying reservoir (a) Young's modulus, (b) Poisson's ratio, (c) Biot coefficient and (d) permeability. 272

6.8 The fault aperture (left) and contact traction (right) one time step before (t_k) and after (t_{k+1}) the time of peak slip for the first slip event during the second injection period for four cases of varying reservoir (a-d) Young's modulus and (e-h) Poisson's ratio. 274

6.9 The tangential fault slip at each node at the time of peak slip for the first slip event during the second injection period for cases of varying reservoir (a-d) Young's modulus, (e-h) Poisson's ratio, (i-k) Biot coefficient and (l-o) permeability.276

6.10 The effective strain over a vertical interval containing the anticlinal caprock and reservoir units at the time of peak slip for the first slip event during the second injection period for cases of varying reservoir (a-d) Young's modulus, (e-h) Poisson's ratio, (i-l) Biot coefficient and (m-p) permeability. Dark green denotes high strain, dark blue denotes low strain. 277

6.11 The fault aperture (left) and contact traction (right) one time step before (t_k) and after (t_{k+1}) the time of peak slip for the first slip event during the second injection period for four cases of varying reservoir (a-d) Biot coefficient and (e-h) permeability. 279

6.12 Plots of stress along the mid-depth of the reservoir unit in the y-direction for four cases of varying reservoir (a) Young's modulus, (b) Poisson's ratio, (c) Biot coefficient and (d) permeability. 280

6.13 The fault aperture (left) and contact traction (right) one time step before (t_k) and after (t_{k+1}) the time of peak slip for the first slip event during the second injection period for four cases of varying fault (a-d) friction coefficient and (e-h) length. The length of the vectors in the contact traction figures are scaled according to magnitude in the same way the color bar functions: the longer the vector, the larger the traction. 283

6.14 The fault aperture (left) and contact traction (right) one time step before (t_k) and after (t_{k+1}) the time of peak slip for the first slip event during the second injection period for four cases of varying fault (a-d) dip and (e-h) strike. The length of the vectors in the contact traction figures are scaled according to magnitude in the same way the color bar functions: the longer the vector, the larger the traction. 288

6.15 Average slip as a function of operation time for four cases of varying (a) fault friction coefficient, (b) fault permeability, (c) fault length, (d) fault dip, (e) fault strike, (f) injection rate, (g) withdrawal rate, (h) horizontal well length, (i) vertical well length, (j) vertical well spacing, (k) hydrogen viscosity, (l) hydrogen density, (m) hydrogen compressibility, and (n) stresses. Zoomed views of the slip in (a)-(g) and (h)-(n) are shown in Figures 6.16 and 6.17, respectively. 290

6.16 Zoomed views of the two main slip periods from Figure 6.15 as a function of operation time for four cases of varying (a) fault friction coefficient, (b) fault permeability, (c) fault length, (d) fault dip, (e) fault strike, (f) injection rate, and (g) withdrawal rate. The left column shows zoomed views of the first slip period and the central column shows zoomed views of the second slip period. Time in years is shown on the x-axes and the average slip in m is shown on the y-axes as in Figure 6.15. 291

6.17 Zoomed views of the two main slip periods from Figure 6.15 as a function of operation time for four cases of varying (h) horizontal well length, (i) vertical well length, (j) vertical well spacing, (k) hydrogen viscosity, (l) hydrogen density, (m) hydrogen compressibility, and (n) stresses. The left column shows zoomed views of the first slip period and the central column shows zoomed views of the second slip period. Time in years is shown on the x-axes and the average slip in m is shown on the y-axes as in Figure 6.15. 292

6.18 The fault aperture (left) and contact traction (right) one time step before (t_k) and after (t_{k+1}) the time of peak slip for the first slip event during the second injection period for four cases of varying hydrogen (a-d) injection rate and (e-h) production rate. 294

6.19 Plots of stress vertically through the center of the model in the z-direction for four cases of varying (a) fault friction coefficient, (b) fault permeability, (c) fault length, (d) fault dip, (e) fault strike, (f) injection rate, (g) withdrawal rate, (h) horizontal well length, (i) vertical well length, (j) vertical well spacing, (k) hydrogen viscosity, (l) hydrogen density, (m) hydrogen compressibility, and (n) stresses 296

6.20 The tangential fault slip at each node at the time of peak slip for the first slip event during the second injection period for cases of varying (a-d) fault friction coefficient, (e-h) fault permeability, (i-l) fault length, (m-p) fault dip, (q-t) fault strike, (u-x) injection rate and (y-bb) withdrawal rate. The color bar ranges from 0.00 to 0.15 m. 298

6.21 The tangential fault slip at each node at the time of peak slip for the first slip event during the second injection period for cases of varying (a-d) horizontal well length, (e-h) vertical well length, (i-l) vertical well-fault spacing, (m-p) hydrogen viscosity, (q-t) hydrogen density, (u-x) hydrogen compressibility and (y-bb) stresses. The color bar ranges from 0.00 to 0.15 m. 299

6.22 The fault aperture (left) and contact traction (right) one time step before (t_k) and after (t_{k+1}) the time of peak slip for the first slip event during the second injection period for four cases of varying vertical (a-d) length and (e-h) spacing. 302

6.23 The fault aperture (left) and contact traction (right) one time step before (t_k) and after (t_{k+1}) the time of peak slip for the first slip event during the second injection period for four cases of varying hydrogen injectant (a-d) viscosity and (e-h) density. 304

6.24 The fault aperture (left) and contact traction (right) one time step before (t_k) and after (t_{k+1}) the time of peak slip for the first slip event during the second injection period for four cases of varying (a-d) hydrogen injectant compressibility and (e-h) fault permeability. 307

6.25 The fault aperture (left) and contact traction (right) one time step before (t_k) and after (t_{k+1}) the time of peak slip for the first slip event during the second injection period for four cases of varying (a-d) stresses and (e-h) horizontal well length. 309

6.26 Fault slip versus moment magnitude for all seismic events resultant from the various simulation sets. Circles, crosses, triangles and squares denote the lowest, second lowest, second highest and highest value of the four tested values in that simulation set, respectively. For example, for the Biot coefficient, 0.25, 0.35, 0.65 and 0.90 was tested. The 0.25 case is represented by a circle, 0.35 by a cross, 0.65 by a triangle and 0.90 by a square. 310

7.1 (a) A solid and wireframe view of the model showing the four rock layers (overburden is cream, caprock is light grey, reservoir is orange, underburden is dark grey). b) A perspective front-right solid and wireframe view of the fault (blue) contained with the reservoir unit and the injection well on the left of the domain (orange) and the withdrawal well on the right of the domain (red). The reservoir and underburden units are removed in order to observe these. c) A top view of the rectangular fault surface. 335

7.2 (a) Wireframe views of the four versions of the model for each refinement case in Table 7.3. The dashed boxes denote the zones of increased refinement. (b) Zoomed views of the mesh at the centre of the underburden unit. (c) Mesh of the fault surface for the five versions of the fault in the model for each refinement case in Table 7.4, for varying amounts of fracture elements E_{frac}. 337

7.3 Plots of average slip as a function of operation time for (a) five cases of different fault refinements represented by different numbers of fault elements, (b) four cases of different bulk rock/domain refinements represented by different numbers of nodes and (c) four cases of different time step. The full discretisation data for each case in (a) and (b) is reported in Tables 7.4 and 7.3 respectively. 338

7.4 Average slip as a function of operation time for four cases of varying reservoir (a) Young's modulus, (b) Poisson's ratio, (c) Biot coefficient and (d) permeability.340

7.5 The apertures of the fault at a time of 1.58 years during the end of the second storage and beginning of the second withdrawal periods for cases of varying reservoir (a-d) Young's modulus, (e-h) Poisson's ratio, (i-l) Biot coefficient and (m-p) permeability. 342

7.6 The individual slip at each node of the fault at a time of 1.58 years during the end of the second storage and beginning of the second withdrawal periods for cases of varying reservoir (a-d) Young's modulus, (e-h) Poisson's ratio, (i-l) Biot coefficient and (m-p) permeability. Note that the scales are not the same in each subfigure. 343

7.7 Plots of effective stress vertically through the center of the model in the z-direction for four cases of varying underburden (a) Young's modulus, (b) Poisson's ratio, (c) Biot coefficient and (d) permeability at a time of 1.58 years. z=0 refers to the centre point of the ground (top) surface. 346

7.8 Fault slip versus time for four cases of varying (a) injection rate, (b) withdrawal rate, (c) fault permeability, (d) friction coefficient and (e) stresses. 349

7.9 Plots of stress vertically through the center of the model in the z-direction for four cases of varying (a) injection rate, (b) withdrawal rate, (c) fault permeability, (d) friction coefficient and (e) stresses. 350

7.10 The apertures of the fault at a time of 1.58 years during the end of the second storage and beginning of the second withdrawal periods for cases of varying (a) injection rate, (b) withdrawal rate, (c) fault permeability, (d) friction coefficient and (e) stresses. 351

7.11 The individual slip at each node of the fault at a time of 1.58 years, during the end of the second storage and beginning of the second withdrawal periods, for cases of varying (a) injection rate, (b) withdrawal rate, (c) fault permeability, (d) friction coefficient and (e) stresses. 353

7.12 The effective strain over a vertical cut through the model at a time of 1.58 years, during the end of the second storage period and start of the second withdrawal period, for cases of (a-d) varying injection rate, (e-h) varying withdrawal rate, (i-l) varying fault permeability, (m-p) varying friction coefficient, and (q-t) varying stresses. 355

7.13 The strain over a vertical interval containing the anticlinal caprock, reservoir and underburden units at a time of 1.58 years during the end of the second storage and beginning of the second withdrawal periods for cases of varying reservoir (a-d) Young's modulus, (e-h) Poisson's ratio, (i-l) Biot coefficient and (m-p) permeability. 358

Nomenclature

A - Rock cross-sectional area to flow

A_{rup} - Rupture area

a_f - Fracture/fault aperture

C^α - Concentration of the solute α

C_m - Compaction coefficient

c_f - Fluid compressibility

Ca - Dimensionless capillary number

d - Damage variable

d_m - Molecular diameter

d_s - Average slip across fault

D - Effective diffusion coefficient

$\boldsymbol{D}$ - Linear elastic stiffness matrix

D_0 - Diffusion coefficient

E - Young's modulus

$\boldsymbol{F}$ - External body force vector per unit volume

G - Shear modulus

G_f - Maximum Irwin energy release rate of any node on a given fracture

G_n - Irwin energy release rate of a given node

G_{max} - Maximum Irwin energy release rate

g - Acceleration due to gravity

g_N - Normal gap function

$\hat{g}_N$ - Initial normal gap function

g_T - Tangential gap function

$\hat{g}_T$ - Initial tangential gap function

h - Reservoir thickness

$\boldsymbol{I}$ - Identity matrix

J^α - Mass flux of the solute α

k - Permeability

k^e - Element Permeability

K_v - Comparative stress intensity factor

K_I - Mode I (tensile) stress intensity factor

K_{IC} - Critical stress intensity factor (mode I fracture toughness)

K_{II} - Mode II (in-plane shear) stress intensity factor

K_{IIC} - Mode II fracture toughness

K_{III} - Mode III (out-of-plane tear) stress intensity factor

K_{IIIC} - Mode III fracture toughness

K_s - Matrix bulk modulus

k_f - Fracture permeability

k_m - Matrix permeability

k_B - Boltzmann constant

k_{eff} - Effective permeability

$k_{f,Total}$ - Representative/total fracture permeability of domain

k_s - Snow permeability

k_z - Vertical permeability

$\mathbf{k}$ - Equivalent permeability tensor

L - Well spacing

M - Mobility ratio

M_L - Local magnitude of seismic event

M_w - Moment magnitude of seismic event

M_0 - Scalar seismic moment release

$\boldsymbol{n}$ - Unit normal vector

n_c - Unit normal vector outward from the fracture faces

n_f - Total number of fractures in domain

P - Reservoir pressure

p - Normal traction

p^e - Element pressure

p_m - Matrix pressure

p_f - Pressure within the fracture

q - Darcy velocity

r - Crack radius

R_f - Hydrogen recovery factor

$R_{v/g}$ - Fayers & Muggeridge dimensionless number

R_0 - Initial radius of the sphere

S_h - Hydrogen saturation

T - Absolute temperature

T_0 - Tensile strength

t - Time

$\{u\}$ - In-plane tensile crack-tip displacement

$\mathbf{u}$ - Displacement vector

$\boldsymbol{u}^f$ - Displacement vector of follower surface

$\boldsymbol{u}^l$ - Displacement vector of leader surface

$u(r)$ - Radial displacement

v - Injection velocity

$\mathbf{v}$ - Darcy velocity

$\mathbf{v^e}$ - Barycentric element velocity

V - Reservoir volume

V_e - Finite element volume

V_Ω - Domain volume

$\{v\}$ - In-plane shear crack-tip displacement

$\{w\}$ - Anti-plane tear crack-tip displacement

$\boldsymbol{x}$ - Position vector

$\boldsymbol{x}^f$ - Position vector of follower surface

$\boldsymbol{x}^l$ - Position vector of leader surface

α - Biot coefficient

β - Fracture growth rate exponent

δ - Dirac delta function

Δa_f - Maximum extension length of a given fracture

Δa_v - Maximum extension length of any node on any fracture

γ - Interfacial tension

Γ - Domain boundary

Γ_c - Fracture boundary

$\dot{\gamma}$ - Slip rate

$\boldsymbol{\varepsilon}$ - Infinitesimal strain tensor

ε_{ci} - Compressive principal strain

ε_{ti} - Tensile principal strain

$\boldsymbol{\varepsilon}_0$ - Initial strain

$\tilde{\varepsilon}$ - Equivalent strain

$\tilde{\varepsilon}_c$ - Critical strain threshold

θ - Dip

κ - Kolosov constant

λ - Lame parameter

μ - Friction coefficient

μ_f - Fluid viscosity

μ_h - Hydrogen viscosity

μ_w - Brine/water viscosity

ν - Poisson's ratio

ρ - Density

ρ_f - Fluid density

ρ_h - Hydrogen density

ρ_w - Brine/water density

$\boldsymbol{\sigma}$ - Cauchy stress tensor

$\boldsymbol{\sigma}_0$ - Initial stress

τ - Tangential traction

τ_c - Cohesion

φ - Fracture deflection angle

ϕ - Porosity

ϕ_f - Fracture volume fraction

$\phi_{f,Total}$ - Representative/total fracture volume fraction of domain

Ω - Domain of interest

∇ - Gradient operator

$\otimes$ - Cross product operator

Acronyms

ACM - Abandoned Coal Mine

AE - Alkaline Electrolyser

APB - Acid-producing Bacteria

BNEF - BloombergNEF

CAES - Compressed Air Energy Storage

CcH_2 - Cryo-compressed H_2

CCS - Carbon, Capture and Storage

CFD - Computational Fluid Dynamics

CGH_2 - Compressed H_2

CH_4 - Natural gas/methane

CO_2 - Carbon dioxide

C++ - The C++ computer language

EC - European Commission

EDTA - Ethylenediaminetetraacetic acid

EIA - United States Energy Information Administration

ETC - Energy Transition Commission

FBE - Fusion-bonded epoxy

FEM - Finite Element Method

GW - Giga-watt

GWh - Giga-watt hour

H_2 - Hydrogen

H_2S - Hydrogen sulphide

HC - Hydrogen Council

HEDPA - Hydroxyethylidene diphosphonic acid

ICGT - Imperial College Geomechanics Toolkit (ICGT)

IEA - International Energy Agency

IRB - Iron (III)-reducing Bacteria

IRENA - International Renewable Energy Agency

kW - Kilo-watt

kWh - Kilowatt hour

LH_2 - Liquid H_2

LOHC - Liquid Organic Hydrogen Carrier

LRC - Lined Hard Rock Cavern

MOF - Metal Organic Framework

MW - Megawatt

MWh - Megawatt hour

NERC - Natural Environment Research Council

NFPA 704 - U.S. Standard System for the Identification of the Hazards of Materials for Emergency Response

NRB - Nitrate-reducing Bacteria

PEM - Polymer Electrolyte Membrane Electrolysers

pH - Potential of Hydrogen

PHREEQC - PH REdox EQuilibrium (in C language) software

PVC - Polyvinyl Chloride

QPE - Quarter-point Element Nodes

RMC - Refrigerated Mined Rock Cavern

SDS - Sodium Dodecyl Sulphate

SI - Sulphur-Iodine Cycle SIF - Stress Intensity Factor

SMR - Steam Methane Reformation

SOE - Solid Oxide Electrolyser

SRB- Sulphate-reducing Bacteria

SRM - Sulphate-reducing Microorganisms

SSC - Sulphide Stress Cracking

STHIIP - Stock Tank Hydrogen Initially In Place

TWh - Terra-watt hour

UHS - Underground Hydrogen Storage

VOF - Volume of Fluid Method

WAG - Water-alternating-gas Injection

WGS - Water Gas Shift Reaction

Chapter 1

Introduction

1.1 Background

Hydrogen as an energy carrier is attracting growing interest from governments, major energy companies, and researchers due to its very high energy density [Osman et al., 2022], versatility in production routes [Incer-Valverde et al., 2023, Qyyum et al., 2021], compatibility with renewable energy systems, potential for decarbonization [Seck et al., 2022, Griffiths et al., 2021], large-scale energy storage potential [Burtonshaw et al., 2024a, Hassanpouryouzband et al., 2021], potential for long duration grid balancing [Le Duigou et al., 2017, Mayyas et al., 2020] and its ability to address challenges in sectors that are difficult to electrify directly, such as heavy industry [Benavides, 2023, Neuwirth et al., 2022, Liu et al., 2021b] and long-haul transportation [Aminudin et al., 2023].

The European Commission (EC) of the European Union reports that up to 25% of future renewable electricity will go towards the production of green hydrogen by 2050 [European Commission, 2020]. The International Renewable Energy Agency (IRENA) and the Hydrogen Council (HC) estimate that hydrogen will constitute 6% [IRENA, 2019b] and 18% [Hydrogen Council, 2017] of the global energy mix by 2050, respectively [IRENA, 2019a]. The United States Energy Information Administration (EIA) reports that global annual energy consumption will increase by nearly 50% from 2018 levels to approximately 267,000 TWh by 2050

[U.S. Energy Information Administration, 2021]. From the hydrogen energy share estimates of IRENA and HC and the global energy consumption estimates of the EIA, this translates to 16,000-48,000 TWh per year of energy from hydrogen being required by 2050. It follows that hydrogen will need to be stored on an enormous scale (ideally multiple TWhs in any given project). Currently, no existing commercial method of hydrogen storage can realistically satisfy such demand.

In a low-carbon energy world, an annual energy dichotomy will be observed, in which for half of the year an excess of renewable energy is produced, and for the other half, a deficit of energy exists [Heinemann et al., 2021]. In order to avoid the use of fossil fuels as seasonal fuels to satisfy this energy deficit, green hydrogen can be synthesised from excess renewable energy during the periods of energy abundance [Heinemann et al., 2021, Burtonshaw et al., 2024a], and then injected into subsurface porous media such as depleted gas fields where it is stored. Subsequently, the hydrogen can be withdrawn during the periods of energy deficit, avoiding the need for fossil fuels. The hydrogen is then either combusted [Shadidi et al., 2021] as a fuel or used as a reactant in a fuel cell [Singla et al., 2021] where the hydrogen molecules are stripped of their electrons to generate an electrical current that can be used to generate power.

Despite there being far less experience of hydrogen storage geologically, relative primarily to other physical-storage techniques (i.e., CGH_2, LH_2 and CcH_2 tanks), but also to some material/chemical-storages, hydrogen storage in depleted oil and gas reservoirs is the most promising method of both efficiently storing hydrogen, and storing enough quantity to satisfy the 16,000-48,000 TWh of future (2050) demand. Consider a depleted hydrocarbon reservoir, with size and characteristics as follows: porosity, $\phi = 0.15$, thickness, $h = 150$ m, area, $A = 2000 \times 2000$ m^2, hydrogen saturation, $S_h = 0.75$, hydrogen recovery factor, $R_f = 0.8$, hydrogen density, $\rho_h = 9$ kg/m^3. The mass of recoverable stored hydrogen is then $\rho_h A h \phi S_h R_f = 486{,}000{,}000$ kg. One kg of hydrogen equates to 33.3 kWh of energy [Ayodele et al., 2021]. Thus, one typical depleted hydrocarbon field can store approximately 16.2 TWh of energy or 1% of the total annual energy consumption of the United Kingdom. This poses the question: how much of the other storage methods are required to equate to such quantities of energy storage? One of MaHyTec's largest CGH_2 tanks (dimensions: 0.84 m $\times$ 1.87 m) can store 4.2 kg of

hydrogen. Therefore, over 115 million of such tanks would be required to match the energy storage capacity of a single depleted hydrocarbon reservoir. 115 million of these tanks would occupy almost the entire land surface of the city of Glasgow. Following the stoichometry of Scheme 1 in Luo et al. [2011], 11 million tonnes of a liquid organic (BN-cyclomethylpentane) would be required to match the energy storage capacity of a single depleted oil/gas field. For contrast, that is not hugely dissimilar to the amount of natural gas (assuming CH_4 composition) consumed by the entire United Kingdom in 2017 (52 million tonnes). Finally, salt caverns have very rarely stored more than 600,000 m^3 (Table 2.3). A salt cavern of 600,000 m^3 at a typical pressure of 10 MPa, would store hydrogen of approximate density 7 kg/m^3 [Heinemann et al., 2021]. This corresponds to one salt cavern having a storage capacity of 4,200,000 kg. Therefore, to store the same quantity of hydrogen as a single typical depleted hydrocarbon field, 116 typical salt caverns would be required. Thus, it is clear that geological hydrogen storage in porous media is the most volumetrically efficient way of storing hydrogen, and the only realistic technique of storing sufficient quantities to meet future demand. However, until late 2023, pure hydrogen had never been stored in a depleted reservoir and therefore the technology remains in an embryonic stage.

Future research problems in depleted reservoir hydrogen storage geomechanics have been identified by numerous authors (i.e., Kumar et al. [2023], Saeed and Jadhawar [2023], Heinemann et al. [2021]), but to date no substantial studies of these key geomechanical phenomena have been performed. Such problems include induced seismicity, mechanical integrity of the caprock (which differs in H_2 storage relative to CO_2 storage due to the fatigue induced from the cyclical injection and withdrawal of the fluid), and surface subsidence, which are investigated in this thesis.

The induced seismicity chapters of this PhD thesis constitute part of the £3.6 million SeisGreen research project. This project, funded by the Natural Environment Research Council (NERC), aims to (1) understand and (2) mitigate the induced seismicity resultant from the injection of fluids into subsurface reservoirs with application to subsurface carbon sequestration, hydrogen storage and geothermal energy production. The SeisGreen project is comprised of seven work packages encompassing mechanical and statistical work on induced seismicity conducted with

both numerical simulations and physical laboratory experiments. The seismicity work in this PhD addresses part of Work Package 5, which aimed to numerically model fluid-induced seismicity across spatial and temporal scales. Specifically, fully-coupled, hydromechanical, quasi-static, linear-elastic simulations were performed to understand both the likelihood and magnitude of induced events during the multi-year storage of gaseous hydrogen and the mechanical characteristics of the reservoir rock that reduce and exacerbate seismicity.

1.2 Motivation

Little to nothing is known with regards to the geomechanical consequences of injecting an ultra-low density ($\sim$ 10 kg/m^3, Heinemann et al. [2021]), ultra-low viscosity ($\sim$ 10μPa s, Heinemann et al. [2021]) fluid such as hydrogen into a depleted gas field. In order to ensure geological hydrogen storage achieves a social license to operate commercially and does not suffer the same fate as the hydraulic fracturing industry (i.e., nationwide bans in the U.K., Cotton [2017]), potential geomechanical phenomena such as induced seismicity, caprock integrity and surface subsidence (Figure 1.1) must be described and understood prior to the onset of operations.

1.2.1 Caprock Integrity

The caprock, which is the rock unit vertically above the lithological unit in which the injection, storage and withdrawal take place (the reservoir unit), is a low permeability stratum that prevents the vertical transmission of fluid, or more accurately, restricts the upward vertical flow rate to such an extent that flow is negligible on human time-scales. However, the cyclical injection and withdrawal of fluids from the reservoir unit can disturb the stress state in the reservoir and caprock. Such disturbances in the stress field, may or may not, (1) induce further growth of pre-existing natural fractures in the caprock and/or (2) induce the development of new cracks. The growth of these cracks and the closure or opening of the crack apertures can heavily influence the fracture permeability and thus the overall caprock permeability. The cracks could grow to such an extent that they fully penetrate the vertical thickness of the caprock and

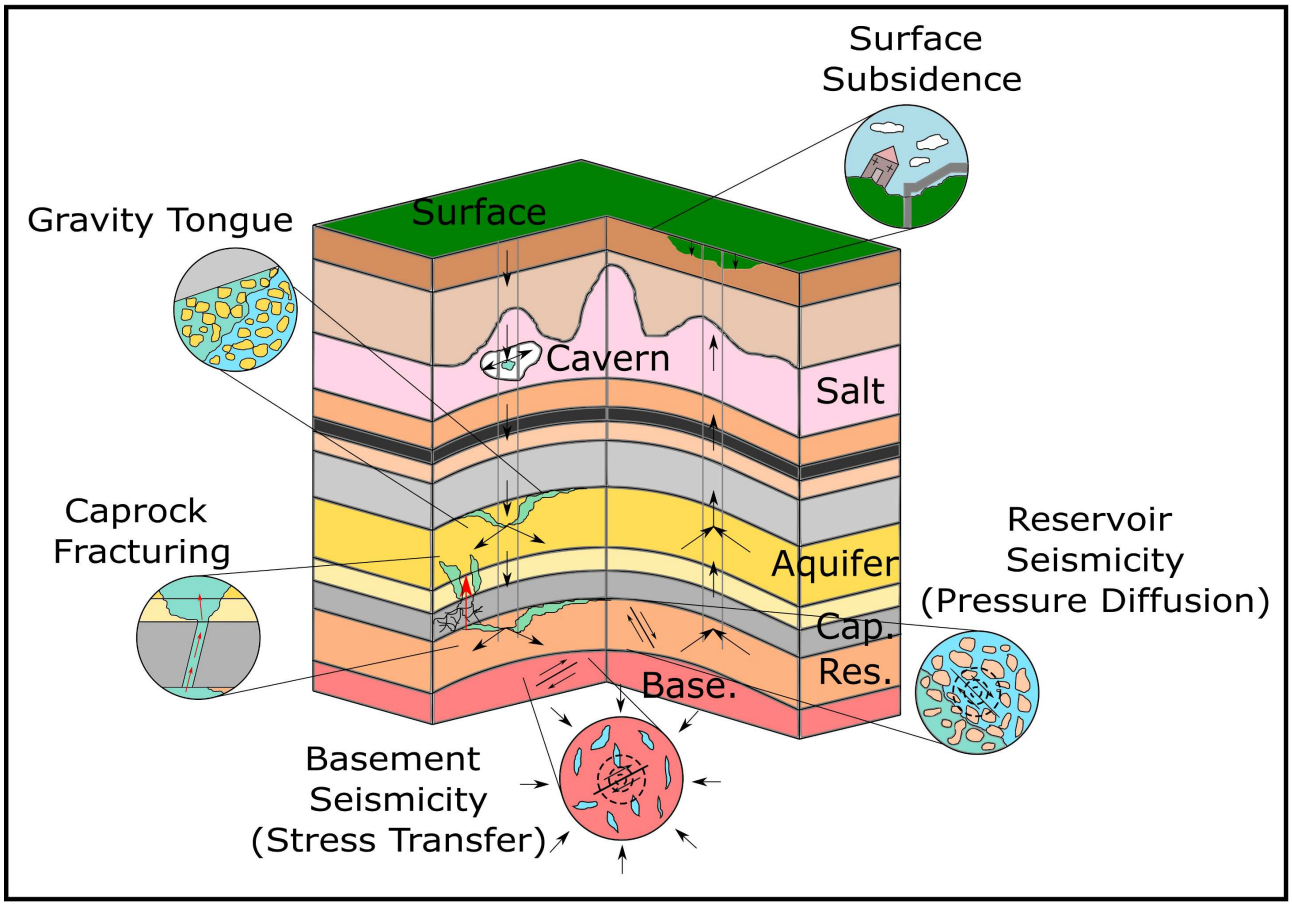


Figure 1.1: Schematic of hydrogen storage underground in a depleted gas reservoir, an aquifer and a salt cavern. Key mechanical and flow risks are highlighted.

thus allow a direct and rapid pathway for hydrogen to leave the reservoir and escape to the overburden, where it could contaminate aquifers or reach surface and ignite. Furthermore, it could result in large economic losses and nationwide energy shortfalls. Alternatively, the cracks may not grow to the point that total mechanical integrity has been lost, but they have grown and opened sufficiently to enhance the caprock permeability to the point at which its capacity to hydraulically seal the hydrogen in place by preventing flow at appreciable rates has been lost. Therefore, the critical question arises, are there any favourable caprock properties and conditions under which the caprock integrity may be lost during hydrogen storage?

1.2.2 Subsidence and Uplift

The cyclical injection and withdrawal of a fluid at high rates is likely to induce cyclical ground deformation at surface. Compaction and expansion of subsurface rock in response to changes

in effective stress lead to such deformation. Especially over relatively small time scales of months, ground elevation changes can cause structural damage to buildings, roads, pipelines and other surface infrastructure. Foundations can crack or buckle leading to costly repairs and safety hazards including the loss of human life. Land sinking can lead to an area or micro-habitats becoming flood-prone and can also compress subsurface aquifers, reducing their permeability and ability to store drinking water, leading to decreases in groundwater availability and increasing pumping costs for industries and agriculture. Both subsidence and uplift could increase stress around faults, inducing seismic events. Therefore, this thesis aims to determine which types of field may enhance or minimise the risk of surface elevation changes.

1.2.3 Induced Seismicity

Given the exceptionally low density of hydrogen at typical reservoir conditions, it is likely that large volumes of hydrogen will need to be injected, especially if the technology is to be scalable to the point where it can constitute a very significant proportion of a nation's energy demand. The mechanical stability of faults depends heavily on the pore pressure in the vicinity of such faults. Increased pore pressure can reduce effective normal stress acting on a fault, promoting slip. Induced seismicity can result in human deaths, the rupturing of subsurface pipelines and wells, subsidence and caprock rupture. Induced seismicity could also induce stricter regulatory and legal constraints and potentially even technological bans if public trust is lost. For example, public pressure in the United Kingdom due to very small magnitude (M_L 1.6 and 2.9) seismic events at the Preston New Road site in Lancashire (Kettlety and Verdon [2021]) has resulted in a nationwide ban on hydraulic fracturing of shale oil, despite the promise of energy independence that it offered. For geological hydrogen storage in depleted fields - especially onshore - to be operationally sustainable far into the future, the potential for seismic events must be fully assessed and qualified prior to implementation. The key question is, are there specific field or operational properties that minimise the likelihood of seismic activity in depleted reservoirs during hydrogen storage?

1.2.4 Objective

This thesis presents for the first time a comprehensive analysis of the key geomechanical consequences of the injection, storage and withdrawal of gaseous hydrogen from depleted gas reservoirs (Figure 1.1). It provides novel insights into which mechanical properties of the caprock, reservoir and underburden units, and which operational properties, exacerbate or minimise geomechanical risk during the implementation of this technology. This will enable particular fields to be prioritised as hydrogen storage candidates, based on the severity of geomechanical risk that a field with those mechanical properties is likely to induce.

The caprock integrity study is the first to explicitly grow and nucleate isolated caprock fractures in a field-scale numerical model, and the first to compute the permeability evolution of a caprock with geomechanically evolving fracture apertures during a fluid storage procedure. Most caprock integrity studies will simply compare overpressure to the caprock fracture pressure as a means of assessing whether the caprock will fail. However, this only impacts the creation of novel fractures. The existing literature does not seem to consider the growth of fatigue cracks. This is problematic because caprocks are microfractured media. They may not fail through the creation of novel fractures, but cyclical loading from rising and decreasing pressures can cause fractures to propagate at stresses below the ultimate tensile strength of the caprock. Most models are implicit fracturing models where rather than representing the fractures as discrete discontinuities in the mesh, fractures are quasi-incorporated by altering the matrix properties in the cells in which a fracture would be present. However, explicit fracturing models are much more accurate as they incorporate the physical laws of fracture mechanics. The few studies that have used explicit fracturing models such as Paluszny et al. [2017] (Heletz) and Salimzadeh et al. [2018] (Goldeneye) examine cold CO_2 injection. The fractures in both are not entirely isolated in the caprock and in Salimzadeh et al. [2018] they are enormous at 250 m, whilst the fractures are stochastically distributed in Paluszny et al. [2017] with no geomechanical significance. Both studies did not require a withdrawal phase.

The subsidence and uplift work is the first to comprehensively assess these phenomena during geological hydrogen storage. Bai and Tahmasebi [2022] did so for an aquifer but used such

low injection rates (order of magnitude too small) and only had a 40 m overburden and 33 m thick reservoir. Therefore the stresses are likely very different to the typical depths we would be interested in for depleted gas reservoir storage. Plus they provided just a simple base case. There reservoir was only 2% porosity which is unrealistic for the majority of high quality storage fields. The work herein is robust compared to others as its been validated against Geertsma's solutions and that of Mehrabian and Abousleiman [2015]. Furthermore, the existing models seem to only consider mechanical parameters such as Young's modulus and Poisson's ratio but we also assessed permeability which was shown to have a large effect on subsidence and uplift. Most models are one-way coupling and the few that are fully-coupled don't include both injection and withdrawal.

No one has considered the potential for induced seismicity during hydrogen storage except those examining reactivation purely from a Mohr-Coulomb failure criterion perspective. Most studies seem to evaluate seismicity based on the CFS, which may tell us the likelihood of slip but it doesn't give us any information on the magnitude of slip and what types of magnitude such events could correspond to, which is critical especially for maintaining our social license to operate. Only one study found was 3-D and this was for a geothermal injection case in an ultra-low permeability crystalline rock which is very different to our high porosity sedimentary reservoirs. 2-D work is limiting because the fault is inherently 1-D and we can only calculate the slip at one point along the depth of the fault, not across the whole fault surface as in this thesis. Therefore, we can calculate on a node-by-node basis the slip and aperture at each point on the 2-D fracture surface, whereas most models assume a constant aperture. This is important because it is known that the length of a fault has an impact on the slip magnitude, so assuming it is infinite in the third plane is unrealistic. Most of the previous studies look at slip along a fault during hydraulic fracturing, but such studies are essentially different as they are highly fractured media. Highly fractured media disrupt the stress field significantly through fracture interaction (stress-shadowing) and altering fluid flow patterns. The stress field on the fault is not solely dependent on the injection. None of these studies included the cyclical injection and withdrawal of a fluid.

The basement seismicity work is novel because other than one study Fan et al. [2019] no one

has numerically computed fault slip along a basement fault. This study only altered reservoir Biot coefficient but we varied a host of underburden properties to assess the impact. This is pivotal because some of the largest induced seismicity results along basement faults including the M5.6 Prague Earthquake in Oklahoma from wastewater injection.

The Imperial College Geomechanics Toolkit (ICGT) is the three-dimensional, hydromechanical, linear-elastic, C++ fracture and rock mechanics code, used to perform these studies. Slight model variations of a generic North sea depleted gas field comprised of a chalk overburden, shale caprock, sandstone reservoir and shale underburden are used to study caprock integrity, surface subsidence and induced seismicity over multi-year cycles of hydrogen storage. The ICGT was primarily used in its native state but some additional code was added during this PhD in order to aid the accuracy and structure of the simulations. New code enabled different storage regimes to be incorporated in one simulation (i.e., injection, storage and withdrawal) rather than just a single regime (i.e., injection), which was not possible in the ICGT prior to this PhD. Furthermore, additional meshing capabilities were added to enable localized refinement of individual, specific rock units or regions that did not have a simple parallel boundary structure (i.e., folded units).

1.3 Thesis Overview

This thesis comprises seven main chapters. Other than the Background Literature Review and Methodology chapters (Chapters 2 and 3, respectively), each chapter incorporates its own review of relevant literature to that geomechanical topic, methodology specific to that sub-study, results, and discussion.

- Chapter 2 provides a comprehensive review of the different methods of hydrogen production, the different existing hydrogen storage technologies including surface and subsurface physical storages, chemical storages and material storages, and all known or potential risks associated with underground hydrogen storage including fluid flow issues, chemical reac-

tions, biological activity and operational considerations. The chapter sets the scene for the analysis of the geomechanical risks of UHS, which have not previously been researched.

- Chapter 3 presents the equations and numerical procedures used in this thesis. This includes the equations of stress and strain, fluid flow laws for laminar flow in the fractures and Darcy flow in the rock matrix, the handling of friction, contact and slip of fracture faces, the Mazars damage model used to determine where to nucleate fractures, Richard's criteria for fracture propagation based on stress intensity factors and the effective and equivalent permeability models used to assess caprock integrity.

- Chapter 4 evaluates the impact of caprock mechanical and natural fracture properties on caprock integrity in terms of crack propagation and caprock permeability evolution through time.

- Chapter 5 evaluates the impact of overburden, caprock and reservoir mechanical properties on ground elevation changes.

- Chapter 6 assesses the impact of reservoir mechanical properties, fault properties, fluid properties and operational properties on fault slip and induced seismicity along faults in direct pressure communication with the propagating hydrogen front. The core mechanism initiating the fault slip is pressure diffusion.

- Chapter 7 assesses the impact of underburden mechanical properties, fault properties and operational properties on fault slip and induced seismicity along basement faults that are entirely isolated from the elevated pressure front that propagates within the reservoir unit. The core mechanism initiating the fault slip is stress transfer.

- Chapter 8 presents a risk matrix summarising which overburden, caprock, reservoir, and underburden properties and which fault properties, fluid properties and operational properties are the most influential in terms of having the potential to exacerbate geomechanical risk (seismicity, subsidence/uplift and caprock failure or permeability degradation). Future work and methodological enhancements are suggested.

1.4 Publications

Much of the work presented in this PhD thesis has been disseminated into multiple journal and conference paper publications. These papers are listed chronologically as follows:

- Burtonshaw, J.E.J., Paluszny, A., and Zimmerman, R. W. (2023). Numerical modelling of induced seismicity along a fault during CO2 injection into a subsurface reservoir. *Proceedings of the 15th International Congress of Rock Mechanics*, 9-14 October 2023, pp. 2795-2800.

  - Included in Chapter 6. Presents a comparison study of the ICGT against COMSOL Multiphysics in modelling fault slip for a published case of CO_2 storage.

- Burtonshaw, J.E.J., Paluszny, A., Mohammadpour, A., and Zimmerman, R. W. (2024a). Effects of Reservoir Mechanical Properties on Induced Seismicity during Subsurface Hydrogen Storage. *Royal Society Philosophical Transactions A*, 382(2276).

  - Forms the basis of Chapter 6. Studies how mechanical properties of reservoir rock such as Young's modulus, Poisson's ratio, Biot coefficient and permeability influence fault slip and induced seismicity along reservoir faults in direct communication with the injection and withdrawal wells.

- Burtonshaw, J.E.J., Paluszny, A., Mohammadpour, A. and Zimmerman, R.W. (2024b). Effects of mechanical properties of the underburden on induced seismicity along a basement fault during hydrogen storage in a depleted reservoir. *iScience*, 27(8).

  - Forms the basis of Chapter 7. Studies how mechanical properties of low permeability underburden rock such as Young's modulus, Poisson's ratio, Biot coefficient and permeability influence fault slip and induced seismicity along basement faults that have no pressure communication with the injection and withdrawal wells.

- Burtonshaw, J.E.J., Paluszny, A., Mohammadpour, A., and Zimmerman, R. W. (2024c). Effects of Underburden Fault Properties, Operational Properties, and Stresses on Induced

Basement Fault Seismicity during Hydrogen Storage in Depleted Gas Fields. *Proceedings of the 58th U.S. Rock Mechanics Symposium*, 23-26 June 2024, Golden, Colorado, paper ARMA-2024-817.

  - Forms part of Chapter 7. Studies how operational properties such as injection rate and withdrawal rate, fault properties such as fault permeability and friction coefficient and *in situ* stresses influence fault slip and induced seismicity along basement faults that have no pressure communication with the injection and withdrawal wells.

Further journal publications are currently in review or are in the process of submission:

- Burtonshaw, J.E.J., Paluszny, A., Mohammadpour, A., and Zimmerman, R. W. (2025a). Effects of Fault, Fluid and Operational Properties on Induced Seismicity Along a Reservoir Fault During Depleted Gas Reservoir Hydrogen Storage.

  - Forms a key part of Chapter 6. Studies how fault properties such as friction coefficient and fault permeability, fluid properties such as hydrogen viscosity and compressibility, and operational properties such as well length, orientations and injection/withdrawal rates influence fault slip and induced seismicity along reservoir faults in direct communication with the injection and withdrawal wells.

- Burtonshaw, J.E.J., Paluszny, A., and Zimmerman, R. W. (2025b). Modelling of the Mechanical and Hydraulic Integrity of the Caprock during Hydrogen Storage in a Depleted Gas Reservoir.

  - Forms the basis of Chapter 4. Studies how different caprock mechanical properties influence (1) the growth of natural fractures and (2) the nucleation of new fractures in the caprock, and thus, the effective permeability evolution of the caprock during hydrogen storage.

- Burtonshaw, J.E.J., Paluszny, A., and Zimmerman, R.W. (2025c). Effect of *in situ* stresses on natural fracture growth and shale caprock integrity during Underground Hydrogen Storage (UHS). *Journal of the Geological Society, under review.*

  - Forms part of Chapter 4. Studies how *in situ* stresses effect the growth of natural fractures in shale caprock and thus, the effective permeability and the equivalent permeability evolution of the caprock.

- Burtonshaw, J.E.J., Paluszny, A., Simeons, E., and Zimmerman, R.W. (2025d). Numerical Simulations of Surface Subsidence and Uplift in a Depleted Gas Reservoir During the Geological Storage of Hydrogen.

  - Forms the basis of Chapter 5. Studies how (1) the mechanical properties of the caprock, reservoir and overburden units and (2) operational properties such as injection rate influence both subsidence and uplift during the injection, storage and withdrawal of hydrogen.

- Burtonshaw, J.E.J., Simeons, E., Paluszny, A., Kanimova, E., Precious, N., and Zimmerman, R.W. (2025e). Simulation of Surface Uplift and Subsidence during Underground Hydrogen Storage (UHS) in a North Sea Depleted Hydrocarbon Field. *Proceedings of the 59th U.S. Rock Mechanics Symposium, 8-11 June 2025, Santa Fe, New Mexico, accepted.*

  - Forms part of Chapter 5. Studies what magnitudes of surface subsidence and uplift could be expected during UHS. Simulation results are compared against analytical solutions for reservoir pressure distribution, reservoir expansion/compaction and surface uplift/subsidence. Provides a validation of the ICGT by comparing against Geertsma's 'Nucleus of Strain' Model.

During the course of this PhD, the research findings were orally presented at multiple international conferences. Chronologically, these were as follows:

- Burtonshaw, J.E.J., Paluszny, A., Thomas, R.N. and Zimmerman, R.W. (2022). The influence of hydraulic fluid properties on induced seismicity during underground hydrogen storage. *American Rock Mechanics Association (ARMA) 56th U.S. Rock Mechanics/Geomechanics Symposium, Santa Fe, New Mexico.*

- Burtonshaw, J.E.J., Paluszny, A. and Zimmerman, R.W. (2023). Numerical Modelling of Induced Seismicity Along a Fault During CO2 Injection into a Subsurface Reservoir. *15th International Society of Rock Mechanics (ISRM) Congress, Salzburg, Austria.*

- Burtonshaw, J.E.J., Paluszny, A. and Zimmerman, R.W. (2023). Effect of Mechanical, Hydraulic, and Fault Properties on Fault Slip during Injection, Storage, and Production of Hydrogen in a Depleted Gas Field. *American Geophysical Union (AGU) 2023, San Franciso, California.*

- Burtonshaw, J.E.J., Paluszny, A., Mohammadpour, A., and Zimmerman, R. W. (2024). Mechanical Caprock Integrity Analysis via Simulations of Fracture Growth during Underground Hydrogen Storage (UHS) in a Depleted Gas Field. *CouFrac 2024: The 4th International Conference on Coupled Processes in Fractured Geological Media, Kyoto, Japan.*

- Burtonshaw, J.E.J., Paluszny, A., Mohammadpour, A. and Zimmerman, R.W. (2024). Effects of Underburden Fault Properties, Operational Properties, and Stresses on Induced Basement Fault Seismicity During Hydrogen Storage in Depleted Gas Fields. *American Rock Mechanics Association (ARMA) 58th U.S. Rock Mechanics/Geomechanics Symposium, Golden, Colorado.*

1.5 Awards

The work in this PhD thesis was awarded the 2024 John S. Archer PhD Research Excellence Award in the Department of Earth Science & Engineering, with an associated monetary prize of £5,000. The winner of the award is decided by the Group of Ten (whom fund raise the prize money), Professor Martin Blunt FREng FRS, Professor Anne Muggeridge, and a panel of other department researchers.

Some of the published work associated with this PhD thesis was used in consideration for awarding the 2025 European Association of Geoscientists & Engineers (EAGE) Marie Tharp

Young European Sustainable Energy Professional of the Year Award with an associated monetary prize of €1,000 to the author of this thesis. The work in this thesis will be presented at the 6th EAGE Global Energy Transition Conference & Exhibition in Rotterdam in October 2025 just prior to receiving the award.

Chapter 2

Review: Hydrogen as a Resource, Storage Methods, and Challenges of Geological Hydrogen Storage

2.1 Types of Hydrogen

Hydrogen can be produced via an abundance of chemical reactions or physical processes, making it a highly versatile fuel. Hydrogen is often given a colour prefix to denote which chemical or physical mechanism has been implemented to yield the hydrogen. Hydrogen can be produced via clean pathways such as electrolysis (green), in which the source of electricity is derived from renewable energy, or via more traditional, greenhouse gas emissions-heavy routes (brown, black, or grey), such as chemical synthesis from fossil fuels. The different 'types' of hydrogen that currently exist are outlined in this section.

2.1.1 Green Hydrogen

Green hydrogen refers to hydrogen that is produced by the electrolysis of water, and critically, where the source of electricity is obtained from renewable energy such as solar, wind, or hydropower [van Renssen, 2020].

A conventional water electrolytic cell or electrolyser requires water, an electrolyte such as sulphuric acid, two electrodes (one anode and one cathode), a source of direct electrical current, and a diaphragm. The electrodes are submerged in a solution containing water and the electrolyte, which is essential for conducting sufficient charge between the electrodes, as pure water contains no free ions [Ursua et al., 2011]. The hydrogen is co-produced with hydroxide ions during the reduction of water at the cathode, and oxygen is subsequently produced as a waste product in association with water as hydroxide ions migrate through the diaphragm and undergo oxidation at the anode, according to [Coutanceau et al., 2017]:

$$\text{Cathode: } 2H_2O\,(l) + 2e^- \longrightarrow H_2\,(g) + 2OH^-\,(aq) \tag{2.1}$$

$$\text{Anode: } 2OH^-\,(aq) \longrightarrow \frac{1}{2}O_2\,(g) + H_2O\,(l) + 2e^- \tag{2.2}$$

$$\text{Overall: } H_2O\,(l) \longrightarrow \frac{1}{2}O_2\,(g) + H_2\,(g) \tag{2.3}$$

The oxygen is vented to the atmosphere or utilised, whilst the hydrogen is captured. The gas separation is ensured by the diaphragm which must be impermeable to gas flow but highly permeable to ion flow [Brauns et al., 2021].

Currently, three main types of electrolyser exist: Alkaline Electrolysers (AEs), Polymer Electrolyte Membrane Electrolysers (PEMs), and Solid Oxide Electrolysers (SOEs). AEs follow the chemical half-cell reactions in Equations 2.1-2.3. They function by the transportation of hydroxide ions from the anode to the cathode through an aqueous alkaline solution such as potassium hydroxide or sodium hydroxide [Azzaro-Pantel, 2018]. The electrodes in AEs are not precious metals and typically consist of nickel coated in an electrocatalytic substance [Brauns and Turek, 2020]. AEs were the first electrolysers to be adopted commercially for hydrogen production [Chisholm and Cronin, 2016] and are the most habitually employed water electrolyzers [Dincer and AlZahrani, 2018, Chisholm and Cronin, 2016], owing to their technological maturity [David et al., 2019], proven reliability and extended lifetimes, sometimes reaching in excess of 30 years [Taibi et al., 2020].

The electrolyte in PEMs is a solid rather than an aqueous solution, and consists of a polymeric plastic membrane. Whilst the migration of hydroxide ions provides the essential role in hydrogen production in AEs, ithe migration of positive hydrogen ions from the anode to the cathode through the solid membrane is the crucial step in hydrogen production from PEMs. The hydrogen ions react with electrons supplied to the cathode via the external circuit to generate the hydrogen gas. The half-cell and overall reactions are specified in Equations 2.4-2.6 [Azzaro-Pantel, 2018].

$$\text{Cathode: } 4H^+ \text{ (aq)} + 4e^- \longrightarrow 2H_2 \text{ (g)} \tag{2.4}$$

$$\text{Anode: } 2H_2O \text{ (l)} \longrightarrow 4H^+ \text{ (aq)} + 4e^- + O_2 \text{ (g)} \tag{2.5}$$

$$\text{Overall: } 2H_2O \text{ (l)} \longrightarrow O_2 \text{ (g)} + 2H_2 \text{ (g)} \tag{2.6}$$

Whilst PEMs require simpler maintenance than AEs, and they do not suffer from corrosion as do AEs, they have high manufacturing costs, which is the main limitation in expanding their use for green hydrogen production [Guo et al., 2019]. These high costs are driven by the necessity to use a number of precious metals such as iridium and platinum at the anode and platinum and gold at the cathode. Other expensive metals such as titanium are also required at both electrodes. The strong oxidative nature of the electrolyser requires such metals to prevent degradation of the cells components [Taibi et al., 2020].

Like PEMs, SOEs utilise a solid membrane as the electrolyte. The electrolytic membrane in SOEs is comprised of a ceramic oxide, typically zirconium dioxide covered in yttrium oxide. In SOEs, steam reacts with electrons supplied by the external circuit at the cathode to form both hydrogen gas and oxygen anions. The oxygen anions are selectively conducted through the solid ceramic oxide, forming oxygen gas at the anode, together with free electrons which traverse the external circuit to begin the process again at the cathode. The half-cell and overall reaction equations are provided in Equations 2.7-2.9 [Azzaro-Pantel, 2018].

$$\text{Cathode: } H_2O\,(g) + 2e^- \longrightarrow H_2\,(g) + O^{2-}\,(aq) \tag{2.7}$$

$$\text{Anode: } O^{2-}\,(aq) \longrightarrow 2e^- + \frac{1}{2}O_2\,(g) \tag{2.8}$$

$$\text{Overall: } H_2O\,(g) \longrightarrow \frac{1}{2}O_2\,(g) + H_2\,(g) \tag{2.9}$$

SOEs require very high operating temperatures of 700-850 °C, well in excess of that of AEs (70-90 °C) and PEMs (50-80 °C). This allows SOEs to obtain part of the energy for separation from thermal energy, reducing electricity requirements. Additionally, the favourable kinetics of the

reactions enable cheaper nickel electrodes to be used. SOEs are limited by short-life times due to fast degradation of the cell components and that they are only currently capable of delivering hydrogen at the kW-scale, well short of the MW to GW-scale required for industrial scale deployment [Taibi et al., 2020]. These issues have prevented SOEs from being commercialised to date [Tong et al., 2019, Harman et al., 2021, Chisholm and Cronin, 2016].

Green hydrogen production accounts for only 0-4% of global hydrogen supply, primarily due to its expense of $6-12 per kg [Fan et al., 2021, WoodMackenzie, 2019]. It is likely to remain costly without significant subsidies from policymakers [Fan et al., 2021], but could become economical in specific markets by 2030 [WoodMackenzie, 2019].

2.1.2 Blue Hydrogen

The production of hydrogen from natural gas only requires a one-stage reaction, but typically involves a two-stage reaction for commercial production. The first-stage of the reaction involves the steam methane reformation (SMR) of natural gas. Natural gas, simplified to methane in Equation 2.10, is added to very hot steam (700-1000 °C) in the presence of a nickel catalyst [Chen et al., 2020, Meloni et al., 2020], generating the desired hydrogen gas and a toxic carbon monoxide waste product [Meloni et al., 2020].

$$CH_4\,(g) + H_2O\,(g) \longrightarrow CO\,(g) + 3H_2\,(g) \tag{2.10}$$

The toxicity of the produced carbon monoxide presents a disposal problem, but it can be reacted with additional hot steam to convert to non-toxic carbon dioxide, whilst simultaneously yielding more of the desired hydrogen. This is known as the water-gas shift reaction (WGS) and is presented in Equation 2.11 [Meloni et al., 2020]. The WGS is catalyzed by both iron and copper based catalysts [Baraj et al., 2020].

$$CO\ (g) + H_2O\ (g) \longrightarrow CO_2\ (g) + H_2\ (g) \tag{2.11}$$

The co-produced carbon dioxide from the WGS reaction is then captured and sequestered in subsurface geological media using Carbon Capture and Storage (CCS) technology, meaning that theoretically no greenhouse gas emissions are released during hydrogen production. For hydrogen to be defined as blue hydrogen, it must have been produced by the SMR or WGS reactions and, critically, must utilise CCS technology to ensure the production process is devoid of greenhouse gas emissions [Noussan et al., 2021]. Recent, concerns have been raised that blue hydrogen does indeed result in significant greenhouse gas emissions, particularly due to unburned fugitive methane. One study found that total carbon dioxide equivalent emissions from blue hydrogen production were only 10% less than grey hydrogen [Howarth and Jacobson, 2021].

Blue hydrogen is considerably more economical ($1.50-3.50 per kg) than green hydrogen due to the hydrogen being produced from natural gas [Birol, 2019, Zapantis, 2021, Powell, 2020]. This has resulted in blue hydrogen (0.98% of global production) comprising more than twice the quantity of green hydrogen (<0.4% of global production) in the global hydrogen mix [Birol, 2019].

2.1.3 Grey Hydrogen

Grey hydrogen is produced in exactly the same manner as blue hydrogen, through the SMR and WGS reactions outlined in Section 2.1.2. The only difference between grey and blue hydrogen is that grey hydrogen allows the carbon dioxide produced in the WGS reaction to be vented to the atmosphere without capture [Dawood et al., 2020], rendering grey hydrogen a greenhouse gas-emissions heavy production route.

Grey hydrogen represents 76% of global hydrogen production [Howarth and Jacobson, 2021,

Birol, 2019], and is thus the dominant source of hydrogen today. This is driven by the readily available supply of natural gas, and the low average production cost of approximately $1.75 per kg [van Renssen, 2020]. Grey hydrogen prices can reach as low as $1 per kg [Flowers, 2020] or below [Ewing, 2020] depending on geography.

2.1.4 Black Hydrogen

Black hydrogen is hydrogen derived from bituminous (black) coal [Birol, 2019], which has undergone the process of coal gasification (see Equation 2.12). Coal gasification involves exposing a source of coal to a hot (750 °C), and sometimes pressurised (<10 MPa), mixture of gases comprised of oxygen and water vapour [Chadwick et al., 1987, Uchida and Harada, 2019, Dincer and Acar, 2015]. The successful generation of hydrogen requires incomplete combustion to occur and thus, the oxygen supplied must be purposely limited. If plentiful oxygen is supplied, then carbon dioxide and water will be produced instead of carbon monoxide and hydrogen, resulting in wasted reactants and no desired end-product. If the reaction advances as expected, then the produced hydrogen is contained in a mixture with carbon monoxide, referred to as 'syngas', 'synthesis gas' or 'coal gas.' The syngas can be refined further by reacting it with additional steam to yield more hydrogen, together with carbon dioxide, which is then vented to the atmosphere (see Equation 2.13).

$$\underbrace{3\mathrm{C\,(s)}}_{\text{Idealized coal}} + \mathrm{O_2\,(g)} + \mathrm{H_2O\,(g)} \longrightarrow \underbrace{3\mathrm{CO\,(g)} + \mathrm{H_2\,(g)}}_{\text{Syngas}} \tag{2.12}$$

$$\mathrm{CO\,(g)} + \mathrm{H_2O\,(g)} \longrightarrow \mathrm{CO_2\,(g)} + \mathrm{H_2\,(g)} \tag{2.13}$$

It is unclear what percentage of global hydrogen production is black hydrogen. However, the International Energy Agency reports that black and brown hydrogen (see Section 2.1.5) together

comprise 23% of the global hydrogen mix [Birol, 2019], signifying that hydrogen production from coal gasification is the second major source of the world's hydrogen. Given that bituminous and sub-bituminous coals constitute approximately 77% of global coal production today, whilst lignite only represents approximately 9% [Prime and Martínez, 2020], it is likely that the majority of hydrogen from coal gasification is black hydrogen.

Hydrogen produced from coal gasification is typically similar in cost to grey hydrogen at $1.25-2.25 per kg [IEA, 2018], but can often be the cheapest of all hydrogen production methods depending on geography, with prices of $1 per kg in China [Kaplan and Kopacz, 2020] and $0.94 per kg in Australia (even inclusive of CCS which is estimated to have a cost of $0.50-1.00 per kg [Powell, 2020]). Whilst hydrogen from coal gasification is economically optimal, it yields the largest carbon dioxide emissions of all the hydrogen production technologies [Dincer and Acar, 2015] with 19 tonnes of carbon dioxide being released per tonne of hydrogen produced, double that of grey hydrogen [Birol, 2019]. Furthermore, the hydrogen-to-carbon ratio of coal-derived hydrogen is 40 times less than grey hydrogen [Birol, 2019], owing to the fact that coal is almost chemically identical to pure carbon, whereas methane is a hydrocarbon.

2.1.5 Brown Hydrogen

Brown hydrogen is hydrogen derived from coal gasification in which the source of coal in Equation 2.12 is lignite instead of bituminous coal (black hydrogen). Brown hydrogen synthesis occurs by the identical processes outlined in Section 2.1.4, and is therefore not repeated here. When combusted, lignite releases on average 5% more carbon dioxide emissions than bituminous coal [Winschel, 1990], rendering brown hydrogen more greenhouse gas-polluting than black hydrogen.

2.1.6 Pink, Purple and Red Hydrogen

Pink hydrogen, also sometimes referred to as purple or red hydrogen, is hydrogen produced through electrolysis in which the source of electricity is provided by nuclear power. Electrolysis

is discussed in detail in Section 2.1.1 on green hydrogen and consequently is not repeated here. In the case of SOEs (see Section 2.1.1), hydrogen may also be referred to as pink hydrogen where the source of steam in Equation 2.7 is produced by heating water with thermal energy derived from nuclear fission [Harman et al., 2021].

Pink hydrogen has yet to see implementation at a commercial scale. It is estimated to have a production cost of $2.24-5.92 per kg, depending on whether AEs, PEMs, or SOEs are used for the electrolysis [Pinsky et al., 2020]. Excluding SOEs from this range, as these are yet to be commercialised and they technically define the subset of pink hydrogen known as purple hydrogen, gives a production cost range of $3.56-5.92 per kg. Therefore, pink hydrogen is significantly more costly than brown, black, or blue hydrogen, but considerably more economical than green hydrogen. Given that the more costly green hydrogen has been commercialised, to a small extent, it is unlikely that economics is the primary driver behind pink hydrogen's total lack of marketisation. Rather, it is likely the immaturity of the technology and the smaller geographical spread of nuclear power (thirty-two countries, of which only fifteen have a nuclear-share of over 20% in their energy mix [IAEA-PRIS, 2021]) relative to renewable power (at least seventy countries [Looney, 2020]) that is behind this.

Various projects are scheduled to demonstrate the viability of pink hydrogen production at scale in the United States, the United Kingdom, and Russia between 2020 and 2030. Rosatom began piloting pink hydrogen production in 2023 with surplus nuclear power from their Kola Nuclear Power Plant in Murmansk Oblast, North-Western Russia. The plant will initially provide 1 MW of nuclear power for the electrolysers, expanding to 10 MW over time. The pilot test may be used to determine whether hydrogen production at scale may be feasible at Rosatom's Kola Nuclear Power Plant-II, scheduled for construction in 2028.

In the United Kingdom, Électricité de France S.A. (EDF), are planning a pink hydrogen demonstration project at the proposed Sizewell C Nuclear Power Plant in Suffolk, East England. If the plant is approved by the Government of the United Kingdom and EDF, then EDF propose to produce up to 800 kg of pink hydrogen per day using nuclear power from Sizewell B. The hydrogen will be used to power equipment and vehicles required for the construction of Sizewell

C. If successful, EDF propose diverting nuclear power from Sizewell C to electrolysers for pink hydrogen production in the early 2030s, during time periods in which solar and wind power are in excess.

In the United States, Pacific North West Hydrogen Fuel LLC (PNW Hydrogen) and the United States Department of Energy will produce pink hydrogen at the Palo Verde Nuclear Power Station in Tonopah, Arizona. The project start date is unclear, but the electrolyser is yet to be built, as funding was only confirmed in October 2021. At any one time, six tonnes of hydrogen can be stored and utilised to produce 200 MWh of electrical power.

The purple and red hydrogen colour terminology, often used interchangeably with the term 'pink hydrogen,' tend to be reserved for specific thermonuclear-based methods for hydrogen production, whilst pink hydrogen is preferred as the general name for lower-temperature nuclear-based conventional electrolysis. Therefore, purple and red hydrogen are considered subsets of pink hydrogen. Purple hydrogen uses thermal energy from nuclear power to perform water splitting by high temperature electrolysis, whilst red hydrogen uses the nuclear-derived thermal energy to perform high-temperature thermochemical and thermocatalytic water splitting.

The method of red hydrogen production closest to commercialisation is through the three-stage sulphur-iodine (SI) cycle [Xu et al., 2017]. In the first stage, sulphuric acid is heated to 850 °C with thermal energy harnessed from nuclear fission, initialising its decomposition into a mixture of gases: water vapour, sulphur dioxide and oxygen (see Equation 2.14). In the Bunsen Reaction (Stage 2, see Equation 2.15), the mixture of gases from Stage 1 are reacted with molecular iodine at 120 °C, producing hydrogen iodide gas and regenerating the initial sulphuric acid in the process. The hydrogen iodide gas is then heated with thermonuclear energy to a temperature of 450 °C in Stage 3 (see Equation 2.16), where it decomposes into molecular iodine that can be recycled and the desired hydrogen gas [Xu et al., 2017]. Red hydrogen has been estimated to cost in the range of $2.18-5.65 per kg [Pinsky et al., 2020], making it economically more favourable than true pink hydrogen, but less economical than purple hydrogen which is costed at $2.24-3.73 per kg [Pinsky et al., 2020].

$$H_2SO_4\,(g) \longrightarrow SO_2\,(g) + H_2O\,(g) + \frac{1}{2}O_2\,(g) \tag{2.14}$$

$$2H_2O\,(g) + SO_2\,(g) + I_2\,(l) \longrightarrow H_2SO_4\,(l) + 2HI\,(g) \tag{2.15}$$

$$2HI\,(g) \longrightarrow I_2\,(g) + H_2\,(g) \tag{2.16}$$

Purple hydrogen is effectively green hydrogen, but created using the high-temperature electrolysis offered by SOEs (see Section 2.1.1). Additionally, in order to be classified as purple hydrogen instead of green hydrogen, the source of thermal energy required to heat water and produce the steam in Equation 2.7 must be supplied from nuclear-derived waste heat rather than via conversion from electrical energy generated from renewable sources. The higher temperatures involved in SOEs relative to other electrolyzers significantly reduces the electricity requirements for electrolysis by using the thermal energy to improve electrical efficiency [Azzaro-Pantel, 2018, Wang et al., 2019].

2.1.7 Yellow Hydrogen

Yellow hydrogen is a specific derivative of green hydrogen in which the electrical power for electrolysis (see Section 2.1.1) is generated from solar power. The term 'yellow hydrogen' is a new phrase in the literature, and is often simply grouped together with other renewable energies and termed 'green hydrogen.' Care must be taken when using this nomenclature, because previous publications have incorrectly referred to pink hydrogen (see Section 2.1.6) as yellow hydrogen [Noussan et al., 2021, Litvinenko et al., 2020]. This term is sometimes even

used to reference electrolysis which relies on a mixture of fossil fuel-based and renewables-based electrical current (grid electricity).

Yellow hydrogen is reported to cost between $3.38-6.84 per kg [Gielen et al., 2019], but Christensen [2020] notes that only the electrolyser and electricity costs are included within the analyses, whilst ignoring other system costs. Furthermore, the electricity prices assumed are overly generous and represent a global best case scenario rather than an average cost [Christensen, 2020]. Wind-derived electrolysis, for which there is no declared name in the literature, and shall henceforth be referred to as cyan hydrogen, is more economical than yellow hydrogen according to the same study [Gielen et al., 2019], with prices of $2.70-4.30, but again these are considered overly optimistic. Whilst, these prices are therefore unlikely to be quantitatively representative of the costs of yellow and cyan hydrogen today, it can be qualitatively inferred that cyan hydrogen is more economical than yellow hydrogen. Therefore, given the average $6-12 cost declared for generalised green hydrogen (see Section 2.1.1), cyan hydrogen is likely to be in the lower part of this range and yellow hydrogen in the higher part.

Even with these overly optimistic prices, yellow and cyan hydrogen remain economically uncompetitive with grey, brown, black, and blue hydrogen. Cyan hydrogen, assuming these highly generous prices, is economically competitive with pink hydrogen, but yellow hydrogen remains considerably more expensive.

2.1.8 White Hydrogen

White hydrogen is naturally-occurring hydrogen, that may require hydraulic fracturing ('fracking') of subsurface geological deposits in order to be produced. It is unique within the hydrogen colour spectrum, as it is the only type of hydrogen that does not require production from a chemical or electrical process - it is natively ready for immediate use.

Until very recently, there were no plans to exploit white hydrogen deposits, nor has any substantial assessment of its resource potential taken place [Truche and Bazarkina, 2019]. However, hundreds of natural hydrogen seepages have already been discovered, many of which are found

in deposits with no obvious association with ultramafic rocks. This implies that our understanding of natural hydrogen production is poor, as the circulation of hydrothermal fluids through ultramafic rocks were previously thought of as playing an essential role in this process [Truche and Bazarkina, 2019]. Interestingly, these white hydrogen deposits appear to be geographically diverse, increasing their future potential as a wide-scale source of hydrogen. Truche and Bazarkina [2019] provides an initial scoping of known white hydrogen deposits, including intra-cratonic seepages, peralkaline granites, ophiolite deposits, mid-ocean ridge deposits, and clay-rich adsorption deposits. Deposits appear to be found across the globe, although appear to be less concentrated in Asia and Eurasia (although this could merely be a result of less publications in these geographies and/or less interest in these resources). Furthermore, a considerable number of these known deposits occur at very large distances from the nearest landmass, making them technically challenging to exploit.

In 1987, Mamadou Ngulo Konare, a villager in the town of Bourakebougou, Mali, bore witness to diggers excavating a borehole in their attempt to find drinking water. The cigarette of one of the drillers initiated a strong wind to blow out from the borehole and a fire ignited. The fire blew a sparkling blue colour in the day-time and a gold colour in the night-time [Hand, 2023]. What they had discovered was not drinking water, but in fact, natural white hydrogen. Multiple reservoirs were found, including karstified and fractured dolostone with sufficient permeability to not require hydraulic fracturing, fractured iron-rich sandstones, and some low-permeability dolerite and granite units. Hydroma became the first company to exploit natural white hydrogen in 2012, where twenty-four wells have been producing hydrogen until the present day. The reservoir has not lost pressure since production began, indicating that the hydrogen is being constantly replenished. This greatly assists project economics since the driving force for fluid flow always remains high, even after we have produced huge volumes of the fluid and without the necessity for the secondary injection of another fluid agent such as water.

In March 2024, the Australian start-up Gold Hydrogen became the second company to extract gaseous white hydrogen from the subsurface in Yorke Peninsula, Australia using wellbores Ramsay-1 and Ramsay-2. The Stock Tank Hydrogen Initially In Place (STHIIP) is 1.3 million

tonnes or 14.5 billion m^3, representing 43.2 TWh of energy. In this case, the hydrogen exists in two reservoirs, the fractured granitic basement as the primary reservoir and cambrian limestones and sandstones as the secondary reservoir. Other known white hydrogen deposits that are being considered for development are shown in Table 2.1.

The main mechanism for white hydrogen production is the serpentinisation of ultramafic igneous rocks. Serpentinisation is the redox reaction that occurs when Fe-rich minerals such as olivine are exposed to hot hydrothermal fluids, typically yielding serpentine and magnetite, and evolving hydrogen gas (see Equation 2.17), which is then stored in natural fractures and any pore space which has been etched out from reactive subsurface fluids. Alternatively, it can seep upwards into overlying sedimentary sequences with suitable caprocks such as impermeable salt, where it resides in the pore space.

$$\underbrace{6Mg_{1.5}Fe_{0.5}SiO_4\,(s)}_{\text{forsterite-rich olivine}} + 7H_2O\,(g/l) \longrightarrow H_2\,(g) + \underbrace{3Mg_3Si_2O_5(OH)_4\,(s)}_{\text{serpentine}} + \underbrace{Fe_3O_4\,(s)}_{\text{magnetite}} \tag{2.17}$$

Artificial serpentinization can even be initiated in the laboratory to generate hydrogen. However, the rate of reaction is slow, with 0-57% serpentinisation after ten days for temperatures between 200 and 320°C and pressures between 20 and 300 MPa [Andreani et al., 2013]. Andreani et al. [2013] performed serpentinization reactions in diamond-anvil cells and found that the rate of reaction can be drastically improved to 100% serpentinization within 1.4-2.4 days within the same temperature and pressure bounds, but by adding a source of aluminium to the reaction, either in the form of ruby microspheres or aluminium hydroxide. The hydrogen produced, now also encompassed by the term white hydrogen, is derived from a totally carbon-free process and could eventually present a hydrogen production route as economic as brown, black and grey hydrogen given the natural abundance of olivine-rich rock. Artificial serpentinization would remove the need to hydraulically fracture natural deposits and the technical challenges of exploiting the many resources located along mid-ocean ridges and subsequently transporting the hydrogen large distances.

Table 2.1: Lithological, geospatial and operational information about white hydrogen deposits around the world. E denotes 'exploration' and P denotes 'production.' M denotes 'main,' S denotes 'secondary' and 'O' denotes 'other'. The references are as follows: [a]Maiga et al. [2023], [b]Frery et al. [2022], [c]Elkhateeb et al. [2019],[d]Apak et al. [2000], [e]Bourdet et al. [2023], [f]Izart et al. [2016], [g]Hemelsdael et al. [2023], [h]Guélard et al. [2017], [i]Zgonnik et al. [2019], [j]Nivin [2019], [k]McMahon et al. [2023], [l]Wood [1972], [m]Gregory et al. [2019], [n]Mathur et al. [2024], and [o]Donze et al. [2020].

Location	Reservoir Lithology	Caprock Lithology	Depth (m)	Discovery Date	Status
Bourakebougou, Mali[a]	M: Karstified/Fractured Dolostone w. Marble Zones, S: Fractured Iron-rich Sandstones, O: Siltstone, Dolerite and Granite	Dolerite Sills	M: 50-110, S: 1310-1460	2012 (1987)	24 P wells
North Perth Basin, Beermullah Trough, Australia[b, c]	M: Sandstone/Coal, S: Gneiss	Shale	M: 2000-14000, S: 8000-18000	2006	Prospecting
Far East Yilgarn Province Officer/Canning Basin, Australia[b, d]	M: Quartzite, S: Interbedded Sansdstone, Shale and Dolostone	Halite	M: 3600-5200, S: 800-2700	Undiscovered	Prospecting
Yilgarn Craton, Australia	Fractured Dacite and Rhyolite	-	0-20000	2021	Prospecting
Ramsay Project, Yorke Peninsula, Kangaroo Island, Australia[e]	M: Fractured Granite, S: Limestone/Sandstone	-	240-1068	2023 (1931)	2 E wells, P wells in 2025
Monzon & Barbastro Fields, Aragon, Spain	M: Sandstone Conglomerate, S: Sandstone	Halite and Shale	0-1400, 3600-3715	2022 (1963)	1 E Well
Lorraine Basin, France[f, g]	Coal	Rhyolite	1093-3000	2023	Applied for E permit
Nemaha Project, Kansas City, United States[h]	M: Fractured Limestone, S: Fractured Gabbro, O: Shale and Arkose	-	0-1215	2009	E permit granted Jul 2024
Geneva Project, Nebraska, United States	unk.	unk.	3400	2019	1 E well
Western Hajar Mountains, Northern Oman[i]	M: Marble, S: Jasper and Limestone, O: Peridotite	-	unk.	2018	Prospecting
Lovozero Loparite Mine, Kola, Russian Federation[j]	Microfractured Granite/Gneiss	-	unk.	1950s	Confirmed from Rare-Earth Ore Mining
Poison Bay, New Zealand	Mylonitic Gneiss	-	unk.	1970	Prospecting
Leopoldshall Potash Mine, Germany[m]	M: Sylvinite, S: Halite	-	unk.	1910	Prospecting
Burro Mountain, California[n]	Iron-rich Dunite	-	>0	1984	Prospecting
Sao Franciso, Brazil[o]	M: Limestone/Dolostone, S: Migmatite	-	320-1240	2019	Prospecting
5 Locations (Korea National Oil Company), South Korea	-	-	-	2022	Prospecting

Table 2.2: Different types of hydrogen, the chemical or physical route by which they were produced, their cost, their percentage of the current global hydrogen mix and their cleanliness in terms of their CO_2 emissions.

Type	Reaction/Process	Reactants	Products	Cost ($/kg)	Current % of H_2 supply	Cleanliness
Green	Wind/Solar/Geothermal/Hydropower-derived Electrolysis	H_2O	H_2, O_2	3.38-12.00	0.5	Carbon-neutral
Blue	SMR, WGS, CCS	CH_4, H_2O	H_2, CO_2	1.50-3.50	1	Carbon-neutral
Brown	Lignite Coal Gasification	C, O_2, H_2O	H_2, CO_2	0.94-2.25	1	Very Heavy CO_2 route
Black	Bituminous Coal Gasification	C, O_2, H_2O	H_2, CO_2	0.94-2.25	21	Very Heavy CO_2 route
Grey	SMR, WGS, no CCS	CH_4, H_2O	H_2, CO_2	1.00-1.75	76	Heavy CO_2 route
Pink	Nuclear-derived Electrolysis	H_2O	H_2, O_2	2.24-5.92	0	Carbon-neutral
White	Serpentinization, Hydraulic Fracturing	$Mg_{1.5}Fe_{0.5}SiO_4$, H_2O	Fe_3O_4, $Mg_3Si_2O_5(OH)_4$	-	0	Carbon-neutral
Purple	Nuclear-derived High-temperature Electrolysis	H_2O	H_2, O_2	2.24-3.73	0	Carbon-neutral
Red	Nuclear-derived High-temperature Thermocatalytic/thermochemical H_2O Splitting	H_2SO_4, I_2	O_2, H_2	2.18-5.65	0	Carbon-neutral
Yellow	Solar-derived Electrolysis	H_2O	H_2, O_2	3.38-6.84	unk.	Carbon-neutral
Turquoise	Pyrolysis	CH_4	C, H_2	1.60-2.47	<0.5	Theoretically Carbon-neutral
Orange	Artificial Redox Reaction	CO_2, H_2O, FeO, MgO/CaO	H_2, Fe_2O_3, $MgCO_3$/$CaCO_3$	-	0	Carbon-neutral

2.1.9 Turquoise Hydrogen

Turquoise hydrogen refers to the pyrolysis of natural gas [Newborough and Cooley, 2020], yielding hydrogen gas and solid carbon ('carbon black'). The reaction is a thermal cracking reaction and is shown in Equation 2.18.

$$\underbrace{CH_4\,(g)}_{\text{idealized natural gas}} \longrightarrow \underbrace{C\,(s)}_{\text{carbon black}} + 2H_2\,(g) \tag{2.18}$$

Natural gas is pumped into a quartz bubble column reactor, partially filled with a molten metal, typically gallium, magnesium, copper or tin [Pérez et al., 2021], through an inlet. The molten metal acts as a thermal transfer medium, heating the rising bubbles of natural gas at temperatures typically in excess of 1000°C. As the natural gas is cracked, the solid carbon produced is deposited on the bubble interface with the gaseous hydrogen encapsulated within. When the bubble reaches the molten metal-air interface at the top of the reactor, the three chemical species (the molten metal, the hydrogen, and the carbon black) are gravitationally segregated due to their density contrasts. The carbon is deposited as residue layers on the top surface of the molten metal and the hydrogen rises to the top of the reactor where it exits through an outlet [Pérez et al., 2021].

Since the carbon species involved in the production of turquoise hydrogen are never oxidised or combusted, no carbon dioxide is released despite the inherent use of fossil fuels. However, carbon dioxide may be released during the heating of the molten metal transfer medium, as this often involves the combustion of natural gas [Timmerberg et al., 2020], so the process is usually not entirely emissions-free. The carbon black co-product is a commodity in its own right, reducing hydrogen production costs if sold commercially. It is primarily used in the strengthening and filling of rubber tyres [Sanchez-Bastardo et al., 2021], but is also routinely used as both an insulating and conducting agent, a pigment and an ultra-violet stabilizer in rubber, ink, coating and plastic applications, and as a soil improver. According to the

stoichiometry of Equation 2.18, a substantial 750 g of carbon black is produced for every 1 kg of methane cracked.

Turquoise hydrogen offers the most economical solution of all the low and no-carbon dioxide production routes with a cost of $1.60-2.47 per kg [Timmerberg et al., 2020] and is only slightly more expensive than grey, brown and black hydrogen. For this reason, turquoise hydrogen offers considerable potential as the main hydrogen production pathway of the future.

Industrial-scale methane pyrolysis for turquoise hydrogen production is still almost exclusively at the Research & Development (R&D) stage. Only one known project is currently functioning: the Monolith Materials, Inc. Olive Creek I Plant in Nebraska, the United States, which came online in 2020. The production rate of turquoise hydrogen is 600 kg/hr. The success has led to the planning and execution of the Olive Creek II Plant, which will produce an additional 600 kg/hr from 2023. In Germany, multiple projects are scheduled. In 2023, Wintershall DEA GmbH and VNG - Verbundnetz Gas Agbo began operation of their planned pilot facility, producing 400 kg of turquoise hydrogen per day. In 2025, BASF SE will bring their turquoise hydrogen pilot plant online. In the United States, start-up C-Zero began operating a pilot facility at the end of 2022, capable of producing 250 kg of turquoise hydrogen per day. Later, they plan to install their first commercial unit with a production rate of 6,000 kg/d. In Australia, the Hazer Group began construction of a 100,000 kg per annum turquoise hydrogen facility in late 2021 and in Russia, Gazprom Neft have announced intentions to begin turquoise hydrogen production in the future, although the hydrogen will not be an end-product, but rather used for oil refining.

2.1.10 Orange Hydrogen

Captured CO_2 can be dissolved in brine, to form an enriched-CO_2 brine injectant. The enriched-CO_2 brine is then pumped down injection wellbores into subsurface reservoirs containing iron (ii) oxide minerals such as magnetite and wüstite. The enriched-CO_2 brine chemically reacts with the magnetite and wüstite, oxidising it in a standard redox reaction to form hematite. Hydrogen gas evolves as a by-product, forming an artificial reservoir of hydrogen [Osselin et al.,

2022]. Simultaneously, the CO_2 in the brine reacts with magnesium and calcium oxide to precipitate new carbonate minerals such as calcite and magnesite. This has two benefits (1) the CO_2 has been converted from a gaseous form to a solid immobile form and (2) the solid precipitation clogs the pore space and reduces permeability which reduces the CO_2's ability to escape even further. However, whilst permeability decreases are beneficial for the sequestration of the CO_2, they are disadvantageous for the withdrawal of the hydrogen.

2.1.11 Summary

A summary of all the chemical and physical methods of hydrogen production discussed in this Section is provided in Table 2.2. Clean hydrogen is the main-focus of future geological hydrogen storage in the context of the energy transition. Whilst green hydrogen is the ultimate goal for geological hydrogen storage, renewable energy needs to become more widespread to make it a more cost-effective method of hydrogen production. In the meantime, blue and turquoise hydrogen offer excellent storage alternatives. In particular, turquoise hydrogen can sustainably use the Earth's substantial natural gas resources without releasing carbon dioxide, since the carbon atoms of the natural gas become carbon soot, offering an excellent route for early commercial-scale geological hydrogen storage.

2.2 Methods of Surface and Subsurface Hydrogen Storage

Methods of hydrogen storage can be categorised into one of two groups: physical-storage or material/chemical-storage. Physical-storage include (1) compressed hydrogen gas (CGH_2) in tanks at pressures typically between 35 and 70 MPa and ambient temperature [Pollet et al., 2014], (2) cooled liquid hydrogen (LH_2) in tanks at temperatures lower than -253°C and at ambient pressure [Sorensen and Spazzafumo, 2018], (3) cryo-compressed liquid hydrogen (CcH_2) in tanks at temperatures lower than -253°C and at typical pressures of 35 MPa [Ahluwalia et al.,

2016], and (4) injection of gaseous hydrogen into subsurface geological media, either engineered or natural salt caverns, engineered steel-lined rock caverns or natural porous media such as aquifers, depleted gas fields and depleted oil fields (Table 2.3). Material and chemical-storages include: (1) adsorbents (i.e., MOF-5, carbon nanotubes, buckminsterfullerene, Peedikakkal and Aljundi [2021], Sridhar and Kaisare [2020]) where hydrogen is held to the surface of the compound by physisorption, (2) liquid organics (i.e., BN-methylcyclopentane, Luo et al. [2011]) where the compound is dehydrogenated usually under intermediate temperatures (i.e., 80°C) and under the action of a catalyst (i.e., $FeCl_2$), (3) interstitial hydrides (i.e., La-Ni Hydride, Ye et al. [2021], Kunce et al. [2017]) where chemisorption of hydrogen to metal (i.e., Ni in La-Ni Hydride) atoms, causes H_2 dissociation, and the produced H^+ ions diffuse into the alloy-hydride lattice, (4) complex hydrides (i.e., sodium alanate, Salehabadi et al. [2020], Ren et al. [2021]) which are metal salts where the anion contains a hydride, and which can be dehydrogenated for hydrogen production typically at high temperatures (i.e., 200°C) under the action of a titanium catalyst and (5) chemical hydrogen (i.e., ammonia borane, Akbayrak and Özkar [2018]) which are hydrogen-containing compounds that are capable of undergoing hydrolysis.

Despite there being less experience of hydrogen storage geologically, relative to other physical-storage techniques (i.e., CGH_2, LH_2 and CcH_2), but also to some material/chemical-storages, it was shown in Section 1.1 that hydrogen storage in depleted oil and gas reservoirs is the most promising method of both efficiently storing hydrogen and storing enough quantity to satisfy the 16,000-48,000 TWh of future (2050) demand.

2.2.1 Surface Storages

2.2.1.1 Physical Storages

2.2.1.1.1 CGH_2 Tanks Compressed hydrogen gas tanks (CGH_2) store hydrogen at very high pressures of 35-70 MPa and standard temperature [Pollet et al., 2014]. Five types of CGH_2 tank exist [Kampker et al., 2024]. A classification is assigned based on the materials used and their structure. Type-I CGH_2 tanks are heavy [Fechte-Heinen et al., 2023] all-metal

(steel/aluminium) tanks; these are typically too heavy to be used in vehicles. Type-II CGH_2 tanks are metal tanks with a composite wrapping on the outside that enables the tank to hold higher pressures whilst reducing weight. The wrapping distributes the stress placed on the tank as it holds compressed hydrogen. The fibres in the wrapping are laid in specific orientations (often in a crisscross pattern) to absorb and distribute the forces acting on the tank's walls. The wrapping typically consists of fibres (such as carbon fibre, glass fibre, or aramid fibre) embedded in a resin matrix (usually epoxy). Type-III tanks include a metal liner with a full composite wrap. 'Full' denotes that the entire tank is encapsulated by the composite wrap, whereas Type-II tanks have a partial wrap. Type-IV CGH_2 tanks have a polymer, rather than metal, liner with a full composite wrap. Type-IV tanks are standard for most hydrogen vehicles. Finally, Type-V CGH_2 tanks do not have a metal or polymer liner. They only have a composite outer structure. Such Type-V tanks are still largely experimental [Moradi and Groth, 2019, Balasooriya et al., 2022].

2.2.1.1.2 LH_2 Tanks Liquid hydrogen tanks (LH_2) store hydrogen at extremely low temperatures, below -253°C, and at standard pressures [Sorensen and Spazzafumo, 2018]. LH_2 tanks are designed to keep hydrogen in its liquid state, whilst preventing boil-off and minimising heat transfer from the surrounding environment. The tanks are typically designed with a double-wall structure where the space between the inner and outer walls is a vacuum [Kim et al., 2023] or filled with insulating materials (like foam) [Wang et al., 2013]. This design minimises heat transfer from the external environment to the liquid hydrogen, helping to maintain the cryogenic temperatures needed. For those tanks using a vacuum between the two walls, heat transfer is reduced by eliminating conduction and convection [Yu et al., 2023]. This helps prevent the hydrogen from absorbing heat and evaporating into the gaseous state.

Boil-off refers to the slow evaporation of liquid hydrogen due to heat entering the tank. Even with the best insulation, boil-off cannot be completely avoided, some hydrogen will always vaporise [Matveev and Leachman, 2023, Kumar and Sleiti, 2024, Yin et al., 2024]. LH_2 tanks are equipped with venting systems to safely release the small amounts of gaseous hydrogen that build up as the liquid evaporates. Recirculation systems can be used to re-liquefy the boil-

off gas [Morales-Ospino et al., 2023], improving efficiency. The materials used in LH_2 tanks need to withstand extreme cold without becoming brittle. Common materials include stainless steel [Ratnakar et al., 2021] and aluminum [Mital et al., 2006], which retain their strength at cryogenic temperatures [Zhirafar et al., 2007].

2.2.1.1.3 CcH_2Tanks Cryo-compressed hydrogen (CcH_2) tanks store hydrogen in the liquid state at temperatures below -253°C, but also at elevated pressures around 35 MPa [Ahluwalia et al., 2016]. They are a relatively new and advanced technology designed to allow hydrogen to be stored at higher densities compared to compressed hydrogen gas or ambient pressure-liquid hydrogen [Yanxing et al., 2019], making it more efficient for certain applications, especially in vehicles. Due to the hydrogen being compressed, the amount of boil-off is less in comparison with LH_2 tanks [Yanxing et al., 2019].

2.2.1.2 Material/Chemical Storages

2.2.1.2.1 Adsorbents Adsorbent-based hydrogen storage is a method for storing hydrogen at relatively low pressures, but often at cryogenic temperatures [Nelson, 2014]. This approach relies on the phenomenon of adsorption (physisorption), where hydrogen molecules physically adhere to the surface of materials rather than being chemically bonded or stored as a liquid or gas under pressure [Bordiga et al., 2005]. Common adsorbent materials include Metal-Organic Frameworks (MOFs) [Lin et al., 2008], carbon nanotubes [Darkrim et al., 2002], and nanofullerene cages [Venkataramanan et al., 2009].

In these materials, hydrogen is attracted to various surface sites through weak London dispersion forces [Bordiga et al., 2005] in which temporary shifts in electron density within the storage molecules, lead to transient dipoles that induce dipoles in the incoming hydrogen molecules. For MOF-5, hydrogen primarily adheres to the open metal sites created by the metal centres (zinc ions), but also the organic linkers (terephthalic acid) that make up the framework to a lesser extent [Peedikakkal and Aljundi, 2021, Nikiforov et al., 2023]. The highly porous nature of MOF-5 and its high surface area [Gangu et al., 2022], increases the number of available sites

for hydrogen adsorption, thus allowing larger amounts of hydrogen to be stored than other material storage options. Some theoretical work has shown that some MOFs such as MOF-177 can be impregnated with a guest substance such as buckminsterfullerene (C_{60}), which in itself is a hydrogen storage adsorbent, to greatly enhance the number of adsorption sites [Durbin and Malardier-Jugroot, 2013].

Various mechanisms can be used to facilitate hydrogen desorption when it is required for usage. Firstly, raising the temperature of the adsorbent material [Chien and Chuang, 2011] can provide the energy needed to overcome the weak van der Waals forces (London dispersion forces) holding the hydrogen molecules on the surface. As the temperature increases, the kinetic energy of the hydrogen molecules also increases, making it easier for them to detach and diffuse from the adsorption sites [Saha and Deng, 2009]. Secondly, reducing the pressure around the adsorbent can also promote desorption [Purewal et al., 2012]. Adsorption is generally more favourable at higher pressures. This can be achieved by creating a vacuum around the adsorbent material [Saha and Deng, 2009] which can result in a rapid release of stored hydrogen. Finally, chemical treatments may potentially be performed to induce changes to the chemical structure of the framework (e.g., when a metal centre in a MOF changes oxidation state) [D'alessandro, 2016]. This can influence the binding strength of the hydrogen.

2.2.1.2.2 Liquid Organics A Liquid Organic Hydrogen Carrier (LOHC) is an organic compound that is liquid under ambient conditions, making it easier to handle and transport compared to gaseous hydrogen [Bollmann et al., 2023]. LOHCs chemically bind hydrogen atoms through hydrogenation reactions and can release them later via dehydrogenation reactions [Bollmann et al., 2023]. Hydrogenation is the process in which hydrogen molecules (H_2) are chemically added to the organic molecule. LOHC molecules typically have unsaturated bonds (i.e., carbon-carbon double bonds) that can readily react with hydrogen. The hydrogenation process involves the addition of hydrogen H_2 to these unsaturated bonds to form a saturated structure [Ali and Shaikh, 2024]. The presence of π-electrons in the double bonds of unsaturated compounds creates sites of higher electron density. Hydrogen molecules, under the right conditions (i.e., intermediate temperatures and the presence of a catalyst), will break

their H-H bond and add across these unsaturated sites. The catalyst provides a surface on which the hydrogen molecules adsorb and dissociate into individual hydrogen atoms. These hydrogen atoms then interact with the unsaturated bonds in the LOHC.

The key reaction for the hydrogenation of the LOHC, N-ethylcarbazole, is [Peters et al., 2015]:

$$\underbrace{C_{14}H_{13}N}_{\text{N-ethylcarbazole}} + 6H_2 \longrightarrow \underbrace{C_{14}H_{25}N}_{\text{perhydro-N-ethylcarbazole}} . \tag{2.19}$$

This reaction is catalysed using a ruthenium catalyst on an alumina porous support at 2-5 MPa and 150°C. The dehydrogentation reaction is then the reverse and occurs at much lower pressures of 0.1-0.3 MPa, but much higher temperatures of 180°C to 260°C [Peters et al., 2015, Morawa Eblagon et al., 2010].

These carriers are designed for reversible storage, meaning they can uptake and release hydrogen multiple times without significant degradation. Examples of LOHCs that can store hydrogen include BN-methylcyclopentane [Luo et al., 2011], N-ethylcarbazole, dibenzyltoluene [Muller et al., 2016], and toluene/methylcyclohexane [Taube et al., 1983].

2.2.1.2.3 Interstitial Hydrides Interstitial hydrides are a class of compounds where hydrogen atoms are stored within the interstitial spaces (or gaps) of a metal or alloy lattice [Keith et al., 2024]. Lanthanum-Nickel alloy (LaN_5) has a hexagonal crystal structure of the $CaCu_5$ type [Yamamoto et al., 2001]. In the hexagonal unit cell, lanthanum (La) atoms and nickel (Ni) atoms are arranged in a layered structure. Lanthanum atoms are larger and occupy specific sites in the structure, while the smaller nickel atoms form more closely packed layers around them, with the alloy held together by strong metallic bonds [Joubert et al., 2021].

Firstly, molecular hydrogen (H_2) dissociates into atomic hydrogen upon interacting with the surface of the nickel metal [Wallace et al., 1979]. The electronic configuration of nickel allows it to interact more readily with hydrogen molecules. Transition metals like nickel have partially

filled d-orbitals, which can accept and share electrons from adsorbed molecules like H_2 [McLellan and Harkins, 1975]. Nickel therefore forms dative covalent bonds with the hydrogen atoms [McLellan and Harkins, 1975] of the hydrogen molecule, weakening the H-H bond and allowing the molecule to dissociate into two hydrogen ions (H^+). These reactions can occur at mild temperatures and pressures of 25°C and 0.2 MPa, respectively [Wallace et al., 1979]. Secondly, the dissociated hydrogen atoms (H^+) diffuse into the metal lattice, occupying interstitial sites between the metal atoms. Thirdly, as more hydrogen ions diffuse into the lattice, the metal becomes saturated, forming a solid-state metal hydride (i.e., LaN_5H_6). When energy (i.e., heat or a drop in pressure) is applied to the metal hydride, the hydrogen ions recombine to form molecular hydrogen (H_2) and are released from the lattice [Wallace et al., 1979].

Other interstitial hydrides have been suggested for hydrogen storage including those based on Pd, TiFe, and PdAgAu. Interstitial hydrides are currently prohibitively expensive due to the aforementioned metals involved [Keith et al., 2024].

2.2.1.2.4 Complex Hydrides Complex hydrides are a class of chemical compounds that consist of a metal (or a metalloid) combined with hydrogen, where the hydrogen exists primarily in the form of hydride ions (H^-). They can be stored at room temperature [He et al., 2019]. These materials typically contain one or more metal cations and include complex anions that hold the hydride ions [Orimo et al., 2007]. For example, in the complex hydride sodium alanate, the hydride ion is a part of a wider $AlH_4{}^-$ alanate anion complex. The hydrogen is ionically bound as hydride ions in the solid-state structure. Upon heating (typically at temperatures around 200 °C [Orimo et al., 2007, Garner and Haycock, 1952]) and under the action of a titanium catalyst [Bogdanovic and Schwickardi, 2001], these complex hydrides undergo thermal decomposition, releasing hydrogen gas:

$$\underbrace{2NaAlH_4}_{\text{sodium alanate}} \longrightarrow \underbrace{2NaH}_{\text{sodium hydride}} + 2Al + 3H_2. \tag{2.20}$$

Other examples of complex hydrides used for hydrogen storage include lithium alanate [Garner and Haycock, 1952] and sodium borohydride [Muir and Yao, 2011]. Complex hydrides are very expensive due to the requirement of a platinum catalyst, which in late-2024 has a price of over $33,000 USD per kilogram.

2.2.1.2.5 Chemical Hydrogen Chemical hydrogen storage involves using hydrogen-rich compounds that release hydrogen through decomposition reactions and can later be regenerated again. Ammonia borane, NH_3BH_3, is a well-known example of a chemical hydrogen storage material due to its high hydrogen content (19.6% by weight) and its ability to release hydrogen through hydrolysis and thermolysis.

When ammonia borane is exposed to water, it undergoes a hydrolysis reaction, producing hydrogen gas according to [Jiang and Xu, 2011]:

$$\underbrace{NH_3BH_3}_{\text{ammonia borane}} + 2H_2O \longrightarrow \underbrace{NH_4BO_2}_{\text{ammonium metaborate}} + 3H_2. \tag{2.21}$$

A catalyst is required to facilitate the reaction and could include any of the following metals: Pt, Pd, Ru, Cu, Co, Ni or Rh [Liu et al., 2020]. The catalyst is often supported on carbon or other solid materials to increase surface area and enhance catalytic activity. The metal catalyst offers a surface that can adsorb ammonia borane molecules. When ammonia borane binds to the catalytic surface, it weakens the B-H bonds because the electrons in these bonds are partially drawn towards the metal atoms. Metals like palladium or platinum have d-electrons that can interact with the electron-rich regions in ammonia borane forming temporary weak interactions between the ammonia borane and the metal. These temporary interactions help stabilise the molecule on the catalyst surface and thus weaken the B-H bonds, as the electron density around the boron and hydrogen is slightly rearranged. The activated B-H bonds are now more accessible to react with water, leading to their breakage and the subsequent release of hydrogen atoms that pair up to form H_2 gas [Liu et al., 2020].

Thermolysis of ammonia borane can also yield hydrogen gas. In a four-step procedure, requiring temperatures between 100 and 500 °C, ammonia borane decomposes according to the net reaction [Demirci et al., 2011]:

$$\underbrace{NH_3BH_3}_{\text{ammonia borane}} \longrightarrow \underbrace{BN}_{\text{boron nitride}} + 3H_2. \tag{2.22}$$

Other chemical hydrogen storage materials include hydrazine borane [Karahan et al., 2011] and methanol/formic acid [Singh et al., 2016].

2.2.2 Subsurface Storages

2.2.2.1 History of Geological Hydrogen Storage

The first time a fluid mixture containing a non-negligible concentration of hydrogen was injected into a subsurface geological system was when town gas was stored at the Beynes aquifer in France (2.3). Also known as coal gas, town gas was used for lighting, cooking, and heating from the early 19th century until the mid/late-20th century [Thomas and Churchill, 2014]. It was widely adopted before natural gas infrastructure was created. The gas was a mixture of hydrogen, methane, carbon dioxide, carbon monoxide, and some other hydrocarbon gases and impurities [Heinemann et al., 2021]. In the case of Beynes, the injectant consisted of 50% hydrogen [DBI GUT, 2017]. At this time, the idea of pure geological hydrogen storage had not been mentioned or thought of.

In 1972, Rosenberg and Gregory [1972] were the first to briefly propose the idea of storing gaseous hydrogen in depleted gas fields. This was then suggested again shortly after by numerous authors such as Dell and Bridger [1975], Magee [1975], Singh [1975], Eldridge [1975], and Pangborn and Gregory [1976] demonstrating a growing interest in the feasibility of storing hydrogen in subsurface depleted gas fields. In 1979, the first analyses of geological hydrogen

storage were published (i.e., Carden and Paterson [1979] and Foh et al. [1979]). These publications were the first to go beyond merely mentioning the potential for subsurface hydrogen storage and to begin the analysis of the relevant physics and chemistry. They included descriptions of the need for cushion gas, the chemical reactions which may occur as a result of the storage of hydrogen, material leakages through the caprock, contamination of the productant by other gases, and diffusion through the caprock.

Very few publications on hydrogen storage in geological media were written between the mid-1980s and 2000. This was primarily driven by the fact that only relatively recently has the greenhouse effect and climate change come to the forefront of the thinking of governments, policy makers, and energy companies. The abundance of fossil fuel reserves, and lack of public pressure for a transition to cleaner energy systems, put the idea of hydrogen storage onto the shelf. The first publication to re-garner interest in geological hydrogen storage was by Venter and Pucher [1997] who analysed the cost of storage for different subsurface bulk hydrogen storage systems (i.e., salt caverns and depleted fields). In 2005, Stone et al. [2005] was the first to provide a scoping of suitable locations of rock salt formations for the storage of hydrogen in salt caverns within the United Kingdom. They were also the first to note the importance of a 'social license to operate' with the statement that "Even if the political will exists [for geological hydrogen storage], there may be resistance from UK residents". In 2009, Lord [2009] provided the first technological feasibility overview since the works of Carden and Paterson [1979] and Foh et al. [1979] nearly 30 years prior. They seem to be the first to mention the possibility of hydrogen embrittlement in the subsurface infrastructure and they were the first to discuss the possibility of subsurface storage methods other than depleted reservoir storage and salt caverns. These included coal mines, lined rock caverns and refrigerated rock caverns. In 2021, Heinemann et al. [2021] published a substantial review of a large number of aspects of geological hydrogen storage from microbial effects and *in situ* chemical reactions to potential fluid flow issues such as flow instabilities. This piece of work led to an explosion in publications relating to geological hydrogen storage, most likely due to the fact it highlights a large number of potential research questions that still need to be answered.

Experience of geological storage of hydrogen in subsurface rock systems is very limited, and

geological storage of pure hydrogen in porous media has only just been implemented for the first time. To date, six known storage projects involving H_2 gas have been implemented in natural or engineered salt caverns (Table 2.3). A salt cavern is an empty void created via designed dissolution, or naturally-existing within salt deposits. Salt caverns have stored gas of the highest hydrogen composition (relative to aquifers and oil/gas fields), but the volumes stored are typically low ($<$ 600,000 m^3), the depths of storage are reasonably shallow ($<$ 1500 m) and the cavern pressures are low ($<$ 15 MPa). There are only three major examples of hydrogen storage in aquifers (Table 2.3), with four further minor examples in Germany (Engelbostel, Bad Lauchstadt, Hähnlein and Eschenfelden, Londe [2021]). In all cases, the hydrogen composition is typically close to 50%, and is thus much lower purity than the examples in salt caverns. The depths of storage are very shallow ($<$ 500 m) and the pressures ($<$ 10 MPa) and temperatures ($<$ 50°C) of storage are also low. In all cases, except that of Ketzin, the storage site was opened to store town gas, a product of coal gasification, existing as a mixture of gases (CH_4, H_2, CO_2, CO and others) and the precursor to natural gas in heating and energy systems. Finally, there are only three case studies of gas storage involving hydrogen within depleted hydrocarbon fields (Table 2.3). All have occurred in depleted gas fields; no hydrogen has ever been stored in a depleted oil field. The stored gas in both the Diadema and first Underground Sun Storage cases consisted of only 10% hydrogen and as such little can be learned from such storage projects for future geological hydrogen storage in depleted hydrocarbon fields. In the case of Diadema, the hydrogen was not intended for storage, merely injected to be bio-converted into methane for later production.

As of 2023, a fluid with over 62% hydrogen concentration had never been injected into a subsurface porous medium, and specifically, a fluid in excess of 10% hydrogen concentration had never been injected into a depleted gas field. In late-2023, RAG Austria's hydrogen storage demonstration facility (the Underground Sun Storage II) became the world's first hydrogen storage project that stores pure hydrogen in a depleted gas reservoir [Andiappan et al., 2023]. In the summer, 4.2 gigawatt-hours (GWh) of energy is stored in the form of green hydrogen in a depleted gas reservoir in Gampern, Upper Austria [Salmachi et al., 2024]. The hydrogen is re-produced during the winter months as an energy source and for material usage. No data is

Table 2.3: All known current and past geological hydrogen storage projects. The four minor salt cavern hydrogen storages in Germany (Engelbostel, Bad Lauchstädt, Hähnlein and Eschenfelden) are excluded from this table. [a][DBI GUT, 2017], [b][Pérez et al., 2016], [c][Kruck et al., 2013], [d][Wolf, 2015], [e][Würdemann et al., 2004], [f][Barbir, 2021], [g][Hévin, 2019], [h][Brugier et al., 2017], [i][Pichler, 2019], [j][Cihlar et al., 2021], [k][Basniev et al., 2010], [l][Andiappan et al., 2023].

Location	Storage type	Gas composition (%)	Pressure (MPa)	Temp. (°C)	Volume (m^3)	Depth (m)	Status
Beynes, FR	Aquifer	50% H_2 [a]	-	-	-	430 [a]	1956/1972 - [a]
Clemens Dome, US	Salt cavern	95% H_2 [a]	7 - 13.5 [c]	-	580e3 [d]	1000 - 1300 [d]	1983 - [c]
Diadema/Hychico, AR	Dep. gas field	10% H_2 [a]	1 [a]	50 [a]	600e3 [b]	600 [a]	2009 - unk [a]
Ketzin, DE	Aquifer	62% H_2, CO_2 [a]	7.7 - 7.8 [e]	-	-	200 - 250 [a]	2008/2010 - [e]
Kiel, DE	Salt cavern	62% H_2 [a]	8 - 10 [a]	-	32e3 [a]	1330 [f]	1971 - [f]
Lobodice, CZ	Aquifer	50% H_2, 25 % CH_4 [a]	9 [a]	34 [a]	-	430 [a]	1965 - [a]
Moss Bluff, US	Salt cavern	-	5.5 - 15.2 [c]	-	566e3 [d]	335 - 1400 [d]	2007 - [c]
Spindletop, US	Salt cavern	95% H_2 [a]	Conf. [g]	-	-	1500 [h]	2014 - [g]
Teesside, UK	Salt cavern	95% H_2, 3-4% CO_2 [a]	4.5 [c]	-	70e3 (3 ×)[d]	370 [d]	1972 - [c]
Underg. Sun Storage I, AT	Dep. gas field	10% H_2 [a]	7.8 [a]	40 [a]	1,200e3 [i]	1000 [a]	2015/2017 - [a] [j]
Yakshunovskoe, RU	Salt cavern	-	-	-	-	-	unk (2010) [k]
Underg. Sun Storage II, AT	Dep. gas field	100% H_2	-	-	-	-	2023 - present [l]

currently publicly available for this project.

2.2.2.2 Salt Caverns

Salt caverns are underground cavities that either naturally exist in salt formations or have been created by purposefully dissolving salt deposits through a process called solution mining. This is the process in which highly-pressured water is injected into the salt formation to dissolve the salt and the resulting brine is pumped out. These caverns have been widely used for storing natural gas, town gas, and compressed air, primarily due to their impermeability, flexibility in withstanding high pressures and high injection and withdrawal rates.

Salt caverns have a number of limitations and deficiencies relative to depleted gas fields. Firstly, they are geographically confined to regions with evaporitic crystalline deposits [Tackie-Otoo and Haq, 2024]. Even in those regions where salt deposits exist, there may be no natural caverns, and thus, additional expense will be incurred in the engineered dissolution of new artificial caverns. Secondly, they are volumetrically inferior. In the Introduction of this thesis, it was calculated that over 100 salt caverns of size 600,000 m^3, which is above the typical value of 500,000 m^3 suggested by Caglayan et al. [2020] and within the range of 32,000-1,000,000 m^3 for domal and bedded salt [Wallace et al., 2021, Crotogino et al., 2010, Aftab et al., 2023, Malachowska et al., 2022, Caglayan et al., 2020, Minougou et al., 2023, Jahanbakhsh et al., 2024, Zhu et al., 2023, Susan Gram, 2019, Hévin, 2019, Stevenson, 2019], would be required to store the same amount

of energy as a single depleted gas field with typical and conservative properties. Even if the typical salt cavern in that calculation had a storage size of 1,000,000 m^3, which is deemed the maximum capacity for a salt cavern [Jahanbakhsh et al., 2024], then approximately seventy caverns would be required. Even with abnormally low assumed reservoir porosities below 10% and thicknesses (only tens of metres), at least tens of salt caverns would be required to match the storage capacity of one depleted gas field. A similar calculation performed by Epelle et al. [2022] suggests one depleted gas reservoir can store the same as almost 400 salt caverns. Thirdly, salt caverns are typically restricted to within 2000 m depth, because the increased pressures and temperatures at greater depths will be conducive to large mechanical deformations of the cavern [Muhammed et al., 2022]. Fourthly, halite, which is a desired host rock for engineered salt caverns due to its very low permeability [Cyran et al., 2023], experiences non-linear creep deformation due to long-term loading resultant from underground storage [Ramesh Kumar et al., 2021, Muhammed et al., 2022], which could elicit structural damage to the storage unit many years into operation. Fifthly, salt caverns are typically not proximal to pre-existing major gas pipelines [Zivar et al., 2021, Muhammed et al., 2022], which may necessitate very large expense for new gas transportation infrastructure. Sixthly, engineered salt caverns may not, from the outset, contain native gas capable of acting as a cushion gas. However, in some cases, such as intrasalt deposits, the cushion gas requirements of salt caverns may actually be less than depleted reservoirs [Valle-Falcones et al., 2022]. Depleted gas fields typically contain some unrecoverable natural gas that satisfies, either entirely or partially, cushion gas requirements [Muhammed et al., 2023b,a, Wallace et al., 2021, Lord et al., 2014]. Again, this will incur significant additional costs. However, the residual native natural gas in some depleted gas fields may not be suitable depending on its exact chemical composition. Large percentage volumes of certain impurities, such as CO_2, could initiate various chemical reactions such as the Sabatier methanogenetic reaction [Senderens and Sabatier, 1902, Tarkowski, 2019, Panfilov, 2010, Perera, 2023] in which the stored hydrogen is converted to methane, reducing the purity of the withdrawn hydrogen stream. The reaction requires the presence of methanogens but was observed to significantly degrade hydrogen concentration by almost 50% during town gas (H_2 and CO_2-rich gas) injection at Lobodice, Czechia [Amigavn et al., 1990, Buzek et al., 1994,

Tarkowski, 2019]. Therefore, reservoirs with high CO_2 remnant natural gas or reservoirs which have already undergone some CO_2 storage should be carefully analysed prior to any potential hydrogen storage to ensure that high concentrations of such methanogens are not present. Despite these deficiencies associated with salt caverns, it must be noted that salt caverns have a number of advantages: (1) large production rates are possible [Heinemann et al., 2021] due to the lack of tortuous and narrow pore spaces associated with subsurface rock and (2) substantial prior experience at the small scale exists in which a near pure hydrogen fluid was cyclically injected, stored and produced [Jahanbakhsh et al., 2024]. Salt caverns can be considered advantageous over depleted gas fields because hydrogen injection into depleted gas fields can promote microbial growth that leads to hydrogen consumption and loss [Thaysen et al., 2021, Gregory et al., 2019, Rivolta et al., 2024]. However, halotolerant and halophilic microbes exist in high-saline environments and as such storage in salt caverns does not significantly reduce microbial consumption of hydrogen [Dopffel et al., 2021, Muhammed et al., 2022].

In conclusion, salt caverns are optimal for satisfying short-term and small-scale energy demand fluctuations, but they cannot realistically satisfy long-term energy deficiencies. Critically, they lack the storage capacity necessary to satisfy the tens of thousands of TWh of future global hydrogen demand [Speight, 2019], which can only be met through storage in subsurface porous media. This is because salt caverns have the capacity to discharge MWh's to GWh's of energy over days to weeks but depleted gas fields have the capacity to deliver TWh's over periods of days to months [Jahanbakhsh et al., 2024]. Yusaf et al. [2022] suggests a lower range than the 16,000-48,000 TWh of this thesis (see Section 1.1). They state that 73 to 568 megatonnes of hydrogen will be required globally by 2050, which equates to 2,433-18,914 TWh assuming 1 kg = 33.3 kWh of energy. Combining the summary analysis of hydrogen demand from Statista [Statista, 2024] covering demand estimates from established organizations such as the Hydrogen Council, the International Energy Agency (IEA), the International Renewable Energy Agency (IRENA), BloombergNEF (BNEF) and the Energy Transition Commisson (ETC), which all estimate 12-22% of world energy demand coming from hydrogen in 2050 with the Thunder Said Energy research consultancy's world energy outlook model [Thunder Said Energy, 2024] for 2050, which estimates 120,000 TWh of energy demand, then hydrogen demand in 2050

will be between 14,400 and 26,400 TWh. Therefore, TWh hydrogen storage solutions such as depleted gas fields are critical to a successful future hydrogen economy.

2.2.2.3 Depleted Gas Fields

Depleted gas fields have been found to be more economical than salt caverns and aquifers [Kumar et al., 2023] and a single field (with thickness = 150 m, area = 4,000,000 m^2, porosity = 0.15, hydrogen density = 9 kg/m^3, hydrogen saturation = 0.75, and recovery factor = 0.8) has the capacity to store the equivalent of 1% of the U.K.'s annual energy consumption [Burtonshaw et al., 2024a]. Depleted gas fields are easy to operate, maintain and develop due to pre-existing infrastructure (i.e., connected gas pipelines, potential re-use of old wells, surface compressors), proven fluid storage integrity (i.e., the caprock largely contained the original hydrocarbon gas in place for hundreds of thousands to millions of years [Song and Zhang, 2013, Paluszny et al., 2020a]) and a wealth of field-specific knowledge and expensive datasets associated with the original exploration and production phases of the gas field. Furthermore, a substantial workforce with the skills already required to operate such fields exists from the petroleum engineering sector. However, no prior experience exists of the injection, storage and production of a fluid comprising pure hydrogen into a depleted gas field [Sambo et al., 2022, Craig et al., 2022, Ershadnia et al., 2023, Burtonshaw et al., 2024a]. In fact, no fluid above 10% H_2 concentration had been injected into such fields prior to 2023 [Burtonshaw et al., 2024a]. Therefore, numerical simulation of geological hydrogen storage is crucial to understanding potential consequences of the technology.

2.2.2.4 Depleted Oil Fields

Generally, hydrogen storage in depleted oil fields has not been considered in the literature. This is primarily owing to greater storage costs associated with fluid separation after withdrawal. Whilst remnant natural gas (1) is largely unreactive with hydrogen, and (2) has a generally simplistic chemical composition consisting primarily of methane with some ethane and propane, remnant oil is highly reactive with hydrogen and consists of tens to hundreds

of chemical constituents that can contaminate the hydrogen product, requiring a much more complex separation.

Some examples of the chemical reactions that may occur between hydrogen and remnant oil in depleted oil reservoirs include the hydrogenation of aromatics, alkenes, carboxylic acids, and asphaltenes. However, it should be noted that these reactions typically require a catalyst for appreciable conversion rates in industrial processes, so their influence on hydrogen loss and contamination in the subsurface is uncertain. Example hydrogenation reactions that could occur include:

$$\underbrace{C_6H_6\,(l)}_{\text{benzene}} + 3H_2 \longrightarrow \underbrace{C_6H_{12}\,(l)}_{\text{cyclohexane}} \tag{2.23}$$

$$\underbrace{RCHCHR'\,(l)}_{\text{generalized alkene}} + H_2 \longrightarrow \underbrace{RCH_2CH_2R'\,(l)}_{\text{generalized alkane}} \tag{2.24}$$

$$\underbrace{RCOOH\,(l)}_{\text{generalized carboxylic acid}} + H_2 \longrightarrow \underbrace{RCH_2OH\,(l)}_{\text{generalized alcohol}} + H_2O\,(l) \tag{2.25}$$

$$\underbrace{C_{80}H_{90}S_2N_2O_3\,(l)}_{\text{an asphaltene}} + 12H_2 \longrightarrow \underbrace{C_{60}H_{100}\,(l)}_{\text{hexacontane}} + \underbrace{2H_2S\,(g)}_{\text{hydrogen sulphide}} + \underbrace{2NH_3\,(g)}_{\text{ammonia}} + 3H_2O\,(g) \tag{2.26}$$

Furthermore, some of the remnant crude oil will still contain some light hydrocarbon components such as ethane, propane, butane and pentane. When the hydrogen is injected and the reservoir pressure increases this can facilitate the lighter components vaporising from the liquid to the gaseous phase, where they dissolve in the hydrogen, contaminating the productant stream. This will be of particular issue in reservoirs of high temperature, which can further

encourage the vaporisation of light and intermediate crude oil components into the stored hydrogen. The final product is then a mixture of a large number of gases, incurring greater separation complexity.

2.2.2.5 Aquifers

Storage of hydrogen in aquifers is a similar process to storage in a depleted hydrocarbon field since both storage modes involve porous and permeable media overlain by low permeability caprocks, often with anticlinal trap geometries. Nevertheless, aquifer storage has a number of drawbacks that depleted gas field storage does not possess. Firstly, specific geological, geophysical, geomechanical, and reservoir data relevant to a specific aquifer is less likely to already exist, relative to depleted fields, because depleted fields had extensive prior economic investment into data acquisition prior to the commercial production of a highly valuable product (natural gas or oil). Therefore, the data acquisition phase prior to storage in aquifers is likely to incur significant additional costs such as new wells [Muhammed et al., 2022], core acquisition and seismic and geophysical surveying. Secondly, aquifers have larger cushion gas requirements because they contain no native gas. Additionally, the producible gas may only occupy 20% of the reservoir unit, with 80% occupied by the non-working cushion gas [Lord et al., 2014, Muhammed et al., 2022], which reduces storage capacity and diminishes the economics of the process. Therefore, it can be seen that aquifers are also inferior to depleted gas fields for satisfying large-scale and long-term energy demand.

2.2.2.6 Other Storages

Other subsurface storages exist that could be used for hydrogen storage, such as hard lined rock caverns [Masoudi et al., 2024, Lemieux et al., 2019], refrigerated mined caverns [Muhammed et al., 2022, Lord, 2009], and abandoned coal mines [Crotogino et al., 2018, Muhammed et al., 2022, Jalili et al., 2011], but these are immature technologies that also lack the volumetric capacity and are geographically restricted to locations of abandoned coal mines or suitable

igneous and metamorphic rocks to be scalable at the level necessary to deliver tens of TWh's of energy and beyond.

2.2.2.6.1 Lined Rock Caverns Lined rock caverns (LRCs) are subsurface caverns mined within hard rock such as igneous and metamorphic rocks. They are sealed with a special lining to create a secure storage system. The internal pressure of the storage system is accommodated by the surrounding hard rock mass and the steel lining ensures that fluid cannot leak out of the cavern [Masoudi et al., 2024].

LRCs pertain to a number of advantages as a hydrogen storage system. Firstly, they can be implemented in locations where other storage options are unfeasible due to the local geology (i.e., salt caverns are not possible where there is no salt formation). Secondly, the steel lining system is designed to be non-porous, ensuring with certainty a 0% leakage rate of the stored product and a 0% contamination of the stored product with other subsurface fluids since it is evacuated prior to operations. Thirdly, the inclusion of the steel lining enables higher pressures to be achieved than storing the fluid at the same depth outside the cavern. This enables a greater volume of hydrogen to be stored and a greater withdrawal rate.

However, the depth at which the cavern is located must exceed a certain threshold. This is because the overburden pressure, resultant from the weight of the overlying rock strata, must always exceed the maximum internal gas pressure of the cavern [Masoudi et al., 2024]. If this condition is not obeyed, the rock mass may uplift and the cavern may fail [Johansson, 2003, Damasceno, 2022, Sofregaz and Gustafsvag, 1999]. Additionally, the cavern must be fitted with a drainage system of perforated polyvinyl chloride (PVC) pipes every 1-2 m along the outside cavern walls. These are required in order to minimize the hydrostatic pressure acting on the steel lining during construction or maintenance. The drainage system is also required to detect and collect any gas leaks [Nilsen and Olsen, 2022, Masoudi et al., 2024].

2.2.2.6.2 Refrigerated Mine Caverns Refrigerated Mined Rock Caverns (RMCs) could potentially be used to store hydrogen in the liquid state in the future [Muhammed et al.,

2022, Zivar et al., 2021, Gianni et al., 2024]. RMCs are an underground storage facility for cryogenic liquids [Freeway, 1998]. They have already been used to store liquefied natural gas (LNG) at temperatures around -160° [Glamheden and Lindblom, 2002, Cha et al., 2007, Park et al., 2010]. They are typically excavated in low permeability geological formations, such as salt or granite, which provide a safe and stable environment for storage. Since they do not incorporate a lining like LRCs [Jacobsson, 1978], the rock surrounding the cavern must act as a natural barrier to prevent leakage. Cooling systems are integrated into the cavern structure to ensure that the temperature remains stable and prevents the stored liquid from vaporising into the gaseous state. The cavern walls may be lined with insulating materials to minimise heat transfer from the surrounding rock to the stored liquid, maintaining the necessary low temperatures [Christenson, 1978]. Such thermal barriers are crucial in reducing energy costs associated with maintaining the required temperature. One core uncertainty on the capability of RMCs storing liquid hydrogen is that hydrogen must be kept at extremely low temperatures (approximately -253°C to remain in a liquid state), not far from absolute zero. Storing a fluid at nearly 100°C cooler than previously done for LNG may be complex and require far more energy, potentially severely impacting the storage economics.

2.2.2.6.3 Abandoned Coal Mines After long periods of coal mining, many coal reserves have been depleted and mines closed. Such old coal mines offer large amounts of empty underground volume, including chambers, tunnels and shafts [Liu and Pei, 2021]. Abandoned coal mines (ACMs) have been touted for hydrogen storage routinely in the literature [Peppas et al., 2023, Saigustia and Robak, 2021, Wu et al., 2024]. The coal seams above the mined areas can act as a natural seal, preventing the escape of hydrogen gas from the cavernous spaces. Whilst the low porosity and permeability of coal seams can prevent upward migration of the hydrogen, the coal can allow some hydrogen to adsorb to the surface which will result in losses of the stored product [Iglauer et al., 2021]. A potential advantage of hydrogen storage in ACMs is that existing infrastructure such as shafts and ventilation systems can be repurposed for hydrogen injection and extraction, reducing the costs and complexities associated with new construction.

2.3 Challenges of Hydrogen Storage in Porous Media

2.3.1 Fluid Flow

2.3.1.1 Viscous Fingering

Hydrogen has a much lower viscosity than all other fluids used in geo-energy applications. The viscosity of hydrogen has a value of between 9 and 12 μPa s for typical reservoir temperatures of 40–120°C and reservoir pressures of 10–50 MPa [Heinemann et al., 2021]. Over the same temperature and pressure ranges, carbon dioxide has a viscosity of 20–75 μPa s [Heinemann et al., 2021], methane-based natural gas is between 15 and 27 μPa s [Heinemann et al., 2021], brine is between 400 and 1,200 μPa s [Francke and Thorade, 2010], and hydraulic fracturing fluid is between 2000 and 1,000,000 μPa s [Burtonshaw et al., 2021].

Saffman-Taylor instabilities [Saffman and Taylor, 1958], also referred to as viscous fingers [Saffman, 1986], can appear in the fluid front of the displacing phase as it traverses through the *in situ* fluid, leading to poor areal sweep efficiency and thus, poor macroscopic sweep efficiency. This phenomenon is exacerbated when the viscosity of the displacing phase is much lower than the viscosity of the *in situ* fluid phase. For miscible displacements, where the injectant (in this case hydrogen) can significantly dissolve in the *in situ* fluid (in this case remnant brine from the primary depletion of the gas field or from secondary injection for pressure support), the miscible mobility ratio, M, governs the formation of viscous fingers and such instabilities occur when M exceeds 1 [Muggeridge et al., 2017]:

$$M = \frac{\mu_w}{\mu_h}, \tag{2.27}$$

where μ_w is the viscosity of the remnant brine and μ_h is the viscosity of injected hydrogen. Taking the highest viscosity value of hydrogen (12 μPa s) and the lowest viscosity value of brine (400 μPa s) in the aforementioned ranges in order to find an approximate minimum value for M, we obtain $M \geq 33.3$. Therefore, viscous fingers are very likely to form as the hydrogen

passes through the brine. This leads to very poor sweep and thus poor storage space efficiency. It should be noted that here M is approximated as the miscible mobility ratio because the immiscible mobility ratio [Muggeridge et al., 2017] requires knowledge of hydrogen and brine relative permeability curves as a function of saturation for the system of interest, which we do not have. Hydrogen does not dissolve strongly in water as hydrogen is a non-polar molecule and water is a polar solvent, but it does exhibit some dissolution, which justifies the first-order simplification of M as the miscible mobility ratio.

Viscous fingers can be minimised by controlling flow rate. Dumore [1964] proposed the following condition, adapted slightly herein, to prevent viscous fingers:

$$v < \frac{\rho_w - \rho_h}{\mu_w \left(\ln M\right)} kg. \tag{2.28}$$

Assuming a reservoir temperature of 120 °C and a reservoir pressure of 25 MPa, approximately we have, a brine density, ρ_w, of 1080 kg/m^3, a brine viscosity, μ_w, of 400 μPa s, a hydrogen density, ρ_h, of 13.5 kg/m^3, a reservoir permeability, k, of 100 mD, and a mobility ratio, M, of 35.7. With these assumptions, the stable injection velocity, v, is approximately 0.06 m/d. Thus, for a reservoir of thickness, $h = 150$ m and width, $w = 4000$ m, the maximal injection rate for viscously stable injection is 36,000 m^3/d. This provides a typical upper limit on realistic injection rate for geological hydrogen storage. Any higher and alternative injection strategies (i.e., water-alternate-gas (WAG) to increase the average injectant viscosity) will be required to ensure that the hydrogen accesses a sufficient proportion of the depleted reservoir pore space.

Paterson [1983] noted that one major consequence of viscous fingering is that the hydrogen front propagates much further out from the injection well than might be expected from a homogeneous circular displacement. Since most depleted gas fields contain an anticlinal trap, such fingering effects may lead to early hydrogen spillage beyond the synclines. Gravity could then conceivably carry the hydrogen away from the main storage plume, never to be recovered again, resulting in losses of the stored commodity.

Ren et al. [2024] performed numerical simulations in a 20 mm × 20 mm square micromodel

with Fluent software using the Eulerian multi-fluid model. Nitrogen, representative of cushion gas, was injected in association with hydrogen, with the hydrogen percentage ranging from 0% to 70%. Viscous fingering was observed, but decreased with increased cushion gas percentage in the injectant mixture due to nitrogen's larger viscosity. Ultimately, the hydrogen saturation increased as the cushion gas percentage increased due to improved areal sweep efficiency.

Dehury et al. [2024] utilized a highly heterogeneous porous micromodel of a saline aquifer to study immiscible two-phase dynamics for hydrogen-brine and nitrogen-brine at high-temperature (323-343 K) and high-pressure (15-25 MPa) conditions. Computational fluid dynamics (CFD) simulations based on the volume of fluid (VOF) method were conducted. Viscous fingering in the hydrogen injectant front was found to occur. In fact, the nitrogen-brine displacement resulted in 35% better gas saturation at breakthrough than the hydrogen-brine displacement, highlighting that viscous fingering is a particularly eminent issue with hydrogen storage.

2.3.1.2 Gravitational Override

The density of hydrogen at a pressure of 15 MPa and a temperature of 90°C is approximately 9 kg/m^3. Within a typical range of reservoir pressures, 0–50 MPa, and a typical range of reservoir temperatures, 40–120°C, the density of hydrogen may range anywhere between 0 and 30 kg/m^3 [Heinemann et al., 2021]. These are extremely low fluid densities relative to other geo-energy injectants over the same 0–50 MPa and 40–120°C pressure and temperature ranges, such as brine (1070–1160 kg/m^3), carbon dioxide (190–850 kg/m^3) and natural gas of CH_4 composition (50–210 kg/m^3). Hydrogen density trends upward with lower temperature and higher pressure [Heinemann et al., 2021].

The injection of hydrogen could theoretically result in gravitational instabilities in the flow-front, resulting from the hydrogen-brine density difference, where the low-density hydrogen propagates as a tongue at the top of the reservoir. The likeliness of gravity tongue formation is governed by the Fayers and Muggeridge [1990] dimensionless number:

$$R_{v/g} = 2\frac{h}{L}\left[\frac{v(1-1/M)\mu_w}{\Delta\rho g k_z} - \theta\right], \tag{2.29}$$

where θ is the dip of the reservoir in radians and L is the well spacing. If $R_{v/g}$ lies between 0 and 1, a gravity tongue will form, but if $R_{v/g} < 0$ the displacement is gravitationally stable Muggeridge et al. [2017]. The condition for stability is thus:

$$v < \frac{\Delta\rho g k_z \theta}{(1 - 1/M)\mu_w}. \tag{2.30}$$

Using the same values as above, $L = 2000$ m and an approximate $\theta = 0.037$ c, the maximal value of v to ensure no gravitational override is 0.0086 m/d, and thus the maximal injection rate is 3440 m^3/d. A value above this would again result in poor vertical sweep of the reservoir and ultimately poor macroscopic sweep (storage) efficiency. With this constraint and that in Section 2.3.1.1 for viscous fingers, we can see that injection rates in the range 0–36,000 m^3/d, and ideally near the lower end of this range (0–3,500 m^3/d), are more realistic of future operations in average reservoirs.

Numerous authors have found that gravitational override occurs during hydrogen displacements into brine. Huang et al. [2023] developed a numerical model based on the Tough and RealGasBrine (T + RGB) simulators. They simulated one hydrogen injection-soak-withdrawal operation in a depleted gas field with an anticlinal structure. Hydrogen rose vertically under gravity, displacing the remnant natural gas and residing all at the top of the storage unit. Feldmann et al. [2016] performed 2-D hydrogen-brine displacement simulations and also found that gravitational override was an issue wtih the hydrogen pooling across the top of the reservoir. Buscheck et al. [2024] found that changing the injectant from pure hydrogen to an equal component hydrogen-methane mix reduced the buoyancy driving force by a factor of 4.7–5.7, highlighting that hydrogen particularly exacerbates gravitational override.

The density of H_2 increases linearly with depth, while the density of brine barely changes with increasing depth. The density of H_2 and brine decreases weakly with increasing temperature. Therefore, the risk of hydrogen gravitational override decreases nearly linearly with depth. Vertical sweep efficiency of hydrogen increases significantly with depth because gravity override

decreases with depth [Buscheck et al., 2024]. Therefore, storing hydrogen in deeper fields may reduce gravitational flow instabilities and improve storage efficiency.

Gravitational override is exacerbated in formations with high vertical permeability [Terry, 2003], which promotes the low density phase to rapdily rise. Lower injection rates also enhance the relative dominance of gravitational to viscous forces, promoting gravitational override [Terry, 2003]. Therefore, whilst lower injection rates may reduce viscous fingering effects and enhance areal sweep (see Section 2.3.1.1), they enhance gravitational effects, hence decreasing vertical sweep. Therefore, the conundrum exists in which the injection rate should not be too low or too high, which highlights the importance of performing fluid flow simulations with specific field and operational properties prior to the onset of operations.

2.3.1.3 Capillary Fingering

Capillary fingering occurs when capillary forces dominate over viscous forces during the displacement of one fluid by another in a porous medium. The dimensionless capillary number, Ca is defined according to [Lee and Tallmadge, 1974, Blunt, 2017b]:

$$Ca = \frac{\mu_f q}{\gamma}, \tag{2.31}$$

where μ_f is the injectant fluid viscosity, q is the Darcy velocity of the injectant and γ is the interfacial tension between the injectant and resident fluid phases. When Ca is low, and capillary forces dominate the displacement, capillary fingers can evolve where the injected phase moves heterogeneously through the resident phase in a few long thin, elongated plumes. This results in poor microscopic sweep (storage) efficiency.

Hosseini et al. [2022] used the pendant drop technique to measure hydrogen-brine interfacial tensions under various pressure-temperature conditions typical of geo-energy storage sites. They found that for a temperature of 100°C and pressure of 15 MPa, the interfacial tension ranged between 57 and 65 mN/m, dependent on the molality of the hydrogen-brine mixture. Therefore,

taking γ to equal 60 mN/m, together with a μ_f of 10 μPa s, then Ca takes values of 2.78×10^{-11}, 1.38×10^{-9}, and 1.11×10^{-8}, for darcy velocities of 1.67×10^{-7}, 8.33×10^{-6} and 6.66×10^{-5} m/s, respectively, which for the cross-sectional area to flow of 4000 m $\times$ 150 m used in the Results chapters of this thesis, corresponds to injection rates of 0.1, 5 and 40 m^3/s, respectively.

Dehury et al. [2024] found that for their high pressure, high temperature (representative of aquifer conditions), immiscible two-phase hydrogen-brine dynamics simulations, capillary fingering was evident in cases with Ca even as high as 2.83×10^{-6} and 5.66×10^{-7}. Therefore, we would certainly expect capillary fingering to be a significant issue at our lower computed values of 2.78×10^{-11}-1.11×10^{-8}. Lysyy et al. [2024] performed experiments with a porous micromodel and delivered hydrogen through a syringe pump to control injection rate. They visually observed that capillary fingering dominated the displacement pattern when $Ca \leq 10^{-7}$. Large capillary fingers both in the direction of and perpendicular to the flow developed and these fingers often completely circumvented the regions of high porosity.

Using a high injection rate will reduce the risk of capillary force instabilities and gravitational override, but it will increase viscous instabilities if the critical injection rate is exceeded (see Section 2.3.1.1). Therefore, whilst this may be a solution, it may be more optimal to add a surfactant to the injectant phase so that the interfacial tension between the hydrogen and brine decreases and the capillary number increases, reducing the risk of capillary fingers whilst not increasing the risk of viscous fingers. Lu et al. [2024] found that adding a sodium dodecyl sulphate (SDS) surfactant to the injected hydrogen, reduced hydrogen interfacial tension and enhanced hydrogen storage capacity by over 200%. Alternatively, injecting first a foam, where bubbles of gas are dispersed in a liquid surfactant injectant, will raise the effective viscosity of the subsequent hydrogen because the hydrogen must navigate around the network of gas bubbles which act as a physical obstruction impeding flow. This will help keep the capillary number high, and minimise the risk of viscous fingers, although at the expense of the amount of hydrogen that can ultimately be stored. Chaturvedi et al. [2022] suggested this idea showing that the initial injection of an air-based foam increased hydrogen storage capacity by a massive 150-270% in sand-pack experiments.

2.3.1.4 Diffusion and Mixing

Diffusion is the process in which solute particles move randomly, due to constant thermal fluctuations, through the resident fluid. A flux of solute particles moves from regions of high concentration of the solute to regions of low concentration. Hydrogen has a much larger effective diffusion coefficient, D, in water than other geo-energy fluids such as CO_2, N_2, CH_4 and air. For a temperature of 50°C, the effective diffusion coefficients for H_2, CO_2, N_2, CH_4 and air are 9.7×10^{-9}, 3.2×10^{-9}, 5.1×10^{-9}, 4.7×10^{-9} and 4.9×10^{-9} m^2/s, respectively [Wise and Houghton, 1966, Lu et al., 2013]. Fick's law of diffusion in porous media states [Fick, 1855, Blunt, 2017a]:

$$J^\alpha = -\phi D^\alpha \nabla C^\alpha, \tag{2.32}$$

where J^α is the mass flux (mass of solute moving per unit area per unit time), ϕ is the porosity, and C^α is the concentration (mass of solute per unit volume of the resident phase). The superscript α refers to the solute of interest. Therefore, for the same storage field and the same concentration gradient, the mass flux is directly proportional to the effective diffusion coefficient. Therefore, we can expect that two to three times the mass of hydrogen will have diffused in a given area in a given time than any other geo-energy injectant.

Hydrogen is much more diffusive than these other gases because the diffusion coefficient, D_0, is inversely proportional to the injectant molecule diameter according to the Debye-Einstein equation [Einstein, 1905]:

$$D_0 = \frac{k_B T}{3\pi\mu_f d_m}, \tag{2.33}$$

and thus the effective diffusion coefficient, D, given by $D = D_0/\phi$, is also dependent on this. Given a hydrogen molecule contains only two electrons and two protons, it has a far smaller molecular diameter than the other aforementioned geo-energy fluid species. Here k_B is the Boltzmann constant with a value of 1.380649×10^{-23} J/K, T is the absolute temperature, and d_m is the molecular diameter.

Nevertheless, some authors estimate that diffusive hydrogen losses from the storage unit are very low and do not exceed 0.1-1% over storage lifetime [Carden and Paterson, 1979, Feldmann et al., 2016]. Accounting for diffusive processes can lead to slightly increased hydrogen plume sizes of up to 7% [Yang et al., 2024]. This is non-ideal as when the plume spreads, the hydrogen dilutes. This renders the stored hydrogen less concentrated which has associated retrieval and separation costs.

Diffusion of the hydrogen into the resident fluid phases can lead to fluid mixing (with the cushion gas, remnant natural gas and the *in situ* brine) leading to contamination of the stored hydrogen. Such impurities in the productant may result in operational and engineering challenges in terms of toxicity, compression and dehydration requirements, due to differing thermophysical properties between a pure hydrogen and partial hydrogen stream, and safety issues [Heinemann et al., 2021]. Pfeiffer and Bauer [2015] conducted flow simulations of a five-well hydrogen storage operation, where the injection occurred near the top of their anticlinal trap structure. They first injected nitrogen cushion gas for 710 days before injecting the working hydrogen gas for 210 days. Then four storage cycles are simulated consisting of hydrogen withdrawal for one week, followed by hydrogen injection for 50 days, and finally followed by a shut-in period of thirty days. They found that the hydrogen concentration of the productant was only 50-80%. Carbon dioxide may be a better cushion gas because at reservoir temperatures and pressures it is far more dense than hydrogen (21-95 times based on the fluid densities discussed in Section 2.3.1.2). Therefore, the working hydrogen and cushion carbon dioxide will not have strong affinity to mix due to their large density contrasts favouring gravity segregation [Oldenburg, 2003].

2.3.1.5 Straining

Fine clay particles can get dislodged from the rock skeleton during subsurface activities and can move through the porous medium in suspension with the flowing fluid [Zeng et al., 2024]. This is a known problem particularly for production wellbores in sandstone reservoirs [Gray and Rex, 1996]. Subsurface fluid activities such as the circulation of drilling fluid, the circulation

of completion fluid, and the injection of acidising treatments can initiate alterations in the attractive and repulsive forces between grains within the rock matrix [Muneer et al., 2020]. The introduction of completion or drilling fluids can change the ionic strength of the reservoir fluid, which may alter the electrostatic forces that hold fines in place. If the reservoir fluid becomes increasingly more charged with the opposite polarity to the mineral fine, then particles can become unstable and are removed from the rock skeleton. Furthermore, acid treatments can physically dislodge part of the rock matrix, leading to fines production. As the fines migrate through the pore space, they can either entirely block pore throats or partially reduce their diameter. This induces formation damage that reduces permeability (a positive skin factor) and thus decreases well productivity [Muneer et al., 2020], which could lead to not honouring hydrogen supply contracts and ultimately causing energy shortfalls.

As noted by Zeng et al. [2024], no studies on fines production during underground hydrogen storage have yet been performed. However, we might expect that because of the smaller viscosity of hydrogen (Section 2.3.1.1) and its high diffusivity (Section 2.3.1.4) relative to other geo-energy fluids, the hydrogen will more easily spread throughout the storage unit and potentially interact with more fines. Furthermore, the large injection rates, likely to be necessary in future hydrogen storage projects in order to meet enormous future hydrogen demand and to account for the very low fluid density, will likely result in much larger pressure changes throughout the storage operations than in other injection-extraction technologies. These high pressure variations could disturb the reservoir rock to a greater extent and lead to greater mobilization of fines particles. However, more research is required to investigate this phenomenon specifically for hydrogen storage.

2.3.1.6 Wettability and Pore-scale Trapping

Wettability refers to the ability of a fluid to spread on or adhere to the solid surface [Donaldson and Alam, 2013], as determined by the interaction between the fluids and the rock/mineral surface. Wettability is often quantified using the contact angle [Young, 1832], which is the angle formed between the tangent to the fluid surface of the more dense fluid phase at the

contact point and the solid surface. The rock surface is said to be water-wet when the brine has a greater affinity for the solid surface than the other fluid phase. Most clean rocks, where the surface of the solid is the same composition as the bulk rock, are naturally water-wet [Blunt, 2017b]. In the case of a sandstone reservoir, the rock is primarily composed of quartz or silicon dioxide. Silicon dioxide is an ionically bonded compound. When water, a polar molecule, is present, there is strong electrostatic attraction between the quartz ions and the hydrogen/oxygen atoms of the water molecules. Therefore, water minimises the surface energy of the solid. Hydrocarbons are covalently bonded compounds and they do not have the capacity for ionic or hydrogen bonding. Therefore, they have much less affinity for the solid surface, and tend to reside away from it, in the centres of the pore space. This means that brine flows throughout the reservoir along the surfaces of the pores and into throats, which are sometimes only large enough to allow one fluid film (the wetting phase), thus trapping the hydrocarbons in the pores indefinitely, in a process called snap-off [Pickell et al., 1966, Lenormand and Zarcone, 1984]. Sometimes, the surface of the rock in a sandstone reservoir may be oil-wet instead of water-wet. In crude oil, high molecular weight hydrocarbon fractions called asphaltenes contain surface active components. Asphalthenes have polar and non-polar ends to their molecular structure. The polar ends can adhere to the solid surface, creating a dirty surface [Buckley and Liu, 1998]. The surface of the rock that is in contact with the fluids now no longer has a crystalline structure but an oleic film covers it [Blunt, 2017b]. The surface can now form van der Waals bonds with the *in situ* hydrocarbons, making it oil-wet as the surface now has an affinity for the hydrocarbon phase. A water-wet rock will have a contact angle between 0 and 90°, whilst an oil-wet rock will have a contact angle between 90 and 180°.

With this in mind, oil reservoirs are more likely to be oil-wet since the oil likely contains at least some asphaltenes. Gas reservoirs are less likely to be oil-wet since gaseous hydrocarbons contain volatile components and not heavy fractions such as asphaltenes. However, this does not prevent natural gas reservoirs from being partially oil-wet because organic acids remnant from the thermal maturation of organic matter into crude oil and natural gas are mobile within the reservoir and make contact with the solid surface.

Hydrogen is a non-polar molecule and thus will not be the wetting phase in a reservoir with

clean rock surfaces. However, if the rock has previously been contacted by organic acids or asphaltenes, the rock is likely to at least have some wettability to hydrogen. In water-wet reservoirs, snap-off could potentially be a significant problem because hydrogen stays in the centre of the pore spaces and gets cut-off by brine in the throats, resulting in unrecoverable hydrogen. Therefore, it is likely better that hydrogen is stored in a system with some hydrogen-wettability to ensure that hydrogen can easily flow to the withdrawal wellbore during extraction.

Iglauer et al. [2021] conducted contact angle measurements on clean quartz-dominant sandstone samples using the Tilted Plate Method. They investigated two cases: one where the surface was kept clean and one in which the surface was prepared with stearic acid to represent the organic acids present in most depleted hydrocarbon fields. For the clean surface, the contact angles always remained water-wet at less than 50°. For the aged surface, the contact angles increased significantly and became weakly water-wet at 50-70° dependent on stearic acid concentration, but not significant enough to become hydrogen-wet. Hashemi et al. [2021] used the Captive-Bubble method to determine the contact angle in samples of homogeneous clean Bentheimer and Berea sandstone, and found that for a host of pressures (20-100 bar) and temperatures (20-50°C), the rock was always water-wet with contact angles betweeen 21.1 and 43.0°. Mirchi et al. [2022] measured the static contact angles of H_2–CH_4 mixtures in both water-wet and oil-wet sandstones and limestones at reservoir conditions using the pendant drop and rising/captive bubble methods. These mixtures are more representative of subsurface hydrogen storage conditions because some remnant natural gas will be present as well as brine prior to hydrogen injection. They observed that H_2–CH_4 mixtures exhibit weakly water-wet behaviour on oil-wet limestone and sandstone with contact angles of 52.4°-71.1°. Therefore, it appears that even in the case of oil-wet rocks, the rock is never hydrogen-wet, which would be more ideal for hydrogen storage.

It may be possible to alter the wettability of the reservoir rock to make it more hydrogen-wet [Perera, 2023]. However, this will incur additional costs. Injecting a surfactant can alter the wettability [Jarrahian et al., 2012] by altering the interfacial tension between the hydrogen and the brine [Fox and Jackson, 1955]. Surfactants contain a hydrophilic head and a hydrophobic tail [Wilson et al., 2019]. For a clean water-wet surface that is ionic in nature, the hydrophilic

head of the surfactant can be attracted to the solid surface where it adheres. The fluids in the pore space now see a hydrophobic surface from the tail-end of the surfactants, and van der Waals forces can form with the hydrogen in the pore space, making the rock more hydrogen-wet [Lykema et al., 2000]. Therefore, surfactant application may potentially be useful in geological hydrogen storage.

2.3.2 Chemical

2.3.2.1 Mineral Dissolution

The presence of calcite within the reservoir rock can be both problematic and beneficial during geological hydrogen storage. Some of the gaseous hydrogen can dissolve in the resident brine forming an aqueous hydrogen-brine solution. The aqueous hydrogen can then dissociate to provide a source of hydrogen ions according to [Bo et al., 2021]:

$$\mathrm{H_2(aq)} \rightleftharpoons 2\mathrm{H^+} + 2e^-. \tag{2.34}$$

The spontaneous dissociation of the resident brine can also provide a second source of hydrogen ions in the reservoir according to:

$$\mathrm{H_2O(l)} \rightleftharpoons \mathrm{H^+} + \mathrm{OH^-}. \tag{2.35}$$

The presence of $\mathrm{H^+}$ ions forms an acidic brine which can attack and dissolve calcite from the rock matrix according to [Bo et al., 2021]:

$$\mathrm{CaCO_3(s)} + \mathrm{H^+} \rightleftharpoons \mathrm{Ca^{2+}} + \mathrm{HCO_3^-}, \tag{2.36}$$

which can enhance the porosity and potentially the permeability of the reservoir rock enabling better injectivity, productivity, and hydrogen storage capacity. However, it can be seen from

Equation 2.34 that lower pH conditions, such as that of the acidic brine, helps drive the equilibrium equation to the left to keep hydrogen in its molecular form. However, in alkaline conditions, the equilibrium equation moves to the right to generate more H^+ ions to neutralise the reservoir conditions, which leads to loss of the stored product: molecular hydrogen. When calcite dissolves it leaves behind $HCO_3{}^-$ ions that create an alkaline environment. This alkaline environment encourages Equation 2.34 to move to the right and leads to the loss of molecular hydrogen. Bo et al. [2021] performed kinetic simulations in PHREEQC (Version 3) to determine the loss of hydrogen over a 30 year storage period in the Mondarra sandstone reservoir. They tested a case where hydrogen gas was not present to determine the influence of hydrogen on the calcite dissolution or whether it was primarily driven by the spontaneous water dissociation-dervied hydrogen ions. They found that without gaseous hydrogen present only 2.9% of the calcite was dissovled but it was 87% in the case with stored gaseous hydrogen, highlighting that hydrogen injection is exacerbating calcite dissolution reactions. They also found that the calcite dissolution led to 2.76% stored hydrogen loss over the 30 year storage period. However, since they do not perform any hydromechanical simulations, they did not address the possibility that the increased calcite dissolution would enhance the porosity and permeability of the rock to enable greater hydrogen storage volumes than would have been possible without calcite dissolution. For the quartz-rich Tubridgi sandstone reservoir, they found that the absence of calcite, resulted in only 0.72% hydrogen loss. Therefore, storage in sandstone reservoirs with minimal calcite may be more optimal for hydrogen storage and care should be taken to store hydrogen in limestone reservoirs.

Laboratory batch experiments in heterogeneous sandstone samples containing sulphate cements, and exposed to hydrogen, showed significant sulphate dissolution for typical depleted reservoir conditions of 40–120°C temperature and 4–20 MPa pressure [Pudlo et al., 2018]. Due to the pore-filling nature of the sulphate cement, the porosity was described as having 'strongly increased' and new flow pathways were created. The dissolution reaction for a sulphate mineral such as gypsum is:

$$CaSO_4 \cdot 2H_2O(s) \rightleftharpoons Ca^{2+} + SO_4^{2-} + 2H_2O(l). \tag{2.37}$$

Perera [2023] claims that due to the fact that pyrite is thermodynamically unstable in the presence of hydrogen, it constitutes the major non-biological geochemical reaction that occurs in a hydrogen storage reservoir. Pyrite is dissolved and replaced by a pyrrhotite precipitate according to:

$$FeS_2(s) + H_2 \rightleftharpoons FeS(s) + H_2S, \tag{2.38}$$

In fact, this reaction was confirmed with hydrogen sulphide production in the Beynes storage facility in France, where hydrogen-containing town gas was injected and dissolved pyrite [Bourgeois et al., 1979]. Truche et al. [2013] showed with physical experiments on claystone samples, representative of caprock, that for a wide range of temperatures (0-250 °C) and pressures between 0-3 MPa, a large amount of pyrite conversion occurred. Depending on the mineral volume changes, which are not quantified, this could either be beneficial or detrimental for hydrogen storage. If the overall porosity increases because the pyrrhotite occupies less rock volume than pyrite, then the caprock permeability could be enhanced degrading the seal capacity of the reservoir.

2.3.2.2 Mineral Precipitation

Clay minerals like kaolinite, illite and chlorite have been found to be precipitated during geological hydrogen storage, along with other minerals such as K-feldspar, pyrite, and calcite [Reitenbach et al., 2015, Gholami, 2023]. However, Gholami [2023] notes that none of these reactions seem to be significant. Sandstone is generally a good storage lithology if calcite is non-prevalent, in which case injectivity degradation is not expected to be significant.

2.3.2.3 Gas Production

Equation 2.38 demonstrates that hydrogen can react with sulphur minerals to generate hydrogen sulphide (H_2S) gas. This can degrade the quality of the hydrogen productant stream requiring

additional separation costs and necessitate additional safety procedures during withdrawal due to its toxicity, potential lethality and high flammibility [Heinemann et al., 2021]. However, dealing with hydrogen sulphide at withdrawal wellbores is not overly problematic given it is relatively routine in conventional oil and gas operations. A further problem relating to hydrogen sulphide gas is that it can exacerbate rock-fluid interactions by altering brine pH [Heinemann et al., 2021]. It's acidic nature could further exacerbate calcite dissolution by providing additional H^+ ions to push Equation 2.37 to the right.

2.3.3 Biological

2.3.3.1 Microbial Hydrogen Consumption

Microorganisms can metabolise hydrogen resulting in loss of stored hydrogen. Major hydrogen-consuming microorganism groups that are prevalent in subsurface rock include methanogens, sulphate-reducing microorganisms (SRMs), homoacetogenic bacteria and iron(III)-reducers [Heinemann et al., 2021]. The microbial consumption is dependent on temperature, pH-value, and salt concentration in reservoir brine [Heinemann et al., 2021].

Methanogens are a type of archaea (single-celled microorganisms) that produce methane as a metabolic byproduct. They consume hydrogen and carbon dioxide to produce methane and water according to [Zabranska and Pokorna, 2018]:

$$4H_2 + CO_2 \rightarrow CH_4 + 2H_2O. \tag{2.39}$$

SRMs are archaea that perform a specific type of anaerobic respiration where sulphate (SO_4^{2-}) is used as a terminal electron acceptor instead of oxygen. SRMs reduce sulphate to hydrogen sulphide gas (H_2S) in the presence of an organic substrate (i.e., butanoic acid) according to [Scarascia et al., 2016]:

$$SO_4^{2-} + C_3H_7COOH \rightarrow H_2S + 2CH_3COOH. \tag{2.40}$$

Homoacetogenic bacteria are a type of microorganism that produce acetate (acetic acid) as their primary metabolic end product. Homoacetogens perform a process known as homoacetogenesis where carbon dioxide is reduced to acetate according to [Fuentes et al., 2021]:

$$2CO_2 + 4H_2 \rightarrow CH_3COOH + 2H_2O. \tag{2.41}$$

Iron (III) reducers (IRBs) are microorganisms that use ferric iron (Fe^{3+}) as a terminal electron acceptor in their metabolic process. An example of a potential iron (III) reduction reaction performed by such bacteria is [Amez et al., 2021]:

$$H_2 + Fe_2O_3 \rightarrow 2FeO + H_2O. \tag{2.42}$$

Veshareh et al. [2022] used the PHREEQC version 3 geochemical modeling software for their hydrogen storage-microbial reaction simulations in a depleted chalk reservoir and found that assuming methanogens and acetogens grow at the slowest speed found in the literature for methanogen/acetogen growth, then methanogenesis and acetogenesis cannot cause more than 0.60% stored hydrogen loss per year. However, when the growth rate assumed was the fastest found in the literature, all of the hydrogen was consumed in just five years of operation. Thaysen et al. [2021] performed a review of the thermophysical conditions in 42 different depleted oil and gas fields and found that only six had conditions capable of sustaining all of the reactions in this section. Depleted fields with temperatures over 122°C are sterile and are not at risk of microbial hydrogen consumption because microorganism life cannot be sustained at temperatures above this [Takai et al., 2008].

Some microbial mitigation strategies have been suggested by various authors. Schwab et al. [2023] showed that by increasing salinity concentration in the reservoir, hydrogen consumption from microbial activity can be significantly reduced, by reducing the sulphate reduction rate. Biocides can be injected into the reservoir to eliminate bacteria, especially SRB colonies. Biocides that can be applied include: glutaraldehyde, dibromonitrilopropionamide,

dodecyl dimethylammonium chloride, chlorine dioxide, tributyl tetradecylphosphonium chloride, alkyl dimethyl benzylammonium chloride, methylisothiazolinone, sodium hypochlorite, dazomet, chloromethylisothiazolinone, dimethyloxazolidine, trimethyloxazolidine, bromosuccinimide, bronopol, and peracetic acid [Bhadariya et al., 2024]. Additionally, hydrogen sulphide scavengers can be injected to deal with the hydrogen sulphide production. These are chemical compounds injected into the reservoir that chemically eliminate the H_2S. Triazine is a commonly used liquid scavenger in oil and gas operations [Montesantos et al., 2022] that converts the H_2S into a water-soluble byproduct called dithiazine. Turkiewicz et al. [2021] used a biocide/hydrogen sulphide scavenger preparation and found that SRB metabolism was extremely reduced and even eliminated in some sample wells.

2.3.3.2 Microbial Clogging

Bacteria can exist in one of two states within the reservoir. Firstly, they can be contained fully within the pore-fluid itself as freely-drifting organisms (plankton). Secondly, they can adhere to the pore and throat walls as a slimy film of biological material. These two forms are interchangeable: the plankton can strike the rock skeleton and adhere or the biofilm can desorb from the rock surface and flow with the pore fluid as plankton [Eddaoui et al., 2021]. This detachment can occur through a variety of mechanisms such as hydrodynamic detachment in which shear forces associated with higher flow velocities or pressures erode the outer layers of the biofilm [Wang et al., 2022], nutrient depletion in which the deeper layers of the biofilm become starved of nutrients so they biologically detach to find a more nutrient-rich environment [Hunt et al., 2004] and through quorom sensing in which the colony can coordinate enzyme release in response to too large population size in order to weaken the biofilm and allow parts of it to break away [Emerenini et al., 2015]. The biofilm can thicken as colony size increases, either to partially fill the pore space, or completely, thus reducing porosity and permeability. This in turn impacts the injectivity and productivity of the wells, along with the ultimate recovery of the hydrogen that has been injected. Reservoir bacteria typically have similar sizes to a typical pore diameter (0.1-1μm) and therefore only the accumulation of a few cells is required to clog an entire pore. A 'bio-plug' is said to have formed. Bio-plugging has been responsible for two

to four orders of magnitude permeability reduction in other geo-energy applications [Eddaoui et al., 2021].

Eddaoui et al. [2021] used a two-phase multicomponent transport model accounting for bio-reactions and bio-contamination and found that microbial clogging significantly reduced vertical flow of hydrogen, leading to a more uniform horizontal hydrogen propagation throughout the reservoir. This is positive because the hydrogen has a natural affinity to rise due to its extremely low density which will (1) induce large buoyancy stresses on the underside of the caprock, (2) lead to poor pore storage capacity utilisation due to gravity tongue formation and (3) lead to larger flowrates of hydrogen attempting to leak vertically through the caprock. Therefore, reduced vertical flow and increased horizontal flow is favourable for UHS.

Liu et al. [2023] performed laboratory experiments on a high-pressure rock micromodel. In one experiment the rock was inoculated with a halophilic SRB strain called *Desulfohalobium retbaense DSM 5692*, whilst the other experiment was kept sterile. They found that the residual hydrogen saturation was approximately 0.045 and 0.085 in the sterilized and bioactive cases, respectively. Therefore, the inclusion of microbial clogging resulted in trapping almost twice the amount of hydrogen. However, in both cases, the residual saturation remained low at less than 10%.

The hydrogen sulphide generated from the action of SRBs (Section 2.3.3.1) will react with any dissolved ferrous iron within the resident pore brine and precipitate FeS-based minerals such as pyrite. If the concentration of oxygen is sufficient, then the dissolved iron can also induce the precipitation of ferric iron minerals such as goethite, magnetite, and ferrihydrite [Dopffel et al., 2021]. Such microbially-induced chemical precipitation can also clog the pore-space reducing porosity and permeability.

2.3.3.3 Microbe-induced Corrosion

Hydrogen sulphide (H_2S), produced in the reservoir from SRBs (Section 2.3.3.1), is highly corrosive to metal-containing materials such as steel. Hydrogen sulphide attacks the iron present

in steel, forming an iron sulphide corrosion product:

$$\mathrm{Fe} + \mathrm{H_2S} \rightarrow \mathrm{FeS} + \mathrm{H_2}. \tag{2.43}$$

This iron sulphide resides on the steel surface and weakens the steel over time by accelerating the corrosion rate [Bai et al., 2016].

Nitrate-reducing bacteria (NRBs) use hydrogen as an electron donor to reduce nitrate to nitrogen gas (N_2) or other nitrogeneous compounds such as ammonia (NH_3). This has indirect consequences on the corrosion of wellbores and subsurface steel-based equipment. Firstly, the products of NRB's metabolism can inhibit the growth of SRBs which reduces hydrogen sulphide production which in turn heavily corrodes steel [Lai et al., 2020, Voordouw et al., 2002]. However, the produced ammonia can cause ammonium nitrate corrosion which induces pitting corrosion [Voordouw et al., 2002] where small but deep cavities form, reducing the structural integrity of the equipment:

$$\mathrm{NH_3} + \mathrm{HNO_3} \rightarrow \mathrm{NH_4NO_3}. \tag{2.44}$$

Since ammonium nitrate, NH_4NO_3, is hygroscopic, it readily absorbs water to create a highly corrosive solution. However, Vargas et al. [2017] found that the corrosivity of nitrate was heavily dependent on pH and that the solution was almost non-corrosive for a pH of close to 7.

Acid-producing bacteria (APBs) metabolise organic compounds present in the reservoir, such as remnant hydrocarbons, generating organic acids such as acetic acid, lactic acid and formic acid [Ibrahim et al., 2018]. These organic acids, although weaker than those mentioned previously, can also induce corrosion on the wellbores. However, they can significantly reduce pH which inhibits the growth of SRBs that strongly contribute to corrosion [Widdel and Back, 2006].

2.3.4 Operational

2.3.4.1 Hydrogen Embrittlement of Surface and Downhole Infrastructure

Hydrogen embrittlement is the process by which metallic materials become brittle and fracture more easily in the presence of hydrogen [Andrew, 1914, Cotterill, 1961, Pfeil, 1926]. Hydrogen embrittlement is a multi-step process consisting of two key sub-processes. Firstly, molecules of hydrogen adsorb onto the metal at the phase-boundary and dissociate into atoms, which can then migrate through the metal lattice. The hydrogen molecules dissociate because the metal surface provides catalytic sites that lower the energy barrier for hydrogen molecule dissociation. Secondly, hydrogen atoms can cause internal pressure by recombining to form hydrogen gas bubbles within dislocations and defects in the metal lattice [Chen et al., 2024, Ghosh et al., 2018]. This results in reduced ductility [Tiwari et al., 2000], making the metal more prone to cracking (hydrogen-induced cracking) and breaking under stress which can lead to sudden and catastrophic failure of the material. The hydrogen atoms can also form metal hydrides that alter the metal's properties making it more brittle. The other form of hydrogen embrittlement is sulphide stress cracking (SSC). SSC specifically occurs in the presence of hydrogen sulphide [Ovbije, 2012]. Therefore, SSC may occur in wells located in reservoirs with large pyrite quantities that generate hydrogen sulphide in the presence of hydrogen (Section 2.38). H_2S dissociates into hydrogen and sulphide ions within the metal. The hydrogen proceeds to contribute to the embrittlement process, while sulphide ions can interact with the metal to form sulphide phases [Ovbije, 2012]. This accelerates crack initiation and propagation and the interaction can weaken the metal further compared to hydrogen alone.

Typical materials used in traditional oil and gas pipelines, wells and components include carbon steel, alloy steel, stainless steel and composite materials [Alamri, 2020, Aberle and Agarwal, 2008, Badeghaish et al., 2019]. Carbon steel, containing high amounts of iron and carbon [Abdulkareem et al., 2019], is susceptible to hydrogen embrittlement. It can become brittle and prone to cracking, especially under high-stress conditions and the susceptibility increases with higher strength grades and higher hydrogen concentrations [Trautmann et al., 2020]. Alloy

steels, typically containing chromium, are also particularly susceptible to hydrogen embrittlement, though their resistance varies based on the specific alloying elements. In fact, Symons [1997] found that high-Cr based steels heavily reduced ductility and promoted embrittlement. The molybdenum can provide some resistance to embrittlement but is not immune [Jo et al., 2020]. Stainless steel is used in corrosive reservoirs [Aberle and Agarwal, 2008]. It often contains large amounts of nickel [Kahraman et al., 2005]. Stainless steels generally exhibit better resistance to hydrogen embrittlement compared to carbon and alloy steels, due to their larger nickel contents. Nickel has been shown to enhance resistance to hydrogen embrittlement processes [Ravi et al., 1993]. One to two orders of magnitude more hydrogen must be adsorbed for some stainless steels to undergo embrittlement relative to other steels [Trautmann et al., 2020, Whiteman and Troiano, 1965]. However, they are not completely immune, particularly under extreme conditions or in the presence of hydrogen sulphide. In some rare cases, composite materials (such as fiberglass) are used, particularly in environments where corrosion resistance is essential [Sebaey, 2019]. These materials are generally not susceptible to hydrogen embrittlement, as they do not contain metals that can interact with hydrogen in the same way. Other metals not mentioned prior such as titanium, zirconium, and vanadium are also susceptible to hydrogen embrittlement [Cotterill, 1961].

Relatively recently, it has been discovered that steel can be designed to be resistant to hydrogen-induced embrittlement through the inclusion of metal carbides such as titanium carbide (TiC) and vanadium carbide (V_4C_3) [Hsu et al., 2020]. These inclusions act as trapping sites for atomic hydrogen that prevent its diffusivity throughout the steel. In particular, ϵ carbide (referring to a specific crystalline structure) has been found to have very strong hydrogen-trapping capabilities [Zhu et al., 2015]. Whilst this is positive for future geological hydrogen storage in that it is not an impossibility to design suitable extraction and transportation technologies to deal with hydrogen, it does render the widespread re-use of existing wells and pipelines a serious engineering challenge. The need to implement new pipelines would be a significant additional cost to geological storage operations. Some engineering solutions have already been reported for the repurposing of natural gas pipelines for hydrogen such as increased monitoring, addition of inhibition gases, pipe-in-pipe structures and inner pipeline coatings [Télessy et al., 2024].

The purity of the H_2 productant can be purposefully reduced by the admixture of other gases that inhibit hydrogen embrittlement such as oxygen (O_2), sulphur dioxide (SO_2) and carbon monoxide (CO) [Barthélémy, 2011, Holbrook et al., 2012]. These gases block the steel surface and therefore prevent the absorption of hydrogen into wells and pipelines. The required concentration of such a gas depends on the admixed gas. Concentration levels of just 2% SO_2 and CO can inhibit hydrogen embrittlement and only a concentration level of 0.015% of oxygen was required to achieve the same [Cerniauskas et al., 2020]. Alternatively, the pipe-in-pipe method could be employed. In this method, old natural gas pipelines and wells can still be used by adding an inner tube such that the hydrogen gas does not contact the old pipeline/well walls but only the new tubing [Télessy et al., 2024]. The inner pipeline is designed to withstand the hydrogen-related difficulties discussed above. A second alternative is the inner coating of the steel pipelines [Télessy et al., 2024]. A non-corrosive substance is coated onto the pipeline walls to prevent hydrogen action. Fusion-bonded epoxy (FBE) is one such coating [Byrnes, 2017]. A powder is applied to the pipeline walls, after the steel has been heated, which melts until it cures. Aluminum and zinc are also potential inner coatings as they are partially resistant to hydrogen embrittlement depending on the exact alloy [Krieg, 2012]. Detailed monitoring and maintenance can also be employed to detect cracks and leaks [Cerniauskas et al., 2020] so that they can be addressed before failure, which could be sufficient as hydrogen embrittlement is a slow process [Télessy et al., 2024].

2.3.4.2 Irrecoverable Pore Space with Each Injection

Unlike other geo-energy storage technologies such as carbon dioxide sequestration, in which the fluid is permanently sequestered into the subsurface to never be withdrawn again, hydrogen storage requires short-time scale (i.e., months) cyclical injection and withdrawal of the fluid. After each injection, the amount of hydrogen that can be withdrawn must be less than the original injection volume. This is because some hydrogen is lost due to diffusive processes (Section 2.3.1.4), due to pore-scale residual trapping (Section 2.3.1.6) and due to diffusion into the metallic lattices of the wellbore steel (Section 2.3.4.1). In particular, the immobile, trapped hydrogen within the pore-space reduces the pore volume available for mobile hydrogen during

the subsequent injection. If trapping is favourable, such as in water-wet storage reservoirs, then eventually the potential storage capacity of the reservoir may become excessively low to the point that storage is no longer economic and hydrogen withdrawal rates become too small to meet contracted demand. This is problematic given that the reservoir may need to store hydrogen for hundreds-thousands of years depending on the development of other energy technologies. Research is required to investigate this phenomenon.

2.3.4.3 Wellbore Scales

Chemical production (withdrawal) scales in wells are hard mineral deposits that form when dissolved minerals in reservoir fluids precipitate out under certain conditions. These scales are often caused by pressure, temperature, or chemical changes during the production of oil, gas, or other fluids [Olajire, 2015]. These deposits accumulate on wellbore walls, tubing, and equipment, reducing flow efficiency [Zhang et al., 2022]. Effective scale management often involves chemical inhibitors [Graham et al., 2002] and regular cleaning.

Theoretically, the hydrogen atoms formed by hydrogen gas dissociation at the wellbore walls can attack the iron in the steel and chemically corrode it. This releases iron ions and hydrogen according to the classical corrosion reaction:

$$\mathrm{Fe} + 2\mathrm{H}^{+} \rightarrow \mathrm{Fe}^{2+} + \mathrm{H}_2. \tag{2.45}$$

If carbon dioxide is present, dissolved in the brine, then the brine has a source of carbonate ions that can react with the corrosion-produced iron ions to form solid iron (II) carbonate scales that build up on the wellbore walls:

$$\mathrm{Fe}^{2+} + \mathrm{CO}_3^{2-} \rightarrow \mathrm{FeCO}_3. \tag{2.46}$$

Chelating agents such as ethylenediaminetetraacetic acid (EDTA) and hydroxyethylidene diphosphonic acid (HEDPA) can be added to the wellbores [Hassan et al., 2020, Ji-jiang et al., 2016].

EDTA binds to Fe ions through coordination bonds. The carboxylate groups ($–COO^-$) and amine groups ($–NH_2$) of EDTA donate electron pairs to the iron ions, forming a chelate ring. This chelation prevents the Fe ions from reacting with the carbonate ions, thereby inhibiting scale formation. Alternatively, polyphosphate inhibitors can be used [Featherston et al., 1959]. These bind with Fe ions to form soluble complexes, thereby reducing the availability of Fe ions to react with carbonate ions for scale formation.

2.3.5 Mechanical

The geomechanical issues with respect to geological hydrogen storage in depleted reservoirs is the core of this thesis. The key issues include induced seismicity, caprock integrity, and surface subsidence. To avoid repetition, these are not discussed here. Rather, discussion around these issues and a review of the limited prior work on this topic is integrated into the Introduction subsection of each of the core Results chapters (Chapters 4, 5, 6 and 7).

2.3.6 Summary

Among the various challenges identified for underground hydrogen (H_2) storage, the most critical factors that demand attention are microbial activity, hydrogen reactivity with reservoir and caprock minerals, and the necessity for tailored engineering of injection and extraction strategies. Each of these challenges not only affects the technical feasibility of storage but also significantly influences the economic viability and operational efficiency of the storage system.

Microbial activity, particularly the action of hydrogenotrophic methanogens and sulfate-reducing bacteria, stands out as a primary concern in many geological settings. These microbes can consume hydrogen, converting it into methane or hydrogen sulfide, which not only results in a loss of stored hydrogen but can also degrade the quality of the gas mixture and pose safety and corrosion issues. This is especially problematic in reservoirs with high organic content or in settings where native microbial populations are abundant. Mitigation strategies such as

biocides or pre-conditioning of reservoirs, while potentially effective, add to operational costs and must be carefully tailored to the specific microbial ecology of the site.

Equally significant is the reactivity of hydrogen with the mineralogical constituents of both the reservoir rock and the caprock. Hydrogen can participate in redox reactions with iron-bearing minerals, potentially altering the porosity and permeability of the storage formation. This reactivity is more pronounced in formations with higher concentrations of reactive minerals, such as sandstones with iron oxides or clay-rich caprocks. Understanding the geochemical environment is thus crucial for selecting appropriate sites and designing storage operations that minimize these interactions.

From an engineering perspective, the challenges of hydrogen's low density and high diffusivity necessitate modifications to conventional gas injection and withdrawal technologies. High injection pressures may be required to achieve desired storage densities, particularly in deep reservoirs, which in turn demands robust infrastructure and increases energy costs. Moreover, hydrogen's propensity for diffusive loss through caprocks and wellbore materials calls for specialized sealing technologies and materials resistant to hydrogen embrittlement.

Considering cost and operational conditions, an optimal storage configuration would likely involve deep, dry sandstone reservoirs with minimal microbial activity and low concentrations of reactive minerals. These conditions favour reduced biological and chemical reactivity and offer good porosity and permeability for efficient gas injection and withdrawal. In such settings, the use of horizontal wells and pressure cycling can enhance storage efficiency, albeit with an increased initial capital investment. Conversely, shallower reservoirs or those with complex mineralogy may be more cost-effective initially but could incur higher operational costs over time due to the need for more intensive monitoring, treatment, and maintenance.

Ultimately, the optimal solution is context-dependent and must balance technical feasibility, cost, and environmental safety. For example, in a mature hydrocarbon basin with existing infrastructure and known reservoir characteristics, retrofitting depleted gas fields could be economically advantageous despite moderate microbial or mineral reactivity challenges. In contrast, in greenfield projects, the upfront cost of thorough site characterization and engineering

customization may be justified by the long-term reliability and performance of the storage system.

2.4 Fluid Properties of Hydrogen

Hydrogen has hydraulic properties that differ significantly from those of other fluids and injectants traditionally deployed for subsurface fluid injection. This section outlines and discusses the properties of gaseous hydrogen at a reservoir pressure of 15 MPa and reservoir temperature of 90°C, which are the reservoir pressures and temperatures employed for the modelling in this thesis.

2.4.1 Density

The density of hydrogen at a pressure of 15 MPa and temperature of 90°C is approximately 9 kg/m^3. Within a typical range of reservoir pressures, 0-50 MPa, and a typical range of reservoir temperatures, 40-120°C, the density of hydrogen may range anywhere between 0 kg/m^3 and 30 kg/m^3 [Heinemann et al., 2021]. These are extremely low fluid densities relative to other geo-energy injectants over the same 0-50 MPa and 40-120°C pressure and temperature ranges, such as brine (1070-1160 kg/m^3), carbon dioxide (190-850 kg/m^3, and natural gas of CH_4 composition (50-210 kg/m^3).

2.4.2 Viscosity

The viscosity of hydrogen is assumed to have values of between 9 and 12 μPa s for typical reservoir temperatures of 40-120 °C and reservoir pressures of 10-50 MPa [Heinemann et al., 2021]. Hydrogen is much less viscous over the same temperature and pressure ranges than other fluids used in geo-energy applications such as carbon dioxide (20-75 μPa s, Heinemann et al. [2021]), methane-based natural gas (15-27 μPa s, Heinemann et al. [2021]), brine (400-1200 μPa s, Francke and Thorade [2010]) and hydraulic fracturing fluid (2000-1000000 μPa s,

Burtonshaw et al. [2021]). Hydrogen has a viscosity of 10.4 μPa s at a pressure of 15 MPa and temperature of 90°.

2.4.3 Compressibility

At 15 MPa and 60 °C, the Z-Factor for hydrogen is 1.06 [Zhou and Zhou, 2001]. The same study shows that the Z-Factor, the measure of how much a real gas deviates from ideal behavior, decreases with increasing temperature at 15 MPa. Thus, extrapolating implies a Z-Factor of approximately 1.04 at 15 MPa and 90 °C. In this case, since the Z-Factor is very close to 1, we will assume it behaves in a sufficiently ideal way, that we can take the isothermal bulk modulus as the pressure. This would give an isothermal compressibility of 6.67×10^{-8} Pa^{-1}. However, at higher reservoir pressures, this approximation is not reasonable. This leaves much uncertainty around the compressibility of hydrogen in its geological storage, and further experimental work may need to be done in this regard, if compressibility is shown to be a key factor for geomechanical storage hazards.

Chapter 3

Methodology of the ICGT

3.1 Stress and Strain

Stress and strain are computed using the finite element method, according to:

$$\boldsymbol{\sigma} = \boldsymbol{D}(\boldsymbol{\varepsilon} - \boldsymbol{\varepsilon}_0) + \boldsymbol{\sigma}_0, \tag{3.1}$$

where $\boldsymbol{\sigma}$ is the Cauchy stress tensor, $\boldsymbol{D}$ is the linear elastic stiffness matrix, $\boldsymbol{\varepsilon}$ is the infinitesimal strain tensor, $\boldsymbol{\varepsilon}_0$ is the initial strain and $\boldsymbol{\sigma}_0$ is the initial stress [Cook, 2007].

Since the system is in static equilibrium, Cauchy's first law of motion:

$$\nabla \cdot \boldsymbol{\sigma} = -\boldsymbol{F}, \tag{3.2}$$

must be obeyed, where ∇ is the divergence operator and $\boldsymbol{F}$ is a vector of the body forces acting on the system externally, per unit volume.

The Intel Pardiso direct solver is utilised to perform matrix inversion of the accumulated FEM matrix. The rock matrix is assumed to be homogeneous, isotropic, and behave as a linear-elastic medium.

3.2 Matrix Flow, Fault Flow and Rock Deformation

Fluid flow through the bulk rock mass is modelled by combining mass conservation of the flowing fluid with Darcy's law, while neglecting inertial effects. The governing equation is:

$$\operatorname{div}\left(\frac{k_m}{\mu_f}\left(\nabla p_m + \rho_f \mathbf{g}\right)\right) = \left[\alpha \frac{\partial(\operatorname{div}\mathbf{u})}{\partial t} + \left(\phi c_f + \frac{\alpha-\phi}{K_s}\right)\frac{\partial p_m}{\partial t}\right] + \frac{k_m}{\mu_f}\frac{\partial p_m}{\partial \mathrm{n}_c}\delta\left(\mathbf{x}-\mathbf{x}_c\right), \quad (3.3)$$

where the function $\delta(\mathbf{x}-\mathbf{x}_a)$ is the Dirac delta function, with $\mathbf{x}_a$ specifying the position of the fracture, c_f is the fluid compressibility, $\boldsymbol{g}$ is the acceleration due to gravity, k_m is the matrix permeability, K_s is the matrix bulk modulus, n_c is the unit normal pointing outward from the fracture wall, p_m is the fluid pressure within the matrix, t is elapsed time, $\boldsymbol{u}$ is the displacement in the rock matrix, α is the Biot coefficient, ϕ is the matrix porosity, and ρ_f is the fluid density.

Fluid flow through the fault assumes a laminar flow model constructed from lubrication theory. The governing equation is:

$$\nabla \cdot \left(\frac{{a_f}^3}{12\mu_f}\nabla p_f\right) = a_f c_f \frac{\partial p_f}{\partial t} + \frac{\partial a_f}{\partial t} - \frac{k_m}{\mu_f}\frac{\partial p_m}{\partial \mathrm{n}_c}, \quad (3.4)$$

where a_f is the fault aperture, p_f is the pressure in the fracture and μ_f is the fluid viscosity.

Fluid flow in the fault/fractures, fluid flow in the bulk rock mass and poroelastic deformation of the rock mass are concomitantly accounted for by the ICGT. Equation 3.2 is transformed into Equation 3.5, which governs the entire deformation field for a saturated rock mass, by combining effective stress and imposing a boundary traction of hydraulic loading on fault walls, and subsequently integrating over each finite element. The final governing differential equation is thus:

$$\int_\Omega \left[\nabla \cdot \left(\boldsymbol{D}\boldsymbol{\varepsilon} - \alpha p_m \boldsymbol{I}\right) + \boldsymbol{F}\right] d\Omega = \int_{\Gamma_c} p_f n_c d\Gamma, \quad (3.5)$$

where $\boldsymbol{I}$ is the identity matrix of second-order, Γ is the domain boundary, Γ_c is the fracture boundary and Ω is the domain of interest. [Salimzadeh et al., 2017a].

3.3 Friction, Contact and Slip

Faults or fractures are discrete discontinuities in the rock mass, represented by two smooth surfaces that act as the fault/fracture faces. When the two surfaces contact one another, a frictional contact constitutive law governs the boundary conditions on the fault surface. The law is derived from the Amontons-Coulomb first law of friction.

A normal gap function, g_N, detects whether contact between fault/fracture surfaces has occurred and enforces displacement constraints. It describes the perpendicular gap between nodes on the two opposing fault/fracture surfaces (the follower, f, and the leader, l, surfaces):

$$g_N = \left(\boldsymbol{x}^f - \boldsymbol{x}^l\right) \cdot \boldsymbol{n} = \left(\boldsymbol{u}^f - \boldsymbol{u}^l\right) \cdot \boldsymbol{n} - \hat{g}_N, \tag{3.6}$$

where $\boldsymbol{x}$ is a position vector, $\boldsymbol{n}$ is the unit normal vector, $\boldsymbol{u}$ is a displacement vector and $\hat{g}_N$ is a scalar defining the normal gap prior to initial displacement.

Once first contact of the fault/fracture faces occurs, an initial tangential gap vector, $\hat{\boldsymbol{g}}_T$ is defined, which measures the tangential displacement between two matching nodes on the follower and leader surfaces before the point of contact, and is given by $\hat{\boldsymbol{g}}_T = (\boldsymbol{I} - \boldsymbol{n} \otimes \boldsymbol{n})(\boldsymbol{u}^f - \boldsymbol{u}^l)_c$. The tangential gap function, $\boldsymbol{g}_T$, measuring the same phenomenon after the point of initial contact, and referred herein as fault slip, x_n, is defined as:

$$\boldsymbol{g}_T = (\boldsymbol{I} - \boldsymbol{n} \otimes \boldsymbol{n}) \left(\boldsymbol{x}^f - \boldsymbol{x}^l\right) = (\boldsymbol{I} - \boldsymbol{n} \otimes \boldsymbol{n}) \left(\boldsymbol{u}^f - \boldsymbol{u}^l\right) - \hat{\boldsymbol{g}}_T. \tag{3.7}$$

The frictional (tangential) traction, τ, is defined based on one of two potential friction states (stick or slip):

$$\begin{cases} \boldsymbol{g}_T = 0 \text{ and } \frac{\partial \boldsymbol{g}_T}{\partial t} = 0 & \text{if } \tau \leq \mu \left|p\right| + \tau_c \text{ (stick)} \\ \tau = \left(\mu \left|p\right| + \tau_c\right) \frac{\frac{\partial \boldsymbol{g}_T}{\partial t}}{\left|\frac{\partial \boldsymbol{g}_T}{\partial t}\right|} & \text{if } \tau > \mu \left|p\right| + \tau_c \text{ (slip)}, \end{cases} \tag{3.8}$$

where p is the normal traction acting on the fault/fracture surfaces, τ_c is the fault/fracture cohesion and μ is the friction coefficient.

The normal and tangential Kuhn-Tucker inequality contact constraints, which are the boundary conditions on the fault/fractures, are written as follows:

$$g_N \geq 0,\ p \leq 0,\ pg_N = 0 \text{ on } \Gamma_c \times [0,T]\,, \tag{3.9}$$

$$\dot{\gamma} \geq 0,\ |\tau| - (\mu\,|p| + \tau_c) \leq 0,\ \dot{\gamma}\,[|\tau| - (\mu\,|p| + \tau_c)] = 0 \text{ on } \Gamma_c \times [0,T]\,, \tag{3.10}$$

where $\dot{\gamma}$ is the slip rate.

The problem is then solved using a four-stage gap-based double-loop Augmented-Lagrangian algorithm to fully resolve the aperture and traction distribution of the fault where gaps are augmented instead of tractions. The algorithm is described in more detail in Nejati et al. [2016] and Nejati [2015].

3.4 Moment Release and Moment Magnitude

The scalar seismic moment, M_0, is given by:

$$M_0 = \frac{E}{2(1+\nu)} \times A_{rup} \times d_s, \tag{3.11}$$

where E is the Young's modulus, ν is the Poisson's ratio, A_{rup} is the rupture area of the fault and d_s is the average slip across the fault surface. The rupture area is computed as the areal region of the fault surface that experiences significant fault slip above 0.5 mm. For slip below this, the fault is said to be in stick, and the area does not contribute to the A_{rup} term. The first term of the three term product on the right hand side, $\frac{E}{2(1+\nu)}$, is known as the shear modulus, G.

The moment magnitude, M_w, of an event, with M_0 specified in units of Nm, is then computed

as [Bormann et al., 2013, Bormann and Di Giacomo, 2011]:

$$M_w = \frac{2}{3}\log_{10} M_0 - 9.1. \tag{3.12}$$

3.5 Fracture Nucleation and Damage

Fractures are nucleated in regions of the matrix for which the damage surpasses a material-specific threshold. Damage is defined as the degradation in the stiffness of the rock. Microscopic flaws within the rock contribute to the development of a 'damaged zone,' characterised by a localised reduction in rock strength [Boukharouba et al., 2009]. A damage model is therefore suitable for describing fracture nucleation because the process takes place at the microscale, where the rock is stressed beyond its proportional limit. Equation 3.1 is adapted using the Mazars damage model [Mazars, 1984] which accurately replicates quasi-brittle behaviour:

$$\boldsymbol{\sigma} = (1-d)[\boldsymbol{D}(\boldsymbol{\varepsilon} - \boldsymbol{\varepsilon}_0)] + \boldsymbol{\sigma}_0, \tag{3.13}$$

where d is the damage parameter. The damage parameter is computed by computing the equivalent strain, according to:

$$\tilde{\varepsilon} = \|\langle \boldsymbol{\varepsilon} \rangle\|_2^2. \tag{3.14}$$

Fractures will nucleate if the equivalent strain exceeds a critical strain threshold, $\tilde{\varepsilon}_c$, according to:

$$\tilde{\varepsilon} \geq \tilde{\varepsilon}_c, \tag{3.15}$$

where $\tilde{\varepsilon}_c$ is taken as T_0/E, where T_0 is the tensile strength of the rock and E is the Young's modulus of the rock before any damage has occurred.

The damage parameter is a linear combination of compression-based and tension-based damage, if the equivalent strain is in excess of the strain threshold [Paluszny et al., 2020b]:

$$
\begin{aligned}
d = &\left(\sum_{i=1}^{3} \frac{\varepsilon_{ti} \langle \varepsilon_i \rangle}{\tilde{\varepsilon}^2}\right)^b \left(1 - \frac{(1 - A_t)\,\varepsilon_c}{\tilde{\varepsilon}} - A_t e^{-B_t(\tilde{\varepsilon} - \varepsilon_c)}\right) \\
&+ \left(\sum_{i=1}^{3} \frac{\varepsilon_{ci} \langle \varepsilon_i \rangle}{\tilde{\varepsilon}^2}\right)^b \left(1 - \frac{(1 - A_c)\,\varepsilon_c}{\tilde{\varepsilon}} - A_c e^{-B_c(\tilde{\varepsilon} - \varepsilon_c)}\right)
\end{aligned}
\tag{3.16}
$$

where ε_{ti} and ε_{ci} are the tensile and compressive principal strains, respectively, the exponent b is a damping factor with a value of 1.06 [Jirasek, 2011], ε_c is the strain threshold; and A_c, B_c, A_t, and B_t, are material parameters that control the uniaxial stress-strain curves in compression, c, and tension, t, respectively. The approach to damage is detailed further in Saceanu et al. [2022].

3.6 Fracture Growth

Stress Intensity Factors (SIFs) quantify the concentration of stress or energy at fracture tips. The stress state at each location on the fracture tip is fully described by three SIFs which correspond to the three linearly independent crack tip deformation modes: tension (K_I), in-plane shear (K_{II}) and anti-plane tear (K_{III}). The SIFs are calculated at the centre of each tip segment by sampling the surrounding stress and displacement fields. This thesis adopts the Displacement Correlation method to compute the SIFs [Barsoum, 1976]. In this methodology, the crack tip displacement formulae must be satisfied by the displacements of the quarter-point (QPE) nodes given by [Nejati et al., 2015]:

$$
\begin{aligned}
\begin{Bmatrix} u \\ v \end{Bmatrix} &= \frac{K_I}{2G}\sqrt{\frac{r}{2\pi}} \begin{Bmatrix} \left[\kappa - 1 + 2\sin^2\left(\frac{\theta}{2}\right)\right]\cos\left(\frac{\theta}{2}\right) \\ \left[\kappa + 1 - 2\cos^2\left(\frac{\theta}{2}\right)\right]\sin\left(\frac{\theta}{2}\right) \end{Bmatrix} \\
&\quad + \frac{K_{II}}{2G}\sqrt{\frac{r}{2\pi}} \begin{Bmatrix} \left[\kappa + 1 + 2\cos^2\left(\frac{\theta}{2}\right)\right]\sin\left(\frac{\theta}{2}\right) \\ \left[1 - \kappa + 2\sin^2\left(\frac{\theta}{2}\right)\right]\cos\left(\frac{\theta}{2}\right) \end{Bmatrix}, \\
\begin{Bmatrix} w \end{Bmatrix} &= \frac{2K_{III}}{G}\sqrt{\frac{r}{2\pi}} \begin{Bmatrix} \sin\left(\frac{\theta}{2}\right) \end{Bmatrix}
\end{aligned}
\tag{3.17}
$$

where ν is Poisson's ratio, E is the Young's modulus, $G = E/2(1+\nu)$ is the shear modulus, and $\kappa = 3$ - 4ν is the Kolosov constant. The method generates excellent approximations to the SIFs (to within 2-3% error, Nejati et al. [2015]) and is very inexpensive computationally [Burtonshaw et al., 2021]. Once the SIFs have been computed from Equation 3.17, the independent components of the stress tensor representing the stress field near the crack tip is given by [Nejati et al., 2015]:

$$\begin{aligned}
\begin{Bmatrix} \sigma_{xx} \\ \sigma_{yy} \\ \sigma_{xy} \\ \sigma_{zz} \end{Bmatrix} &= \frac{K_I}{\sqrt{2\pi r}} \begin{Bmatrix} \cos\left[\frac{\theta}{2}\left(1 - \sin\left(\frac{\theta}{2}\right)\sin\left(\frac{3\theta}{2}\right)\right)\right] \\ \cos\left[\frac{\theta}{2}\left(1 + \sin\left(\frac{\theta}{2}\right)\sin\left(\frac{3\theta}{2}\right)\right)\right] \\ \cos\left(\frac{\theta}{2}\right)\sin\left(\frac{\theta}{2}\right)\cos\left(\frac{3\theta}{2}\right) \\ 2\nu\cos\left(\frac{\theta}{2}\right) \end{Bmatrix} \\
&+ \frac{K_{II}}{\sqrt{2\pi r}} \begin{Bmatrix} \sin\left[\frac{\theta}{2}\left(-2 - \cos\left(\frac{\theta}{2}\right)\cos\left(\frac{3\theta}{2}\right)\right)\right] \\ \sin\left(\frac{\theta}{2}\right)\cos\left(\frac{\theta}{2}\right)\cos\left(\frac{3\theta}{2}\right) \\ \cos\left[\frac{\theta}{2}\left(1 - \sin\left(\frac{\theta}{2}\right)\sin\left(\frac{3\theta}{2}\right)\right)\right] \\ -2\nu\sin\left(\frac{\theta}{2}\right) \end{Bmatrix}, \\
\begin{Bmatrix} \sigma_{xz} \\ \sigma_{yz} \end{Bmatrix} &= \frac{K_{III}}{\sqrt{2\pi r}} \begin{Bmatrix} -\sin\left(\frac{\theta}{2}\right) \\ \cos\left(\frac{\theta}{2}\right) \end{Bmatrix}
\end{aligned} \tag{3.18}$$

where r and θ are polar coordinates describing the location of the centre-point of the element of interest within the finite element mesh from the crack tip. The magnitude of the vector connecting these two points is given by r and the orientation of the vector from the fracture plane in the anticlockwise direction is given by θ.

The Richard mixed mode failure criterion governs fracture propagation [Richard et al., 2014]. This criterion represents a combined response to all three deformation modes. An intact region of rock will fail, and a fracture will propagate, when the comparative stress intensity factor, K_v, exceeds (or equals) the local critical SIF of the rock, K_{IC}. The Richard failure criterion is

$$K_v = \frac{K_I}{2} + \frac{1}{2}\sqrt{K_I^2 + 4(\alpha_1 K_{II})^2 + 4(\alpha_2 K_{III})^2} \geq K_{IC}, \tag{3.19}$$

where α_1 and α_2 are calculated as $\alpha_1 = K_{IC}/K_{IIC}$ and $\alpha_2 = K_{IC}/K_{IIIC}$ respectively. K_{IC},

K_{IIC}, and K_{IIIC} are the mode I, II and III fracture toughness respectively. Once the stress intensity factors are computed, a set of growth vectors are approximated, which inform a change of geometry of the system.

If the Richard propagation failure criterion is satisfied, then the angle of the subsequent propagation vector is computed. The in-plane angle of propagation, known as the fracture deflection angle [Thomas et al., 2020a], φ, is given by:

$$\varphi = \mp \left[A \frac{|K_{II}|}{K_I + |K_{II}| + |K_{III}|} + B \left(\frac{|K_{II}|}{K_I + |K_{II}| + |K_{III}|} \right)^2 \right], \tag{3.20}$$

where A = 140° and B = -70° The approach to fracture growth is detailed further in Thomas et al. [2020a] and Thomas et al. [2020b].

3.7 Fracture Extension

Once the Richard failure criterion specified in Equation 3.19 has been achieved, and the fracture deflection angle has been computed according to Equation 3.20, the extension length, which governs the quasi-static propagation of the fracture, for each node on each of the fracture tips must be computed. It is important that this is computed on a node-by-node basis because in order to replicate crack patterns from physical experiments, the entire crack front cannot grow at one uniform velocity [Renshaw and Pollard, 1994]. Local variations in stress are known to occur due to fracture interaction effects [Thomas et al., 2017] and thus it is critical that the fracture growth is not enforced to be uniform everywhere on the tip otherwise such effects would be masked. Fatigue fracture growth adheres to the Paris-type criterion in a power-law formulation [Pugno et al., 2006]:

$$\frac{\mathrm{d}a}{\mathrm{d}N} = c \left(\frac{G}{G_{max}} \right)^{\beta}, \tag{3.21}$$

which assesses the progression of a fracture tip over successive load cycles, where a is the magnitude of the crack advance, N is the number of load cycles, c is a material specific constant, G is the Irwin energy release rate at a given tip, G_{max} is the maximum Irwin energy release

rate at any point on any of the fractures in the domain and β is the fracture growth rate exponent. According to this criterion, the expansion of a fracture front is directly related to the Irwin energy release rate at each point along the fracture. Consequently, the point experiencing the highest energy release rate exhibits the fastest growth, while other points expand at comparatively slower rates. For domains containing numerous three-dimensional fractures such as that herein, Equation 3.21 is adapted and decomposed to form a two-stage Paris-type law governing the fracture extension [Thomas et al., 2020b]:

$$\Delta a_f = \Delta a_v \left(\frac{G_f}{G_{max}} \right)^{\beta_f} \tag{3.22}$$

$$\Delta a_n = \Delta a_f \left(\frac{G_n}{G_f} \right)^{\beta_n}. \tag{3.23}$$

In this treatment, two values of β are used rather than one (β_f, the fracture growth rate exponent and, β_n, the tip growth rate exponent). In each growth step, a maximum extension length at any node on any fracture, Δa_v, is chosen. The maximum Irwin energy release rate, G_n of any node, n, on a given fracture, f, is given by G_f. The maximum extension length of a given fracture, Δa_f, is then a result of the chosen Δa_v and the accumulation of energy at the fracture tip. This Δa_f value is then inputted into the second step to compute the local tip extension of a given node, Δa_n. Therefore, the constraint $\Delta a_n \leq \Delta a_f \leq \Delta a_v$ is always obeyed. Laboratory experiments and outcrop observations in brittle rocks showed that β_f is approximately equal to 0.35 [Renshaw and Pollard, 1994].

3.8 Permeability

The upper and lower bounds on the actual effective permeability, k_{eff}, of fractured rock masses are described by the classical Hashin-Shtrikman bounds [Hashin and Shtrikman, 1962]:

$$k_m + \frac{3k_m \left(k_f - k_m\right) \phi_f}{3k_m + \left(k_f - k_m\right)\left(1 - \phi_f\right)} \leq k_{eff} \leq k_f - \frac{3k_f \left(k_f - k_m\right)\left(1 - \phi_f\right)}{3k_f - \left(k_f - k_m\right)\phi_f}, \tag{3.24}$$

where k_f is the fracture permeability and ϕ_f is the fracture volume fraction. Provided that the matrix permeability is far smaller than the fracture permeability and that the fracture volume fraction is far less than one, then Equation 3.24 reduces to [Zimmerman and Paluszny, 2023]:

$$k_m \leq k_{eff} \leq k_m + \frac{2k_f\phi_f}{3} = k_m + k_s, \tag{3.25}$$

where k_s is the Snow permeability [Snow, 1969] given by $\frac{2k_f\phi_f}{3}$. Physically, Equation 3.25 tells us that the effective permeability of a fractured rock mass must be above the matrix permeability, which would be the permeability of an entirely unfractured rock (k_m), and that the effective permeability must be below the sum of the permeabilities of the unfractured rock and the sole permeability of an infinite set of fractures (k_s). Other bounds for effective permeability exist but the Hashin-Shtrikman bounds are considered superior because they are at least as strict as other bounds such as the Wiener bounds [Wiener, 1912]. The permeability of each individual fracture, k_f is described by the cubic law [Zimmerman and Bodvarsson, 1996] which states that $k_f = h^2/12$ where h is the fracture aperture denoted by g_N in this work as described in Section 3.3. Once each fractures permeability and each fractures volume fraction is computed, the product of a total representative fracture permeability, $k_{f,Total}$, and total representative fracture volume fraction, $\phi_{f,Total}$, is computed according to:

$$k_{f,Total}\phi_{f,Total} = \sum_{i=1}^{n_f} k_{f,i}\phi_{f,i}, \tag{3.26}$$

where n_f denotes the total number of fractures in the domain. The total representative fracture permeability-fracture volume fraction product, $k_{f,Total}\phi_{f,Total}$ is then substituted into Equation 3.25 as $k_f\phi_f$.

The effective permeability computed in this work, $k_m + k_s$, assumes that the fractures are through-going, and that the domain is completely interconnected and flow is percolating. Many of the geomechanically grown fracture sets shown in this thesis are below the percolation threshold. In such cases, the resulting equivalent permeability will be only slightly higher than the matrix permeability. Therefore, the effective permeability results in this thesis represent the worst-case scenario in which all the fractures are through-going.

The equivalent permeability of the caprock is calculated using the method of Lang et al. [2014]. The Laplace problem models the flow of an incompressible fluid:

$$\nabla \cdot (k^e \nabla p) = 0, \tag{3.27}$$

where k^e is the element permeability, ∇p is the pressure gradient and ∇ is the divergence operator. For fracture surface elements, the assigned permeability is equal to the fracture permeability computed from the cubic law [Zimmerman and Bodvarsson, 1996] and for matrix volumetric elements, a fixed value (1×10^{-21} m^2 for the default shale caprock) is used. After the pressure field has been solved for, the barycentric velocity of a given element, $\mathbf{v^e}$, is computed by Darcy's Law:

$$\mathbf{v^e} = -\frac{k^e}{\mu_f}\boldsymbol{\nabla} p^e, \tag{3.28}$$

where p^e is the element pressure. Subsequently, Darcy's law can be applied:

$$\mathbf{v} = -\frac{\mathbf{k}}{\mu_f}\nabla p, \tag{3.29}$$

where $\mathbf{k}$ is the equivalent permeability tensor, consisting of eigenvalues k_1, k_2, and k_3, $\mathbf{v}$ is the Darcy velocity and μ_f is the viscosity. The following volume-weighted element averages for the fluxes ($\langle v_i \rangle$) and pressure gradients ($\left\langle \frac{\partial p}{\partial x_i} \right\rangle$) along the three coordinate axes ($i = x,y,z$) :

$$\langle v_i \rangle = \frac{1}{V_\Omega} \sum_e \int_{V_e} v_i^e dV_e, \tag{3.30}$$

$$\left\langle \frac{\partial p}{\partial x_i} \right\rangle = \frac{1}{V_\Omega} \sum_e, \int_{V_e} \frac{\partial p^e}{\partial x_i} dV_e \tag{3.31}$$

are then substituted into Equation 3.29 to compute the equivalent permeability tensor. The nomenclature in Equations 3.30 and 3.31 is as follows: V_Ω is the domain volume, V_e is the volume of finite element, e, and $\frac{\partial p^e}{\partial x_i}$ is the pressure gradient of element e in direction i.

In matrix form, the equation to be solved is written as:

$$\begin{bmatrix} \begin{bmatrix} \left\langle \frac{\partial p}{\partial x} \right\rangle^x & \left\langle \frac{\partial p}{\partial y} \right\rangle^x & \left\langle \frac{\partial p}{\partial z} \right\rangle^x \\ 0 & 0 & 0 \\ 0 & 0 & 0 \end{bmatrix} & \begin{bmatrix} 0 & 0 & 0 \\ \left\langle \frac{\partial p}{\partial x} \right\rangle^x & \left\langle \frac{\partial p}{\partial y} \right\rangle^x & \left\langle \frac{\partial p}{\partial z} \right\rangle^x \\ 0 & 0 & 0 \end{bmatrix} & \begin{bmatrix} 0 & 0 & 0 \\ 0 & 0 & 0 \\ \left\langle \frac{\partial p}{\partial x} \right\rangle^x & \left\langle \frac{\partial p}{\partial y} \right\rangle^x & \left\langle \frac{\partial p}{\partial z} \right\rangle^x \end{bmatrix} \\ \begin{bmatrix} \left\langle \frac{\partial p}{\partial x} \right\rangle^y & \left\langle \frac{\partial p}{\partial y} \right\rangle^y & \left\langle \frac{\partial p}{\partial z} \right\rangle^y \\ 0 & 0 & 0 \\ 0 & 0 & 0 \end{bmatrix} & \begin{bmatrix} 0 & 0 & 0 \\ \left\langle \frac{\partial p}{\partial x} \right\rangle^y & \left\langle \frac{\partial p}{\partial y} \right\rangle^y & \left\langle \frac{\partial p}{\partial z} \right\rangle^y \\ 0 & 0 & 0 \end{bmatrix} & \begin{bmatrix} 0 & 0 & 0 \\ 0 & 0 & 0 \\ \left\langle \frac{\partial p}{\partial x} \right\rangle^y & \left\langle \frac{\partial p}{\partial y} \right\rangle^y & \left\langle \frac{\partial p}{\partial z} \right\rangle^y \end{bmatrix} \\ \begin{bmatrix} \left\langle \frac{\partial p}{\partial x} \right\rangle^z & \left\langle \frac{\partial p}{\partial y} \right\rangle^z & \left\langle \frac{\partial p}{\partial z} \right\rangle^z \\ 0 & 0 & 0 \\ 0 & 0 & 0 \end{bmatrix} & \begin{bmatrix} 0 & 0 & 0 \\ \left\langle \frac{\partial p}{\partial x} \right\rangle^z & \left\langle \frac{\partial p}{\partial y} \right\rangle^z & \left\langle \frac{\partial p}{\partial z} \right\rangle^z \\ 0 & 0 & 0 \end{bmatrix} & \begin{bmatrix} 0 & 0 & 0 \\ 0 & 0 & 0 \\ \left\langle \frac{\partial p}{\partial x} \right\rangle^z & \left\langle \frac{\partial p}{\partial y} \right\rangle^z & \left\langle \frac{\partial p}{\partial z} \right\rangle^z \end{bmatrix} \\ \begin{bmatrix} 0 & 1 & 0 \\ 0 & 0 & 1 \\ 0 & 0 & 0 \end{bmatrix} & \begin{bmatrix} -1 & 0 & 0 \\ 0 & 0 & 0 \\ 0 & 0 & 1 \end{bmatrix} & \begin{bmatrix} 0 & 0 & 0 \\ -1 & 0 & 0 \\ 0 & -1 & 0 \end{bmatrix} \end{bmatrix} \begin{bmatrix} k_{xx} \\ k_{xy} \\ k_{xz} \\ k_{yx} \\ k_{yy} \\ k_{yz} \\ k_{zx} \\ k_{zy} \\ k_{zz} \end{bmatrix} = \begin{bmatrix} \langle v_x \rangle^x \\ \langle v_y \rangle^x \\ \langle v_z \rangle^x \\ \langle v_x \rangle^y \\ \langle v_y \rangle^y \\ \langle v_z \rangle^y \\ \langle v_x \rangle^z \\ \langle v_y \rangle^z \\ \langle v_z \rangle^z \\ 0 \\ 0 \\ 0 \end{bmatrix} \tag{3.32}$$

where x, y and z are the coordinate axes.

Chapter 4

Effect of Mechanical, Fluid, Crack and Operational Properties on Mechanical and Hydraulic Caprock Integrity during UHS

4.1 Introduction

The successful storage of hydrogen within a subsurface reservoir requires an overlying sealing unit. This sealing unit must be of low permeability, typically less than 10^{-18} m^2 [Kivi et al., 2022], and mechanically stable to ensure the integrity of the entire storage system. Mudstones/shales [Jia et al., 2023, Wang et al., 2024c], cemented or tight sandstones/siltstones [Tibane et al., 2021, Fischer et al., 2013], halites [Abdel-Azeim et al., 2023], anhydrites [Kirkland, 2024, Jalalifar et al., 2021, Liao et al., 2020] and some chalks [Zhang et al., 2017] constitute most caprocks due to their low permeabilities. The caprock must also be resistant to deformation: minimizing new damage and fracture growth and either containing few major faults or being insusceptible to the reactivation and growth of pre-existing faults and fractures contained within it [Paluszny et al., 2017]. If the caprock is either hydraulically or mechanically compro-

mised, then stored hydrogen can escape and leak into the overburden [Newell and Martinez, 2020], resulting in potentially serious economic, social, and operational consequences. In a future energy mix, in which hydrogen constitutes a significant proportion [Capurso et al., 2022, Burtonshaw et al., 2024a], loss of hydrogen may result in energy supply shortages that cannot easily be mitigated without the use of emergency fossil fuels. Large losses of hydrogen may result in a loss of reservoir pressure, which may reduce well productivity during withdrawal periods, again resulting in energy supply shortages. Furthermore, unlike hydrocarbons which are naturally occurring, green hydrogen must be synthesised at the surface with an associated financial cost [Burtonshaw et al., 2024b]. Hydrogen does occur naturally, but these deposits are not currently exploited, at not least beyond the pilot scale (i.e., Whitcombe et al. [2024]), and the economics and logistics of their exploitation is not well understood [Truche and Bazarkina, 2019]. The loss of significant percentages of stored hydrogen, which cannot later be sold, could lead to significant economic losses for businesses. Potential social issues surrounding caprock integrity may also arise. If the caprock fails in an onshore system, and hydrogen leaks from the storage reservoir into overlying units, then aquifers may become contaminated with hydrogen and remnant natural gas. Although, gaseous hydrogen is largely insoluble in water [Wiebe and Gaddy, 1934], chemical treatment costs for separation will be incurred that previously did not exist, and further treatment infrastructure would need to be constructed. The public may become agitated with the concept of hydrogen or natural gas having contacted their drinking water, risking the loss of a social license to operate as observed with minor induced seismicity during hydraulic fracturing in the United Kingdom [Kettlety and Verdon, 2021, Cao et al., 2022, Cotton, 2017]. Furthermore, caprock integrity and well integrity are critical with hydrogen storage relative to other geo-energy storage types, because hydrogen has NFPA 704's highest rating of 4 on the flammability scale [Cavaliere, 2023]. Ignition is possible with a hydrogen-to-air volumetric ratio of as low as 0.04 [Le et al., 2023]. Therefore, if hydrogen leaks all the way to surface, explosions could occur which could be catastrophic onshore.

Depleted oil and gas fields are strong candidates for geological hydrogen storage, because they have proven over million-year time scales to have contained hydrocarbons without major leakages. However, the introduction of a foreign fluid into the subsurface, together with short-time

scale cycling of reservoir pressure, may perturb caprock stresses, induce new fractures, and re-activate faults, leading to a loss of mechanical integrity. Very low density fluids, of less than 10 kg/m^3 [Heinemann et al., 2021] density, such as hydrogen, have never been stored in porous media [Burtonshaw et al., 2024a]. Large buoyancy forces may develop from the storage of such a fluid, exerting large stresses on the underside of the caprock, that could encourage greater fracture growth or greater opening of fracture apertures relative to other geo-energy storage technologies.

Hydrogen may be lost through the caprock via two main mechanisms: (1) loss of mechanical integrity of the caprock, wherein fractures nucleate and grow in the caprock to such an extent that they eventually fully penetrate the height of the caprock and as such provide a very high permeability, direct leakage pathway from the storage reservoir to the overburden. (2) Loss of hydraulic integrity of the caprock, in which the spatially widespread nucleation and growth of smaller-scale fractures increases the permeability of the caprock without enabling direct physical communication between the storage reservoir and the overburden unit. In this case, the increased permeability may potentially be sufficient for hydrogen to flow from reservoir to overburden over reasonably short time-scales.

Caprock integrity has been examined through a variety of modelling procedures and numerical methods for the case of gaseous CO_2 injection and storage without withdrawal [Paluszny et al., 2020a]. Most studies examine caprock integrity by comparing overpressure with a threshold fracture pressure. Some studies assess caprock integrity by accounting for fracture growth either through implicit [McDermott et al., 2016, Akhurst et al., 2017, Gor et al., 2013a, Gor and Prévost, 2013, Gor et al., 2013b, Orlic et al., 2011, Pourtoy et al., 2013] or explicit fracturing models [Paluszny et al., 2017, Salimzadeh et al., 2018]. Implicit fracturing models do not explicitly represent fractures as discrete entities in the computational mesh but rather, the model captures the effects of fracture propagation through modifications to the properties of the surrounding rock matrix. These modifications occur due to changes in the stress and strain fields within the reservoir during the injection, and the model implicitly accounts for the creation and growth of fractures based on predefined criteria relative to these changes in stress and strain. Implicit fracturing methods are computationally efficient and are often used

in large-scale reservoir simulations where detailed modelling of individual fractures may not be feasible. In explicit fracturing models, fractures are represented as discrete entities within the computational mesh. They are defined by their orientation, length/radius, aperture and permeability. These models track the evolution of each fracture individually, simulating their initiation, growth, and interaction with other fractures and the reservoir matrix based on direct physical laws of fracture mechanics. Explicit fracturing methods provide a high level of detail and accuracy in capturing fracture behavior but are computationally more intensive compared to implicit methods. Explicit fracturing models for CO_2 caprock integrity studies are rare and are restricted to those of Paluszny et al. [2017] and Salimzadeh et al. [2018].

Some studies examine caprock integrity by computing fracture permeabilities, and thus effective caprock permeability [Iding and Ringrose, 2010], but in order to be accurate these require fully-coupled and temporal explicit fracturing models, which are already limited within the storage integrity literature. In order to compute fracture permeability accurately, fracture apertures cannot be kept constant as in many fracture growth studies (i.e., Iding and Ringrose [2010]), but rather must geomechanically evolve throughout the simulation. No previous study involving any fluid has studied permeability alteration in an explicit fracturing model with geomechanical evolution of the fracture aperture. It is important to assess permeability alteration because the occurrence of new tensile fracturing within the caprock does not automatically signify the existence of a pathway for fluid flow. For growth to translate to containment loss, the effective permeability of the caprock must be enhanced significantly. It is important to utilise 3D models for such studies because 3D predictions of growth and resultant effective permeability are known to deviate substantially from 2D equivalents [Lang et al., 2014]. Previous 2D and 3D fracture growth studies have suggested that accounting for mechanically realistic apertures may result in a lower predicted permeability [Paluszny and Matthai, 2010, Thomas et al., 2020b] and in 3D, fractures can geomechanically interact such that the opening of fracture apertures may be constrained by the shadow zone of neighbouring fractures [Salimzadeh et al., 2017b, Thomas et al., 2017], leading to a further reduction in the permeability of the system than otherwise predicted.

Numerical methods used to study caprock integrity with thermohydromechanical coupling and

fracture growth include the Finite Element Method (FEM), Integral Finite Difference Method (IFD), Finite Difference Method (FDM), and the Finite Volume Method [Paluszny et al., 2017]. These studies either have full thermohydromechanical coupling, one-way thermohydromechanical coupling, or iterative thermohydromechanical coupling. Discrete Element Method (DEM) and Boundary Element Method (BEM) are less commonly implemented in this field of work because generating and maintaining a suitable mesh for such methods can be challenging, especially when dealing with complex geometries and evolving fracture networks at the very large scale. Furthermore, whereas DEM and BEM can incorporate mechanical interactions, their capability to seamlessly integrate thermohydraulic and mechanical processes are limited. This coupling is crucial for accurately modelling the behaviour of caprock under the influence of thermal, hydraulic, and mechanical stresses. Methods such as DEM and BEM are computationally expensive, especially when simulating large-scale problems with complex geometries and material properties. Caprock integrity studies often require simulations spanning significant spatial and temporal scales, making DEM and BEM impractical due to their high computational demands.

Few documented cases of caprock failure or caprock-induced fluid leakage exist within porous media such as depleted oil fields, depleted gas fields and aquifers. Notably, that of (1) the In Salah CO_2 sequestration project and (2) the Joslyn Creek bitumen reservoir. The use of the term 'caprock-induced fluid leakage' highlights that this does not include fluid leakage spatially past the caprock via wellbore integrity issues, as this work is concerned with the geomechanical integrity of the caprock only.

The lower 200 m portion of the caprock of the Krechba field, which is the storage system at the In Salah CO_2 project in Algeria, experienced damage during the injection of supercritical CO_2 [White et al., 2014b]. The main hypothesis is that the injectant fluid pressure exceeded the fracture pressure of the caprock. Leak-off tests, formation integrity tests and step-rate tests were performed. The fracture gradient of the caprock, which is a measure of the mud pressure required to induce fractures in the rock at a certain depth, was found to be within the range 1.35 - 1.70 sg where sg is specific gravity (equivalent mud weight), with 1 sg = 0.1 bar/m. Bottom-hole pressure data suggest that between November 2005 and September

2006, the maximal potential fracture gradient of 1.70 sg was exceeded. In February 2006, a double-lobe uplift pattern appeared on the InSAR satellite surface deformation maps. This was considered abnormal because reservoir pressurisation should be somewhat homogeneous leading to elliptical uplift patterns, unless the reservoir had strong permeability heterogeneity, which was disproved. Dilating vertical cracks in an elastic half space are known to induce trough-like uplifts at the ground surface, and this supports the idea that new hydrofractures were induced in the caprock and then dilated on pressurisation from escaped CO_2. Therefore, it was concluded that CO_2 escaped the reservoir unit and entered the lower caprock. Nevertheless, full caprock integrity was not compromised because the main 900 m carboniferous Visean mudstone caprock overlying the lower caprock was mechanically undamaged and thus, CO_2 is presumed not to have leaked into the overburden or to surface.

Fluid leakage to the surface through the caprock did occur at the Josyln Creek oil sands bitumen reservoir in Alberta, Canada operated by Total SA, after a catastrophic failure of the Clearwater caprock on May 18th 2006 [Carlson, 2012]. In this project, Steam-Assisted-Gravity-Drainage (SAGD) was implemented as an Enhanced Oil Recovery (EOR) technology to volatilise the bitumen, which is too deep to be mineable, enabling it to flow to a horizontal extraction well underlying the horizontal injection well via gravity. Although little geomechanical literature exists on the incident, Carlson [2012] suggests that when hot steam was pumped into the injection well, well geysering occurred due to pockets of gas forming within the remnant cold water condensate as it was heated, leading to very high pressure transients associated with the phase change and resulting in a fracture through the caprock to the surface. According to an article in the 'Oil & Gas Journal' website on May 30th 2014 entitled 'Total suspends work on Joslyn SAGD oil sands project,' the caprock breach affected a 125 m $\times$ 75 m areal region and the released steam caused rock projectiles to be launched as high as 300 m above the surface crater and produced a 1 km dust plume. As a result, production from the reservoir was terminated indefinitely in May 2014, and the $11 billion USD project was abandoned. This mechanistic caprock failure is unlikely to occur in geological hydrogen storage because (1) hydrogen is not expected to exhibit phase changes because it needs to be cooled to less than -235°C to become a liquid (at any pressure) and (2) injection and extraction wells are

likely to be vertical, not horizontal, so vertical fractures are not expected to emanate from the wellbore. Nevertheless, this case highlights the seriousness of potential caprock failure and why it is important to study prior to commercialisation of hydrogen storage in depleted gas fields.

In this chapter, the Imperial College Geomechanics Toolkit (ICGT) is utilised to assess the hydraulic and mechanical integrity of caprocks during the injection, storage and withdrawal of gaseous hydrogen. A field-scale 4000×4000×3300 m model of a generic North Sea depleted gas field comprising of an overburden, 100 m thick shale caprock, reservoir and underburden is designed to perform the study. An initial 5×5 array of pre-existing natural fractures is initialized in the centre of the caprock and the explicit growth of such fractures is computed over a period of many years. The evolution of the effective permeability of the fractured caprock region is computed over the entire storage period to assess the hydraulic integrity of the caprock through time. A series of parametric studies are performed to assess the impact of fracture and mechanical properties on the fracture growth and caprock permeability, revealing which properties exacerbate or minimise loss of hydraulic integrity. Furthermore, a number of shorter simulations are performed to assess the impact of caprock properties on the nucleation of new fractures in the caprock.

4.2 Literature Review

This section reviews previous work examining the mechanical, chemical and hydraulic integrity of caprocks during hydrogen injection and the mechanical integrity of caprocks during the storage of other geo-energy fluids such as CO_2. Whilst previous studies examining the mechanical integrity of the caprock and reservoir rock in geological porous media during the injection of hydrogen gas are minimal (Section 4.2.1), some similar studies have been performed for the injection of supercritical and liquid carbon dioxide (Section 4.2.4). Table 4.1 summarises many more caprock mechanical, chemical or hydraulic integrity studies during hydrogen or carbon dioxide storage.

4.2.1 Mechanical Caprock Integrity during Hydrogen Storage

Bai and Tahmasebi [2022] conducted one of only three prior studies that have directly examined the mechanical integrity of the caprock during the geological storage of hydrogen. However, this was modelled for a specific saline aquifer (Powder River Basin, Wyoming, USA) and not a depleted oil and gas field. They construct a 3-D Mechanical Earth Model of size approximately 24,000×26,000×6000 m^3 based from petrophysical, geometrical and geomechanical data taken from the CarbonSAFE project. Simulations are believed to have been performed in the commercial software Petrel [Nemes, 2023] and contain over 475,000 grid cells. The caprock is an impermeable shale and the reservoir unit is initially saturated with brine at hydrostatic equilibrium. Cushion hydrogen gas is first injected for two years at a rate of 120,000 m^3/d, followed by three years of hydrogen injection-extraction cycles. Each year of operation is sub-divided into a 243-day injection period at a rate of 300,000 m^3/d, followed by a 122-day extraction period. They studied the integrity of both the target formation and the caprock in terms of the Mohr-Coulomb criterion and found that for three injection-extraction cycles both the reservoir rock and caprock were mechanically stable. After each extraction stage, the reservoir pressure is reduced resulting in increased effective stress, shifting the Mohr-Coulomb envelope further to the right and enhancing mechanical stability. After each injection stage, the reservoir pressure increased, resulting in reduced effective stress, shifting the Mohr-Coulomb envelope further to the left, and reducing mechanical stability. With each subsequent injection-extraction cycle, the Mohr-Coulomb envelope moved closer to the failure line. Whilst both lithologies were stable after three cycles, the trend could imply that with years or decades of injection-extraction cycles, the Mohr-Coulomb failure line may finally be intersected, especially in the reservoir rock. They found that the caprock is more likely to remain stable because the translation of the Mohr's circle to the left is extremely small with each injection-extraction cycle, owing to the poor hydraulic connectivity between the high permeability reservoir and low permeability caprock. Thus, the pore pressure increase in the caprock is likely small and therefore, so is reduction in effective stress.

This work is limited by no inclusion of pre-existing faults, fractures and discontinuities in

any of the rock units. Caprocks, especially those comprised of shale, of depleted oil and gas fields are often fractured media [Rutqvist and Tsang, 2002, Lavrov, 2016, Dewhurst et al., 2018, Gheibi et al., 2018, Antropov et al., 2017, Kolawole et al., 2021]. The existence of pre-existing planes of weakness would make failure more favourable relative to a non-fractured rock. Furthermore, as a result of excluding pre-existing cracks, the work does not quantify how caprock permeability changes through time. The caprock may maintain overall mechanical integrity (no development of major faults), but deformation and growth of existing cracks may enhance caprock permeability such that the hydraulic integrity of the reservoir rock is compromised and leakage to the caprock occurs. This could reduce reservoir pressures such that the natural pressure drive to the wellbores from the reservoir during hydrogen extraction is significantly reduced impacting hydrogen production flow rates and total extractable volumes.

Laalam et al. [2023] injected and withdrew gaseous hydrogen from their numerical model of the Inyan Kara formation, a primarily sandstone and siltstone reservoir containing small amounts of shale and coal in North Dakota, USA, that is now used for wastewater disposal. Their model was 3-D and constructed using the FEM CMG-Builder software. Only one injection-withdrawal annual cycle is simulated. They assess the changes in effective stress in terms of the Mohr-Coulomb diagram and found that changes in effective stress state in the caprock are minimal and the Mohr's circle remains very distant from the Mohr-Coulomb failure envelope. Therefore, the caprock should remain mechanically stable.

Tenthorey et al. [2024] used a preliminary model of the Otway International Test Centre (OITC) depleted gas reservoir in Australia, where future geological hydrogen storage may potentially occur. Various gases (i.e. hydrogen, methane, and carbon dioxide) were injected for six months and withdrawn for six months over a period of ten years in separate simulations. A one-way coupled approach was implemented, whereby pressure and temperature are computed at particular time steps by a reservoir simulator and a separate geomechanical simulator computed the stress and strains at those steps. Therefore, the induced changes in stress and strain do not impact the pressure and temperature. They found that hydrogen has much less thermal impact on the reservoir and caprock, in terms of temperature magnitude and spatial extent, than methane and carbon dioxide. For example, for the same rock thermal conductivities and

specific heat capacities, when hydrogen was injected and withdrawn from the reservoir for ten annual cycles, the altered temperature plume covers a distance of 96 m from the injection wellbore with a maximum temperature discrepancy from the original temperature of 20 °C. For the simulation, where carbon dioxide was injected and withdrawn instead, the altered temperature plume covers a distance from the injection wellbore four times as large as in the hydrogen simulations, with a maximum temperature discrepancy from the original temperature of 55°C. Thus, temperature effects on caprock integrity are much less likely during hydrogen storage than during carbon dioxide storage and natural gas production. When the thermal conductivity of the caprock was reduced from 4.5 W m^{-1} K^{-1} to 0.65 W m^{-1} K^{-1} and the specific heat capacity of the caprock was increased from 1800 kJ m^{-3} K^{-1} to 3500 kJ m^{-3} K^{-1}, the plume of altered temperature decreased even further to a lateral extent of just 71 m from the injection well, showing that temperature effects during hydrogen storage can be reduced even further depending on the rock thermal properties. Furthermore, they report the fracture pressure as a function of depth from simulations for all three fluids. They found that the fracture pressure drops below the bottomhole borehole pressure by the largest amount for CO_2, then CH_4 and then H_2. The average fracture pressure, which is a quantity measuring the pressure required to induce fractures or cracks in a rock formation, were 6.75 lbs/gallon, 8.00 lbs/gallon and 9.70 lbs/gallon in the CO_2, CH_4 and H_2 cases respectively, suggesting that caprock fracturing is less likely during hydrogen storage relative to other geo-energy activities.

However, a simple comparison of fracture pressures may not be sufficient to fully quantify caprock integrity. Injection rate and fluid viscosity can have significant effects on fracture interactions [Burtonshaw et al., 2021, Ishida et al., 2004, Stanchits et al., 2014]. Burtonshaw et al. [2021] performed a study where the stress interaction between natural and hydraulic fractures was examined during the injection of hydraulic fracturing fluid into a model of the Longmaxi shale, Sichuan Basin, China. They found that higher injection rates and higher viscosities will maximise tensile failure and the balance of tensile-to-shear effects on the fractures. This results in wider fractures which enhances the rock permeability. Furthermore, they found that mode III tear failure of the fractures is enhanced when viscosity and injection rate are high, which enhances fracture connectivity by diverting the fracture plane from its original path. Therefore,

the very low viscosity of hydrogen may assist in limiting fracture tensile failure and interconnectivity and thus limit permeability increase of the caprock. However, the very high injection rates that are needed in hydrogen storage relative to CO_2 storage and natural gas production would act to enhance tensile failure and mode III tear failure, thus potentially optimising the conditions for enhanced caprock permeability. Tenthorey et al. [2024] used the same injection rate when varying the fluid between CH_4, CO_2 and H_2, whereas realistically in hydrogen storage the injection rate in H_2 storage may need to be up to two orders of magnitude larger or perhaps even more.

4.2.2 Chemical Caprock Integrity during Hydrogen Storage

Using the United States Geological Survey's PHREEQC geochemical software, Zeng et al. [2023] found that the caprock is likely to have strong chemical integrity during hydrogen storage, with the geochemical interactions between hydrogen, brine and shale only affecting a few metres of caprock directly above the reservoir unit, implying that even relatively thin shale caprocks of tens of metres will still remain a chemical seal. Three shale samples of Ordovician age from the Canning Basin, Western Australia with different mineralogical compositions (calcareous, argillaceous and sillaceous shale) were selected for testing. The highest dissolution of any mineral by volume, over a 30 year storage period, was less than 1% implying the caprock will remain chemically stable. Furthermore, loss of hydrogen via chemical reactions with the CO_3^{2-}, HCO_3^- or SO_4^{2-} in the caprock was found to be insignificant with less than 0.2% hydrogen loss due to redox reduction from H_2 to CH_4/H_2S.

However, Bensing et al. [2022] conducted tests on Jurassic claystone samples from Untersturmig, Germany, in which the samples were treated with a brine-H_2 mixture, in which the brine was NaCl at 10 wt%. Subsequently, the samples were analyzed with Broad Ion Beam-Scanning Electron Microscopy (BIB-SEM). Unlike when pure H_2 was applied to the samples, the brine-H_2 mixture resulted in significant etching and dissolution of calcite grains, especially in the form of fossil fragments. The increased porosity may result in increased permeability through increased connected porosity, and a decrease in caprock strength and stiffness, which would

both reduce caprock integrity. Furthermore, hydrogen is consumed in reacting with calcite leading to losses of the stored resource, although such losses are not large. Therefore, caprocks with high calcite concentrations may be more susceptible to loss of chemical integrity. This work was limited though in that the samples were tested at room temperature, not reservoir temperature.

Labus and Tarkowski [2022] conducted a comprehensive geochemical modelling study using the Geochemist's Workbench 11 (GWB) geochemical simulator to simulate claystone and mudstone caprock samples from the Zaosie and Chabowo Anticlines in Poland at pressures and temperatures, not exceeing 12.5 MPa and 50°C, respectively. Hydrogen is injected for 1000 days, followed by a storage period of 182 days, and then a production period of 182 days. Porosity and mineral fraction changes were reported at each stage. During the injection phase it was found that caprock porosity typically increased, and these increases were significant (between 7 to 65% increases), suggesting that hydrogen injection may chemically reduce hydraulic caprock integrity, by increasing porosity and coincidentally permeability. Although, in one claystone sample with high amounts of anorthite, the porosity decreased by 17.3%, which would chemically enhance the hydraulic integrity of the caprock. The caprocks which increased porosity, had high amounts of goethite which have a higher volume than the newly crystallised replacement phases, pyrrhotite and iron (II) oxide. Hydrogen injection increases the pH of the fluid mixtures in the subsurface which aids decomposition of pyrite into pyrrhotite, which again has a smaller volume than the primary phase, resulting in increased porosity. Caprocks with high amounts of anorthite, resulted in porosity decreases because the secondary mineral phases resultant from the anorthite decomposition (prehnite, gibbsite, and laumontite) had a larger net volume than the decomposed anorthite. Thus, caprocks with large amounts of goethite and pyrite may reduce hydraulic integrity of the caprock, whilst caprocks with large amounts of anorthite may enhance hydraulic integrity.

4.2.3 Hydraulic Caprock Integrity during Hydrogen Storage

Aghaei et al. [2023] conducted a wettability analysis on anhydrite caprock samples from a gas

field in North Iran at subsurface conditions. They found that, irrespective of temperature (30-75°C) and pressure (3-20 MPa), the contact angle remained approximately 20°, implying the caprock is always strongly water-wet in the presence of brine and hydrogen. Therefore, the caprock is likely to have a high sealing capacity because the hydrogen is the non-wetting phase and will be preferentially trapped in the pores by phenomena such as snap-off. Although, it must be noted that this work assumed a clean rock surface. It may be the case that the caprock is not water-wet for rocks which have high amounts of organic content or that have previously experienced asphaltene deposition from oil residing in the pore space. However, this is likely only an issue for depleted oil reservoirs and not depleted gas reservoirs, since natural gas does not contain asphaltenes.

In fact, Al-Mukainah et al. [2022] found that at subsurface temperatures and pressures of 50 °C and 0-7 MPa respectively, some caprock samples could show weakly hydrogen-wet conditions when the Total Organic Content (TOC) is high. They conducted wettability analysis of samples from the Eagle-Ford Shale and the Wolf-Camp Shale using SEM. The Eagle-Ford sample was representative of high TOC (3.83%), whilst the Wolf-Camp sample was representative of low TOC (0.30%). It was found that the contact angles for the Wolf-Camp sample were between 55° and 65° implying moderately-weak water-wet conditions, but for the Eagle-Ford sample the contact angles varied between 80° and 100° implying some mixed-wet to weakly hydrogen-wet conditions, although these were found at very low pressures of less than 2 MPa. Therefore, shale caprocks with high TOC may preferentially trap brine in the centres of the pore space and preferentially allow hydrogen to flow along the walls of the pores, which is not ideal for a seal rock.

Ali et al. [2021] found that the caprock wettability was highly dependent on the presence of organic acids. They calculated contact angles for a mica/H_2/brine system using the Tilted Plate Method, at 50°C and 20-25 MPa, with and without the presence of the organic Stearic acid at 10^{-2} mol/L. The mica was used to represent the caprock, since mica is often ubiquitous in shale caprocks. It was found that without the organic acid, the mica was water-wet with advancing and receding contact angles of 49.7° and 43.8° respectively. However, when the organic acid was added, the mica became mixed-wet to weakly hydrogen-wet with advancing

and receding contact angles of 98.8° and 90.8° respectively. Therefore, a caprock with organic acids present, may preferentially trap brine and preferentially allow hydrogen to permeate, reducing the hydraulic integrity of the caprock.

Andiappan et al. [2023] conducted permeation measurements at 10 MPa and 40°C on shale caprock core taken from the Hall formation. They found that the permeability to natural gas and hydrogen was almost identical with a maximum difference of only 1.3 nD. Therefore, it may be concluded that a caprock that can store natural gas successfully is likely to also maintain its hydraulic integrity in the presence of hydrogen.

Salina Borello et al. [2024] conducted adsportion and desorption tests on mudstone caprock samples taken from the Argille del Santerno Formation. They compared the adsorption and desorption of the samples to methane (natural gas) and to hydrogen and found that diffusion coefficients through the caprock for hydrogen were 1×10^{-10} m^2/s to 6×10^{-8} m^2/s and for methane from 9×10^{-10} m^2/s to 2×10^{-8} m^2/s. Therefore, the diffusion of hydrogen through the caprock is only slightly more favourable than for methane, suggesting that loss of hydraulic caprock integrity via diffusion is unlikely.

Alanazi et al. [2023] analyzed the contact angles of three separate systems: (1) H_2/Brine/Rock, (2) CH_4/Brine/Rock and (3) H_2-CH_4/Brine/Rock in Jordanian oil shale samples at temperatures of 323 K and 0.1-1600 psi. They found that the contact angle of the H_2/Brine/Rock system was the lowest and that of the CH_4/Brine/Rock system was the highest. The H_2-CH_4/Brine/Rock contact angle was in between the two end-member cases. This implies that caprock shales are less wetting to hydrogen than to natural gas, so that a caprock that prevented natural gas flow should also prevent hydrogen flow. They also varied the TOC of their samples and found that a significant increase in wettability occurs in all cases from intermediate-wet ($70° < \theta < 110°$) to weakly gas-wet ($110° < \theta < 130°$) as the TOC increased. Therefore, caprocks with high TOC could potentially be weakly hydrogen-wet, thus preferentially encouraging upward hydrogen flow.

4.2.4 Caprock Integrity during CO_2 Storage

Gor et al. [2013a] conducted a 2-D 5000 × 1820 m numerical study of CO_2 injection using the DynaFlow finite element code. CO_2 was continuously injected over a period of 12 years into a 20 m aquifer, underlain by a 900 m aquitard and overlain by a 900 m caprock of low 100 nD permeability. They computed the horizontal effective stresses that developed across the caprock over the study period and found that after just 3.4 years the stresses in the caprock shifted from compressive to tensile, reaching tensile stresses of up to 3.8 MPa for a CO_2 injection temperature of 40-50°C. Given that the tensile strength of some shales can be significantly less than these tensile stresses [Jin et al., 2018], it is likely that such stresses will lead to the formation of new fractures within the caprock. However, when the injection temperature is increased to 60°C or above, the initial compressive stresses in the caprock are unaffected and no tensile stresses are induced, suggesting higher temperature injection may be more beneficial for maintaining mechanical caprock integrity. Furthermore, it was found that the injection temperature only induces the tensile stresses if the aquifer permeability was small. For an injection temperature of 50°C, the initial compressive stresses were maintained when the aquifer permeability was 500 mD, but tensile stresses of over 1 MPa were induced when the aquifer permeability was only 50 mD. Thus, the permeability of the injection unit below the caprock, has a strong effect on the likeliness of mechanical failure in the caprock. They found that shear failure is also a risk in the caprock. For a CO_2 injection temperature of 40°C, the mobilised friction angle reached values of 53° in the caprock after 12 years, significantly surpassing the shear strength of the caprock. Even after three years, the mobilised friction angle had reached 30°, suggesting some shear failure. As the injection temperature was reduced, the risk of shear failure increased. However, whether this resultant fracturing is detrimental to the overall caprock mechanical or hydraulic integrity is dependent on their length and ability to propagate. Fractures were not explicitly modelled in this work.

Paluszny et al. [2017] performed a 3-D, fully-coupled, thermohydromechanical field-scale study of CO_2 storage in a 5000×2500×400 m numerical model of the Heletz CCS Pilot site in Israel. Twenty fractures were incorporated in a spatially random manner into the caprock and

represented as circular flaws of radius 10 m. Cold CO_2 was injected into the aquifer unit at a rate of 2 kg/s for 1 year. The advancement of the temperature plume was noted to induce localised stress release, triggering short propagation episodes primarily associated with downward growth in the direction of the Aquifer. This is positive in that if fractures do not exhibit strong growth vertically upward then the caprock cannot become mechanically compromised because fractures will not fully penetrate the height of the caprock and as such the hydraulic isolation of the overburden from the reservoir unit remains.

Salimzadeh et al. [2018] constructed a full-scale field model of dimensions 10,000×6000×4000 m of the Goldeneye gas condensate field in the North Sea, United Kingdom. A 3-D, fully-coupled, thermohydromechanical study of cold CO_2 injection at a temperature of 20°C into the 83°C reservoir was conducted. Four large-sized circular fractures of 250 m radius were modelled, and each of these fractures crossed the reservoir-caprock interface. Thermoelastic stresses were found to play a dominant role in deforming the reservoir, significantly influencing the distribution of fracture apertures within it. Conversely, poroelastic deformation primarily governed the aperture of fractures within the caprock. The injection of cold fluid into the reservoir layer leads to matrix contraction, exerting compression on the caprock layer and reducing fracture aperture, which has the effect of reducing caprock effective permeability by reducing the contributions from the individual fracture permeabilites. Injecting warmer fluid or employing a lower Young's modulus matrix mitigated thermoelastic effects.

Vilarrasa et al. [2013] injected liquid CO_2 into a 100 m vertically thick aquifer unit that is overlain and underlain by low permeability seal rocks of 200 m thickness. The model was 2-D and extends 20,000 m in the lateral direction. The overburden is not explicitly modelled because it is argued that its very low stiffness means it need not be included. The injection rate is set to an equivalent of 1 Mt/year. They studied fault reactivation during this CO_2 injection, which has important consequences for integrity because if faults are sufficiently reactivated that propagation can lead to full penetration of the caprock and/or offset of the reservoir and caprock layers leads to pathways through the seal, then integrity can be compromised and the stored fluid will no longer be contained. The impact of thermal effects on the mechanical stability of the modelled rocks became significant with large temperature differences between

injectant and *in situ* fluid and rigid rock formations. Thermal contraction mobilised greater friction angles within the aquifer, resulting in the shear displacement of pre-existing fractures and faults. While shear slip within the aquifer can be beneficial by increasing permeability and enhancing CO_2 injectivity, it is noteworthy that the mobilised friction angle in the seals did not rise when liquid CO_2 was injected, but even decreased in stress conditions where the maximum principal stress is vertical. These findings are positive in that they suggest fault reactivation in the caprock is not more favourable as a result of CO_2 storage than in the fault's native state and that when the maximum principal stress is vertical, the storage of CO_2 can actually decrease the likelihood of fault reactivation relative to its native state.

Study	Activity/fluid	Type	Methodology	Findings
Mechanical Integrity				
Bai and Tahmasebi [2022]	Aquifer H_2 storage	FEM	Mohr-Coulomb analysis	Stable caprock - failure line not intersected
Laalam et al. [2023]	Depleted HC H_2 storage	FEM	Mohr-Coulomb analysis	Stable caprock - failure line not intersected
Tenthorey et al. [2024]	Depleted gas H_2 storage, CO_2, CH_4	FEM	Fracture pressure, temperature plume	Temperature least important and fracture pressure most for H_2 storage
Ciancimino et al. [2024]	H_2	Experimental	Cyclical triaxial tests (M/HPTA)	Fragile cyclic failure (>15 cycles)
Gor et al. [2013a]	Aquifer CO_2 sequestration	Analytical	1-D diffusion & single KGD frac. geometry	Very high 200 m/min frac. propagation rate in first minute after initiation
Paluszny et al. [2017]	Depleted HC CO_2 sequestration	FEM	3-D fully-coupled THM w. growth of 1-20 frac.	Mech. integrity maintained - frac. grow downward toward reservoir, not upward
Salimzadeh et al. [2018]	Depleted gas CO_2 sequestration	FEM	3-D iteratively-coupled THM w. growth of 4 frac.	No propagation when inj. temp. > 40°C. No upward propagation, all cases
Vilarrasa et al. [2013]	Aquifer Liquid CO_2 sequestration	FEM	3-D fully-coupled THM	Mobilized friction angle does not increase, decreases when $\sigma_v = \sigma_1$
Han et al. [2024]	Aquifer CO_2 sequestration	FDM	HM coupling w/o fractures	Uniformity of p increases w. time, so insignificant bending load on caprock
Aminaho et al. [2024]	Depleted HC CO_2 storage, H_2S, SO_2	FVM	2-D reactive transport, brittleness index	Δ K, ϕ, B_I negligible for CO_2/CO_2-H_2S injectants and cyclical CO_2 storage
Nath et al. [2024]	Depleted HC CO_2 sequestration	Experimental	Diametrical compression tests w. 3D-DIC	Heterogeneities (frac./lamination/mineral %) led to changes in failure pattern
Tan et al. [2024]	Depleted HC CO_2 sequestration	Analytical	1-D geomech. model from well log & MC analysis	Stable caprock - failure line not intersected
Alvarez et al. [2023]	Aquifer CO_2 sequestration	FEM	3-D two-phase flow w. 8-component geochem. model	$1{\times}10^6$ m^3/d inj. rate led to failure (fault reactivation), 275 m^3/d did not
Wang et al. [2024c]	Depleted HC general fluid injection	FEM	MC, Mogi-Coulomb and TMNS constitutive models	Highest strain near injector at cap-res, stable caprock using all methods
Shen et al. [2024]	Depleted oil CO_2 sequestration	FEM	2-D M, σ&ϵ compared to damage factor w. VT	Min p_f: 6.995 MPa to 8.089 MPa. More quartz = greater stability
Bai et al. [2024]	Aquifer CO_2 sequestration	FEM	3-D MEM from 1-D well log MEMs using SGS	Stable caprock - failure line not intersected in any cells
Mu et al. [2024]	H_2, CH_4, H_2O	Experimental	Nanoidentation technology and XRD	H_2O enhances H_2/rock reaction increasing caprock elastic modulus
Cerasi et al. [2022]	CO_2	Experimental	Triaxial tests, non-destructive stiffness test w. CO_2	Diffusion into cap. affects poroelas. properties of OB, alters expected cap. σ'
Trujillo et al. [2021]	CO_2	Experimental	Coring, HRA, well-logs, triaxial testing	Shale can sustain fracture gradients up to 7 MPa above hydrostatic pressure
Thompson et al. [2021]	CO_2	Analytical	Relations for framework stiffness, Δp, $\Delta\epsilon$, $\Delta\sigma'$	Undrained effects in cap. do not lead to unfavourable tensile conditions
Hydraulic Integrity				
Aghaei et al. [2023]	H_2	Experimental	Contact angle analysis via CBM	For T 30-75°C and p 3-18 MPa, all samples strongly water-wet ($17<\theta^\circ<30$)
Al-Mukainah et al. [2022]	H_2	Experimental	Contact angle analysis via modified-SDM	Hydrogen-wet (θ=99.9°) w. high TOC at 0.1 MPa, intermediate-wet (θ=89.7°) at 1.4 MPa
Ali et al. [2021]	H_2	Experimental	Contact angle analysis via the TPM	Mica intermediate-wet at higher p, lower T, and increasing stearic acid conc.
Andiappan et al. [2023]	H_2, CH_4	Experimental	Gas permeation measurements to CH_4 and H_2	Same order of magnitude K both gases. On average, H_2 cores slightly < K
Salina Borello et al. [2024]	H_2, CH_4	Experimental	Adsorption/desorption tests w. DGVS	D_c: H_2 = $1{\times}10^{-10}$-$6{\times}10^{-8}$ m^2/s, CH_4 = $9{\times}10^{-10}$-$2{\times}10^{-8}$ m^2/s
Alanazi et al. [2023]	H_2, CH_4	Experimental	Contact angle analysis via the TPM	$\theta >$ for CH_4 than H_2. Very high TOC (13-18%) = hydrogen-wet (up to 120°)
Minardi et al. [2021]	CO_2	Experimental	Step-wise injection and residual method w. OC	Shale had very low snap-off pressure of 3.5 MPa, cap. CO_2 trapped easily
Chemical Integrity				
Zeng et al. [2023]	H_2	Numerical	Geochem. computer program PHREEQC & KBM	All mineral dissolution < 1% in 30 yrs, H_2 only affects first few m of caprock
Bensing et al. [2022]	H_2	Experimental	Hydrogen treatment, analyzed with BIB-SEM	Calcite in caprock dissolves (< 30 days), increasing ϕ, K and decreasing strength
Labus and Tarkowski [2022]	H_2	Numerical	Geochemist's Workbench 11 Geochem. simulator	H_2 increases fluid mixture pH encouraging pyrite destabil. = increased ϕ
Xue et al. [2023]	CH_4	FEM	2-D fully-coupled two-phase flow model	Gas P increase in cap. leads to matrix adsorption expansion reducing a_f/K
ter Heege [2023]	H_2, N_2	Experimental	Samples encased in PTFE tubes, put in PCT	For intermediate depth fields, H_2 exposure has little effect on E, none on ν
Al-Yaseri et al. [2023]	H_2	Experimental	XRD, XRF, SEM, polished w. DF & cleaned	Calcite precipitation in cap. pores due to organic content at 9.65 MPa/75°C

Table 4.1: Studies examining the mechanical, chemical or hydraulic integrity of the caprock during hydrogen storage and the mechanical integrity of the caprock during carbon dioxide storage. Some studies involving other fluids such as natural gas are included. The following acronyms are used: a_f = fracture aperture, ΔB_I = brittleness index, BIB-SEM = broad ion beam-scanning electron microscopy, cap-res = caprock-reservoir interface, CBM = captive bubble method, CH_4 = methane or represents natural gas, D_c = diffusion coefficient, DF = diamond foil, DGVS = dynamic gravimetric vapor/gas sorption system, DIC = digital image correlation, FDM = finite difference method, FEM = finite element method, FVM = finite volume method, HC = hydrocarbon field, HRA = heterogeneous rock analysis, KBM = kinetic batch modelling, KGD = Khristianovich-Geertsma-de Klerk fracture, M = mechanical model, MC = Mohr-Coulomb, M/HPTA = medium and high pressure triaxial apparatuses, OB = overburden, OC = oedometric cell, P = pressure, p = pore pressure, p_f = fracture pressure, PCT = plastic centrifugal tubes, SDM = sessile drop method, SGS = sequential gaussian simulation, T = temperature, THM = thermohydromechanical, TMNS = triple-mean-normal-stress, TOC = total organic carbon, TPM = tilted plate method, VT = Voronoi tessellation technique, w/o = 'without', XRD = x-ray diffraction, XRF = x-ray fluorescence, Δ = 'change in', σ = stress, σ' = effective stress, ϵ = strain.

4.3 Methodology

A three-dimensional model of a depleted gas field with dimensions 4000 m × 4000 m × 3300 m is constructed (Figure 4.1). The anticlinal model contains four lithological units, typical of North sea systems: a chalk overburden, a shale caprock, a sandstone reservoir and a shale underburden. A substantial literature review (Table 6.4) of depleted and still-producing North Sea oil and gas fields was conducted in order to find realistic parameter ranges for mechanical and lithological properties for each of the four units. Values for such properties in each unit were prescribed to be middle-values or averages of that found in the literature review and are shown in Table 4.2. Many of these values relate to the Britannia and Leman fields in the North Sea, which could be used for potential hydrogen storage, and the Goldeneye field for which a near-complete parameter space is somewhat well reported. Where values for these units in these fields could not be found, a value was taken from a similar North sea analogue rock, and where that was not possible, a generalised typical value for that lithology was used. Stresses are prescribed such that the *in situ* reservoir stresses of 45 MPa reflect that found in mutliple North Sea fields at such depths. Additional parameters used herein that were not required in Chapter 6 and thus were not included in the literature review of model parameters in that chapter include fracture toughness and ultimate tensile strength. The fracture toughnesses in Table 4.2 for the overburden, caprock, reservoir and underburden are referenced from Brevik [2016], Liu [2015], Rao et al. [2007] and Vishal et al. [2022], respectively. The ultimate tensile strengths in Table 4.2 for the overburden, caprock, reservoir and underburden are referenced from Brevik [2016], Vishal et al. [2022], Suhett Helmer [2014] and Vishal et al. [2022], respectively. All of the default model parameters are described in Table 4.2.

Hydrogen is stored for three years in the majority of simulations unless specified otherwise. Each annual cycle consists of a five-month injection, two-month storage, and five-month withdrawal period. Hydrogen is injected at a rate of 5.00 m^3/s through a horizontal wellbore 500 m from the left boundary of the domain and that penetrates 4000 m in the x-direction and is withdrawn at a rate of 4.25 m^3/s through a horizontal wellbore 500 m from the right boundary of the domain that also penetrates 4000 m in the x-direction. The withdrawal rate is set to a lower value

Table 4.2: The mechanical, fluid, geometrical, and lithological properties and the *in situ* stresses of the four different lithologies within the model. The properties of the fractures in the caprock unit are also provided. The symbology in the table is as follows: k = permeability, ϕ = porosity, h = thickness, E = Young's modulus, ν = Poisson's ratio, α = Biot coefficient, ρ_b = rock density, σ_t = tensile strength, K_{IC} = fracture toughness, ρ_f = fluid density, μ = fluid viscosity, c = fluid compressibility, σ_h = minimum horizontal *in situ* stress at base, σ_H = maximum horizontal *in situ* stress at base, σ_V = *vertical *in situ* stress at top (i.e. just the overlying vertical stress due to the sea water not the overlying rock), Δa_v = maximum extension length at any node on any fracture, β_f = fracture growth rate exponent, β_n = tip growth rate exponent and r_i = initial radius of fractures. The table is adapted from Burtonshaw et al. [2024a] and Burtonshaw et al. [2024b].

Property	Overburden	Caprock	Reservoir	Underburden
Mechanical				
Lithology	Chalk	Shale	Sandstone	Shale/Coal
k (m^2)	3.0×10^{-15}	1.0×10^{-21}	1.0×10^{-13}	1.0×10^{-21}
ϕ	0.30	0.05	0.15	0.05
h (m)	2300 - 2400	100	150	650 - 750
E (Pa)	4.5×10^{9}	1.5×10^{10}	1.5×10^{10}	4.0×10^{10}
ν	0.35	0.35	0.15	0.35
α	0.87	0.93	0.35	0.93
ρ_b (kg/m^3)	2080	2500	2500	2500
σ_t (Pa)	1.78×10^{6}	10.40×10^{6}	6.07×10^{6}	10.60×10^{6}
K_{IC} (Pa $\sqrt{\text{m}}$)	0.139×10^{6}	0.330×10^{5}	0.880×10^{6}	0.480×10^{6}
Fluid				
Fluid	Brine	Brine	Hydrogen	Brine
ρ_f (kg/m^3)	1058	1042	9	1037
μ (μPa s)	561.0	357.5	10.4	296.0
c (Pa^{-1})	4.47×10^{-10}	4.57×10^{-10}	6.67×10^{-8}	4.68×10^{-10}
Stresses				
σ_h (MPa)	-	-	58.5	-
σ_H (MPa)	-	-	58.5	-
σ_V (MPa)	-	-	0.9800517*	-
Fractures				
β_f (-)	-	-	0.35	-
β_n (-)	-	-	1.00	-
Δa_v (m)	-	-	0.5256	-
r_i (m)	-	-	1	-

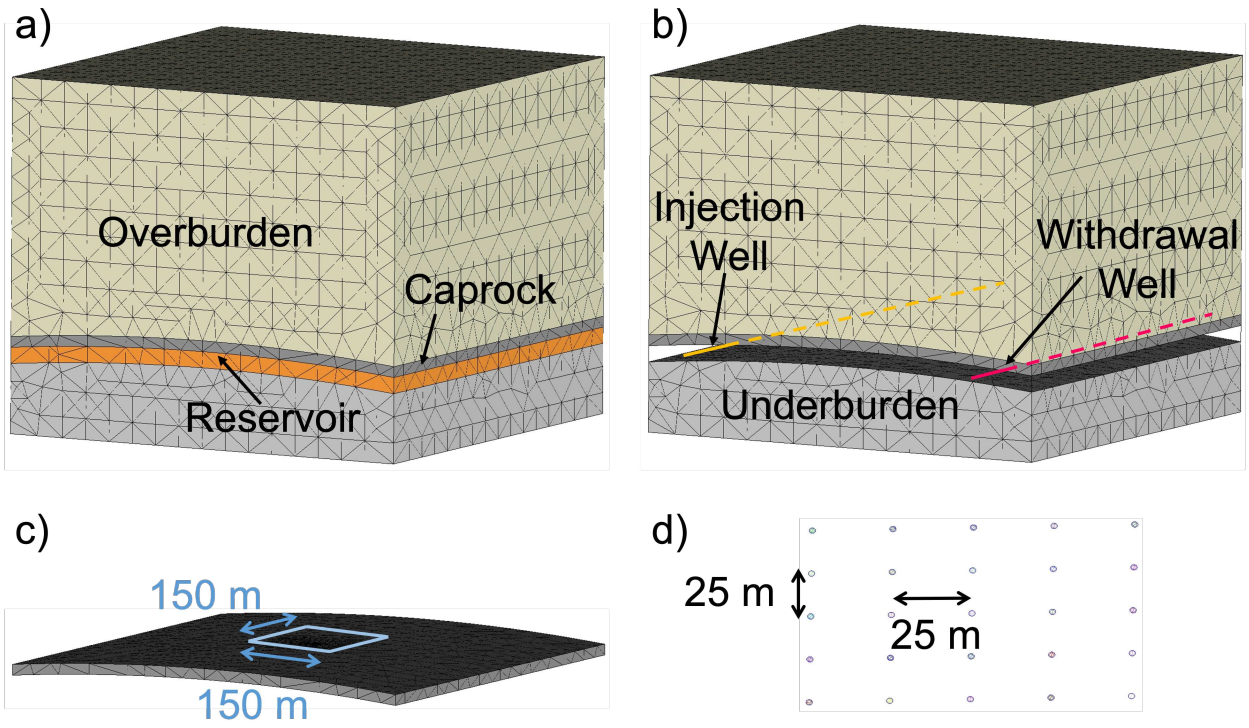


Figure 4.1: (a) A 3-D perspective view of the model displaying the four distinct lithological units: a chalk overburden in cream, a shale caprock in grey, a sandstone reservoir in orange and a shale/coal underburden in light grey. (b) The same as (a) with the sandstone reservoir unit removed so that the location of the injection (amber) and withdrawal (pink) wellbores can be seen. The dashes display the trace of the wellbores within the reservoir unit if the caprock and overburden units were removed. (c) The caprock unit showing the dimensions and location of the naturally fractured region of the caprock. For clarity, the box is diagrammatically exaggerated in size relative to the 4000×4000 m x-y dimensions of the caprock. (d) The initial fracture array that is located within the blue region in (c). In the default simulation case, the fractures are oriented vertical and all exist in the same x-y plane such that all fractures are centred at the same depth of 2350 m, which is the mid-depth of the caprock. The caprock region outside of the blue box in (c) is unfractured.

than the injection rate because in reality it will never be possible to withdraw an equivalent volume to that which we inject due to pore scale trapping, diffusion, microbial metabolism, and chemical consumption. Given the ultra-low density of hydrogen, the high injection rate is prescribed to ensure sufficiently large masses of hydrogen are delivered to the rock during the injection periods. In this chapter, the injection rate specified corresponds to 591,300,000 kg of hydrogen stored or approximately 19.7 TWh of energy stored annually, which is approximately 1% of the total annual energy demand of the United Kingdom [Burtonshaw et al., 2024b].

In this study, a simplified annual cycle was used comprising 5 months of hydrogen injection, 2

months of storage, and 5 months of withdrawal. This setup is useful for exploring seasonal-scale storage but does not capture the full range of temporal variability likely to be encountered in real-world hydrogen storage operations. In practice, injection and withdrawal cycles may be significantly more dynamic, reflecting the complex and often unpredictable nature of energy demand and supply. Natural gas (currently fulfilling a role hydrogen may occupy in the future) is stored and dispatched in patterns that include daily, weekly, and seasonal cycles. For example, in response to cold weather or supply constraints, natural gas withdrawal can ramp up quickly, with national energy ramp rates reaching as high as 5 GW per hour. Moreover, week-long energy storage needs for the UK can reach approximately 1 TWh, indicating the requirement for storage systems that can flexibly respond to short-term energy imbalances. Similarly, operational data from European gas storage sites reveal a range of storage strategies, including high-frequency cycling in some facilities. These realities suggest that future hydrogen storage systems may need to accommodate a broader array of temporal patterns, including more frequent and rapid cycling than modelled in the base case. Therefore, future work should consider incorporating variable cycling rates and intra-annual operation modes to more closely reflect operational demands.

In the growth simulations, initial circular flaws of radius 1 m are imposed in the caprock. A total of twenty-five caprock fractures are arranged into a 5×5 array in the x-y plane (Figure 4.1c,d). Each fracture has a spacing of 25 m in the x and y directions, and all are centred at a depth of 2,350 m, unless specified otherwise. The initial natural fracture array is chosen to be restricted to the centre of the caprock and not throughout because otherwise, (1) simulation artefacts arise as a result of boundary effects in the stress field, where fractures nearer the model boundaries grow considerably more than those fractures nearer the model centre in response to larger stress near the boundaries, and (2) the computational expense of the simulation grows very significantly as the number of fractures increases. The maximum extension length at any node on any fracture, Δa_v, is set to a value of 0.5256 m per step because this is equivalent to a typical crack growth speed for shale [Dong et al., 2019]. However, these shale crack growth speeds can vary very significantly [Nara et al., 2011, Chandler et al., 2018, Maruvanchery, 2019] and as such a number of simulations are performed to assess the impact of this parameter on

Table 4.3: Fracture and mechanical properties of the different growth and nucleation simulations performed. The nomenclature is: ψ = normal fracture orientation vector, r_i = initial fracture radius at time t=0, Δa_v = maximum extension length at any node on any fracture per step, s_{xy} = fracture spacing for simulations with fractures in the x-y plane, s_{xz} = fracture spacing for simulations with fractures in the x-z plane, K_{IC} = caprock mode I fracture toughness, E = caprock Young's modulus, ν = caprock Poisson's ratio, α = caprock Biot coefficient, k = caprock permeability, k_{fN} = caprock normal fracture leak-off permeability, and σ_t = caprock ultimate tensile strength.

Simulation	Case 1	Case 2	Case 3	Case 4	Case 5	Case 6
Growth: Fractures						
s_{xy} (m)	25.0	7.5	10.0	15.0	-	-
s_{xz} (m)	10.0	15.0	20.0	25.0	-	-
ψ (-)	(1 0 0)	(1 1 1)	(0 0 1)	(0 1 1)	(1 0 1)	(0 1 0)
r_i (m)	1.0	0.2	2.0	5.0	-	-
Δa_v (m)	0.5256	1.0512	5.2560	52.5600	-	-
Growth: Mechanical						
K_{IC} (Pa $\sqrt{\text{m}}$)	0.33×10^5	0.60×10^5	1.00×10^5	0.46×10^6	-	-
E (GPa)	15	2	28	43	-	-
ν (-)	0.35	0.11	0.19	0.27	-	-
α (-)	0.93	0.40	0.60	0.77	-	-
k (m^2)	1×10^{-21}	1×10^{-23}	1×10^{-20}	1×10^{-19}	-	-
k_{fN} (m^2)	1×10^{-15}	1×10^{-20}	1×10^{-18}	1×10^{-11}	-	-
Nucleation: Mechanical						
σ_t (MPa)	10.4	30.0	44.0	50.0	-	-

the solution.

In the nucleation simulations, fractures are allowed to nucleate in the caprock unit. Fractures have the potential to grow and nucleate at each step according to that outlined in Sections 3.5-3.6 of Chapter 3. In order to avoid boundary effects, limits are imposed to prevent fractures nucleating near the boundaries of the model; no fractures can form within 1600 m from the left, right, back, and front domain boundaries respectively. Therefore, fractures can only form within an 800×800 m region in the centre of the model. Limits are also imposed to prevent fractures from only forming in clusters; no fractures can form within 50 m of a previously nucleated fracture. This is necessary because the algorithm nucleates cracks in descending order from the most damaged element in the domain. Thus, one can expect that the next most damaged element in the domain, is the element next to such an element.

A number of numerical experiments, listed in Table 4.3, are performed. A parametric analysis

is conducted whereby in each simulation the default model parameters specified in Table 4.2 are used, except one given caprock property (either mechanical or fracture property), which is altered keeping everything else constant. This is conducted to isolate the effect of a single caprock property on the fracture growth, fracture nucleation, and fracture aperture behaviour and thus the caprock permeability temporal evolution.

4.4 Mesh Effects

It is not expected that the refinement of the mesh should have significant effects on the results. This is because the extension of each fracture is determined by computation at the fracture tip nodes and not within the elements themselves. Therefore, the comparative stress intensity factor is computed at a given fracture node and if the critical stress intensity factor is exceeded, the node moves by a length equal to Δa_n, which is a function of the Irwin energy release rate, at an angle given by the Richard fracture deflection angle, which is a function of multimode stress intensity factors. After this growth, the domain is re-meshed to conform to the new fracture node geometries and thus, the growth is independent from the mesh selection. In order to demonstrate that this is indeed true, four simulations were performed with different mesh refinements. A volumetric region of x-y-z dimensions 600×600×325 m is defined at the centre of the caprock which encompasses the 150×150×100 m caprock study area (Figure 4.1c) that contains the natural fracture array. Therefore, this region encompasses the full vertical extent of the caprock (150 m) and more. In each of the four simulations, all the physical properties of the system are left unchanged and are equal to that given in Table 4.2. The only change between each of the simulations is the refinement of the mesh in the 600×600×325 m volumetric region at the caprock centre. The number of elements in this region is varied from a coarse case of approximately 160,000 to a more refined case of nearly three quarters of a million elements (Figure 4.2a-d).

The effective permeability of each case is shown in Figure 4.2e. It is observed that the effective permeability is insensitive to changes in the mesh refinement, reflecting the fact that the

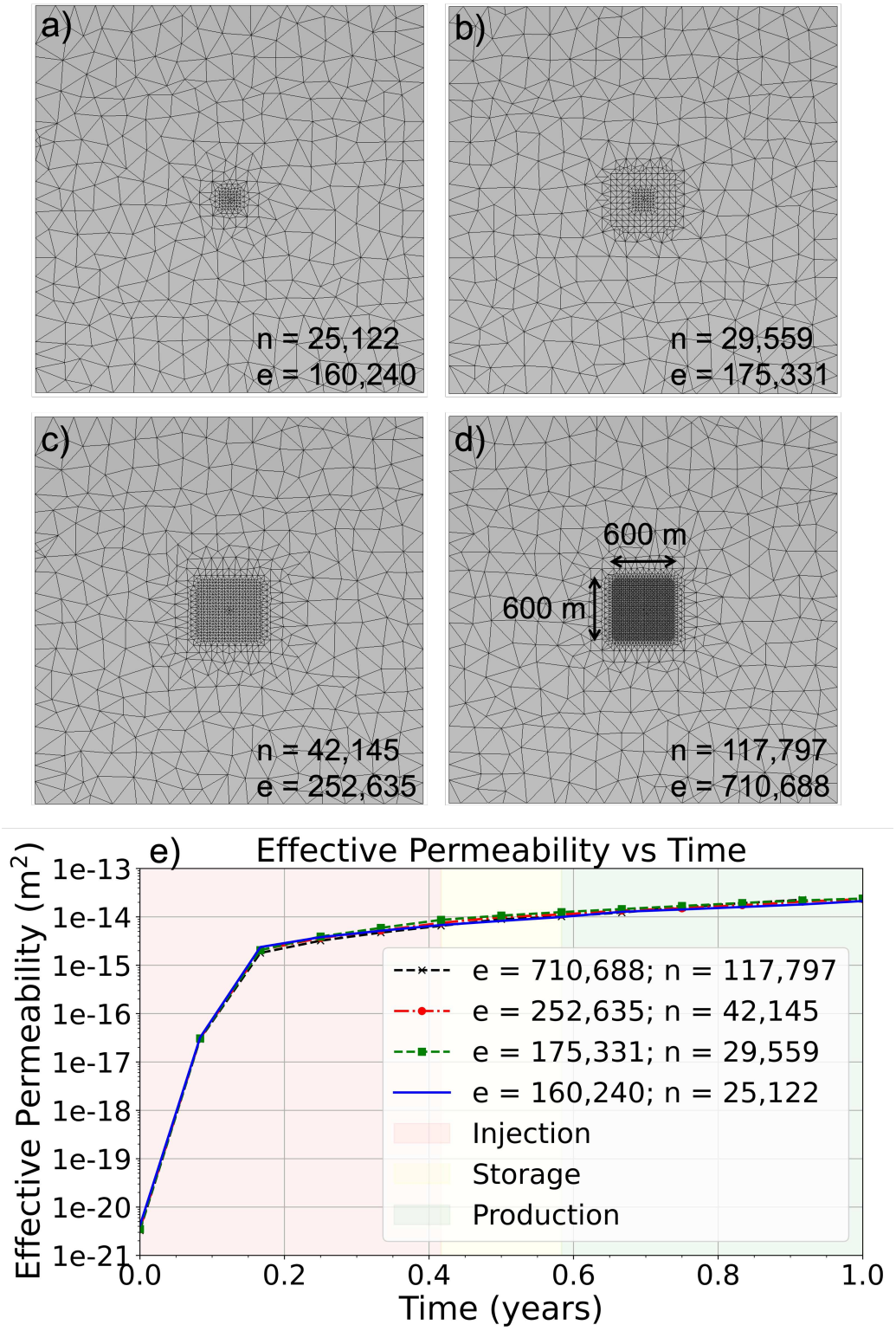


Figure 4.2: (a-d) Plane views (x-y) of the mesh along the top surface of the caprock in four simulations of different caprock refinement. The number of nodes in the model is denoted by 'n' and the number of elements is denoted by 'e'. The refinement increases in ascending order of figure lettering: (a) is the coarsest case and (d) is the most refined case. (e) Effective permeability of the 150×150×100 m caprock region versus time for one cycle of hydrogen injection, storage and withdrawal.

computed fracture geometry is very similar in all cases. The difference between the effective permeability of the four cases after a time of one year is only approximately 1 mD (5% relative difference). No systematic trend in effective permeability is observed with increasing or decreasing mesh refinement: the second coarsest case (175,331 elements) and the most refined case (710,688 elements) have the highest permeability at the end of the study period, with the coarsest case (160,240 elements) and the second most refined case (252,635 elements) having the lowest permeability. The small differences in computed effective permeability are primarily related to small differences in aperture. Since the effective permeability computation relies on the average aperture of each of the fractures which itself is the average of the aperture at each node on a given fracture surface, then any small variations in these values can have a noticeable impact on the effective permeability value due the quadratic relationship of fracture permeability with aperture. Small differences in caprock pressure distribution due to the differences in mesh refinement can impact these apertures.

In summary, these results provide confidence that the mesh is not significantly influencing the fracture growth behaviour and thus the effective permeability. For the remainder of the simulations performed in this work, the mesh in Figure 4.2b is used containing approximately 175,000 elements and 30,000 nodes. This mesh results in a computational run-time for the simulations herein of approximately one week per simulation for three years of storage time, whereas the mesh in Figure 4.2d has a simulation run-time of approximately one month per simulation if run for three years of storage time. Therefore, given the computational expense of using a more refined mesh and the fact that the difference in effective permeability results are minimal, a coarser mesh is implemented in this work.

4.5 Results

The results section is divided into three subsections, structured as follows: (1) a number of parametric studies in which the effects of caprock fracture properties such as fracture size, orientation, and spacing on caprock fracture growth and integrity are assessed (Table 4.3); (2)

a number of parametric studies in which the effects of caprock mechanical properties such as Young's modulus, Poisson's ratio, permeability and Biot coefficient on caprock fracture growth and integrity are assessed (Table 4.3); and (3) a parametric study in which the effects of caprock tensile strength on the nucleation of new caprock fractures is assessed. Plots of effective permeability, dimensionless P_{32}, P_{21} per fracture and images of the final fracture network are provided for each case to help assess the caprock integrity.

Despite starting with an initially symmetric array of equally sized and oriented fractures in the caprock, a heterogeneous fracture network evolves over time. This results from the asymmetries in the injection and withdrawal setup in the reservoir below. Since we inject fluid from one side of the domain and withdraw it from the opposite side, the pressure and stress distribution in the reservoir and caprock no longer remains homogeneous. As soon as one fracture starts to propagate even slightly ahead of its neighbours due to these asymmetries, it can alter the local stress field in the caprock. This is called the stress shadow effect: a growing fracture relieves (or amplifies) stress in its vicinity and may suppress (or amplify) growth of nearby fractures or redirect their paths. This feedback loop rapidly compounds initial differences. Once fractures start growing heterogeneously, regions of varied permeability develop in the caprock, which then introduces further asymmetries that cause varied growth extents.

4.5.1 Effect of Initial Fracture Array

4.5.1.1 Initial Fracture Size

Four simulations were performed to assess the impact of initial fracture size on the fracture growth and permeability alteration of the caprock. All model properties were defined according to Table 4.2 in each simulation, with the only property changing between the simulations being the initial radius of the natural fractures in the 5×5 array. The fracture radii tested were 0.2 m, 1.0 m, 2.0 m and 5.0 m.

Figures 4.3a-d show the state of the fracture network at the end of the three year storage period. When the fractures were very small (r = 0.2 m), the fractures grew somewhat homogeneously

with the majority of fractures having very similar fracture sizes. Additionally, the fractures grew in a quasi-circular manner with many of the fractures retaining a near-circular geometry. When the fractures were large ($r = 5.0$ m), the fractures also grew in a quasi-circular manner with few fractures forming ellipsoidal or polygonal/pointed fractures. However, unlike the $r = 0.2$ m case, the resultant fracture network has some heterogeneity in fracture size with some moderately sized fractures amongst much larger fractures. The two cases in between these end-member cases, with $r = 1.0$ m and $r = 2.0$ m, grew in a much more heterogeneous manner with a few fractures growing to a very large extent and many fractures experiencing very little growth. It can be seen that for these cases, the very large fractures tend to be found in the immediate vicinity of very small fractures and very small fractures are often found sandwiched between much larger fractures (i.e., first row, fourth row and fifth row of fractures in Figure 4.3b for the $r = 1.0$ m case).

Figure 4.5a shows the dimensionless P_{32} of the fractured caprock region, which is a parameter that demonstrates the degree to which the fracture areas have grown relative to their initial state. A clear systematic trend in P_{32} is found in which P_{32} increases with smaller initial fracture radii. This trend does not appear to be linear but appears to accelerate with smaller fracture radii. For example, when the fracture radii were decreased to 2.0 m from 5.0 m, the P_{32} value increased by less than 1 for most of the three year study period, but when the fracture radii were decreased from 2.0 m to 1.0 m (a smaller percentage reduction from 5.0 m to 2.0 m), the P_{32} value increased by approximately 70. When the radii were decreased from 1.0 m to 0.2 m, the increase in P_{32} accelerated again with an increase of over 4400. Figure 4.3 also reveals that the area of the larger fractures ($r = 2.0$ m and $r = 5.0$ m) seems to be tending toward a maximum value by the end of the third withdrawal period implying that the fracture network may be reaching its maximal size in these cases. The smaller initial fracture sizes show that by the end of the third withdrawal period the fracture network still seems to be showing signs of continued growth, especially in the $r = 0.2$ m case as the P_{32} curve is still steeply increasing. Therefore, it could be the case that the larger the natural fractures, the smaller the operation time before the fracture network reaches a state of mechanical stability.

Figures 4.4a-d shows the P_{21} per fracture of the fractured caprock region, which is a parameter

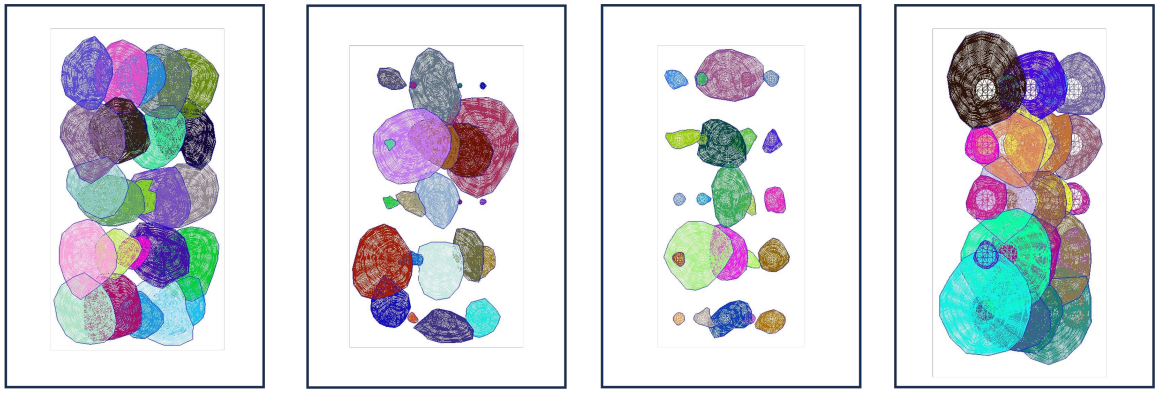
that displays how the fracture lengths have evolved through time. The largest initial radius case of 5.0 m resulted in the largest fractures at the end of the three year storage period, with two fractures having a P_{21} value above 0.001 compared to zero in any of the other cases. Additionally, the gradient of the curves reveals that in the 0.2 m case, all but one of the fractures are still in a state of growth at the end of the study period. Contrastingly, in the 2.0 m case, all but two fractures have a flattened P_{21} curve potentially implying a cessation of growth.

The total average aperture in each case is shown in Figure 4.6a. This is the average of the average aperture of each fracture at a given time. Each fracture is assigned an average aperture by averaging the aperture at each node on the fracture surface at a given time and then the average of all these average values across all fractures is taken to obtain the 'total average aperture.' It can be seen that there is no systematic change in aperture with increasing or decreasing initial fracture radius and that the aperture is similar in all cases.

The effective permeability plot in Figure 4.7a shows no systematic change in caprock effective permeability with increasing or decreasing initial fracture size. The cases with the smallest and largest natural fractures resulted in the largest permeability, with the intermediate size cases, resulting in lower permeability. However, during the early stages of the initial injection period, before the caprock permeability curves begin to stabilize, it is observed that the effective permeability increases with larger natural fracture size which is to be expected because before the fractures have significant time to grow, the cases with larger initial fractures have a larger fracture void fraction and thus have a larger permeability. The final permeability difference between the largest and smallest permeability cases (r = 0.2 m and r = 2.0 m) was a very significant 200 mD.

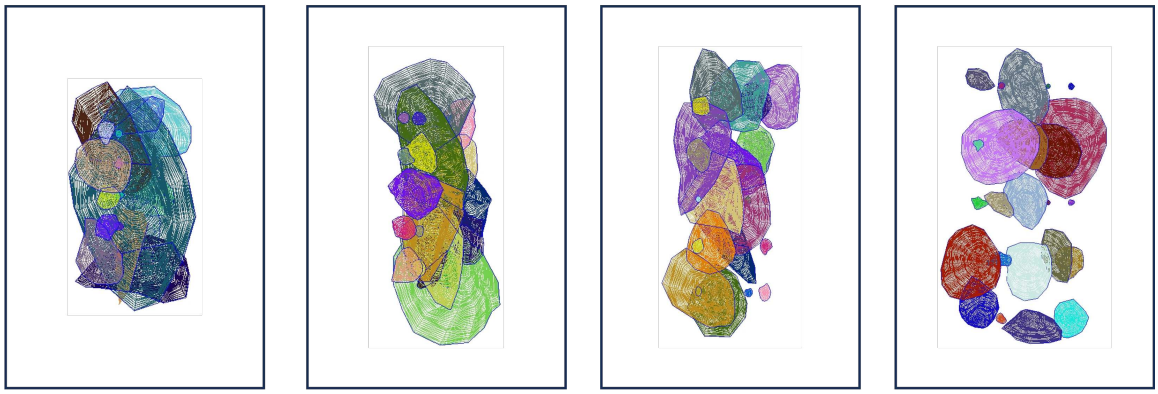
4.5.1.2 Initial Fracture Spacing

Six simulations were performed to assess the impact of initial fracture spacing on the fracture growth and permeability alteration of the caprock. All model properties were defined according to Table 4.2 in each simulation, with the only property changing between the simulations being the initial spacing of the natural fractures in the 5×5 array. The natural fracture spacings



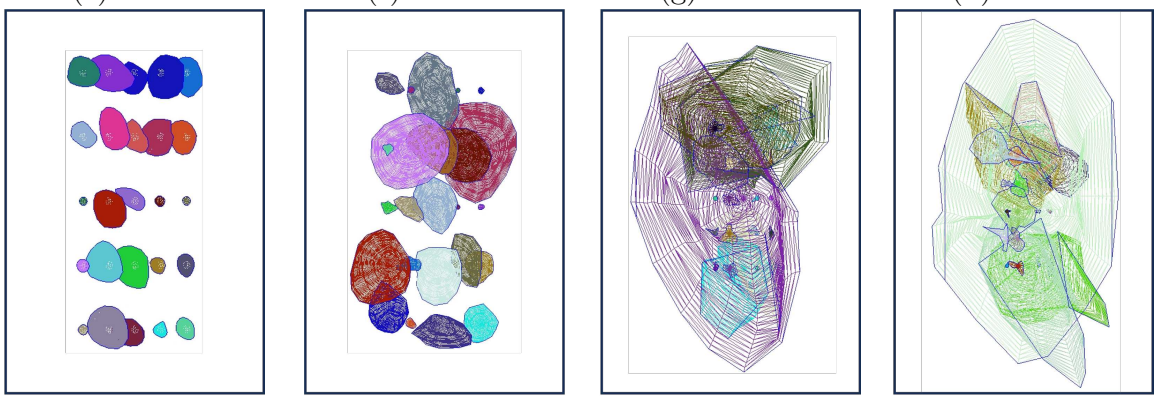
(a) 0.2 m (b) 1.0 m (c) 2.0 m (d) 5.0 m

s_i



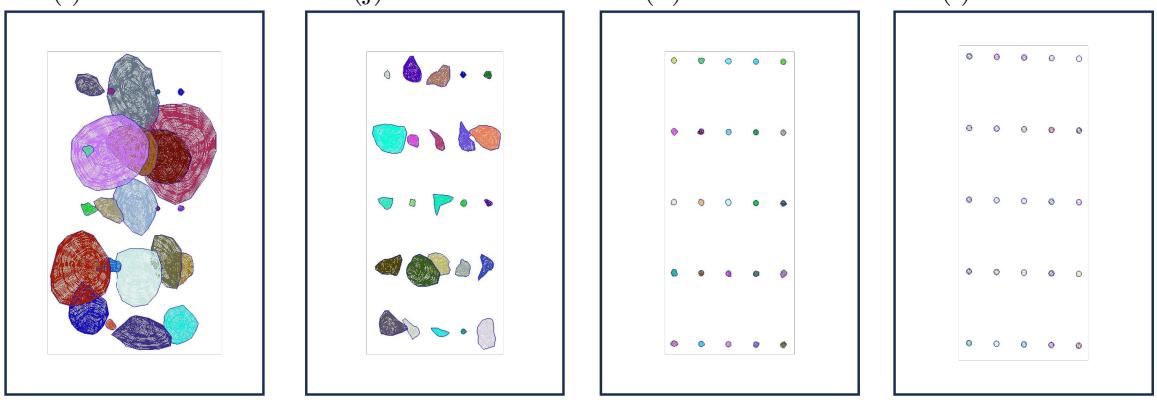
(e) 7.5 m (f) 10.0 m (g) 15.0 m (h) 25.0 m

Δa_v



(i) 0.1314 m (j) 0.5256 m (k) 2.1024 m (l) 2.5000 m

K_{IC}



(m) 0.033 MPa $m^{0.5}$ (n) 0.060 MPa $m^{0.5}$ (o) 0.10 MPa $m^{0.5}$ (p) 0.46 MPa $m^{0.5}$

Figure 4.3: The final state of the fracture network after three years of hydrogen storage for four cases of (a-d) initial natural fracture radius, (e-h) initial horizontal natural fracture spacing, (i-l) crack propagation velocity, and (m-p) caprock fracture toughness.

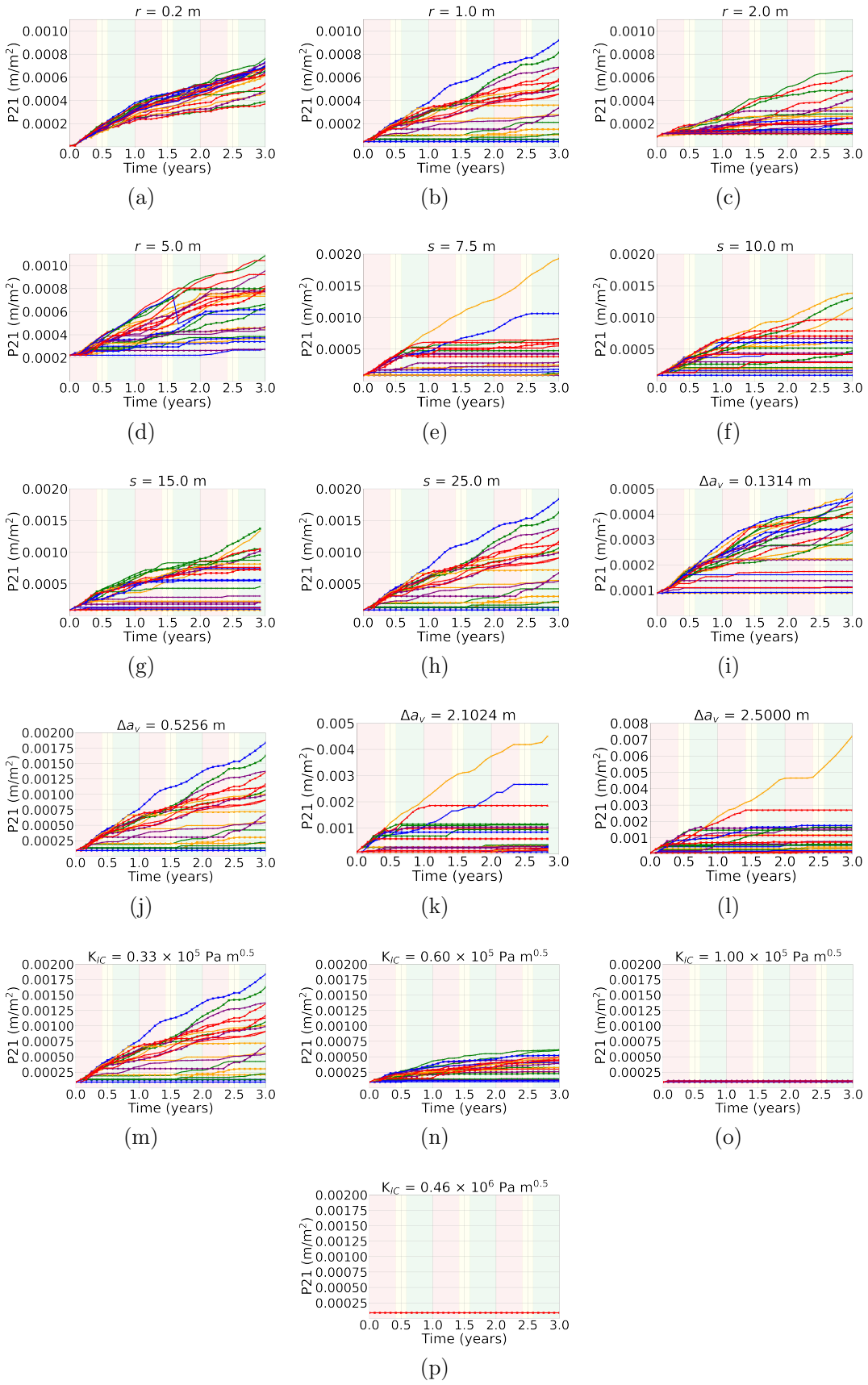


Figure 4.4: P_{21} versus time for four cases of varying (a-d) initial natural fracture radius, (e-h) initial horizontal natural fracture spacing, (i-l) crack propagation velocity and (m-p) caprock fracture toughness. Note that the y-axes are not the same in each case. Marker size has no physical meaning.

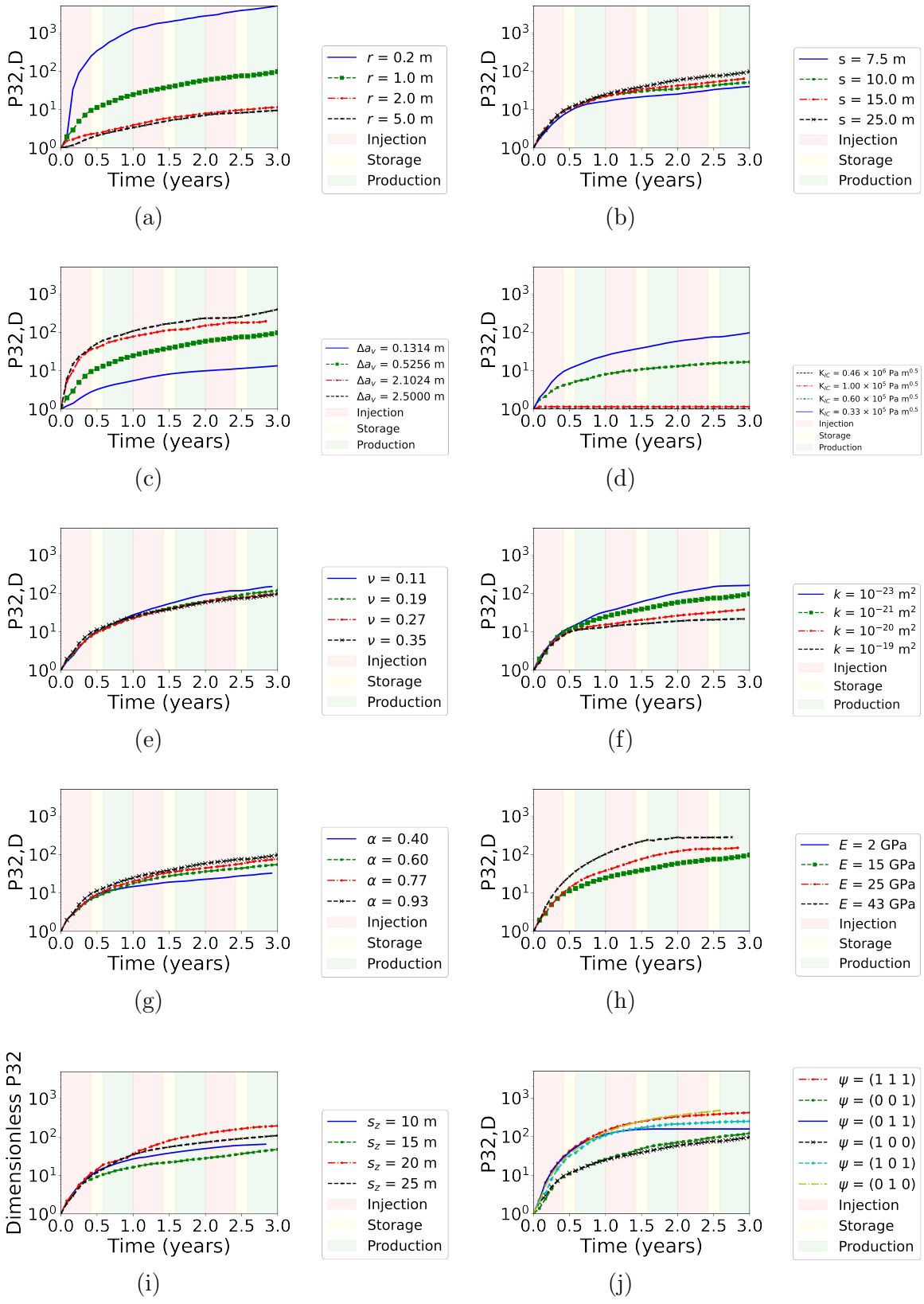


Figure 4.5: Dimensionless P_{32}, $P_{32,D}$, versus time for four cases of varying (a) initial natural fracture radius, (b) initial horizontal natural fracture spacing, (c) crack propagation velocity, (d) caprock fracture toughness, (e) caprock Poisson's ratio, (f) caprock matrix permeability, (g) caprock Biot coefficient, (h) caprock Young's modulus, (i) initial vertical natural fracture spacing, and (j) initial natural fracture orientation. The y-axis is logarithmic.

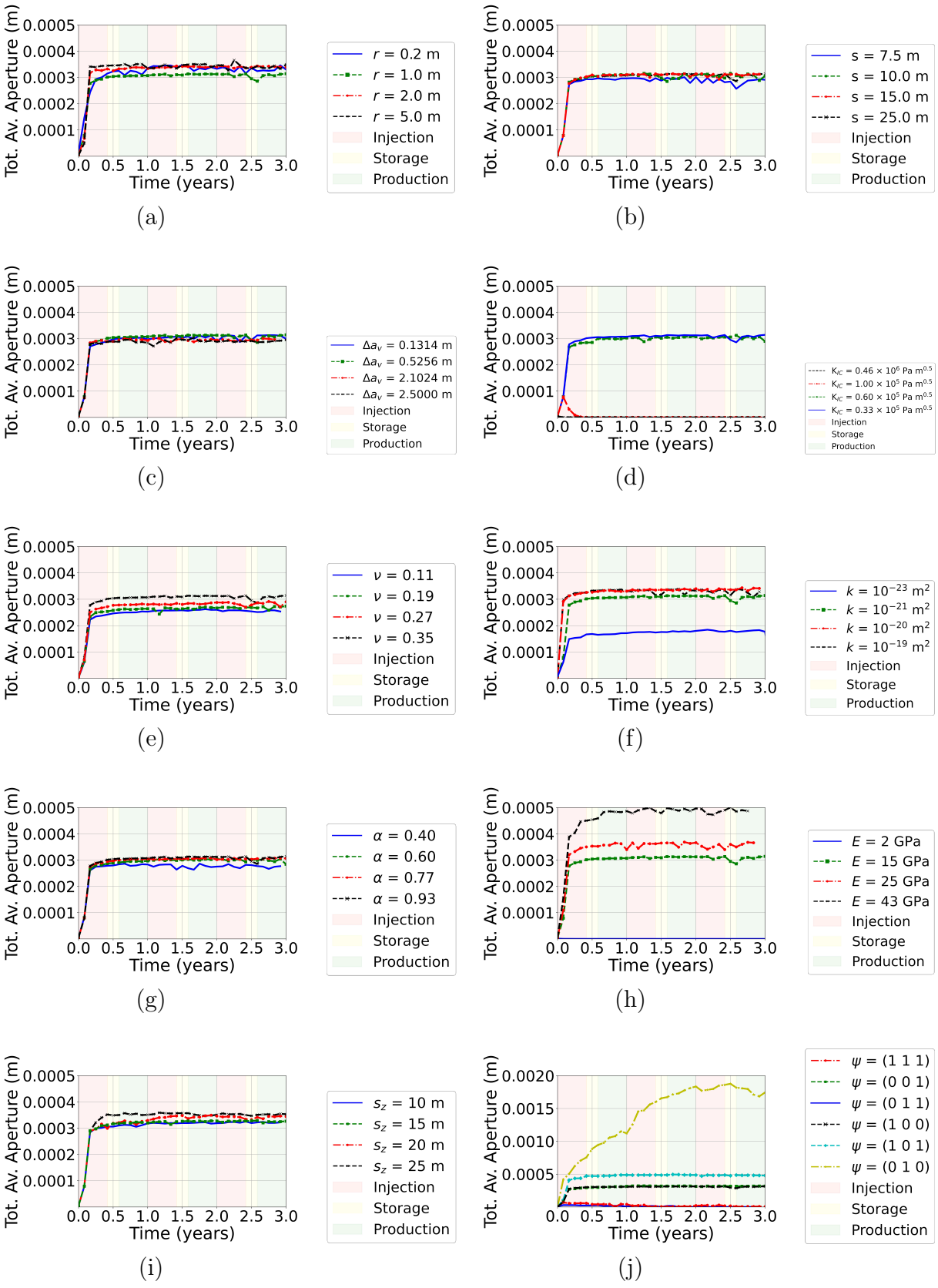


Figure 4.6: Total average aperture of all fractures versus time for four cases of varying (a) initial natural fracture radius, (b) initial horizontal natural fracture spacing, (c) crack propagation velocity, (d) caprock fracture toughness, (e) caprock Poisson's ratio, (f) caprock matrix permeability, (g) caprock Biot coefficient, (h) caprock Young's modulus, (i) initial vertical natural fracture spacing, and (j) initial natural fracture orientation.

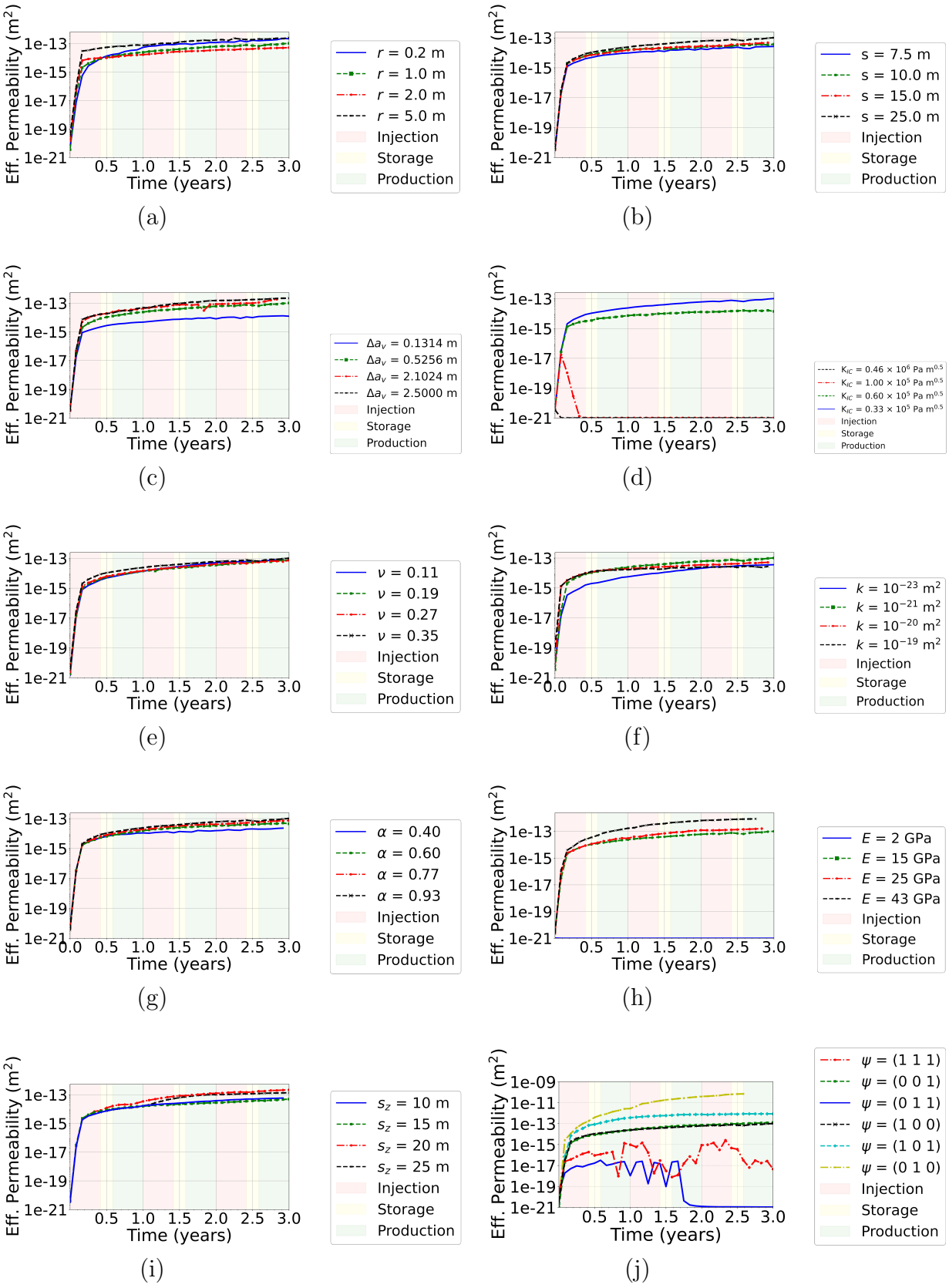


Figure 4.7: Effective permeability of the fractured caprock region versus time for four cases of varying (a) initial natural fracture radius, (b) initial horizontal natural fracture spacing, (c) crack propagation velocity, (d) caprock fracture toughness, (e) caprock Poisson's ratio, (f) caprock matrix permeability, (g) caprock Biot coefficient, (h) caprock Young's modulus, (i) initial vertical natural fracture spacing, and (j) initial natural fracture orientation.

tested were 7.5 m, 10 m, 15 m and 25 m. Natural fracture spacings of up to 25 m were tested because this was the maximum spacing reported by Carlson and Mercer [1991] for Devonian shale through history matching of production data from hundreds of wells across the Eastern United States. The minimum fracture spacing tested was 7.5 m. Ideally, this would be much lower and in the range of 0.10 m, but such small spacings induce numerical issues.

Figures 4.3e-h show the state of the fracture network at the end of the three year storage period. When the fracture spacing was large as in the 25 m case, a heterogeneous network of large and small fractures developed. The fractures grew in a quasi-circular manner and very large fractures were often found in the vicinity of very small fractures (i.e., row 2 column 5 in Figure 4.3h). Some very large fractures grew such as that in row 2 column 5 of Figure 4.3h. When the spacing decreased to 15 m, the fracture network still remained very heterogeneous with some large and some small fractures but more of the fractures were ellipsoidal or more pointed in geometry and less were quasi-circular. Many of these ellipsoidal fractures had their main axis pointing in a near-vertical direction (pointing horizontally in real physical space, i.e., the fractures in row 2 column 2 and row 4 column 3 of Figure 4.3g). When the spacing decreased further to 10 m, a few more of the fractures became more ellipsoidal in geometry with the green, orange and yellow fractures in Figure 4.3f all having a very ellipsoidal geometry with their main axes pointing vertically (horizontally in reality). Despite these small differences in geometry, the fracture networks in all three of the 10 m, 15 m and 25 m spacing cases were very similar. Only in the 7.5 m case, the case with the smallest natural fracture spacing, did a significantly different network evolve. This fracture network was very heterogeneous with many small fractures and a few very large fractures such as the teal fracture in the centre of the fracture network. This fracture now occupies more than the entire width of the original fracture network (> 30 m).

Figure 4.5b shows the dimensionless P_{32} of the fractured caprock region. A small trend is observed in which fracture area increased with increased spacing. At the end of the three year study period, the P_{32} of the fractured caprock region for the 7.5 m, 10.0 m, 15.0 m and 25.0 m cases was 38, 51, 62 and 83 showing fairly small differences in areal extent between the cases. The P_{21} plots in Figures 4.4e-h show that in the 7.5 m, 10.0 m, 15.0 m and 25.0 m

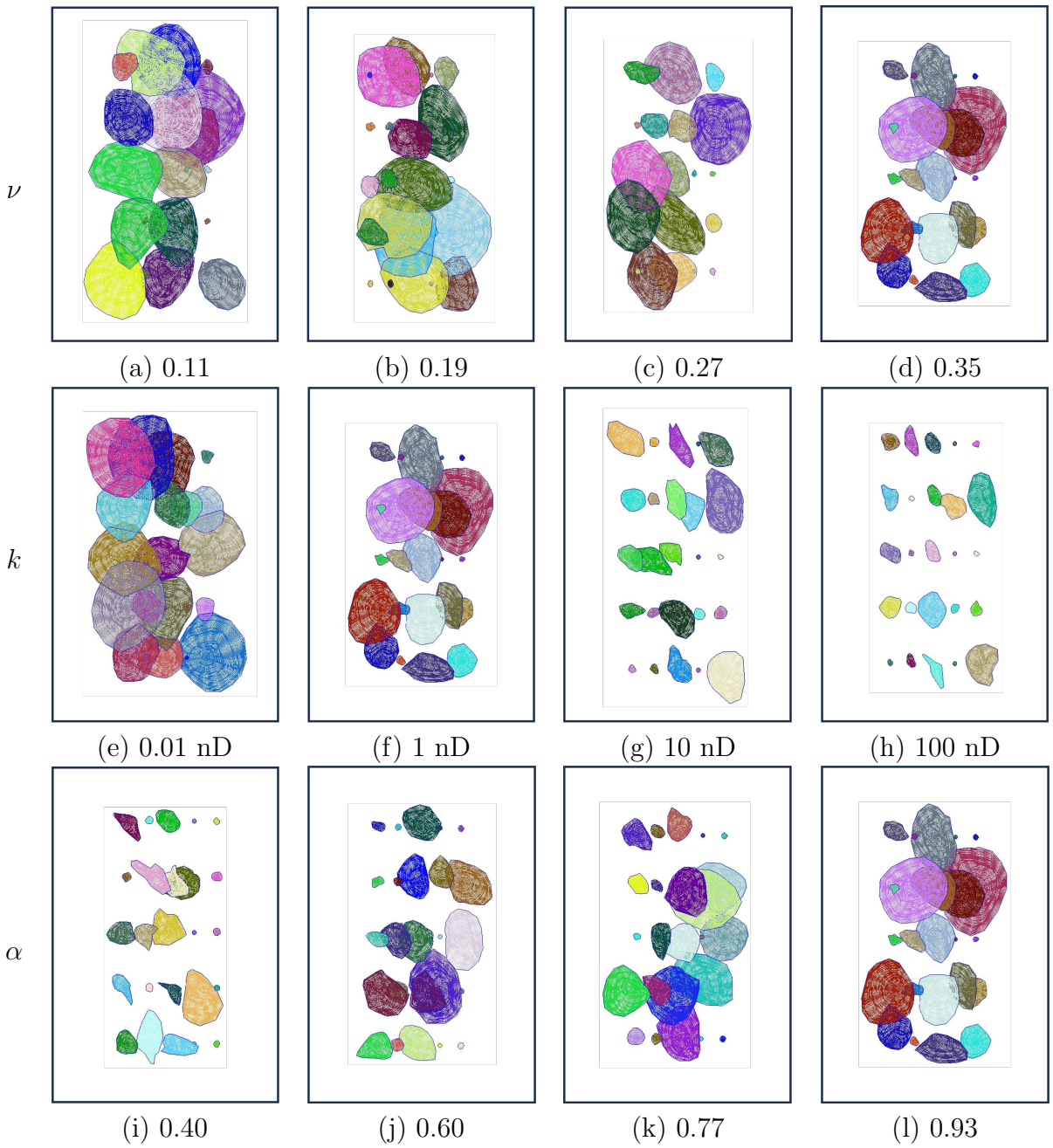
cases, the number of fractures still growing at the end of the study period was 4, 6, 7, and 13, respectively. Therefore, the number of fractures that have fully arrested decreases as initial spacing increases. Furthermore, in the 7.5 m spacing case only one fracture shows a moderately increasing gradient suggesting non-negligible continued growth (the largest fracture in teal in Figure 4.3e). For the largest spacing cases (i.e., 15.0 m and 25.0 m) many of the fractures show steep gradients at the end of the P_{21} curves implying significant further growth.

The total average aperture in each case is shown in Figure 4.6b. Very little difference is seen in total average aperture between the cases. This is especially true between the largest spacing cases of 15.0 m and 25.0 m, where the apertures are essentially identical. This total average aperture decreases very slightly when the spacing is reduced from 15.0 m to 10.0 m at times throughout the simulation with a maximal difference of 26 microns with those cases, but even then for the majority of the storage operation there was no difference with the 15.0 and 25.0 m cases. Only when the spacing was reduced to 7.5 m did a noticeable reduction in total average aperture of the fractures occur and even then this was only a maximum of approximately 30 microns, but it was sustained throughout the majority of the storage operation.

The effective permeability plot in Figure 4.7b shows that the effective permeability increased as the spacing of natural fractures increased. This is because the further apart the fractures are initially, the less stress shadowing they experience from neighbouring fractures and the greater the propensity they have for growth. The effective permeability at the end of the three year study period in the 7.5 m, 10.0 m, 15.0 m and 25.0 m cases was 23 mD, 57 mD, 63 mD, and 110 mD. Before the end of the first storage year, the effective permeability of all four cases was very similar, but beyond this point the effective permeability of the 25.0 m spacing case began to increase at a considerably faster rate than the three smaller spacing cases which all remained very similar.

4.5.1.3 Initial Fracture Orientation

Four simulations were performed to assess the impact of the natural fracture orientation on the fracture growth and permeability alteration of the caprock. All model properties were



(a) 0.11 (b) 0.19 (c) 0.27 (d) 0.35

(e) 0.01 nD (f) 1 nD (g) 10 nD (h) 100 nD

(i) 0.40 (j) 0.60 (k) 0.77 (l) 0.93

Figure 4.8: The final state of the fracture network after three years of hydrogen storage for four cases of (a-d) caprock Poisson's ratio, (e-h) caprock matrix permeability, and (i-l) caprock Biot coefficient

defined according to Table 4.2 in each simulation, with the only property changing between the simulations being the orientation of the natural fractures in the 5×5 array. The orientations tested were (1 0 0), (1 1 1), (0 0 1), (0 1 1), (1 0 1) and (0 1 0), where (x y z) represents the unit normal vector pointing outward from the fracture faces. These correspond to strike/dips of 0°/90°, 45°/54.7°, 0°/0°, 90°/45°, 0°/45°, and 90°/90°, respectively. These orientations were selected randomly because in reality the fractures could strike and dip at any angle.

Figures 4.9i-n show the state of the fracture network at the end of the three year storage period. In the majority of cases, the fractures form geometries that are almost perfectly circular (i.e., (1 1 1), (0 1 1), (1 0 1), and (0 1 0)). Only in the (1 0 0) and (0 0 1) cases did some of the fractures form more quasi-circular, ellipsoidal or angular geometries. When the fractures were inclined to some degree (i.e., not perfectly vertical or horizontal), the fractures always formed almost perfectly circular geometries (i.e., (1 1 1), (0 1 1), (1 0 1)) but when the fractures were perfectly vertical or horizontal, the fractures often formed non-circular geometries (i.e., (1 0 0) and (0 0 1)). The (1 0 0), (1 1 1), (0 1 1) and (1 0 1) cases all displayed heterogeneous fracture networks by virtue of the fact that the fractures varied in size considerably. The (0 1 0) and (0 0 1) cases yielded much more homogeneous fracture networks with all fractures having very similar sizes. In the (0 1 0) case, the fractures grew to such an extent that the five fractures in each row all overlapped forming five huge fractures (one per row). Furthermore, these fractures grew to such an extent vertically that by the end of the three year storage period, they had almost reached the reservoir-caprock and caprock-overburden interfaces, risking mechanical failure of the caprock.

Figure 4.5j shows the dimensionless P_{32} of the fractured caprock region. At the end of the three year study period, the P_{32} of the fractured caprock region for the (1 0 0), (1 1 1), (0 0 1), (0 1 1), (1 0 1) and (0 1 0) cases were 83, 420, 100, 136, 232 and 464, showing that the resultant fracture surface area is highly dependent on the orientation of the natural fractures. The dimensionless P_{32} plot also shows that (1 1 1), (0 1 1), (1 0 1) and (0 1 0) cases grew more rapidly in the early stages of the storage operations and reach a near mechanically stable state where there is very minimal growth by the end of the study period, whereas the (1 0 0) and (0 0 1) cases grow more slowly but are still showing signs of continual growth at the end of the

study period by virtue of the increasing gradient in the P_{32} plot.

The total average aperture in each case is shown in Figure 4.6j and varies drastically dependent on initial natural fracture orientation. The (1 1 1) and (0 1 1) cases have the smallest average aperture of all the cases, with values of 33 microns and 20 microns, respectively. Additionally, in both of these cases, the total average aperture broadly decreases with time. Then, the (0 0 1) and (1 0 0) cases have larger total average apertures than the (1 1 1) and (0 1 1) cases, possessing values of 330 microns and 310 microns, respectively. Therefore, the (0 0 1) and (1 0 0) cases have essentially identical total average apertures and these are approximately one order of magnitude larger than the apertures of the (1 1 1) and (0 1 1) cases. The (1 0 1) case has the second largest apertures of all six cases with an average value of 490 microns. Finally, the (0 1 0) case has the largest aperture of all six cases, and it has no typical aperture value since in this case the aperture continuously increases with time from the onset of initial injection until the end of the second withdrawal period. After this, the aperture plateaus at an average value of 1.8 mm, and may even potentially be showing signs of decreasing at the end of study period. Therefore, the aperture in the (0 1 0) case is almost two orders of magnitude larger than the aperture in the (1 1 1) and (0 1 1) cases.

The effective permeability plot in Figure 4.7j shows that the effective permeability at the end of the study period in the (1 0 0), (1 1 1), (0 0 1), (0 1 1), (1 0 1) and (0 1 0) was 100 mD, 0.06 mD, 110 mD, 1×10^{-6} mD, 3000 mD and 95000 mD, respectively. After approximately 1.7 years, the (0 1 1) case reverses its effective permeability returning to approximately the caprocks original permeability prior to the onset of hydrogen storage.

4.5.1.4 Crack Propagation Velocity

Four simulations were performed to assess the impact of the maximum extension length, Δa_v, which represents the crack propagation velocity, on the fracture growth and permeability alteration of the caprock. All model properties were defined according to Table 4.2 in each simulation, with the only property changing between the simulations being the maximum extension length of the natural fractures in the 5×5 array. The maximum extension lengths tested

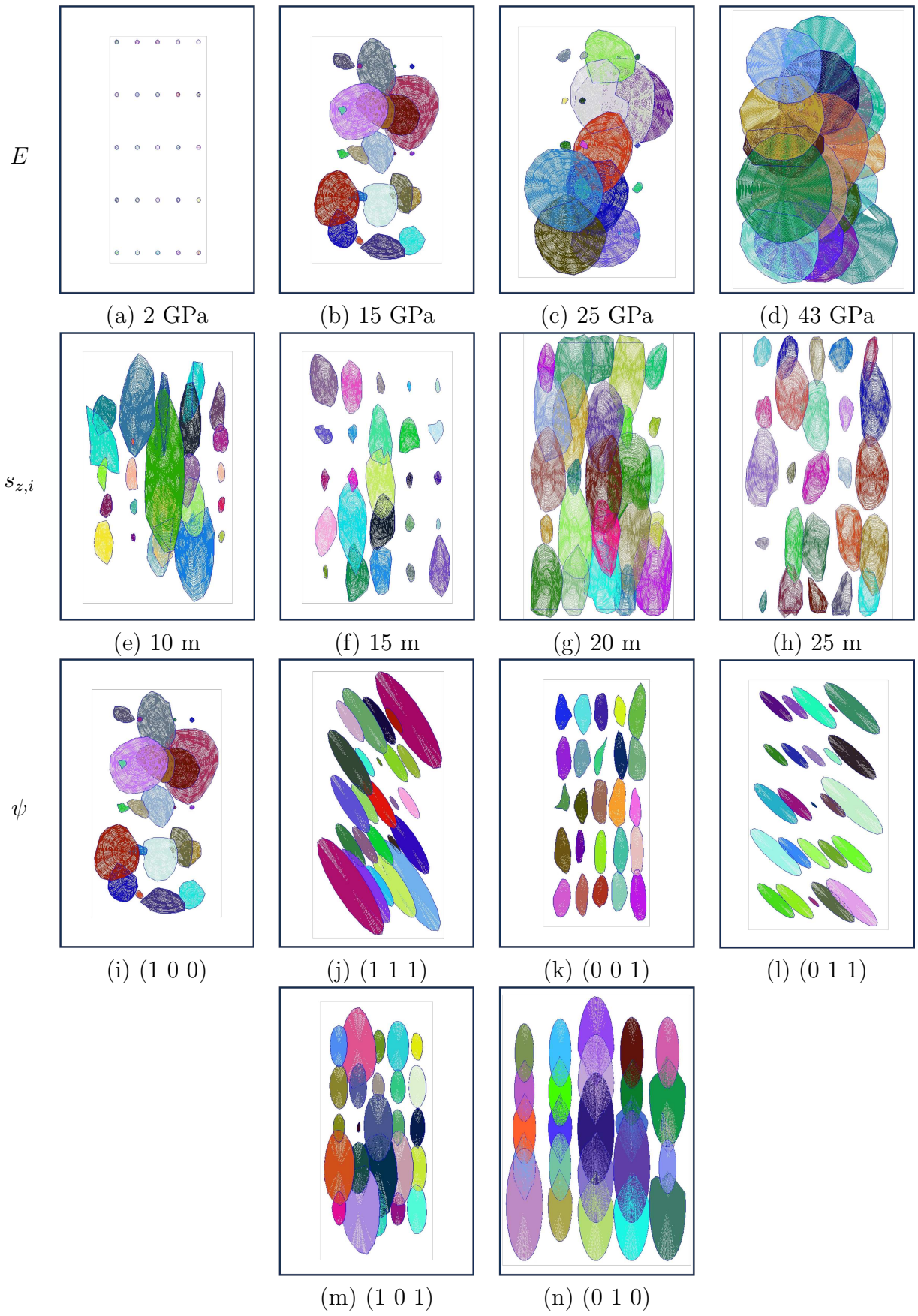


Figure 4.9: The final state of the fracture network after three years of hydrogen storage for four cases of (a-d) caprock Young's modulus, (e-h) initial natural fracture vertical spacing, and (i-n) initial natural fracture orientation. Note that for the vertical spacing and orientation cases, the diagrams have been re-oriented to fit in the same shape boxes as the Young's modulus cases.

were 0.1314 m, 0.5256 m, 2.1024 m and 2.5000 m per time step, which corresponds to crack propagation velocities of 5×10^{-8} m/s, 2×10^{-7} m/s, 8×10^{-7} m/s and 1×10^{-6} m/s, respectively.

Figures 4.3i-l show the state of the fracture network at the end of the three year storage period. The geometry of the fracture networks are very different in each case. For a small crack propagation velocity such as that in the 0.1314 m case, the fractures are fairly homogeneous all having similar sizes in the most part, and all grow in a quasi-circular manner. When the crack propagation velocity was increased to that in the 0.5256 m case, a more heterogeneous fracture network develops with some large fractures and some small fractures. The majority of the fractures are either ellipsoidal or quasi-circular in geometry, with little angularity. Typically, the largest fractures are located in the vicinity of the smallest fractures (i.e., the fractures in row 1 column 3, row 2 column 5 and row 2 column 2) and small fractures are often sandwiched between two larger fractures (i.e., row 4 columns 1,2 and 3). When the crack propagation velocity was increased to that in the 2.1024 m case, the heterogeneity in the fracture network drastically increased. Some huge fractures evolve whilst other fractures barely grow. The angularity of the fractures also increases with many of the smaller fractures being sharp and pointed. Finally, when the crack propagation velocity was further increased to that in the 2.5000 m case, the heterogeneity in the network becomes even greater. A massive fracture develops which penetrates the full thickness of the caprock, thus propagating into the overlying overburden unit and the underlying reservoir unit. Some very angular and polygonal fractures develop and many of the fractures become particularly pointed in the horizontal direction.

Figure 4.5c shows the dimensionless P_{32} of the fractured caprock region. The dimensionless P_{32} increases substantially as the crack propagation velocity increases, highlighting that the total crack surface area increases as the crack propagation velocity increases. The 0.1314 m, 0.5256 m, 2.1024 m and 2.5000 m cases yielded P_{32} values of 9, 80, 200 and 360, respectively. For the smaller crack propagation velocity cases (i.e., 0.1314 m and 0.5256 m), the P_{32} seem to be almost reaching a stable value at the end of the three year study peripd, but for larger crack propagation velocities (i.e., 2.1024 m and 2.5000 m), the P_{32} curves show a steepening gradient at the end of the three year point.

Figures 4.4i-l show the P_{21} per fracture of the fractured caprock region. It can be seen in all cases that the vast majority of fractures have become mechanically stable, keeping the same fracture length for a long while prior to the end of the study period. In the 0.1314 m, 0.5256 m, 2.1024 m and 2.5000 m cases, the number of fractures still growing in length at the three year point was 11, 11, 4 and 1 respectively, showing that the number of fractures still growing after three years decreases as the crack propagation velocity increases. In the 2.1024 m and 2.5000 m cases, the largest fracture in both cases is still growing, implying that the network permeability could become even more heavily dominated by one fracture.

The total average aperture in each case is shown in Figure 4.6c. No systematic trend in total average aperture with increasing crack propagation velocity was found. In all four cases, the total average aperture was essentially the same at a value of 3 mm, showing that the aperture is insensitive to changes in crack propagation velocity.

The effective permeability plot in Figure 4.7c shows that as crack propagation velocity increased, the effective permeability of the fractured caprock region increased. The final effective permeability in the 0.1314 m, 0.5256 m, 2.1024 m and 2.5000 m cases was 13 mD, 95 mD, 185 mD and 220 mD.

4.5.1.5 Vertical Fracture Spacing

Four simulations were performed to assess the impact of vertical fracture spacing on the fracture growth and permeability alteration of the caprock. In these cases, the initial horizontal 5×5 array of natural fractures used in all the other growth simulations in this work were removed. It was replaced with an initial vertical 5×5 array of natural fractures in the same central region of the caprock. All other model properties were defined according to Table 4.2 in each simulation; the only property changing between the simulations was the vertical fracture spacing. The vertical fracture spacings tested were 10 m, 15 m, 20 m and 25 m. No reliable data on the range of realistic vertical fracture spacings in shale caprock could be found. Therefore, the upper limit of 25 m was specified to be the same as that found for general fracture spacings in any direction (Section 4.5.1.2). Ideally, the lower end of the range would have tested smaller

vertical spacings than 10 m, but this introduced numerical issues associated with such small elements between the individual fractures.

Figures 4.9e-h show the state of the fracture network at the end of the three year storage period. When the vertical fracture spacing was smallest at 10 m, a very heterogeneous fracture network evolved. This is highlighted by the fact that the fracture surface area is smallest in the 10 m case, but the 10 m case has the largest fracture (Figure 4.11e). Furthermore, in the smallest two vertical spacing cases (10 m and 15 m), the geometry of the fractures is more angular and polygonal, whereas the fractures become much more quasi-circular and ellipsoidal for larger vertical spacings (20 m and 25 m). Despite the smaller growth extents in the 10 m case, fracture columns 3 and 4 (Figure 4.9e) show that the fractures have overlapped and joined into two large vertical fractures, which could lead to mechanical failure of the caprock if they overcome the full caprock thickness. In the 20 m case, the fractures have grown to a very large extent. The fractures in columns 2 and 4 have overlapped and formed two very large vertical fractures, and the fractures in column 3 have very almost accomplished the same. The two newly formed, very large fractures in columns 2 and 4 fully penetrate the caprock thickness, providing a direct pathway for hydrogen to flow from the reservoir, through the caprock, and into the overburden. The caprock has lost mechanical integrity. In the 25 m case, the fractures do not grow to as large extents as the 20 m case, but grow more than the 10 m and 15 m cases. None of the fractures overlap to form one continuous large fracture, although the fractures in column 5 (Figure 4.9h) have almost accomplished this. The fractures in this case have penetrated the caprock-reservoir interface, but they cease further downward growth into the reservoir unit, forming blocky shapes at their base (row 5 in Figure 4.9h). The growth ceases because the fracture toughness of the sandstone reservoir is approximately 27 times larger than that of the shale caprock. Therefore, whilst the stress intensity at the fracture tips is sufficient to propagate the fractures in the shale, it is insufficient to propagate them in the sandstone.

Figure 4.5i shows the dimensionless P_{32} of the fractured caprock region. No systematic trend in dimensionless P_{32} was found with increasing or decreasing vertical fracture spacing. The final dimensionless P_{32} values at the end of the study period for the four cases were 58, 40, 198 and 104, for the 10 m, 15 m, 20 m and 25 m cases respectively. Therefore, an intermediate vertical

spacing of 20 m appears to exacerbate the fracture growth, with smaller total fracture surfaces areas for spacings smaller and larger than this. Generally, smaller vertical spacings seem to reduce fracture growth since the final P_{32} values of the 10 m and 15 m cases were approximately less than half of the 20 m and 25 m cases.

The total average aperture in each case is shown in Figure 4.6i. It was found that as the vertical spacing increased, the fracture apertures increased. However, the difference between the cases was relatively small. The average aperture for the 10 m, 15 m, 20 m and 25 m cases was 320 microns, 325 microns, 340 microns, and 355 microns, respectively.

The effective permeability plot in Figure 4.7i shows no systematic trend with increasing or decreasing vertical fracture spacing. The final effective permeability in the 10 m, 15 m, 20 m and 25 m cases was 68 mD, 52 mD, 232 mD, and 147 mD, respectively. Whilst no systematic trend was found, within this range, it can be seen the larger vertical spacings result in enhanced effective caprock permeabilities.

4.5.2 Effect of Caprock Mechanical Properties

4.5.2.1 Fracture Toughness

Four simulations were performed to assess the impact of fracture toughness on the fracture growth and permeability alteration of the caprock. All model properties were defined according to Table 4.2 in each simulation, with the only property changing between the simulations being the fracture toughness of the caprock. The fracture toughnesses tested were 0.33×10^5 Pa $m^{1/2}$, 0.60×10^5 Pa $m^{1/2}$, 1.00×10^5 Pa $m^{1/2}$ and 0.46×10^6 Pa $m^{1/2}$.

Figures 4.3m-p show the state of the fracture network at the end of the three year storage period. When the fracture toughness was 0.46×10^6 Pa $m^{1/2}$, the fractures exhibited no growth. When the fracture toughness was 1.00×10^5 Pa $m^{1/2}$, the fractures exhibit a very small amount of growth but rapidly reach a state of mechanical equilibrium again with no further growth. Even when the fracture toughness was decreased further to 0.60×10^5 Pa $m^{1/2}$, the majority of

fractures still do not experience large amounts of growth. In this case the final fracture network is heterogeneous in terms of both fracture sizes and fracture geometry with some rounded fractures (i.e., row 2 column 1 in Figure 4.3n) and some highly angular fractures (i.e., row 2 column 3/4 and row 3 column 3 in Figure 4.3n). When the fracture toughness was decreased further to 0.33×10^5 Pa $m^{1/2}$, finally significant fracture growth was observed. A heterogeneous fracture network evolved with some very small fractures and some huge fractures. In the locations where huge fractures formed, very small fractures are often found in their vicinity. An example of this include the huge fracture in row 2 column 5 of Figure 4.3m, where two very small fractures with minimal growth are located above and below. Further examples of this include the fractures at row 1 column 3 and row 2 column 2. The dimensionless P_{32} in Figure 4.5d shows that in the 0.33×10^5 Pa $m^{1/2}$ case, the fracture area increased by approximately a factor of 100 from before the onset of initial injection and in the 0.60×10^5 Pa $m^{1/2}$ case, the fracture area increased by approximately a factor of 10.

Figures 4.4m-p show the P_{21} per fracture of the fractured caprock region. The 0.60×10^5 Pa $m^{1/2}$ case reveals that almost all fractures, except two, show no signs of continued growth beyond the three year study period. These fractures seem to have reached mechanical equilibrium. Even the two fractures which have some non-zero gradient at the 3.0 year point, do not show signs of steep increase, and thus, are unlikely to grow considerably more. The two fractures showing continual growth are two of the four largest fractures in this case suggesting that beyond the study period any small further growth will lead to an even more heterogeneous network. In the 0.33×10^5 Pa $m^{1/2}$ case, approximately half of the fractures are still showing signs of growth at the end of the study period and some have steep gradients at this point suggesting that considerably more growth could be possible. The larger fractures show the steepest gradients at this point and thus are likely to become much larger implying that again that the fracture network heterogeneity is likely to increase. Furthermore, the largest fractures in the 0.33×10^5 Pa $m^{1/2}$ case are as much as three times larger than the 0.60×10^5 Pa $m^{1/2}$ case.

The total average aperture in each case is shown in Figure 4.6d. It was found that total average aperture increased broadly as fracture toughness decreased. However, the difference in total fracture aperture between the 0.33×10^5 Pa $m^{1/2}$ and 0.60×10^5 Pa $m^{1/2}$ cases was very small

with a maximal difference between the two cases of 27 microns. In the 1.0×10^5 Pa $m^{1/2}$ case, the aperture of the fractures increases very slightly at the onset of injection at the coincident time in which the fractures grew. Once the fractures ceased growing, the aperture closed again. In the 0.46×10^6 Pa $m^{1/2}$ case, where no growth took place, the total average aperture of the fractures never deviated from their original value, thus resulting in no permeability change due to either increases in fracture length or due to aperture opening.

The effective permeability plot in Figure 4.7d shows that as fracture toughness decreases, the effective permeability of the fractured caprock region increases. The final permeability difference between the largest and smallest caprock fracture toughness cases was huge, spanning nearly eight orders of magnitude. In the 1.0×10^5 Pa $m^{1/2}$ case, the effective permeability increases at early times to approximately 2×10^{-17} m^2, before then returning to a very low value.

4.5.2.2 Young's Modulus

Four simulations were performed to assess the impact of caprock Young's modulus on the fracture growth and permeability alteration of the caprock. All model properties were defined according to Table 4.2 in each simulation, with the only property changing between the simulations being the Young's modulus of the caprock. The Young's moduli tested were 2 GPa, 15 GPa, 25 GPa, and 43 GPa. The intermediary values (i.e., 15 GPa and 25 GPa) were not chosen with a specific statistical methodology and as such are randomly chosen between the end points from the literature review.

Figure 4.9a-d show the state of the fracture network at the end of the three year storage period. The geometry of the fracture network drastically depends on the caprock Young's modulus. When the Young's modulus was very small (i.e. 2 GPa), the caprock natural fractures did not grow at all and thus all fractures remained at their initial 1 m radius size with a purely circular geometry. When the Young's modulus was increased to 15 GPa, a heterogeneous fracture network developed with some very small fractures and some large fractures. This heterogeneity increased further when the Young's modulus was increased to 25 GPa, with little

further growth of the smaller fractures, but very significant growth increases with the larger fractures. The fracture network in the 25 GPa case had more quasi-circular fractures than the 15 GPa case, which had a few examples of ellipsoidal and pointed fractures. In both cases, very large fractures develop between very small fractures (i.e., the fractures in column 5, row 1,2 and 3 in both Figure 4.9b and 4.9c). When the Young's modulus was large (i.e., 43 GPa), the vast majority of fractures grew to very large extents, with a fairly homogeneous fracture size and geometry distribution. Nearly all fractures formed a quasi-circular geometry. The fractures grew to such an extent that many within a given column overlapped, combining to form one much larger fracture.

The dimensionless P_{32} and the P_{21} are shown in Figures 4.5h and 4.11a-d respectively. A trend was found in the dimensionless P_{32} in which P_{32} increased as caprock Young's modulus increased. It can be seen that in the 43 GPa case, the P_{32} essentially reaches a stable value after approximately 1.6 years, and the same can be said in the 25 GPa case after a time of approximately 2.3 years. In the 15 GPa case, the gradient of the P_{32} curve at 3.0 years, shows that the fractures are still significantly growing at the end of the study period. Therefore, in the Young's moduli range of 15 GPa to 43 GPa, it is observed that as Young's modulus increases, it takes a longer amount of time for the fracture network to approach mechanical equilibrium. The final P_{32} values in the 2 GPa, 15 GPa, 25 GPa, and 43 GPa cases was 1, 90, 140 and 280, respectively.

The total average aperture in each case is shown in Figure 4.6h. It was found that the total average aperture systematically increased as Young's modulus increased. When the Young's modulus was low (i.e., 2 GPa), the fractures essentially remained closed. The stabilised total average aperture value in the 15 GPa, 25 GPa, and 43 GPa cases was 310 microns, 370 microns and 490 microns, respectively. When the Young's modulus was increased by 10 GPa from 15 GPa to 25 GPa the increase in aperture was 6 microns and when it was increased by approximately 30 GPa (three times as much) from 15 GPa to 43 GPa, the increase in aperture was 18 microns (three times as much). This demonstrates an approximately linear increase in aperture value with caprock Young's modulus in this range.

Figure 4.7h shows the effective permeability versus time. As Young's modulus increased, effective permeability of the fractured caprock region increased. The final effective permeability value in the 2 GPa, 15 GPa, 25 GPa and 43 GPa cases was 1×10^{-6} mD, 102 mD, 161 mD and 868 mD, respectively.

4.5.2.3 Poisson's Ratio

Four simulations were performed to assess the impact of fracture toughness on the fracture growth and permeability alteration of the caprock. All model properties were defined according to Table 4.2 in each simulation, with the only property changing between the simulations being the Poisson's ratio of the caprock. The Poisson's ratios tested were 0.11, 0.19, 0.27 and 0.35. The intermediary values (i.e., 0.19 and 0.27) were chosen to be equidistant (0.08) from the end points derived from the literature review.

Figures 4.8a-d show the state of the fracture network at the end of the three year storage period. The fracture networks are very similar in all cases, with large fractures dispersed with small fractures leading to a heterogeneous fracture network. In all cases, the fractures grow in a quasi-circular manner with very few ellipsoidal or angular fractures. In all cases, the largest fractures are typically found in the immediate vicinity of very small fractures, especially where the small fractures are sandwiched in between large fractures. Examples of this include the fractures in row 4 columns 1,2 and 3, row 4 columns 3, 4 and 5, row 4 columns 1,2 and 3, and row 4 columns 1,2 and 3 in the 0.11, 0.19, 0.27 and 0.35 cases respectively.

The dimensionless P_{32} is shown in Figure 4.5e. A trend was found in which as Poisson's ratio decreases, the fracture area increases. For Poisson's ratios between 0.19 and 0.35, this trend was not strong with a difference of only 1 in the dimensionless P_{32} of the 0.19 and 0.27 cases, and much less than this between 0.27 and 0.35. When the Poisson's ratio of the caprock was decreased from 0.19 to 0.11, this increase in P_{32} was slightly larger with a difference of 2 between the cases. Nevertheless, the areal size of the fractures are essentially the same in all cases.

The total average aperture in each case is shown in Figure 4.6e. It was found that the total

average aperture systematically increased as Poisson's ratio increased. Furthermore, the degree of increase in the total average aperture as Poisson's ratio increased, accelerated as the Poisson's ratio became larger. For example, when the Poisson's ratio was increased to 0.19 from 0.11, the total average aperture increased by approximately 11 microns. Then, when the Poisson's ratio was increased from 0.19 to 0.27, the total average aperture increase was larger at approximately 18 microns. Finally, when the Poisson's ratio was increased from 0.27 to 0.35, the total average aperture increase was even larger at approximately 30 microns.

Figure 4.7e shows an effective permeability versus time plot that reveals that there was no systematic change in effective permeability with Poisson's ratio and that the final effective permeabilities of the fractured caprock region were nearly the same in all four cases. There was a systematic trend in effective permeability with Poisson's ratio after the first year of operations, with effective permeability increasing with larger Poisson's ratio, but this did not hold beyond this time.

4.5.2.4 Initial Matrix Permeability

Four simulations were performed to assess the impact of the matrix permeability on the fracture growth and permeability alteration of the caprock. All model properties were defined according to Table 4.2 in each simulation, with the only property changing between the simulations being the matrix permeability of the caprock. The matrix permeabilities tested were 0.01 nD, 1 nD, 10 nD and 100 nD. The intermediary values (i.e., 1 nD and 10 nD) were not chosen with a specific statistical methodology and as such are randomly chosen between the end points from the literature review.

Figures 4.8e-h show the state of the fracture network at the end of the three year storage period. The fracture networks show that as the matrix permeability decreased, the larger the areal extent of the fractures on average. Furthermore, in the lower matrix permeability cases (i.e., 0.01 nD and 1 nD), the majority of fractures were quasi-circular in geometry, whereas more angular (i.e., the fracture in row 1 column 3 of Figure 4.8g) and ellipsoidal fractures (i.e., the fracture in row 2 column 5 of Figure 4.8h) were present in the higher matrix permeability cases

(10 nD and 100 nD). Fracture networks in matrixes of permeability 1 nD, 10 nD and 100 nD were particularly heterogeneous with some large and some small fractures. This heterogeneity was significantly reduced for very low matrix permeabilities such as 0.01 nD, where the majority of fractures were of similar areal sizes. In the larger matrix permeability cases (i.e., 1 nD, 10 nD and 100 nD) it was commonplace that large fractures formed in the vicinity of small fractures and small fractures were sandwiched between two larger fractures (i.e., row 3 column 1,2 and 3 in Figure 4.8h, row 1 column 1,2 and 3 in Figure 4.8g, and row 4 column 1,2 and 3 in Figure 4.8f).

The dimensionless P_{32} is shown in Figure 4.5f. It was found that as matrix permeability decreased, the P_{32} of the fractured caprock region increased. The areal extent of the fracture network grew at a similar rate for all cases during the first injection period. The P_{21} plots for each case are shown in Figures 4.10e-h. It is observed that the number of fractures that are still growing at the end of the study period for the 0.01, 1, 10 and 100 nD cases are 5, 12, 7 and 2, respectively. The two fractures that are still growing in the 100 nD case, show very shallow gradients at the three year point, thus displaying minimal growth.

The total average aperture in each case is shown in Figure 4.6f. It was found that the total average aperture was highly variable between the cases and that fracture apertures increased as matrix permeability increased. However, the total average aperture was nearly identical in the two largest matrix permeability cases (10 nD and 100 nD).

Figure 4.7f shows an effective permeability versus time plot for the matrix permeability cases. The plot reveals that no systematic trend in effective permeability with increasing/decreasing matrix permeability was found but that the matrix permeability had a strong effect on the final effective permeability of the caprock. The final effective permeability in the 0.01, 1, 10 and 100 nD cases was 28 mD, 110 mD, 48 mD and 18 mD, respectively.

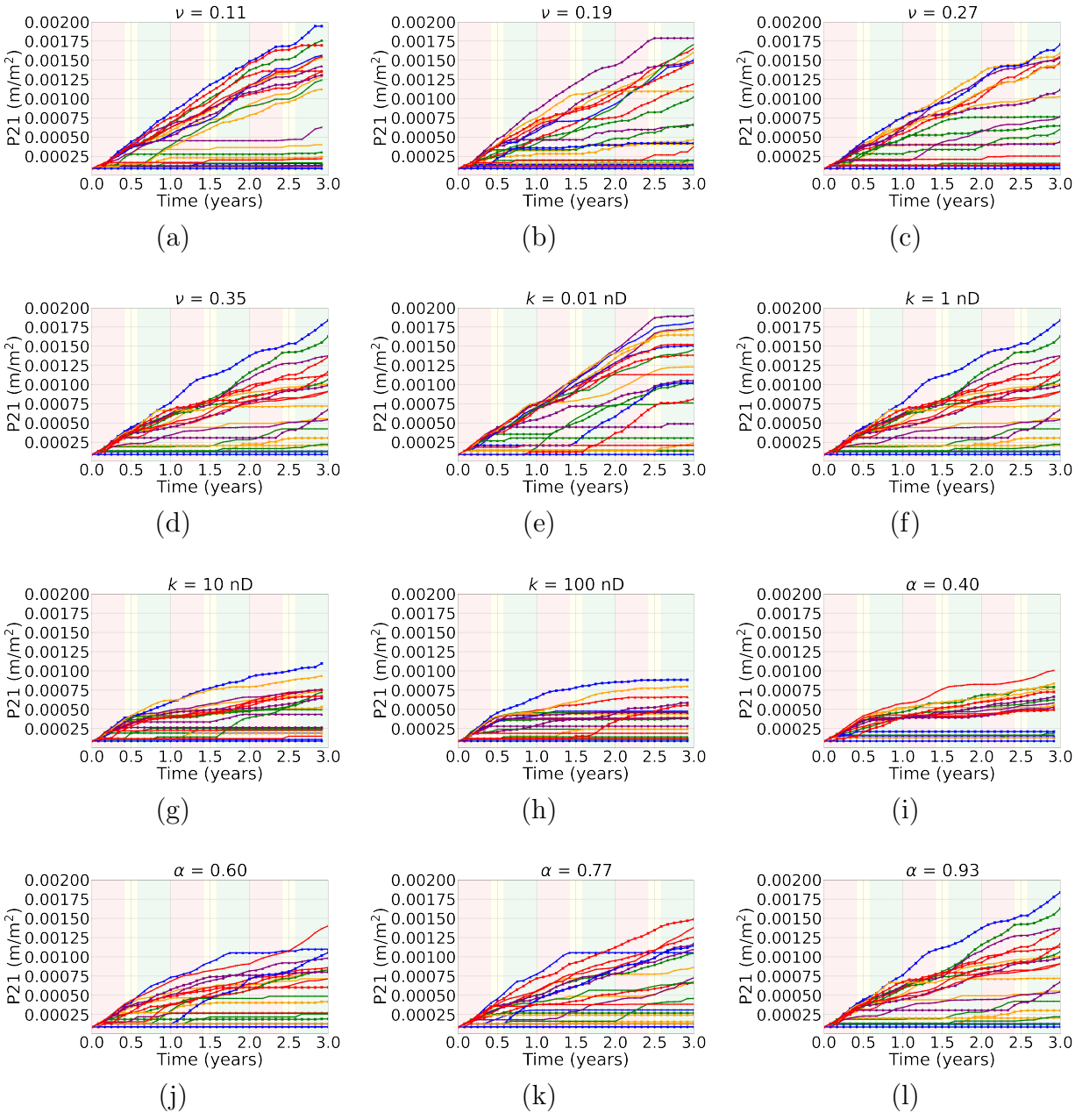


Figure 4.10: P_{21} versus time for four cases of varying (a-d) caprock Poisson's ratio, (e-h), caprock matrix permeability, and (i-l) caprock Biot coefficient. Note that the y-axes are not the same in each case. Marker size has no physical meaning.

4.5.2.5 Biot Coefficient

Four simulations were performed to assess the impact of the Biot coefficient on the fracture growth and permeability alteration of the caprock. All model properties were defined according to Table 4.2 in each simulation, with the only property changing between the simulations being the Biot coefficient of the caprock. The Biot coefficients tested included 0.40, 0.60, 0.77 and 0.93. The intermediary values (i.e., 0.60 and 0.77) were not chosen with a specific statistical methodology and as such are randomly chosen between the end points from the literature review.

Figures 4.8i-l show the state of the fracture network at the end of the three year storage period. The areal extent of the fractures decreased as Biot coefficient decreased. Furthermore, the fractures became slightly more angular and pointed when the Biot coefficient decreased, with more quasi-circular fracture geometries at larger Biot coefficients. This is especially noticeable in the 0.40 case in Figure 4.8i, where many of the fractures have highly angular geometries (i.e., the fractures in row 2 column 2, row 4 column 1, row 4 column 3, and row 1 column 1). All four cases display heterogeneous final fracture networks with some much larger fractures and some much smaller fractures. The dimensionless P_{32} is shown in Figure 4.5g, which reinforces the observation that the areal extent of the fractures decreased as Biot coefficient decreased. The final P_{32} values for the 0.40, 0.60, 0.77 and 0.93 cases was 30, 55, 81 and 100, highlighting a substantial difference between the cases.

The final P_{21} value after three years of storage operations, shown in Figures 4.10i-l, show that the largest fracture in each network decreased in length when the Biot coefficient decreased. For example, the final P_{21} in the 0.93, 0.77, 0.60 and 0.40 cases was 0.00184 m^{-1}, 0.00148 m^{-1}, 0.00140 m^{-1} and 0.00102 m^{-1}. Few of the fractures in the 0.40 and 0.60 cases are showing steep gradients in P_{21} at the end of the study period suggesting further growth is likely to be minimal, whereas the opposite is true for the 0.77 and 0.93 cases.

The total average aperture in each case is shown in Figure 4.6g. It can be observed that as Biot coefficient decreased, the total average aperture decreased. However, for the 0.60, 0.77 and 0.93

cases, whilst the aperture did decrease as Biot coefficient decreased, this was a tiny change and the aperture was essentially the same in each case. For these three cases, the average aperture was 300 microns, 306 microns and 310 microns respectively. Only when the Biot coefficient decreased to 0.40, did the decrease in total average aperture become substantial with an average value of 277 microns.

Figure 4.7g shows an effective permeability versus time plot for the Biot coefficient cases. The plot demonstrates that as Biot coefficient decreased, the effective permeability of the fractured caprock region decreased. The final effective permeability at the end of the three year study period for the 0.40, 0.60, 0.77 and 0.93 cases was 23 mD, 61 mD, 80 mD and 110 mD, respectively.

4.5.3 Stresses

Eight simulations were performed to assess the impact of the horizontal *in situ* stresses on the fracture growth and permeability alteration of the caprock. All model properties were defined according to Table 4.2 in each simulation, with the only property changing between the simulations being the horizontal *in situ* stresses acting on the vertical model boundaries. The homogeneous *in situ* stresses tested were 15 MPa/15 MPa, 30 MPa/30 MPa, 45 MPa/45 MPa and 60 MPa/60 MPa. The heterogeneous *in situ* stresses tested were 30 MPa/45 MPa, 45 MPa/30 MPa, 65 MPa/75 MPa, and 75 MPa/65 MPa.

Figure 4.12 shows the state of the fracture networks at the end of the three year storage period. The fracture networks show that for the homogeneous stresses in Figures 4.12a-d, the areal extent of the fractures increases as the stress magnitude increases, especially in the range 15 MPa to 45 MPa, with no further increases in areal extent in the 60 MPa case relative to the 45 MPa case. This is confirmed in the P_{32} versus time plot in Figure 4.13a, where the final P_{32} values in the 15 MPa/15 MPa, 30 MPa/30 MPa, 45 MPa/45 MPa and 60/60 MPa cases was 29, 51, 97 and 95 respectively. Despite the areal extent of the fractures being very similar in the 45/45 MPa and 60/60 MPa cases, there is one major difference in the evolved fracture networks. In the 60 MPa/60 MPa case, one column of fractures has nearly grown to such an extent as

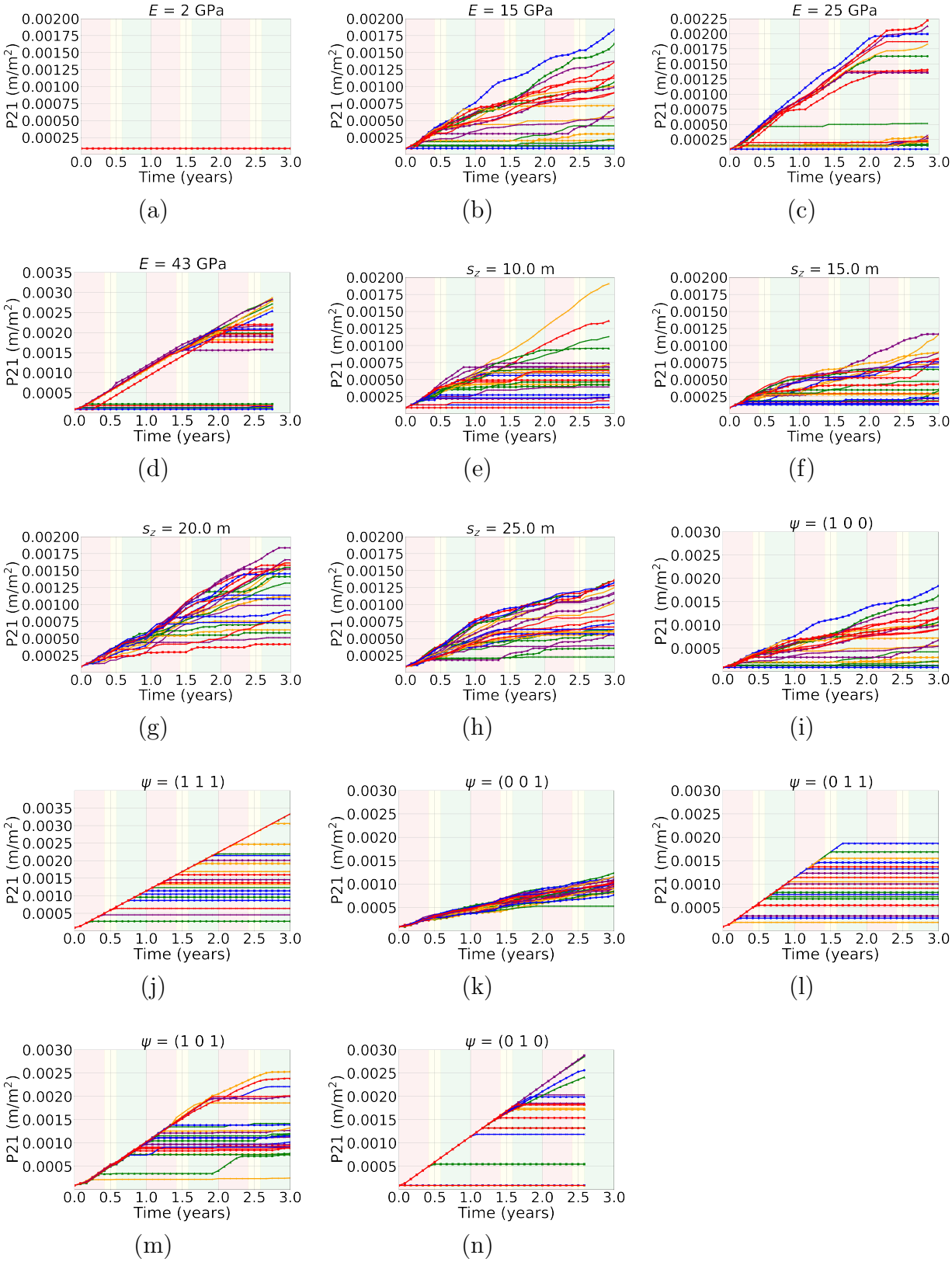


Figure 4.11: P_{21} versus time for four cases of varying (a-d) caprock Young's modulus, (e-h) initial vertical natural fracture spacing, and (i-n) initial natural fracture orientation. The y-axes are not the same in each case. Marker size has no physical meaning.

to have combined into one single very large fracture (see fracture column 3 in Figure 4.12d). This can be seen where the fractures in row 3,4 and 5 have overlapped and combined into one and the fractures in row 1 and 2 have done the same. Only a small amount of rock matrix is left between these two fracture chains and is likely to combine beyond the three year storage period, providing a very high permeability pathway for fluids to migrate rapidly through the caprock. One common phenomenon seen in all the homogeneous fracture networks is fracture interaction. Small fractures are often found sandwiched between much larger fractures such as the fractures in row 5, columns 1, 2 and 3 of the 30 MPa/30 MPa case (Figure 4.12b), in row 4, columns 1, 2 and 3 of the 45 MPa/45 MPa case (Figure 4.12c) and in row 2, columns 3,4 and 5 of the 60 MPa/60 MPa case (Figure 4.12d). Furthermore, the largest fractures are almost always found in the direct vicinity of the smallest fractures such as the fractures in column 5, rows 1 and 2 of the 45 MPa/45 MPa and 60 MPa/60 MPa cases (Figure 4.12c,d).

The fracture networks show that for the heterogeneous stresses in Figures 4.12e-h, there is no systematic change in fracture areal extent at the end of the three year study period with increased *in situ* stress magnitude. This is confirmed in the P_{32} versus time plot in Figure 4.13a which shows that the final P_{32} value of 117 in the 45 MPa/30 MPa case is actually larger than the value of 96 in the 65 MPa/75 MPa case. The final P_{32} value of the 30 MPa/45 MPa, 45 MPa/30 MPa, 65 MPa/75 MPa, and 75 MPa/65 MPa cases was 56, 117, 97 and 139 respectively. Therefore, broadly as the stress magnitude increases, the fracture growth extent increased but the dominant factor influencing the final areal extent of the fractures was whether or not the stress was larger in the x-direction than the y-direction. This is reinforced by Figure 4.14, which shows in subfigures e-h, that the largest fracture lengths are found in the cases where the stress in the x-direction is larger than the stress in the y-direction with three and one fractures in the 45 MPa/30 MPa and 75 MPa/65 MPa cases above a P_{21} value of 0.00175 respectively. No fractures were above this value in the 30 MPa/45 MPa and 65 MPa/75 MPa cases. For the 15 MPa/15 MPa, 30 MPa/30 MPa, 45 MPa/45 MPa, 60 MPa/60 MPa, 30 MPa/45 MPa, 45 MPa/30 MPa, 65 MPa/75 MPa and 75 MPa/65 MPa cases respectively, the number of fractures with a P_{21} value above 0.00150 after three years was 0, 0, 2, 2, 0, 4, 3, and 6, respectively. This again highlights two things, larger fracture lengths can be expected

with larger stress magnitudes, but also larger fracture lengths can be expected for significantly heterogeneous stresses relative to homogeneous stresses, and that longer fracture evolve when the stress in the x-direction (i.e., when the unit normal to the fracture faces is parallel to the wellbores) is larger than the y-direction.

The total average aperture in each case is shown in Figure 4.13b. For the homogeneous stress cases, it can be observed that total average aperture systematically increased with increased *in situ* stress magnitude. The average aperture in the 15 MPa/15 MPa, 30 MPa/30 MPa, 45 MPa/45 MPa, and 60 MPa/60 MPa cases was 0.000070 m, 0.000190 m, 0.000315 m, and 0.000425 m, respectively. Therefore, the aperture approximately linearly increases as the *in situ* stress magnitude increases: when the *in situ* stresses increase by 15 MPa in both directions, the aperture increases by 0.000120 m from 15 MPa to 30 MPa, by 0.000125 m from 30 MPa to 45 MPa and by 0.000110 m from 45 MPa to 60 MPa showing an increase of between 0.000110-0.000125 m for every 15 MPa increase. We also observe for heterogeneous stresses, that as the stress magnitude increased, the average fracture apertures increased. The green and cyan aperture curves map one another very closely, as do the yellow and red curves in Figure 4.13b. The green and cyan curves represent the 30 MPa/30 MPa and 30 MPa/45 MPa cases, whilst the yellow and red curves represent the 45 MPa/30 MPa and 45 MPa/45 MPa cases respectively. Therefore, it is observed that it is the stress in the x-direction which controls the fracture aperture and the y-direction stress has only a negligible effect on the fracture aperture. The apertures are therefore larger in the heterogeneous cases with larger x-direction stress, which is reinforced by the fact that the 75 MPa/65 MPa case yielded the largest apertures as it has the largest x-direction stress of any of the tested cases.

Both the effective and equivalent permeabilities, shown in FIgure 4.15, show the same qualitative trend for the homogeneous cases. As the magnitude of the horizontal *in situ* stresses increases, the caprock permeability increases. For the 15 MPa/15 MPa, 30 MPa/30 MPa, 45 MPa/45 MPa and 60 MPa/60 MPa cases, the final caprock effective permeabilities were 0.7 mD, 14 mD, 103 mD and 330 mD and the final caprock equivalent permeabilities were 2.83 nD, 2.88 nD, 3.02 nD and 3.07 nD, respectively.

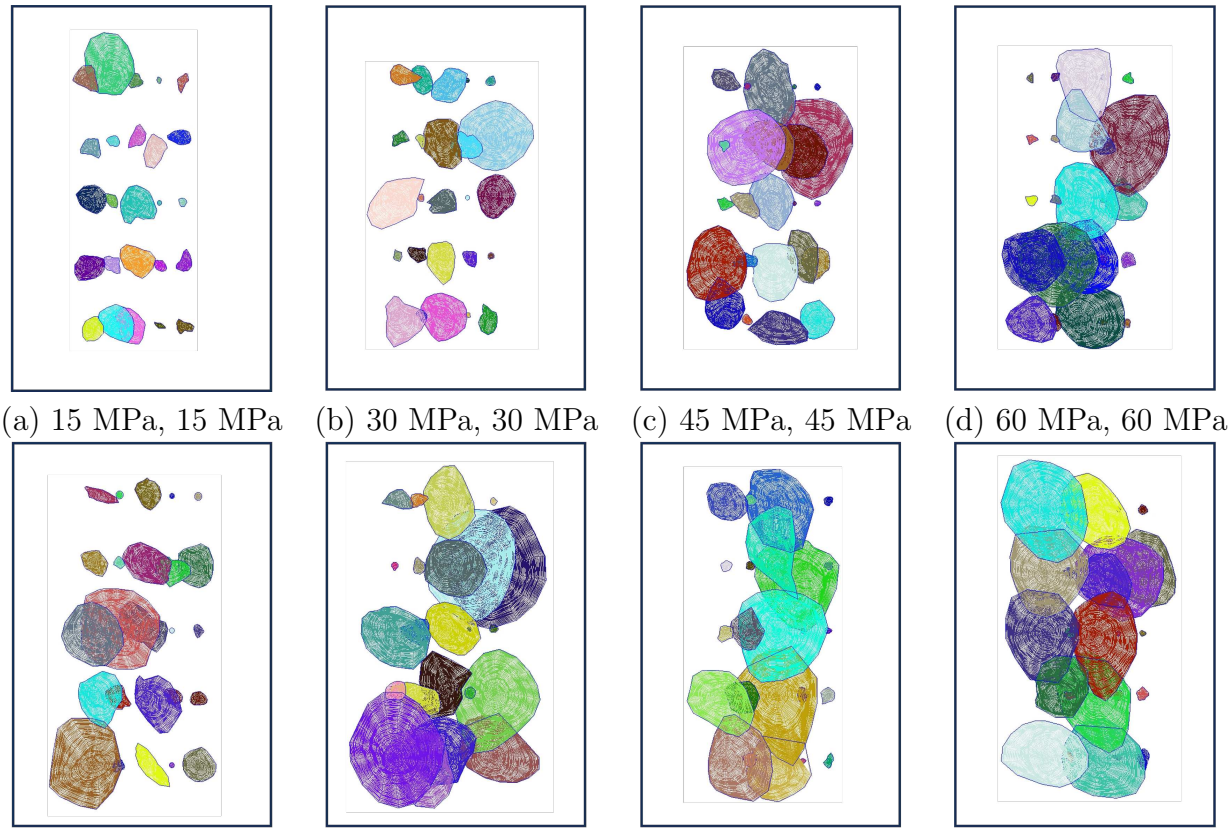
The effective and equivalent permeabilities also show the same qualititative trend for the heterogeneous cases. The 75 MPa/65 MPa case, followed by the 65 MPa/75 MPa case, followed by the 45 MPa/30 MPa case, followed finally by the 30 MPa/45 MPa case show the largest effective and equivalent permeabilities. For the 30 MPa/45 MPa, 45 MPa/30 MPa, 65 MPa/75 MPa and 75 MPa/65 MPa cases, the final caprock effective permeabilities were 13 mD, 130 mD, 335 mD and 412 mD and the final caprock equivalent permeabilities were 2.92 nD, 3.18 nD, 3.29 nD and 3.50 nD, respectively.

The effective and equivalent permeabilities display many orders of magnitude difference. The final effective permeabilities in Figure 4.15b vary within the approximate range of milliDarcies to hundreds of milliDarcies, whereas the equivalent permeabilities in Figure 4.15a vary within the range of 2-4 nanoDarcies.

Figure 4.16 shows the diagonal components of the equivalent permeability tensor: k_{xx}, k_{yy} and k_{zz}. These represent the permeability in the x, y and z directions respectively. The permeability in the x-direction, shown in Figure 4.16a, does not change with time over the study period and is not dependent on the horizontal *in situ* stresses. The permeability in the y-direction, shown in Figure 4.16b, has the highest values of all three principal permeability components, with values as high as 4.67 nD compared to 2.80 nD and 3.27 nD in the x and z-directions respectively. In all of the eight stress cases, the following identity is obeyed: $k_{yy} > k_{zz} > k_{xx}$.

For the homogeneous cases, as horizontal stress magnitude increases, both k_{yy} and k_{zz} increase. For the 15 MPa/15 MPa, 30 MPa/30 MPa, 45 MPa/45 MPa and 60 MPa/60 MPa cases, the final k_{yy} was 2.87 nD, 2.91 nD, 3.27 nD and 3.40 nD, and the final k_{zz} was 2.85 nD, 2.93 nD, 3.05 nD and 3.05 nD for the same cases, respectively. In the heterogeneous stress cases, for the 30 MPa/45 MPa, 45 MPa/30 MPa, 65 MPa/75 MPa and 75 MPa/65 MPa cases, the final k_{yy} was 3.02 nD, 3.59 nD, 4.18 nD and 4.67 nD and the final k_{zz} was 2.94 nD, 3.23 nD, 3.07 nD, and 3.28 nD for the same cases, respectively. The trend for the homogeneous cases shows that k_{yy} and k_{zz} increased with increasing stress magnitude. Given that the difference in final k_{yy} and k_{zz} between the cases was 0.53 nD and 0.20 nD, respectively, the *in situ* stress state has a much stronger influence on k_{yy}. For the heterogeneous cases, it was also broadly seen that

as the stress magnitudes became larger, the k_{yy} and k_{zz} also increased. However, this was not always the case. For example, for k_{zz}, the 45 MPa/30 MPa case had a much larger final value than the 65 MPa/75 MPa case, despite the larger stress magnitudes in the latter case.



(a) 15 MPa, 15 MPa (b) 30 MPa, 30 MPa (c) 45 MPa, 45 MPa (d) 60 MPa, 60 MPa

(e) 30 MPa, 45 MPa (f) 45 MPa, 30 MPa (g) 65 MPa, 75 MPa (h) 75 MPa, 65 MPa

Figure 4.12: The final state of the fracture network after three years of hydrogen storage for eight cases of varying *in situ* horizontal stresses (σ_x, σ_y). (a-d) Homogeneous stress cases and (e-h) heterogeneous stress cases.

4.5.4 Fracture Nucleation: Tensile Strength

Four simulations were performed to assess the impact of caprock tensile strength on the caprock integrity with respect to the inducement of new caprock fractures. All model properties were defined according to Table 4.2 in each simulation, with the only property changing between the simulations being the tensile strength of the caprock. However, in these nucleation simulations, the initial 5×5 array of caprock natural fractures used in the rest of this work is removed. The initial caprock is fully mechanically intact (unfractured) and only induced fractures after the onset of first injection are considered.

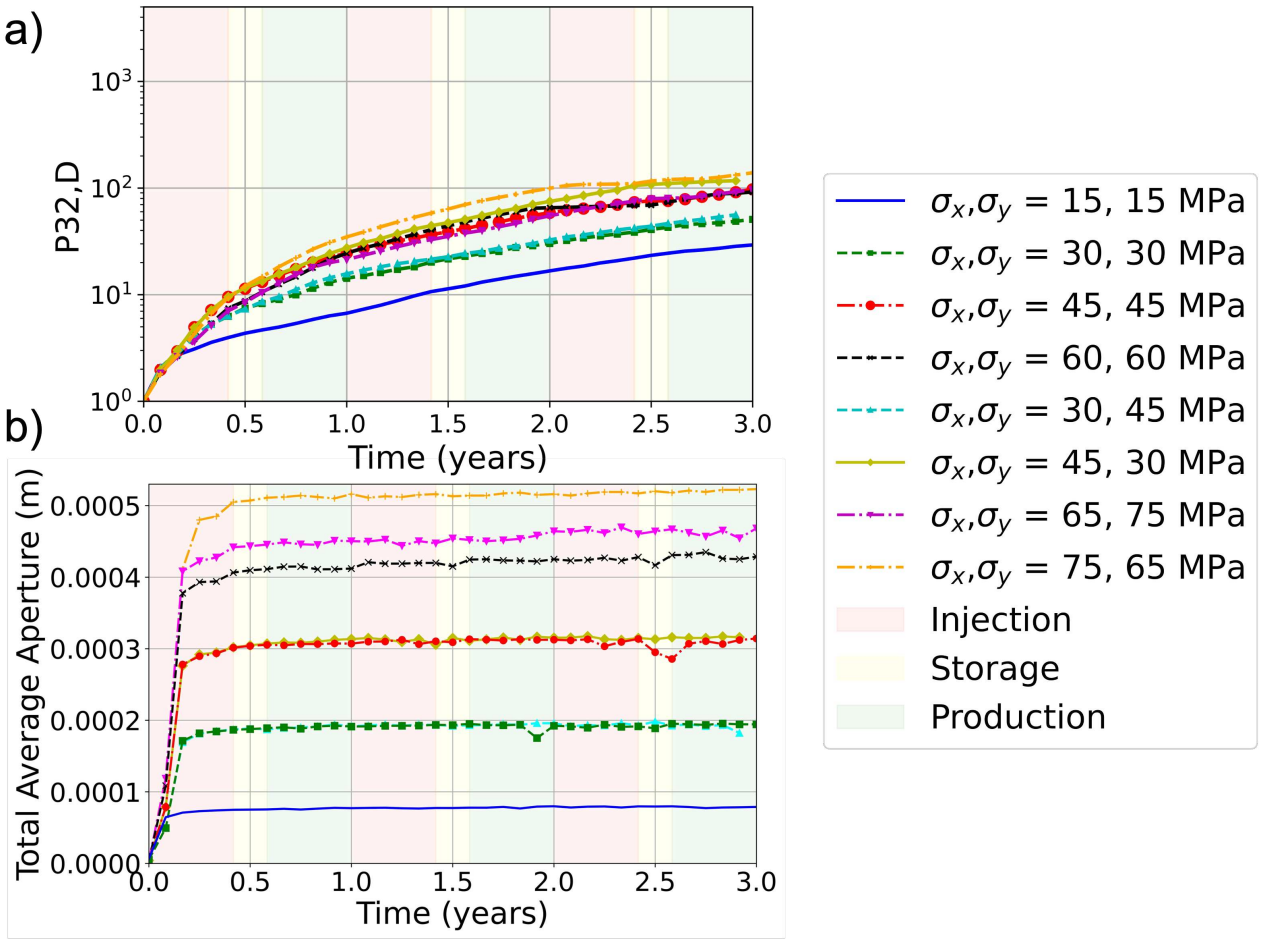


Figure 4.13: (a) The dimensionless P_{32} and (b) the total average aperture of the fractured caprock region. The total average aperture is the average of the average aperture of all fractures.

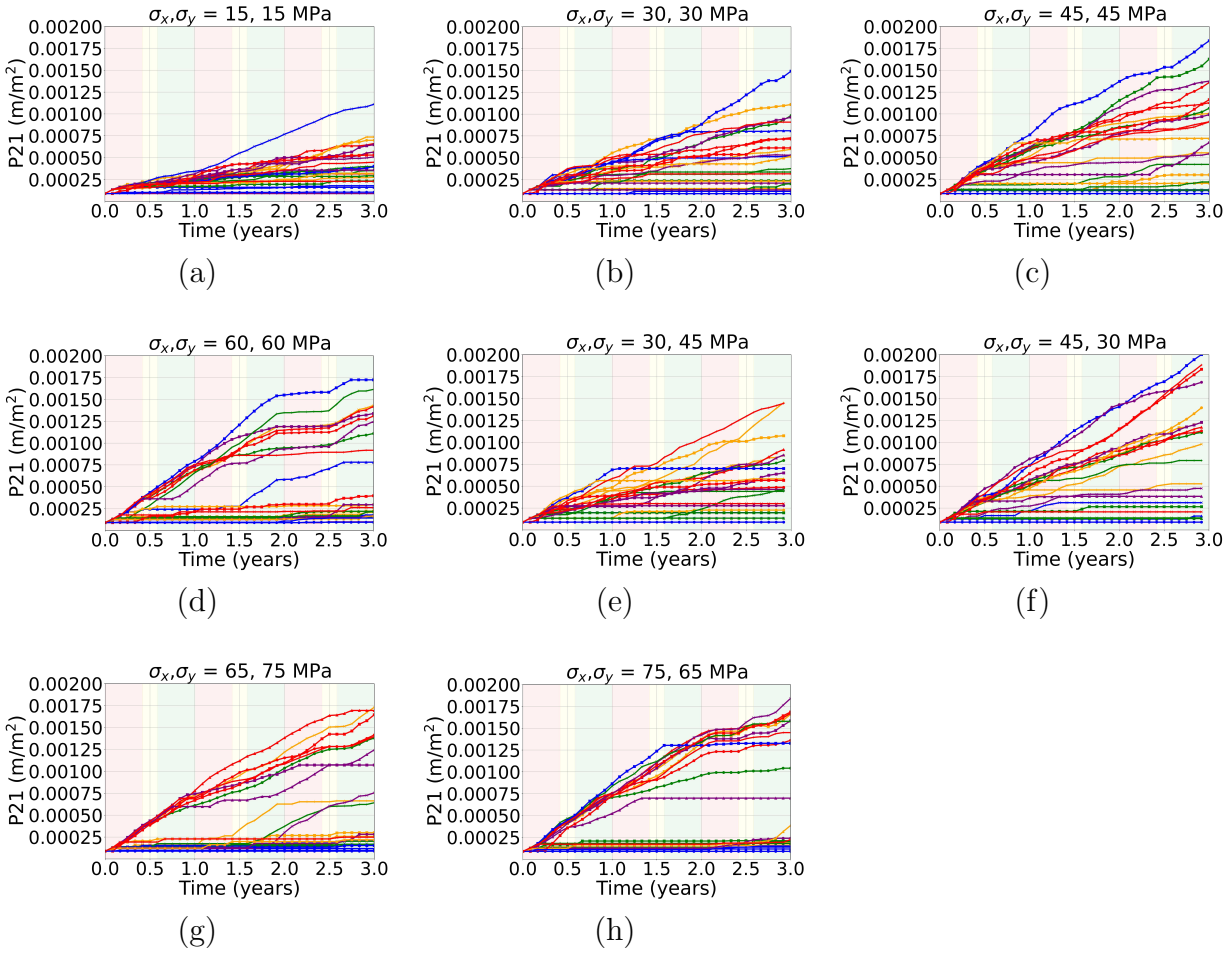


Figure 4.14: P_{21} versus time for eight cases of varying horizontal *in situ* stresses. (a-d) Homogeneous stress cases and (e-h) heterogeneous stress cases.

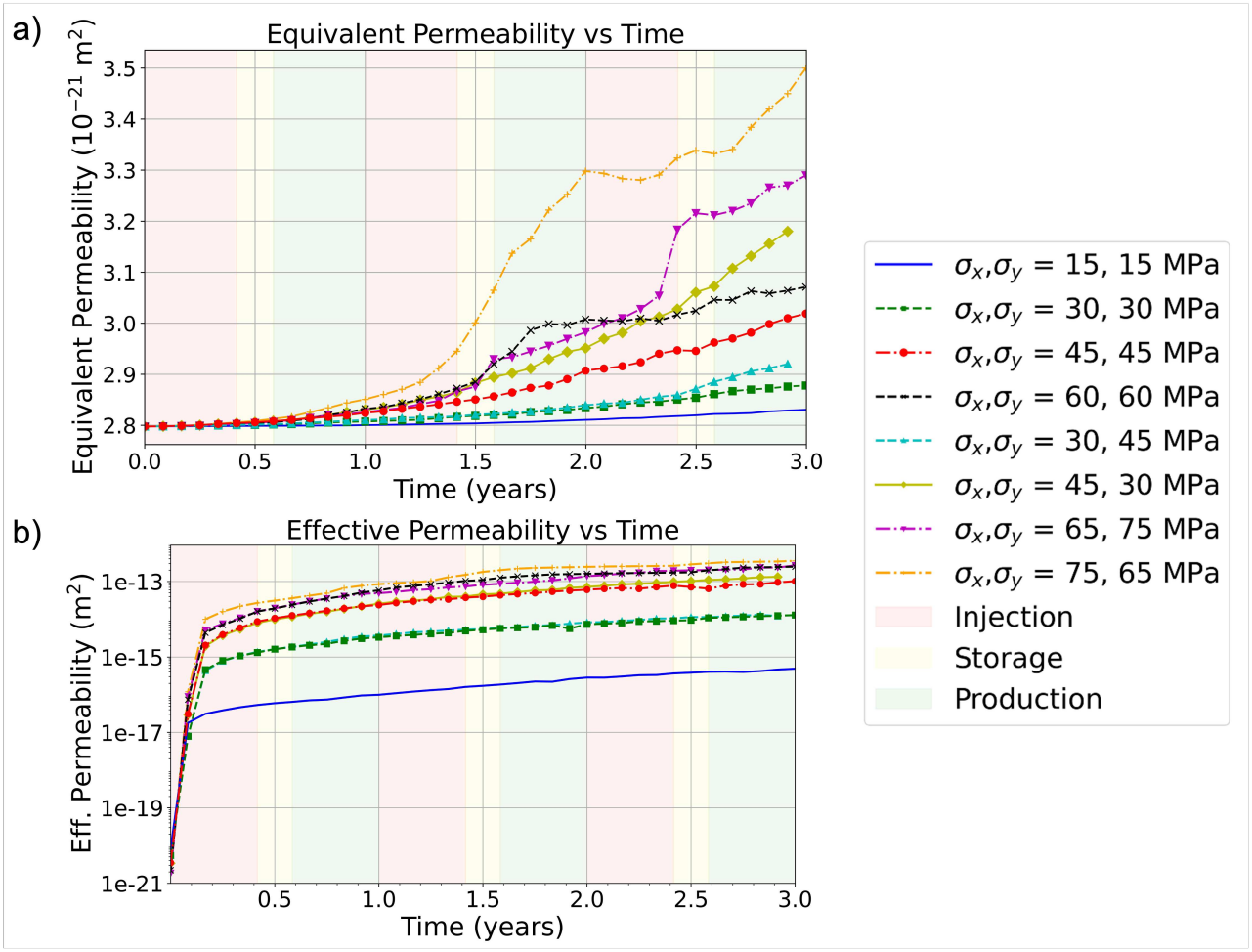
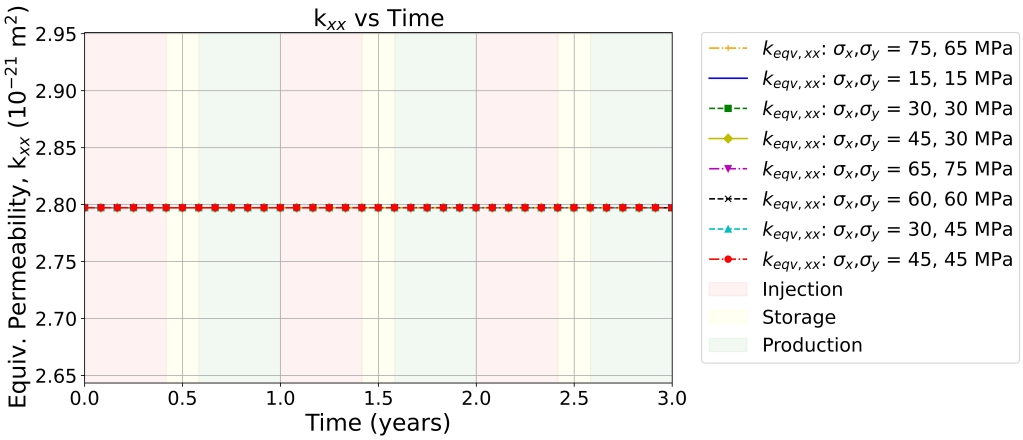
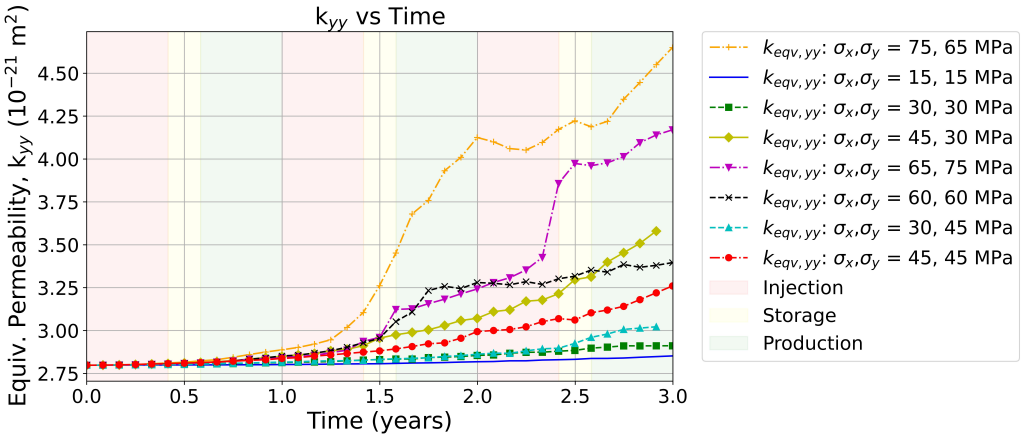


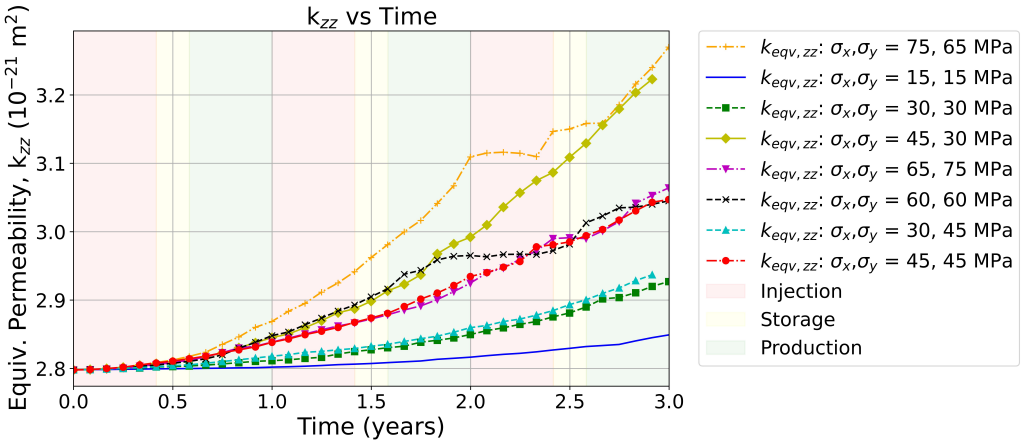
Figure 4.15: Comparison of equivalent and effective permeabilities. (a) Lang et al. [2014] geomechanical equivalent permeability versus time and (b) Snow [1969] effective permeability versus time for eight cases of varying horizontal *in situ* stresses.



(a)



(b)



(c)

Figure 4.16: Lang et al. [2014] geomechanical equivalent permeability versus time for eight cases of varying horizontal *in situ* stresses. (a) in the x-direction, (b) y-direction and (c) z-direction, respectively.

The induced fracture networks for each case (10.4 MPa, 30 MPa, 44 MPa and 50 MPa) are shown in Figure 4.17. It is observed that in the 50 MPa case, no new fractures are induced for the entirety of the three year study period. In all other cases, new caprock fractures are induced because the induced caprock damage is sufficient to exceed the tensile strength. In each case, it is observed that the majority of the fractures are vertical fractures with a smaller population of horizontal fractures. The horizontal fractures often form in the direct vicinity of the vertical fractures, especially in the 10.4 MPa and 30.0 MPa cases. In all cases, the horizontal fractures also typically form broadly within a region bounded either side by a group of vertical fractures. This is particularly obvious in the 44.0 MPa case.

The broad location and number of fractures is not a direct result of a physical process. The maximum number of induced fractures is capped at thirty because for every additional fracture, the simulation time increases significantly, and becomes prohibitively slow beyond this amount. The location of the fractures at the mid-point of the model is due to a restriction in which the fractures can only form in an 800×800 m region at the centre of the model to avoid boundary effects in the stress field and should not be taken to suggest that fractures will only form in this location.

4.6 Discussion

It should be noted that the findings in this work do not suggest that caprocks will hydraulically or mechanically fail during geological hydrogen storage. In all cases, the default fracture toughness was set to 0.33×10^5 Pa $m^{1/2}$, which as discussed in Section 4.6.1.5, was the lowest value for the fracture toughness of a shale caprock found in the literature. If the fracture toughness is sufficiently high then the initial fractures do not grow and the effective permeability is not enhanced, maintaining the caprock integrity. The results herein show the influence of various parameters on permeability enhancement when the fracture toughness is sufficiently low for natural fracture propagation in the caprock.

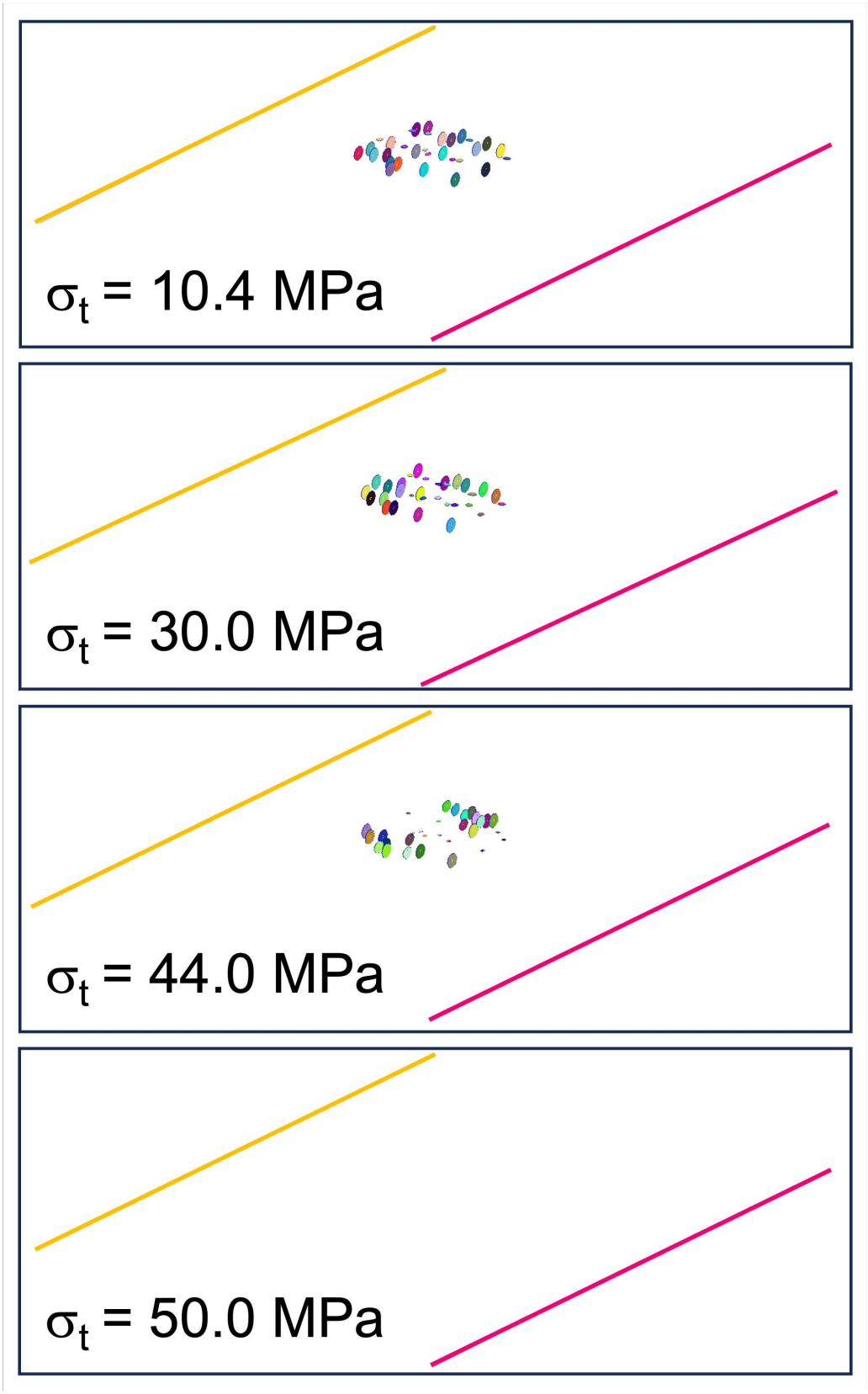


Figure 4.17: The state of the induced fracture networks within the caprock unit at the end of three years of hydrogen storage in four simulations with varying caprock tensile strength.

4.6.1 Initial Fracture Size

Schaaf et al. [2017] performed an extensive characterisation of natural fractures within the Agardhfjellet formation shale caprock and found that fracture sizes ranged from less than 0.1 m to over 2.0 m. The modal fracture size within the fracture population was approximately 0.2 m. These sizes correspond to the sizes analysed in this work (0.2 m, 1.0 m and 2.0 m). The 5.0 m case was tested to see what might occur in a less common case in which the natural fractures were larger, and corresponds to the upper limit of the common fracture population sizes found in the shale samples examined by Ladeveze et al. [2018]. Although, they note that occasionally fractures could reach up to 30 m.

The very significant 200 mD final permeability difference between the largest and smallest permeability cases ($r = 0.2$ m and $r = 5.0$ m) reveals that the size of the natural fractures have a large impact on the hydraulic integrity of the caprock. Given that the effective permeability is high in the 0.2 m case and the P_{32} results show signs of continued growth beyond the study period, caprocks with very small natural fractures may exacerbate hydraulic caprock integrity loss. Similarly, the effective permeability is high for very large fractures (i.e., $r = 5.0$ m), so natural fractures at the extremities of realistic population sizes lead to the greatest loss of hydraulic integrity. Although this is for different reasons: when the fractures are large their initial size contributes considerably to their permeability and their average aperture is slightly larger which enhances the contribution of the fracture permeability. Whereas, when the fractures are very small, stress shadowing is minimised, thus not shielding the stress around neighbouring fractures, keeping the stress at fracture nodes high and encouraging homogeneous growth.

No matter the size of the fractures, within the tested range, the caprock integrity is still completely lost for a caprock with the default parameters (excluding radius) in Table 4.2 since the permeabilities are well in excess of an acceptable value of approximately 10^{-18} m^2. Nevertheless, the smaller the fractures, the larger the growth from the initial state, and thus, caprocks with very small natural fractures (0.2 cm) should ideally be avoided, unless other caprock mechanical properties are favourable such that the effect of initial fracture radius is overridden.

4.6.1.1 Initial Fracture Spacing

Natural fracture spacing in shales is a property that is highly variable dependent on the given shale formation. Very small natural fracture spacings of 0.01-0.10 m were reported in Devonian shale samples by Schettler et al. [1989]. Slightly larger spacings such as 0.30-0.60 m were reported by Walton and McLennan [2013] for Antrim shale samples. Larger fracture spacing again of up to 1 m were reported for samples of Agardhfjellet formation shale caprock by Schaaf et al. [2017]. Natural fracture spacings of as large as 25 m were reported by Carlson and Mercer [1991] for Devonian shale through history matching of production data from hundreds of wells across the Eastern United States. With these ranges in mind, the maximum fracture spacing tested was 25 m. The minimum fracture spacing tested was 7.5 m. Ideally, this would be much lower and in the range of 0.10 m, but such small spacings induce a core problem. Extremely small elements would be needed to cover such spacing between fractures, which would require tens of millions of finite elements in such a large-scale model inducing impossibly long simulation run-times, and therefore fracture spacings of less than 7.5 m, with elements of workable size, create mesh issues where the fractures become undefined. Therefore, with the simulations involving this parameter (the fracture spacing), the results should not be deemed definitively extractable to all situations because for a caprock with natural fractures spaced on the order of mm's to cm's, the interaction behaviour of the fracture stress fields may be different.

The final difference in effective permeability between the 7.5 m and 25.0 m spacing cases, that had the lowest and highest effective permeability respectively, was only 87 mD showing that the fracture spacing did not have a large effect on the final effective permeability. Nevertheless, the larger the fracture spacing between the natural fractures, the higher the effective permeability. This is positive for the smaller fracture spacings much below 7.5 m that could not be tested in this work. It follows that one would expect less areal growth of fractures that are initially closer together and thus the effective permeability would also be less. Even more so because the total average aperture was shown to also decrease significantly when the fracture spacing was smallest, so one would expect the apertures to also be smaller, reducing the fracture

permeabilities that contribute to the effective permeability of the caprock. However, when the fracture spacing was smallest (i.e., 7.5 m case), a very large fracture developed and that fractures P_{21} showed signs of continual growth due to its steep gradient just before the three year point. Therefore, it is possible that this fracture will grow to such an extent that it will eventually intersect the full thickness of the caprock, implying that even if the hydraulic integrity of the caprock is not at risk as much as higher spacing cases, total mechanical integrity could be lost, in which a single fracture provides a direct and rapid pathway for hydrogen to leak from the reservoir into the overburden and then to surface. This is unlikely however, given that the fracture is primarily propagating in the horizontal plane. Furthermore, the fact that less fractures seem to be showing signs of growth at the end of the study period as the fracture spacing decreases positively implies that at lower fracture spacings than those tested here, the fracture growth in the caprock may have fully arrested before the three year point, becoming mechanically stable much more quickly. The number of fractures still growing at the end of the three year period decreased with decreasing fracture spacing because when the fractures are closer together the stress fields around the fractures interact more strongly. When the stress fields of neighbouring fractures overlap to an increasing extent, regions of lower stress intensity develop in the space between fractures, which reduces the energy available for further fracture propagation. The reduced fracture apertures with decreased fracture spacing are also attributed to this, where fracture interaction reduces the tensile stress around the fractures slightly reducing their ability to open. This is also exacerbated because when fractures are more closely spaced together, there is less elastic shale matrix between fractures to accomodate expansion of the fractures faces, thus limiting the potential aperture.

4.6.1.2 Initial Fracture Orientation

Natural fractures in shale can of course take any orientation, dependent on the tectonic stress history of the rock formation of interest. As a result of this potential variance, six simulations were performed covering a range of different natural fracture orientations.

The maximal difference in effective permeability after three years between the highest (0 1

0) and lowest (0 1 1) permeability cases was a huge 11 orders of magnitude. This highlights that the initial orientation of the natural fractures has a very strong control on the effective permeability evolution and the potential risk of caprock hydraulic integrity loss. For the exact same operation conditions, when the fractures are described by a normal vector of (0 1 1), the maximal effective permeability was only 0.05 mD and this decreased to approximately 1 nD after the first 1.5 years, whereas when the fractures are described by a normal vector of (0 1 0), the maximal effective permeability was approximately 95,000 mD. This is the difference between a caprock which can only transmit very small percentages of the stored hydrogen for a short period of time and a caprock which has become a high-quality reservoir unit and no longer has any sealing capacity. Therefore, it is key to understand the orientation of the natural fractures in the caprock of any potential storage field if the caprock also has low fracture toughness, in order to de-risk caprock hydraulic integrity loss.

The (1 0 0) case had the smallest increase in fracture surface area. This is because in this case the fractures are vertical and the fracture normal is aligned with the x-axis. Since the *in situ* horizontal stresses are equal in both directions, there is no differential horizontal stress other than that added due to the fluid flow in the underlying reservoir unit. As a result, there is not significant differential stress to drive significant fracture propagation when the fractures have this orientation. Therefore, the growth is limited. The (0 0 1) case had the next smallest increase. In this case, the fractures are horizontal and the fracture normal is alligned with the x-axis. In this case, the fracture mechanics is primarily governed by the *in situ* vertical stress due to the weight of the overlying rock. These stresses are higher than the *in situ* horizontal stresses and they are compressive in nature which acts to minimise fracture growth. The (0 1 1), (1 0 1) and (1 1 1) cases then exhibit the next largest growth. In these cases, the fractures are orientated at an angle to the principal stress directions and as a result, the fractures experience a combination of shear and normal stresses, facilitating mixed-mode loading, which enables the fractures to propagate under a wider range of conditions and promotes growth. The (0 1 0) case has the largest increase in fracture surface area because although they are orientated vertically like the (1 0 0) case, and thus the external stress field in the horizontal plane is the same in both directions, in the (0 1 0) orientation the fractures faces are parallel to the

horizontal injection wellbore and the faces are therefore perpendicular to the flow of the injected hydrogen. This leads to larger tensile stresses exerted on the fractures as the fractures become more pressurised. This also explains why the (0 1 0) case has the highest total average aperture which is one-to-two orders of magnitude larger than the other cases.

The (0 1 0) case has the highest permeability because of three factors. This case has (1) the highest aperture, (2) the largest increase in fracture surface area relative to the initial state and (3) the fractures have grown to such an extent that each row of fractures has mechanically combined into 5 single very large fractures which enhances the fracture permeability. Although the (0 1 1) and (1 1 1) cases had significant fracture growth relative to other cases, their much lower apertures dominate the effective permeability computation, thus resulting in lower effective permeabilities than in the other cases.

The (0 1 1) case reverses its permeability increase because the apertures close after 1.5 years in the second withdrawal period. The fractures stop growing a short time before this, approximately at the end of the second injection period, and this is because during repeated injection and withdrawal cycles, stress redistribution around the fractures leads to an increase in effective stress acting normal to the fracture plane which inhibits their ability to grow further and acts to close the fractures. Shortly after, during the second withdrawal period, the reduction in pore pressure further increases the effective stress acting on the fractures acting to close them further.

4.6.1.3 Crack Propagation Velocity

The velocity with which a fracture can propagate is highly variable between rock types and within rock types. Using a Double-Cantilever Beam (DCB) setup and processing the samples with a reciprocating diamond-impregnated wire saw to prevent the sample from splitting, Dong et al. [2019] found a crack propagation velocity of 0.1 μm/s in shale samples from the Longmaxi Formation, Sichuan Basin, China. Contrastingly, much higher values of crack propagation velocity in shales were found by Chandler et al. [2018] using time-resolved radiograph imaging of the fracture evolution. These values ranged from 30 to 470 μm/s. The 0.1 μm/s value

from Dong et al. [2019] corresponds to a velocity of 0.05 μm/s in opposing directions which corresponds to an extension length of 0.1314 m per time step. This is why 0.1314 m is used as the lowest fracture extension length used in this work. The other three cases, 0.5256 m, 2.1024 m and 2.5000 m correspond to larger crack propagation velocities, but values as high as those corresponding to 470 μm/s could not be tested as the rapidity of this fracture growth leads to very large, pointed/angular fractures which disrupt the continuity of the mesh causing the simulation to terminate because fracture node pairs on opposing fracture surfaces cannot be found. Thus, 2.5000 m is the upper restriction possible on the crack propagation velocity.

The maximal difference in effective permeability after three years between the highest (2.5000 m) and lowest (0.1314 m) permeability cases was a very large 207 mD, highlighting that the crack propagation velocity is a critical parameter in assessing the potential loss of hydraulic integrity of the caprock. In this case, the total average aperture was found to be insensitive to changes in crack propagation velocity, and thus the differences in the effective permeability evolution are entirely a function of the fracture lengths.

Furthermore, it was found in the 2.5000 m case that one of the fractures grew to such an extent that it fully penetrated the full height of the caprock such that the fracture tips penetrate into the overlying overburden and into the underlying reservoir. In this case, the mechanical integrity of the caprock can be said to have been lost because now there is a direct pathway for hydrogen in the reservoir to leak into the high permeability overburden rapidly. This could have negative environmental and economical consequences. Loss of the commercial product could result in an inability to uphold contracts with customers and in a futuristic nation in which hydrogen storage satisfies renewable energy deficits during winter months, wide-scale energy shortages could result where there is insufficient hydrogen available and no renewable energy, meaning fossil fuels may need to be combusted in emergencies, releasing CO_2. Furthermore, hydrogen could leak up through the high permeability overburden to surface where it could catch a spark and ignite. Therefore, storage in caprocks of very low fracture toughness and high crack propagation velocities should be avoided. Few experimental studies report crack propagation velocities in shales and given the impact of its variability to the caprock permeability, this is an important parameter for storage companies to characterise prior to the onset of operations.

The number of fractures still growing at the end of the three year study period decreased as the crack propagation velocity increased, with only 1 fracture still showing signs of growth in the 2.5000 m case at this point. This trend occurs because faster growing fractures dissipate the driving stress intensity more efficiently along their length alleviating localised stress concentrations more rapidly. Therefore, there is quicker attainment of stress equilibrium around the fractures and earlier crack arrest.

The increased heterogeneity of the fracture network with increased crack propagation velocity can be explained as follows. At higher crack propagation velocities, the fractures that initially propagate consume a larger portion of the available stress energy in the caprock, leading to rapid stress relief elsewhere. This combined with the fact that as the fractures grow larger, they create stress shadows which are regions of reduced stress intensity, in their vicinity which further inhibits the growth of other fractures. These two factors explain why high crack propagation velocities result in more heterogeneous fracture networks dominated by a few very large fractures.

4.6.1.4 Vertical Fracture Spacing

The final difference in effective permeability between the 15 m and 20 m spacing cases, that had the lowest and highest effective permeability respectively, was a very substantial 180 mD showing that the initial vertical fracture spacing had a large effect on the final effective permeability of the caprock.

The total average fracture aperture increases slightly with increasing vertical fracture spacing. This is because when the fractures are spaced further apart, the fractures interact less. As a result, the stress field in the vicinity of a given fracture remains less disturbed than if the spacing was smaller. This results in larger stress concentrations around each individual fracture that facilitate larger apertures. When the vertical fracture spacing is small, neighbouring fractures reduce the stress surrounding the fracture, resulting in less available energy to open fracture faces apart as the fracture propagates.

Generally, the smaller spacings result in smaller final fracture surface areas and the larger spacings results in larger final fracture surface areas. This is once again due to the fact that wider spacings reduce stress around surrounding fractures to a lesser extent, which favours growth. However, despite this broad trend, the trend is not completely systematic. For example, the 20 m case results in larger fracture surface areas than the 25 m case. This is because in the 25 m case, the fractures initially intersect the caprock-reservoir interface and due to the much higher reservoir fracture toughness, the fractures cannot propagate significantly in the downward direction and thus there growth extent is more limited than in the 20 m case where all fractures are surrounded by shale. The fractures also initially intersect the overburden-reservoir interface which prevents fracture growth upward as well, further reducing the growth potential. Therefore, if the caprock was thicker such that larger vertical spacings (i.e., 25 m, 30 m, 50 m etc) were possible without initially intersecting the caprock-reservoir interface, we may expect the fracture surface areas to increase systematically as the spacing continued to increase. At least until some spacing is reached in which the fractures have zero interaction on each others stress-fields, in which case we would expect the growth extents to plateau and not increase further with increased spacing. The 10 m case resulted in more total fracture surface area than the 15 m case due to stronger interaction effects. Many of the fractures are smaller in the 10 m case than the 15 m case as expected due to the fact stress is reduced at the fracture tips when the fractures are closer due to stress shadowing. However, interaction in places has resulted in a few much larger fractures than that present in the 15 m case which dominate the total surface area and is sufficient to ensure the 10 m case has slightly more fracture surface area than the 15 m case. The very large fracture in the 10 m case resides next to much smaller fractures because the large fracture has consumed the majority of the available stress-energy in this region. It does this because once it gets a slight growth advantage over its neighbours, the stress intensity at its fracture tips increases (whilst decreasing elsewhere) because the mode I stress intensity factor is proportional to the square-root of the fracture half-length.

No systematic trend in effective permeability was found with increasing/decreasing vertical fracture spacing due the slightly opposing influences on the fracture apertures and the fracture growth extents. For example, the 20 m case results in an effective permeability slightly above

the 25 m case because even though the 25 m case has higher fracture apertures that enhance the fracture permeability contribution to the caprock permeability, the fractures are larger in the 20 m spacing case and this overcomes the smaller apertures.

4.6.1.5 Fracture Toughness

The smallest value of fracture toughness that could be found reported in the literature for a shale caprock was 0.33×10^5 Pa $m^{1/2}$ from nano-indentation experiments on samples of Antrim and Opalinus clay shale using Berkovich and Cube corner nanoindenters [Liu, 2015]. However, fracture toughness of shale can be far larger with values of as high as 0.49×10^6 Pa $m^{1/2}$, 1.65×10^6 Pa $m^{1/2}$, and 1.38×10^6 Pa $m^{1/2}$ reported by Vishal et al. [2022], Han et al. [2021] and Wen et al. [2024], respectively. Therefore, a range of 0.33×10^5 Pa $m^{1/2}$ to 0.46×10^6 Pa $m^{1/2}$ was simulated to account for the minimum value possible. No higher than 0.46×10^6 Pa $m^{1/2}$ is tested, because although shale caprocks can have larger fracture toughnesses, no growth occurred at 0.46×10^6 Pa $m^{1/2}$ and thus, by definition of the fracture toughness, no growth will occur at larger values.

Between the two cases that showed significant growth (0.33×10^5 Pa $m^{1/2}$ and 0.60×10^5 Pa $m^{1/2}$), the difference in effective permeability at the end of the study period was a substantial 85 mD and it ranged from 100 mD to 1 nD between the largest and smallest cases. Therefore, fracture toughness is a key parameter influencing the resultant effective permeability of the caprock, and is the difference between total loss of caprock hydraulic integrity (i.e., 0.33×10^5 Pa $m^{1/2}$) and zero change in sealing capacity from its original value (0.46×10^6 Pa $m^{1/2}$). Therefore, the caprock fracture toughness must be characterised in the laboratory prior to the onset of potential hydrogen storage operations.

Even in the 1.0×10^5 Pa $m^{1/2}$ case, where the fractures do not grow from their initial size, except at the onset of injection, the effective permeability of the caprock region increases significantly for a short time to just less than 20 μD which is enough for some fluid leakage from the reservoir into the caprock. The magnitude of this increase is primarily driven by the substantial increase in fracture apertures rather than as a direct result of the very minimal amount of fracture

growth. In this case, the initial injection induces stress intensity at some of the fracture tips that is just enough to exceed the fracture toughness, thus inducing growth. Once the fractures grew a small amount, a new mechanical equilibrium is reached in which the stress intensity no longer exceeds the critical threshold. The fracture growth is enough to allow some fluid loss into the caprock which increases caprock pore pressure and reduces the effective stress in the vicinity of the fractured region ensuring that the critical threshold for growth is not exceeded. The surrounding rock matrix can now better accommodate additional stress without further propagation. Then, the caprock recovers elastically once the stress in the caprock is redistributed following the cessation of fracture propagation, which causes the rock matrix to push backward as the strain energy stored within it is recovered. This results in the closure of the fracture apertures that opened slightly following the initial injection, and this results in a final effective permeability that has decreased again.

4.6.1.6 Young's Modulus

Burtonshaw et al. [2024a] performed a literature review for the mechanical properties of the same rock units used in a similar model to that used in this work. They found that North sea gas reservoirs had caprocks with Young's moduli in the range 1.45-43 GPa. Therefore, in this work, the caprock Young's modulus was varied between 2 GPa and 43 GPa to cover this range. This range is also inline with other studies on shales such as 4.2-6.0 GPa for the Draupne shale [Agofack et al., 2019], 5-40 GPa for the Heather shale [Rahman et al., 2020], 5-27 GPa for the Draupne shale [Rahman et al., 2020], and 5-36 GPa for Alberta Long Lake shale [Dovletov, 2022]. For some non North-sea shale, the Young's modulus can be in excess of 43 GPa. For example, Rybacki et al. [2015] studied nineteen different shale samples, and found that three samples had very large Young's moduli of 62, 70 and 83 GPa. Although, it must be noted that the other sixteen of the nineteen samples had a Young's modulus of less than 49 GPa, highlighting that the 2-43 GPa range in this work covers the majority of shales.

The maximal difference in final effective permeability between the cases was huge with a caprock with nano-Darcy permeability in the 2 GPa case and a caprock with a permeability of over

800 mD in the 43 GPa case. This highlights that the caprock Young's modulus is a critical parameter in whether a caprock will maintain or lose hydraulic integrity. The effective permeability increased with increasing Young's modulus because both the fracture apertures and the fracture growth followed the same trend, thus combining to enhance permeability as Young's modulus increased. A higher Young's modulus rock, is a stiffer rock, with greater capability to store elastic energy when subjected to a given stress. Therefore, more energy is available for release allowing fractures to propagate further. The lower Young's modulus rock deforms more readily under the same stress, consuming energy during the deformation, and leaving little at the crack tips to promote significant crack propagation. In the 2 GPa case, the deformation is so significant that it prevents the stress intensity at the fracture tips from reaching the critical value for growth. Additionally, the larger Young's moduli rocks resist the compressional *in situ* stresses, resulting in larger fractures apertures. When the Young's modulus was smaller, the compressional *in situ* stresses are more efficient in deforming the rock, squeezing the fracture walls inward and resulting in smaller apertures. Furthermore, with higher Young's modulus caprocks, the surrounding matrix is stiff, resists deformation, and leads to large stress concentrations within the fractures which act to drive the fracture faces apart, whereas for small Young's moduli, the stress is dissipated into the matrix, leading to minimal stress acting internally on the fracture walls, meaning they reside closer to one another.

The more homogeneous fracture network observed for very high Young's modulus values (i.e. 43 GPa) occurs because in these very stiff rocks, the stress is uniformly distributed throughout the caprock because they do not easily accomodate localized deformation. Therefore, this results in more consistent fracture propagation. The highly heterogeneous fracture networks observed for intermediate Young's moduli values (i.e. 15 GPa and 25 GPa) occur because the matrix allows significant deformation which means that certain parts of the caprock deform more readily in response to the subjected stress. These localised stress concentrations can initiate the growth of certain fractures earlier, which then disturbs the stress in the vicinity of other fractures leading to further growth disparities. This phenomenon is known as fracture interaction and occurs due to stress shadowing or stress amplification [Thomas et al., 2017].

4.6.1.7 Poisson's Ratio

Burtonshaw et al. [2024a] performed a literature review for the mechanical properties of the same rock units used in a similar model to that used in this work. They found that North sea gas reservoirs had caprocks with Poisson's ratios in the range 0.11-0.37. Therefore, in this work, the caprock Poisson's ratio was varied between 0.11 and 0.35 to cover this range. Even for non-North sea shales, other authors report similar ranges for shale of 0.20-0.37 for Ordos Basin samples [Dou et al., 2023], 0.12-0.34 for Longmaxi Formation samples [Nie et al., 2023], and 0.05-0.38 for samples from seven different locations including the Kimmeridge shale [Sayers, 2013].

The maximal difference in effective permeability after three years between the highest and lowest permeability cases was only 15 mD highlighting that the Poisson's ratio does not have a large influence on the effective permeability of the caprock. The lack of systematic trend in the final effective permeability with changing Poisson's ratio can be explained due to the competing contributions of the fracture lengths/areas and the fracture apertures. For example, the highest and lowest Poisson's ratio cases (0.11 and 0.35) result in the highest effective permeabilities. This is explained through the fact that when the Poisson's ratio is larger, the fracture apertures are larger, but the P_{32} value that highlights areal growth is lower. This contrast leads to the extremity Poisson's ratio cases having higher effective permeabilities than more typical values (i.e., 0.19-0.27) which don't have large apertures or fracture extents. The fracture aperture increased with increased Poisson's ratio because a larger Poisson's ratio enables the caprock to exhibit more lateral expansion when exposed to the compressive overburden stresses from above and the buoyant hydrogen plume stresses acting on the caprock from below. This lateral expansion of the caprock exerts tensile stresses on the fracture faces enhancing their aperture and this is probably exacerbated in the default case in this work where the fractures are vertically oriented and are therefore favourably orientated in the direction of lateral expansion. The fracture growth is slightly less with higher Poisson's ratio because the lateral deformation that the caprock experiences redistributes the stress more evenly across the fracture surfaces, reducing the localised stress intensity at the fracture tips slightly.

As the caprock Poisson's ratio increased, the aperture increased and the increase accelerated as the Poisson's ratio got larger. This implies that in the event that the caprock had an abnormally high Poisson's ratio (i.e., 0.40-0.45), beyond that tested in this work, it might be expected that significantly more lateral expansion of the caprock occurs, exerting larger tensile stresses on the caprock natural fractures, resulting in much larger apertures. Although, the fractures may grow less with higher Poisson's ratio, this effect was less strong, and thus might have less effect in reducing the permeability enhancing-effect of much larger apertures. Therefore, whilst this work demonstrates that effective permeability is not strongly affected by Poisson's ratio in the range 0.11-0.37, care should be taken storing hydrogen in a system with a caprock with Poisson's ratios much higher than this without further simulations to the contrary.

4.6.1.8 Initial Matrix Permeability

The literature review on mechanical properties of rock units in Burtonshaw et al. [2024a] found that North Sea gas reservoirs had shale units with permeabilities varying over many orders of magnitude and encompassing the range 0.007 nD to 6.62 mD. The higher end of this range is more relevant for shale underburdens, as opposed to shale caprocks, as this permeability would be too excessive for the caprock to act as a seal. Kivi et al. [2022] noted that a caprock could have a maximum permeability of 1000 nD to prevent leakage of stored carbon dioxide, so a better range would be 0.007 nD to 1000 nD specifically for shale caprock. In fact, Armitage et al. [2011] found that caprock in the Krechba field where supercritical CO_2 is being stored had permeability ranging from 0.01 nD to 100 nD, which is within the 0.007 nD to 1000 nD range. Therefore, the matrix permeabilities tested in this thesis range from 0.01 nD to 100 nD.

The maximal difference in effective permeability after three years between the highest (1 nD) and lowest (10 nD) effective permeability cases was a significant 92 mD, which highlights that the initial matrix permeability of the caprock has a significant effect on the final fracture network and the permeability evolution. The lack of a systematic trend in effective permeability with increasing/decreasing matrix permeability is due to the competing effects of the natural fracture lengths and their apertures. For example, the areal extent of the fractures was by far

the largest in the smallest matrix permeability case (0.01 nD), but the effective permeability of the caprock in this case after three years was only the third highest of the four cases and was a very considerable 82 mD less than the 1 nD matrix permeability case. In this example, the larger fracture apertures of the 1 nD matrix permeability case relative to the 0.01 nD case had a greater effect on the effective permeability than the fact that the fractures were smaller than in the 0.01 nD case. This is logical given that the fracture permeability is quadratically related to the fracture aperture.

The trend in total average fracture aperture can be explained by an understanding of the differential stress acting on the fracture. The 10 nD and 100 nD cases, which are the highest matrix permeability cases, had the highest total average fracture apertures. This is because the high matrix permeability allows for significant fluid flow from the fracture into the matrix and this pressure diffusion out of the fracture reduces the pressure in the fractures, which results in a reduced differential stress around the fracture due to a more uniform pressure distribution between the fractures and the matrix and a more uniform pressure distribution across the rock mass. This reduced differential stress reduces the forces driving fracture closure, allowing fracture apertures to remain large. When decreasing the matrix permeability to 1 nD from 10 nD, the total average aperture decreased slightly. This is because only moderate fluid flow from the fracture to the matrix can occur due to the fact the matrix is now less permeable. In this case, the differential stress around the fracture only increases slightly from the 10 nD case, and so the fractures have only slightly lower apertures. When the matrix permeability was further decreased from 1 nD to 0.01 nD, limited fluid flow can occur from the fracture to the matrix, which means that a much higher differential stress around the fractures is maintained which acts to considerably close the fracture apertures.

The increasing systematic trend in areal fracture extent with decreased matrix permeability is explained by virtue of higher stress concentrations in the vicinity of the fractures when the matrix permeability is lower, which assists in keeping the comparative SIF above the fracture toughness promoting growth. Very steep pressure gradients exist at the interface between fracture and low permeability matrices that strengthens the stress field as fluid pressure is not easily dissipated.

The effective permeability plot shows that caprocks with intermediate matrix permeability (approximately 1 nD) tend to exacerbate hydraulic integrity loss. This is negative in the sense that the majority of caprocks have permeabilities around this value and the 100 nD and 0.01 nD cases are much more geologically uncommon. However, the final effective permeability values are still high in all cases so when the fracture toughness is favourable for growth, no matrix permeability value can prevent total hydraulic failure of the caprock.

4.6.1.9 Biot Coefficient

The Biot coefficient is a parameter which seems to be poorly constrained for shale within the literature and the few studies that do exist show a very large range. For intact and remoulded samples of Opalinus clay shale, Kivi et al. [2022] found Biot coefficients of 0.69 and 0.74 respectively. For 27 samples of Bakken shale, He et al. [2016] found that the Biot coefficient could vary between 0.57 and 0.70, and that the Biot coefficient varied considerably within this range dependent on whether the samples were taken perpendicular or parallel to the shale bedding planes. More extreme values were reported by Luo et al. [2015] and Ma and Gutierrez [2021] for claystone/shale samples of 0.36 and 0.99, respectively. Therefore, four cases were tested within this found range of 0.36 to 0.99, with values of 0.40, 0.60, 0.77 and 0.93, to respect this wide range of potential values.

The maximal difference in effective permeability after three years between the cases was a noticeable 87 mD, which highlights that the Biot coefficient has a substantial influence on the effective permeability of the caprock. In the case of Biot coefficient, both the fracture surface area and the average fracture apertures increased with increased Biot coefficient. As a result, both of these effects constructively combine to result in effective permeability increasing as Biot coefficient increases. The lower the Biot coefficient of the storage field's caprock, the better for maintaining hydraulic and mechanical integrity of the system.

The fracture surface area decreased with decreased Biot coefficient because with a lower Biot coefficient, the pore pressure has a diminished effect on reducing the effective stress within the caprock. Higher effective stress means that the rock matrix is under greater compressive

stresses, making it less likely for fractures to propagate. With higher Biot coefficients, fractures propagate more easily because the effective stress is reduced to a greater extent to allow the rock to fail in tension or shear more often.

The total average aperture of the fractures decreases with decreased Biot coefficient also because of the following. When the Biot coefficient is smaller, the effective stress in the caprock remains higher and thus the rock matrix experiences a greater degree of compression, which acts to close pore space and fracture apertures.

4.6.1.10 Stresses

The fracture toughness chosen in this work has a very significant influence on the growth of the fracture network and thus, the final permeability of the caprock. The caprock fracture toughness used in this work was 0.33×10^5 Pa $m^{1/2}$, which was the lowest value of shale caprock fracture toughness that could be found in the literature. This value was chosen to bound how the fracture network and permeability would evolve in the worst-case scenario in which growth is most favourable. This value was experimentally measured on samples of Opalinus and Antrim clay shale by Liu [2015]. Much larger values, one to two orders of magnitude above that used in this work, are more common for shale caprocks such as 0.49×10^6 Pa $m^{1/2}$ [Vishal et al., 2022], 1.65×10^6 Pa $m^{1/2}$ [Han et al., 2021], and 1.38×10^6 Pa $m^{1/2}$ [Wen et al., 2024]. Therefore, it should not be inferred from the results in this work that hydrogen storage at a large range of *in situ* stress conditions invokes total hydraulic caprock failure. The results in this work are merely used to assess the relative impact of *in situ* stresses on the fracture network and permeability evolution. When the fracture toughness was increased to values at or above 1×10^5 Pa $m^{1/2}$, no growth of the pre-existing natural fractures occurred and thus the caprock maintained its initial permeability and mechanical state throughout the simulated hydrogen storage period, ensuring no loss of integrity.

In the homogeneous *in situ* stress cases, the fracture surface area increased as stress magnitude increased, at least until a value of 45 MPa was reached, and thereafter further increases in stress magnitude did not induce additional growth. This increasing trend occurs because higher stress

magnitudes result in greater stress intensities at fracture tips, making it easier for fractures to propagate. Higher *in situ* stress magnitudes translate to higher stress intensity at fracture tips because the mode I stress intensity factor is directly proportional to the applied *in situ* stresses according to $K_I = Y \cdot \sigma_x \sqrt{\pi a}$, where Y is a dimensionless geometry factor dependent on crack shape and size and the loading conditions, σ_x is the applied *in situ* stress perpendicular to the fracture plane and a is the crack length. A higher stress state implies that more energy is stored in the caprock, which can be released when the fractures propagate, allowing them to grow to greater extents. The 60/60 MPa case does not induce any further fracture growth than the 45/45 MPa case, because the caprock has already reached a mechanical stress saturation point when the *in situ* stresses are 45 MPa. The fractures grow in such a manner, that interaction leads to a highly heterogeneous network with some very large and small fractures. Eventually, the large fractures become so large that they stress-shadow the other fractures preventing additional growth. Thus, additional stress is inefficient in promoting additional growth as the 45 MPa case is already sufficient to generate such a heterogeneous fracture network. Additionally, the maximum extension length of the fractures per time step is set to 0.2628 m, which corresponds to a typical fracture propagation velocity of 0.1 μm/s in shale [Dong et al., 2019], meaning that additional stress does not drive larger fractures because the maximal growth of the growing fractures has almost been reached.

For the homogeneous cases, the average fracture apertures increased with increased *in situ* stress magnitude. At first glance, this may seem counterintuitive. As the compressive stresses acting perpendicular to the fracture plane increases, one may expect the fracture aperture to be smaller due to a greater resistance to opening. However, the complex coupling between stress, pressure and caprock mechanical properties plays a key role. As the horizontal stresses that the rock is externally subjected to are increased in magnitude, the rock matrix poroelastically deforms, undergoing greater lateral compaction, reducing the matrix porosity. When the porosity decreased, the caprock fluid pore pressure increased because the same volume of rock is now occupying a smaller space. The pore pressure increases sufficiently to overcome the additional *in situ* horizontal stresses meaning that the larger homogeneous stress cases have a lower effective stress. This process is exacerbated because the higher stress cases resulted in considerably

greater fracture growth, and those much larger fractures enhance caprock permeability, allowing more of the stored hydrogen to enter the caprock in the higher homogeneous *in situ* stress cases, further pressurising the caprock which is already experiencing horizontal compaction. The lower effective stresses then promote fracture opening resulting in larger apertures in the higher stress magnitude cases. This phenomenon reinforces the importance of fully-coupled models.

The trend in growth extent in the heterogeneous cases is less obvious than in the homogeneous cases. The most to least growth went from the 75/65 MPa case to the 45/30 MPa case to the 65/75 MPa case to the 30/45 MPa case. Therefore, the growth is maximized when σ_x exceeds σ_y and is minimised when σ_y exceeds σ_x. The 75 MPa case grows the most because according to $K_I = Y \cdot \sigma_x \sqrt{\pi a}$, the mode I stress intensity increases with increased σ_x which is largest in this case. When K_I is large, mode I growth is favoured. Using this explanation, one may expect the next largest growth case to be the 65/75 MPa case. However, it was the 45/30 MPa case. This is because in the 65/75 MPa case, although the mode I stress intensity factor is large and so should promote in-plane fracture propagation, the very large σ_y exerts large clamping forces on the fracture in plane laterally, reducing the growth. Therefore, the 45/30 MPa case grows more because even though the mode I stress intensity factors are less than in the 65/75 MPa case, the 30 MPa σ_y exerts far smaller compressive clamping forces meaning σ_x is the dominant control on the in-plane growth behaviour in the 45/30 MPa case compared to σ_y in the 65/75 MPa case. The 30/45 MPa case grows the least because the compressive clamping forces are moderately high and the tensile forces due to σ_x-induced stress intensity are very small.

In the heterogeneous cases, it was found that the 30 MPa/45 MPa case had a total average aperture essentially identical to the 30 MPa/30 MPa case and that the 45/30 MPa case had a total average aperture essentially identical to the 45 MPa/45 MPa case. This highlights that the average aperture is dependent on σ_x and not σ_y. This is logical because σ_x is in the direction perpendicular to the fracture plane and the aperture of a fracture is directly dependent on the effective stress experienced in the direction perpendicular to the fracture plane and not the in-plane direction.

For the homogeneous cases, the effective and equivalent caprock permeability increased with increased horizontal stresses. This reflects the fact that higher stresses resulted in larger fracture surface areas and apertures. For the heterogeneous cases, the effective and equivalent caprock permeability was largest in the 75 MPa/65 MPa and smallest in the 30 MPa/45 MPa case due to the fact that the fracture surface areas and apertures were largest and smallest in these cases, respectively. Although the 45/30 MPa case had slightly larger fracture surface areas than the 65 MPa/75 MPa case, the 45/30 MPa case had a smaller effective and equivalent permeability because the 65 MPa/75 MPa case had much larger fracture apertures than the 45 MPa/30 MPa case.

The effective permeability model of Snow [1969] was shown to correctly predict the qualitative changes between the cases, but quantitatively, there was orders of magnitude difference compared to the equivalent permeability methodology of Lang et al. [2014]. This is because Snow assumes that the fractures are infinite in extent in all directions such that the fractures are through-going within the studied 150 m $\times$ 150 m area. This results in a completely interconnected network such that the fluid can percolate. Once the percolation threshold is reached, it is known that rapid rises in permeability occur, which is why the effective permeabilities are so high. In reality, all of the geomechanical fracture sets grown in the present work are significantly below the percolation threshold. Only the 75 MPa/65 MPa case in Figure 4.12 displays a system of fractures where some of the fractures have fully-overlapped to form much larger fractures that span the whole domain in the horizontal direction and even then these haven't grown to encompass the entire vertical thickness of the caprock. The equivalent permeability of the 75 MPa/65 MPa shows a steepening increase toward the end of the study period, that is higher than all other cases, highlighting the fact that the fractures may be approaching the percolation threshold. In all of the cases, there is still a significant volume of ultra-low permeability shale matrix between the fractures which prevents appreciable flow through the caprock, keeping the equivalent permeability on the order of nanoDarcies. This comparison demonstrates that the Snow model should not be used to predict the true permeability of the caprock, but rather should be used as a worst-case scenario, upper-bound for the permeability, if fractures have become inter-connected and widespread. The Snow permeabilities in Figure

4.15 tend toward some final, non-increasing value. This value represents the equivalent permeability value that would be reached after many years of storage (under the given operational and mechanical properties), if the fractures were to continue to grow until they fully inter-connect and allow percolation.

The decomposed equivalent permeability along the principal axes showed that the permeability in the x-direction does not change with varied stress state or with time. This is because of the initial orientation of the natural fractures. The normal to the fracture faces is in the x-direction such that growth is restricted to the y-z plane. Since, the fractures cannot grow in the x-direction, the fluid traveling in the x-direction will not find significantly easier flow paths through the caprock. As a result of this, essentially the same volume of low-permeability shale rock matrix exists in the x-direction at the end of the simulations as does at the onset of the initial injection.

The final k_{yy} of the caprock is always higher than the final k_{zz}. This is because of the configuration of the initial fracture array. The 5×5 fracture array exists in the x-y plane such that the array is five fractures wide in the x-direction and five fractures wide in the y-direction. However, there is no stacking of fractures in the vertical direction: the array is one fracture tall in the z-direction. Therefore, as the fractures grow over time, they provide more length, connectivity, and permeability in the y-direction due to the greater number of fractures. No connectivity can occur in the z-direction.

In the heterogeneous stress cases, it was observed that the 45 MPa/30 MPa case yielded higher k_{zz} than the 65 MPa/75 MPa case, despite the fact that the stress magnitudes are smaller. This is because the 45 MPa/30 MPa case has a significantly higher horizontal differential stress than the 65 MPa/75 MPa case (15 MPa relative to 10 MPa). Differential stress in the horizontal plane drives fracture propagation in the plane perpendicular to the plane where the differential stress exists. This means higher differential stress promotes fracture growth in the z-direction which is why the fractures are larger in this direction in the 45 MPa/30 MPa case (see Figures 4.12f,g), leading to higher z-permeability.

Linear-Elastic Fracture Mechanics (LEFM) is a widely used and effective approach for assess-

ing fracture growth, but it does have some limitations. LEFM assumes that materials behave elastically up until the point of fracture, meaning it does not account for any permanent deformation (plasticity) that may occur before or after fracture initiation. In materials like chalk and shale, which can exhibit some plastic deformation under high stress conditions, this assumption might not fully capture the nuances of fracture behaviour. Plastic deformation can influence the redistribution of stresses and potentially alter the growth patterns of fractures in ways that a purely elastic model may not predict. Specifically, the inclusion of plasticity would allow the shale to absorb some of the applied stress, thereby reducing the stress intensity at fracture tips and slowing down or even arresting fracture propagation, leading to smaller fracture surface areas and thus potentially smaller final permeabilities. Therefore, the exclusion of plasticity may lead to slight overpredictions on the caprock permeability. Furthermore, plastic zones could develop around the fracture tips that alter the stress distribution in such a way that fractures could be deviated from their paths predicted from a purely elastic model, leading to small differences in the final geometry of the fracture network.

However, the use of a linear-elastic approach remains highly valuable, especially in certain contexts such as multi-year, fully-coupled, large-scale, hydrogen storage simulations. LEFM offers a simpler and more computationally efficient method for analysing fracture growth, making it advantageous for preliminary studies or large-scale models such as in this present work where computational efficiency is crucial. Additionally, when the stress levels within the caprock are within the elastic range of the materials involved, LEFM can provide accurate and insightful predictions. Its well-established theoretical foundation and broad applicability make it a reliable tool for assessing the effects of different *in situ* stress conditions on fracture behaviour. While incorporating plasticity might be necessary for certain scenarios to capture more complex behaviors, especially at the very small-scale, LEFM still serves as a robust and practical first approach.

4.6.1.11 Fracture Nucleation: Tensile Strength

The maximal tensile strength of shale found in the literature was 197.37 MPa for samples of Ordos Basin sandwich shale using a TAW-1000 servo-controlled triaxial rock mechanics experimental system [Dou et al., 2023]. Other large tensile strengths for shale are reported such as the 76 MPa for samples of Cambrian Silurian Black shale extracted from Shizhu County, Chongqing, China PR and measured using Semi-Circular Bending (SCB) tests [Shi et al., 2018a]. Typically, however, the tensile strength of shales are often much lower. Tensile strengths of 3.82-13.5 MPa were reported for the Longmaxi shale [Liu et al., 2021a, Lan et al., 2019], 2.29-10.35 MPa for the Agardhfjellet shale [Abbas, 2015], 3.96-5.53 MPa for the Rurikfjellet shale [Abbas, 2015], 11.5 MPa for the Mancos shale [Petrie et al., 2014], and 14.03-25.62 MPa for Banjiuguan shale [Li et al., 2024].

For the stress conditions (47 MPa vertical stress above caprock and 39 MPa horizontal stresses) and operational conditions (injection rates of 5 m^3/s) in this work, a tensile strength of almost 50 MPa is required to prevent inducement of new caprock fractures and ensure mechanical and hydraulic integrity of the caprock are maintained. For values of 44 MPa or lower, new fractures will develop. However, this does not necessary confirm the loss of mechanical or hydraulic integrity of the caprock. This is dependent on the subsequent growth of the fractures which has been analysed throughout this paper. For example, it was observed in Section 4.5.2.2, if the Young's modulus of the rock is low (i.e. 2 GPa), the fractures will not grow and their apertures remain low and thus the fractures do not fully penetrate the caprock thickness to provide a direct flow pathway and they do not sufficiently enhance the effective caprock permeability to allow fluids to pass through it sufficiently quickly.

For most shale caprocks, the combination of these operating conditions with the relatively high *in situ* stresses will induce mechanical damage to the caprock, and with favourable caprock mechanical properties, hydraulic integrity loss is likely. Therefore, it is possible that the hydrogen cannot be injected at as high rates as 5 m^3/s, at least when the *in situ* stresses are of this magnitude. It is possible that when the *in situ* stresses are lower, the high rate may not be prohibitive because the lower *in situ* stresses allow for larger stress increase due to the

large fluid pressure before reaching the critical stress needed to exceed the tensile strength of the caprock. This will be the focus of future work, but it is clear that very high injection rates such as 5 m^3/s should not be used in fields with caprocks of both low tensile strength (< 45 MPa) and high *in situ* stresses (> 35 MPa).

Figure 4.17 shows that in the 10.4 MPa, 30 MPa and 44 MPa cases, a mix of both horizontal and vertical fractures form. Often two groups of vertical fractures form separated from one another by a group of horizontal fractures in between. Furthermore, the horizontal fractures often form in close vicinity to vertical fractures. The majority of fractures are vertical because of the *in situ* stress state. The horizontal stresses of 39 MPa at the depth of the caprock are slightly less than the 47 MPa vertical stress due to the overlying rock weight. As a result, the minimum compressive stress is in the horizontal direction, and since fractures propagate perpendicular to the minimum compressive stress, the majority of the fractures are vertical. The horizontal fractures form because of a combination of factors. Firstly, once the injection begins, the reservoir pore pressure increases, and the effective vertical stress decreases which reduces the compressive vertical loading on the caprock and allows the caprock to vertically expand. As this occurs, the *in situ* stress state becomes more homogeneous with all three stress states being very similar, until the horizontal stresses just exceed the vertical stress, meaning the minimum compressive stress direction is then the vertical. Fractures therefore propagate perpendicular to this, in the horizontal plane. Secondly, once the vertical fractures nucleate, their interaction creates zones of stress relief and stress amplification. Parallel to the plane of the vertical fractures, horizontal stress is relieved by propagation in that direction. However, perpendicular to the plane of these vertical fractures, due to elasticity, the rock must now carry the load that was previously balanced by the horizontal stress parallel to the fracture. Therefore, the horizontal stress perpendicular to the vertical fractures increases, bringing the stress state closer to homogeneity. Eventually, the horizontal stress just exceeds the vertical stress and the fractures propagate horizontally. The fact that the horizontal fractures are broadly in a group in between the vertical fractures is partly due to the fact that the nucleation algorithm induces a crack in the elements that are most damaged in descending order until the maximum number of induced cracks at that step (specified by the user) has been induced. Since, the middle of

the fractured region has a damage slightly less than the outer part (where the vertical fractures have been induced), the vertical fractures are induced with a space in between them, that then alters the stress state in between, encouraging horizontal fracture nucleation. In reality, if the number of cracks specified to be nucleated was larger, this whole region might be filled with more vertical fractures before the onset of horizontal fracture nucleation, resulting in a more homogeneous fracture orientation distribution. Therefore, this total separation is likely partially a physical artefact. This artefact occurs more in the 44.0 MPa case than the 10.4 MPa or 30 MPa cases. Nevertheless, the purpose of this particular set of simulations was to explore the tensile strength at which fractures will be nucleated rather than the geometrical nature of the resultant network.

4.7 Conclusion

A three-dimensional, fully-coupled, hydromechanical, linear-elastic fracture mechanics simulator, the Imperial College Geomechanics Toolkit (ICGT) was implemented to study fracture growth, fracture nucleation and permeability alteration in the caprock unit of a large-scale 4000×4000×3300 m model of a generic North sea gas reservoir. Parametric studies of fracture properties (i.e., initial size, orientation and spacing) and caprock mechanical properties (i.e., Young's modulus, Poisson's ratio, fracture toughness) was performed to understand the influence of certain parameters on the hydraulic and mechanical integrity of the caprock. Furthermore, simulations were performed in which the *in situ* horizontal stress state was varied in order to assess the sensitivity of the results to different stress conditions that could be found in subsurface reservoirs. Both homogeneous and heterogeneous horizontal stresses were examined. The Lang geomechanical equivalent permeability was computed and compared against the results for Snow effective permeability. Results were found that can guide the choice of a potential hydrogen storage field dependent on the mechanical properties of the caprock of such a field. It was found that:

- Significant growth of pre-existing natural fractures only occurred for fracture toughnesses

of less than 1×10^5 Pa $m^{1/2}$. Above this, the fractures did not grow, suggesting that at the operating conditions of 5 m^3/s, the caprock will maintain integrity if it has a fracture toughness above 1×10^5 Pa $m^{1/2}$. For values less than 0.6×10^5 Pa $m^{1/2}$, under the same conditions, total loss of hydraulic integrity can be expected.

- Smaller initial fractures grew appreciably more than larger fractures. Surface area of fractures of radius 0.2 m and 5.0 m grew 4400 and 8 times from their pre-injection value, respectively.

- The effective permeability decreased substantially as horizontal fracture spacing decreased. For fractures horizontally spaced 7.5 m and 25.0 m, the final effective permeability of the fractured caprock region was 23 mD and 110 mD, respectively.

- The natural fracture orientation had a huge influence on the final effective permeability of the caprock. Large fracture surface areas and apertures led to the caprock having a permeability of 95,000 mD when the normal vector to the fracture faces was (0 1 0), allowing for complete loss of hydraulic integrity, whereas when it was (0 1 1), the final effective permeability was the initial pre-injection value.

- The caprock Poisson's ratio had minimal effect on the hydraulic integrity of the caprock.

- The initial matrix permeability of the caprock did not influence the effective permeability in a systematic manner, but did substantially effect the value of the final effective permeability. This is due to somewhat opposing trends in growth extents and aperture alterations with increasing/decreasing matrix permeability.

- As Biot coefficient decreased, the effective permeability of the caprock decreased. Lower Biot coefficients help to keep effective stress in the caprock high, minimising apertures and fracture propagation.

- Young's modulus had a major effect on the caprock's hydraulic integrity. Low Young's moduli (2 GPa) resulted in no fracture growth or permeability change, but large Young's moduli (43 GPa) led to coalescence of multiple fractures into single very large fractures and a final effective permeability of almost 1 D.

- For an injection rate of 5 m^3/s and a stress state at the depth of the caprock of σ_h = 39 MPa, σ_H = 39 MPa and σ_V = 47 MPa, a caprock tensile strength of over 44 MPa is needed to prevent the inducement of new fractures and maintain caprock integrity.

- No systematic change in effective permeability was observed with increasing vertical fracture spacing. Broadly, however, the larger the vertical spacing, the greater the loss of hydraulic integrity of the caprock.

- The equivalent permeability results demonstrate that even at very high injection and withdrawal rates up to 5 m^3/s, and very low caprock fracture toughness (0.33×10^5 Pa $m^{1/2}$) the hydraulic integrity of the caprock will not be lost after three years of hydrogen storage irrespective of the stress state. The caprock equivalent permeability was maintained on the order of nanoDarcies, and only increased by a maximum of 0.7 nD.

- For homogeneous stresses, the larger the magnitude of the *in situ* horizontal stresses, the larger the fracture growth and the larger the caprock permeability enhancement.

- For heterogeneous stresses, broadly the larger the magnitude of the *in situ* horizontal stresses, the larger the fracture growth and the larger the caprock permeability enhancement. However, the magnitude of the differential stress plays a more dominant role; larger horizontal differential stresses lead to greater fracture growth in the plane perpendicular (vertical plane) to the differential stress, even when the stress magnitudes are smaller.

- The mechanical integrity of the caprock is not lost in three years of geological hydrogen storage. However, in the highest stress case (75 MPa/65 MPa), which is unusually high for typical subsurface conditions, some of the fractures are not far from cross-cutting the entire caprock thickness. This potentially highlights that mechanical integrity could be lost in such a case after a long period of time. Caution should be taken when storing hydrogen in very high stress state reservoirs having very low shale fracture toughness.

- The Snow effective permeability model does not yield a temporally accurate quantitative computation of the permeability evolution of a caprock, but rather represents the worst-case scenario if the fractures grow to such an extent that they are through-going and

completely interconnected such that the percolation threshold is exceeded.

Chapter 5

Effect of Mechanical and Operational Properties on Surface Uplift and Subsidence during UHS

5.1 Introduction

Injection of a fluid can lead to pore pressure increases in the reservoir unit that cause an upward vertical displacement at surface known as surface uplift. Conversely, the withdrawal of a fluid results in pore pressure decreases that cause downward vertical displacement, known as surface subsidence [Niu et al., 2017, Bohloli et al., 2018, Shirzaei et al., 2016]. The changes in pore pressure in the reservoir unit occur hundreds to thousands of metres below the surface where the uplift or subsidence is observed. This is possible because of poroelastic stress changes that lead to cumulative elastic deformation at surface [Chambers et al., 2024]. The pore pressure perturbations force the porous reservoir unit to poroelastically expand (during injection) and contract (during withdrawal), which exerts upward stresses and downward stresses, respectively, on the overlying lithological units [Bohloli et al., 2018]. The total lithostatic stress or overburden load, which is the weight of the rock above the reservoir unit, is balanced by the effective vertical intergranular stress [Gambolati et al., 1996]. When fluid is withdrawn, stress is transferred

from the fluid to the rock skeleton, increasing effective stress and resulting in the compaction of the reservoir and adjacent formations. When fluid is injected, stress is transferred from the rock skeleton to the fluid, reducing effective stress and allowing for the reservoir rock and neighbouring units to expand.

However, surface deformation does not always occur during fluid extraction or injection. The mechanisms for understanding when and when not surface deformation will occur is poorly understood [Deng et al., 2020]. Important factors likely include injection and withdrawal rates, the presence or absence of natural or pre-existing discontinuities, mechanical properties of the reservoir rock, caprock and overburden, fracture properties and the total injected volumes, durations and the depths at which the injection and withdrawal occurs [Deng et al., 2020, Teatini et al., 2011].

Surface subsidence can have serious economic, social and environmental consequences. Subsidence can cause uneven settling of the ground beneath buildings leading to differential settlement of foundations which leads to foundation cracks, tilting or sinking of the building [Cooper, 2008, Ukleja, 2018, Bru et al., 2013]. As the foundations lose support, they may fail to adequately take the load of the structure leading in the most extreme cases to instability, collapse and subsequent death of hundreds of people [Ohenhen and Shirzaei, 2022]. Subsidence can damage underground utility lines, such as water pipes, sewer lines, gas pipelines, and electrical conduits [Bai et al., 2020, Feng et al., 2008]. As the ground displaces, such structures may become bent, crushed, or severed, leading to service disruptions, leaks, or ruptures. This can result in loss of essential services, property damage, and safety hazards for residents. Subsidence can also cause deformation and cracking of roadways and pavements, making them uneven and unsafe for travel [Kontogianni et al., 2007, Shi et al., 2018b]. Differential ground settlement along road surfaces can create bumps, depressions, or potholes, increasing the risk of accidents and vehicle damage. Cracked or damaged roadways may need to be repaired or replaced, resulting in costly infrastructure maintenance and traffic disruptions. Subsidence increases the propensity for flooding by altering surface drainage patterns [Wang et al., 2021, Holzer and Galloway, 2005]. As the ground subsides, natural or engineered drainage systems may become ineffective or blocked, causing water to accumulate and infiltrate buildings or roadways. Drainage infras-

tructure, such as culverts, stormwater pipes, and drainage ditches, may need to be modified or repaired to mitigate flood risks and prevent property damage. Furthermore, subsidence-induced flooding can heavily influence habitat health. Terrestrial habitats such as wetlands, forests, and grasslands, can be inundated with flood waters leading to the loss of vegetation and habitat for wildlife [White and Tremblay, 1995, Morton et al., 2005]. Species that rely on these habitats for nesting, foraging, breeding or simply existing in the case of plant species, may be displaced, experience reduced reproductive success, or killed leading to population declines [Dobben and Slim, 2012]. Subsidence can induce compaction of subsurface reservoirs [Pei et al., 2023] which leads to decreased reservoir storage capacity by reducing porosity and permeability. This also leads to decreases in injectivity and productivity meaning higher injection pressures are needed during injection, thus incurring additional injectant compression costs. Surface subsidence can also result in induced seismicity [Deng et al., 2020, Juncu et al., 2020] and can alter stress distribution within subsurface rock formations. As the overlying rock mass settles or contracts due to subsidence, it redistributes stress to surrounding areas, including faults and fractures in the subsurface. This redistribution of stress due to compaction can lead to the reactivation of pre-existing faults or the initiation of new fractures, potentially inducing seismic events. Subsidence can also induce changes in pore pressure by reducing the porosity and permeability of subsurface rock units. This can facilitate the migration of fluids which can promote the lubrication of faults and fractures, reducing their frictional strength or reducing the effective normal stress acting on the fault and facilitating slip. Subsidence resulting from fluid withdrawal may trigger regulatory scrutiny and legal proceedings [de Waal and Schouten, 2020]. Authorities may impose restrictions or monitoring requirements on activities to mitigate risks to public safety and environmental integrity. Legal disputes over liability for damages and compensation for affected parties may arise, requiring resolution through litigation or regulatory mechanisms. Surface uplift could lead to similar issues as those discussed here for subsidence.

The key example of fluid extraction-induced subsidence was natural gas production from the Groningen field which has been a significant issue since the 1960s. Production from the field peaked in the 1970s, with extraction rates reaching as high as almost 7 billion ft^3/day according to data from the Dutch Petroleum Company [U.S. Energy Information Administration,

2020]. Over time, the removal of gas from the reservoir led to significant reductions in reservoir pressure, causing the ground to sink. Subsidence has been recorded at as much as 40 cm in some areas, especially in regions near the center of the field [van Thienen-Visser et al., 2015]. Some degree of subsidence has occurred over the entire reservoir surface area of approximately 900 km^2 [van Thienen-Visser et al., 2015]. The gradual sinking of the land, combined with increased seismic activity in the region, prompted concerns for infrastructure and safety, leading to a significant reduction in production in recent years. By 2023, the production rate had been cut to below 0.2 billion ft^3/day [U.S. Energy Information Administration, 2020], as the Dutch government announced plans to phase out production entirely by the mid-2020's to mitigate further subsidence and earthquake risks. The development of chronic stress health conditions in local residents of the Groningen field, due to reported feelings of powerlessness and being endangered, will result in at least five deaths per year according to Postmes et al. [2024], should the subsidence continue.

Due to the ultra-low density of hydrogen, enormous volumes of hydrogen will need to be stored to meet future energy demand. Such large volumes will induce fluid overpressures well in excess of typical fluid pressure increases associated with the injection of other fluids for other geo-energy technologies. Larger pore pressure increases and pore pressure reductions associated with hydrogen injection and withdrawal could induce much larger magnitudes of uplift and subsidence relative to that seen from Carbon Capture and Storage (CCS) and natural gas storage. Furthermore, the low density hydrogen may pool at the top of the reservoir, exerting very large buoyancy stresses against the underside of the caprock [Heinemann et al., 2021, Perera, 2023] which could yield additional caprock flexure and deformation that is ultimately transferred to surface in the form of uplift. Alternatively, new fractures could be induced in the reservoir and caprock as a result of these high pressures and stresses that facilitate stress release and dissipation, thus counteracting this expected increased surface uplift.

In this chapter, the ICGT is implemented to study the influence of overburden, reservoir and caprock mechanical properties such as Biot coefficient and permeability, and operational properties such as injection rate on the surface deformation. The ICGT's capability to compute subsidence and uplift is validated against Geertsma's classical 'nucleus of strain' model and

their extended model including the effects of a free surface.

5.2 Literature Review of Numerical and Experimental Studies of Subsidence and Uplift

This section reviews previous work examining uplift and subsidence during the injection and withdrawal of geo-energy fluids. Once again, almost nothing prior has been done to experimentally or numerically examine these phenomena during UHS in depleted gas reservoirs other than the one study mentioned in Section 5.2.1. Therefore, this Section also higlights key studies of uplift and subsidence from other semi-analogous geo-energy technologies such as CO_2 storage and natural gas production. However, it should be noted that none of these analogous technologies concern both the injection and withdrawal of a fluid as will be necessary with UHS, and thus only examine either uplift or subsidence, not both.

Tables 5.1 and 5.2 summarize many more real field cases and experimental or numerical studies, respectively, than those chosen for discussion in this Section. Table 5.1 provides details on the typical magnitudes of subsidence and uplift that have occurred in deployed geo-energy projects around the world and Table 5.2 details already existing conclusions learned from numerical and experimental studies from the literature.

5.2.1 Surface Subsidence and Uplift from Hydrogen Storage

Bai and Tahmasebi [2022] simulated three annual cycles of hydrogen storage in a 3-D model of the Powder River Basin saline aquifer in Wyoming, USA. Each cycle consisted of a 243 day injection period, followed by a 122 day withdrawal period. Injection and withdrawal occur through the same well and the injection rate was 300,000 sm^3/d. The withdrawal rate is not constrained to one value, but rather the wellbore pressure was kept constant during the withdrawal stage. The withdrawal rate therefore varied between 350,000 and 450,000 sm^3/d, with the withdrawal rate increasing as the number of storage cycles increased. They found a

maximum surface uplift of 1.55 cm after the three storage cycles. After just the first injection stage, nearly the whole ground surface experienced some degree of uplift with a maximum of 1.3 cm in the proximity of the well, and the uplift increased with each subsequent cycle. It can be expected that the surface uplift will increase with more injection-extraction cycles. The surface uplift and subsidence during the injection and withdrawal periods respectively, was always maximized in the near-wellbore region, because the pressure changes were largest here. The relatively large magnitude of uplift (cm's) primarily reflects the thin nature of the reservoir unit (33 m). The injection rate used in this work corresponds to 2,700,000 kg of stored hydrogen per day, but potentially masses over an order of magnitude larger than this may need to be stored. Therefore, realistically the surface uplift and subsidence could be much larger than that found in Bai and Tahmasebi [2022].

5.2.2 Surface Uplift from CO_2 Storage

Arjomand et al. [2024] investigated the surface deformations observed through InSAR data and numerical simulations of the InSalah CO_2 storage site, focusing primarily on two wells: KB502 and KB503. For KB502, a fault zone (F12) was incorporated into the model to replicate the observed double-lobe surface uplift pattern. Sensitivity analyses are performed to fine-tune fault properties and reservoir permeability to match simulation results with observed data. Similarly, for KB503, a fractured zone is considered to influence surface deformation, resulting in elongated uplift patterns. Sensitivity analyses on hydraulic conductivity of this zone are conducted to align simulation results with InSAR observations. The study underscores the importance of considering the hydromechanical properties of geological features, such as fault and fractured zones, in numerical simulations of surface deformation. By incorporating anisotropic reservoir permeability and orthotropic materials, the simulations could accurately predict realistic uplift patterns and magnitudes. Uplifts of up to 3 cm were observed over an injection period of 7 years. CO_2 injection into wellbore KB502 started in April 2005 with a rate of 280,000 m^3/day until mid-2007. The ground surface deformation increased rapdily above the well with a rate of 5 mm/year. Injection into this wellbore was then stopped and surface deformation remained

largely unchanged, although injection continued in November 2009, and a few months later an approximate additional 5 mm of uplift occurred above the well.

Rinaldi et al. [2017] injected CO_2 into a four-layer numerical model of the In Salah Aquifer in Algeria which included a low 8 mD permeability reservoir unit and caprock. Two simulations were performed, one which included a fractured zone in the caprock and one which only considered intact caprock. It was found that the uplift was up to 50% larger when the caprock contained fractures. This shows that excluding fractures could have a significant influence on computed subsidence or uplift values.

5.2.3 Surface Subsidence from Natural Gas/Oil Production

Giani et al. [2018] used coupled fluid flow and geomechanical modelling to explore how production of natural gas impacts compaction and surface subsidence. The study used a synthetic case of a multi-layered, weakly compacted offshore gas reservoir, integrating geological, fluid flow, and geomechanical data from an existing gas-bearing formation in offshore Croatia. The numerical simulations demonstrated that the stress-strain behaviour of the system remains in the elastic domain, meaning deformation due to production is minimal (around 10^{-4} m/m) because of limited variations in net effective stress, providing confidence that elastic modelling is valid for subsidence studies during fluid extraction processes. They also concluded that ground-level subsidence differences between one-way and two-way coupling techniques were negligible, though they were more pronounced at the reservoir level.

Zhang et al. [2016] used a simple one-way 3-D numerical model of an oil reservoir undergoing oil production to characterize the effects of various parameters on calculated surface subsidence. These parameters included the withdrawal rate and reservoir properties such as Young's modulus. They found that in a 15 m thick reservoir, as withdrawal rate was varied from 50 to 150 STB/d, the maximal subsidence after a period of 20 years increased from 6 to 18 mm. They additionally found that subsidence linearly increased with increased withdrawal rate. They varied the Young's modulus of the reservoir rock in a very narrow and abnormally low range of 1 to 3 GPa, and found that the Young's modulus had a huge effect on subsidence magnitude

even across such a small parameter space. When the Young's modulus of the reservoir rock was only 1 GPa, the subsidence was 23 mm, which dropped to 11 mm and then to 8 mm when the Young's modulus was increased to 2 and 3 GPa, respectievly. Therefore, a higher reservoir Young's modulus could drastically reduce the final subsidence profiles. They did not test more reaslitic values of Young's modulus or the influence of the Young's modulus of the overburden or caprock materials, which constitute the majority of the rock volume beneath the surface.

5.2.4 Surface Uplift from Water Injection

Jiang [2021] used a poroelastic simulation framework to model surface displacements caused by wastewater injection into a very permeable (250 mD) deep reservoir. The analysis considers two reservoir types: open systems, where fluid can migrate beyond the injection zone, and sealed systems, where movement is constrained by lateral faults. The simulations vary injection rates, total fluid volumes, and reservoir properties such as elastic modulus and Biot coefficient. They varied the reservoir Young's modulus in the sealed reservoir case between high values of 15 to 35 GPa and found that uplift increased significantly from 0.8 cm to 2.4 cm to 6.7 cm as Young's modulus was decreased from 35 to 24 to 15 GPa. The effect of Young's modulus was less significant but still important in the open reservoir case. The sealed and open reservoir cases yielded similar uplift magnitudes, and in the sealed case as Biot coefficient was increased from 0.29 to 0.39 to 0.49, the uplift increased from 2.2 cm to 2.8 cm to 3.4 cm, respectively, showing that increased reservoir Biot coefficient increases observed uplift. They also found that the caprock thickness had a huge effect on uplift when the reservoir was open but no effect when the reservoir was closed. For the open case, the uplift increased from 1.4 cm to 2.1 cm to 2.9 cm as the caprock thickness increased from 100 m to 500 m to 1000 m, showing that as caprock thickness increases, the uplift increases.

Niu et al. [2017] injected water into a 2-D fully-coupled hydromechanical model that included Cam-Clay plasticity. They found that the surface uplift above interbeds is considerably smaller than reservoirs without them. This is because the shale interbed is a heterogeneity in the reservoir that experiences plastic deformation. Therefore, highly heterogeneous layered reservoirs

with either spatially extensive or a significant number of mudstones baffles should be treated differently to the high quality reservoir rocks considered in this work.

5.3 Methodology

A full-scale four-layer model of a generic North sea gas field of dimensions 4000×4000×3300 m was constructed (Figure 5.1). The four lithological units are a chalk overburden, a shale caprock, a sandstone reservoir and a shale underburden. A single, dual-purpose wellbore of length 100 m strikes in the y-direction of the model. The well is parallel to the left and right boundaries of the model and equidistant from both in the model centre. The well lies in the reservoir unit at its mid-depth, which is at a depth of 2475 m. This well therefore acts as an injector well during the time periods of hydrogen injection and then switches to a production well during the periods of hydrogen withdrawal. The caprock and reservoir units are folded to be representative of the anticlinal nature of most North sea field structural traps.

The mechanical properties of the rocks and fluids in each layer are shown in Table 7.2. The fault properties in that table are not relevant in this Chapter as no fractures or faults are studied. A literature review of the values of each relevant mechanical property for each of the four lithologies used in this work is provided in Table 6.4. That table presents these values for three different potential North Sea H_2 storage candidate fields: the Leman field, the Britannia field and the Goldeneye field. The values in Table 7.2 are taken from the 'overall range' of all three of those fields.

No thermal coupling is used in this work. To partially account for the effect of temperature on the fluid mechanical properties, an *in situ* brine of differing density, viscosity and compressibility is prescribed in each lithological unit from P-T correlations according to the P-T conditions that would occur at the middle-depth of that unit if temperature was directly incorporated (Table 7.2).

Unless specified otherwise, hydrogen is injected at a rate of 10 m^3/s for five months, stored with no fluid injection or extraction for two months and withdrawn at a rate of 8.5 m^3/s for a

Table 5.1: Known field cases of induced subsidence or uplift resultant from subsurface injection, storage and withdrawal technologies. 'Subs.', 'Up.' and 'Aq.' denotes the words 'Subsidence', 'Uplift' and 'Acquisition' respectively. Subsidence is denoted by negative values in the 'Total Subs./Up. (cm)' column and uplift is denoted by positive values. References are as follows: [a]Maghsoudi et al. [2018], [b]Wang et al. [2020],[c]Motagh et al. [2017], [d]Rutqvist et al. [2009], [e]Liu et al. [2017], [f]Bawden et al. [2001],[g]Barba-Sevilla et al. [2018], [h]Heimlich et al. [2015], [i]Zheng et al. [2023], [j]Shi et al. [2019], [k]van Thienen-Visser and Breunese [2015], [l]Erban et al. [2014], [m]Feng et al. [2008],[n]Wösten et al. [1997], [o]Herrera et al. [2010],[p]Aobpaet et al. [2013], [q]Teatini et al. [2011], [r]Shirzaei et al. [2016], [s]Ji et al. [2016], [t]Yang et al. [2015], and [u]Staniewicz et al. [2020].

Case	Activity	Data Aq. Method	Subs./Up. Rate (mm/year)	Total Subs./Up. (cm)	Total Area (km^2)
Subsidence					
Bandung, West Java, Indonesia[a]	Groundwater Extraction	PS-InSAR of ALOS PALSAR/Sentinel-1A	-20.1 to -63.6	-	22.85
Rafsanjan plain, Southeastern Iran[c]	Groundwater Extraction	InSAR time-series and in situ measurements	> -50	59.58	-
Sebei Field, Qinghai Province, China PR[e]	Biogas (CH_4+CO_2) Production	InSAR of Sentinel-1	-5 to -70	1-19	-
Santa Ana Basin, Los Angeles, California[f]	Groundwater Extraction	GPS and InSAR	-6 to -13	6	-
Groningen Oil Field, Netherlands[k]	Gas Extraction	Optical Leveling and InSAR	-3	-30	200
Mekong Delta, Vietnam [l]	Groundwater Extraction	InSAR, using 78 ALOS PALSAR Interferograms	-2.8 to -31	-	-
Datun, China[m]	Groundwater Extraction	-	27.58	86.3	33.1
Peat Swamps of Johore, Malaysia[n]	Groundwater Extraction/Peat Swamp Draining	Analysis of irrigation and drainage data	-10 to -30	140	950
Murica, Spain[o]	Groundwater Extraction	TerraSAR-X and ERS/ENVISAT data	-5 to -35	-	-
Samut Prakarn-Thepharak[p]	Groundwater Extraction	InSAR Time-series Analysis	-10 to -30	10	80
Karamay Oilfield, Xinjiang, China PR[s]	Oil Production	GAMMA InSAR of ALOS	< -25	-	355
Pecos, Permian Basin, Texas, USA[u]	Hydraulic Fracturing-Based Oil Production	InSAR of Sentinel-1	-	< -4	900
Uplift					
Wayang Windu, West Java, Indonesia[a]	Geothermal H_2O Injection	PS-InSAR of ALOS PALSAR/Sentinel-1A	9.1 to 15.4	-	0.875
Patuha, West Java, Indonesia[a]	Geothermal H_2O Injection	InSAR of Sentinel-1A	0.05 to 7.2	-	0.0475
Changning, Shuanghe, China PR[b]	Solution Mining of Salt	InSAR of Sentinel-1	10 to 20	-	108.75
In Salah, Algeria[d]	CO_2 Injection for CO_2 Storage	InSAR	5	15	-
Santa Ana Basin, Los Angeles, California[f]	Water Injection	GPS and InSAR	5 to 9	5	-
Cushing, Oklahoma, USA[g]	Wastewater Injection	- Spatiotemporal Correlation Analysis of DInSAR	28 to 39	4 to 5.5	66
Landau, Upper Rhine Graben, Germany[h]	Geothermal H_2O Injection	PS-InSAR/InSAR of TerraSAR-X	10 to 45	4.5	7.16
Winkler County, West Texas, USA[i]	Wastewater Injection	InSAR of Sentinel-1A/B	15	8	62.475
Fengcheng Oil Field, Xinjang, China[j]	CO_2 Injection	Small Baseline Subset InSAR (SBS InSAR)	80 to 120	40	17.25
Las Vegas Valley, Nevada, USA[q]	Groundwater Injection	InSAR	2 to 10	2.8	-
Krechba Gas Field, Algeria[q]	CO_2 Injection	PSInSAR	5	2	19.6
Timpson, East Texas, USA[r]	Wastewater Injection	InSAR of ALOS	0.5 to 3	-	230
Karamay Oilfield, Xinjiang, China PR[s]	Wastewater Injection	GAMMA InSAR of ALOS	9 to 60	20	1.5
Scurry County, West Texas, USA[t]	CO_2 Injection for CO_2-EOR	Baseline Subset InSAR of ALOS	-	< 10	300

Study	Activity/fluid	Type	Details	Methodology	Findings
Subsidence					
Pham et al. [2019]	Groundwater Extraction	FEM	3-D fully-coupled HM	FEEFLOW with SUB+ plug-in and PSUB pre-processing software	Even when wells have same prod. rate, areas far from the constant total head boundaries have most subsidence
Giani et al. [2018]	Natural Gas Production	FEM/FDM	3-D one-way coupled HM	Three models (geological, flow and geomechanics) built from data set of an existing gas-bearing formation	Effective stress increase was only 4-5 MPa; Stress-strain evolution always stays within elastic domain
Kihm et al. [2007]	Groundwater Extraction	FEM	3-D fully-coupled HM	COWADE123D model of aquifer composed of loam layer underlain by a sand layer on flat bedrock	Subsidence greatest near pumping well and decayed to negligible at distances > 100 m
Ye et al. [2016]	Groundwater Extraction	FEM	3-D one-way coupled HM	16-year sim. using two models (groundwater flow and geomechanical) of aquifer systems in central Shanghai	Fixed & traction-free BCs are tested. Subsidence differences are limited to very near model boundaries
Bai and Tahmasebi [2022]	Hydrogen Storage	FEM	3-D one-way coupled HM	Lower Sundance Fm. (CarbonSAFE Project). H_2 injected for 2/3rds of a year, extracted for 1/3rd, no storage	After 1st, 2nd, 3rd withdrawal cycles, subsidence was 6.5 mm, 3.5 mm, 4 mm. Max. subsIdence not above well
Ferronato et al. [2008]	Gas/Oil Production	FEM	2-D one-way coupled HM	5000 m long producing reservoir, compartmentalized into 4 sections. Faults vs no faults tested	Presence of faults reduces subsidence slightly (< 2 cm), subsidence insenstive to fric. angle
Zhang et al. [2016]	Oil Production	FEM	3-D one-way coupled HM	Sensitivity analysis of prod. rate, res. thickness, res. Young's mod., Poisson's ratio on subsidence	Subsidence increases approx. linearly with decreasing Young's mod. Subsid. increases with decreasing Poisson's ratio
Finol and Ali [1975]	Oil Production	FDM	2-D coupled HM	Multiphase fluid flow, black oil simulator with oil production and some gas injection	For same res. compaction, surface subsid. increases as burial depth increases. Subsidence increases for thicker reservoir
Baú et al. [2004]	Groundwater Extraction	FEM	3-D one-way coupled HM	Five-layer model of cylindrical aquifer, different boundary conditions tested (no-flow/fixed pressure)	Imperm. BCs overestimates surface subsid. Larger aquifer/caprock hydraulic conduct. ratio, the smaller the impact of BCs
Alassi [2008]	Fluid Extraction	DEM	2-D one-way coupled HM	PFC-2D (Particle Flow Code) with 20 m uniform particles in hexagonal packing	Subsidence is max. above extraction point. 3.5% error compared to Geertsma's soln. at extract. point, up to 30% further away
Tzampoglou and Loupasakis [2019]	Dewatering Coal Mine	FEM	3-D coupled HM	Plaxis FEM code, models have over 10 strata with fault present, Anargiroi, Fanos and Valtonera settlements	Greater proportion of silt/clay layers relative to sand increases subsidence. Dip angle of fault has little effect on subsid.
Kiryukhin et al. [2014]	Geothermal Fluid Extraction	FEM	3-D fully-coupled THM	TOUGH-FLAC3D sims of the Mutnovsky Geothermal Field with no horiz. displace. on side/bototm boundary	Average subsidence of 5 cm across the model, cause 75% pressure decline and 25% cooling. Only 1^oC cooling occurred
Yao et al. [2023]	Geothermal Fluid Extraction	FEM	3-D one-way coupled HM	COMSOL Multiphysics sims of (1) carbonate karst and (2) sandstone geothermal reservoirs in North China	For same water level drawdown, subsidence in karst was 0.29 mm/yr and 8.9 mm/yr in sandstone. Lithology is important
Uplift					
Jiang [2021]	Wastewater Injection	FEM	2-D fully-coupled HM	COMSOL Multiphysics sims of a 7-layer model inc. reservoir and caprock using inj. rate of 0.05 m^3/min	Res. Young's mod., porosity and depth have large impacts on uplift. Good sealing enhances horiz. displacement more than vert.
Zhang et al. [2018]	CO_2 Sequest.	FEM	3-D fully-coupled THM	TOUGHREACT and FLAC3D sims of four-layer In Salah aquifer model with inj. rate of 7.5 kg/s	Uplift has an approximately linear relationship with inj. rate/pressure. Uplift increased with increased caprock perm.
Niu et al. [2017]	Water Injection	FEM	2-D fully-coupled HM	ABAQUS with Cam-Clay plasticity model. Three-layer model with res. and cap. Res. has clay interbeds	Surface uplift above interbed deviates considerably from that without. Uplift is lower with interbeds
Li and Laloui [2016]	CO_2 Sequest.	FEM	2-D fully-coupled THM	Multiphase flow, 5-layer model inc. aquifer and caprock of the In Salah system, 4.5 years sim.	Cold CO_2 cooling effect further decreased min. effective stress beyond that from increases in the pressure
Zhang et al. [2018]	Water Injection	Experimental	Sand/clay container with pressure pump	$100\times$ 10×50 cm^3 container, H_2O injected at base, displacement monitored	Uplift decays away from well, uplift increases non-linearly with inj. pressure. Presence of clay exacerbates uplift.
Kumar et al. [2022]	Fluid Injection	FEM	2-D one-way coupled HM	Bergermeer gas field model, modified Cam Clay model and creep, 3 cycles of inj. and withdrawal	Uplift max. above injection point. 1.12 cm of uplift after two inj. cycles for 5.2 MPa pressure increase
Bai and Tahmasebi [2022]	Hydrogen Storage	FEM	3-D one-way coupled HM	Lower Sundance Fm. (CarbonSAFE Project). H_2 injected for 2/3rds of a year, extracted for 1/3rd, no storage	After 1st, 2nd, 3rd injection cycles, uplift was 13 mm, 7.5 mm and 5 mm. Max. uplift above well
Elyasi et al. [2016]	CO_2 EOR Injection	FEM	3-D partially-coupled HM	FORTRAN 90 interface code couples ECLIPSE reservoir and ABAQUS geomech. simulators	Uplift linearly increasing with time, approx. 25 cm uplift for inj. rate of 200 million scf/day
Rinaldi et al. [2017]	CO_2 Sequest.	FEM	3-D fully-coupled HM	iTOUGH-PEST and TOUGH-FLAC sims. CO_2 inj. into 4-layer model of In Salah Aquifer	Caprock with fractures enhances uplift by 2-3 mm relative to intact caprock. Dormant vs active fracture had no effect
Khan et al. [2018]	CO_2 Sequest.	FEM	3-D fully-coupled HM	CMG-GEM sims in Arab Jubaila fractured carbonate reservoir model. Fractures not directly modelled	Appreciably lower uplift for sequential inj.-prod. than simultaneous. Uplift increased linearly with inj. pressure
Yin et al. [2010]	Steam EOR Injection	FEM	3-D fully-coupled THM	Multiphase flow, displace.-discon. used for elastic non-thermal zone, 840 m$\times$840 m$\times$20 m reservoir at 1000 m	Uplift was max. above injection well. Max. uplift = 1.1 mm, decaying to < 0.5 mm within 400 m from well
Pearse et al. [2014]	Steam EOR Injection	FEM/FDM	2-D one-way coupled THM	CMG-STARS sims of steam-assisted gravity drainage of bitumen in Athabasca oil sands model	Uplift was max. above injection well. After 3 years heating, max. uplift = 4.6 cm, uplift was 0 cm beyond 200 m
Zheng et al. [2019]	Wastewater Injection	FEM	3-D coupled HM	Defmod sims of wastewater inj. 3-layer model inc. cap., res. Surface-to-res fault versus no fault tested	Presence of fault reduces surface subsidence area and magnitude: 1.83 mm compared to 2.5 mm without

Table 5.2: Literature review of studies examining surface subsidence and uplift from various geo-energy technologies such as hydrogen storage, CO_2 sequestration, wastewater disposal, natural gas production, EOR, coal mine dewatering and geothermal.

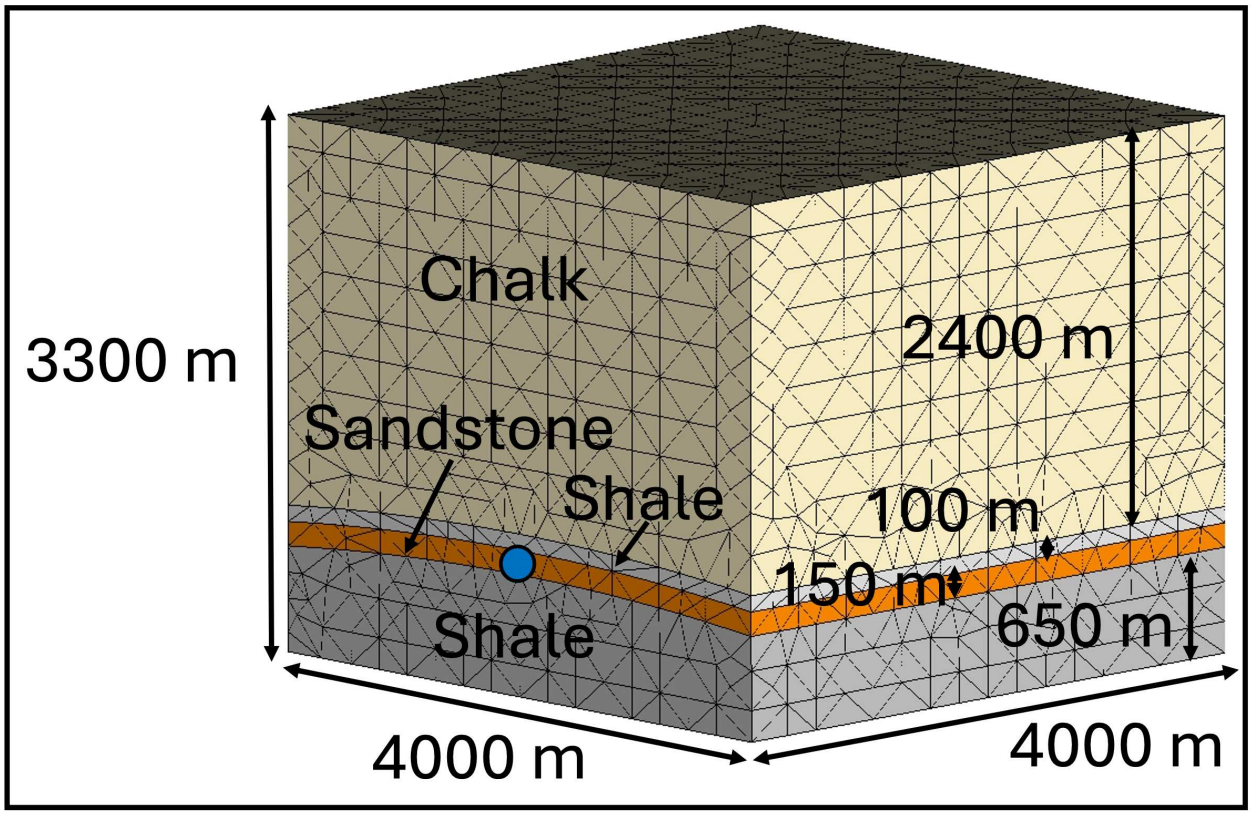


Figure 5.1: Depleted gas field model containing chalk overburden (beige), shale caprock (light grey), sandstone reservoir (orange) and shale underburden (darker grey). A horizontal wellbore of 100 m length is located at the centre of the model and strikes parallel to the right boundary that is visible. Its depth is denoted by the blue circle.

further five months. This injection-storage-withdrawal schedule is repeated for a total of three years.

Sets of simulations are performed for different mechanical properites of different rock units in the model. In each set, a given mechanical property (i.e., Young's modulus, Poisson's ratio, Biot coefficient, matrix permeability) for a given lithological unit (i.e., caprock, overburden, reservoir) is varied across four simulations, keeping all other properties constant across those four simulations. This allows the direct influence of a given property on the surface deformation to be constrained, thus highlighting the values of various mechanical properties that may minimize surface deformation. The same procedure is followed for operational properties such as the injection rate. The numerical simulation cases conducted are shown in Table 5.3.

The model is discretized using a mixed finite element formulation, which is particularly effective for solving complex coupled problems. Numerical simulations of subsidence and uplift during fluid injection or withdrawal from reservoirs must capture the strong interactions between mechanical deformation in the surrounding rock, and the fluid flow. Using the same-order finite elements for such simulations can lead to numerical instabilities and non-physical behavior in the pressure solutions [Haga et al., 2012]. In the present study, Taylor-Hood elements were used for disretization, a type of mixed finite element method in which displacement is modelled using second-order elements, and fluid pressure is approximated with first-order elements [Fortin and Brezzi, 1991]. This approach satisfies the inf-sup stability condition [Murad and Loula, 1994] and prevents numerical oscillations, allowing accurate capture of the interactions between the field variables, and providing a more stable and precise solution.

5.4 Validation against Geertsma's Solutions

5.4.1 Nucleus of Strain

In order to provide confidence that the ICGT simulator can compute compaction and subsidence accurately, its computational predictions are compared against the classical analytical solution

Table 5.3: The four simulation cases run for each mechanical property (Young's modulus, Biot coefficient, Poisson's ratio and permeability) of each unit to examine the effect of such properties on surface subsidence/uplift.

Property	Case 1	Case 2	Case 3	Case 4
Reservoir				
Young's Modulus (GPa)	5	15	40	60
Biot Coefficient (-)	0.35	0.65	0.85	1.00
Poisson's Ratio (-)	0.00	0.15	0.23	0.30
Permeability (m^2)	0.1×10^{-15}	10×10^{-15}	100×10^{-15}	1500×10^{-15}
Caprock				
Young's Modulus (GPa)	2	15	28	43
Biot Coefficient (-)	0.65	0.80	0.93	1.00
Poisson's Ratio (-)	0.11	0.19	0.27	0.35
Permeability (m^2)	1×10^{-23}	1×10^{-21}	1×10^{-20}	1×10^{-19}
Overburden				
Young's Modulus (GPa)	1	4.5	10	35
Biot Coefficient (-)	0.70	0.79	0.87	1.00
Poisson's Ratio (-)	0.20	0.29	0.35	0.42
Permeability (m^2)	0.1×10^{-15}	3×10^{-15}	15×10^{-15}	100×10^{-15}

of Geertsma [Fjaer, 2008, Geertsma, 1973], known as the 'Nucleus of Strain' Model. Geertsma considered a spherical reservoir that is undergoing depletion, surrounded by non-reservoir rock, where there is no difference in the elastic properties of the two rock units. The displacement at some radial distance, r, from the centre of the spherical reservoir, $u(r)$, is given by:

$$u(r) = u_0 \frac{R_0^2}{r^2}, \tag{5.1}$$

where u_0 is related to the volume change of the spherical reservoir and R_0 is the initial radius of the sphere. Specifically, u_0 is given by:

$$u_0 = -\frac{C_m V \alpha \Delta P}{4\pi R_0^2}, \tag{5.2}$$

where α is the Biot coefficient, P is the reservoir pressure, V is the reservoir volume, and C_m is the compaction coefficient or uniaxial compressibility expressed as:

$$C_m = \frac{1}{E_{fr}} \frac{(1+\nu_{fr})(1-2\nu_{fr})}{(1-\nu_{fr})} = \frac{1}{3K_{fr}} \frac{1+\nu_{fr}}{1-\nu_{fr}} = \frac{1}{\lambda_{fr} + 2G_{fr}}, \tag{5.3}$$

where E is the Young's modulus, ν is the Poisson's ratio, K is the bulk modulus, λ is the Lame parameter, G is the shear modulus, and the subscript 'fr' refers to framework (rock skeleton).

By combining Equations 5.1, 5.2 and 5.3, Geertsma arrived at the following expression that describes the displacement field at all locations in the material surrounding the depleting sphere for an infinite medium:

$$u(r) = -\frac{C_m}{4\pi} V \alpha \Delta P \frac{1}{r^2}. \tag{5.4}$$

The sphere has radius 1 m and is encapsulated by a cube of dimensions 120 m $\times$ 120 m $\times$ 120 m. The rock surrounding the spherical reservoir is set to have an ultra-low permeability of 1×10^{-21} m^2 such that as little of the reservoir fluid depletion is associated with the leakage of the fluid into the surrounding material as numerically possible. Ideally the surrounding material

would have a permeability equivalent to 0 m^2 to prevent any leakage whatsoever, so that any compaction is only associated with pressure loss due to fluid extraction from the withdrawal wellbore. However, very low permeabilities induce significant numerical oscillations and errors in the results such that a permeability of zero cannot be assigned to the second unit without heavily contaminating the solution. The elastic, geometric and operational properties of the sphere and the second rock unit are given in Table 5.4.

Property	Sphere	Rock
V (m^3)	4.189	1,727,995.810
E (GPa)	20	20
ν (-)	0.25	0.25
Δp_f (Pa)	100	-
α (-)	1.0	1.0

Table 5.4: Properties of the sphere and the surrounding rock used in the ICGT replication model of Geertsma's 'nucleus of strain' model.

Geertsma's solution is plotted in black in Figure 5.2 and is compared against the results of the equivalent replicated ICGT simulation. An excellent match is observed, except at the boundary between the sphere and the surrounding low permeability material. This localized error results from multiple factors. Firstly, the low permeability material surrounding the depleting sphere is in fact a zero permeability material in Geertsma's analytical solution. However, the ICGT simulator has difficulty solving displacement and pressure fields when there is very significant permeability contrasts between materials (such as the 10^{-13} m^2 of the sphere and the 0 m^2 of the surrounding material) and when the magnitude of the permeability is extremely low ($< 10^{-21}$ m^2). Therefore, the surrounding material must be modelled as having some low, but non-zero permeability. Therefore, a very small amount of the fluid leaks from the surrounding material that is near to the interface between the two materials and into the sphere. This means the pressure reduction is very slightly more than in reality, as more fluid is withdrawn than expected, which enhances the observed subsidence at these very small distances. Secondly, some of the error relates to the fact that the sphere is relatively coarse to aid run time and does not have a perfectly spherical shape (Figure 5.3b). The slightly irregular shape of the sphere allows stress concentrations to form due to the geometrical asymmetries, altering the displacement

pattern near the interface. Ultimately, the minor error at the reservoir depth is not detrimental since we are interested in studying the displacement pattern at surface, thousands of metres away from the reservoir. Surface subsidence or uplift results from the integrated response of the entire displacement field in the medium, which is dominated by far-field effects rather than localized discrepancies near the sphere's interface. At larger radial distances, the displacement field becomes smoother, and deviations due to interface irregularities or mesh-induced errors diminish. This aligns more closely with Geertsma's model predictions. Therefore, as long as the error diminishes to very small magnitudes, as seen in Figure 5.2, at moderate distances, this is not problematic for the evaluation of the surface subsidence or uplift.

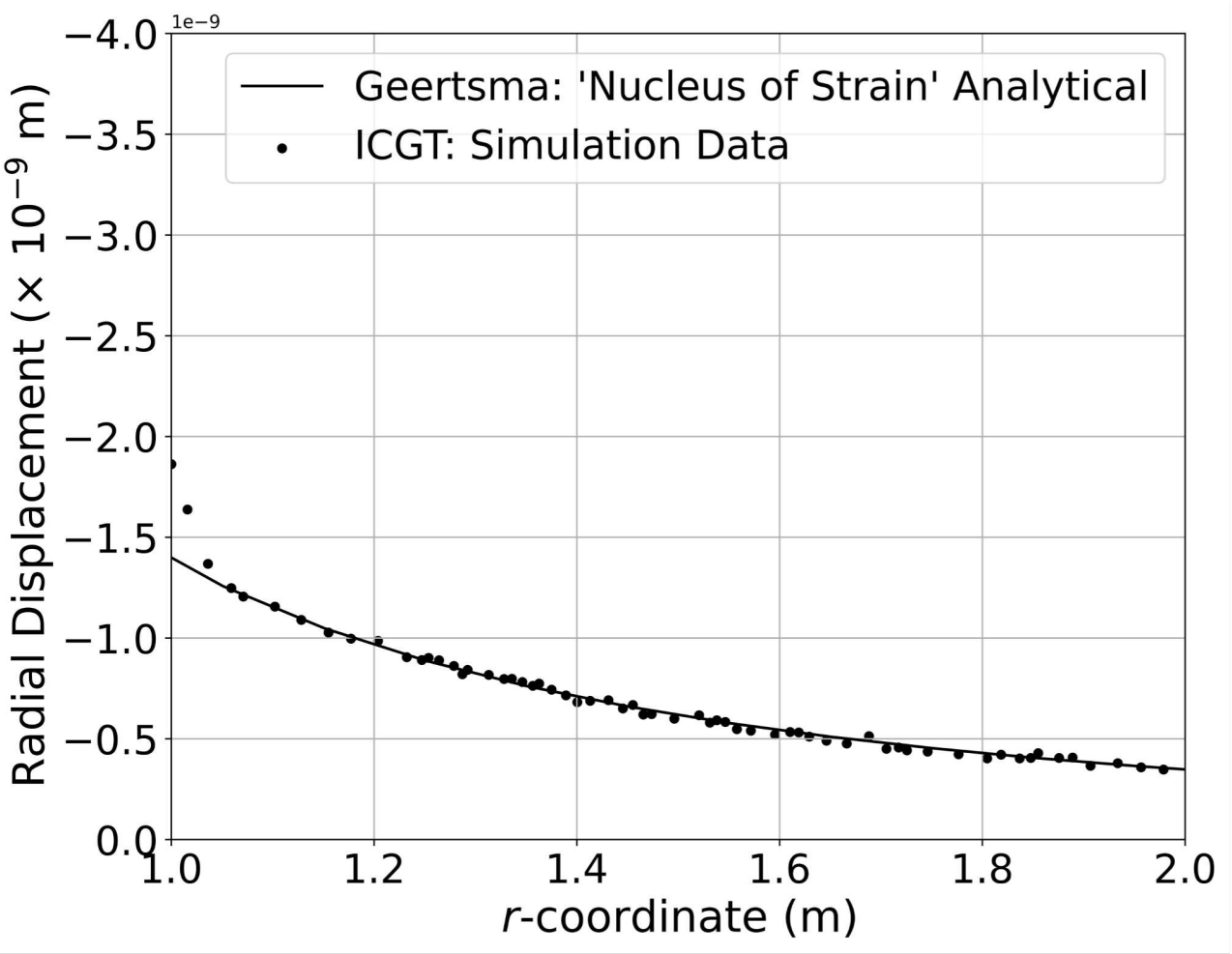


Figure 5.2: Comparison of Geertsma's nucleus of strain model to the ICGT computation of displacements.

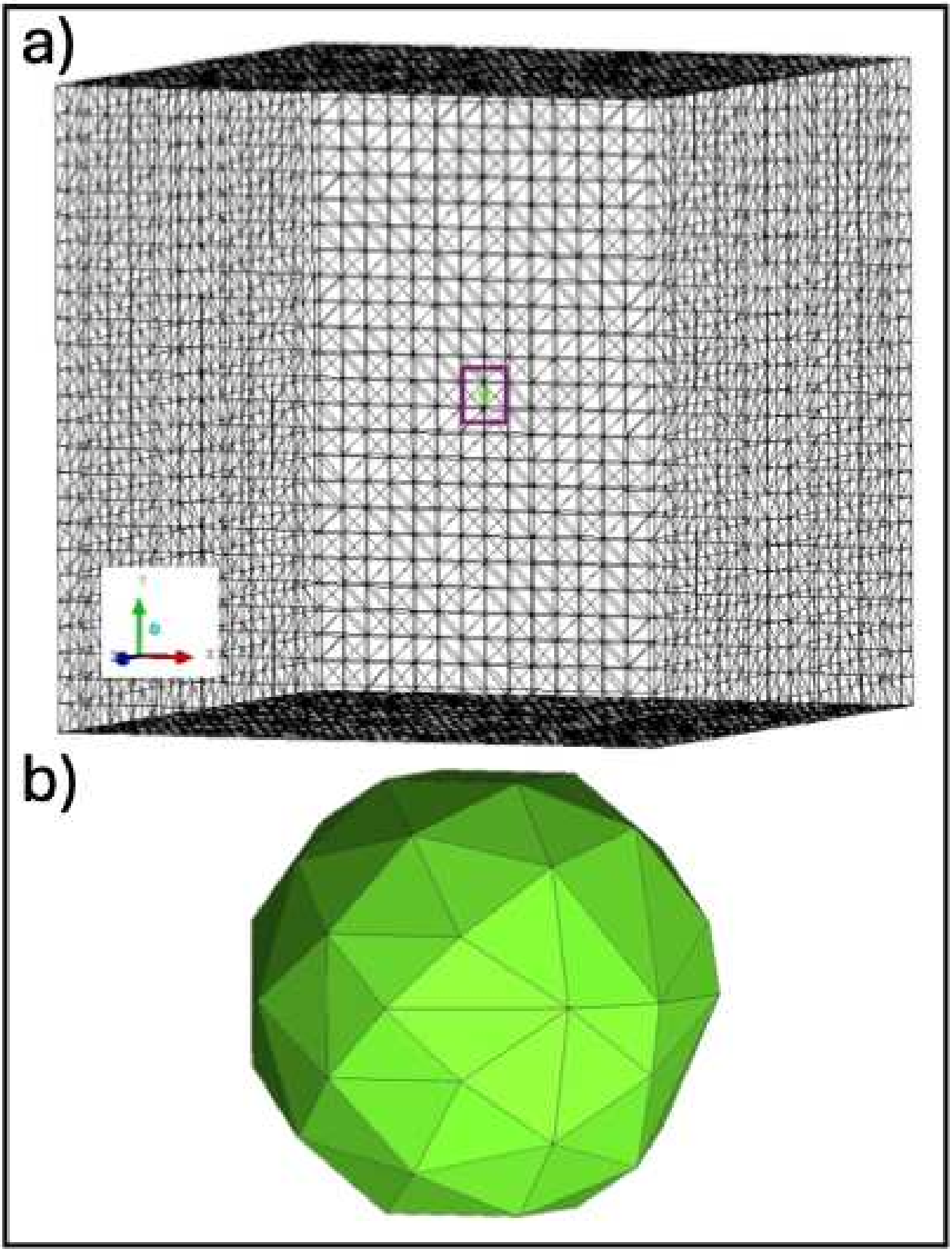


Figure 5.3: The 120 × 120 × 120 m^3 model used within the ICGT to replicate Geertsma's 'nucleus of strain' scenario. The purple box highlights the location of the 1 m radius sphere at the model centre. (b) The depleting sphere enlarged from (a).

5.4.2 Extended Nucleus of Strain with Effect of Free Surface

Geertsma then considered the influence of a nearby free surface on the displacement (zero vertical stress) and provided an analytical solution for the displacement over the surface. The Geertsma model in Section 5.4.1 assumes an infinite, unbounded medium, which is successfully replicated in the ICGT by embedding the depleting sphere far away from any boundary. Therefore, the sphere essentially had no defined 'top' or 'surface' to impose specific constraints on stress or displacement. The deformation propagates isotropically from the source of compaction, without encountering a boundary where stresses or displacements need to change behaviour. However, in this model Geertsma's boundary conditions change from an infinite medium to a zero vertical stress top surface, which will inevitably impact the deformation and displacement field. To account for this in the ICGT, the model in Section 5.4.1 is altered by translating the depleting sphere vertically upward from the centre of the model, very far from model boundaries, to just 2 m below the upper surface.

Geertsma's analytical solution for surface displacement accounting for a free surface is given by:

$$\vec{u} = \frac{C_m\,(1-\nu)}{\pi} V \alpha \Delta P \frac{\vec{R_1}}{R_1^3}, \tag{5.5}$$

where $\vec{u}$ is the displacement (which is in the direction of $\vec{R_1}$ on the surface), C_m is the compaction coefficient given by equation 5.3, $\vec{R_1}$ is the displacement vector of a point of interest anywhere in the rock from the centre of the sphere, and R_1 is the distance between the point of interest and the centre of the depleting sphere.

Figure 5.4 shows the displacement as a function of distance along the line across the surface that passes through the centre point and starts and terminates at the mid-point of the left and right boundaries of the top surface of the model. The results show an excellent match. Only near the origin is a non-negligible error observed, where a maximal error of 3.3% is found. The origin refers to the surface point directly above the depleting sphere. The error here is explained by the same mechanisms as in Section 5.4.1. The imperfect spherical nature of the

sphere due to the element sizes and the non-zero permeability of the sphere-surrounding rock are the main contributors to this error. Figure 5.5 shows a zoomed in view of the pressure field at the very small scale (several metres of rock) that highlights this, clearly showing that the pressure has declined outside of the sphere outline and assymetries and coarseness in the sphere geometry has caused some distortion of the pressure field. These irregularities in the pressure field all occur within less than 3 metres width of rock, which is the x-coordinate range where some non-negligble error is observed compared to Geertsma's solution (Figure 5.4).

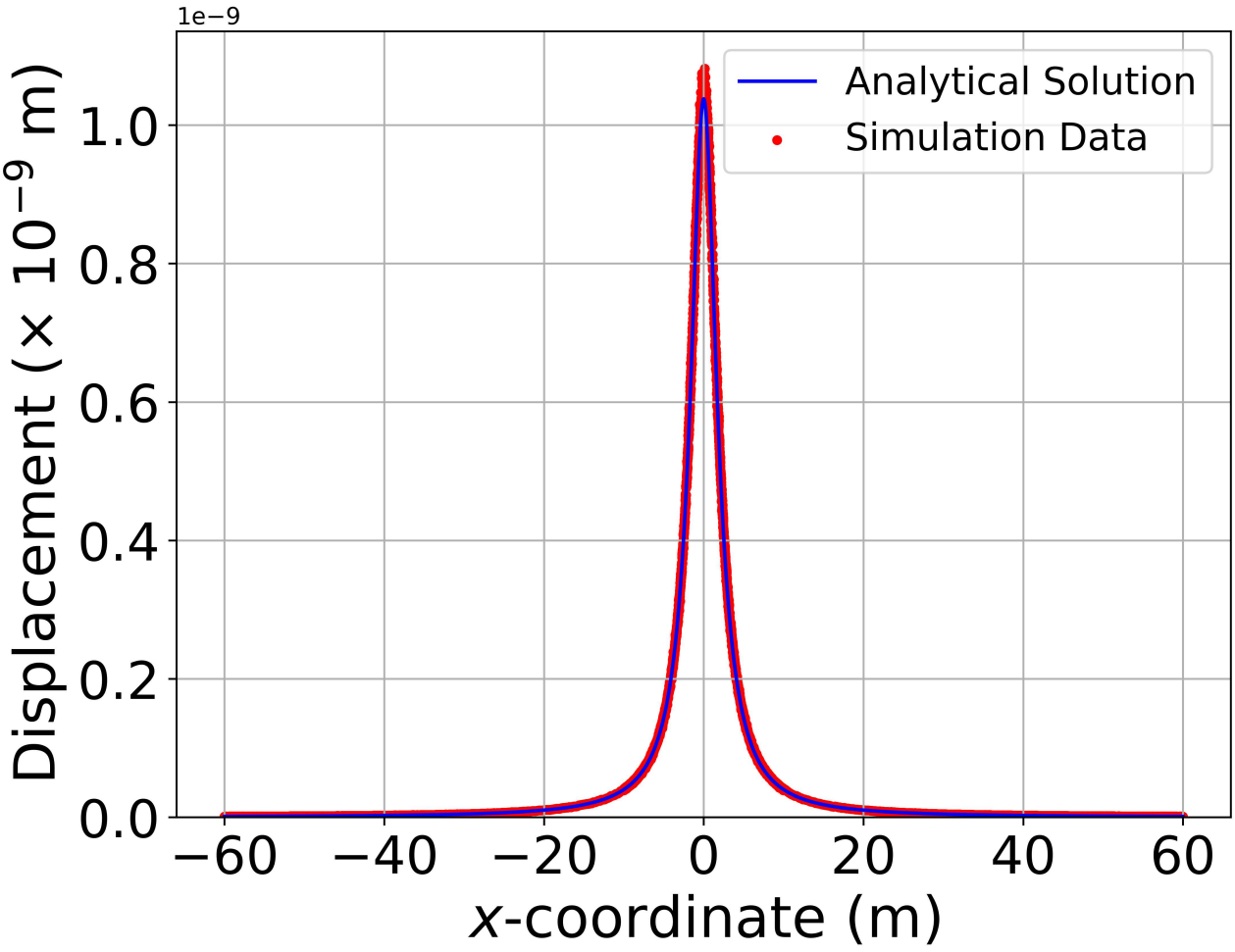


Figure 5.4: Comparison of Geertsma's nucleus of strain model with free surface to the ICGT computation for the displacement along the line on the model surface, passing through the surface center, and starting and terminating from the left and right boundaries.

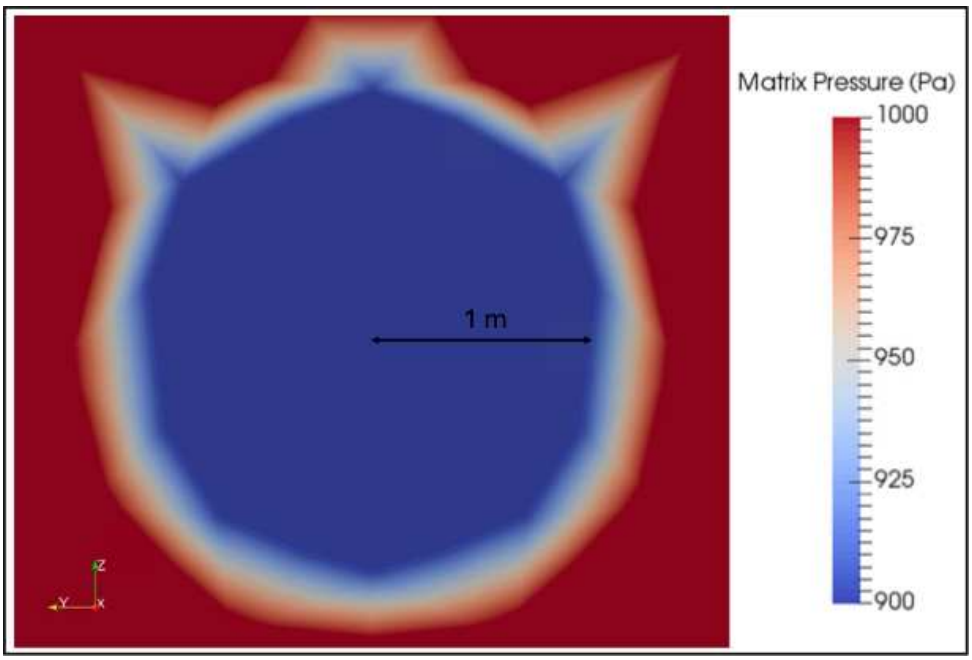


Figure 5.5: Zoomed view of the pressure field at and around the depleting sphere at the very small scale.

5.5 Mesh Effects

Four simulations were performed to assess the impact of the chosen mesh on the uplift versus time solution. This is especially important given that it was already observed with the Geertsma validation (Section 5.4) that a relatively coarse mesh around the fluid withdrawal point can induce small errors in the computed compaction in the surrounding region of rock. Therefore, a different mesh refinement was used in each simulation (Figure 5.6) to understand this impact. All four cases have a region of ultra-high refinement around the multi-purpose wellbore, which is the rectangular white region in all subplots of Figure 5.6. The 28,206 and 130,840 node cases shown in the bottom row of Figure 5.6 have an equally dense mesh throughout the entire volume (excluding the highly-refined zone around the well). The 153,639 and 290,725 cases then use an additional highly refined volume of 500 m $\times$ 500 m $\times$ 3300 m centred at the middle of the model around the wellbore. Each mesh case had between approximately 30,000 and 300,000 nodes and the results are shown in Figure 5.7. It was found that the net uplift versus time solution converged to the same solution as the number of nodes reached approximately 150,000 nodes and when a highly-refined region around the wellbore was present (top row of Figure 5.6). The 28,206 node case was too coarse and yielded a completely erroneous solution. This results

from the fact that the element sizes are so large that the pressure and stress distributions are significantly different to that in the more refined models. In the 130,840 node case, a small error of approximately 2% was found relative to the 153,639 and 290,725 cases. This is attributed to needing more refinement around the wellbore as in the 153,639 and 290,725 cases. The remainder of this work will use the 153,639 node mesh.

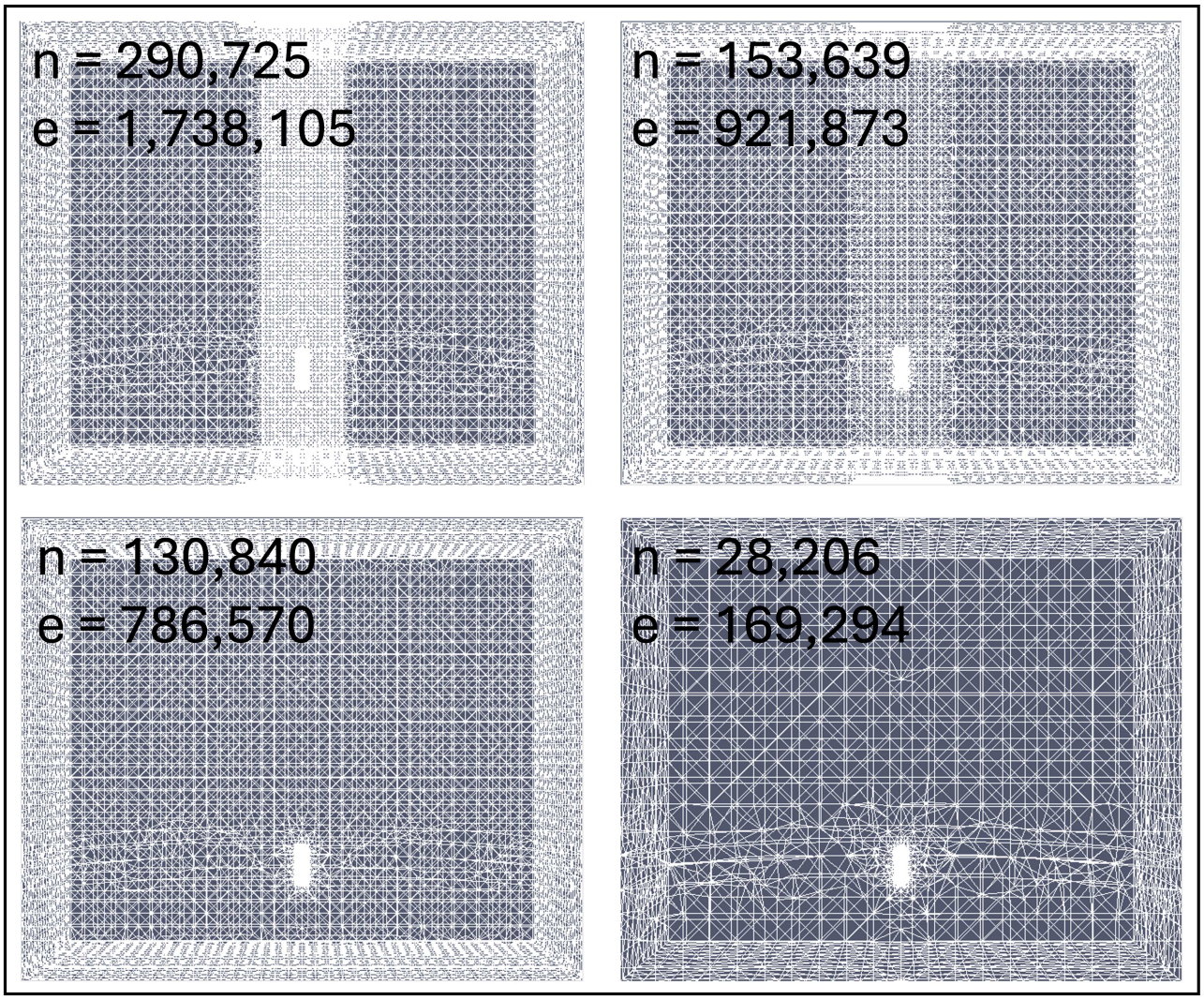


Figure 5.6: Four different meshes used to examine the effect of mesh refinement on the net uplift versus time solution.

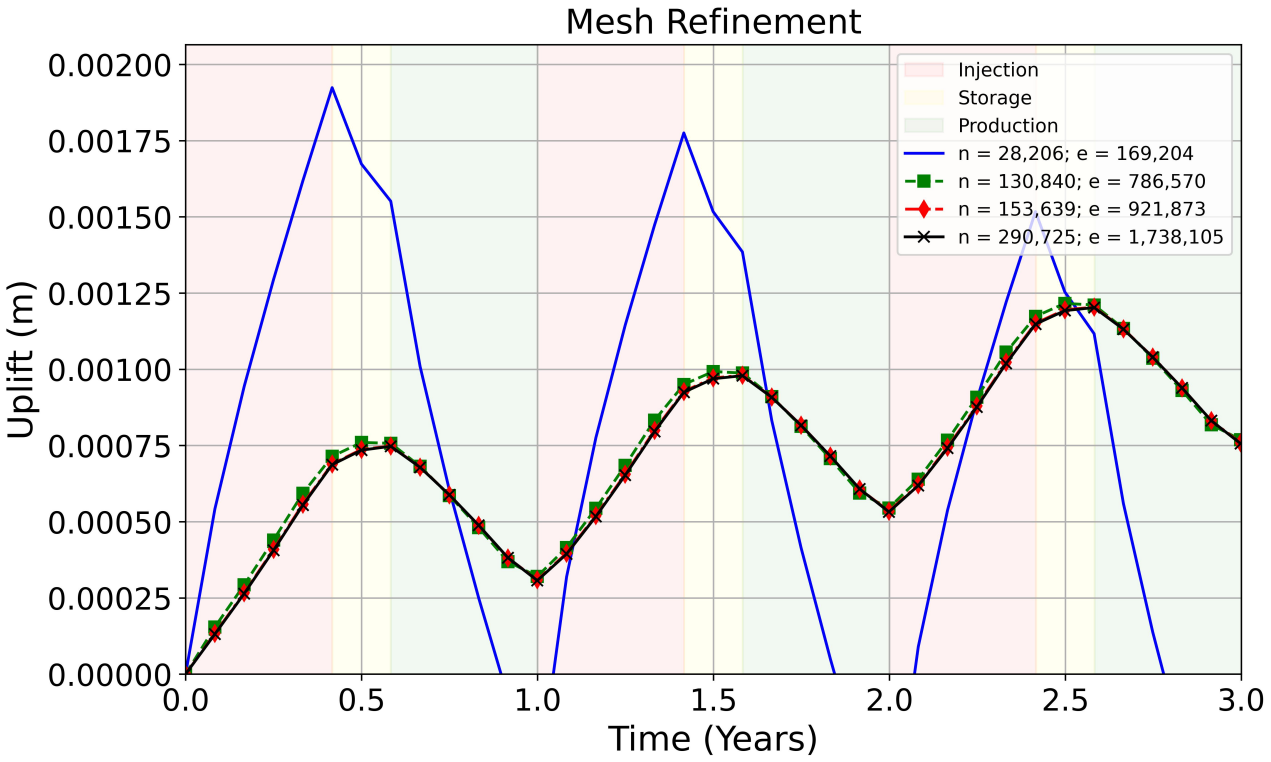


Figure 5.7: Net uplift versus time for four cases of varying mesh refinement.

5.6 Results

5.6.1 Base Case

Figure 5.8 shows the reservoir pressure, $P(R,t)$ as a function of radial distance from the wellbore, R, and time since the onset of injection, t. The simulator shows an excellent match with the known analytical solution [Zimmerman, 2018]:

$$P(R,t) = P_i - \frac{\mu_f Q}{2\pi k H}\left[\frac{R^2}{2R_e^2} + \frac{2kt}{\phi\mu c R_e^2} - ln\left(\frac{R}{R_w}\right) - \frac{3}{4} + ln\left(\frac{R_e}{R_w}\right)\right], \tag{5.6}$$

where P_i is the initial reservoir pressure, μ_f is the fluid viscosity, Q is the volumetric flowrate, k is the reservoir permeability, H is the reservoir thickness, R is the radial coordinate, R_e is the reservoir's outer radius, ϕ is the porosity, c is the total compressibility (sum of the formation and fluid compressibilities), and R_w is the wellbore radius.

Figure 5.9b shows the evolution of the net uplift of the surface point directly above the reservoir

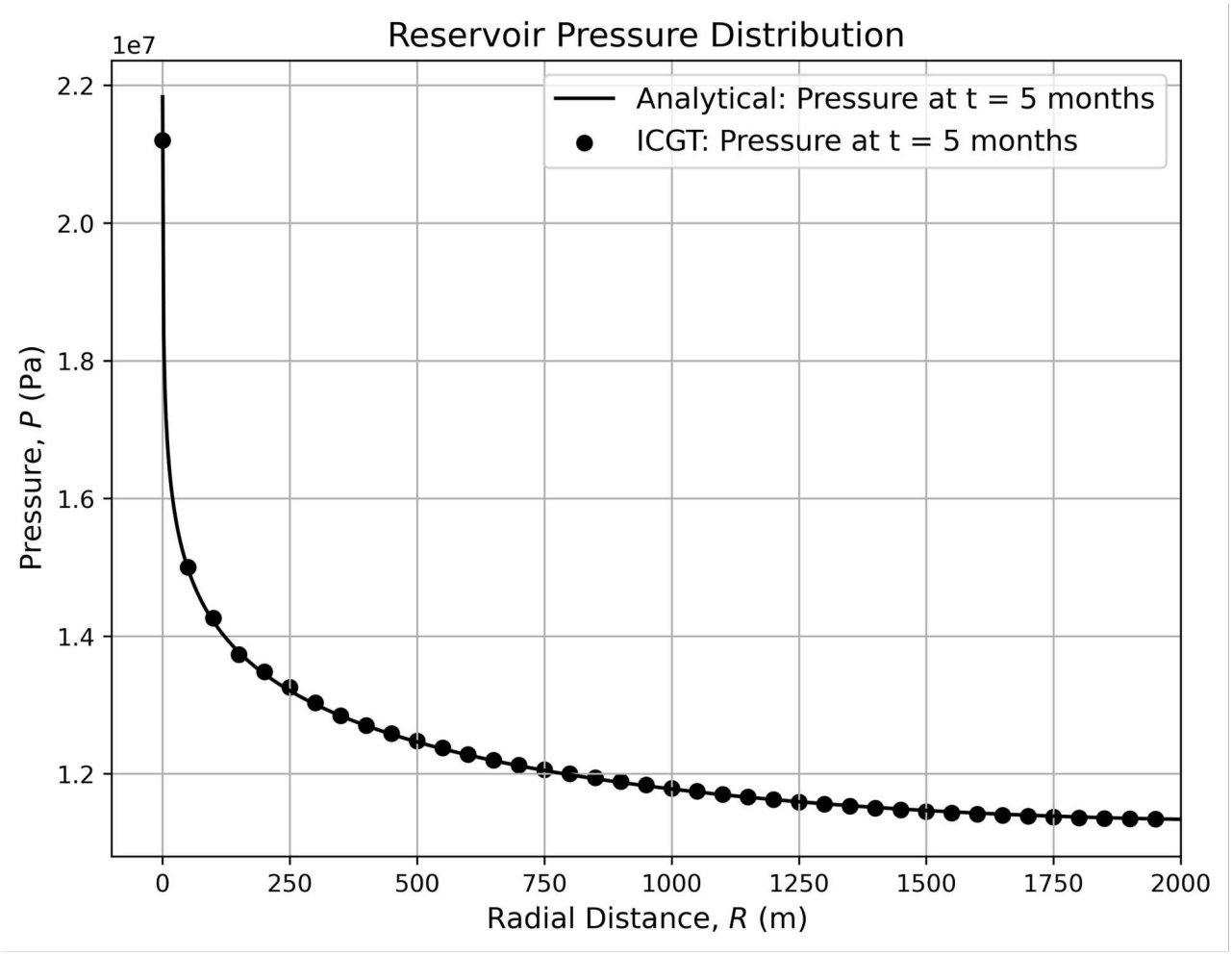


Figure 5.8: Reservoir pressure with radial distance from the well after five months of injection (end of first injection period).

(and model) centre through time. It can be seen that the maximal net uplift after three cycles is only 1.21 mm. During the injection periods, the surface uplifts in response to the elevated reservoir pressure which causes the reservoir to expand due to effective stress reduction. This expansion is propagated up through to the surface but with a significantly decayed magnitude. Figure 5.9a shows the uplift at the reservoir and caprock levels after five months (the end of the first injection period). The maximal uplift at the top of reservoir is approximately 12.3 mm. This decays considerably to 0.72 mm above the very thick (2300 m) overburden. The bottom of the reservoir moves vertically downward by 7.6 mm. Therefore the total reservoir expansion, Δh_{sim}, is 12.3 + 7.6 mm = 19.9 mm. Analytically, the expected reservoir expansion, $\Delta h_{analytical}$, is given by Fjaer [2008]:

$$\Delta h_{analytical} = \alpha C_m H \Delta P, \tag{5.7}$$

where α is the reservoir Biot coefficient, C_m is the uniaxial compaction coefficient (given by Equation 5.3), H is the initial reservoir thickness, and ΔP is the average reservoir pressure increase. Therefore, $\Delta h_{analytical} = 0.35 \times 6.3 \times 10^{-11} \times 150 \times 5{,}924{,}332.04 = 19.6$ mm. The analytical and simulation reservoir expansions show excellent alignment.

Mehrabian and Abousleiman [2015] provided an analytical solution for the surface deformation above a reservoir unit that is embedded within elastic strata of different mechanical properties, and which is subjected to pore pressure variations resulting from fluid extraction or injection. The model is basic in the sense that in only accounts for the Young's modulus, the Poisson ratio, and the Biot coefficient of the layers, the magnitude of the pressure disturbance, and the geometry of the reservoir laterally and with respect to the surface. It does not include the effects of possible slight arching of the reservoir below the caprock, as is the case in the present model. Furthermore, it assumes that there is only one rock unit between the surface and the reservoir, when in reality, and in the present computational model, multiple rock units will be present, having varying mechanical properties. Nevertheless, the Mehrabian and Abousleiman [2015] model can be used to give a rough expectation of the magnitude of the uplift.

The Mehrabian and Abousleiman [2015] surface uplift solution is given by:

$$\frac{u_z(0,0)}{\alpha C_m \Delta P H} = -\left(\frac{1+\mu-2\nu}{\mu}\right)\left(\frac{1}{\sqrt{1+\rho^2}}-1\right)+\left(\frac{\mu-1}{\mu}\right)\left(\frac{\rho^2}{\sqrt{(1+\rho^2)^3}}\right), \qquad (5.8)$$

where $u_z(0,0)$ is the surface uplift at the point on the surface located directly above the center of the reservoir, μ is ratio of the overburden and reservoir shear moduli, G, and ρ is the ratio of the radial distance that the injectant pressure front has propagated at a time, t, to the depth to the top of the reservoir unit, d. Firstly, computing μ for the present model gives $G_{over}/G_{res} = [4.5/(2(1+0.35))]/[15/(2(1+0.15))] = 0.256$. The parameter ρ takes the value $R_e/d = 2257/2400 = 0.940$. This calculation assumes that the injectant pressure front has propagated fully to the edge of the reservoir, R_e. This assumption is reasonable, according to the following calculation. Zimmerman [2018] showed that after an elapsed time t, the pressre pulse propagates a distance R into the reservoir, according to the equation $t = \phi\mu c\mathrm{R}^2/k$. Using the property values from Table 7.2, it follows that the pressure pulse will reach the edge of the reservoir in $(0.15\times10.4\times10^{-6}\times66.7\times10^{-9}\times2257^2)/(100\times10^{-15}) = 61$ days.

Substituing the μ and ρ values into Equation 5.8 yields $u_z(0,0)/(\alpha C_m H\Delta P) = 0.0198$, which leads to a surface uplfit at the center of the reservoir of $u_z(0,0) = 0.0198\alpha C_m H\Delta P = 0.4$ mm. After this same five month period, the simulation gave 0.7 mm of uplift at the same center point on the surface (end of first injection in Figure 5.9b). The two results are reasonably close, and provide support for the validity of the simulated uplift values. As mentioned above, small differences are to be expected, due to the idealizations contained in the Mehrabian and Abousleiman [2015] model. In particular, this simulation has a thin caprock between the reservoir and overburden units with different mechanical properties, whereas Mehrabian and Abousleiman assume uniform properties above the reservoir.

To demonstrate that this analytical calculation does indeed give a reasonable approximation of the magnitudes that could be expected from a specific fluid injection procedure, we perform this analysis again for the CO_2 storage model of Rutqvist [2012], and compare the analytical prediction to the simulated result. The model properties are not all explicitly stated in Rutqvist

[2012], but can be found in Rutqvist et al. [2010]. That model has a 900 m thick overburden on top of a 900 m thick caprock before reaching the reservoir. Therefore, we will compute two values using the Mehrabian and Abousleiman [2015] model, one assuming the entire unit above the reservoir has the properties of the caprock, and one assuming that the entire unit above the reservoir has the properties of the overburden. Assuming the caprock constitutes the top layer, $\mu = G_{cap}/G_{res} = [20/(2(1+0.15))]/[6/(2(1+0.20))] = 3.478$, and $\rho = R_e/d = 5642/1800 = 3.134$. Equation 5.8 then yields $u_z(0,0) = 3.0$ cm. Using the overburden properties yields $\mu = G_{over}/G_{res} = 0.25$, in which case Equation 5.8 yields $u_z(0,0) = 4.6$ cm. Therefore, it can be concluded that the expected uplift should be on the order of a few centimetres in this case. The simulation in Rutqvist (2012) found 1.2 cm of uplift at the central surface point after the three years. Once again, there is some rough agreement between the "analytical" and simulated uplift values. The slightly larger difference between the analytical and simulated values in the model of Rutqvist [2012], as compared to the present work may possibly be explained by the fact that Rutqvist's model has a much thicker caprock unit (900 m) between the overburden and reservoir, rendering the approximation of a single layer between the surface and reservoir less appropriate.

Once injection ceases, the surface uplift essentially plateaus since there is no additional increase in mean reservoir pressure. Figure 5.9b shows that the central surface point does continue to uplift very slightly after injection has ceased with an increase of 0.05 mm after the 0.72 mm of uplift due to the first injection period. This represents a 7% increase in uplift even after the injection has ceased. This occurs because despite the fact that the reservoir pressure directly below this surface point (at the wellbore) is no longer increasing, the hydrogen has its highest pressure at the injection well and continues to diffuse deeper into the reservoir in order to achieve pressure equilibrium. Therefore, after injection ceases the outer portions of the reservoir become more pressurized than during the injection period and as such, the outer portions of the reservoir undergo additional expansion. Since the overlying caprock is relatively stiff with a Young's modulus of 15 GPa and it has a very low permeability of 1 nD preventing upward flow of hydrogen into the caprock, the caprock resists the upward expansion and deformation of the outer reservoir and the internal vertical stresses within the reservoir are redistributed

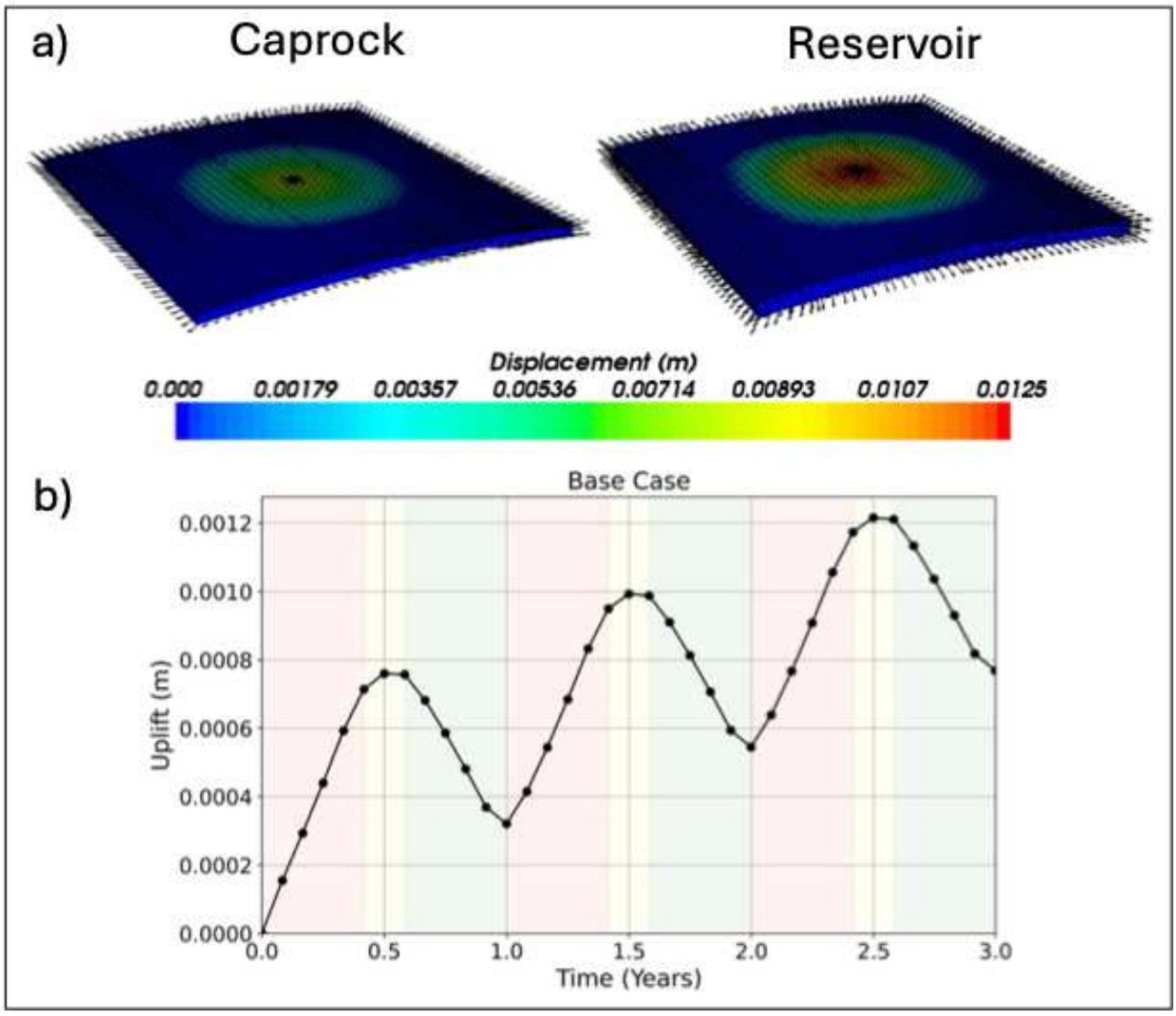


Figure 5.9: Base case. (a) The vertical uplift along the top surface of the caprock and reservoir units after five months of injection. (b) Uplift versus time at the centre point of the model top surface.

and spread over a wider area, leading to a slightly elevated surface uplift at the centre during the storage period.

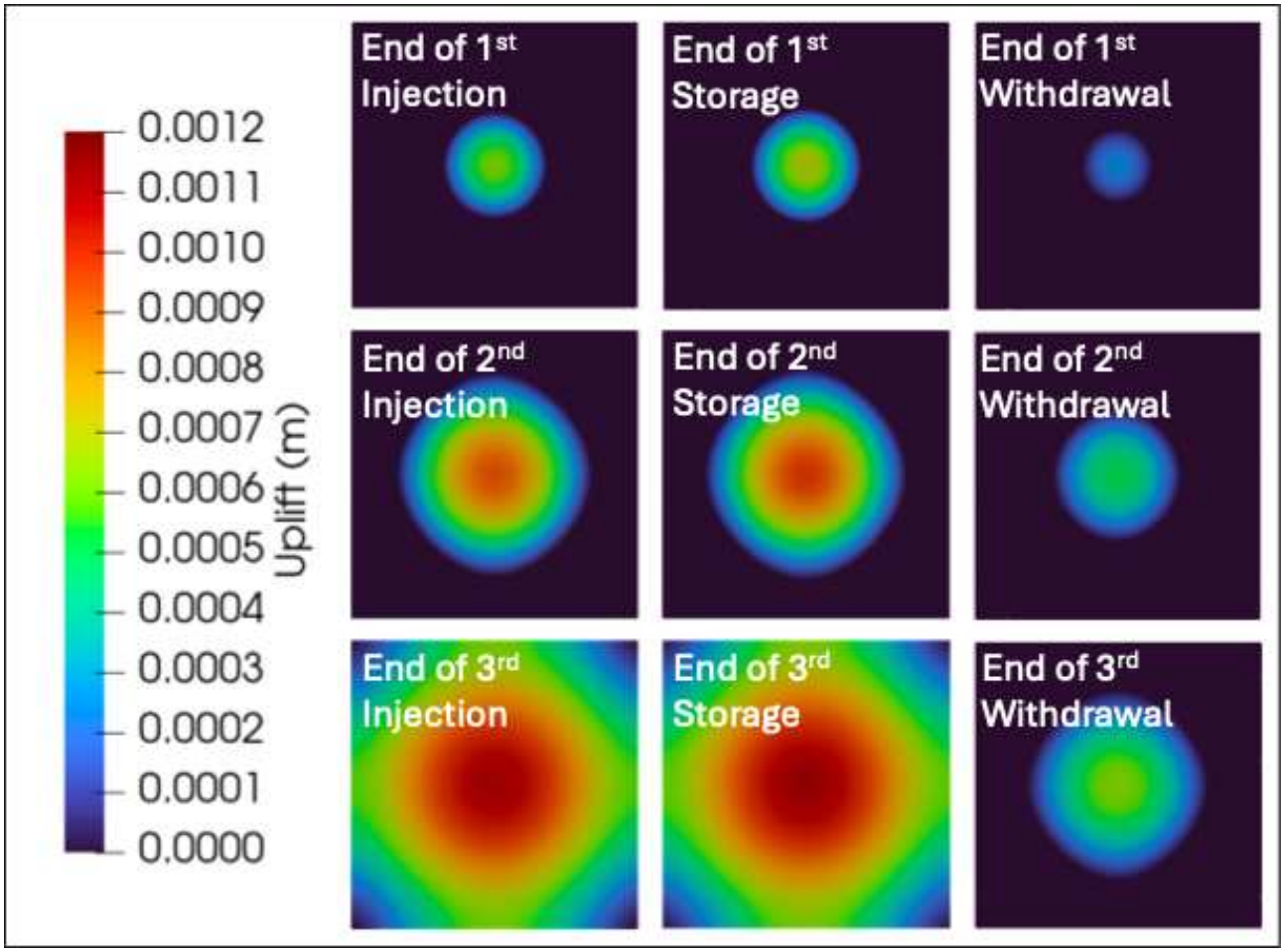


Figure 5.10: The net uplift across the base case model surface at selected key times.

During the withdrawal periods, the fluid pressure in the reservoir decreases and the effective stress increases, causing the reservoir to compact and thus leading to subsidence at surface. Given that the injection rate is 10 m^3/s and the withdrawal rate is 8.5 m^3/s, it is logical that the surface does not return to its original displacement of zero, since some residual pressure from the injection remains in the reservoir. One might expect, since the withdrawal-injection rate ratio is 85%, that the ratio of the uplift during the injection/storage period to the subsidence during the withdrawal period would be approximately 85%. However, if we examine the second injection/storage period and the second withdrawal period in Figure 5.9b, the uplift and subsidence within those periods is 0.63 mm and 0.45 mm respectively, which yields an uplift-subsidence ratio of just 71%. During withdrawal, the pore pressure decreases, which re-

duces the expansive reservoir stresses from the earlier injection and might be expected to cause a 'mirror-image' stress reversal. However, this reversal is incomplete because the withdrawal rate is lower than the injection rate (85%), and thus pressure reduction propagates more slowly through the reservoir. This creates pressure gradients between the central region (near the well) and the outer edges, leaving outer parts of the reservoir still under expanded stress conditions that act to give some upward (expansive) stress component at the centre of the reservoir, reducing the net compressive downward stress components directly associated with the pressure reduction at the well.

5.6.2 Injection Rate

Figure 5.11 shows that as injection rate increases, the uplift increases. This is obvious given that the more pressurized the reservoir becomes, the greater the reduction in effective stress and the greater the expansion of the reservoir, which manifests itself as greater surface uplift. The maximal uplift in the 0.01, 1, 10 and 40 m^3/s cases was 0.0013 mm, 0.12 mm, 1.21 mm and 4.84 mm, respectively. Therefore, the surface uplift linearly increased with increased injection rate. The injection rate increases the reservoir pressure in a predictable manner. Darcy's law informs us that for a given reservoir geometry, permeability and fluid viscosity, the pressure increase is proportional to the injection rate. Surface uplift is primarily caused by induced volumetric strain resultant from pressure changes in the reservoir rock. Since the deformation is proportional to the change in pressure in an elastic regime, surface uplift is also proportional to the injection rate. Zhang et al. [2018] performed three-dimensional, fully-coupled, thermohydromechanical simulations of CO_2 injection into a model of the In Salah Aquifer and also found that the surface uplift was directly proportional with the injection rate.

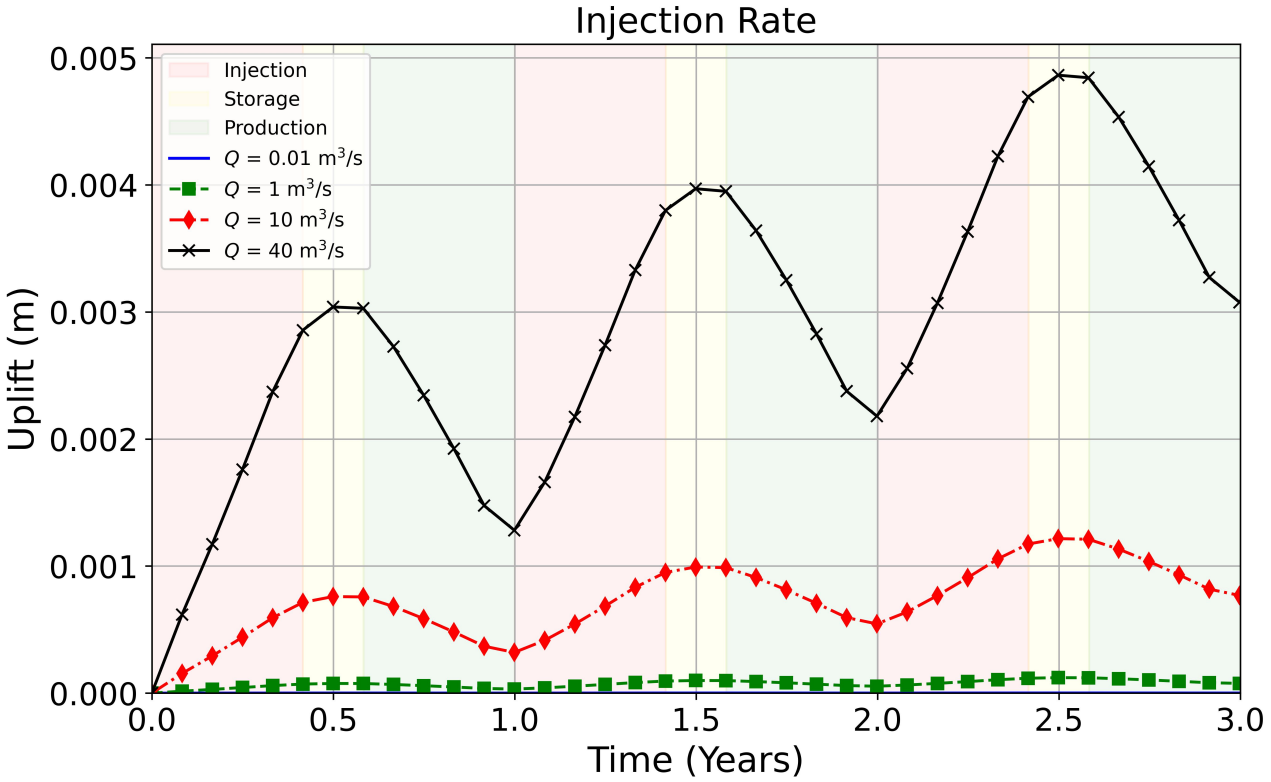


Figure 5.11: The net uplift versus time at the centre point on the surface for four cases of varying injection rate.

5.6.3 Young's Modulus

5.6.3.1 Reservoir

Four simulations are run in which the reservoir Young's modulus is varied between 5 and 60 GPa to determine the effect of reservoir Young's modulus on uplift and subsidence. Figure 5.12a shows the evolution of the uplift at the surface center through time. It was found that as reservoir Young's modulus decreased, surface uplfit increased. This is because the softer reservoirs (lower Young's moduli) undergo significant volumetric expansion under the same injection pressure. This expansion translates into upward displacement of the overlying rock that propagates to surface in the form of uplift. For high reservoir Young's moduli in the range 40-60 GPa, there was no surface uplift. This is because the stiff reservoir resists deformation and absorbs the majoirty of the stress internally in the form of stored internal elastic energy. The little stress that is transferred to the caprock is so small that it decays to zero through the thousands of metres of rock that lie above before the surface is reached.

The increase in uplift as reservoir Young's modulus decreased is not linear with decreasing Young's modulus. The magnitude of uplift accelerates as Young's modulus decreases. This is shown in Figure 5.12a, where a 20 GPa decrease from 60 GPa to 40 GPa, yielded no additional uplift. A further 25 GPa decrease from the 40 GPa case to the 15 GPa case, yielded some minor additional uplift (a maximum of 1.21 mm). However, a further 10 GPa decrease from 15 GPa to 5 GPa, yielded a very significant additional uplift of up to 13 mm (over 10 times the change between the 40 and 15 GPa case). Therefore, it is clear that the smaller the reservoir Young's modulus, the more detrimental hydrogen storage could be to the risk of uplift.

The 5 GPa case yields far more net surface uplift relative to the larger Young's modulus cases for the following reason. Surface uplift is directly proportional to the Uniaxial Compaction Coefficient (C_m) in Geertsma's solutions. The Uniaxial Compaction Coefficient is inversely proportional to the Young's modulus of the reservoir rock. Therefore, according to the analytical solutions, the surface uplift would follow a $1/E$ shaped graph where E is the Young's modulus. In such a plot, as we move closer to the origin, the value on the y-axis would begin to increase rapidly, which reinforces the observed behaviour.

5.6.3.2 Caprock

Four simulations are run in which the caprock Young's modulus is varied between 2 and 43 GPa to determine the effect of caprock Young's modulus on uplift and subsidence. The same monotonous increasing trend in uplift with decreasing reservoir Young's modulus is not observed for decreasing caprock Young's modulus. In the caprock Young's modulus range of 15 GPa to 43 GPa, the opposite was found to be true, where surface uplift increased as caprock Young's modulus increased (Figure 5.12b). However, when the caprock Young's modulus was reduced to a very low value of just 2 GPa, the trend was broken, and the highest uplift was observed (Figure 5.12b). This lack of a systematic trend is explained by the fact that there are two different deformation mechanisms present at the lower (2 GPa) and higher (15-43 GPa) ends of the Young's moduli range tested.

At very low caprock Young's moduli such as 2 GPa, the caprock is very soft, and behaves in an

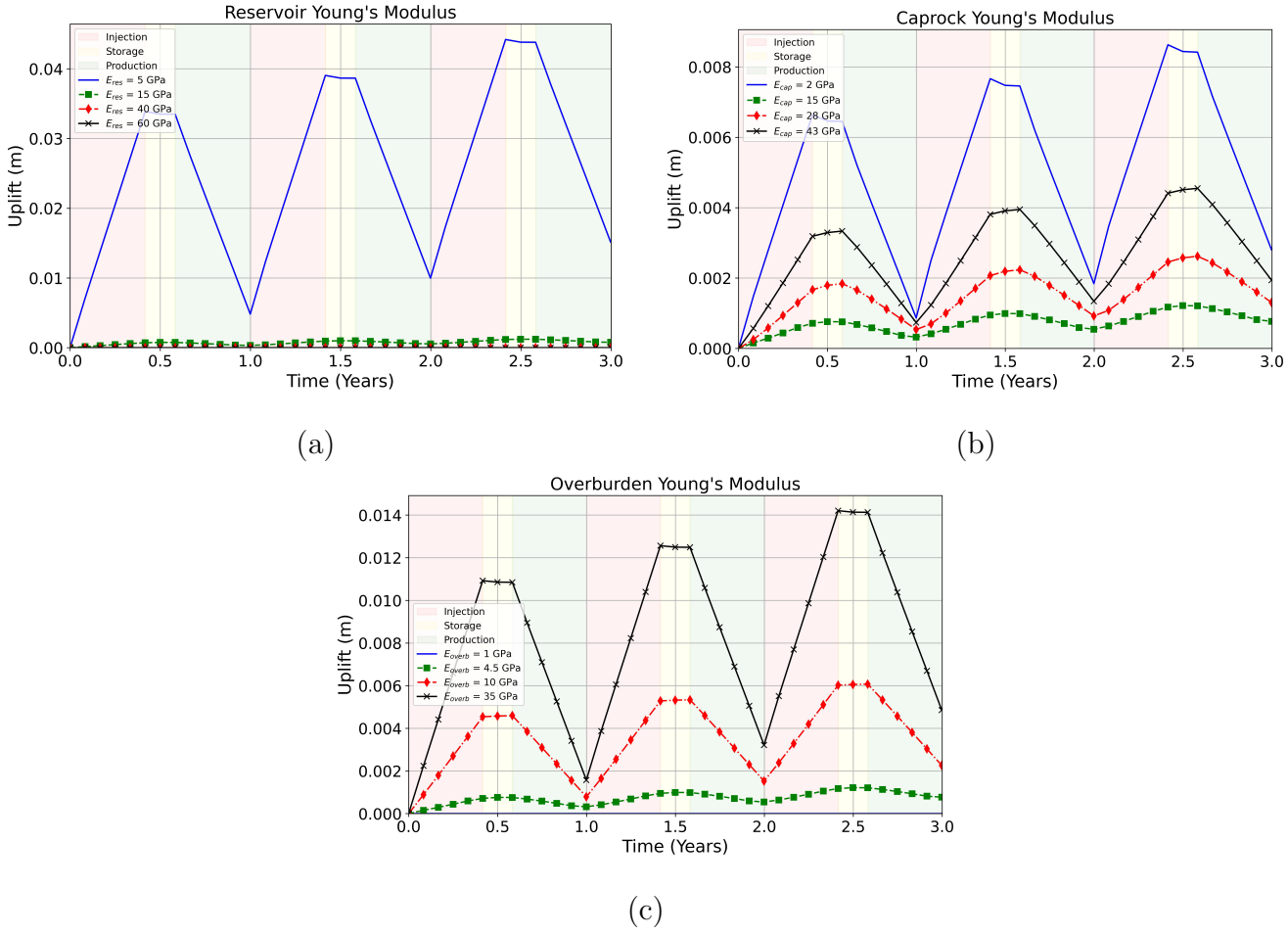


Figure 5.12: The net uplift versus time at the centre point on the surface for three cases of varying (a) reservoir, (b) caprock, and (c) overburden Young's modulus.

extremely flexible manner. Such flexibility allows it to deform with ease, concentrating almost all of the reservoir deformation directly upward. A total lack of lateral stress redistribution, which is provided with stiffer caprocks, allows a near maximal potential uplift to be achieved above the wellbore.

However, as the Young's modulus increased from 2 GPa to 15 GPa, a mechanical transition occurs in which the caprock transforms from being extremely flexible to more elastic. It now has some capability to resist the applied stress from the underlying reservoir. For such stiff caprocks in the range 15-43 GPa, the higher the Young's modulus, the more the caprock resists lateral deformation and the more stress that is transmitted vertically upward into the overburden and the more uplift that manifests at surface.

To visualize this consider the following analogy. The 2 GPa case is as if the reservoir is covered by a thin, very soft rubber sheet (like balloon material). When the sheet feels the upward expansion of the reservoir beneath, as it becomes pressurized during hydrogen injection, the sheet deforms very significantly in a localized manner directly above the point at which the force is applied (directly above the wellbore). The 15 GPa case is like having a moderately stiff, rubber sheet. When it feels the applied force of the reservoir expansion beneath, some vertical deformation occurs, but much of the applied stress gets redistributed laterally, leading to a more expansive deformation area. Thus, less stress is directed upward, leading to less uplift. For the 28 and 43 GPa cases, consider much stiffer plastic sheets overlying the reservoir. When these sheets feel the applied force from beneath, they do not deform easily. However, materials (especially rocks and sheets), tend to deform more easily in the direction of the applied force. Especially, given that the *in situ* vertical stress is less than the *in situ* horizontal stresses in this work, vertical deformation is energetically more favourable. Therefore, this stress has to go somewhere, and thus is forced upward and into the overburden. The 43 GPa case is stiffer than the 28 GPa case, so allows even less lateral deformation, transmitting more stress in the vertical direction leading to greater uplift.

5.6.3.3 Overburden

Four simulations are run in which the overburden Young's modulus is varied between 1 and 35 GPa to determine the effect of overburden Young's modulus on uplift and subsidence. Figure 5.12c shows that as overburden Young's modulus increased, the surface uplift at the surface centre increased. Higher Young's modulus, stiffer overburdens, are less able to deform laterally, which forces the deformation to concentrate and be transmitted efficiently in the vertical direction. Softer overburdens deform easily, spreading the stress from the reservoir and caprock beneath over a large overburden volume, leading to less vertical deformation reaching the surface as uplift. The 1 GPa overburden case was so soft that the overburden deformed internally to such a significant extent that none of the induced stress reached the surface and no vertical uplift was observed.

Another interesting phenomenon can be seen at the transition between the injection and storage periods in Figure 5.12c. For the 4.5 GPa case which is the base case, shown more clearly with the smaller y-axis scale in Figure 5.9b, the uplift continues to increase slightly during the storage period, after hydrogen injection has ceased. When the overburden Young's modulus is increased to 10 GPa, the uplift essentially plateaus once the injection ceases, and then when the Young's modulus is increased further to 35 GPa, the uplift begins to reduce slightly during the storage period after injection ceases. This shows that the mechanical deformation depends on overburden Young's modulus even after injection ceases. This transition from increased uplift to plateaued uplift to decreased uplift as overburden Young's modulus increased relates to the fact that stiffer overburdens are already significantly resisting deformation due to their greater rigidity even during injection. As soon as the applied stress from the increased pressure in the underlying reservoir begins to decrease, a more rigid material will elastically recover more quickly, which is why the high Young's modulus overburden case sees some subsidence as soon injection ceases. For the 4.5 GPa case, the stress is being redistributed throughout the overburden during injection such that it is not as easy for the rock to quickly return to its pre-stressed state.

5.6.4 Biot Coefficient

5.6.4.1 Reservoir

Four simulations are run in which the reservoir Biot coefficient is varied between 0.35 and 1.00 to determine the effect of reservoir Biot coefficient on uplift and subsidence. Figure 5.13a shows that as reservoir Biot coefficient increased, the net surface uplift at the surface centre increased. Given that the effective stress, σ', is given by $\sigma' = \sigma$ - αp where σ is the total stress, α is the Biot coefficient and p is the pore pressure, for a given pore pressure, the effective stress is lower for greater Biot coefficient. Lower effective stresses promote volumetric reservoir expansion which induces stress and strain changes in the caprock and overburden that propagate to the surface in the form of higher net uplift.

The reservoir Biot coefficient has a relatively large impact on the percentage change in uplift between the cases with the high reservoir Biot coefficient of 1.00 representing a 48% increase in uplift from the low reservoir Biot coefficient of 0.35. Nevertheless, the magnitudes of these net uplifts remain insignificant at 1.79 mm and 1.21 mm for the 1.00 and 0.35 cases respectively.

When the Biot coefficient is low at 0.35, the net uplift follows a smooth sinusoidal evolution with time, in which uplift occurs during the injection period, the uplift essentially plateaus during the storage period, and then the surface begins to subside instantaneously once withdrawal begins and the pressure is reduced at the wellbore. However, this smooth sinusoidal type behaviour disappears when the Biot coefficient increases to high values of 0.85 and 1.00. In these cases, the surface continues to uplift significantly during the storage periods, albeit at a reduced rate. In fact, the surface even continues to uplift for 2-3 months into the withdrawal period even though the pressure at the wellbore is decreasing. Then, delayed, the surface suddenly responds to the reducing pressure during withdrawal, subsiding a lot in a one month period. After this, the surface does not continue to subside much more despite the fact that the withdrawal continues. When the injeciton resumes, the surface takes a couple of months to show significant uplift, representing a delayed uplift response to the increasing pressure at the well.

The smooth sinusoidal behaviour of the net uplift with time and the fact that the uplift responds

almost instantaneously to a change in operational regime in the low Biot coefficient case, occurs because when the Biot coefficient is only 0.35, only 35% of the pore pressure contributes to altering the effective stress, which weakens the hydromechanical coupling. The rock skeleton is therefore less sensitive to changes in pore pressure, and so the reservoir responds more uniformly and predictably. The rock appears to be stiffer because the pore pressure changes have less effect on the rock skeleton. This stiffness causes the deformation to be more localized and immediate. For the higher reservoir Biot coefficient, delayed responses in the uplift-time curve are seen following a change in operational regime. In such cases, any change in pore pressure significantly impacts the deformation of the rock skeleton. This introduces time-dependent effects like uneven deformation due to pore pressure gradients across the reservoir. These cause slower, spatially distributed deformation that takes some time to propagate through the elastic rock framework. The strong coupling due to high Biot coefficient causes significant changes in the stress field, with stresses being redistributed across the reservoir. This redistribution takes time to equilibrate, slowing the overall response. For low Biot coefficient, the rock deformation is primarily governed by pore pressure diffusion. The mechanical response is therefore closely tied to how quickly pressure equilibrates. Whereas at high Biot coefficient, elastic deformation of the rock skeleton is more prominent and is influenced by pressure gradients, leading to delayed and spatially distributed responses.

For the 0.85 and 1.00 cases, the uplift continues during the storage and withdrawal periods despite no fluid being injected, and the pressure near the well either stabilizing (during storage) or reducing (during withdrawal). This is because the pressure gradients within the deeper reservoir still remain and the higher pressures at the outer regions continue to drive slow deformation due to the strong coupling. The ongoing expansive deformation then propagates inward through the elastic rock skeleton, causing the surface to continue uplifting slightly during storage, even with the reservoir pore pressure near the well decreasing. This inward propagation counteracts the subsidence that would normally occur near the well, causing the surface to continue uplifting slightly at the center (directly above the well).

In the high Biot coefficient cases, we then observe a sudden subsidence half-way through the withdrawal periods. As the withdrawal continues, the pressure gradients in the outer reservoir

begin to equilibrate and return to values closer to their original state. Eventually, this causes enough of a pressure reduction in the outer reservoir, that a critical threshold is exceeded in which the outer reservoir's ability to support the reservoir rock's expanded state diminishes. It can no longer resist compactive deformation. When this occurs, the reservoir compacts rapidly in response.

At late times in the withdrawal periods, after the sudden zone of subsidence, the subsidence is seen to slow dramaticallty. This is because after the compaction event in the reservoir, the pore space shrinks substantially. Now the grains are essentially packed more tightly, there is less space for the grains to move (compact further) or rearrange under additional stress reductions. The bulk stiffness of the rock has increased, allowing it to resist further compression more effectively.

When injection resumes after the first withdrawal cycle, the surface takes a couple of months to show significant uplift due to the pre-expanded state of the reservoir. Following on from the previous withdrawal period, the reservoir is left in a slightly expanded condition relative to its initial state, as the net fluid balance results in an increase in pore pressure and a slight volumetric expansion of the rock. The reservoir rock skeleton is now less responsive to the initial pressure increases during the second injection cycle. The pre-expansion provides resistance to further deformation, meaning that the same amount of pressure increase has a reduced effect on the reservoir's volume compared to the first injection cycle. Furthermore, the pressure redistribution within the reservoir is slower, as some reservoir regions retain lower pressures from the previous cycle, thus delaying uniform expansion. Consequently, surface uplift is minimal after the injection resumes as the reservoir takes time to fully respond to the increased pore pressure.

5.6.4.2 Caprock

Four simulations are run in which the caprock Biot coefficient is varied between 0.65 and 1.00 to determine the effect of caprock Biot coefficient on uplift and subsidence. Figure 5.13b shows that as caprock Biot coefficient increased, the net surface uplift at the surface centre increased.

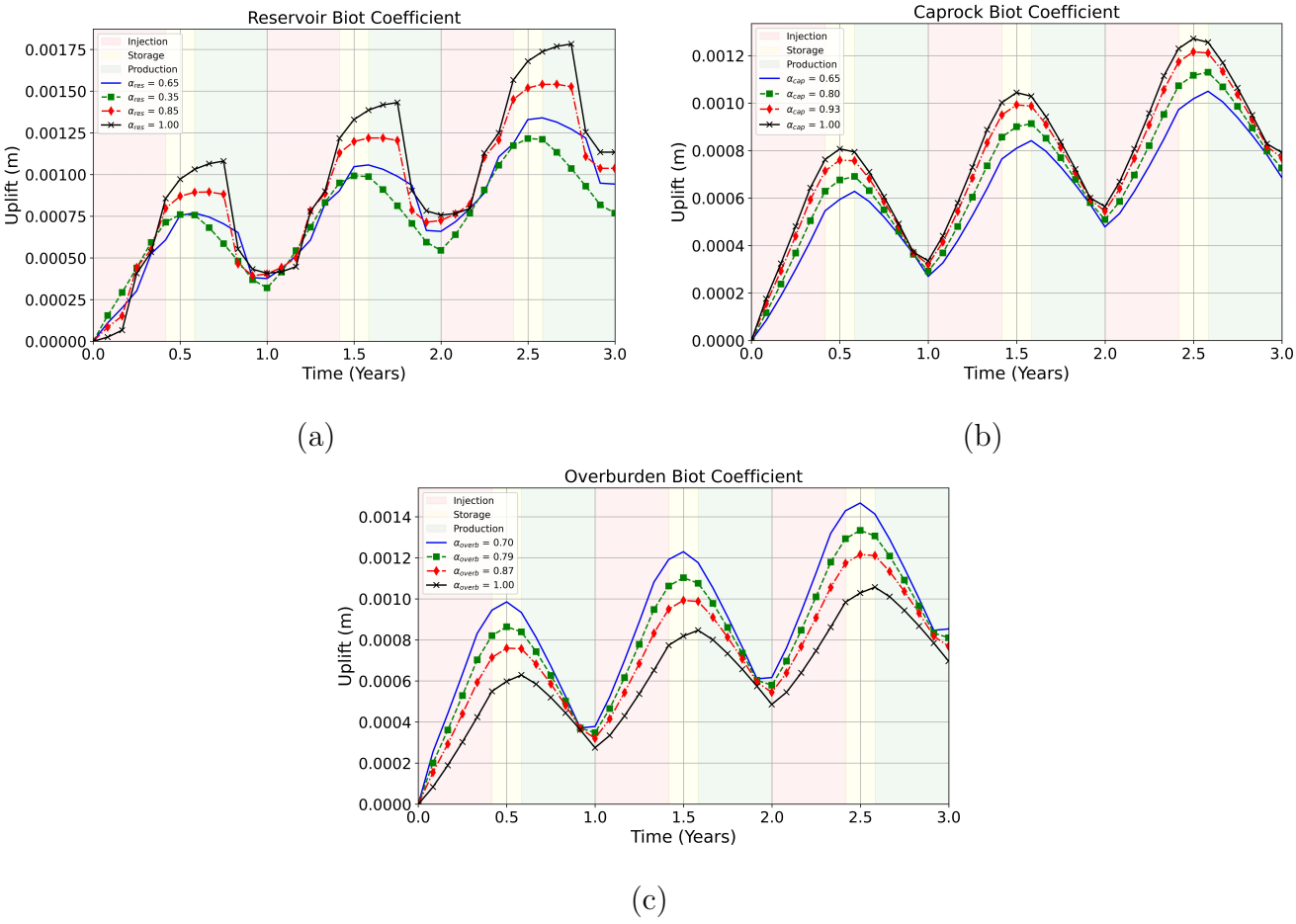


Figure 5.13: The net uplift versus time at the centre point on the surface for three cases of varying (a) reservoir, (b) caprock, and (c) overburden Biot coefficient.

The higher the Biot coefficient, the greater the effective stress reduction for a given pressure state, and since the permeability of the caprock is extremely low at 1 nD and does not allow hydrogen flow, the caprock brine pressure remains similar in all four cases. Therefore, the effective stress reduction enhances volumetric strains and expansion of the caprock when the Biot coefficient is higher, manifesting as larger surface uplift.

During the storage periods, a slgiht difference in the uplift response is observed between the four caprock Biot coefficient cases. When the Biot coefficient is low at 0.65, the surface uplift continues to increase substantially during the storage period despite no alteration in reservoir pressure. At 0.80, the surface uplift also continues to increase during the storage period but to a lesser extent. At 0.93, the degree of further surface expansion has decreased further such that the surface uplift has essentially plateaued during the storage period. Finally, at 1.0, the surface subsides a little during the course of the storage period. At low caprock Biot coefficients, the caprock is stiff and does not deform easily for a given reservoir pressure state. Therefore, the stress-induced from the reservoir pressure is not easily dissipated, keeping it concentrated within the reservoir and allowing the reservoir to continue to expand, resulting in increased surface uplift. At the high caprock Biot coefficients, the caprock can expand much more readily in response to the expansive stresses of the reservoir beneath. This dissipates the reservoir stresses throughout the caprock, lowering the expansive stress state in the reservoir, and in the 1.0 case, lowering it to such an extent to allow it to begin subsiding.

5.6.4.3 Overburden

Four simulations are run in which the overburden Biot coefficient is varied between 0.70 and 1.00 to determine the effect of overburden Biot coefficient on uplift and subsidence. Perhaps counterintuitively, Figure 5.13c shows that as overburden Biot coefficient increased, the net surface uplift at the surface centre decreased. When the overburden Biot coefficient is high, the overburden deforms more easily due to reduced effective stress. Therefore, when the reservoir unit expands during pressurization with hydrogen, the overburden deforms more easily than the lower overburden Biot coefficient cases. Due to its greater propensity to deform, it also

redistributes a greater proportion of the stresses throughout the overburden leading to a wider-scale deformation. A greater degree of lateral deformation occurs, meaning that there is a lower proportion of the stress transmitted from the reservoir and caprock below to contribute to vertical uplift above the well. For lower overburden Biot coefficients like 0.70, the overburden is stiffer and more resistant to deformation. Therefore, the stresses from the expanding reservoir below are less able to deform the overburden. As a result, the overburden doesn't easily relieve stress laterally, thus providing a greater share of the transmitted stress for vertical expansion, resulting in greater uplift at the surface.

5.6.5 Poisson's Ratio

5.6.5.1 Reservoir

Four simulations are run in which the reservoir Poisson's ratio is varied between 0.00 and 0.30 to determine the effect of reservoir Poisson's ratio on uplift and subsidence. Figure 5.14a shows that as reservoir Poisson's ratio increased, the net surface uplift at the surface centre increased.

When the reservoir is pressurized by the injected hydrogen it begins to expand. As it expands, it exerts lateral stresses on the caprock at the reservoir-caprock interface. The impermeable caprock does not have the high fluid pressure that the reservoir has. Therefore, there is no physical mechanism by which the caprock can easily expand laterally as it is confined by the compressive horizontal stresses that are larger than the vertical stress of the weight of the rock above. There is no means to counteract such stress and allow lateral expansion as in the reservoir. Therefore, the caprock resists this lateral stress from the reservoir, concentrating it vertically instead, causing the caprock to bulge upward.

When the reservoir Poisson's ratio is higher, the reservoir can expand more laterally in response to the increasing internal hydrogen fluid pressure. This generates larger lateral stresses at the caprock-reservoir interface that are transmitted into the caprock. As a result of the caprock's inabillity to deform laterally, it funnels this larger stress vertically upward, yielding larger surface uplift for higher reservoir Poisson's ratio. In the 0.00 case, the reservoir is per-

fectly incompressible in the lateral direction. The reservoir does not expand in the horizontal direction. All transmitted vertical strain is in the vertical direction. As a result, there is no bulging effect on the caprock resulting in less vertical uplift than the higher Poisson's ratio cases. Less stress is transmitted to the caprock in this case.

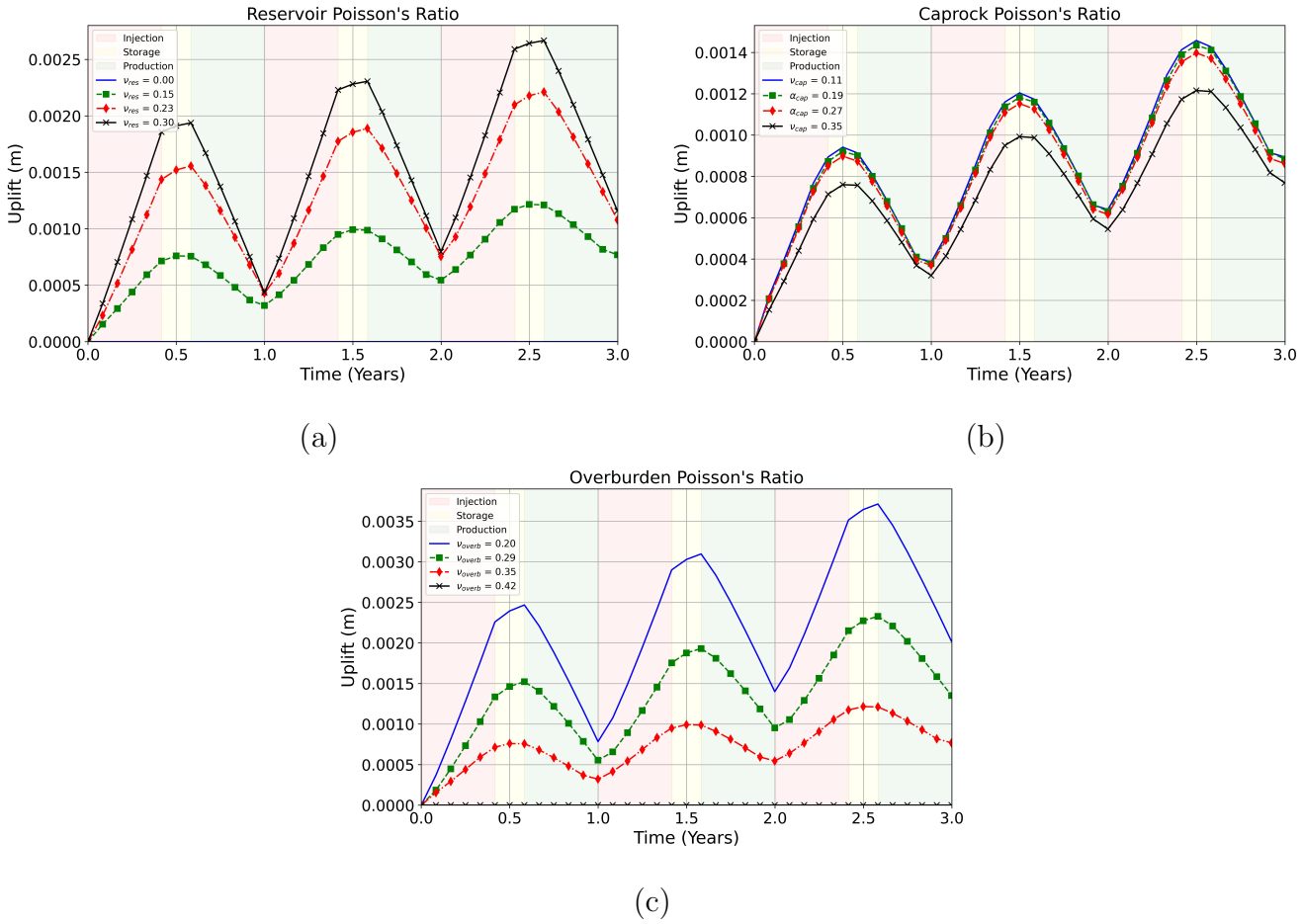


Figure 5.14: The net uplift versus time at the centre point on the surface for three cases of varying (a) reservoir, (b) caprock, and (c) overburden Poisson's ratio.

5.6.5.2 Caprock

Four simulations are run in which the caprock Poisson's ratio is varied between 0.11 and 0.35 to determine the effect of caprock Poisson's ratio on uplift and subsidence. Figure 5.14b shows that as caprock Poisson's ratio increased, the net surface uplift at the surface centre decreased.

A lower caprock Poisson's ratio means that for a given amount of the stress transmitted from the reservoir unit, the caprock can deform less in the lateral direction. Therefore, in the

lower caprock Poisson's ratio cases, the caprock resists lateral deformation and funnels the transmitted stress from the reservoir up vertically into the overburden, leading to elevated surface uplift. When the caprock Poisson's ratio is larger, slightly more lateral deformation can occur, which means a lower proportion of the transmitted stress from the reservoir is available to be transmitted further in the vertical direction to the overburden. Hence, the net surface uplift is less.

The difference in maximal surface uplift between the four cases for the caprock Poisson's ratio was 0.25 mm compared to a value of 2.64 mm for the reservoir Poisson's ratio cases. Therefore, the reservoir Poisson's ratio had a nearly 1000% larger influence on the surface uplift than the caprock Poisson's ratio. This reflects the discussion in Section 5.6.5.1. Since the *in situ* horizontal stress state is larger than the weight of the overlying overburden, the caprock is resistive to lateral deformation almost whatever the value of its Poisson's ratio. Therefore, there is little influence on the vertical surface uplift because the stress transmitted from the reservoir is essentially all transmitted upward anyway for the same expansive reservoir stress state, irrespective of the caprock Poisson's ratio.

5.6.5.3 Overburden

Four simulations are run in which the overburden Poisson's ratio is varied between 0.20 and 0.42 to determine the effect of overburden Poisson's ratio on uplift and subsidence. Figure 5.14c shows that as overburden Poisson's ratio increased, the net surface uplift at the surface centre decreased.

When the overburden Poisson's ratio is low, the overburden deforms more easily in the vertical direction, allowing for greater surface uplift. When the overburden Poisson's ratio is high, the overburden preferentially deforms in the horizontal direction rather than the vertical direction. Given the huge thickness of the overburden ($>$ 2000 m), the mechanical stress transmitted upward from the expanding reservoir is dissipated in the lateral direction, meaning little stress remains for vertical deformation. In fact, in the 0.42 overburden Poisson's ratio case, none of these transmitted mechanical stresses are transmitted vertically through the full thickness of

the overburden because they are fully absorbed through lateral deformation. As a result, no surface uplift occurs in this case.

5.6.6 Permeability

5.6.6.1 Reservoir

Four simulations are run in which the reservoir permeability is varied between 0.1 mD and 1500 mD to determine the effect of reservoir permeability on uplift and subsidence. Figure 5.15a shows that as reservoir permeability increased, the net surface uplift at the surface centre increased.

When the reservoir permeability is high, such as in the 1500 mD and 100 mD cases, the fluid rapidly flows through the reservoir during the injection periods, pressurizing the reservoir and initiating wide-scale expansive stresses that propagate through the caprock and overburden to surface in the form of uplift. For low reservoir permeabilities, the fluid takes far longer to flow away from the wellbore, and in a given period of time, the fluid will have propagated into a much smaller proportion of the reservoir. Therefore, the expansive stresses only develop over a small proportion of the reservoir and less stress is therefore transmitted to the overlying layers, resulting in less surface uplift.

The 1500 mD and 100 mD cases yield near-identical uplift-time curves. This is because the permeability is sufficiently high already at 100 mD to allow rapid fluid flow throughout the reservoir under the high injection pressure. In both cases, the reservoir experiences the maximum expansive stress that it can do given the pore pressure increase.

In the 0.1 mD case, no uplift or subsidence is observed. In this case, the reservoir permeability is so small that the hydrogen injectant remains much more concentrated around the wellbore, and thus, only a small proportion of the reservoir experiences expansive stresses. These stresses are insufficient to have not decayed out over the course of the 2400 m of rock that lies above the reservoir, before reaching the surface.

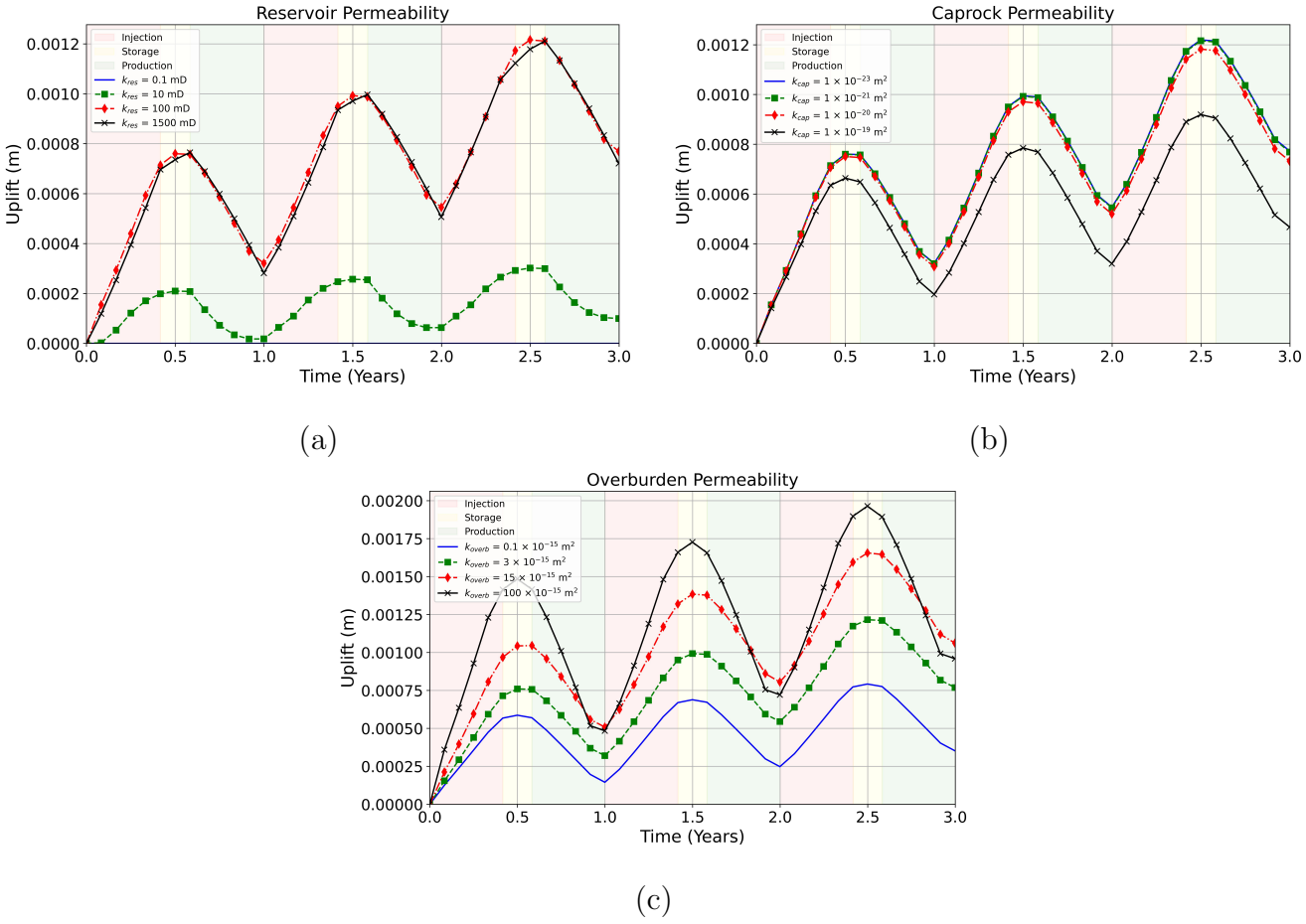


Figure 5.15: The net uplift versus time at the centre point on the surface for three cases of varying (a) reservoir, (b) caprock, and (c) overburden permeability.

5.6.6.2 Caprock

Four simulations are run in which the caprock permeability is varied between 1×10^{-23} m^2 and 1×10^{-19} m^2 to determine the effect of caprock permeability on uplift and subsidence. Figure 5.15b shows that as caprock permeability increased, the net surface uplift at the surface centre decreased.

When the caprock permeability was very low (i.e., the 1×10^{-23} m^2 and 1×10^{-21} m^2) cases, the net uplift-time curve was essentially identical. In these cases, the caprock is impermeable to the flow of hydrogen from the underlying reservoir. Therefore, pore pressure changes in the reservoir remain constrained within the reservoir unit. The expansive stresses in the reservoir remain high and these get transmitted into the caprock and overburden resulting in high vertical uplift at the surface. Since in both these cases the caprock allows zero hydrogen penetration, the reservoir pressure is the same in both cases, and thus, the magnitude of the expansive stresses are the same, leading to identical uplift profiles. When the permeability of the caprock is increased from 1×10^{-21} m^2 to 1×10^{-20} m^2, the caprock allows a very small amount of hydrogen to flow from the reservoir. Now, the retained reservoir pressure in this case is slightly lower than when the caprock has a lower permeability, and as a result, the expansive reservoir stresses are reduced. This leads to less stress transmitted vertically into the caprock and hence, less uplift at surface. When the caprock permeability is increased further to 1×10^{-19} m^2, the combination of high reservoir pressure due to the high injection rate and the relatively high caprock permeability is sufficient to allow appreciable drive for flow of hydrogen into the caprock. The retained reservoir pressure is now significantly less than the other cases and as a result the magnitude of the expansive reservoir stresses declines considerably. Therefore, there is less stress transmitted into the caprock and overburden and less surface uplift.

5.6.6.3 Overburden

Four simulations are run in which the overburden permeability is varied between 0.1×10^{-15} m^2 and 100×10^{-15} m^2 to determine the effect of overburden permeability on uplift and

subsidence. Figure 5.15c shows that as overburden permeability increased, the net surface uplift at the surface centre increased.

During injection, the effective stress in the reservoir reduces, and the reservoir begins to expand. As the reservoir expands, it exerts upward mechanical stresses on the thin caprock which transmit through to the overburden. These upward stresses push against the overburden, leading to both deformation in the form of some upward bulging but also causing compression in the vertical direction beneath the overburden. When the overburden is compressed from beneath, its porosity decreases. Given that the pores of the overburden contain incompressible brine, the reduction in pore volume increases the pore pressure. This is a poroelastic effect in which changes in mechanical stress directly affect pore pressure. In the lower permeability cases (i.e., 0.1×10^{-15} m^2), the elevated pore pressure remains more localized because the pressure front cannot propagate quickly. However, for higher overburden permeabilities (i.e., 100×10^{-15} m^2), the fluid redistributes much more freely, spreading the elevated pressure over a larger area. This makes it easier for the overburden to deform uniformly and results in more efficient transmission of the reservoir's expansive forces to the surface, resulting in greater uplift. A larger area of elevated overburden pressure, generates greater bulging stresses at surface.

5.7 Discussion

In the base case, the results show that for a reservoir of similar thickness, areal extent and depth, even at very high injection rates, the surface is not prone to significant changes in elevation during the underground storage of gaseous hydrogen. A maximum surface uplift of 1.21 millimeters over three years is generally considered negligible and is unlikely to pose significant risks to buildings or infrastructure. For context, in geotechnical engineering of structures such as foundations, buildings, roads, and pavements, the general guideline for the maximum threshold on differential settlement varies between 1/500 and 1/1000 [Burgess, 2019, LABC Warranty, 2021] and it is 1/750 for surface machinery/equipment [Wahls, 1981]. This means that the vertical surface displacement between two points cannot be any larger than 1/500th,

1/750th or 1/1000th of the distance between those two points or cracking and structural failure can occur. For example, a 5 m wide house, cannot have more than 5 mm difference in vertical elevation beneath it or the structure will collapse. Our maximal surface uplift at the centre of 1.21 mm is the equivalent of saying that the difference in uplift between any two points across the entire field length of 4000 m (2000 m either side of the centre point) does not exceed 1.21 mm (Figure 5.10). Therefore, the differential uplift never exceeds values on the order of 5 mm over very short distances of just a few m.

When the injection rate is increased to 40 m^3/s, at the absolute upper limit of the volumes of hydrogen per unit time that may need to be injected, the maximal uplift was 4.84 mm (see Section 5.6.2). Even at such a high injection rate, the uplift still remains below this general 5 mm differential settlement limit and this 4.84 mm variance in uplift occurs laterally over hundreds of metres, not the 5 metre distance it would need to occur over to induce damage. Therefore, even at extremely high injection rates, the uplift is not likely to pose significant risk to surface infrastructure and equipment. However, this degree of subsidence may or may not have subsurface risks such as initiating or exacerbating seismicity, which should be investigated in the future.

The Young's modulus results highlight some cases in which surface uplift could pose risks to surface equipment and infrastrucutre. When the Young's modulus of the reservoir rock is very low, such as 5 GPa, 44.30 mm of uplift was observed after three years of operation. The combination of high injection rate and easily deformable rock in direct contact with the injection plume resulted in huge surface uplift. Therefore, storage of hydrogen in low Young's moduli reservoirs should be avoided, especially if large rates are required. High Young's modulus overburdens (> 35 GPa) and low Young's modulus caprocks (< 2 GPa) also exacerbate surface uplift, although do not result in overly problematic uplift magnitudes. Nevertheless, care should be taken in storing hydrogen in such reservoirs as the uplift could become more problematic after many years (beyond the three years examined here).

For a host of reservoir, caprock and overburden Biot coefficients between 0.35 and 1, a significant variation in surface uplift, even at very high injection rates, was not observed. In the caprock,

overburden and reservoir cases, the variation in maximal uplift after three years was only 0.24 mm, 0.44 mm and 0.58 mm, respectively. Therefore, the Biot coefficient of the rock units does not have a significance influence on surface uplift magnitudes, when compared to other properties such as the Young's modulus.

The caprock Poisson's ratio had an insignifcant impact on surface uplift. However, the reservoir and overburden Poisson's ratio had a 956% and 1388% larger impact on the net surface uplift than the caprock Poisson's ratio, respectively, showing the uplift is much more sensitive to these properties. Despite this, the maximal uplift magnitudes after three years still remain well below 5 mm. Nevertheless, care should be taken in storing hydrogen in systems with high reservoir Poisson's ratio (i.e., > 0.30) and low overburden Poisson's ratio that have compressive *in situ* stress regimes, since for many more storage cycles (i.e., 20 years of storage), the uplift magnitudes could become problematic from a surface risk perspective, if they continue to follow a linear increase with time.

The reservoir permeability had a moderate influence on surface uplift. Low permeability reservoirs of less than 10 mD induced no more than 0.3 mm of net uplift after three annual cycles. Reservoir permeabilities of over 100 mD had no further effect on uplift beyond a maximal amount of 1.21 mm, which is still an unproblematic amount of ground elevation change. The caprock permeability had essentially no effect on the degree of net uplift in the typical caprock permeability range of 10^{-23} to 10^{-20} m^2, and only decreased by 0.25 mm when it was increased to 10^{-19} m^2. No matter the caprock or reservoir permeability, the uplift was never of high enough magnitude to be a worry to the structural integrity of surface equipment or infrastructure. Therefore, no limitations on reservoir or caprock permeability for uplift/subsidence-safe storage should be enforced. When the overburden permeabilitiy was altered between 0.1 mD and 100 mD, the 100 mD case yielded approximately 2 mm of net uplift after three years. Whilst this is an insignificant amount of uplift after three years, if the uplift was to continue following a linear trend with more injection-storage-withdrawal cycles, it could become problematic over longer time scales like 20 years. A clear trend was found in which higher overburden permeabilities increased the net surface uplift and so equally, if the overburden had higher permeability than that tested here (perhaps a partially unconsolidated sand of near 1 D permeability), then

it follows, that large uplift magnitudes may be expected. Therefore, hydrogen storage in fields with thick overburden sequences of high permeability (> 100 mD) should be demoted on a list of potential candidate storage fields if possible.

The results in this chapter assume elastic deformation of the reservoir, caprock, and overburden. Several physical mechanisms that may occur during operation that could influence subsidence and uplift dynamics have not been included. Plastic deformation, which may become significant if the stress state in the reservoir or surrounding formations exceeds the yield strength of the rock, is not included. For example, in the unlikely scenario of higher injection rates than the already high value of 10 m^3/s employed herein, or during prolonged storage over much larger time periods leading to cumulative stress buildup, plastic deformation could result in irreversible strain. This would manifest as permanent uplift at the surface or localized uplift/subsidence near the wellbore, diverging from the elastic predictions of fully reversible deformation predicted here.

Futhermore, fracturing and subsidence-induced fault reactivation are other potential processes not included in these simulations. Fractures may form in the reservoir or caprock, particularly if pre-existing faults or weak zones are present in the system or at high injection or withdrawal pressures. The likelihood of this also depends on the tensile strength of the rock. If fractures do indeed form, stress could be redistributed more heterogeneously, leading to localized areas of amplified uplift or subsidence, especially in the proximity of fracture clusters. The creation of high-permeability flow pathways due to fracturing could result in more rapid pressure diffusion throughout the reservoir, altering the spatial and temporal distribution of deformation by disrupting the formation of expansive reservoir stresses.

Geochemical rock-fluid interactions are not included in these simulations. For example, the precipitation of new minerals in the reservoir after hydrogen injection begins could alter the mechanical properties of the reservoir rock, such as Young's modulus or Biot coefficient. Reactions that reduce stiffness or increase permeability, such as mineral dissolution, may enhance the deformation that occurs in the reservoir during subsequent injection-storage-withdrawal cycles.

Under the geological and operational conditions considered, where injection rate is 10 m^3/s over moderate injection times of only months and where the reservoir is assumed to not contain pre-existing weaknesses, plastic deformation and fracturing are unlikely to dominate. However, if the injection rate was to significantly exceed this value, and much larger reservoir pressures ensued or if storage operations are continued over decades, such considerations may be critical. Incorporating these phenomena in additional future work would refine predictions and provide a more comprehensive understanding of deformation under extreme or long-term conditions.

5.8 Conclusions

In this chapter, three-dimensional, hydromechanical simulations of surface uplift and subsidence during injection, storage and withdrawal of gaseous hydrogen from an analogue depleted North sea gas field were performed. Prior to this, compaction within the rock model during fluid withdrawal and surface subsidence during fluid withdrawal was validated against Geertsma's 'nucleus of strain' and 'nucleus of stain with free surface' models, respectively. Subsequently, hydrogen storage was studied for a high injection rate of 10 m^3/s and withdrawal rate of 8.5 m^3/s over three years with each annum comprising of a 5-month injection period, 2-month storage period, and 5-month withdrawal period. Plastic deformation and fracturing was not included. All rock units were assumed to be linear-elastic. The key findings and conclusions include:

- For high injection rates such as 10 m^3/s, hydrogen should not be stored in reservoirs of very low Young's modulus (i.e., < 5 GPa). Maximal uplift was over 4.4 cm in just three years.
- Surface uplift and subsidence is not very sensitive to variation in Biot coefficient. In the caprock, overburden and reservoir cases, the variation in maximal uplift after three years was only 0.24 mm, 0.44 mm and 0.58 mm, respectively.
- The surface uplift linearly increased with increased injection rate.

- Net surface uplift increased as reservoir and caprock Young's modulus decreased. Uplift increased as overburden Young's modulus increased.
- Net surface uplift increased as reservoir and caprock Biot coefficient increased. Uplift increased as overburden Biot coefficient decreased.
- Net surface uplift increased as reservoir Poisson's ratio increased. Uplift increased as caprock and overburden Poisson's ratio decreased.
- Net surface uplift increased as reservoir and overbruden permeability increased. Uplift decreased as caprock permeability increased.

Chapter 6

Effect of Mechanical, Fluid, Operational and Fault Properties on Fault Slip and Induced Seismicity along Reservoir Faults during UHS

6.1 Introduction

Fault reactivation and induced seismicity can occur along faults for various reasons. Firstly, during injection procedures the pore pressure can increase significantly, which according to Terzaghi's effective stress principle [Skempton, 1960], results in reductions in effective stress. Normal effective stress reductions bring Mohr's circle closer to the Mohr-Coulomb failure line [Mohr, 1882, 1914], and thus induce fault slip. A lower effective normal stress means there is less frictional resistance holding the fault in place, making it easier for the fault to slip if it is already close to a critical stress state. Secondly, injection can lead to stress changes well beyond the spatial extent of the increased pore pressure front [Segall and Lu, 2015, Chang and Segall, 2016a]. Distal aureoles of elevated shear stress can develop which increase the likelihood of exceeding the fault shear strength, thus inducing fault slip [Chang and Segall, 2016b,a]. During

withdrawal, pore pressure can decrease, causing the reservoir unit to experience compaction, which can perturb the fault stress state, inducing slip [Haug et al., 2018]. Induced seismicity has been ubiquitous along reservoir faults across a number of geo-energy applications. For example, in natural gas production [Boitz et al., 2024], CO_2 storage [Vilarrasa et al., 2019], wastewater disposal [Grasso et al., 2021], geothermal injection and production [Zbinden et al., 2020], and hydraulic fracturing [Hui et al., 2021a]. However, relatively little is known about the factors which influence such induced seismicity beyond the simplistic effect of pore pressure increases.

Table 6.1 categorizes cases of induced seismicity along reservoir faults based on the geo-energy fluid injection or withdrawal technology in use. Seismicity along reservoir faults is often less than magnitude 3 and the highest recorded event was magnitude 4.5 in the case of hydraulic fracturing for shale oil at Fort St. John in Canada. The magnitude of induced seismic events varies across technologies, ranging from minor tremors with magnitudes of no more than 1.7 (i.e., in CO_2 storage cases) to more significant seismic events between magnitude 3.5 and 4.5, such as those associated with hydraulic fracturing for oil/gas production and geothermal reservoir permeability enhancement. This discrepancy is primarily associated with the difference in pressures involved. When purposely fracturing a formation to enhance reservoir permeability for improved oil production or geothermal injectivity/productivity, novel fractures are created under very high pressure injection providing more sites for microseismicity and large pressure changes that can promote destabilizion of existing faults. During CO_2 storage, fracturing of the formation is avoided since ideally permeability is kept low to minimize the flow and potential subsequent leakage of CO_2. Therefore, any seismicity that does occur must be along pre-existing faults if they are present and given the lower injection pressures, the reservoir pressure does not increase as rapidly and effective stress is not reduced to the same extent. Therefore, faults tend to be more stable in CO_2 storage cases. However, low magnitude seismicity in CO_2 storage does not necessarily imply low magnitude seismicity in hydrogen storage. Firstly, hydrogen can be up to 85 times less dense than CO_2, and therefore to achieve the storage masses necessary for large-scale hydrogen energy storage, huge volumes of hydrogen may need to be stored, thus invoking much larger reservoir pressure increases. Larger reservoir pressure

increases yield greater reductions in effective normal stress along faults bringing them closer to failure and thus increasing the potential for seismicity. Secondly, unlike CO_2 storage which only involves monotonous-directional changes in reservoir pressure, due to no requirement to later withdraw the CO_2, hydrogen storage additionally requires withdrawal which leads to cycling of the reservoir pressure over short periods of time. Table 6.1 demonstrates that large magnitude induced seismicity relating to compaction (i.e., Groningen) can occur when fluid is withdrawn in the case of natural gas or oil production, which could therefore also be a problem in UHS.

Therefore, in this chapter, the Imperial College Geomechanics Toolkit (ICGT) is used to examine fault slip and induced seismicity along a reservoir fault during hydrogen storage into a numerical model of a depleted gas field for a simulated time of three years. Parametric studies are conducted to assess the influence of mechanical properties (i.e., Young's moudulus, Poisson's ratio), fault properties (i.e., friction coefficient, fault permeability), operational properties (i.e., injection rate, withdrawal rate), fluid properties (i.e., density and compressibility) and stresses (i.e., homogeneous versus heterogeneous) on induced seismicity along faults in direct hydraulic communication with the storage reservoir.

6.2 Literature Review

Fluid mechanical, operational, and rock mechanical properties can all influence fault slip and induced seismicity during both the injection and withdrawal of a fluid. This section reviews previous studies from geo-energy fields examining the effects of varying mechanical properties on inferred fault slip, in particular Young's modulus, Poisson's ratio, Biot coefficient and matrix intrinsic permeability. A summary of some of the findings in this Section are provided in Table 6.2, which also summarizes findings of the effects of varying fluid mechanical (i.e., fluid viscosity, fluid compressibility, fluid density), operational (i.e., injection rate, withdrawal rate), fault (i.e., dip, length) and other mechanical (i.e., rock compressibility, *in situ* stresses) properties on induced fault slip and seismicity.

Table 6.1: Key cases of induced seismicity occurring along faults in direct hydraulic communication with the injection/production well from a variety of geo-energy technologies. [a]Kaven et al. [2015]; [b]Verdon et al. [2015]; [c]Gan and Frohlich [2013]; [d]Brown et al. [2004]; [e]Verdon [2016]; [f]Paap et al. [2014]; [g]White et al. [2017]; [h]White et al. [2014a]; [i]Rodríguez-Pradilla and Verdon [2024]; [j]Clarke et al. [2014]; [k]Esmaeilzadeh and Eaton [2021]; [l]Farahbod et al. [2015]; [m]Fasola et al. [2019]; [o]Cheng et al. [2023]; [p]Majer and Peterson [2007]; [q]Zhou et al. [2022]; [r]Baisch et al. [2010]; [s]Hjörleifsdóttir et al. [2020]; [t]Baisch et al. [2006]; [u]Flóvenz et al. [2015]; [v]Urban and Lermo [2013]; [w]Richter et al. [2020]; [x]Rutledge et al. [1994].

Location	Earthquake Magnitudes	Causes & Notes
CO_2 Storage		
Decatur, Illinois, U.S.[a]	-1.13 to 0.95	535,000 sm^3/day CO_2 injected into high k, high ϕ 460m-thick Mount Simon Sandstone Aquifer.
In Salah, Central Sahara, Algeria[b]	< 1.7	CO_2 injected into Krechba gas reservoir water-leg at up to 1.4 million sm^3/day. 20 m-thick sandstone reservoir with k = 10 mD and 13-20% ϕ.
Ketzin, Brandenburg, Germany [f]	-2.5 to 0.5	Injected at average rate of 19.7 sm^3/day into 80 m-thick Stuttgart formation that contains interbedded high k channel sandstones and low k flood-plain mudstones.
Aquistore, Saskatchewan, Canada[g,h]	< -1	214,000-321,000 sm^3/day injected into Winnipeg/Deadwood formation sandstone aquifer. No faults present.
Enhanced Oil Recovery (EOR)		
Cogdell Oil Field, Texas, U.S. [c,d]	< 4.4	2.8 million sm^3/day injection into carbonate platform reservoir. High lateral/vertical heterogeneity, fractures, solution-enlarged fractures and caverns are common.
Weyburn Oil Field, Saskatchewan, Canada[e]	-3.5 to -0.5	CO_2 injected at 80 to 460 m^3/day into the Midale carbonate containing a marly layer and a vuggy layer.
Aneth Oil Field, Utah, U.S. [o]	-1.2 to 0.8	3800 events occurring along two reservoir faults during CO_2-EOR. Distant M3.7 could be due to the stress perturbation from the CO_2 plume.
Hydraulic Fracturing Improved Oil Recovery (IOR)		
Fylde Peninsula, Lancashire, U.K.[i,j]	< 2.9	Vertical, multiple stage hydraulic fracturing operation in 1000 m-thick Bowland shale. Seismicity along fault hundreds of metres below injection point.
Fort St. John, British Columbia, Canada[k]	2.6 to 4.5	Hydraulic fracturing operation in the Montney Septimus shale field. Mainshock due to reactivation of normal fault. Lateral variation in pore pressure exacerbate seismicity.
Horn River Basin, British Columbia, Canada [l]	1.1 to 3.7	Magnitude never exceeded 3 when inj. rate was less than 650 m^3/day. The largest events required inj. rate of over 5000 m^3/day. Seismicity simultaneous to months after inj.
Eagle Ford Shale, Texas, U.S. [m]	0-4	Normal slip parallel to the minimum horizontal *in situ* stress. Stepped variation in injection rate correlated with seismicity rate.
Sichuan Basin, China [n]	< 1.5	Hydraulic fracturing (HF) operation in the Wufeng-Longmaxi shale formation. Average injection rate was 14 m^3/min. 5 day delay between onset of HF and first event.
Geothermal		
The Geysers Geothermal Field, California, U.S. [p]	< 3	Injection-induced 'clouds' of earthquakes extend primarily downward from injection wells. Cloud appears shortly after injection begins. Larger magnitude 4 events occur but not correlated with injection scheme.
Deep Heat Mining Project, Basel, Switzerland [q]	< 3.4	21-day hydraulic stimulation of granitic reservoir in the southern Rhine Graben led to seismicity of M2.6 within 6 days. Multiple post-shutdown events of > M3.
Soultz-sous-Forets, France [r]	-2 to 2.9	Shear dilation stimulation at rates of 0.03-0.05 m^3/s in a highly-fractured granite resulted in 114,000 induced events primarily along a pre-existing large fault. The large M2.9 occurred after shut-in.
Husmuli, Iceland [s]	< 4	Re-injection of geothermal brine caused an immediate increase in seismicity rate, culminating in two large events after several weeks. Associated uplift of 2 cm during this time. Wells located in highly fractured fissure swarm of Hengill volcano.
Cooper Basin, Moomba, Australia[t]	< 3.7	27,000 events during the hydraulic stimulation of a granite at rates of over 0.04 m^3/s. The large events often occured after the cessation of hydraulic treatment.
Krafla, Iceland	< 2 2.2 [u]	Injection rate of 0.04-0.06 m^3 resulted in almost immediate seismicity. Rising earthquake pattern delineates a fault along which magma has heated the injectant causing it to rise. Seismicity mainly in permeable zones.
Los Humeros Geothermal Field, Mexico [v]	< 3.2	Production-related seismicity due to unexpected very-high permeability path resulting in higher than expected production rates. Layered igneous system inc. ignimbrites, basalts, andesites and tuffs.
Natural Gas/Oil Production		
Groningen, Netherlands [w]	< 3.6	First event recorded was M2.4 in 1991, 30 years after initial gas production from Rotliegend sandstone. Magnitude of events consistently increased through time culminating in M3.6 (res. compaction) in 2012, whereafter production was greatly limited.
Ekofisk, North Sea, Norway [x]	-6 to 0	Oil production from the Ekofisk and Tor naturally-fractured chalk formations. Fm has very high ϕ of 32%. Seismicity is due to shear-failure.

6.2.1 Mechanical Properties

6.2.1.1 Poisson's ratio

Zbinden et al. [2017] demonstrated that for the same production rate, for a given value of Young's modulus, as Poisson's ratio was reduced, the likeliness of intersecting the Mohr-Coulomb failure line increased owing to the fact that at smaller Poisson's ratios, the differential stress is becoming larger. Therefore, Poisson's ratio is likely to be an important parameter in controlling production-induced earthquakes. Meng et al. [2020] implemented a 2D 500 $\times$ 500 m plane-strain hydraulic fracturing model containing a 50 m length natural fracture at 45° to the water injection wellbore. They varied the Poisson's ratio between 0.1 and 0.3 and found that as the Poisson's ratio decreases, the fracture slip increases for a given value of the Young's modulus. However, the difference in slip was on the sub-centimetre scale. At high Young's modulii of greater than 30 GPa, the difference in slip was a maximum of only 2 mm between Poisson's ratios of 0.1 and 0.3. The difference in slip between the Poisson's ratio cases increased as Young's modulus decreased, with a maximal difference in slip of approximately only 12 mm between Poisson's ratios of 0.1 and 0.3 at a Young's modulus of 5 GPa. Essentially, the fault slip was insensitive to the tested range of Poisson's ratio. Therefore, it is implied that during fluid injection Poisson's ratio may not have a significant effect on fault slip.

6.2.1.2 Young's modulus

Meng et al. [2020] varied the Young's modulus of the rock during water injection for hydraulic fracturing and assessed the slip along the fault in their model, which the borehole intersects. They found a very strong dependence of slip on Young's modulus, which was varied between 5 and 50 GPa. The slip was shown to decrease as Young's modulus increased, with approximately 120 mm difference in slip between the Young's moduli cases of 5 and 50 GPa. For Young's modulii $>$ 30 GPa, the difference in slip is negligible ($<$ 7.5 mm), but Young's modulus appears to be an important parameter affecting fault slip when it takes a value of $<$ 30 GPa. Hui et al. [2021b] performed a sensitivity analysis on fault slip under varying mechanical and operational

properties within a 4000 × 4500 × 500 m four-layer hydraulic fracturing model containing a single fault that is penetrated by two horizontal wellbores. The four layers were constructed to be representative of the Durvenay, Swan Hills, Cambrian and Precambrian formations within the Duvernay East Shale basin which had previously experienced a local magnitude 4.18 induced earthquake from hydraulic fracturing. They did not quantify the slip but instead measured the change in the Coulomb failure stress (CFS) between the cases. They varied the Young's modulus between 2.17 and 6.52 GPa and found that as Young's modulus increased, the change in CFS decreased, implying that the likelihood of seismicity decreases as Young's modulus increases, which is consistent with results reported by Meng et al. [2020]. However, the difference in the change in CFS between the cases was small at only 0.5 MPa between the 2.17 and 6.52 GPa cases. The sensitivity analysis ranked Young's modulus as a much less important factor on fault slip than the distance between the fault and hydraulic fractures, the permeability of the fault and the injection rate, but slightly more important than the reservoir permeability and the Biot coefficient.

6.2.1.3 Biot coefficient

Fan et al. [2019] conducted three dimensional finite element simulations in ABAQUS to assess seismic fault reactivation along a 20 m width fault within a crystalline basement unit when injecting wastewater into an overlying sedimentary reservoir. They varied the Biot coefficient in two separate cases: $\alpha = 0.79$ and $\alpha = 0.44$, and assessed the impact on the CFS. They found that a decrease in the reservoir Biot coefficient caused a decreased induced normal stress and thus an increase in induced CFS, meaning that as reservoir Biot coefficient decreases, the probability of slip increases. In the hydraulic fracturing work of Hui et al. [2021b], in the model resembling the Duvernay East Shale Basin, they varied the Biot coefficient between 0.22 and 0.66 and also found that as Biot coefficient decreases the change in CFS increases slightly, thus concluding again that as Biot coefficient decreases the probability of slip increases. They also concluded that in a sensitivity analysis of the fault-hydraulic fracture separation, the fault permeability, the injection rate, the Young's modulus, the reservoir permeability and the Biot coefficient that the Biot coefficient has the least impact on CFS and thus the least impact on

slip of that parameter list. However, poroelastic stress perturbations have been recognised as a mechanism by which seismicity can be induced [Chang and Segall, 2016b, Segall and Lu, 2015]. Changes in pore pressure generate poroelastic stresses which alter the total stress state of the reservoir and the surrounding lithological units, potentially inducing slip. While pore pressure diffusion resulting in effective normal stress reduction is the dominant mechanism for inducing slip in conductive faults within the reservoir or in conductive faults that are hydraulically connected to the reservoir, poroelastic stresses dominate slip on low permeability faults within the basement unit. As such, poroelasticity can be a key mechanism for driving slip at further distances from the injection point beyond the region of elevated pore pressure. As such, it is remarkable that Hui et al. [2021b] deemed the Biot coefficient a largely insignificant parameter for governing the change in CFS and thus the likeliness of slip. No study appears to have directly assessed the impact of Biot coefficient on the fault slip, and it is important that any numerical method used to investigate induced seismicity has poroelastic coupling in which the pore pressure changes induce changes in stress and changes in stress induce changes in pore pressure.

6.2.1.4 Intrinsic permeability and porosity

Mortezaei and Vahedifard [2015] conducted numerical 2D single-phase CO_2 injection experiments in a domain containing a 1 km length fault, in which the permeability of the reservoir unit was varied between 10^{-12} and 10^{-14} m^2. They found that the fault slip was largest in the low permeability case, owing to greater pore pressure build-up, but also found that the time to rupture was larger. Mortezaei and Vahedifard [2015] also varied the reservoir porosity between 0.10 and 0.20 and found that slip was identical regardless of porosity.

Table 6.2: Summary of the Literature Review. The 'Effect on Slip/Seismicity' column refers to the subsequent effect on slip/seismicity as that parameter increases in value.[a]Meng et al. [2020], [b]Hui et al. [2021b],[c]Zbinden et al. [2017], [d]Dal Zilio et al. [2022], [e]Fan et al. [2019], [f]Mortezaei and Vahedifard [2015], [g]Alghannam and Juanes [2020], [h]Ji et al. [2022b], [i]Nepveu et al. [2016], [j]Sijacic et al. [2017], [k]Deng et al. [2021], [l]Chang and Segall [2016b], [m]Mazzoldi et al. [2012], [n]Anyim and Gan [2020], [o]Rutqvist et al. [2013]

.

Property	Numerical Method	Geo-energy Type	Method	Cases	Fault Loc.	Mode	Effect on Slip
Mechanical							
Young's Modulus	2D Coupled HM FEM[a], 3D Coupled HM FEM[b]	Hydraulic Fracturing[a,b]	Fault Slip[a], CFS[b]	5-50 GPa[a], 2-7 GPa[b]	Res[a,b]	Inj[a,b]	Decreases[a,b]
Poisson's Ratio	2D Coupled HM FEM[c,a]	Natural Gas Production[c], Hydraulic Fracturing[a]	Mohr-Coulomb[c], Fault Slip[a]	0.10-0.25[c], 0.10-0.30[a]	Res[c,a]	Prod[c], Inj[a]	Decreases[c], Insensitive[a]
Rock Compressibility	2D Coupled HM FEM[d]	Fluid Injection[d]	Qualitative Seismicity Type[d]	10^{-11}-10^{-10} Pa^{-1}[d]	Res[d]	Inj[d]	Insensitive[d]
Biot Coefficient	3D Coupled HM FEM[e,b]	Wastewater[e], Hydraulic Fracturing[b]	CFS[e,b]	0.44 and 0.79[e], 0.22-0.66[b]	Base[e], Res[b]	Inj[e,b]	Decreases slightly[e,b]
Permeability[f]	2D Coupled THM FEM[f]	CO_2 Storage[f]	Fault Slip[f]	10^{-12}-10^{-14} m^3/s[f]	Res[f]	Inj[f]	Time to failure decreases[f]
Porosity	2D Coupled THM FEM[f]	CO_2 Storage[f]	Fault Slip[f]	0.10-0.20[f]	Res[f]	Inj[f]	Insensitive[f]
Hydraulic							
Fluid Compressibility	2D Coupled HM FEM[d]	Fluid Inj[d]	Qualitative Seismicity Type[d]	10^{-11}-10^{-7} Pa^{-1}[d]	Res[d]	Inj[d]	Decreases[d]
Inj Rate	2D Spring-Slider[g], Cyl Granite Samples[h]	Fluid Injection[g,h]	Critical Stiffness Analysis[g], Strain Gauge/AE Hypocenter Analysis[h]	0.25-1.0[g], 0.2-0.8 mL/min[h]	Res[g,h]	Inj[g,h]	Increases[g,h]
Production Rate	2D Coupled HM FEM[c], Bayesian Change Point[i,j]	Natural Gas Production[c,i,j]	Fault Slip[c], Statistical Analysis[i,j]	2.5-10 m^3/s[c]	Res[c]	Prod[c,i,j]	Insensitive[c], Increases[i,j]
Fault							
Friction Coefficient	2D Coupled HM FEM[k,l]	Hydraulic Fracturing[k], Water Inj[l]	Fault Slip[k], Poroelastic Stress Change[l]	0.20-0.60[k], 0.10-0.75[l]	Res[k], Base[l]	Inj[k,l]	Insensitive[k], Decreases[l]
Fault Permeability	2D Coupled THM FEM[m], 3D Coupled THM FEM[n]	CO_2 Storage[m], Geothermal[n]	Fault Slip[m,n]	10^{-15}-10^{-17} m^3/s[m], 10^{-12}-10^{-16} m^3/s[n]	Res[m,n]	Inj[m,n]	Insensitive - time to failure increases[m], Generally decreases[n]
Fault Length	2D Coupled HM FEM[a]	Hydraulic Fracturing[a]	Fault Slip[a]	10-100 m[a]	Res[a]	Inj[a]	Increases[a]
Stress							
σ_H/σ_V	2D Coupled THM FEM[m],	CO_2 Storage[m], Hydraulic Fracturing[o]	Fault Slip[m,o]	0.65-0.70[m], 0.50-0.55[o]	Res[m,o]	Inj[m,o]	Decreases[m,o]

6.2.2 Fault Properties

6.2.2.1 Friction Coefficient

The friction coefficient is a parameter that represents the ratio of the frictional force between two fault faces to the normal force pressing them together. It quantifies the amount of resistance encountered when one fault face attempts to, and does, move against the other.

In the 2-D plane-strain Abaqus Finite Element Method (FEM) hydraulic fracturing simulations of Deng et al. [2021], containing two pre-defined faults F1 and F2 and a pre-defined hydraulic fracturing path, they varied the friction coefficient, μ, of the two faults to observe the influence of μ on the slip on F1 and F2. They found that friction coefficients between 0.2 and 0.6 had a strong effect on fault slip with a maximum of 0.18 mm and 0.29 mm difference in slip between the cases for faults F1 and F2 respectively. This represents a relative change of 13.1% and 35.4% between the 0.2 and 0.6 cases for the two faults. Whilst the change in slip was small in absolute magnitude, the results did indicate a clear trend that as friction coefficient increases so does the fault slip. The small absolute change can be explained by the fact that the work employs a very small injection rate of 0.001 m^3/s.

Chang and Segall [2016b] studied the poroleastic response of faults in the underburden unit to fluid injection into the overlying reservoir unit. The model contained three lithological units: a mudrock caprock, a sandstone reservoir and a basement unit. Time-dependent earthquake nucleation and full poroelastic coupling was included. Two cases of varying friction coefficient were examined: 0.10 and 0.75. The poroelastic stress change was weakly negative in the 0.75 case, but strongly positive in the 0.10 case. Therefore, it was concluded that the lower the friction coefficient, the higher the seismicity rate for faults in the underburden. Thus, it appears friction coefficient can have differing influences on fault slip depending on the location of the fault from the injection point and the lithological unit the fault lies within.

6.2.2.2 Fault Permeability

Fault permeability refers to the ability of a fault to allow fluids, such as hydrogen, to flow through it, which depends on fault aperture. High fault permeability means fluids can move easily along the fault, which can impact fluid migration and pressure distribution in subsurface reservoirs. Conversely, low permeability indicates restricted fluid flow. The degree to which a fault transmits fluid influences pressure distribution within and in the vicinity of the fault which influences fault slip.

Mazzoldi et al. [2012] performed two-phase CO_2 injection experiments using the TOUGH-FLAC 2D FEM simulator, varying the fracture permeability between 10^{-17} and 10^{-15} m^2. For this range, it was found that the fault slip was essentially insensitive to fault permeability. The 10^{-15} and 10^{-17} m^2 cases resulted in 0.4 cm and 0.7 cm more slip than the 10^{-16} m^2 case respectively. Therefore, no systematic change in slip with increasing fault permeability was found.

Anyim and Gan [2020] conducted 3-D geothermal injection experiments using the TOUGHREACT-FLAC3D simulator in a 600 $\times$ 15 $\times$ 600 m model containing a strike-slip fault of length 424 m with a dip angle of 45 °. They varied the fault permeability between 10^{-12} and 10^{-16} m^2 to study the effect on slip and found generally that as fault permeability increases the slip decreases with approximately 2.2 cm difference between the 10^{-12} and 10^{-15} m^2 cases. However, the smallest fault permeability they tested, 10^{-16} m^2, yielded the smallest slip, again displaying some potential non-convergence in the results. It must be noted that some of these fault permeabilities (i.e., 10^{-12} m^2) are well in excess of the low permeability crystalline host rock.

Deng et al. [2021] performed 2-D hydraulic fracturing simulations in a fully coupled hydromechanical model containing two predefined 10 m faults (F1 and F2) and where only a single pre-defined hydraulic fracturing path was considered. The injection point lies laterally below F1, which is laterally below F2. They vary the fault permeability between 10^{-15} and 10^{-14} m^2 and assess the slip on both faults. The slip on F2 is invariant to the fault permeabilities tested with a maximum of 0.03 mm of difference in slip between the cases. The slip on F1 showed

that again as fault permeability increased, fault slip decreased slightly, although the variation was only about 0.6 mm between the 10^{-15} and 10^{-14} m^2 cases.

Rutqvist et al. [2013] performed a similar study to Mazzoldi et al. [2012] but for hydraulic fracturing, varying fracture permeability between 10^{-17} and 10^{-19} m^2. At the time of rupture the slip progressively got larger as fault permeability increased (2 to 9 mm from 10^{-18} to 10^{-17} m^2) for a uniform injection rate.

6.2.2.3 Fault Length

In the 2-D plane-strain FEM hydraulic fracturing work of Meng et al. [2020], which modelled Coulomb friction between the fracture surfaces and temporally applied a fluid pressure to the fault surface, the length of the fracture was varied between 10 and 100 m and it was found that the length of the fracture had a significant influence on the observed fracture slip. They found that as fracture length increased the slip at its center approximately linearly increased. As fracture length was changed from 10 m to 100 m, the slip experienced along the natural fracture increased by 30 – 55 mm (depending on dip angle).

6.2.2.4 Fault Roughness and Orientation

In this study, fault geometry is represented using a smooth, planar macro-fracture, and fault surface roughness is not explicitly incorporated into the induced seismicity simulations. While surface roughness is known to influence rupture nucleation, propagation, and stress redistribution, modelling it accurately poses significant challenges. Roughness can occur across a wide range of spatial scales, from centimetres to hundreds of metres, and would require extremely high-resolution meshing and detailed geological input data, which were unavailable at the reservoir scale. Moreover, incorporating roughness in numerical models often introduces computational instability and complexity, especially in coupled hydro-mechanical simulations. Consequently, the use of a smooth fault surface provides a simplified, yet tractable, representation of fault mechanics suitable for assessing first-order geomechanical behaviour under

hydrogen injection conditions.

Additionally, the orientation of the fault used in the simulations was selected in a semi-random manner, not based on site-specific data. This reflects the fact that, in many real-world storage sites, the subsurface fault fabric may be complex, with faults potentially oriented in any direction relative to the in-situ stress field. As such, the chosen orientation serves to explore a plausible scenario rather than a definitive site-specific case. Future studies could improve on this by incorporating probabilistic fault orientation distributions or site-calibrated structural models, where data allows.

6.2.3 Operational Properties

6.2.3.1 Injection Rate

Injection rate defines the volume of hydrogen delivered to the reservoir unit in a unit time. Injection rate influences the pore pressure within the reservoir unit which alters the effective stress in the vicinity of faults, which governs slip behaviour.

Assuming the same cumulative injected volume, higher injection rates are more likely to induce earthquakes [Alghannam and Juanes, 2020]. Alghannam and Juanes [2020] tested two constant injection rate and one linear ramp-up injection schedules with their spring-poroslider model of a fault segment in contact with a reservoir and found that the higher constant injection rate case resulted in a greater deviation in the dimensionless shear stiffness from the dimensionless critical shear stiffness. This owes to the greater rate of increase in the pore pressure. The linear ramp-up case, where injection rate was gradually increase in small steps, resulted in a lower likeliness of induced seismicity since the increase in the rate of pore pressure increase is smaller. Therefore, a gradual step-up injection schedule is likely to reduce seismic risk relative to an abrupt high constant rate injection schedule, provided the pore pressure stabilizes between injection stages.

Ji et al. [2022b] used low permeability granite samples with critically stressed sawcut faults to

perform injection experiments. They performed these tests at various confining pressures and injection rates. The nucleation length of a seismic event was reduced for higher injection rates, and events associated with smaller nucleation lengths resulted in larger fault slip displacements. It was concluded that higher injection rates are linked to higher seismic hazard.

6.2.3.2 Withdrawal Rate

Withdrawal rate defines the volume of hydrogen extracted from the reservoir unit in a unit time. Withdrawal rate, like injection rate, influences the pore pressure within the reservoir unit, which alters the effective stress in the vicinity of faults. Withdrawal of fluid can also lead to compaction which can increase the vertical loading acting on a fault.

During fluid injection pore pressure increases result in effective normal stress reductions acting on the fault plane, moving the Mohr-Coulomb envelope towards failure [Skempton, 1960, Jaeger et al., 2009]. Unlike injection-induced earthquakes, production-induced earthquakes cannot be explained with the same mechanism. Production reduces the pore pressure, resulting in effective normal stress increases along the fault plane, seemingly rendering the fault more stable [Skempton, 1960, Jaeger et al., 2009]. However, production-induced events are typically compaction-related [Moein et al., 2023, Zbinden et al., 2017]. The pore pressure reduction alters the stress state within the reservoir. The change in the effective horizontal stress is given by $\Delta\sigma'_h$ = -$\alpha(\nu/1-\nu)\Delta P$ and the change in the effective vertical stress is given by $\Delta\sigma'_V$ = -$\alpha\Delta P$ [Zbinden et al., 2017]. The extra term $\nu/1-\nu$ in the change in effective horizontal stress equation ensures that for any value of ν (except 0.5) the change in effective vertical stress must always be greater than that for the horizontal stress. As such, during production the differential stress can increase significantly resulting in growth in the Mohr-Coulomb circle, possibly enabling it to intersect the failure criterion.

Zbinden et al. [2017] implemented a 2-D model with an overburden aquifer, a shale caprock, a 100 m thick porous and weak gas reservoir and a low permeability basement. The model contains a fault with 80° dip. Coupled hydrothermomechanical simulations were performed using the TOUGH-FLAC simulator and the gas production rate was varied in three numerical

experiments between 0.08×10^9, 0.15×10^9 and 0.31×10^9 m^3/year (2.5 – 10 m^3/s). The fault slip was almost invariant to production rate with a peak slip difference of 0.4 cm between the smallest and largest rate cases.

However, Nepveu et al. [2016] and Sijacic et al. [2017] used statistical methods to examine seismicity at the Groningen natural gas field. Increases and reductions in production rate correlated with increases and reductions in seismicity with a delay in the seismicity of 2 – 8 months following the production change. Thus, the effects of production rate on fault slip and induced seismicity are not unanimously agreed upon.

6.2.4 Fluid Properties

6.2.4.1 Fluid Viscosity

Fluid viscosity is a measure of the resistance of a fluid to flow. It quantifies the internal friction within the fluid as it moves, determining how easily the fluid can deform or change shape. Fluid viscosity impacts the dynamic weakening (reduction in dynamic fault friction coefficient) mechanisms acting on a fault by altering the dimensionless Sommerfeld number and the associated macroscopic lubrication regime [Cornelio et al., 2019]. Higher fluid viscosities are likely to promote unstable fault slip [Ji et al., 2022a].

Higher viscosity fluids promote the likeliness of the elasto-hydrodynamic (EHD) fault fluid lubrication regime [Ji et al., 2022a, Cornelio et al., 2019] in which the normal effective stress on the fault is supported solely by the fault fluid pressure. EHD is an effective mechanism in weakening a fault during seismic activity [Cornelio and Violay, 2020a]. Furthermore, more viscous fluids take longer to flow along a fault and have less affinity for leak-off and thus can induce higher fluid overpressures. Additionally, their presence promotes shear-induced compaction [Cornelio and Violay, 2020b], both of which increase the magnitude and likelihood of induced seismicity. However, shear-test experiments are still required to confirm this [Ji et al., 2022a].

6.2.4.2 Fluid Compressibility

Fluid compressibility is a measure of how much a fluid's volume changes in response to changes in pressure. It quantifies the degree to which a fluid can be compressed or compacted under pressure. When fluids are injected into or withdrawn from subsurface reservoirs, the pore pressure within the surrounding rock formations changes. Compressible fluids, such as gases or gas-rich fluids, can undergo significant changes in volume in response to pressure variations. This change in volume leads to corresponding changes in pore pressure. Elevated pore pressure can reduce the effective stress acting on faults, making them more prone to slip.

Dal Zilio et al. [2022] developed a 2-D numerical model containing a planar strike-slip fault embedded within a viscoporoelastoplastic medium considering only mode-II plane strain. The type of seismicity (earthquake, slow-slip event or stable aseismic creep) was monitored for different bulk rock-fluid compressibility pairs within the ranges 10^{-11} - 10^{-7} Pa^{-1} for fluid compressibility and 10^{-11} - 2×10^{-10} Pa^{-1} for bulk rock compressibility. This investigation was replicated for two different cases of rock porosity (0.01 and 0.10). They found that the type of seismicity at a given fluid compressibility was invariant to the bulk rock compressibility. Additionally, for a given bulk rock compressibility, the seismic hazard decreased with increasing fluid compressibility; that is, the likeliness of aseismic creep increases and the likeliness of earthquakes decreases as fluid compressibility increases. Their results imply for a hydrogen compressibility of 6.67×10^{-8} Pa^{-1} and a bulk rock compressibility of 5×10^{-11} Pa^{-1}, stable aseismic creep is expected. These are the fluid and rock compressibilities for a reservoir temperature and pressure of 90°C and 15 MPa and a typical reservoir rock respectively. A temperature of 90°C is the arithmetic average of the reservoir temperatures of the Leman, Britannia and Goldeneye fields which are 137°C [Camm et al., 2020], 83°C [Shell, 2015a] and 51.7°C [Hillier, 2003], respectively. The pressure was selected through a similar process but the averaged value of 29 MPa was abnormally high compared to most depleted reservoirs, so the value was decreased to 15 MPa without any statistical method. However, they find that as the porosity is increased, the onset of aseismic creep is pushed to higher fluid compressibilities with the risk of slow-slip events increasing at fluid compressibilities that at a lower porosity resulted in aseismic creep.

The work is limited in that porosities above 10% are not considered and many storage reservoir rocks have porosities above this such as the Utsira sandstone formation (which has a porosity of 35-39%) which is the storage unit at the Sleipner CO_2 project [Pratikna et al., 2022]. Sandstones typically have porosities in the range 14-46% [Karu, 2012]. If the trend can be extrapolated, it may imply that at higher reservoir porosities, for typical hydrogen compressibilities, the expectation of aseismic creep may evolve into slow-slip seismicity. Furthermore, little knowledge exists around the fluid compressibility of hydrogen at reservoir temperatures and pressures, as until now there has been few uses of hydrogen at such high P-T conditions. Additionally, the work qualitatively describes the seismicity but does not quantitatively assess the slip at these different bulk rock-fluid compressibilites.

6.2.5 Stresses

Mazzoldi et al. [2012] performed further two-phase CO_2 injection experiments to those mentioned in Section 6.2.2.2, whereby the horizontal-to-vertical stress ratio was varied between 0.65 and 0.70. Fault slip was strongly dependent on this ratio. Fault slip increased from approximately 8 to 17 cm as σ_H/σ_V was decreased from 0.70 to 0.65.

Rutqvist et al. [2013] made similar conclusions during a case of water injection for hydraulic fracturing into a 2-D 2×2 km plane strain model of the Marcellus Shale. The model included a 1 km long fault dipping at 80°. The injection point was located within the fault. It was found that for a σ_H/σ_V ratio of 0.5, the fault slip in a 3 hour period of injection was 5 to 12 times larger than at 0.525 and 0.55, reinforcing that slip increases as σ_H/σ_V decreases. However, the effect of individual stress magnitudes at the same σ_H/σ_V ratio was not examined.

6.2.6 Summary

Factors such as the injectant density, fault dip, fault strike, well length, and well-fault spacing on induced fault slip have not been explored. Injectant fluid density may be an important parameter influencing induced fault slip. Buoyancy forces derived from injecting a low density

fluid can increase the vertical loading acting on the fault and reduce the horizontal loading (to satisfy stress equilibrium) and thus this can alter the differential stress causing the Mohr's circle to grow in radius and thus increase the likelihood of intersecting the Mohr-Coulomb failure line. Vilarrasa et al. [2021] attributes this buoyancy mechanism to the slip induced along the Amposta fault at the Castor Underground Natural Gas Storage site in Spain. Given hydrogen is a couple of orders of magnitude less dense than natural gas, this could be an even greater issue during geological hydrogen storage.

This literature review demonstrates that relatively little work has been done to quantify the influence of individual parameters on fault slip and potential seismic risk. Furthermore, there is a shortage of three-dimensional studies: only one study in this literature review was 3-D (see the work of Anyim and Gan [2020] in Section 6.2.2.2) and this was for a geothermal project in which injection occurs into a low-permeability crystalline rock. The 2-D nature of the work is limiting in that fault slip can only be computed at a single point along each depth interval across the fault because the fault is inherently 1-D. The Imperial College Geomechanics Toolkit (see Section 3) used for the work in this thesis has the advantage that due to its 3-D nature, the full spatial distribution of the slip across the 2-D fault surface can be computed by node-to-node comparison of nodes on opposing fault surfaces using a follower-leader formulation. This also allows critical fault parameters such as fault aperture (and contact traction) to be geomechanically computed spatially in 2-D across the entire fault surface and does not impose one constant, or alternatively computes one single, fault aperture as 2-D works must.

Furthermore, the majority of these results are derived from hydraulic fracturing studies, that incorporate hydraulic fractures as well as natural fractures. Thus, the slip computed on the natural fractures are not solely a function of the injection. Additional fractures significantly influence the stress field around the natural fractures and faults due to fracture interaction. Therefore, effects such as stress-shadowing (Paluszny et al. [2020b], Thomas et al. [2017], Burtonshaw et al. [2021]) most likely make these works different problems to that of an unfractured porous reservoir. Other potential issues with comparing to hydraulic fracturing studies include the fact that the natural pre-existing discontinuities are small-scale fractures and not large-scale faults, and the length of the discontinuity has already been shown to have a significant influence

on the slip [Meng et al., 2020]. Even comparing findings with the two works from CO_2 storage are problematic because the pore pressure monotonously increases, and due to the fact that only injection is present, with no subsequent production, cyclical changes in pore pressure and induced stress and strain are not considered, which is critical in understanding fault slip during H_2 storage.

6.3 Comparison of Slip against CO_2 Storage Study

Burtonshaw et al. [2023a] conducted a comparison study, in which the predictions of the ICGT were compared against the predictions of COMSOL Multiphysics for the computation of fault slip during a case of CO_2 injection from the literature [Mortezaei and Vahedifard, 2015]. Mortezaei and Vahedifard [2015] constructed a 2D FEM 2000 $\times$ 2000 m thermohydromechanical model of a layercake subsurface system consisting of five layers: an upper aquifer, an upper caprock, a reservoir, a lower caprock and a lower aquifer unit. The model contains one fault, of length 1000 m and dip 80°, which penetrates to some extent all five structural units. CO_2 was injected at a rate of 0.02 kg/s. They performed a parametric study, varying the permeability and porosity of the reservoir units, and subsequently assessing the change in the slip along the fracture. In the work of Burtonshaw et al. [2023a], the model was replicated in the ICGT and extended to 3D and a hydromechanical study was conducted. The thermal aspect of the work in Mortezaei and Vahedifard [2015] was partially accounted for by assigning fluids of different densities, viscosities and compressibilites to each lithological unit depending on the corresponding temperature and pressure at the mid-depth of each unit. Burtonshaw et al. [2023a] found that the discrepancy between the peak slip across the fault surface between the ICGT and COMSOL results (Figure 6.1) was small and to within the cm-scale (3 cm, 1 cm and 5 cm in the 10^{-12}, 10^{-13} and 10^{-14} m^2). Differences in slip elsewhere along the fault surface can be attributed to differences in the modelling procedures: (1) 2D (COMSOL) vs 3D (ICGT), (2) thermohydromechanical (COMSOL) vs hydromechanical (ICGT), (3) potential differences in the methodology for slip computation and (4) constant apertures (COMSOL) vs. geomechanically-controlled apertures (ICGT). A host of further published validations, compar-

isons and studies for the ICGT in relevant fields applicable to the work herein, such as carbon dioxide sequestration and fracture physics have been performed (i.e., Salimzadeh et al. [2018]).

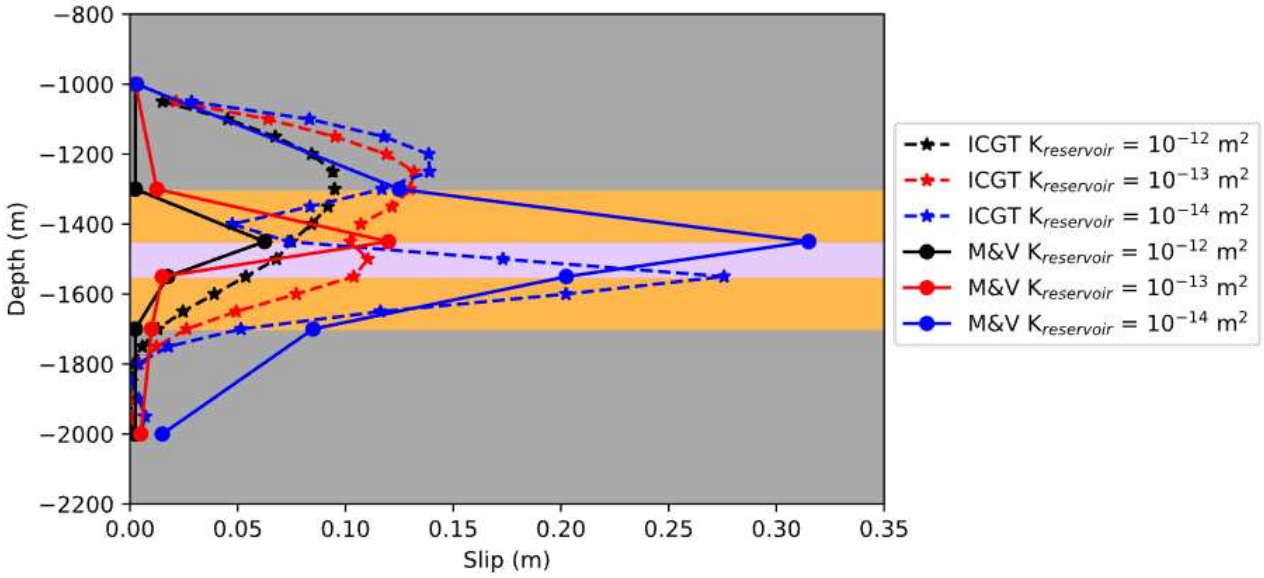


Figure 6.1: Model depth versus slip along the fault for different reservoir permeabilities. The results are presented after injection times of approximately 110 days, 280 days and 1400 days in the 10^{-12}, 10^{-13} and 10^{-14} m^2 cases respectively, as in the numerical comparison paper. The fault exists with vertical coordinates between 1000 and 2000 m. The solid black line represents the numerical solution of Mortezaei and Vahedifard [2015] and e denotes elements. The dashed lines represent results generated from the ICGT.

6.4 Methodology

A numerical model is constructed to study the injection, storage and withdrawal of hydrogen. The model has $x \times y \times z$ dimensions of 4000 m × 4000 m × 3300 m and is shown in Figure 6.2. The model contains an anticlinal structure consisting of a caprock (light grey layer) and a reservoir unit (orange layer), bound from above by a low permeability overburden (cream layer) and from below by a low permeability underburden (dark grey layer). The mechanical, geological, and geometrical properties of each of these layers, as well as fluid and fault properties, are given in Table 6.3. The *in situ* stresses are applied symmetrically such that the *in situ* horizontal stresses at the mid-point of the reservoir unit are approximately 45 MPa, which obey the normal faulting regime that predominates in the Central and Southern North Sea [Williams et al., 2014, Hillis and Nelson, 2005]. Prescribed mechanical, geological and

geometrical properties correspond to a generic North Sea reservoir where data was available (primarily an average from the Leman, Britannia and Goldeneye Fields, Table 6.4). The fault properties are generalized.

Gaseous hydrogen is injected into the sandstone reservoir unit through a single horizontal wellbore that penetrates the whole length of the model in the y-direction, at a depth of 2,475 m, 500 m away in the x-direction from the left boundary of the model (Figure 6.2). Simulations are run for a total time of three years. In each annual cycle, the hydrogen is injected for a total time of five months at a constant injection rate of 20 m^3/s. After the five month injection period, the hydrogen remains in place with no withdrawal or storage taking place for a total of two months (5,256,000 seconds). Finally, the hydrogen is withdrawn for the remaining five months of the year, via a second horizontal wellbore, also at a depth of 2,475 m and 500 m away from the right boundary of the model in the negative x-direction. Therefore the injection and withdrawal well are separated by a distance of 3000 m in the x-direction. The withdrawal rate is set to a constant 17 m^3/s, such that the withdrawal rate is 85% of the injection rate, accounting for the fact that not all the injected hydrogen will be recoverable. The chosen injection rate may at first seem large because the density of the injected hydrogen is extremely low relative to other geo-energy fluids. However, in order to store sufficiently large masses of hydrogen to comprise a significant and useful proportion of the energy mix, in short time periods of months, the injection rate will coincidentally have to be large.

The simulation is composed of two stages: (1) a pre-injection equilibration period which allows the model to reach the initial pressures set and (2) the injection period, lasting five months, a storage period lasting two months and a withdrawal period lasting five months. During the second stage, the fault slip is monitored.

The model contains a single fault (Figure 6.2), modelled as a rectangular flaw of dimensions 2000 $\times$ 198.5 m, and centred at a depth of 2,475 m, such that the fault resides in the reservoir unit. The fault orientation in the final simulations (see Section 6.7) is described by a strike of 45°, a dip of 45°, and a dip direction of 135°, whereas the fault orientation in the mesh convergence simulations (see Section 6.5) is described by a strike of 0°, a dip of 45°, and a dip

direction of 90°. The fault terminates at the top 10 m below the caprock-reservoir interface and at the bottom 10 m above the reservoir-underburden interface. The fault in the final simulations (see Section 6.7) is defined by the four points: (-760, 654, -2410), (-654, 760, -2540.00), (654, -760, -2410) and (760, -654, -2540), whereas in the mesh convergence simulations (see Section 6.5), it is defined by the points: (-1000, -75, -2410), (-1000, 75, -2540), (1000, -75, -2410) and (1000, 75, -2540.00).

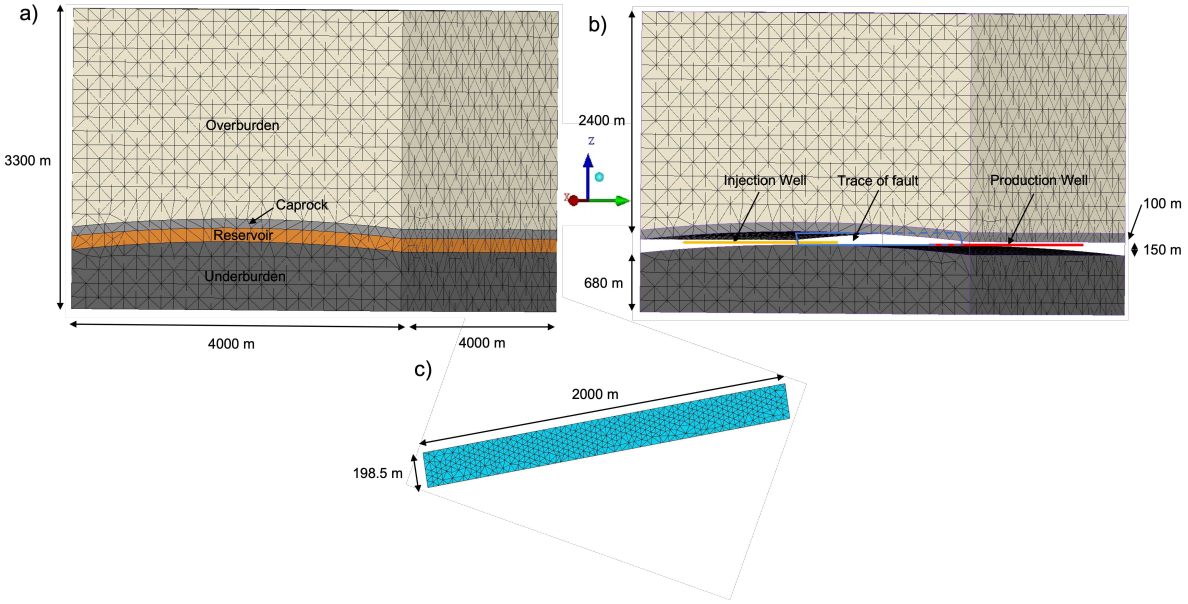


Figure 6.2: (a) A solid and wireframe view of the model showing the four rock layers (overburden is cream, caprock is light grey, reservoir is orange, underburden is dark grey). b) A perspective front-right solid and wireframe view of the fault (cyan) contained with the reservoir unit and the injection well on the left of the domain (orange) and the withdrawal well on the right of the domain (red). The reservoir unit is removed in order to observe these. c) A top view of the rectangular fracture surface.

6.5 Mesh Effects

6.5.1 Domain Mesh Refinement

A total of five separate simulations (Table 6.5) in which the refinement of the bulk rock mesh is varied between each simulation were performed. These simulations utilized meshes with element numbers between approximately 45,000 and 690,000, and node numbers between approximately 7,300 and 110,000. Figure 6.3 shows the refinement for each of the cases. In the cases with 7,276

Table 6.3: The mechanical, geometrical, geological, fluid dynamic, and fault properties and the *in situ* stresses of the four different rock layers within the models. The symbology in the table is as follows: k = Permeability, ϕ = Porosity, h = Thickness, E = Young's modulus, ν = Poisson's ratio, α = Biot coefficient, ρ_b = Rock Density, K = Bulk Modulus, σ^* - Uniaxial Tensile Strength, ρ_f = Fluid Density, μ = Fluid Viscosity, c = Fluid Compressibility, σ_h = minimum horizontal *in situ* stress at base, σ_H = maximum horizontal *in situ* stress at base, σ_V = vertical *in situ* stress at top, L = fault length, w = fault width, θ = fault dip, ψ = fault orientation to North and x = fault centroid location (x,y,z). The properties herein are derived from the 'Overall Range' column of Table 4.

Property	Overburden	Caprock	Reservoir	Underburden
Mechanical				
Lithology	Chalk	Shale	Sandstone	Shale/Coal
k (m^2)	3.0×10^{-15}	1.0×10^{-21}	1.0×10^{-13}	1.0×10^{-21}
ϕ	0.30	0.05	0.15	0.05
h (m)	2300 - 2400	100	150	650 - 750
E (GPa)	4.5×10^9	1.5×10^{10}	1.5×10^{10}	1.5×10^{10}
ν	0.35	0.35	0.15	0.35
α	0.87	0.93	0.35	0.93
ρ_b (kg/m^3)	2080	2500	2500	2500
K (Pa)	9.75×10^9	1.333×10^{10}	2×10^{10}	1.333×10^{10}
σ^* (Pa)	1.0×10^6	1.3×10^6	2.0×10^6	1.3×10^6
Fluid				
Fluid	Brine	Brine	Hydrogen	Brine
ρ_f (kg/m^3)	1058	1042	9	1037
μ (μPa s)	561.0	357.5	10.4	296.0
c (Pa^{-1})	4.47×10^{-10}	4.57×10^{-10}	6.67×10^{-8}	4.68×10^{-10}
Stresses				
σ_h (MPa)	-	-	58.5	-
σ_H (MPa)	-	-	58.5	-
σ_V (MPa)	-	-	0.9800517	-
Fault				
L (m)	-	-	2000	-
w (m)	-	-	183.8	-
θ (°)	-	-	45	-
ψ (°)	-	-	0	-
x (m)	-	-	(0,0,2475)	-

Table 6.4: Literature review of values of reservoir, underburden/caprock and overburden properties and their sources or the sources from which data was taken to compute a value for that field. The range for each property is given in the 'overall range' column, from which the values in Table 3 were chosen. The subscripts R, A, E, W, T, B, A-s, B-s, C-s denote range, average, east, west, top, bottom, A-sand, B-sand and C-sand respectively. KC, CM and NSC refer to Kimmeridge Clay, Coal Measures Rocks and North Sea Chalk respectively. KC is the underburden rock for the Britannia and Goldeneye Fields, whereas CM is the underburden for the Leman Field. North Sea Chalk is the overburden rock for the Britannia and Goldeneye Fields. References from which each property was extracted were: E_{res} - Monsees et al. [2021], Camm et al. [2020], Shell [2014]; K_{res} - Hillier [2003], Camm et al. [2020], Shell [2015a]; $\rho_{b,res}$ - Hillier [2003], Camm et al. [2020], Shell [2015b]; ν_{res} - Ji et al. [2018], Dvorkin and Nur [1996], Shell [2014]; $c_{r,res}$ - Noy et al. [2012], Camm et al. [2020], Shell [2014]; ϕ_{res} - Hillier [2003], Camm et al. [2020], Shell [2015a]; E_{und} - Khandelwal and Singh [2009], Sayers [2013], Kumar et al. [2012]; K_{und} - Karacan [2009], Huang et al. [2022], Gaus et al. [2019], Hawthorn [2004]; $\rho_{b,und}$ - Khandelwal and Singh [2009], Bell et al. [1997], Hornby [1998]; ν_{und} - Khandelwal and Singh [2009], Sayers [2013]; ϕ_{und} - Curtis et al. [2012], Hawthorn [2004], Huang et al. [2022], Hornby [1998]. The sources for the property values of the overburden and the caprock, assuming a chalk overburden and shale caprock as in the Britannia and Goldeneye fields are as follows: E_{over} - Descamps et al. [2017], Olsen [2007]; K_{over} - Keszthelyi et al. [2016]; $\rho_{b,over}$ - Japsen [1998]; α_{over} - Olsen et al. [2008], Gommesen et al. [2007]; ν_{over} - Gommesen et al. [2007]; $c_{r,over}$ - Alam et al. [2012]; ϕ_{over} - Keszthelyi et al. [2016], Gommesen et al. [2007]; α_{cap} - Thompson et al. [2021]. The remaining caprock properties: E_{cap}, K_{cap}, $\rho_{b,cap}$, ν_{cap}, $c_{r,cap}$ and ϕ_{cap} are set to be equal to the underburden properties.* denotes that the value is not specifically for that field but is the value for the equivalent lithological unit in another geographical location or outcrop or if that was not available, the value of a similar rock type. The properties used in Table 6.3 are derived from the 'Overall Range' column herein.

Property	Leman Field	Britannia Field	Goldeneye Field	Overall Range
Reservoir				
E_{res} (GPa)	R: 0.32 - 12.68 * A: 7.18 *	R: 20.6 - 86.2	R: 8.5 - 18.5	0.32 - 86.2
K_{res} (mD)	A-s: 1.02 - 2.45 B-s: 6.03 - 15.60 C-s: 0.55 - 4.67	R: 0.1 - 200 A: 60 (E), 30 (W)	R: 700 - 1500 A: 790	0.1 - 1500
$\rho_{b,res}$ (kg/m^3)	A-s: 2330 - 2600 B-s: 2280 - 2530 C-s: 2390 - 2620	R: 2350 - 2830 A: 2350 (T), 2650 (B)	R: 2013 - 2256	2013 - 2830
α_{res}	-	-	-	-
ν_{res}	R: -0.13 - -0.06 *	R: 0.20 - 0.30 *	R: 0.14 - 0.20	-0.13 - 0.30
$c_{r,res}$ (Pa^{-1})	A: 4.5×10^{-10}*	R: 1.3×10^{-11} - 1.7×10^{-10} A: 3.9×10^{-11} (T), 3.4×10^{-11} (B)	A: 7.83×10^{-11}	3.4×10^{-11} - 4.5×10^{-10}
ϕ_{res} (%)	A-s: 12.05 - 13.70 B-s: 13.54 - 15.06 C-s: 9.30 - 12.61	R: 10 - 18 A: 15	A: 25	9.3 - 25
Underburden/Caprock				
E_{und} (GPa)	R: 1.45 - 3.37 (CM)*	R: 18 - 43 (KC)*	R: 5 - 15 (KC)*	1.45 - 43
K_{und} (mD)	R: 0.0004 - 0.005 (CM)* R: 0.09 - 6.62 (CM)*	R: 2×10^{-6} - 5×10^{-6} (KC)*	R: 7×10^{-9} - 5×10^{-6} (KC)*	7×10^{-9} - 6.62
$\rho_{b,und}$ (kg/m^3)	R: 2430 - 2560 (CM)*	A: 2690 (KC)*	R: 1750 - 2150 (KC)*	1750 - 2690
α_{und}	-	-	-	-
ν_{und}	R: 0.14 - 0.37 (CM)*	R: 0.11 - 0.275 (KC)*	-	0.11 - 0.37
$c_{r,und}$ (Pa^{-1})	-	-	-	-
ϕ_{und} (%)	R: 0.51 - 4.14 (CM)*	R: 0 - 3.3 (KC)* A: 2.5 (KC)*	R: 0.3 - 19.9 (KC)*	0 - 19.9
Overburden				
E_{over} (GPa)	-	R: 1 - 10 *	R: 1 - 7 (NSC)* A: 4 - 5 (NSC)*	1 - 10
K_{over} (mD)	-	R: 1 - 5 (NSC)*	-	1 - 5
$\rho_{b,over}$ (kg/m^3)	-	A: 2050 (T) (NSC)* A: 2110 (B) (NSC)*	-	2050 - 2110
α_{over}	-	R: 0.7 - 1.0 (NSC)*	R: 0.75 - 0.90 (NSC)*	0.7 - 1.0
ν_{over}	-	R: 0.29 - 0.37 (NSC)*	-	0.29 - 0.37
$c_{r,over}$ (Pa^{-1})	-	-	-	-
ϕ_{over} (%)	-	R: 10 - 48 (NSC)*	R: 4 - 41 (NSC)*	4 - 48

and 34,043 nodes the entire domain is refined equally. In the cases with 61,863 and 113,561 nodes the domain is additionally refined in a box of dimensions 2500 × 400 × 450 m centred at the fault centroid such that the fault is fully encompassed by a region of high refinement. In the case with 93,620 nodes the domain is refined additionally in a larger box of dimensions 4000 × 4000 × 650 m also centred at the fault centroid. Within each of these 'refined boxes,' the refinement is not uniform throughout. This refinement is somewhat random dependent on the value of the mesh density flag chosen in the simulator. Running the same simulation again resulted in slightly different meshes in this zone but the results were unaffected by this.

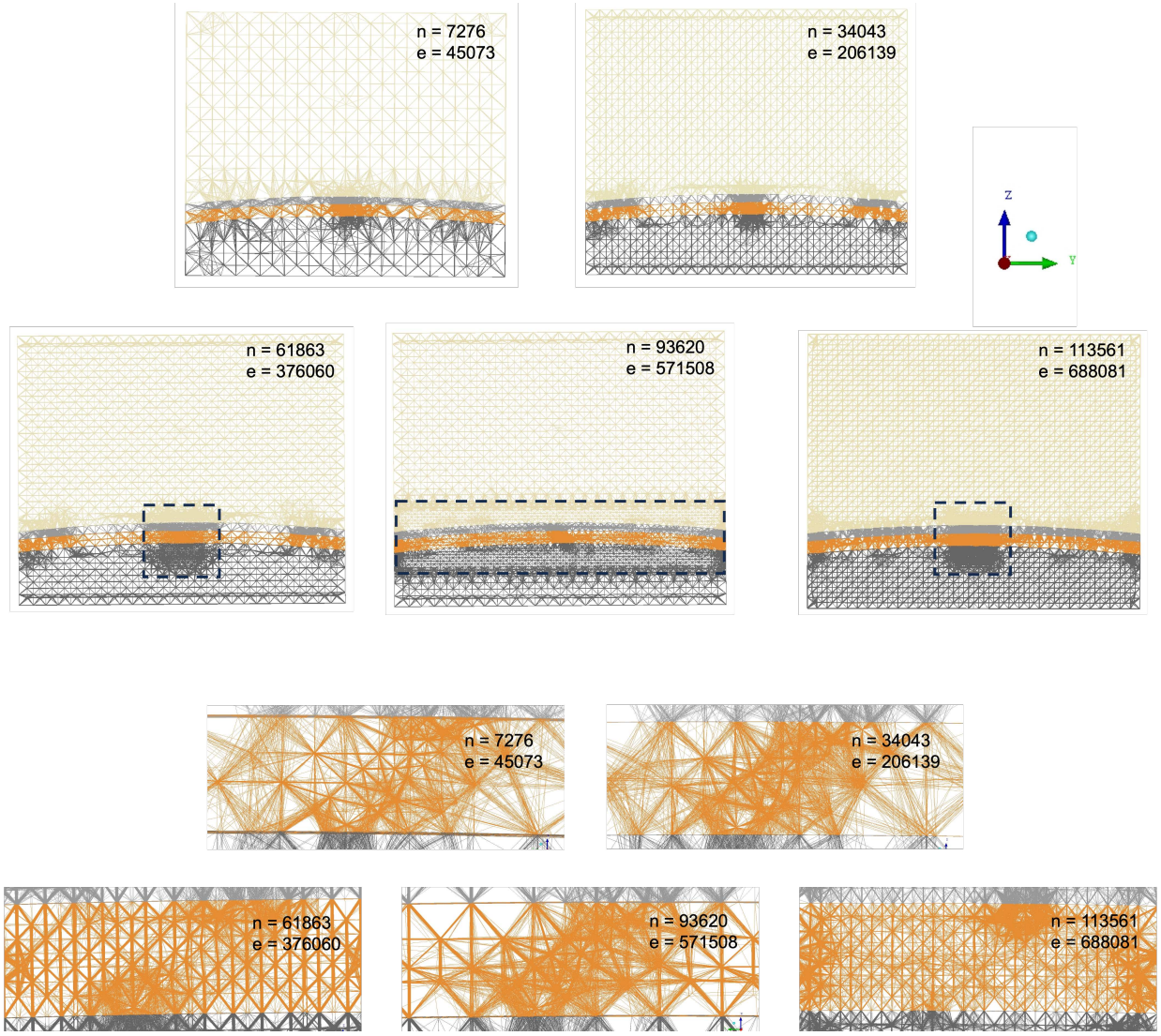


Figure 6.3: (Top) Wireframe views of the five versions of the model for each refinement case in Table 6.5. The dashed boxes denote the zones of increased refinement. (Bottom) Zoomed views of the mesh at the centre of the reservoir unit.

Plots of average slip as a function of time since the onset of the first injection period for each

Table 6.5: Five simulation cases run to examine the effect of domain refinement on the slip solution.

Simulation Case	Nodes	Elements	Fracture Elements
Case 1	7,276	45,073	701
Case 2	34,043	206,139	668
Case 3	61,863	376,060	732
Case 4	93,620	571,508	682
Case 5	113,561	688,081	1202

refinement case are shown in Figure 6.5a. The solution converges to within 1 cm provided that the number of elements and the number of nodes are at least 200,000 and 34,000 respectively. Therefore, the remaining simulations in this work will utilize the mesh with 206,139 elements and 34,043 nodes. Finer refinement than this increases the simulation time to nearly a week for less than a cm accuracy improvement in solution. The case with only 7,276 nodes is offset because the injection pressure in this case has not converged.

6.5.2 Fault Mesh Refinement

Five simulations (Table 6.6) in which the refinement of the fault mesh is varied are performed. In each case, the entire domain is refined using the same refinement as Case 2 from Section 6.5.1. These simulations utilized fault meshes with element numbers between approximately 110 and 5,500 elements. Figure 6.4 shows the refinement for each of the cases.

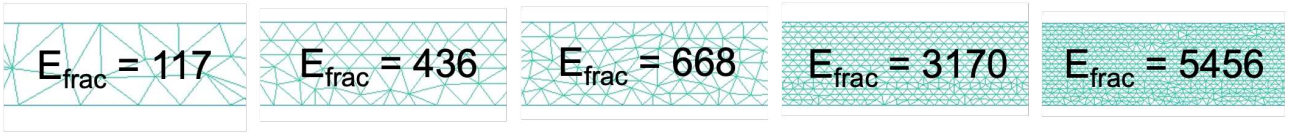


Figure 6.4: Mesh of the fault surface for the five versions of the fault in the model for each refinement case in Table 6.6, for varying amount of fracture elements E_{frac}.

Plots of average slip as a function of time since the onset of the first injection period for each fault refinement case are shown in Figure 6.5b. The solution again converges to within 1 cm provided that the number of elements is at least approximately 440. Only in the case of a fault with only 117 elements did the slip solution significantly diverge, predicting 3 cm less slip during

the first and second slip events. Therefore, the remaining simulations utilize a 'refined' fault mesh with 668 elements. Finer refinement than this, such as the case with 5,456 fault elements, leads to a substantially longer simulation time, but leading to a 1 cm accuracy improvement in the slip solution.

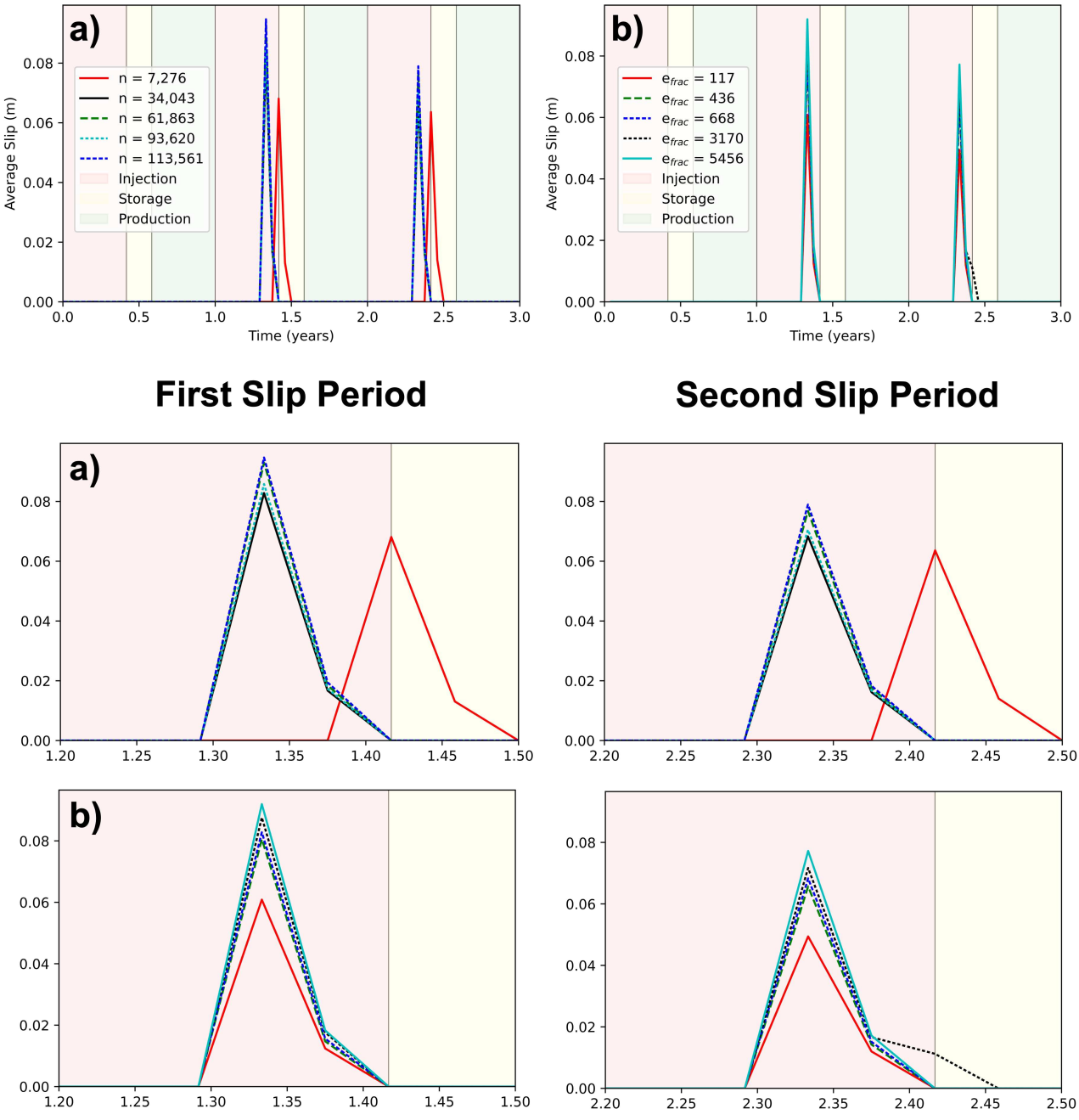


Figure 6.5: Plots of average slip as a function of operation time for (a) five cases of different bulk rock/domain refinements represented by different numbers of nodes and (b) five cases of different fault refinements represented by different numbers of fault elements showing two distinct slip events. A zoomed view of the two slip periods for both (a) and (b) are shown below.

Table 6.6: Five simulation cases run to examine the effect of fracture refinement on the slip solution.

Simulation Case	Nodes	Elements	Fracture Elements
Case 1	16,594	100,800	117
Case 2	17,960	109,517	436
Case 3	34,043	206,139	668
Case 4	41,842	251,167	3170
Case 5	91,641	546,919	5456

6.6 Numerical Experiments

This section outlines the various numerical simulations that were performed in this work. Four sets of simulations are performed in which four simulations are run per set. Each set corresponds to a particular mechanical property, either Young's modulus, Poisson's ratio, Biot coefficient, or permeability. Within each set, each one of these properties in the reservoir unit is parametrically varied four times in four separate simulations so that the influence of each mechanical property on induced fault slip can be studied. Table 6.7 summarizes the test cases for the simulations. The values in each case are selected to cover the full range of potential values that each property was found to take in various depleted North sea oil and gas fields.

Table 6.7: Mechanical properties of the different simulation cases. E = Young's modulus, k = Permeability, α = Biot coefficient, and ν = Poisson's ratio. The subscript 'res' refers to the reservoir unit.

Simulation	Default Case	Case 2	Case 3	Case 4
E_{res} (GPa)	15	10	40	60
k_{res} (mD)	100	5	25	800
α_{res}	0.35	0.25	0.65	0.90
ν_{res}	0.15	0.00	0.10	0.30

6.7 Results

6.7.1 Effect of Mechanical Properties

6.7.1.1 Young's Modulus

The Young's modulus of the reservoir sandstone is varied between 10 GPa and 60 GPa, and the influence on average slip as a function of time is shown in Figures 6.6a and 6.7a. It is found that as reservoir Young's modulus increases, the magnitude of the fault slip typically decreases. For the 10 GPa, 15 GPa, 40 GPa and 60 GPa cases, the number of distinct slip events are 2, 2, 0 and 0 respectively. For the first slip event during the second injection period, the fault slip for the 10 GPa, 15 GPa, 40 GPa and 60 GPa cases is 11.42 cm, 9.34 cm, 0 cm and 0 cm respectively. For the second slip event during the third injection period, the fault slip for the 10 GPa, 15 GPa, 40 GPa and 60 GPa cases is 8.50 cm, 6.85 cm, 0 cm and 0 cm respectively. The Young's modulus therefore has a significant effect on slip: for high reservoir stiffnesses, we can expect the fault to be completely stable, whereas for low reservoir stiffnesses substantial motion could be expected with these injection rates and properties.

The contact traction, fault aperture, and fault slip at each node on the fault surface for the four different cases are shown in Figures 6.8 and 6.9 respectively. Prior to the fault slipping, the contact tractions and fault aperture remain fairly uniform, but a sudden change in contact traction and a sudden increase in aperture is observed at the time of the events. Figure 6.8 shows that as the Young's modulus increases, the magnitude of the contact traction increases. Figure 6.8 shows that prior to the event, as the Young's modulus increases the fault aperture increases, with the fault becoming progressively more open. However, it is also noted that as the Young's modulus increases, the change in the average fault aperture between the time step before and at the slip event decreases, and the aperture after the event decreases for increasing Young's modulus. The larger increases in fault aperture reflect a larger reduction in normal contact tractions. As the contact between the two fault surface is reduced, the greater propensity there is for the fault to slip tangentially (Figure 6.9) as there is less friction between

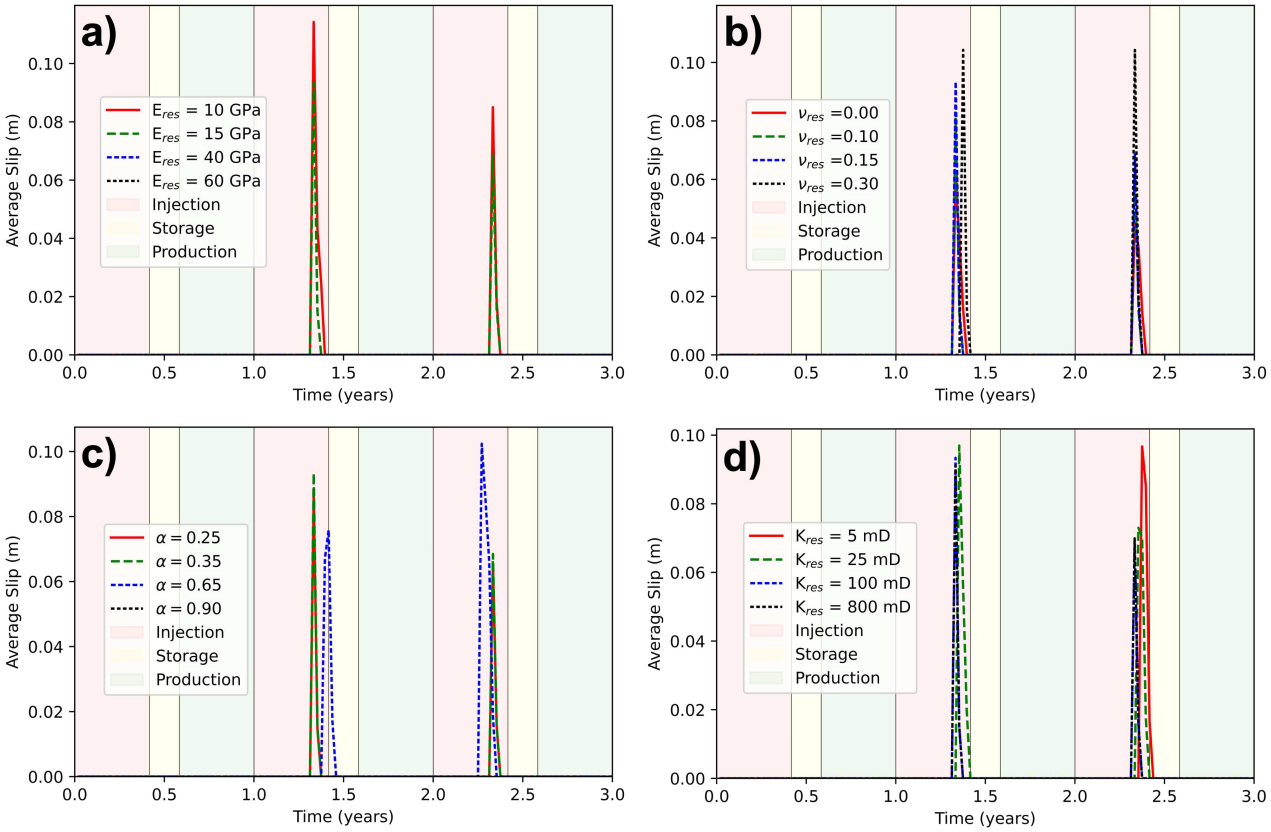


Figure 6.6: Average slip as a function of operation time for four cases of varying reservoir (a) Young's modulus, (b) Poisson's ratio, (c) Biot coefficient and (d) permeability. Zoomed views of the slip peaks can be found in Figure 6.7.

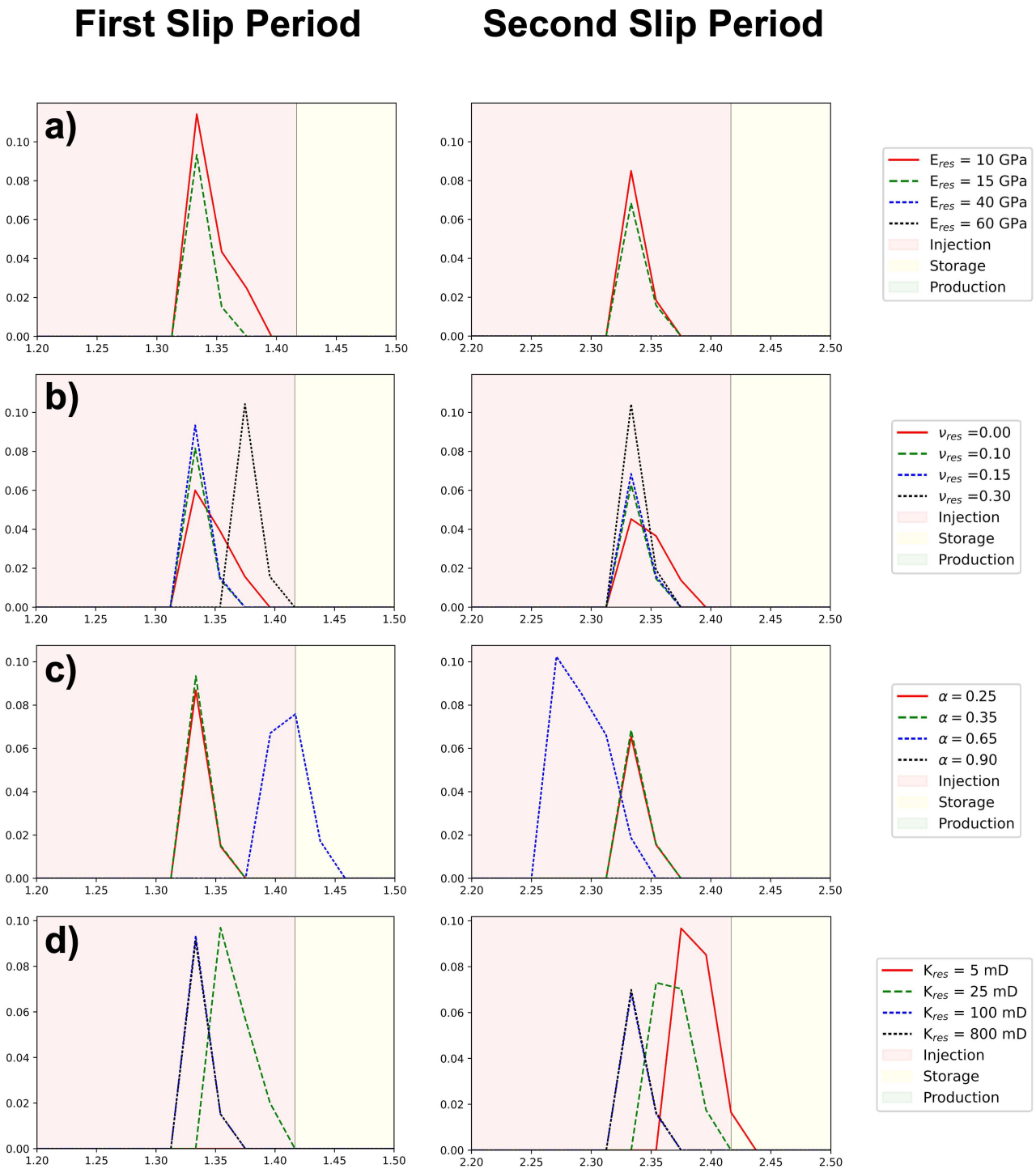


Figure 6.7: Zoomed views of the two distinct slip periods as a function of operation time from Figure 6.6 for four cases of varying reservoir (a) Young's modulus, (b) Poisson's ratio, (c) Biot coefficient and (d) permeability.

the two fault surfaces. In the cases with a reservoir Young's modulus of 40 GPa and 60 GPa, there is no change in the fault aperture (Figure 6.8). This is reflected in the fact that no change in the contact traction is observed (Figure 6.8). The contact traction is large and supplied by all normal traction which keeps the fault closed and locked, thus no change in tangential traction is observed.

Furthermore, examining the stress-strain state at the time of slip, the strain induced in the reservoir unit increases significantly as the Young's modulus decreases (Figure 6.10). For the 40 GPa and 60 GPa case, no strain is induced in the reservoir, and the lack of elastic deformation means that the fault geometry is not influenced, thus it is no surprise we observe no slip. Increased effective strain correlates with increased fault slip.

Taking into account Equations 3.11 and 3.12, and assuming that all the slip is released instantaneously, the upper bound for the moment magnitude of the potential induced seismicity for the first slip event in the 10 GPa and 15 GPa cases is 3.50 and 3.56 respectively. Therefore, despite the fault slip increasing as Young's modulus decreases, the maximum potential seismicity decreases slightly as Young's modulus decreases, below 40 GPa, above which no slip occurs. This is because the decrease in the rigidity modulus as Young's modulus decreases, outweighs the small-to-moderate increase in slip as Young's modulus decreases.

6.7.1.2 Poisson's ratio

The Poisson's ratio of the reservoir sandstone is varied between 0.00 and 0.30, and the influence on average slip as a function of time is shown in Figures 6.6b and 6.7b. It is found that as reservoir Poisson's ratio increases, fault slip increases. For the first slip event during the second injection period, the fault slip for the 0.00, 0.10, 0.15 and 0.30 cases is 6.00 cm, 8.16 cm, 9.34 cm and 11.38 cm respectively. For the second slip event during the third injection period, the fault slip for the 0.00, 0.10, 0.15 and 0.30 cases is 4.53 cm, 6.29 cm, 6.85 cm and 10.43 cm respectively. The Poisson's ratio therefore has a significant effect on slip: for higher reservoir Poisson's ratio, we can expect nearly double the fault slip in the 0.30 case than the 0.00 case.

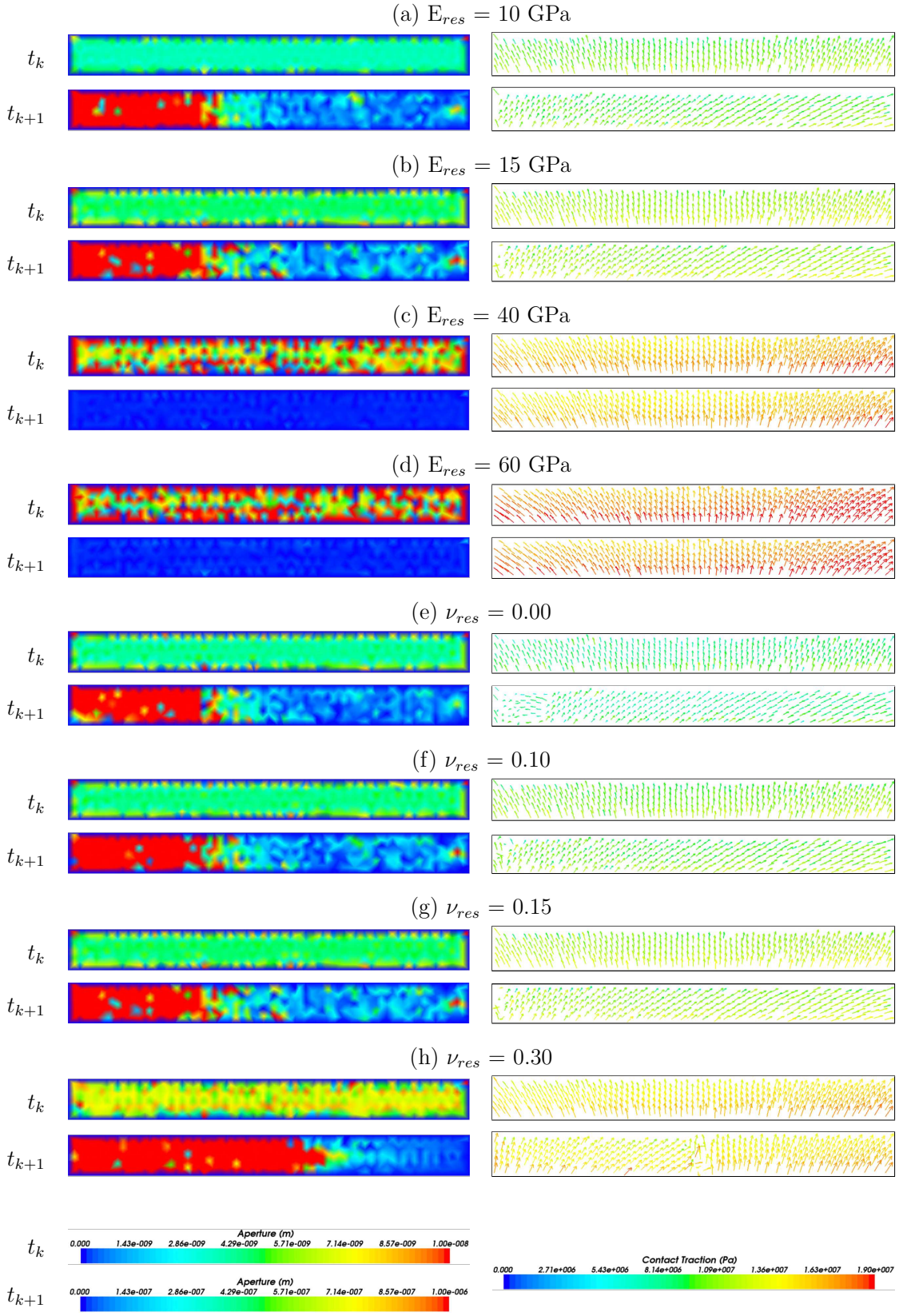


Figure 6.8: The fault aperture (left) and contact traction (right) one time step before (t_k) and after (t_{k+1}) the time of peak slip for the first slip event during the second injection period for four cases of varying reservoir (a-d) Young's modulus and (e-h) Poisson's ratio.

The contact traction along the fault, the fault aperture and the fault slip at each node on the fault surface for the four different cases are shown in Figures 6.8, 6.8 and 6.9 respectively. Figure 6.8 shows that as Poisson's ratio increases the magnitude of the contact traction also increases. Figure 6.8 shows that as the Poisson's ratio increases the fault aperture prior to the slip event increases slightly, with the fault becoming more open with higher Poisson's ratio. As the Poisson's ratio increases, especially beyond $\nu = 0.15$, the fault aperture after the slip event increases. A larger portion of fracture surface area opens in the $\nu = 0.30$ case, not just the portion of the fault closest to the injection wellbore. Again, the larger change in fault aperture mirrors the larger fault slip. The larger the sudden increase in fault aperture, the larger the sudden reduction in normal contact traction, and the greater propensity the fault has to slip tangentially. Interestingly, although the magnitude of the fault slip is the largest in the 0.30 case, the fault area of which the slip occurs is also the smallest. For approximately half of the fault, there is no tangential fault slip (Figure 6.9) because the contact traction at this point is fully supplied by normal contact traction with no tangential component (Figure 6.8) and the fault remains effectively closed in this zone.

Taking into account Equations 3.11 and 3.12, and assuming that all the slip is released instantaneously, the upper bound for the moment magnitude of the potential induced seismicity for the first slip event in the 0.00, 0.10, 0.15 and 0.30 cases respectively, is as follows: 3.47, 3.53, 3.56, and 3.38. Therefore, unlike the trend in the fault slip, the maximum potential seismicity does not progressively increase as Poisson's ratio increases. In fact, the magnitude of the maximum potential seismicity was the smallest in the highest Poisson's ratio case ($\nu = 0.30$), owing to the combination of the reduced slip area (Figure 6.9) and the reduced rigidity modulus of the fault, and was largely insensitive in the range 0.00 to 0.15.

6.7.1.3 Biot Coefficient

The Biot coefficient of the reservoir sandstone is varied between 0.25 and 0.90, and the influence on average slip as a function of time is shown in Figures 6.6c and 6.7c. A systematic change in the slip with Biot coefficient is not found. For the first slip event during the second injection

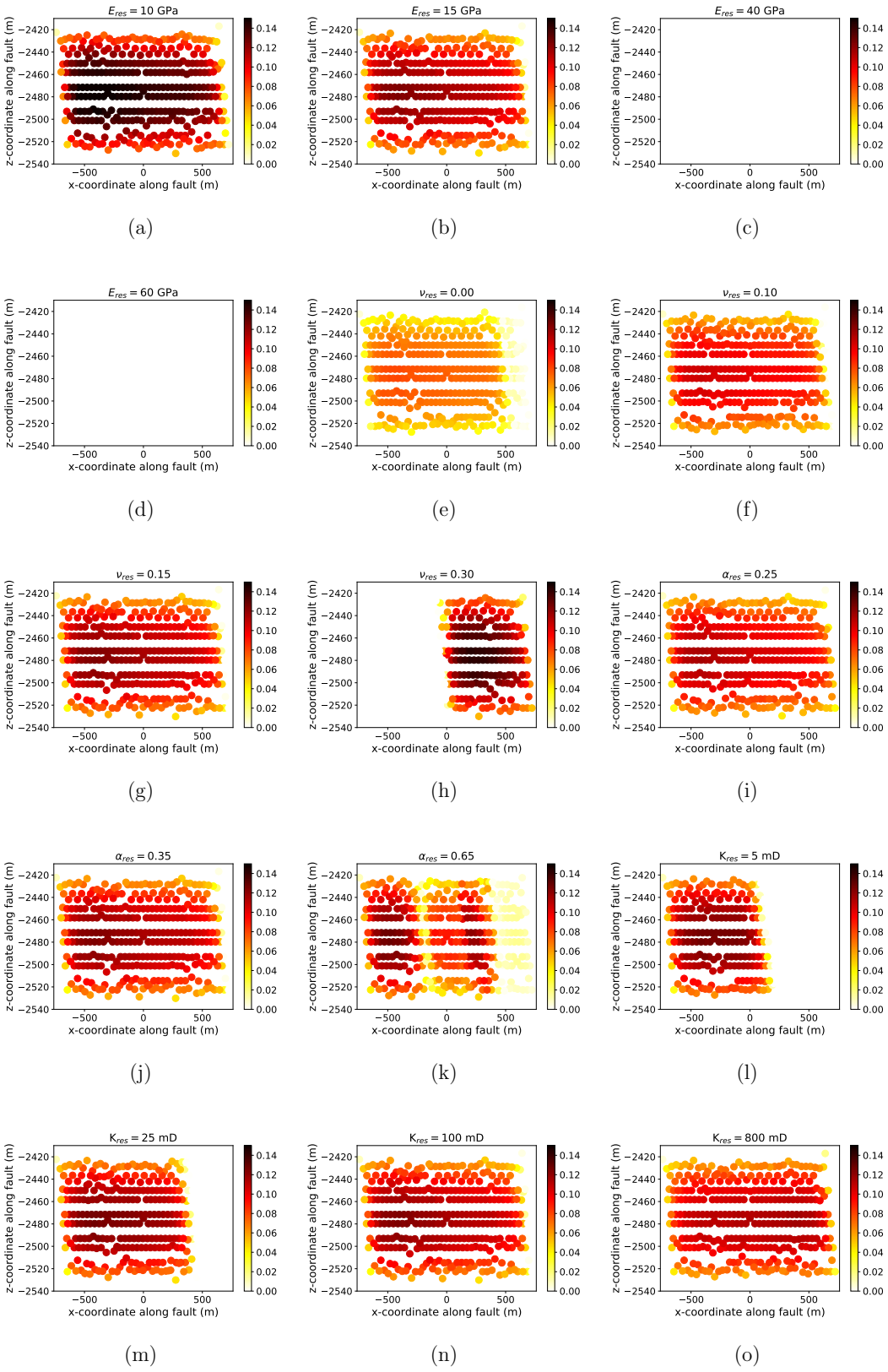
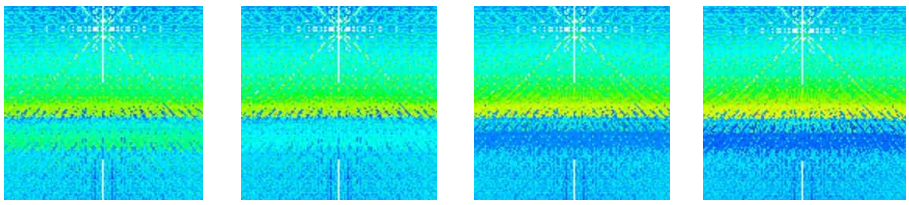
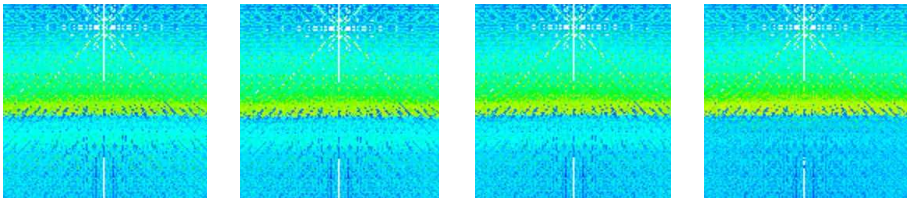


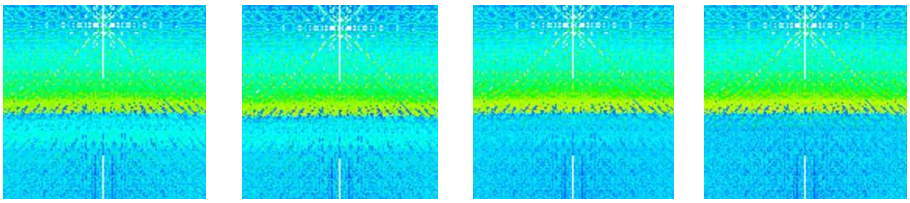
Figure 6.9: The tangential fault slip at each node at the time of peak slip for the first slip event during the second injection period for cases of varying reservoir (a-d) Young's modulus, (e-h) Poisson's ratio, (i-k) Biot coefficient and (l-o) permeability.



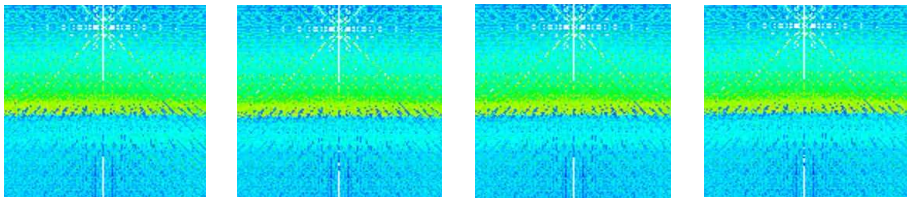
E_{res} (a) 10 GPa (b) 15 GPa (c) 40 GPa (d) 60 GPa



ν_{res} (e) 0.00 (f) 0.10 (g) 0.15 (h) 0.30



α_{res} (i) 0.25 (j) 0.35 (k) 0.65 (l) 0.90



K_{res} (m) 5 mD (n) 25 mD (o) 100 mD (p) 800 mD

Figure 6.10: The effective strain over a vertical interval containing the anticlinal caprock and reservoir units at the time of peak slip for the first slip event during the second injection period for cases of varying reservoir (a-d) Young's modulus, (e-h) Poisson's ratio, (i-l) Biot coefficient and (m-p) permeability. Dark green denotes high strain, dark blue denotes low strain.

period, the fault slip for the 0.25, 0.35, 0.65 and 0.90 cases is 8.69 cm, 9.34 cm, 7.58 cm and 0 cm respectively. For the second slip event during the third injection period, the fault slip for the 0.25, 0.35, 0.65 and 0.90 cases is 6.55 cm, 6.85 cm, 10.24 cm and 0 cm respectively. For the first event, it can generally be observed that as Biot coefficient increases, the magnitude of the peak slip decreases: the slip is almost identical in the 0.25 and 0.35 cases, but decreases considerably by the 0.65 case, and then continues to decrease where the fault is completely stable by the 0.90 case. However, this trend is not repeated for the second event. At values of the Biot coefficient less than 0.65, the fault slip is not significantly dependent on the Biot coefficient. However, in the range 0.65 to 0.90, the Biot coefficient significantly controls the fault slip.

The contact traction and the fault aperture, the fault slip at each node on the fault surface, the strain, and the stress state for the four different cases is shown in Figures 6.11, 6.9, 6.11, 6.10 and 6.12, respectively. Figure 6.11 shows that as Biot coefficient increases, the magnitude of the contact traction also increases, although not significantly until the 0.90 case. Figure 6.11 shows that generally as the Biot coefficient increases the fault aperture prior to the slip event increases, with the fault becoming progressively more open with higher Biot coefficient. As the Biot coefficient increases in the range 0.25 to 0.65 the fault aperture after the slip event increases; however, above 0.65 the fault aperture remains closed. The slips at each individual node (Figure 6.9) in the 0.65 case are more varied than that observed in the 0.25 and 0.35 cases, with the distribution of slip across the fault surface being less smooth. Furthermore, in the 0.65 case, it is observed that a region in which tangential slip is low, near the middle of the fault and near the right side (Figure 6.9) has developed relative to the 0.25 and 0.35 cases. Therefore, it is likely that at values of the Biot coefficient between 0.65 and 0.90, the average fault slip will continue to decrease as these regions of the fault surface that are in stick grow, until a value of the Biot coefficient is reached, in which the entire fault surface area is in stick such as the 0.90 case.

Taking into account Equations 3.11 and 3.12, and assuming that all the slip is released instantaneously, the upper bound for the moment magnitude of the potential induced seismicity for the first slip event in the 0.25, 0.35, and 0.65 cases respectively, is as follows: 3.53, 3.56, and

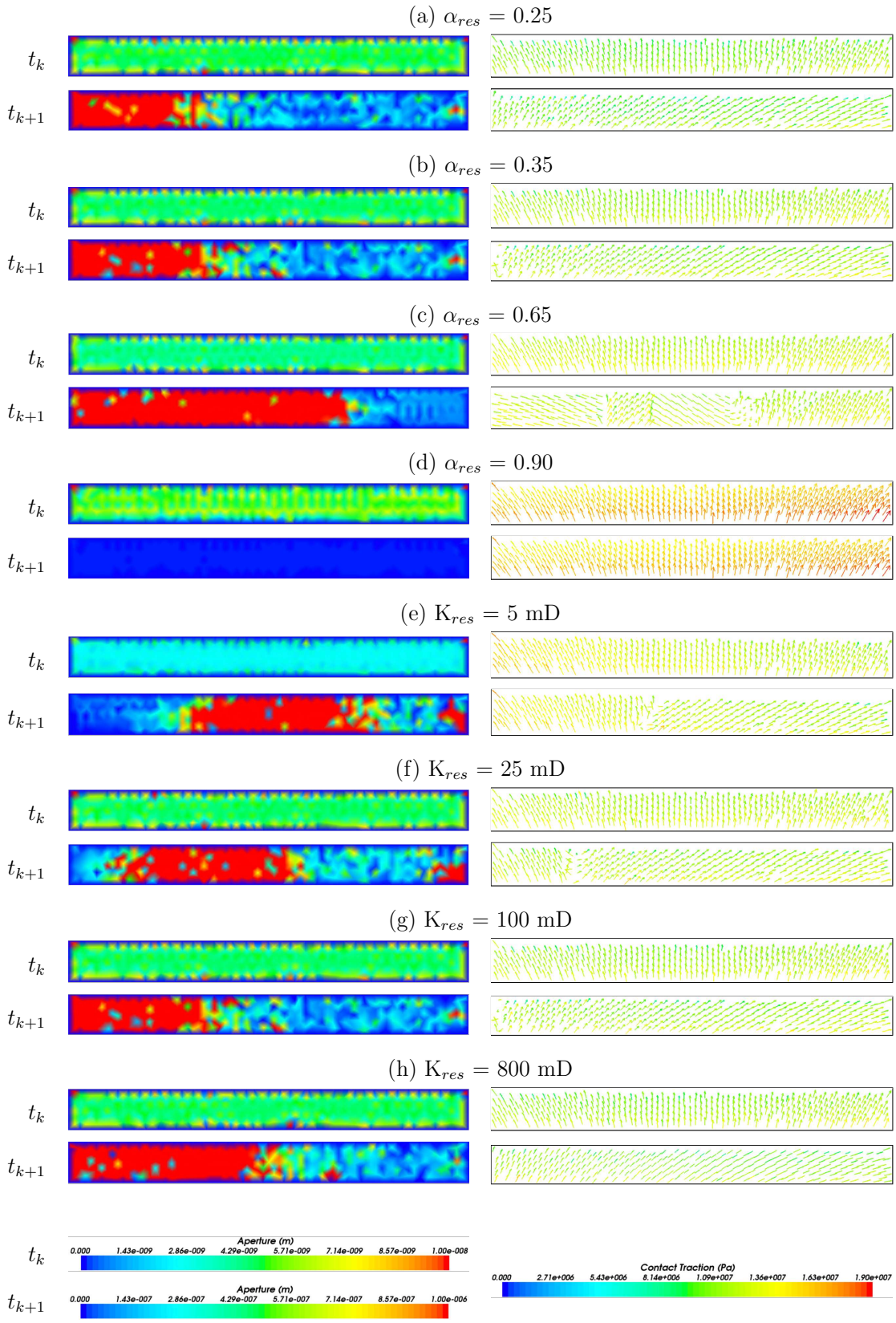


Figure 6.11: The fault aperture (left) and contact traction (right) one time step before (t_k) and after (t_{k+1}) the time of peak slip for the first slip event during the second injection period for four cases of varying reservoir (a-d) Biot coefficient and (e-h) permeability.

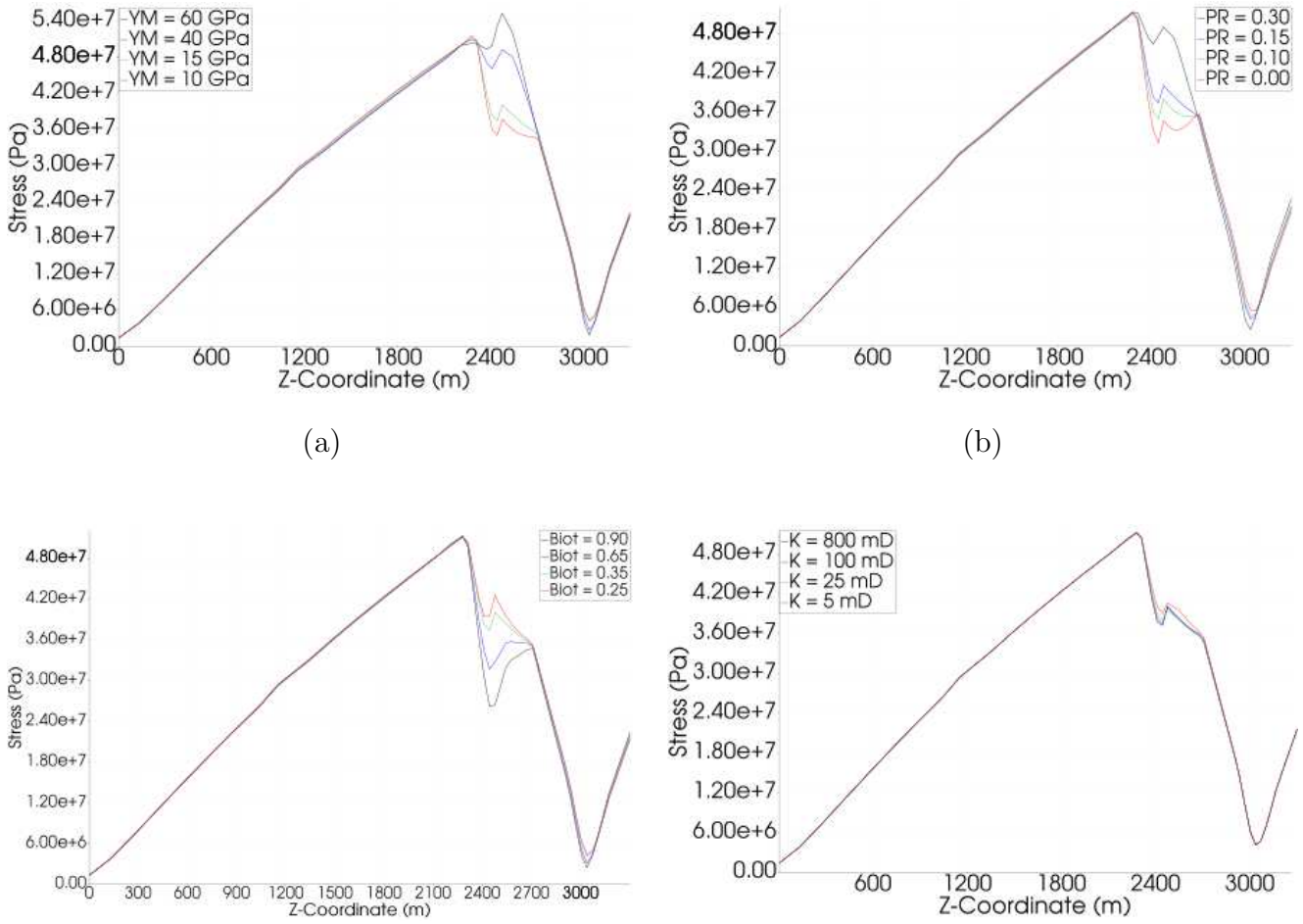


Figure 6.12: Plots of stress along the mid-depth of the reservoir unit in the y-direction for four cases of varying reservoir (a) Young's modulus, (b) Poisson's ratio, (c) Biot coefficient and (d) permeability.

3.42. Therefore, as with the fault slip, generally the maximum potential seismicity decreases slightly as Biot coefficent increases. The strain in the reservoir unit is seen to be similar in the 0.25 and 0.35 cases, in which the slip is very similar, but the strain decreases as Biot coefficient increases above 0.35, reflecting the decreased fault slip with increasing Biot coefficient (Figure 6.10).

6.7.1.4 Permeability

The permeability of the reservoir sandstone is varied between 5 and 800 mD, and the influence on average slip as a function of time is shown in Figures 6.6d and 6.7d. It is found that for the reservoir permeabilities tested, the magnitude of the induced fault slip is similar. For the first slip event during the second injection period, the fault slip for the 5 mD, 25 mD, 100 mD and 800 mD cases is 9.67 cm, 9.70 cm, 9.34 cm and 9.12 cm respectively. A small trend is seen here where as permeability increases the magnitude of the peak fault slip decreases. For the second slip event during the third injection period, the fault slip for the 25 mD, 100 mD and 800 mD cases is 7.30 cm, 6.85 cm, and 6.99 cm respectively. The second slip event for the 5 mD case did not occur by the end of the 3-year study period. The permeability therefore has no major effect on the magnitude of the slip, although it is generally seen that as the permeability increases, the magnitude of the average fault slip decreases slightly. The permeability does have an effect on the time in which the slip occurs. The higher the permeability of the reservoir unit, the earlier the induced slip occurs. This is because the fault pressure at a given time varies depending on the permeability. It takes longer for the fluid front from the injection wellbore to reach the fault, and then leak-off into the fault, when the permeability is smaller. The 800 mD and 100 mD cases coincide temporally, although one would expect the 800 mD case to have slipped earlier than the 100 mD case. The only reason this does not occur is because of the time step size, which is large enough to mask the small time difference. As such, the slip appears to be at identical times in the 100 and 800 mD cases, although if very small time steps were feasible, it would be initiated very slightly before (a few days). The slip event is only significantly delayed when the intrinsic rock permeability approaches the fracture permeability which is 1 mD. Therefore, when the intrinsic permeability is well in excess of the fracture

permeability (the 800 mD, 100 mD and 25 mD cases), the delay in the slip is minor but, when the intrinsic permeability is close to the fracture permeability (the 5 mD case), the slip event is significantly delayed. Therefore, the fracture permeability is likely to be a key parameter affecting the timing of the seismicity.

The contact traction along the fault, the fault aperture, the fault slip at each node on the fault surface, the strain and the stress state for the four different cases is shown in Figures 6.9, 6.10, 6.11, and 6.12, respectively. The contact traction, aperture and strains show no significant differences in the 25 mD, 100 mD and 800 mD cases, and in this case, the magnitude of the fault slip is not significantly impacted. The slip at each individual node across the fault surface (Figure 6.9) shows an interesting trend, as the reservoir permeability decreases, the proportion of the fault in stick increases and the proportion of the fault in slip decreases. Taking into account Equations 3.11 and 3.12, and assuming that all the slip is released instantaneously, the upper bound for the moment magnitude of the potential induced seismicity for the first slip event in the 5 mD, 25 mD, 100 mD and 800 mD cases is 3.42, 3.49, 3.56 and 3.55.

6.7.2 Effect of Fault Properties

6.7.2.1 Friction Coefficient

The friction coefficient of the fault in the reservoir sandstone was varied between 0.20 and 0.99, and the influence on average slip as a function of time is shown in Figures 6.15a and 6.16a. It was found that as the fault friction coefficient increased, the magnitude of the fault slip increased. For the 0.20, 0.50, 0.75 and 0.90 cases, the number of distinct slip events were 2, 2, 3 and 3 respectively, implying that as fault friction coefficient increases as does the number of distinct slip events within the tested range of 0.20-0.99. For the first slip event during the first injection period, the fault slip for the 0.75 and 0.90 cases was 22.71 cm and 21.93 cm respectively. For the second slip event during the second injection period, the fault slip for the 0.20, 0.50, 0.75 and 0.90 cases was 2.73 cm, 9.34 cm, 12.85 cm and 13.51 cm respectively. For the third slip event during the third injection period, the fault slip for the 0.20, 0.50, 0.75 and

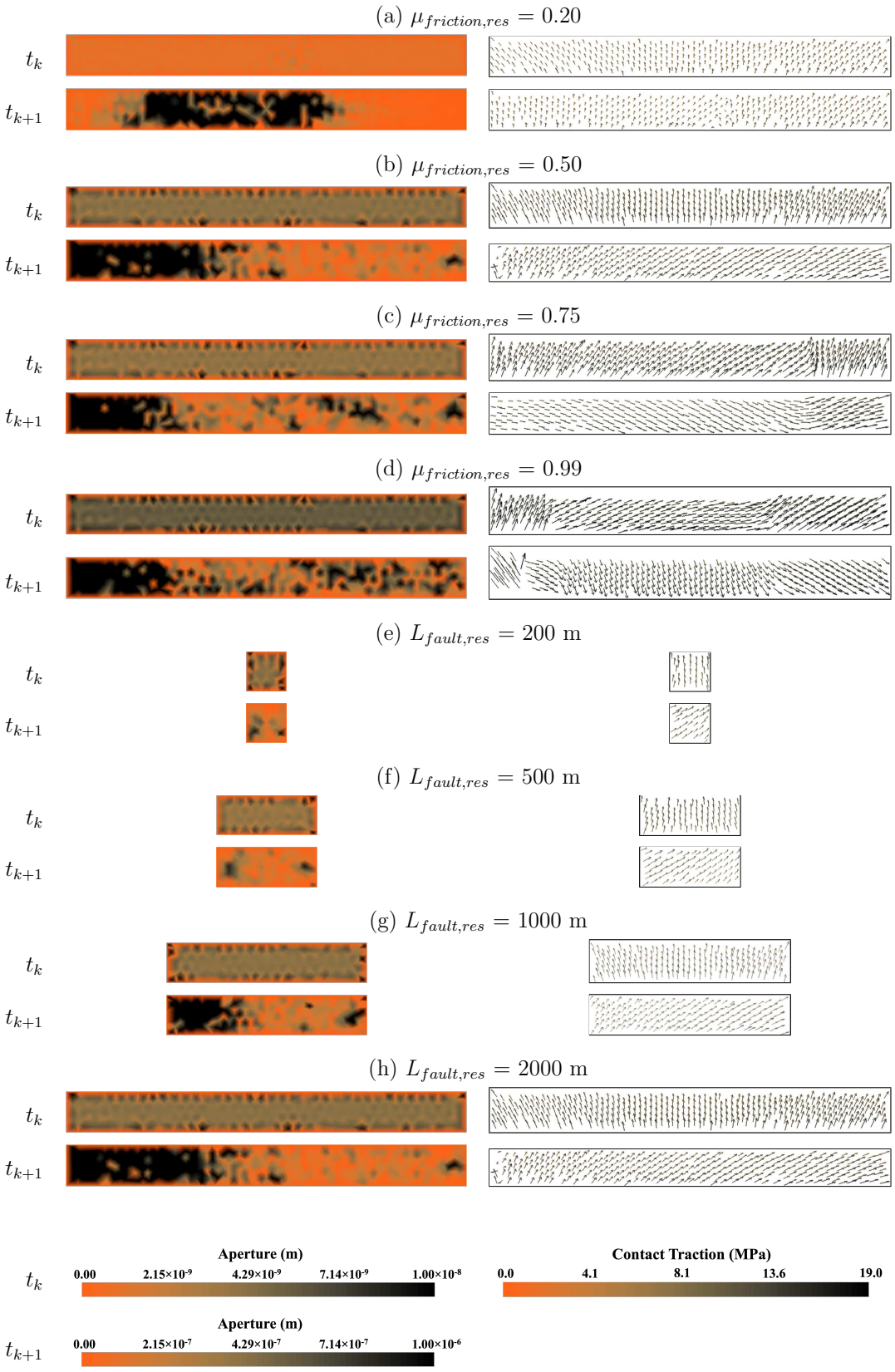


Figure 6.13: The fault aperture (left) and contact traction (right) one time step before (t_k) and after (t_{k+1}) the time of peak slip for the first slip event during the second injection period for four cases of varying fault (a-d) friction coefficient and (e-h) length. The length of the vectors in the contact traction figures are scaled according to magnitude in the same way the color bar functions: the longer the vector, the larger the traction.

0.90 cases was 3.16 cm, 6.85 cm, 11.30 cm and 15.94 cm respectively.

The contact traction along the fault, the fault aperture and the fault slip at each node on the fault surface for the four different cases are shown in Figures 6.13 and 6.20 respectively. A sudden change in the directions of the contact tractions and a sudden increase in aperture was observed at the time of the events. Figure 6.13 shows that as the friction coefficient increased, the magnitude of the contact traction increased. Figure 6.13 shows that after the event, as the friction coefficient increased, the fault aperture broadly increased, with the fault becoming progressively more open. It was also seen that the fault aperture after the slip event was on average slightly larger across the fault as the friction coefficient increased. The reduction in the magnitude of the contact traction before the slip event to at the slip event was largest in the 0.99 case, followed by the 0.75 case, with minimal change in the 0.20 and 0.50 cases. In the 0.20 case, there was minimal change in aperture (except in the middle of the fault) and this was reflected in the fact that there was no change in contact traction in these areas. Also in the 0.20 case, the slip was not ubiquitous across the whole fault as it was in the other cases (Figure 6.20), with half of the fault locked with no slip.

The first slip event during the first injection period (Figure 6.15a) only occurs in the high friction coefficient cases (0.75 and 0.99) but not in the low-intermediate cases (0.20 and 0.50). In the 0.75 and 0.99 cases, the magnitude of the contact tractions are considerably higher than in the 0.20 and 0.50 cases, and the resultant apertures are much larger. In the 0.75 and 0.99 cases, the increase in aperture after the event relative to before was up to 3 orders of magnitude, whereas no change was seen in the 0.20 and 0.50 cases.

Taking into account Equations 3.11 and 3.12, and assuming that all the slip is released instantaneously, the upper bound for the moment magnitude of the potential induced seismicity for the first slip event in the 0.75 and 0.99 cases was 3.72 and 3.67 respectively. For the second slip event in the 0.20, 0.50, 0.75 and 0.99 cases, it was 3.01, 3.56, 3.65 and 3.66 respectively.

6.7.2.2 Fault Permeability

The initial fault permeability in the reservoir sandstone was varied between 0.001 mD and 10,000 mD, and the influence on average slip as a function of time is shown in Figures 6.15b and 6.16b. It was found that the fault slip was generally insensitive to the fault permeability, except in the 0.001 mD case where the fault permeability was many (five) orders of magnitude less than the reservoir matrix permeability. For the first slip event during the second injection period, the fault slip for the 1 mD, 100 mD and 10,000 mD cases was 9.34 cm, 8.85 cm and 9.32 cm. For the second slip event during the third injection period, the fault slip for the 1 mD, 100 mD and 10,000 mD cases was 6.85 cm, 7.23 cm and 7.16 cm. No slip occurred in the 0.001 mD case. No systematic change in fault slip as fault permeability increased was found.

The contact traction along the fault, the fault aperture and the fault slip at each node on the fault surface for the four different cases are shown in Figures 6.24 and 6.20 respectively. A sudden change in the directions of the contact tractions and a sudden increase in aperture was observed at the time of the events. Figure 6.24 shows that the magnitude of the contact tractions are very similar in the 1 mD, 100 mD and 10,000 mD cases, but in the 0.001 mD case where no slip occurs, they are substantially higher. Figure 6.24 shows that the fault aperture after the slip event was larger across the fault on average as the fault permeability increased.

Taking into account Equations 3.11 and 3.12, and assuming that all the slip is released instantaneously, the upper bound for the moment magnitude of the potential induced seismicity for the first slip event in the 1 mD, 100 mD and 10,000 mD cases is 3.56, 3.54 and 3.56 respectively.

6.7.2.3 Fault Length

The length of the fault in the reservoir sandstone was varied between 200 m and 2000 m, and the influence on average slip as a function of time is shown in Figures 6.15c and 6.16c. It was found that as the fault length increased, the magnitude of the fault slip increased. For the first slip event during the second injection period, the fault slip for the 200 m, 500 m, 1000 m and 2000 m cases was 4.23 cm, 7.29 cm, 8.54 cm and 9.34 cm respectively. For the second slip event

during the third injection period, the fault slip for the 200 m, 500 m, 1000 m and 2000 m cases was 3.64 cm, 5.81 cm, 6.61 cm and 6.85 cm respectively.

The contact traction along the fault, the fault aperture and the fault slip at each node on the fault surface for the four different cases are shown in Figures 6.13 and 6.20 respectively. A sudden change in the directions of the contact tractions, where tangential slip was induced, and a sudden increase in aperture was observed at the time of the events. Figure 6.13 shows that as the fault length increased, the average fault aperture increased. In the 1000 m and 2000 m cases large increases in fault aperture were seen, relative to before the event, of up to three orders of magnitude, whereas in the 200 m and 500 m cases, the fault aperture increases less than 2 orders of magnitude.

At the depths of the reservoir unit, the stress decreased slightly as fault length increased (Figure 6.7.3.2c).

Taking into account Equations 3.11 and 3.12, and assuming that all the slip is released instantaneously, the upper bound for the moment magnitude of the potential induced seismicity for the first slip event in the 200 m, 500 m, 1000 m and 2000 m cases was 2.66, 3.08, 3.33 and 3.56 respectively.

6.7.2.4 Fault Dip

The dip of the fault in the reservoir sandstone was varied between 30° and 80°, and the influence on average slip as a function of time is shown in Figures 6.15e and 6.16e. In each of the fault dip cases, the fault has a strike of 0°. No systematic change in fault slip was found with increasing fault dip. For the 30.0°, 45.0°, 63.4° and 80.0° cases, the number of distinct slip events were 2, 3, 2 and 2 respectively, implying that fault slippage events were promoted when the fault dip was 45°. In fact, for the 45° case, the first slip event shortly after the initial injection had the largest magnitude of any slip event for all of the dip cases, with 18.17 cm of slip. No slippage was seen at this time for any of the other dip cases. For the slip event during the second injection period, the fault slip for the 30.0°, 45.0°, 63.4° and 80.0° m cases was 14.80 cm, 5.20

cm, 9.34 cm and 1.74 cm respectively. For the slip event during the third injection period, the fault slip for the 30.0°, 45.0°, 63.4° and 80.0° m cases was 12.83 cm, 5.14 cm, 6.85 cm and 1.70 cm respectively. Therefore, fault dip had a very significant effect on the fault slip.

The contact traction along the fault, the fault aperture and the fault slip at each node on the fault surface for the four different cases are shown in Figures 6.14 and 6.20 respectively. A sudden change in the directions of the contact tractions, where tangential slip was induced, and a sudden increase in aperture was observed at the time of the events. Figure 6.14 shows that in the largest dip case of 80.0°, the contact traction along the fault was far lower than the other cases, which correlates with the lowest observed slip. On average, the fault aperture across the fault surface area increased as fault dip increased. Broadly, the magnitude of the contact traction decreased as fault dip increased, although the contact traction was very slightly larger in the 45.0° case than the 63.4° case.

At the depths of the reservoir unit, the stress was largest in the largest fault dip case of 80.0° (Figure 6.7.3.2d), suggesting that the normal stress acting on the fault was largest when the fault had a dip of 80.0°. This reinforces the reduced slip seen in the 80.0° case.

Taking into account Equations 3.11 and 3.12, and assuming that all the slip is released instantaneously, the upper bound for the moment magnitude of the potential induced seismicity for the slip event during the second injection period in the 30.0°, 45.0°, 63.4° and 80.0° cases was 3.69, 3.39, 3.56, and 3.07, respectively. The upper bound for the moment magnitude of the potential induced seismicity for the first event in the 45.0° case was 3.75.

6.7.2.5 Fault Strike

The strike of the fault in the reservoir sandstone was varied between 0° and 135°, and the influence on average slip as a function of time is shown in Figures 6.15d and 6.16d. No systematic change in fault slip was found with increasing fault strike. For the slip event during the second injection period, the fault slip for the 0°, 45°, 90° and 135° m cases was 9.34 cm, 9.34 cm, 7.97 cm and 9.46 cm, respectively. For the slip event during the third injection period, the

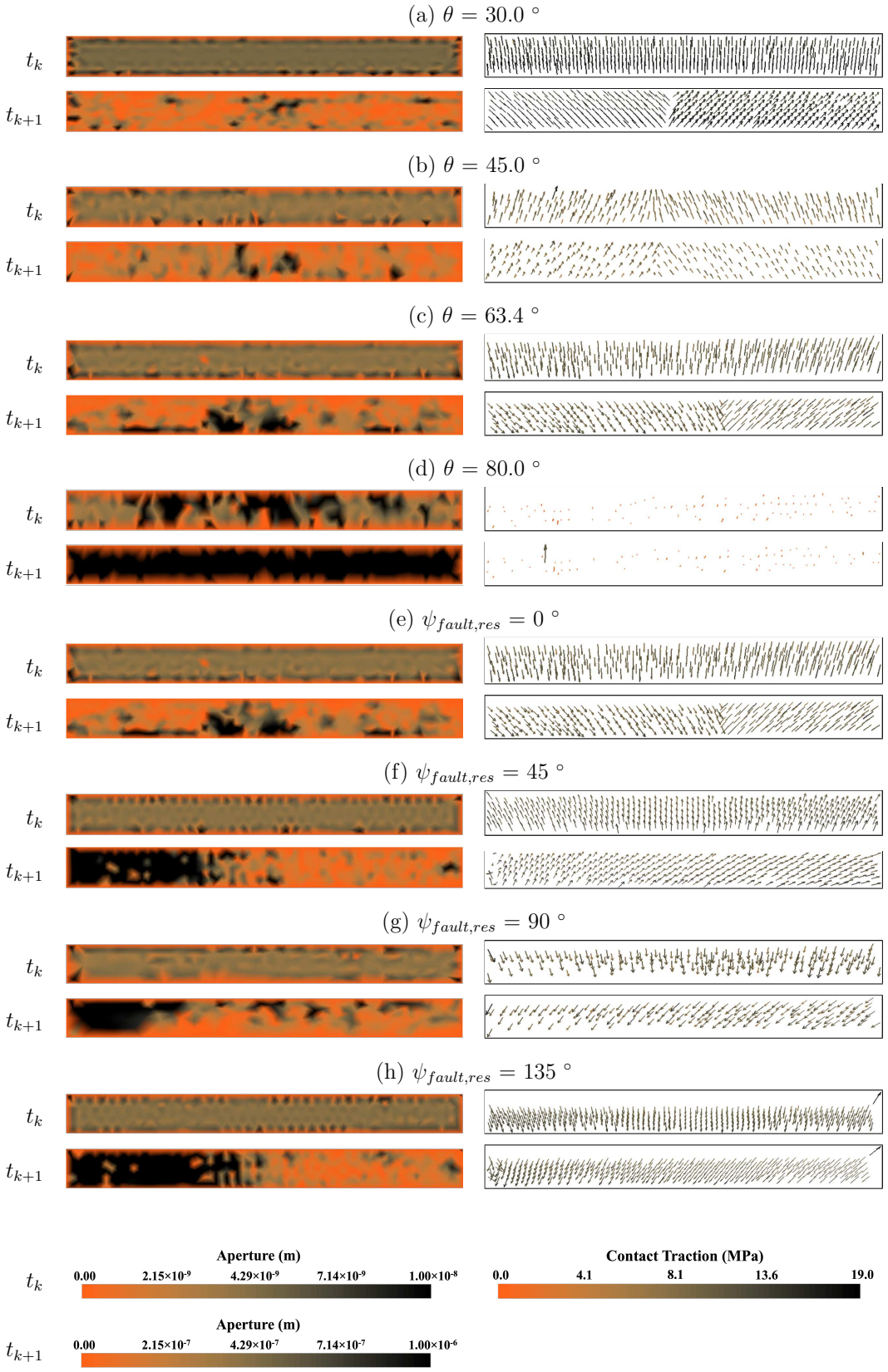


Figure 6.14: The fault aperture (left) and contact traction (right) one time step before (t_k) and after (t_{k+1}) the time of peak slip for the first slip event during the second injection period for four cases of varying fault (a-d) dip and (e-h) strike. The length of the vectors in the contact traction figures are scaled according to magnitude in the same way the color bar functions: the longer the vector, the larger the traction.

fault slip for the 0°, 45.0°, 90° and 135° m cases was 6.85 cm, 6.85 cm, 5.76 cm and 8.43 cm, respectively. Therefore, fault strike has a small influence on the magnitude of the fault slip. Slip was minimized when the fault was oriented in the y-direction (90°).

The contact traction along the fault, the fault aperture and the fault slip at each node on the fault surface for the four different cases are shown in Figures 6.14 and 6.20 respectively. A sudden change in the directions of the contact tractions, where tangential slip was induced, and a sudden increase in aperture was observed at the time of the events. Figure 6.14 shows little difference in the magnitude of the contact tractions 6.14 between the cases, which supports the lack of significant difference in observed slip. However, it can be seen that the contact traction in the 90° was slightly lower than the other cases, which correlates with the fact that the 90° case had the lowest slip. The effective stress profiles (Figure 6.7.3.2e) are also all very similar irrespective of fault strike, which further elucidates the lack of significant influence strike has on fault slip.

Taking into account Equations 3.11 and 3.12, and assuming that all the slip is released instantaneously, the upper bound for the moment magnitude of the potential induced seismicity for the slip event during the second injection period in the 0°, 45°, 90° and 135° m cases was 3.56, 3.56, 3.51, and 3.56, respectively. Therefore, the maximum magnitude of the potential induced seismicity was largely insensitive to changes in fault strike.

6.7.3 Effect of Operational Properties

6.7.3.1 Injection Rate

The injection rate into the reservoir sandstone was varied between 2 m^3/s and 30 m^3/s, and the influence on average slip as a function of time is shown in Figures 6.15f and 6.16f. As expected, it was found that as the injection rate increased, the fault slip increased. For the first slip event during the second injection period, the fault slip for the 20 m^3/s and 30 m^3/s cases was 9.34 cm and 12.51 cm respectively. For the second slip event during the third injection period, the fault slip for the 20 m^3/s and 30 m^3/s cases was 6.85 cm and 11.76 cm respectively. There was

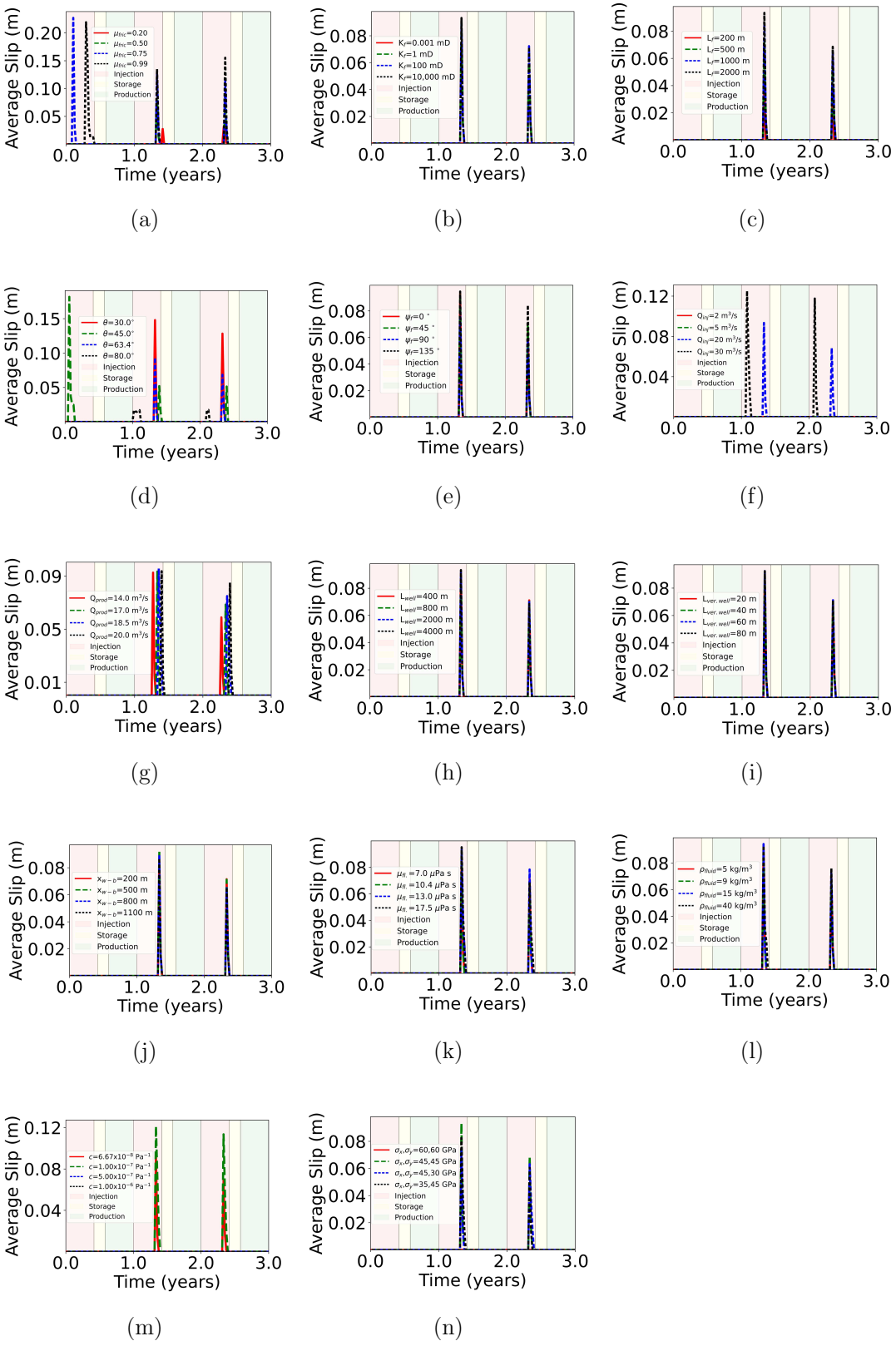
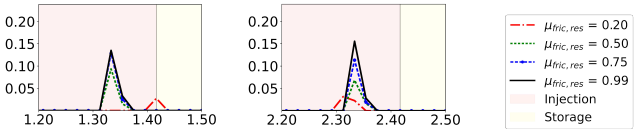
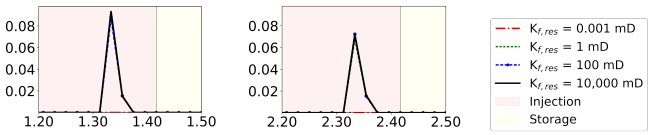


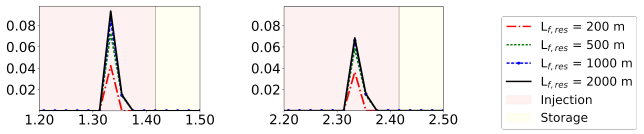
Figure 6.15: Average slip as a function of operation time for four cases of varying (a) fault friction coefficient, (b) fault permeability, (c) fault length, (d) fault dip, (e) fault strike, (f) injection rate, (g) withdrawal rate, (h) horizontal well length, (i) vertical well length, (j) vertical well spacing, (k) hydrogen viscosity, (l) hydrogen density, (m) hydrogen compressibility, and (n) stresses. Zoomed views of the slip in (a)-(g) and (h)-(n) are shown in Figures 6.16 and 6.17, respectively.



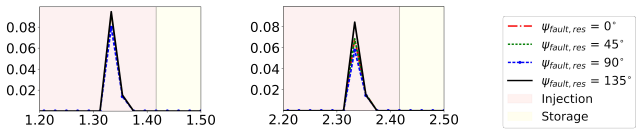
(a)



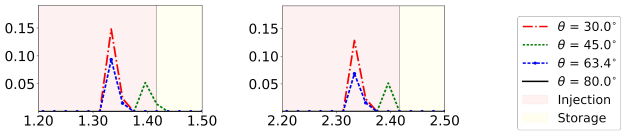
(b)



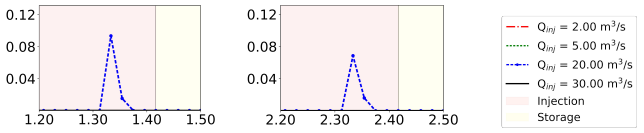
(c)



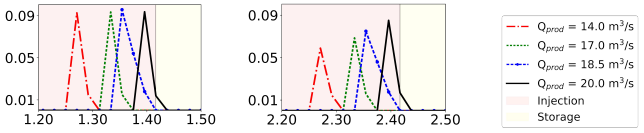
(d)



(e)

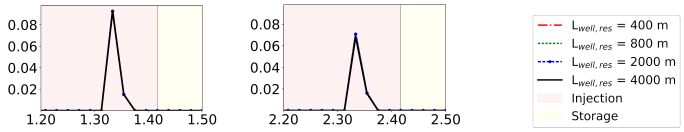


(f)

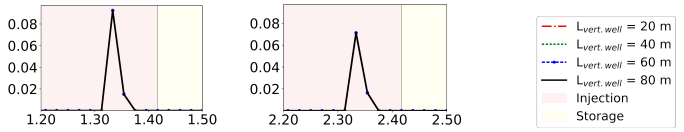


(g)

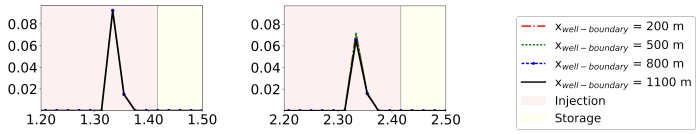
Figure 6.16: Zoomed views of the two main slip periods from Figure 6.15 as a function of operation time for four cases of varying (a) fault friction coefficient, (b) fault permeability, (c) fault length, (d) fault dip, (e) fault strike, (f) injection rate, and (g) withdrawal rate. The left column shows zoomed views of the first slip period and the central column shows zoomed views of the second slip period. Time in years is shown on the x-axes and the average slip in m is shown on the y-axes as in Figure 6.15.



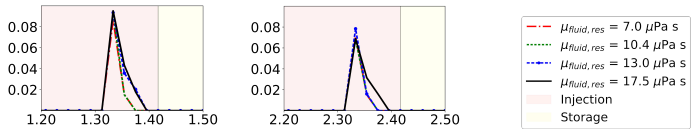
(a)



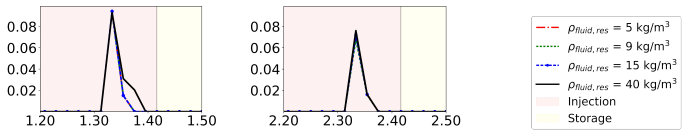
(b)



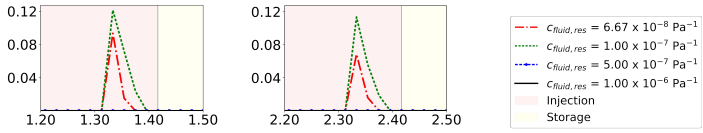
(c)



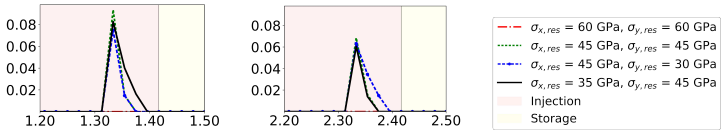
(d)



(e)



(f)



(g)

Figure 6.17: Zoomed views of the two main slip periods from Figure 6.15 as a function of operation time for four cases of varying (h) horizontal well length, (i) vertical well length, (j) vertical well spacing, (k) hydrogen viscosity, (l) hydrogen density, (m) hydrogen compressibility, and (n) stresses. The left column shows zoomed views of the first slip period and the central column shows zoomed views of the second slip period. Time in years is shown on the x-axes and the average slip in m is shown on the y-axes as in Figure 6.15.

no slip induced when the injection rate was 2 m^3/s or 5 m^3/s.

The contact traction along the fault, the fault aperture and the fault slip at each node on the fault surface for the four different cases are shown in Figures 6.18 and 6.20 respectively. A sudden change in the directions of the contact tractions, where tangential slip was induced, and a sudden increase in aperture was observed at the time of the events. Figure 6.18 shows that as the injection rate increased, the contact traction along the fault decreased. Furthermore, the degree to which the traction was dominated by tangential components increased as the injection rate increased, with the contact traction almost fully supplied by high normal contact tractions in the 2.0 m^3/s and 5.0 m^3/s cases, which keeps the fault locked in these cases. Figure 6.18 also shows that the fault aperture increased as injection rate increased.

Taking into account Equations 3.11 and 3.12, and assuming that all the slip is released instantaneously, the upper bound for the moment magnitude of the potential induced seismicity for the first slip event in the 20.0 m^3/s and 30.0 m^3/s cases was 3.56 and 3.64 respectively. No event was triggered in the 2.0 m^3/s or 5.0 m^3/s cases. Therefore, as injection rate increased, the magnitude of the seismic event increased.

6.7.3.2 Withdrawal Rate

The withdrawal rate from the reservoir sandstone was varied between 14 m^3/s and 20 m^3/s, and the influence on average slip as a function of time is shown in Figures 6.15g and 6.16g. Generally, it was found that as withdrawal rate increased, the magnitude of the fault slip increased. For the first slip event, this trend was very small, but for the second event it was more pronounced (Figure 6.7.2.5g). Furthermore, as withdrawal rate increased the time to event initiation was increased. For the first slip event during the second injection period, the fault slip for the 14.0 m^3/s, 17.0 m^3/s, 18.5 m^3/s and 20.0 m^3/s cases was 9.26 cm, 9.34 cm, 9.57 cm and 9.36 cm respectively. For the second slip event during the third injection period, the fault slip for the 14.0 m^3/s, 17.0 m^3/s, 18.5 m^3/s and 20.0 m^3/s cases was 5.89 cm, 6.85 cm, 7.49 cm and 8.50 cm respectively. Essentially, the larger the withdrawal rate, the larger the fault slip during the injection periods. However, the withdrawal rate was not a strong control on the fault slip with

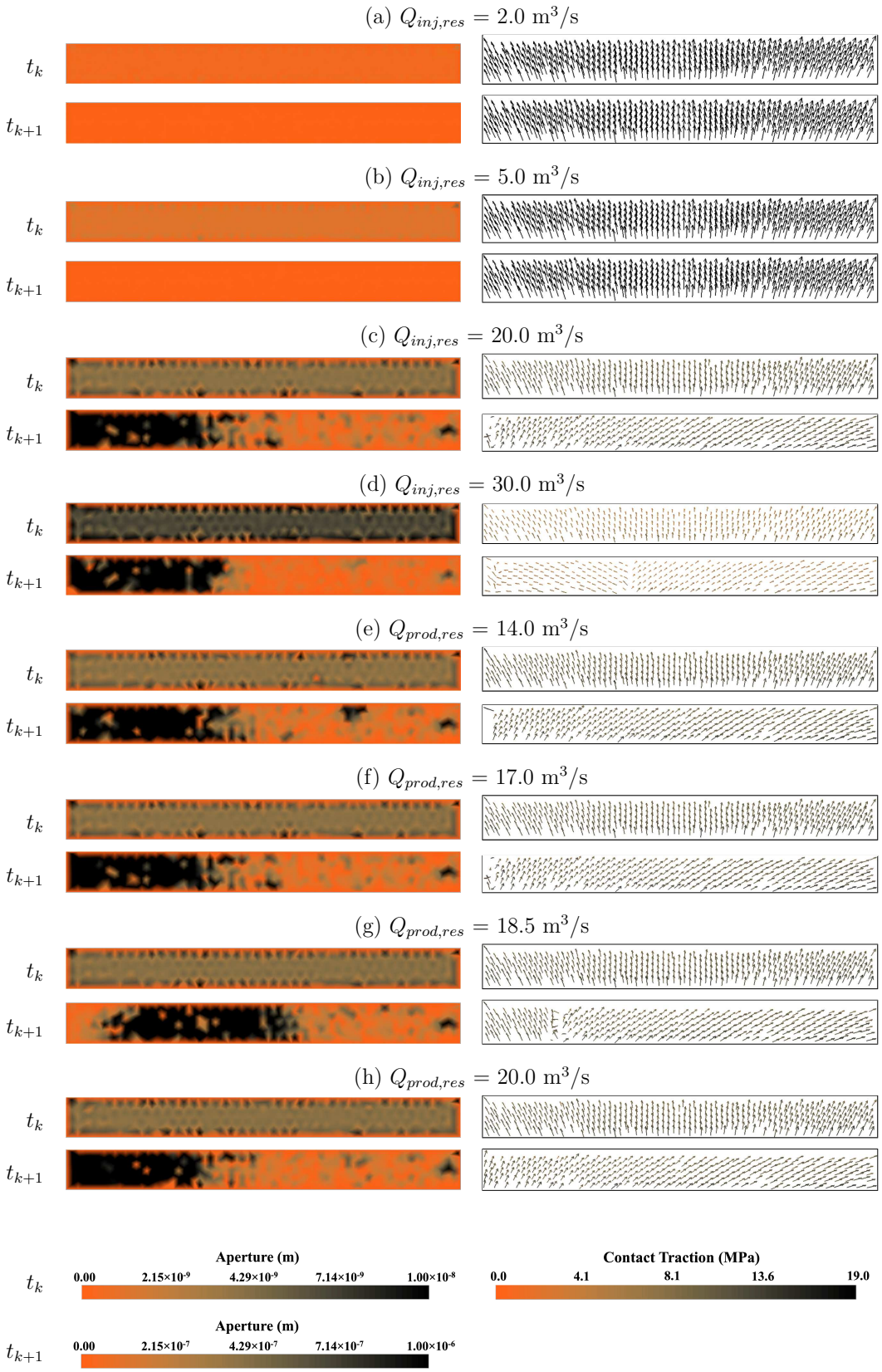


Figure 6.18: The fault aperture (left) and contact traction (right) one time step before (t_k) and after (t_{k+1}) the time of peak slip for the first slip event during the second injection period for four cases of varying hydrogen (a-d) injection rate and (e-h) production rate.

only approximately 3.1 mm range between the cases for the first slip event and 2.6 cm range for the second event.

The contact traction along the fault, the fault aperture and the fault slip at each node on the fault surface for the four different cases are shown in Figures 6.18 and 6.20 respectively. A sudden change in the directions of the contact tractions, where tangential slip is induced, and a sudden increase in aperture is observed at the time of the events. Figure 6.18 shows very little difference in the magnitudes of the contact tractions or the aperture distributions for all four cases.

Taking into account Equations 3.11 and 3.12, and assuming that all the slip is released instantaneously, the upper bound for the moment magnitude of the potential induced seismicity for the first slip event in the 14.0 m^3/s, 17.0 m^3/s, 18.5 m^3/s and 20.0 m^3/s cases is 3.55, 3.56, 3.48 and 3.56 respectively. Therefore, the magnitude of the induced seismicity is almost invariant to production rate.

6.7.3.3 Horizontal Well Length

Both the injection and withdrawal wellbore lengths were varied (at the same time) between 400 m and 4000 m, and the influence on average slip as a function of time is shown in Figures 6.15h and 6.17a. It was found that the slip was insensitive to changes in the well lengths within the tested ranges. For the first slip event during the second injection period, the fault slip for the 400 m, 800 m, 2000 m and 4000 m cases was 9.24 cm, 9.23 cm, 9.25 cm and 9.34 cm respectively. For the second slip event during the third injection period, the fault slip for the 400 m, 800 m, 2000 m and 4000 m cases was 7.11 cm, 7.10 cm, 7.08 cm and 6.85 cm respectively.

The contact traction along the fault, the fault aperture and the fault slip at each node on the fault surface for the four different cases are shown in Figures 6.25 and 6.21 respectively. A sudden change in the directions of the contact tractions, where tangential slip was induced, and a sudden increase in aperture was observed at the time of the events. Figure 6.25 shows very little difference in the magnitudes of the contact tractions for all four cases, which is why

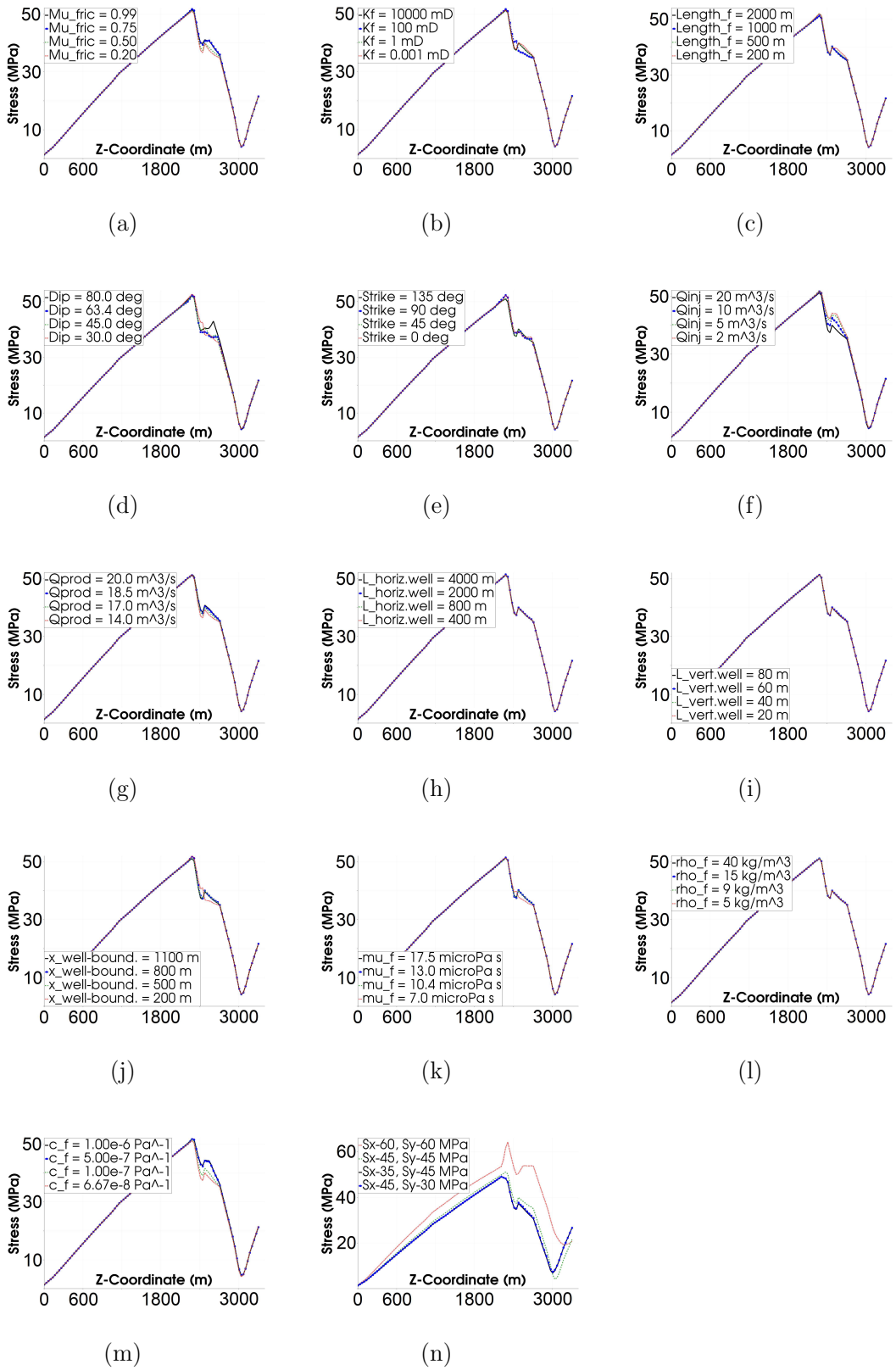


Figure 6.19: Plots of stress vertically through the center of the model in the z-direction for four cases of varying (a) fault friction coefficient, (b) fault permeability, (c) fault length, (d) fault dip, (e) fault strike, (f) injection rate, (g) withdrawal rate, (h) horizontal well length, (i) vertical well length, (j) vertical well spacing, (k) hydrogen viscosity, (l) hydrogen density, (m) hydrogen compressibility, and (n) stresses

the fault slip was not strongly influenced by well length. Figure 6.25 shows that there was a change in the way the aperture was spatially distributed across the fault surface in the four cases.

At the depths of the reservoir unit, the stress profiles indicate that the stress was insensitive to changes in the horizontal well length (Figure 6.7.3.2h). This supports the lack of sensitivity that changes in horizontal well length had on the slip.

Taking into account Equations 3.11 and 3.12, and assuming that all the slip is released instantaneously, the upper bound for the moment magnitude of the potential induced seismicity for the first slip event in the 400 m, 800 m, 2000 m an 4000 m cases is 3.55, 3.55, 3.55 and 3.56. Therefore, the well length has no effect on the magnitude of the induced seismicity.

6.7.3.4 Vertical Well Perforation Length

The horizontal wellbores used in the previous section and described in Section 6.4, are removed and replaced with vertical wells, to assess the influence of the type of wellbore on the induced seismicity. Both the vertical injection and withdrawal wellbore lengths were varied (at the same time) between 20 m and 80 m, and the influence on average slip as a function of time is shown in Figures 6.15i and 6.17b. These lengths are not the total vertical length of the wellbore from the sea bed, but rather refer to the vertical lengths of the wellbore that are perforated. It was found that the slip was insensitive to changes in the vertical well perforation lengths. For the first slip event during the second injection period, the fault slip for the 20 m, 40 m, 60 m and 80 m cases was 9.22 cm, 9.22 cm, 9.24 cm and 9.24 cm, respectively. For the second slip event during the third injection period, the fault slip for the 20 m, 40 m, 60 m and 80 m cases was 7.09 cm, 7.09 cm, 7.12 cm, and 7.11 cm respectively. Therefore, there was a miniscule trend that broadly suggested as vertical well perforation length increased, fault slip increased. However, this difference between the cases was a maximum of 300 microns.

The contact traction along the fault, the fault aperture and the fault slip at each node on the fault surface for the four different cases are shown in Figures 6.22 and 6.21 respectively. A

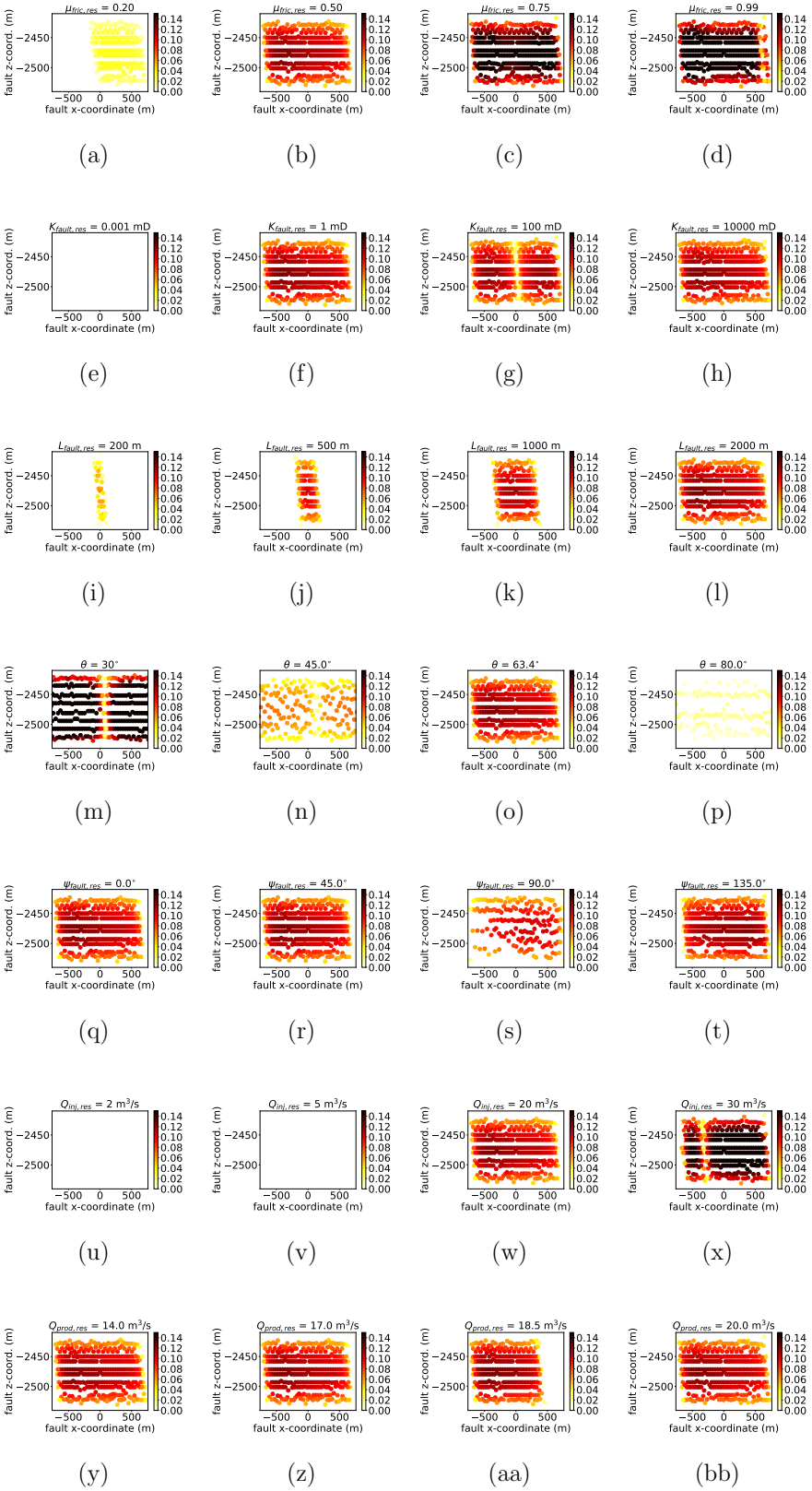


Figure 6.20: The tangential fault slip at each node at the time of peak slip for the first slip event during the second injection period for cases of varying (a-d) fault friction coefficient, (e-h) fault permeability, (i-l) fault length, (m-p) fault dip, (q-t) fault strike, (u-x) injection rate and (y-bb) withdrawal rate. The color bar ranges from 0.00 to 0.15 m.

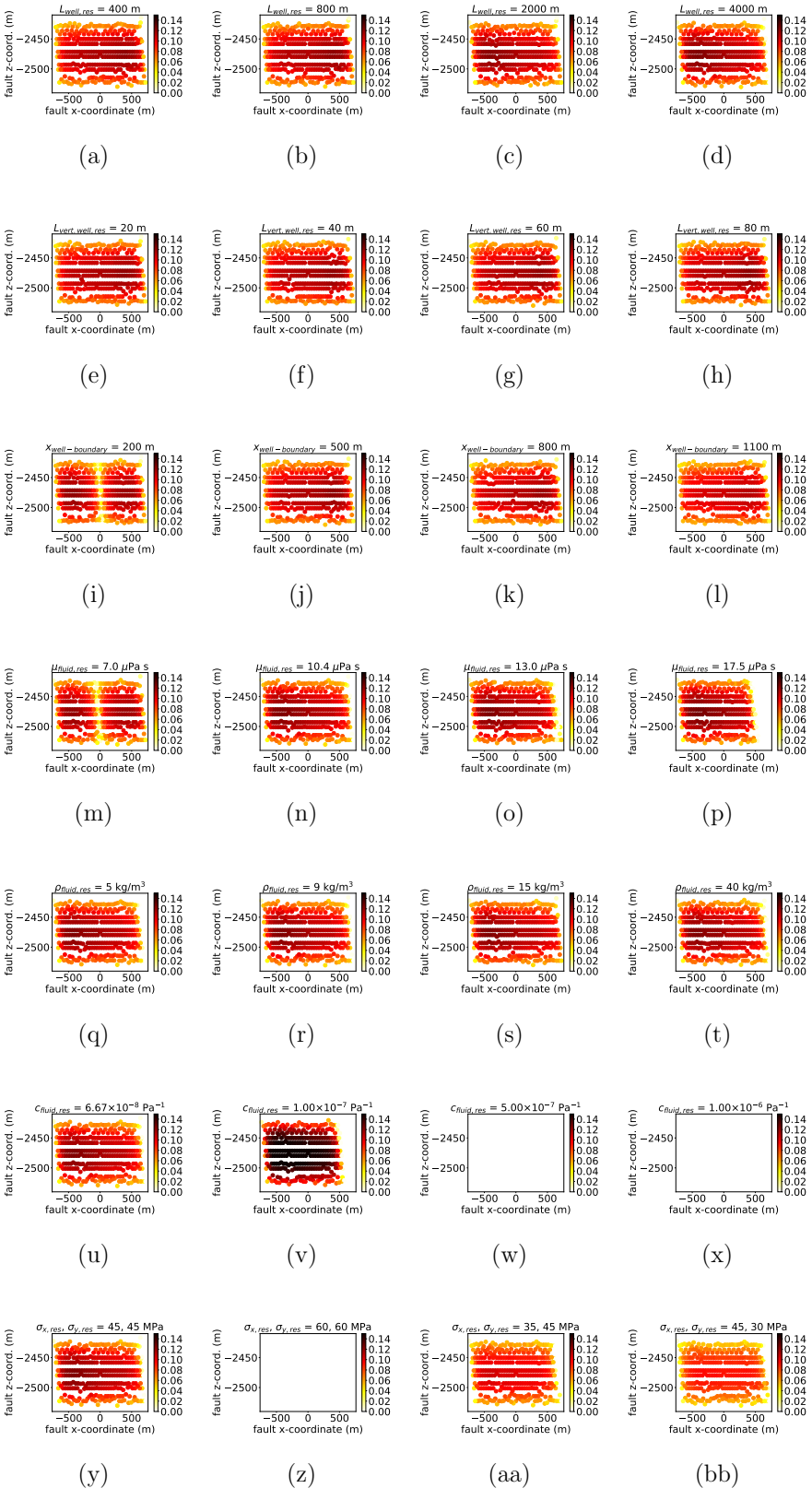


Figure 6.21: The tangential fault slip at each node at the time of peak slip for the first slip event during the second injection period for cases of varying (a-d) horizontal well length, (e-h) vertical well length, (i-l) vertical well-fault spacing, (m-p) hydrogen viscosity, (q-t) hydrogen density, (u-x) hydrogen compressibility and (y-bb) stresses. The color bar ranges from 0.00 to 0.15 m.

sudden change in the directions of the contact tractions, where tangential slip was induced, and a sudden increase in aperture was observed at the time of the events. Figure 6.22 shows very little difference in the magnitudes of the contact tractions or apertures for all four cases, which is why the fault slip was not strongly influenced by well length.

At the depths of the reservoir unit, the stress profiles indicate that the stress was insensitive to changes in the horizontal well length (Figure 6.7.3.2i), which further supports the lack of sensitivity that the slip had on changes in vertical well length.

Taking into account Equations 3.11 and 3.12, and assuming that all the slip is released instantaneously, the upper bound for the moment magnitude of the potential induced seismicity for the first slip event in the 20 m, 40 m, 60 m and 80 m cases was 3.55, 3.55, 3.55, and 3.55 respectively. Therefore, the vertical well perforation length has no effect on the maximum magnitude of the potential induced seismicity.

6.7.3.5 Well-Fault Spacing

The distance between the vertical well mentioned in Section 6.7.3.4 and the fault was varied and the influence on average slip as a function of time is shown in Figures 6.15j and 6.17c. This distance was varied by keeping the fault in the same location as described in Section 6.4, but by moving the injection and withdrawal wellbores by some horizontal distance from the left and right boundaries of the domain simultaneously. Thus the case labelled 1100 m has the wellbores closest to the fault and the case labelled 200 m has the wellbores furthest from the fault. For the first slip event during the second injection period, the fault slip for the 200 m, 500 m, 800 m and 1100 m cases was 8.71 cm, 9.24 cm, 8.97 cm, and 8.69 cm. For the second slip event during the third injection period, the fault slip for the 200 m, 500 m, 800 m and 1100 m cases was 7.15 cm, 7.11 cm, 6.54 cm, and 6.54 cm, respectively. Even though the trend for the second slip event shows that as fault-well spacing decreased, fault slip decreased, this trend was not replicated for the first event. Therefore, no systematic change in fault slip was found for changing fault-well spacing. Furthermore, the magnitude of the fault slip was largely insensitive to changes in well-fault distance.

The contact traction along the fault, the fault aperture and the fault slip at each node on the fault surface for the four different cases are shown in Figures 6.22 and 6.21 respectively. A sudden change in the directions of the contact tractions, where tangential slip was induced, and a sudden increase in aperture was observed at the time of the events. Figure 6.22 shows that the magnitude of the contact traction was almost the same in all four cases, which supports the lack of slip sensitivity to the well-fault spacing. The spatial distribution of the high aperture regions did change depending on the well-fault spacing (Figure 6.22). When the well and fault was either very far apart (200 m case) or very close together (1100 m case), the fault aperture was spatially asymmetric with large aperture regions at one end of the fault and low aperture regions at the other. When the well and fault were at intermediate distances to one another (500 m and 800 m cases), the spatial aperture distribution showed high aperture regions at both ends of the fault.

Taking into account Equations 3.11 and 3.12, and assuming that all the slip is released instantaneously, the upper bound for the moment magnitude of the potential induced seismicity for the first slip event in the 200 m, 500 m, 800 m and 1100 m cases was 3.54, 3.55, 3.54, and 3.53 respectively. Therefore, the well-fault spacing has almost no effect on the maximum magnitude of the potential induced seismicity.

6.7.4 Effect of Fluid Properties

6.7.4.1 Hydrogen Viscosity

The hydrogen viscosity injected into the reservoir sandstone was varied between 7.0 μPa s and 17.5 μPa s, and the influence on average slip as a function of time is shown in Figures 6.15k and 6.17d. This range was designed to cover the full range of viscosities that hydrogen can take at all realistic reservoir temperatures and pressures. For the first slip event during the second injection period, the fault slip for the 7.0 μPa s, 10.4 μPa s, 13.0 μPa s and 17.5 μPa s cases was 8.63 cm, 9.34 cm, 9.35 cm and 9.52 cm respectively. For the second slip event during the third injection period, the fault slip for the 7.0 μPa s, 10.4 μPa s, 13.0 μPa s and 17.5 μPa s

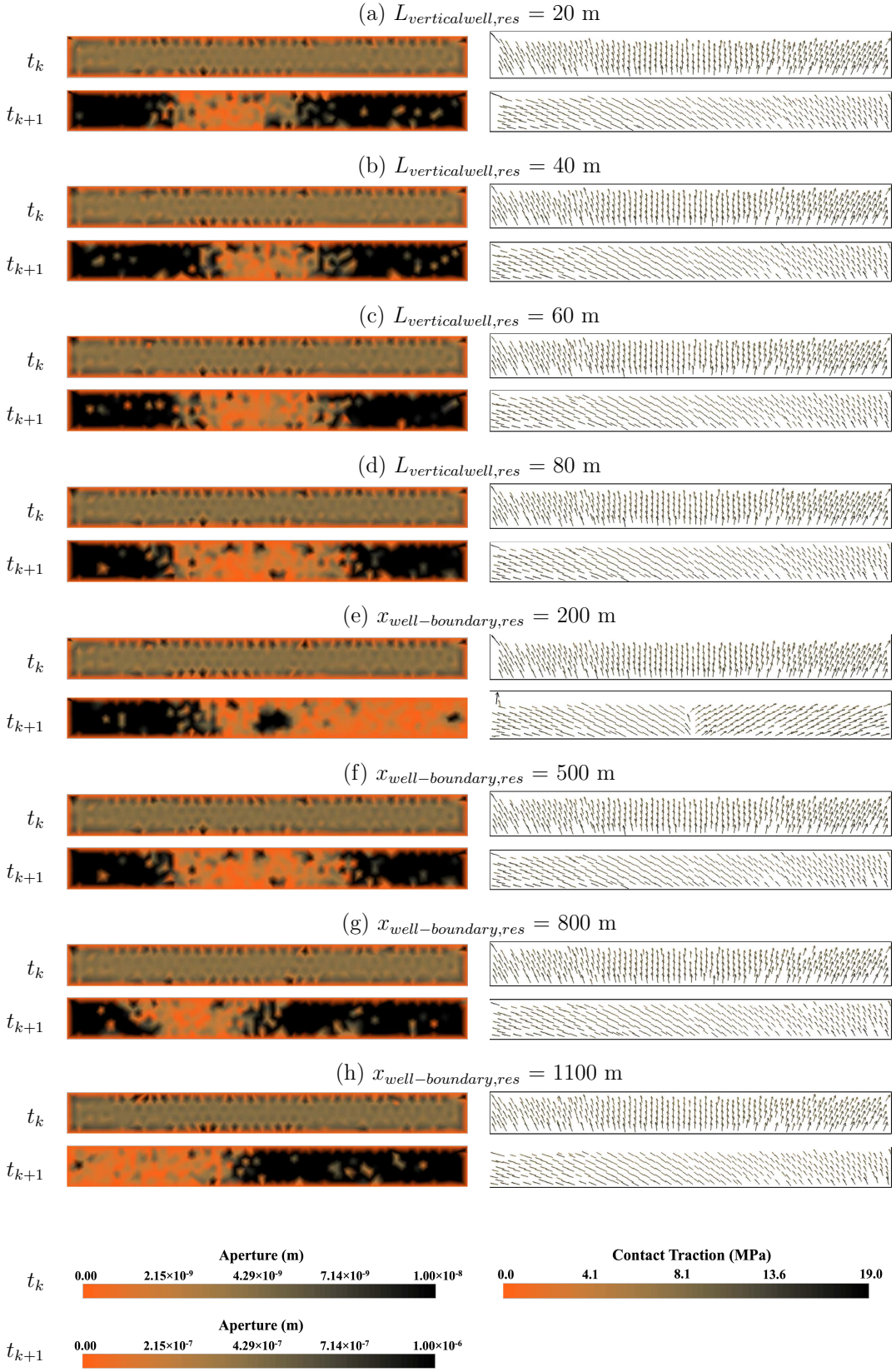


Figure 6.22: The fault aperture (left) and contact traction (right) one time step before (t_k) and after (t_{k+1}) the time of peak slip for the first slip event during the second injection period for four cases of varying vertical (a-d) length and (e-h) spacing.

cases was 7.09 cm, 6.85 cm, 7.84 cm and 6.88 cm respectively. The first event shows a weak trend, in which as hydrogen viscosity increases, the fault slip increases. However, the second event does not show a systematic change with increasing hydrogen viscosity. As such, no trend can be established, but in any case, the slip varies insignificantly as the hydrogen viscosity was changed within this range.

The contact traction along the fault, the fault aperture and the fault slip at each node on the fault surface for the four different cases are shown in Figures 6.23 and 6.21 respectively. A sudden change in the directions of the contact tractions, where tangential slip was induced, and a sudden increase in aperture was observed at the time of the events. From the fault slip at each individual node on the fault surface (Figure 6.21), we see that in the highest viscosity case (17.5 μPa s), an approximately 250-350 m portion of the fault was in stick and does not experience slip.

Taking into account Equations 3.11 and 3.12, and assuming that all the slip is released instantaneously, the upper bound for the moment magnitude of the potential induced seismicity for the first slip event in the 7.0 μPa s, 10.4 μPa s, 13.0 μPa s and 17.5 μPa s cases was 3.53, 3.56, 3.56 and 3.51. Therefore, the hydrogen viscosity has very little effect on the magnitude of the induced seismicity, and no systematic trend with increasing hydrogen viscosity was found.

6.7.4.2 Hydrogen Density

The hydrogen density of the fluid injected into the reservoir sandstone was varied between 5 kg/m^3 and 40 kg/m^3, and the influence on average slip as a function of time is shown in Figures 6.15l and 6.17e. This range was designed to cover the full range of densities that hydrogen can take at all realistic reservoir temperatures and pressures. For the first slip event during the second injection period, the fault slip for the 5 kg/m^3, 9 kg/m^3, 15 kg/m^3 and 40 kg/m^3 cases was 9.34 cm, 9.34 cm, 9.43 cm and 9.30 cm respectively. For the second slip event during the third injection period, the fault slip for the 5 kg/m^3, 9 kg/m^3, 15 kg/m^3 and 40 kg/m^3 cases was 7.23 cm, 6.85 cm, 7.20 cm and 7.61 cm respectively. No systematic change with increasing hydrogen density was found for either event. Furthermore, the fault slip was very

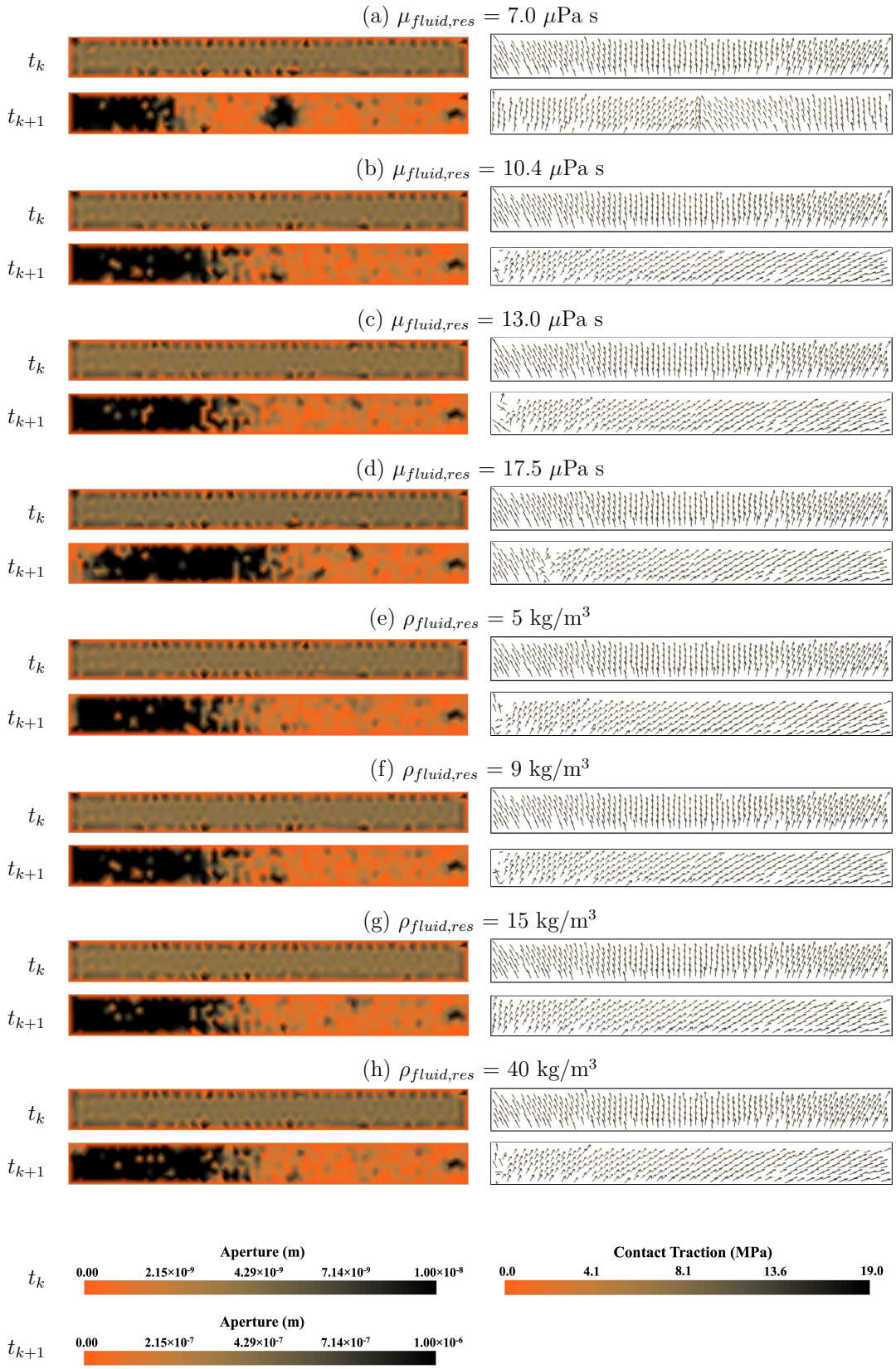


Figure 6.23: The fault aperture (left) and contact traction (right) one time step before (t_k) and after (t_{k+1}) the time of peak slip for the first slip event during the second injection period for four cases of varying hydrogen injectant (a-d) viscosity and (e-h) density.

similar irrespective of potential density and thus, it can be concluded that irrespective of the reservoir temperature or pressure, the fault slip is not dependent on hydrogen density.

The contact traction along the fault, the fault aperture and the fault slip at each node on the fault surface for the four different cases are shown in Figures 6.23 and 6.21 respectively. A sudden change in the directions of the contact tractions, where tangential slip is induced, and a sudden increase in aperture is observed at the time of the events. Figure 6.23 shows essentially no difference in the magnitudes of the contact tractions and apertures for all four cases, which is why the fault slip is not strongly influenced by the hydrogen density. Furthermore, the stress profiles at the depth of the reservoir unit indicate that the stress was insensitive to changes in the hydrogen density (Figure 6.7.3.2l). This supports the lack of sensitivity that changes in hydrogen density had on the slip.

Taking into account Equations 3.11 and 3.12, and assuming that all the slip is released instantaneously, the upper bound for the moment magnitude of the potential induced seismicity for the first slip event in the 5 kg/m^3, 9 kg/m^3, 15 kg/m^3 and 40 kg/m^3 cases is 3.56, 3.56, 3.56 and 3.55. Therefore, the hydrogen density has almost no effect on the magnitude of the induced seismicity.

6.7.4.3 Hydrogen Compressibility

The hydrogen compressibility of the fluid injected into the reservoir sandstone was varied between 6.67×10^{-8} Pa^{-1} and 1.00×10^{-6} Pa^{-1}, and the influence on average slip as a function of time is shown in Figures 6.15m and 6.17f. For the first slip event during the second injection period, the fault slip for the 6.67×10^{-8} Pa^{-1}, 1.00×10^{-7} Pa^{-1}, 5.00×10^{-7} Pa^{-1} and 1.00×10^{-6} Pa^{-1} cases was 9.34 cm, 12.13 cm, 0 cm and 0 cm, respectively. For the second slip event during the third injection period, the fault slip for the 6.67×10^{-8} Pa^{-1}, 1.00×10^{-7} Pa^{-1}, 5.00×10^{-7} Pa^{-1} and 1.00×10^{-6} Pa^{-1} cases was 6.85 cm, 11.35 cm, 0 cm and 0 cm, respectively. Therefore, no systematic change in fault slip was found with increasing hydrogen compressibility. The fault slip was strongly influenced by the hydrogen compressibility in the range 6.67×10^{-8} Pa^{-1}-1.00×10^{-7} Pa^{-1}.

The contact traction along the fault, the fault aperture and the fault slip at each node on the fault surface for the four different cases are shown in Figures 6.24 and 6.21 respectively. A sudden change in the directions of the contact tractions, where tangential slip is induced, and a sudden increase in aperture is observed at the time of the events. Figure 6.24 shows that the magnitude of the contact traction along the fault is strongly influenced by the hydrogen compressibility. As the hydrogen compressibility increased, the magnitude of the contact traction also increased. In the large compressibility cases (5.00×10^{-7} Pa^{-1} and 1.00×10^{-6} Pa^{-1}), very large contract tractions were observed that are almost entirely composed of normal contact traction, which helps keep the fault locked and stable, which is reflected by the small apertures in these cases (Figure 6.24). Even though the magnitude of the fault slip is larger in the 1.00×10^{-7} Pa^{-1} case relative to the 6.67×10^{-8} Pa^{-1}, the proportion of the fault surface area in slip is smaller in the 1.00×10^{-7} Pa^{-1} case (Figures 6.21u and 6.21v). This supports the trend that fault slip became less likely as hydrogen compressibility increased.

At the depths of the reservoir unit, the stress profiles indicate that the stress is considerably smaller in the 6.67×10^{-8} Pa^{-1} and 1.00×10^{-7} Pa^{-1} cases, relative to the 5.00×10^{-7} Pa^{-1} and 1.00×10^{-6} Pa^{-1} cases.

Taking into account Equations 3.11 and 3.12, and assuming that all the slip is released instantaneously, the upper bound for the moment magnitude of the potential induced seismicity for the first slip event in the 6.67×10^{-8} Pa^{-1} and 1.00×10^{-7} Pa^{-1} cases was 3.56 and 3.58, respectively. No event was induced in the 5.00×10^{-7} Pa^{-1} and 1.00×10^{-6} Pa^{-1} cases. Therefore, the hydrogen compressibility has a strong effect on the magnitude of the induced seismicity.

6.7.5 Effect of Stresses

The x and y stresses at the mid-depth of the reservoir sandstone are varied in four cases, two of which involve homogeneous stresses at 45 MPa and 60 MPa and two of which involve heterogeneous stresses (45 MPa/35 MPa and 35 MPa/45 MPa in the x/y directions), and the influence on average slip as a function of time is shown in Figures 6.15n and 6.17g. It was found that the two homogeneous cases bound the fault slip. When both the x and y stresses

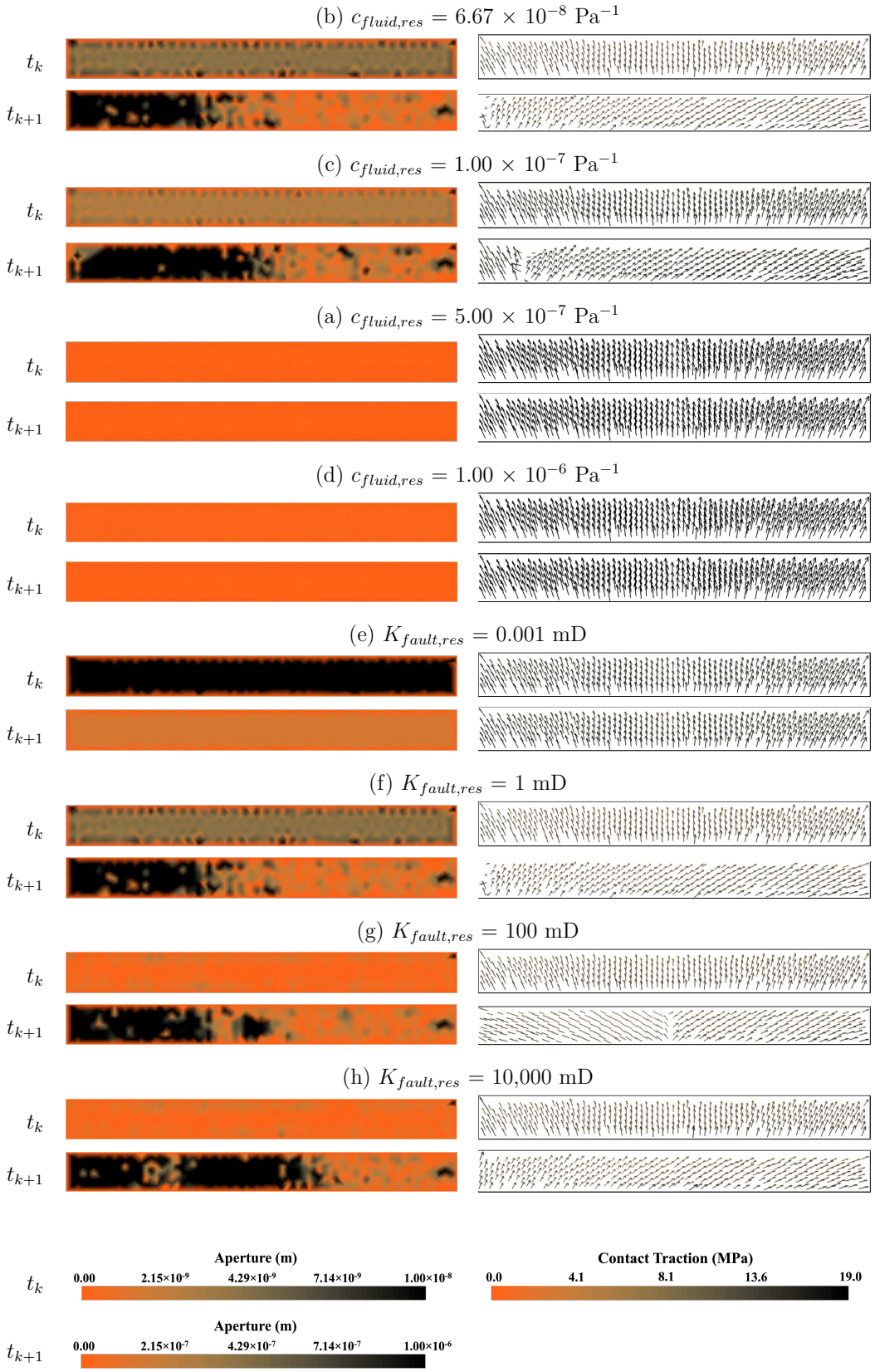


Figure 6.24: The fault aperture (left) and contact traction (right) one time step before (t_k) and after (t_{k+1}) the time of peak slip for the first slip event during the second injection period for four cases of varying (a-d) hydrogen injectant compressibility and (e-h) fault permeability.

are 45 MPa, the fault slip was the largest, and when both the x and y stresses are 60 MPa the fault slip was the lowest (the fault was completely stable). For the heterogeneous stresses, the fault slip lies between these two cases and very similar slip was found. For the first slip event during the second injection period, the fault slip for the 35 MPa/45 MPa, 45 MPa/45 MPa, and 45 MPa/35 MPa cases was 8.24 cm, 9.34 cm and 7.46 cm respectively. For the first slip event during the second injection period, the fault slip for the 35 MPa/45 MPa, 45 MPa/45 MPa, and 45 MPa/35 MPa cases was 6.05 cm, 6.85 cm and 6.32 cm respectively. The fault slip was 0 cm in the 60 MPa/60 MPa case.

The contact traction along the fault, the fault aperture and the fault slip at each node on the fault surface for the four different cases are shown in Figures 6.25 and 6.21 respectively. A sudden change in the directions of the contact tractions, where tangential slip was induced, and a sudden increase in aperture was observed at the time of the events. Figure 6.25 shows that when the magnitude of the stresses was large, the magnitude of the contact traction also increased. In the 60 MPa/60 MPa case, large normal contact tractions are observed with little tangential component. No change in aperture was seen. Very little difference was seen in the aperture and contact traction distributions for the 45 MPa/45 MPa, 35 MPa/45 MPa and 45 MPa/35 MPa cases.

The stress profile at the reservoir depth supports the lack of fault slip in the 60 MPa/60 MPa case (Figure 6.7.3.2n). The stress at this depth is much larger than the other three cases, meaning that the effective normal stress acting on the fault is much larger than that in the other three cases.

Taking into account Equations 3.11 and 3.12, and assuming that all the slip is released instantaneously, the upper bound for the moment magnitude of the potential induced seismicity for the first slip event in the 35 MPa/45 MPa, 45 MPa/45 MPa, and 45 MPa/35 MPa cases was 3.52, 3.56, and 3.49. There was no event in the 60 MPa/60 MPa case. Therefore, the magnitude of the induced seismicity was largely insensitive to heterogeneous versus homogeneous stresses, at least for non-drastic differences in σ_x and σ_y, but it was strongly influenced by the absolute magnitude of the stresses.

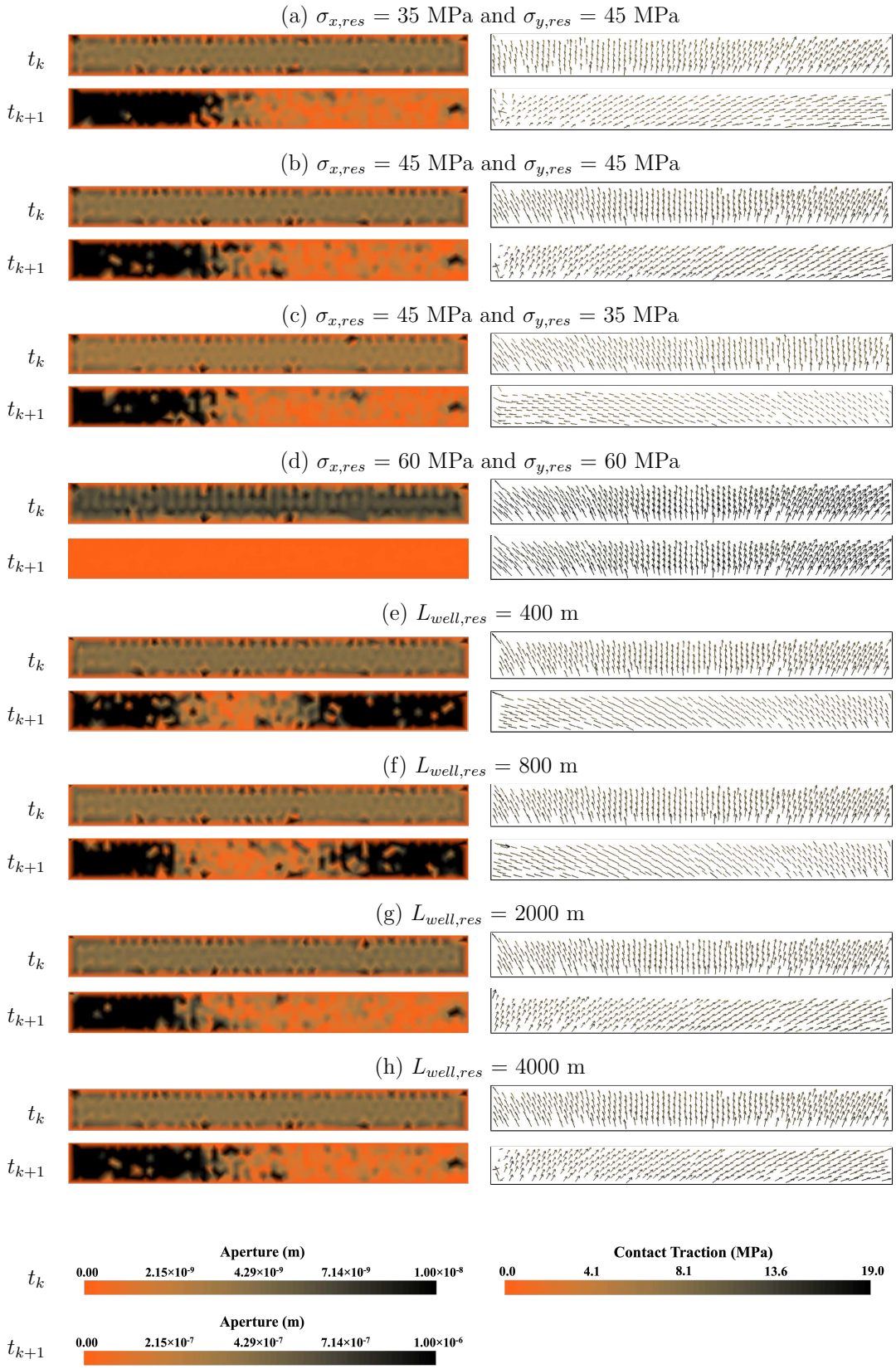


Figure 6.25: The fault aperture (left) and contact traction (right) one time step before (t_k) and after (t_{k+1}) the time of peak slip for the first slip event during the second injection period for four cases of varying (a-d) stresses and (e-h) horizontal well length.

6.8 Discussion

In future commercialized hydrogen storage projects, enormous volumes of hydrogen must be injected and stored in the reservoir in order to sufficiently assist in satisfying future energy demand. Hydrogen has an ultra-low density of 9 kg/m^3 at 15 MPa and 90°C, which implies that injection rates for geological hydrogen storage will need to be far in excess of those used for CO_2 storage or wastewater injection. The injection rate used in this work of 20 m^3/s is designed to be a worst-case scenario in terms of seismic hazard, so that the upper bounds on the magnitude of potential induced seismicity during geological hydrogen storage can be quantified. This rate corresponds to an equivalent 78,761,160,000 kWh of stored energy (~79 TWh), which is approximately 5% of the national annual energy demand of the United Kingdom. The injection rate simulations conducted herein demonstrate that even at rates of 25% of this injection rate (i.e., 5 m^3/s), the fault was entirely stable for three storage cycles. All the events in this work are shown in Figure 6.26.

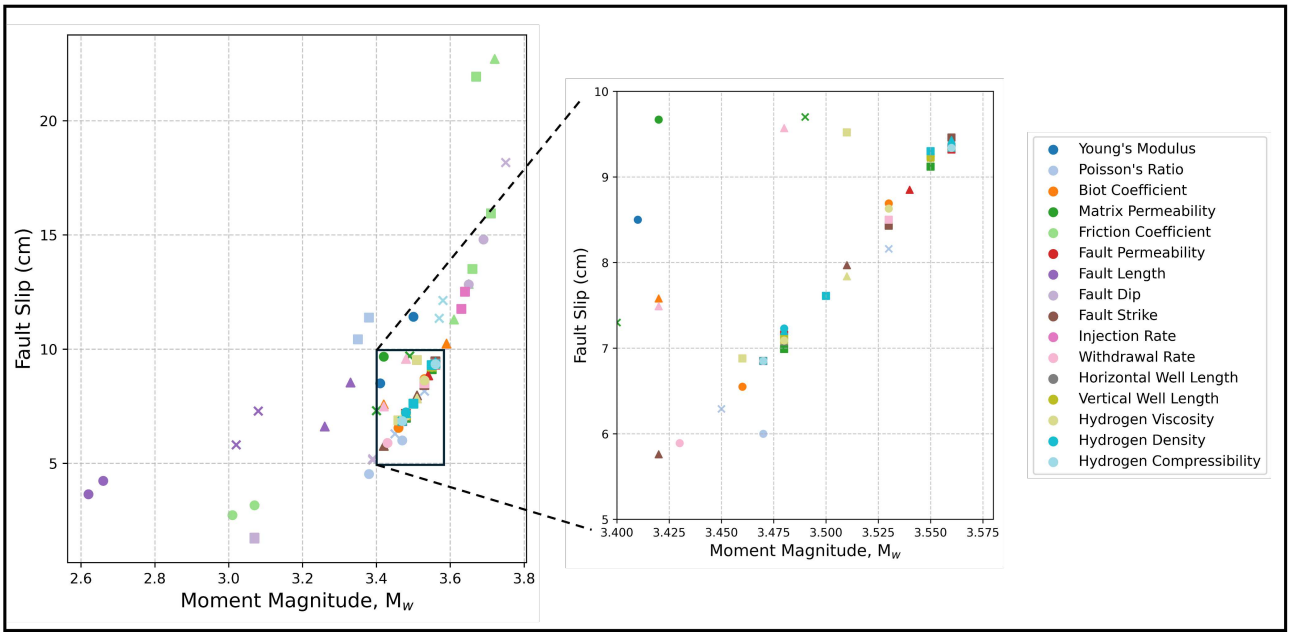


Figure 6.26: Fault slip versus moment magnitude for all seismic events resultant from the various simulation sets. Circles, crosses, triangles and squares denote the lowest, second lowest, second highest and highest value of the four tested values in that simulation set, respectively. For example, for the Biot coefficient, 0.25, 0.35, 0.65 and 0.90 was tested. The 0.25 case is represented by a circle, 0.35 by a cross, 0.65 by a triangle and 0.90 by a square.

6.8.1 Young's Modulus

As Young's modulus increases, the average fault slip and maximum potential event magnitude decreases. For Young's modulii over 40 GPa, the fault was completely stable. The strain induced in the reservoir unit decreased with increasing Young's modulus.

The reduction in fault slip as Young's modulus increased, found in this work, is in line with that found by Meng et al. [2020] in their hydraulic fracturing work. They varied the Young's modulus of their one-unit formation between 5 GPa and 50 GPa, and studied the slip along a natural fracture which was spatially penetrated by their injection wellbore. The slip continuously decreased from a maximum of 12 cm in the 5 GPa case to 1-2 cm in the 50 GPa case, owing to a decrease in strain, which is what we observe in this hydrogen storage case (Figure 6.10).

6.8.2 Poisson's Ratio

As Poisson's ratio increases, the average fault slip increases. However, the maximum potential event magnitude was the smallest in the highest Poisson's ratio case ($\nu = 0.30$) because a large proportion of the fault surface was found to be in stick. Therefore, the maximum potential event magnitude reduces with higher Poisson's ratio.

The only other study examining the effect of Poisson's ratio on fault slip during an injection procedure was that of Meng et al. [2020] in their 2D hydraulic fracturing work. They found that the fault slip is insensitive to changes in Poisson's ratio in the range 0.1-0.3, whereas we found that in this range the average fault slip can vary between approximately 3 to 4 cm. The work here has the advantage of being 3D, with a 2D fault such that the distribution of slip across the realistic 2D fault surface can be studied. Whereas, a 2D model with a 1D fracture surface is restricted to computing the fracture slip at just one point along the depth of the fault. Furthermore, the work is considerably different here in the sense that the pressure cycles up and down (injection and withdrawal), rather than systematically increasing, and that the fault does not, or comes close to, spatially intersecting the injection wellbore, which is likely a different problem, since the fault automatically becomes highly pressurized.

6.8.3 Biot Coefficient

No systematic trend in fault slip with increasing Biot coefficient was found. The fault was completely stable in the highest Biot coefficient case ($\alpha = 0.90$). The magnitude of the average fault slip was nearly identical in the $\alpha = 0.25$ and $\alpha = 0.35$ cases, and was not significantly different in the 0.65 case. Therefore, the fault slip only differed significantly for high Biot coefficient cases (above $\alpha = 0.65$), where the fault becomes more stable.

The Biot coefficient of the reservoir formation is varied and the influence on fault slip is assessed. Hui et al. [2021b] simulated three cases of Biot coefficient of 0.22, 0.44 and 0.66 and assessed the change in Coulomb Failure Stress (CFS) along a pre-existing fault during hydraulic fracturing. They found that the CFS was effectively the same, with only 0.4 MPa difference between the 0.22 (2.7 MPa) and 0.66 (2.3 MPa) cases, implying that the fault is likely to have similar stability irrespective of the Biot coefficient within this range. The findings of this study are consistent with less than 2 cm difference in slip between the 0.25 and 0.65 cases for the first event. In fact, the slight decrease in CFS as Biot coefficient increases implies a slight decrease in expected fault slip as Biot coefficient increases, as observed for the first event in the present paper. Although, given that the work of Hui et al. [2021b] involves large networks of hydraulic fractures, the proximity of this work to that is uncertain. Fan et al. [2019] concluded the same as Hui et al. [2021b], but their work examined the change in CFS along a basement fault, which again is a different problem to the one studied herein.

6.8.3.1 Permeability

The magnitude of the average fault slip was largely insensitive to changes in intrinsic permeability, although as permeability increased the fault slip tended to decrease slightly. The time of the first event was dependent on intrinsic permeability, with the fault first slipping at later times with smaller permeabilities. The delay was stronger when the intrinsic permeability was closer to the fracture permeability, potentially indicating that the fracture permeability has a strong control on the timing of the seismicity.

Comparing these results to the literature, Mortezaei and Vahedifard [2015] injected CO_2 for sequestration with no withdrawal in a 2D model, and found that as permeability decreased, the magnitude of the fault slip increased, which is what we observe here; although the relationship is not strong. They also found that the timing of the first rupture was delayed as permeability decreased, which is observed herein also. This work, relative to that, benefits from the fact that the slip is computed across a 2D fault surface, showing a full spatial distribution of fault slip. Whereas, the 2D nature of the work in Mortezaei and Vahedifard [2015], constrains the fault to a 1D nature, meaning the slip is essentially being computed at just one point along the fault at each depth interval.

6.8.4 Friction Coefficient

Friction coefficient had a very significant effect on slip. As reservoir fault friction coefficient increased within the tested range, average fault slip increased.

For high friction coefficients (>0.75), slip events were more numerous and additional large magnitude events (M_w 3.67 to 3.72) were induced near the onset of the initial injection, that did not occur at lower friction coefficients (<0.50). Friction coefficient had a strong control on fault slip with the slip for the events during the second and third injection periods being approximately 5 times larger in the 0.99 case relative to the 0.20 case, and event magnitudes for the second event varied largely between 3.01 and 3.66. For low friction coefficients (<0.20) the slip was minimal and constrained to be no more than a few centimetres. Higher friction coefficient resulted in higher shear stresses which promoted this behaviour. Not only did slip decrease as friction coefficient decreased, but in the 0.20 case (the smallest friction coefficient tested), part of the fault surface was in stick which could imply at friction coefficients less than 0.20 there may be no slip anywhere across the fault. The lowest event magnitude occurred for the 0.20 case which can be attributed to this reduced fault area in slip. The much lower magnitude in the 0.20 case can be attributed to the fact that only half the fault area was in slip.

The lower friction coefficient case took longer to first slip because in higher friction scenarios,

stress concentrates more along the fault plane due to the higher resistance to slip. This concentrated stress leads to a more focused buildup of shear stress in critical areas, accelerating the approach to the initial slip condition. Whereas when the friction coefficient is less, stress is less prone to concentrate in the vicinity of the fault, thus taking longer for the critical stress to be reached.

Deng et al. [2021] conducted 2-D hydraulic fracturing simulations on two pre-existing faults and found that when the friction coefficient was increased from 0.2 to 0.6, the slip along the faults also increased, and by up to 35.4%. This supports the findings herein and the conclusion that as friction coefficient increases, average fault slip and induced seismic magnitude increases. More accumulated energy is required to initiate movement along faults with high friction coefficients, and thus more energy is released when the slip occurs [Ngo, 2019].

6.8.5 Fault Permeability

For fault permeabilities above the reservoir intrinsic permeability, the fault slip was insensitive to fault permeability. However, when the fault permeability is less than the reservoir matrix permeability, the fault slip drastically reduced to zero throughout the storage cycles. This represents a situation where you have a cataclasite rock or where the fault may have been mineralized or filled with a low permeability crystalline precipitate.

The 0.001 mD case, which yielded the least slip, had the smallest fault aperture after the event. This is because high normal contact tractions helped keep the fault closed and locked. Low fault permeability limits the ability of hydrogen to flow into the fault zone. Consequently, injected hydrogen or changes in reservoir pressure take longer to propagate through the fault. This restricted flow reduces the magnitude and rate of pore pressure increase within the fault zone. Without significant hydrogen movement into the fault zone, the pore pressure does not increase substantially. Lower pore pressures increase the effective normal stress on the fault, which can inhibit fault slip.

In the 2-D hydraulic fracturing and 2-D CO_2 injection works of Deng et al. [2021] and Maz-

zoldi et al. [2012], respectively , it was found that fault slip was also insensitive to changes in fault permeability for fault permeabilities above the matrix permeability, as found in this work. However, the 3-D geothermal work of Anyim and Gan [2020] found that as fault permeability increased, the slip decreased slightly with approximately 2.2 cm difference in the fault permeability range of 10^{-12} and 10^{-15} m^2. This differs from this work in that the injection occurs into a low-permeability non-porous basement rock, so its applicability in comparison to this work is unclear given our model of a high-permeability porous reservoir rock. Additionally, fluid injection in this study is for the purpose of geothermal energy and thus temperature modelling is included. For higher permeability faults, the fluid is more prone to leak-off from the rock matrix into the fault, reducing heat transfer from the rock into the fault zone via conduction. Therefore, less thermal stress is induced which may be why the fault slips less when the permeability is higher. Furthermore, the smallest fault permeability they computed, 10^{-16} m^2, generated the smallest slip of all cases, which counteracts the trend observed in the range 10^{-12} and 10^{-15} m^2 cases. This case matched what we observe: that the fault slip was minimized for the lowest fault permeability case. It can be concluded from the findings of these works and herein that for fault permeabilities of less than or equal to 10^{-16} m^2, the fault slip is minimal. When the fault permeability is lower than the intrinsic rock permeability, the pressure front from the injection wellbore will preferentially flow around, rather than into, the fault. The hydrogen does not leak off from the rock matrix into the fault as efficiently as at higher fault permeabilities and thus, the fault is not pressurized to the same extent. Less pressure increase in the fault, means less effective normal stress reduction and thus less propensity to fail.

6.8.6 Fault Length

Fault length had a significant effect on the fault slip. As reservoir fault length increased, average fault slip increased. The maximum potential event magnitude almost linearly increased with fault length: a M_w 2.66 event occurred for a fault length of 200 m, but the magnitude increased by almost 1 (ten times more intense) to M_w 3.56 when the fault length was increased by a factor of 10 to 2000 m. This was due to reduced slip and reduced fault rupture area as fault

length decreased. This owed to decreased effective normal stress as fault length increased, which promotes slip. This occurs because longer faults redistribute the resultant stresses from the increased pore pressure front propagating from the injection wellbore over a larger area, leading to a more spatially widespread reduction in effective normal stress.

For the first slip event, the fault slip in the 2000 m case was over double that in the 200 m case. Even at the high injection rates used herein, following this trend, one would expect that for small-scale faults on the scale of tens of metres in length, the fault slip may be negligible. Significant slip occurs only on faults of large scale (100 m or more in length).

Meng et al. [2020] performed a 2-D hydraulic fracturing study where they directly applied a fluid pressure to the fracture surface. Fracture length was varied between 10 and 100 m and they equally found that slip was very sensitive to fracture length, with fracture slip approximately linearly increasing with increasing fracture length.

6.8.7 Fault Dip

The magnitude of the induced seismicity was significantly influenced by the fault dip. It is perhaps no surprise events were more numerous and larger in the 45° case, because shear stresses are maximal on a plane at 45° to the principal stress σ_1, which is the case herein. For very steeply dipping faults (i.e. 80.0°), the slip was minimized.

In the largest dip case of 80.0°, the aperture after the event was far greater than in the other dip cases, and the greater the fault aperture, the less contact between the fault surfaces, which results in less accumulation of frictional stress and thus less resultant slippage.

The contact traction was very slightly larger in the 45.0° case than the 63.4° case, because in the 45.0° case, some of the contact traction had already been dissipated by the slippage shortly after the onset of injection, which did not occur in the other cases.

The recommendation in this study that reservoirs with steeply dipping faults (>60°) should be prioritized for geological hydrogen storage is well supported by the theoretical framework

developed by Sibson [1985]. In his seminal paper on fault reactivation, Sibson demonstrated that the likelihood of fault slip under a given stress state is highly dependent on the fault's orientation relative to the principal stress directions. For a normal faulting regime, which is typical of many sedimentary basins suitable for hydrogen storage, faults dipping approximately 60° to the horizontal are optimally oriented for reactivation. This corresponds closely with the intermediate-dip faults (45-65°) modelled in this study that had the greatest slip.

6.8.8 Injection Rate

As injection rate increased, average fault slip increased very significantly beyond 20 m^3/s. When injection rate increased 50% from 20 m^3/s to 30 m^3/s, the average fault slip increased by approximately 72%, showing that fault slip increases at a rate beyond a linear increase. However, for injection rates of 5 m^3/s or lower, the fault does not slip. Therefore, no seismicity is expected for low-to-intermediate injection rates. Slip increases with increased injection rate because the effective normal stress on the fault decreases as injection rate increases due to increased pore pressure. It is positive that the fault does not slip until rates of beyond 5 m^3/s. If hydrogen is stored in smaller quantities across many fields, such high rates as those used herein may not be necessary, and thus, the risk of seismicity in a given field would reduce dramatically.

The laboratory spring-poroslider model of Alghannam and Juanes [2020], representative of a fault in contact with a reservoir unit, showed that higher injection rates generated greater deviations between the dimensionless shear stiffness and the dimensionless critical shear stiffness, implying enhanced propensity for slip. Large slips are induced herein because of the large pore pressure increases associated with such huge volumes of stored hydrogen. It may be possible for the same large injection volume to decreases the slip found in this work, by using a gradual step-up injection schedule as proposed in Alghannam and Juanes [2020]. However, given with hydrogen storage that there is only a short-time period (a few months) to store as much hydrogen as possible for use during the periods of energy deficit, large rates may be required from the start to maximize storage volumes, making this impractical.

6.8.9 Withdrawal Rate

As withdrawal rate increased, the average fault slip increased and the time to event initiation was increased. This is because for a larger withdrawal rate during the withdrawal periods, when the subsequent injection period begins the reservoir pressure is lower than for the cases with lower withdrawal rate because more hydrogen has been recovered. Therefore, it takes more injection volume in the next injection period before the critical pressure on the fault is reached to initiate the slip. Conversely, for smaller withdrawal rates, the reservoir pressure remains high before the next injection period onsets and the fault failure pressure is achieved quicker at a given injection rate.

The very little difference in the magnitudes of the contact tractions or the aperture distributions for all four withdrawal rate cases supports why the fault slip is not strongly influenced by withdrawal rate. The little change in aperture and contact traction is attributed to the fact that the range of withdrawal rates tested was small, varying only by 6 m^3/s between the cases. The tested range is small because in reality we will need to withdraw similar amounts to that we injected previously. The lowest case 14 m^3/s only represents 70% recovery of the injected fluid, and therefore represents the lowest withdrawal rate one would expect (relative to the injection rate) in a real reservoir setting.

The bayesian and classical statisical analyses of Nepveu et al. [2016] and Sijacic et al. [2017] respectively, showed that increases and reductions in production rate correlated with increases and reductions in seismicity at the Groningen Natural Gas Field, which is the trend seen herein. However, it must be noted that the pore pressure monotonously decreases at Groningen because gas is only withdrawn, not injected, and the events therefore occur during withdrawal due to reservoir compaction. Whereas in this work, the events are injection-derived, but their timing is influenced by the withdrawal rate in the previous production cycles which influences the stress state at a given time during the subsequent injection. Thus, the mechanisms for these events are different, even if the same trend was found.

6.8.10 Horizontal Well Length

Interestingly, even though the magnitude of the fault aperture was invariant to changes in wellbore lengths (Figure 6.25), there was a change in the way the aperture was distributed. For larger wellbore lengths (i.e., >2000 m), the fault aperture distributions show that the fault aperture was large at one end of the fault and much smaller at the other end. Whereas for small wellbore lengths (i.e., <800 m), the fault aperture distributions show that large aperture zones develop at both ends of the fault. This is likely because when the wellbore length was much smaller than the fault length, hydrogen pressurizes both ends of the fault more uniformly at any given time because fluid from one end of the 0° striking wellbore only has a slightly larger distance to travel to reach the 45° striking fault than the fluid from the other end of the wellbore. Conversely, when the wellbore length was much larger than the fault, hydrogen pressurizes the closest end of the fault much quicker than the other end, such that any any given time, the hydrogen front has reached one end of the fault but is far from the other end, resulting in this higher aperture at one end of the fault.

6.8.11 Hydrogen Viscosity

Fault slip was largely insensitive to changes in the hydrogen viscosity. Therefore, irrespective of the reservoir temperature and pressure, which governs the viscosity in reality, the viscosity will not have a significant mechanical effect on the fault slip. Although, the first slip event indicated that as viscosity increased, fault slip increased, but the difference in slip was less than 2 mm between the 10.4, 13.0 and 17.5 μPa s cases. The aperture of the fault was found to increase slightly as viscosity increased, reflecting the fact that more viscous fluids have less affinity to leak-off into the surrounding matrix, and thus larger fault fluid overpressures result, which enhanced the propensity for slip.

The very little difference in the magnitudes of the contact tractions and apertures for all four viscosity cases supports why the fault slip was not strongly influenced by the hydrogen viscosity. The highest viscosity case (17.5 μPa s) tested showed that some portion of the fault surface

area became in stick which could imply that if the viscosity was higher, a greater proportion of the fault may enter stick, and seismicity would be less likely.

In the literature, it is suggested that higher viscosity fluids promote the elasto-hydrodynamic (EHD) fault fluid lubrication regime ([Ji et al., 2022a, Cornelio et al., 2019]). This is where the fault surfaces are not in contact and the normal effective stress acting on the fault is supported by the fault fluid pressure. This reduces the frictional strength of the fault. It has been found to be a very effective mechanism in weakening faults and initiating seismic activity [Cornelio and Violay, 2020a]. The increased aperture observed herein with increased hydrogen viscosity is reflecting higher fault fluid pressures, reflecting this process. The trend is weak because the range of hydrogen viscosities tested is very small since hydrogen's viscosity remains almost uniform for all the temperature and pressure ranges possible for subsurface storage reservoirs.

6.8.12 Hydrogen Compressibility

Much uncertainty exists around the compressibility of hydrogen at the very high temperatures and pressures of subsurface depleted gas fields. At a pressure of 15 MPa and temperature of 90°C, hydrogen has a Z-Factor of approximately 1 suggesting that it would behave as an ideal gas and that the reciprocal of the isothermal bulk modulus can be taken as the fluid compressibility. However, at higher temperatures and pressures this may not be the case. As such, the hydrogen compressibility assuming ideal gas behaviour of 6.67×10^{-8} Pa^{-1} is tested together with three larger compressibilities up to two orders of magnitude larger to cover this uncertainty

Broadly, as hydrogen compressibility increased, the average fault slip decreased. Effective stress on the fault was reduced as compressibility decreased, enhancing the fault's propensity to slip. Depending on the compressibility, the maximum potential event magnitude varied drastically from no event to M_w 3.58, demonstrating that the compressibility of the injected hydrogen is a key parameter. Broadly it was seen that in the range 5.00×10^{-7} Pa^{-1}-1.00×10^{-6} Pa^{-1}, the fault is completely stable, implying that the larger the injectant compressibility, the lower the risk of inducing fault slip.

The magnitude of the induced seismicity for the 6.67×10^{-8} Pa^{-1} and 1.00×10^{-7} Pa^{-1} cases is less sensitive to hydrogen compressibility than the slip because of the fact that a proportion of the fault surface is in stick in the 1.00×10^{-7} Pa^{-1} case (Figure 6.21v), which reduced the rupture area.

Dal Zilio et al. [2022] injected an unspecified fluid into a 2-D numerical model containing a fault. They did not quantitatively report slip, but they qualitatively reported the type of seismicity that occurred as either earthquake, slow-slip event or stable aseismic creep for different bulk rock-fluid compressibility pairs in the range 10^{-11} < fluid compressibility (Pa^{-1}) < 10^{-7}. They reported that for a given bulk rock compressibility, the seismic hazard decreased (aseismic creep became more likely than induced earthquakes) with increasing fluid compressibility. This supports the direct slip results herein, that at higher possible fluid compressibilites the fault does not slip. These findings make physical sense because a high compressibility fluid can dissipate some of the accumulated strain, but low compressibility fluids cannot, and thus the fault takes a greater degree of the accumulated strain.

6.8.13 *In Situ* Stresses

Homogeneous stresses may promote or inhibit reservoir fault slip depending on their absolute magnitude. The higher the homogeneous stresses, the more likely the fault is to be stable and induced seismicity avoided. For lower homogeneous stresses, large fault slip can result. As the magnitude of the homogeneous *in situ* stresses increased from 45 MPa to 60 MPa, the fault slip decreased very significantly from 9.34 cm to 0 cm. The normal effective stresses on the fault are much larger in the 60 MPa cases, keeping the fault stable. The heterogeneous horizontal stress cases, which had one of the stresses with magnitude less than 45 MPa, did not show a very significant difference to the homogeneous 45 MPa case in terms of the fault slip. This probably relates to the fact that the *in situ* stresses and the pore pressure are similar in magnitude for these cases, meaning that the pore pressure is the primary control on the slip; but only when the stresses were increased to 60 MPa, was the slip behaviour significantly different, which is the only case where the *in situ* stresses were much larger than the pore pressure, thus in this

case the *in situ* stresses govern the slip behaviour.

Mazzoldi et al. [2012] and Rutqvist et al. [2013] varied the σ_H/σ_V ratio in their 2-D CO_2 injection and water injection for hydraulic fracturing studies respectively. Mazzoldi et al. [2012] found when σ_H/σ_V was increased from 0.65 to 0.70, the fault slip decreased by 53%. When Rutqvist et al. [2013] increased the σ_H/σ_V ratio from 0.525 to 0.55, the fault slip decreased by a factor of between 5 and 12. In the work herein, the 45 MPa case represents a σ_H/σ_V ratio of 0.87 and the 60 MPa case represents a σ_H/σ_V ratio of 1.15. This trend was also observed herein that as σ_H/σ_V increased from 0.87 to 1.15, the fault slip decreased very strongly from nearly 10 cm of slip to none.

6.8.14 Limitations of Modelling Procedure

A quasi-static model of fault slip has been implemented in this work. The model incorporates a sequence of static models over different time intervals. It accounts for changes in reservoir properties, fluid distributions, and fault tractions, apertures and positioning but does so in discrete steps. A dynamic model would account for the rapid propagation of seismic waves and the short time-scale dependent behaviour of stress and strain, providing a more accurate representation of fault slip as it evolves at shorter time scales. Furthermore, complex rupture dynamics, including the exact nucleation and arrest of fault slip, and variations in slip velocity are not considered as they would be in a dynamic model. Dynamic models consider the full energy budget, including the partitioning of energy into seismic radiation, heat, and fracture energy, offering a more comprehensive understanding of the physical processes involved. The quasi-static assumption cannot capture the interaction of individual fault segments during rapid slip events which limits its ability to provide real-time assessments of seismic hazards associated with fluid injection and withdrawal. Nevertheless, there is a strong precedent in the literature to use the quasi-static assumption in numerical models of fault slip during the large field-scale injection and withdrawal of fluids (i.e., Mazzoldi et al. [2012], Zbinden et al. [2020], Mortezaei and Vahedifard [2015], Rutqvist et al. [2013]). This is because of the computational complexities and expense of handling multiple time-scales: from the less than a second in

which a fault ruptures to the years over which fluid is injected and withdrawn. Fluid injection and withdrawal in the context of geological storage occur over extended periods of months to years, leading to relatively slow changes in the stress and pressure fields. This slow rate of change justifies the quasi-static assumption that dynamic effects such as rapid accelerations are negligible. Since the dominant factors in the fault slip behaviour are the variations in pore pressure and resulting stress distributions and not the accelerations of the rock mass, the quasi-static model effectively captures the primary factors. The same quasi-static methodology used herein was used in the validation study of Burtonshaw et al. [2023b] where fault slip was shown to be similar to a published case of CO_2 injection into an aquifer [Mortezaei and Vahedifard, 2015].

This study uses a static friction model based on the Coulomb criterion to describe fault behaviour, identifying two states: stick and slip, according to Equation 3.8. In the stick state, frictional traction is less than or equal to the sum of cohesion and the product of the friction coefficient and normal contact traction. In the slip state, frictional traction exceeds this sum. While this might seem like a modelling constraint, employing the rate-and-state model introduces additional uncertainties. The parameters a and b for the rate-and-state model vary significantly across different faults and geological formations, complicating model calibration. Moreover, data for a and b for the specific rock units in this study are scarce. The static friction model used here partially addresses the 'evolution effect' seen in the rate-and-state model by accounting for changes in fault aperture over time due to geomechanical-fluid interactions. As fault apertures evolve, both tangential and normal tractions change, influencing the frictional stick-and-slip states on the fault. Consequently, frictional resistance varies due to mechanical and hydraulic changes over time. However, this model does not explicitly account for cementation of fault rocks [Romano et al., 2022, Williams and Fagereng, 2022], the sealing and closure of faults through mineral precipitation [Yehya and Rice, 2020], fault gouge compaction [Proctor et al., 2020], stress-induced cementation [Ji et al., 2022] and pressure solution [Hunfeld et al., 2020, Bedford et al., 2023]. Thus, it does not fully capture the complexity of fault aging and healing, which are challenging to model accurately. It should be noted that rate-and-state effects usually lead to negligible variations in the effective friction coefficient (approximately

within +/- 0.05) over time. As a result, we anticipate minimal deviation in slip behaviour compared to the findings presented in this study.

Seismic slip occurs when movement along a fault line triggers an earthquake [Wallace, 2020], resulting in the sudden release of built-up stress. This release fractures surrounding rocks, generating seismic waves that travel through the Earth. Aseismic fault slip involves movement along a fault line without significant seismic wave production. This movement can be slow and continuous or episodic, allowing for gradual stress relief. Since this study does not simulate wave propagation, it cannot definitively differentiate between seismic and aseismic slip. However, seismic slip rates can vary from fractions of a millimeter to several meters per event, while aseismic creep rates typically range from fractions of a millimeter to several centimeters per year [Wallace, 2020]. This annual aseismic creep rate corresponds to a maximum of approximately 0.58 mm per week, which aligns with the time step used in this research. Observations suggest slip occurrences exceeding several centimeters within a single time step, supporting seismic activity. The moment magnitudes provided in this study represent the maximum potential magnitudes, assuming all slip within a given time step occurs instantaneously. Therefore, they act as constraints on the upper limits of potential magnitudes, rather than predictions, due to the indiscernible distribution of slip within a single time step.

One further limitation of the modelling procedure that should be noted is the inability to represent fault sealing mechanisms such as clay smearing, cataclasis, chemical precipitation, and diagenesis. Specifically, the absence of clay smearing and cataclasis modelling may result in underestimating the fault's capacity to act as a barrier to fluid flow, while not accounting for chemical precipitation and diagenesis might overlook changes in fault strength and stability over time. If these fault zone processes were considered, they could have significantly influenced a range of parameters, most notably permeability and fault slip behavior. Cataclasis, the mechanical breakdown of grains due to shear, can either increase or decrease permeability depending on the extent to which generated microfractures form a connected network. In scenarios where cataclasis results in a well-connected microfracture system, fault zone permeability may increase, promoting fluid flow and pore pressure diffusion along the fault, thereby facilitating fault slip under elevated fluid pressures. Conversely, in cases where cataclastic grains clog

pore spaces, permeability may decrease, leading to pressure compartmentalization and localized stress concentrations. Clay smearing, which occurs when ductile clay-rich layers are dragged along a fault plane, typically acts as a sealing mechanism. This can reduce permeability sharply and create hydraulic barriers that isolate compartments within the reservoir. Under such conditions, pore pressure buildup adjacent to the smears could increase the effective normal stress on the fault plane, potentially delaying or localizing slip. In fault zones with heterogeneous clay distribution, this could result in complex slip patterns and spatially variable reactivation potential.

6.9 Conclusion

The Imperial College Geomechanics Toolkit (ICGT), a fully-coupled, three-dimensional, hydromechanical simulator was applied to study fault slip and induced seismicity during multi-year geological hydrogen storage in a full-scale depleted gas reservoir model. Fault slip was examined along a fault that is fully contained within the reservoir unit in which the injection and withdrawal occurred. Parametric analyses were undertaken in order to quantitatively understand which storage fields, in terms of their mechanical and fault properties and stresses, are optimal for minimizing seismic risk during hydrogen storage and which operational and injectant fluid properties minimize potential seismicity. For fault slip along reservoir faults, it was found that:

1. Of the mechanical properties, Young's modulus and Poisson's ratio had the strongest control on the fault slip, and Biot coefficient to a lesser extent. The magnitude of the fault slip was insensitive to changes in reservoir permeability.

2. Increasing friction coefficient results in increased fault slip magnitude per time step and increased number of slippage events. High friction coefficients induced the second and third largest events of all fourteen parametric analyses, with M_w 3.72 and 3.67 in the 0.75 and 0.99 cases.

3. Fault permeability had little influence on fault slip, except when the fault permeability was much smaller than the matrix permeability, where no slip occurred. Thus, faults that have been filled with mineral precipitates will reduce seismic risk.

4. Average fault slip increased significantly with increasing fault length, suggesting that reservoir with large-scale faults could be more prone to seismicity.

5. Fault dip had a significant effect on fault slip. When the fault dipped at 45°, the largest event of all fourteen parametric analyses was observed with M_w 3.75. When the dip was very large (80°), the maximal slip decreased by over 90% relative to the 45° case.

6. As injection rate increased, fault slip increased. Very high injection rates were required to enable the fault to slip. At rates of $5 m^3/s$ or less the fault was fully stable.

7. As withdrawal rate increased, fault slip increased and the time to event initiation increased. The event magnitude varied by only 0.08 across the tested withdrawal rates, implying withdrawal rate does not have a significant influence on the magnitude of the fault slip.

8. As hydrogen compressibility increased, fault slip broadly decreased. As compressibility increased from 1.00×10^{-7} Pa^{-1} to 5.00×10^{-7} Pa^{-1}, fault slip decreased strongly from 11.35 cm to 0 cm. Therefore, the higher the compressibility of the hydrogen injectant, the lower the seismic risk.

9. Fault strike (at least in a homogeneous stress field), horizontal well length, vertical well perforation length, vertical well-fault spacing, hydrogen viscosity and hydrogen density have very little effect on the induced fault slip.

The mechanical, fault, fluid and operational properties were shown to have a strong influence on the maximum potential magnitude of induced seismicity, with M_w varying between no event and 3.75. Therefore, such properties should be strongly considered and assessed prior to the beginning of storage operations. Reservoirs containing faults with low friction coefficient ($<$ 0.50), fault permeability below the matrix permeability (i.e. high degrees of mineralization)

and high fault dips ($> 60°$) should be prioritized for geological hydrogen storage, at least in terms of reducing seismic hazard. The reservoir rock with high Young's modulus (>40 GPa), high Poisson's ratio (>0.30) and high Biot coefficient (>0.65) is found to yield the minimum slip during the simulation of hydrogen storage. Furthermore, the injected hydrogen should have as high compressibility as possible ($> 5.00\times10^{-7}$ Pa^{-1}). Therefore, the injection temperature and pressure should be carefully selected to ensure as high compressibility as possible.

As small injection rate and withdrawal rate as logistically possible should be used because the fault was shown to be completely stable when the injection rate was reduced to 5 m^3/s or less. Utilizing many fields with smaller stored quantities of hydrogen, rather than few fields with huge stored quantities, will reduce seismic risk. Alternatively, potentially spreading the injection volume across multiple injection wellbores in one field may also reduce this risk, but this needs to be subject of future work.

Chapter 7

Effect of Mechanical, Fluid, Operational and Fault Properties on Fault Slip and Induced Seismicity along Basement Faults during UHS

7.1 Introduction

Induced seismicity on basement faults due to the injection of a fluid in an overlying reservoir unit is a well-known phenomenon. Examples of induced seismicity along basement faults include those from wastewater injection [Hearn et al., 2018, Horton, 2012, Zhang et al., 2013, Verdon, 2014, Hornbach et al., 2015, McGarr et al., 2015], CO_2 injection [Cao et al., 2021, Chang et al., 2022] and geothermal [Buijze et al., 2019, Megies and Wassermann, 2014, Küperkoch et al., 2018]. When injecting a fluid, the pore pressure in the reservoir increases, which reduces the effective stress acting on a fault within the reservoir unit, enabling the fault to slip at stress conditions lower than it otherwise would [Ellsworth, 2013, Wang et al., 2024a, Scuderi et al., 2017, Bao and Eaton, 2016, King Hubbert and Rubey, 1959, Shapiro et al., 2003, McGarr, 2014]. However, for faults in basement units, the low permeability of basement/underburden

rocks means that the elevated pore pressure front often remains restricted to the overlying reservoir unit. Therefore, the most common mechanism for fault slip along basement faults during injection is the formation of localised aureoles of elevated shear stress or reduced normal stress, that form due to poroelastic stress and strain transfer beyond the portions of rock where the injectant pressure front has diffused, and which lead to failure [Barbour et al., 2017, Segall and Lu, 2015, Fan et al., 2019, Chang and Segall, 2016a,b]. This poroelastic stress and strain transfer results from the contraction and expansion of the reservoir rock in response to fluid withdrawal and injection, respectively, which perturbs the stress state outside the reservoir. Sometimes, low permeability basement faults can slip due to the elevated pore pressure front, if the basement fault also propagates into the reservoir unit, thus allowing direct fluid communication between the reservoir and underburden [Fan et al., 2019, Ogwari et al., 2018, Hornbach et al., 2015, Langenbruch et al., 2018, Zhang et al., 2013].

A linkage between subsurface fluid injection and induced seismicity has been known since the early 1960's. In 1961, a 12,000-foot well was drilled at the Rocky Mountain Arsenal Chemical Weapons facility in Denver, United States. for the injection of hazardous wastewater into the subsurface [Evans, 1966]. Within a few months of the onset of injection, tremors began, and over 700 small to modest magnitude earthquakes occurred between 1962 and 1966 [Evans, 1966]. The U.S. Army later shut in the wellbore in 1966 [Whitney, 2019], but earthquakes continued to occur, including one of magnitude 4.8 in 1967 [Kuchment, 2016], as the pressure front propagated toward other faults. Earthquakes continued until 1981 according to reports from local residents. In 1969, the United States Geological Survey (USGS) performed injection experiments in Chevron's Rangely oil reservoir in Colorado [Kuchment, 2016]. They found that earthquakes ceased when the injection rate was reduced below a critical level and were initiated when the injection rate exceeded this critical level. In the early 2000's, a boom in shale gas exploration occurred [Wang and Krupnick, 2015]. With this came the need to dispose of large quantities of waste brine. In 2008, in the proximity of the Barnett Shale formation in Texas, United States, a cluster of earthquakes in the nearby town of Cleburne was linked to the wastewater disposal. Seismometer readings showed that 180 small earthquakes occurred between late-October 2008 and late-May 2009 [Frohlich, 2012]. Earthquakes also

resulted from operations south of Fort-Worth in June 2009 [Frohlich et al., 2011], Guy and Greenbrier in Arkansas [Park et al., 2020] and Youngstown, Ohio in March 2011 [Kim, 2013]. It was clear that earthquakes were occurring in regions that are not prone to seismicity, and rates of seismicity were drastically enhanced in the years following injection procedures relative to the years prior. The injection of supercritical carbon dioxide for Carbon, Capture and Storage (CCS) resulted in a sequence of microseismic events at the In Salah site in Algeria in 2004 [Cao et al., 2021]. On November 6th 2011, wastewater injection in Oklahoma, the United States lead to the largest ever induced seismic event, with a magnitude of 5.6, known as the 'M5.6 Prague earthquake' [Yeck et al., 2017]. Significant damage resulted, with the collapse of building walls and chimneys and people were injured [Boak, 2016], showing that it is crucial to understand the physical causes of induced seismicity and how it can be reduced or avoided.

Although some numerical studies have examined seismicity and the mechanical properties that influence it along reservoir faults, no previous study has examined induced seismicity along underburden faults during hydrogen storage, and no previous study has attempted to quantify the underburden mechanical properties which are optimal for reducing fault slip and seismic risk during the deployment of any geo-energy injection technology. This is critical to study because Table 7.1 in comparison to Table 6.1 shows that some of the largest induced seismic events have occurred along basement faults (as have the majority of induced events [Hemami et al., 2021]), and some of these have only small pressure changes of less than 0.2 MPa, such as near magnitude 5 and 6 seismicity in the basement in Milan, Kansas and below the Arbuckle formation in North-Oklahoma respectively, both where wastewater was being injected [Zoback and Smit, 2023, Hearn et al., 2018].

Table 7.1: Cases of induced seismicity occurring along underburden/basement faults below the injection/extraction unit for a variety of geo-energy technologies. [a]Kaven et al. [2015]; [b]Yeck et al. [2016]; [c]Horton [2012]; [d]Keranen et al. [2013]; [e]Goebel et al. [2016]; [f]Lee et al. [2019]; [g]Seeber et al. [2004]; [h]Schultz et al. [2017]; [i]Kim [2013]; [j]Glasgow et al. [2021].

Location	Earthquake Magnitude	Notes
CO_2 Storage		
Decatur, Illinois, U.S.[a]	-0.7 to 1.26	1000 tonnes/day CO_2 injected into overlying sandstone Aquifer. The basement rhyolite has clay-rich matrix and is fractured.
Hydraulic Fracturing		
Fox Creek, Alberta, Canada[h]	< 4.1	9.4 m^3/min hydraulic frac fluid injected into Duvernay shale. Events occurred in top few hundred m's of Precambrian crystalline basement.
Geothermal		
Pohang, South Korea[f]	5.5	Creation of artificial geothermal reservoir in low-permeability crystalline basement via hydraulic fracturing. Loss of > 160 m^3 of drilling fluid that transferred additional pressure of > 20 MPa to the fm.
Wastewater Disposal		
Fairview, Oklahoma, U.S.[b]	5.1	10,000-40,000 barrels of wastewater per day injected into the porous Arbuckle Formation, directly above the crystalline basement containing critically stressed faults.
Arkoma Basin, Arkansas, U.S.[c]	< 4.7	Injection into Paleozoic sedimentary formation that overlays igneous and metamorphic crystalline basement containing critically stressed Guy-Greenbrier fault.
Prague, Oklahoma, U.S.[d]	< 5.7	Seismicity delayed almost 20 years from initial injection, and 5 years after largest increase in wellhead pressure. Occurred due to stress-transfer.
Southern Central Valley, California, U.S.[e]	< 4.6	Injection into 20-30 m thin turbiditic sand lenses (Monterey formation) above very low permeability gneissic basement. Seismicity along White Wolf fault.
Ashtabula, Ohio, U.S.[g]	< 4.3	0.3×10^6 m^3 injected over 8 years into the overlying Paleozoic section resulting in seismicity in the fractured Grenville precambrian basement. Both units are hydraulically isolated.
Youngstown, Ohio, U.S.[i]	< 3.9	All 109 earthquakes occured exclusively in the precambrian basement. Periods of quiescence in seismicity mirror the lows in injection pressure and volumes.
Raton Basin, Colorado/N. Mexico, U.S.[j]	< 5.3	Seismicity occurs along long (< 3 km), reactivated faults with variable faulting regimes and strikes within the precambrian basement.

In the present chapter, the ICGT [Paluszny and Zimmerman, 2013, Thomas et al., 2020a] is used to study fault slip and induced seismicity along a single fault located in the underburden unit (below the reservoir unit in which injection, storage, and withdrawal takes place) of a four-layer, 4000×4000×3300 m, anticlinal, depleted gas field during hydrogen storage. Simulations cover a period of three years, in which each annual cycle consists of a five-month injection period, two-month storage period, and five-month withdrawal period. A parametric analysis is undertaken for four underburden mechanical properties: Young's modulus (5-40 GPa), Poisson's ratio (0.10-0.35), Biot coefficient (0.60-1.00) and matrix permeability (7.0×10^{-24} m^2-1.0×10^{-16} m^2). These parameter ranges are designed to cover all realistic values for the underburden of various depleted North Sea candidate fields found in the literature (Table 6.4). For each mechanical property, a total of four cases are run, in which only that property is varied. In each case, average fault slip versus time is shown for a time period of three years. This analysis particularly helps to understand two fundamental questions relating to the geological storage of hydrogen in depleted fields: (1) to what extent are underburden faults prone to slip and induced seismicity? and (2) what underburden mechanical properties would be most advantageous and disadvantageous in our pursuit to minimise seismic events during injection, storage and production?

7.2 Methodology

A numerical model with dimensions 4000 m × 4000 m × 3300 m (Figure 7.1) was constructed to study the injection, storage and withdrawal of gaseous hydrogen. The model is similar to that used in Chapter 6, except that there is no fault in the reservoir unit, and instead, a fault is emplaced in the underburden unit. The model represents a generic North Sea reservoir, with typical lithologies (chalk overburden, shale caprock, sandstone reservoir and shale underburden) and geometry (anticlinal structure, with the reservoir bound from above and below by a low permeability seal). The mechanical and fluid properties (Table 7.2) are prescribed based on a literature search of depleted North Sea oil and gas fields (Table 6.4) – the majority of the parameters come from the Leman, Britannia and Goldeneye fields for which data was available. The fault properties are generic.

Gaseous hydrogen is injected at 40.0 m^3/s into the reservoir through a horizontal wellbore that penetrates the whole x-direction of the model and is produced through a second wellbore of the same dimensions at 34.0 m^3/s at the opposite end (y-direction) of the model. Both wellbores are at a depth of 2,475 m. Simulations are run for three annual cycles with each annual cycle consisting of a 5-month injection period, a 2-month storage period, and a 5-month withdrawal period. The model contains a solitary fault of dimensions 2000 m x 1000 m, that is centred at a depth of 2,950 m, and is fully encapsulated within the low-permeability underburden unit. The fault strikes parallel to the injection and withdrawal wellbores.

The boundary conditions for the simulation are defined as follows: *In situ* stresses are imposed as Neumann boundary conditions. Initially, matrix pore pressure is in equilibrium with mechanical stresses, and a series of hydrostatic steps are conducted to establish equilibrium before the injection phase commences. Injection and withdrawal processes are represented as volumetric fluxes applied at the respective well elements. Modelling injection and withdrawal as volumetric fluxes at discrete well elements assumes a simplified representation of fluid flow within the reservoir because it presumes homogeneity in fluid distribution and pressure propagation within the reservoir because of the assumed homogeneity in rock properties such as reservoir permeability. Furthermore, in reality wellbore perforations are never perfectly spaced and of identical size. Therefore, fluid delivery to the rock is unlikely to be perfectly distributed along the well length. This may lead to slightly different pressure distributions in the reservoir which may slightly influence stress and strain transfer from the reservoir into the underburden, leading to small differences in the magnitude and timing of fault slip.

The domain is spatially discretised with isoparametric linear tetrahedra internally, and with isoparametric linear triangles on the model boundaries and fault (Figure 7.1). The model contains 15,428 triangular surface elements, of which 3898 are on each fault face, and 238,281 tetrahedral elements in the volume.

The fault exists as two rectangular surfaces that are connected at the fault tips, making a negative volume within the mesh. The slip is computed at each node on the fault surfaces and a weighted-average is used to compute the average fault slip used in the Results Section:

Table 7.2: The geological, mechanical, geometrical, fluid dynamic, and fault properties and the *in situ* stresses of the four different rock layers within the models. The symbology in the table is as follows: k = permeability, ϕ = porosity, h = thickness, E = Young's modulus, ν = Poisson's ratio, α = Biot coefficient, ρ_b = rock density, K = bulk modulus, σ^* - uniaxial tensile strength, ρ_f = fluid density, μ = fluid viscosity, c = fluid compressibility, σ_h = minimum horizontal *in situ* stress at base, σ_H = maximum horizontal *in situ* stress at base, L = fault length, w = fault width, $a_{f,r}$ = residual aperture, θ = fault dip, ψ = fault orientation to North and x = fault centroid location (x,y,z).

Property	Overburden	Caprock	Reservoir	Underburden
Mechanical				
Lithology	Chalk	Shale	Sandstone	Shale/Coal
k (m^2)	3.0×10^{-15}	1.0×10^{-21}	1.0×10^{-13}	1.0×10^{-21}
ϕ	0.30	0.05	0.15	0.05
h (m)	2300 - 2400	100	150	650 - 750
E (Pa)	4.5×10^{9}	1.5×10^{10}	1.5×10^{10}	4.0×10^{10}
ν	0.35	0.35	0.15	0.35
α	0.87	0.93	0.35	0.93
ρ_b (kg/m^3)	2080	2500	2500	2500
σ^* (Pa)	1.0×10^{6}	1.3×10^{6}	2.0×10^{6}	1.3×10^{6}
Fluid				
Fluid	Brine	Brine	Hydrogen	Brine
ρ_f (kg/m^3)	1058	1042	9	1037
μ (μPa s)	561.0	357.5	10.4	296.0
c (Pa^{-1})	4.47×10^{-10}	4.57×10^{-10}	6.67×10^{-8}	4.68×10^{-10}
Stresses				
σ_h (MPa)	-	-	58.5	-
σ_H (MPa)	-	-	58.5	-
Fault				
L (m)	-	-	-	2000
w (m)	-	-	-	1000
$a_{f,r}$ (m)	-	-	-	1.0×10^{-6}
θ (°)	-	-	-	53.1
ψ (°)	-	-	-	0
x (m)	-	-	-	(0,0,2475)

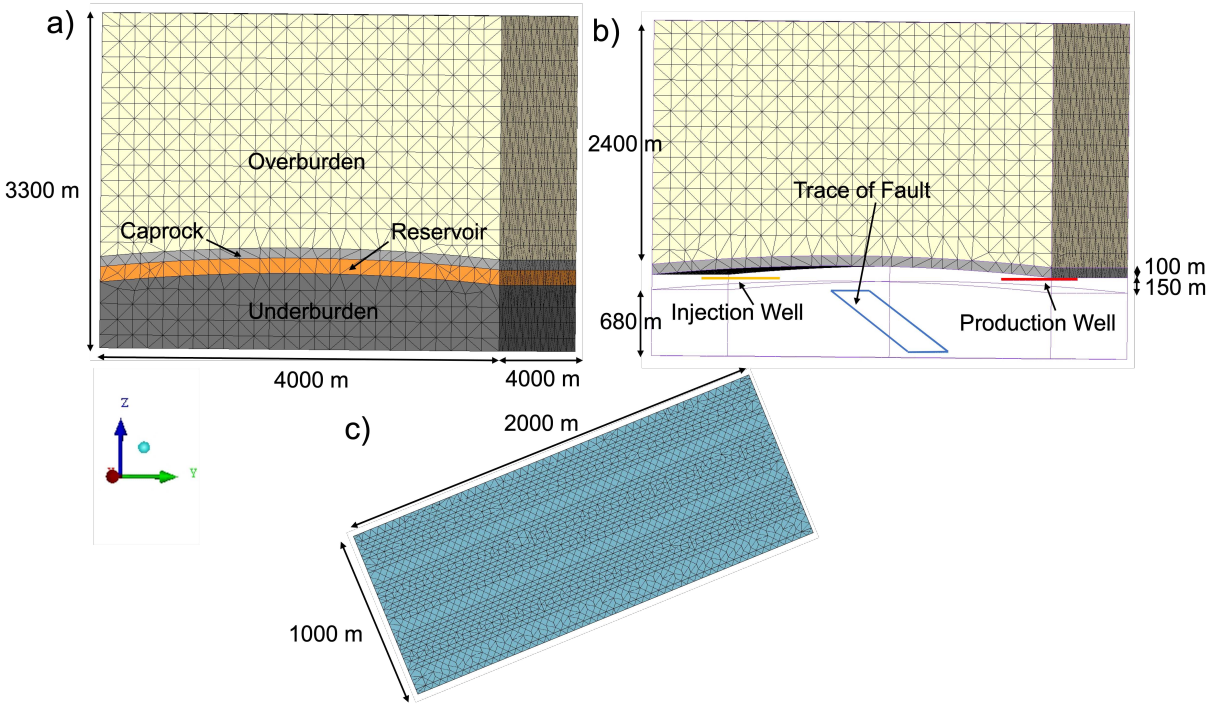


Figure 7.1: (a) A solid and wireframe view of the model showing the four rock layers (overburden is cream, caprock is light grey, reservoir is orange, underburden is dark grey). b) A perspective front-right solid and wireframe view of the fault (blue) contained with the reservoir unit and the injection well on the left of the domain (orange) and the withdrawal well on the right of the domain (red). The reservoir and underburden units are removed in order to observe these. c) A top view of the rectangular fault surface.

$$d = \sum_{n=1}^{N} x_n \cdot \frac{A_n}{A_T}, \tag{7.1}$$

where d is the average fault slip at a given time step, x_n is the slip at the node of interest, n, A_n is the area surrounding the node of interest and A_T is the total fault surface area.

7.3 Mesh and Time Step Effects

In order to ensure that the fault slip solution as a function of time is not dependent on the refinement of the meshes used or the time step used, an extensive study of the effects of the bulk rock domain and the fault mesh refinements, and the time steps, are performed in the following sections.

7.3.1 Domain Mesh Refinement

A total of four simulations were performed to assess the impact of the bulk rock domain mesh refinement on the average fault slip as a function of time. The four cases are summarised in Table 7.3, and vary from a coarse case with approximately 17,000 nodes and 95,000 elements, to a very refined mesh with approximately 125,000 nodes and 750,000 elements. In Cases 1 and 2, the entire domain is refined evenly, in Case 3, a box surrounding the fault of dimensions 2500×1050×750 m is refined more than the remaining domain and in Case 4, the same box is refined to a greater extent than in Case 3. The domain meshes are shown in Figure 7.2a. The results are shown in Figure 7.3b. It is found that provided that the bulk rock mass is discretised with approximately at least 43,000 nodes and 253,000 elements, then the fault slip solution is typically the same to within 0.1 mm (100 microns). Case 1 was found to be too coarse to accurately yield the solution with very large numerical errors generated. Thus, for the remaining simulations in this work the bulk rock mass will be discretised according to Case 2, which suffers from less numerical errors than Cases 3 and 4, and is computationally less expensive.

Table 7.3: Four simulation cases run to examine the effect of domain refinement on the slip solution.

Simulation Case	Nodes	Elements	Fault Elements
Case 1	16,532	94,943	3826
Case 2	42,856	253,709	3898
Case 3	51,664	307,095	3827
Case 4	125,339	748,302	3865

7.3.2 Fault Mesh Refinement

A total of five simulations were performed to assess the impact of the fault mesh refinement on the average fault slip as a function of time. The five cases are summarised in Table 7.4, and vary from a coarse case with approximately 700 elements to a very refined case with approximately 6,250 elements. The fault meshes are shown in Figure 7.2c. The results are shown in Figure

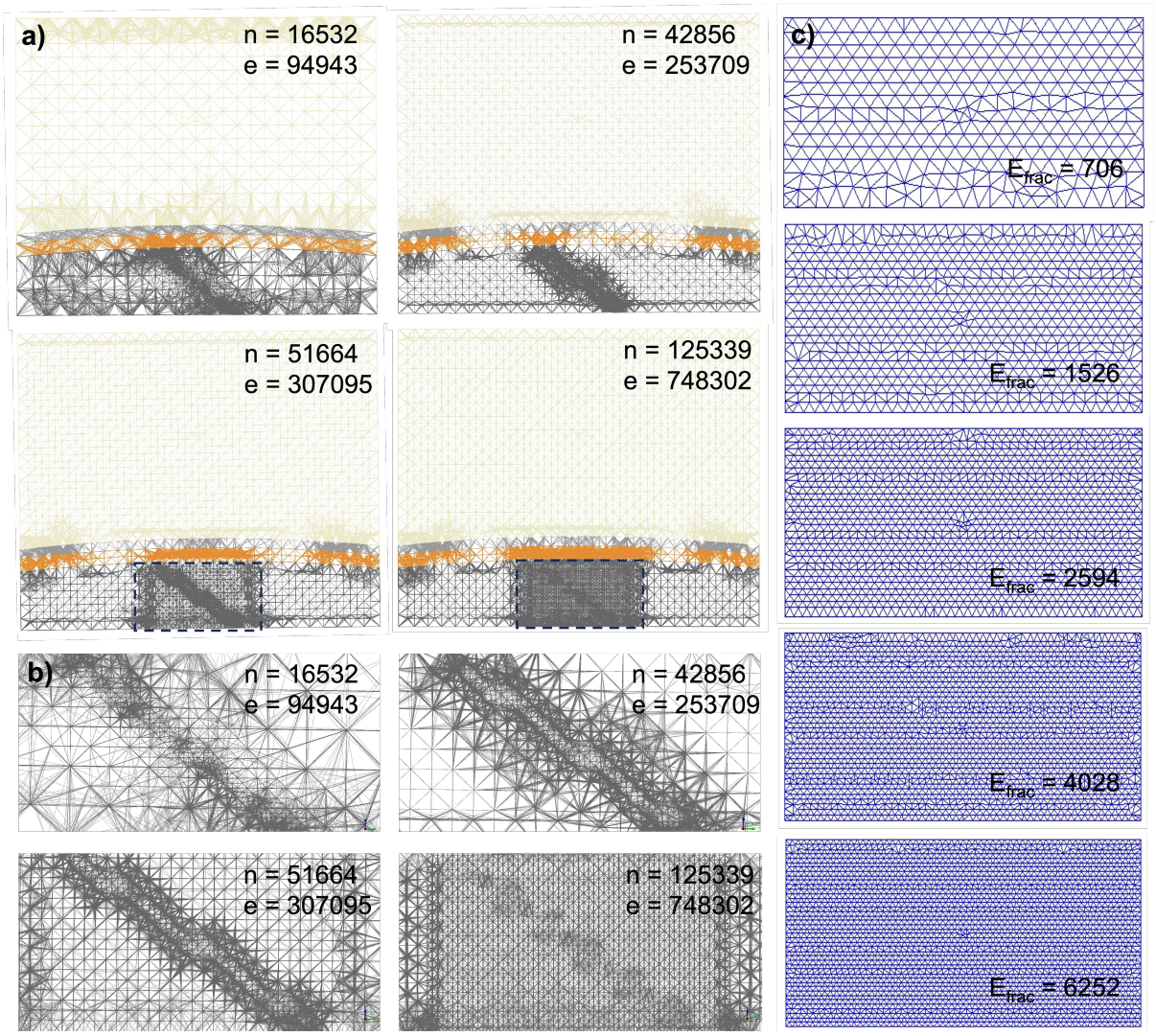


Figure 7.2: (a) Wireframe views of the four versions of the model for each refinement case in Table 7.3. The dashed boxes denote the zones of increased refinement. (b) Zoomed views of the mesh at the centre of the underburden unit. (c) Mesh of the fault surface for the five versions of the fault in the model for each refinement case in Table 7.4, for varying amounts of fracture elements E_{frac}.

7.3a. It is found that provided that the fault is discretised into at least approximately 1500 elements, then the fault slip solution is the same to within a maximum difference of 0.3 mm (300 microns). Only in the coarsest case, with 706 fault elements, was the fault slip solution significantly different, with up to approximately 1.5 mm difference. Thus, for the remaining simulations in this work the fault will be discretised according to Case 4, although Cases 2 and 3 would have also been acceptable.

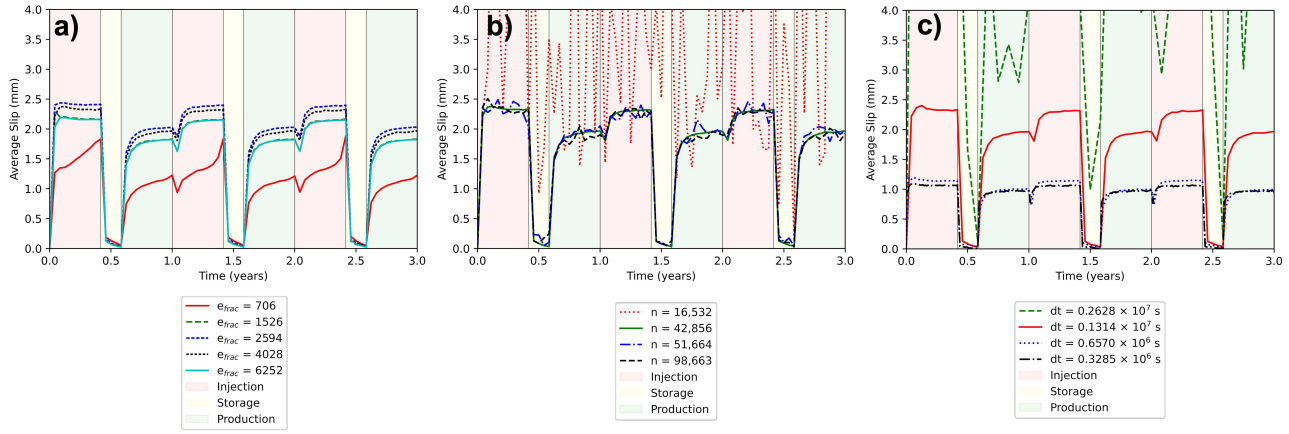


Figure 7.3: Plots of average slip as a function of operation time for (a) five cases of different fault refinements represented by different numbers of fault elements, (b) four cases of different bulk rock/domain refinements represented by different numbers of nodes and (c) four cases of different time step. The full discretisation data for each case in (a) and (b) is reported in Tables 7.4 and 7.3 respectively.

Table 7.4: Five simulation cases run to examine the effect of fault refinement on the slip solution.

Simulation Case	Nodes	Elements	Fault Elements
Case 1	17,603	105,927	706
Case 2	21,604	119,139	1526
Case 3	23,363	138,125	2594
Case 4	42,855	253,697	4028
Case 5	61,445	363,785	6252

7.3.3 Time Step

A total of four simulations were performed to assess the impact of the time step on the average fault slip as a function of time. The time steps tested included 0.2628×10^7 s, 0.1314×10^7 s, 0.657×10^6 s, and 0.3285×10^7 s. Time steps smaller than this were not tested due to the computational constraint of realistic simulation run time. The results are shown in Figure 7.3c. It is found that provided a time step of at least 0.657×10^6 s is used, the fault slip solution converges to the same result. Time steps slightly larger than 0.657×10^6 s replicate the same trend in slip but there are large inaccuracies such as in the 0.1314×10^7 s case, whereas time steps much larger than 0.657×10^6 failed to replicate the same trend in slip and were extremely inaccurate. Given time steps of 0.657×10^6 s or lower yield the same result, the 0.657×10^6 s case

is chosen for the simulations performed in this work in order to reduce computational time.

7.4 Results

This section outlines the results from the numerical experiments outlined in the methodology Section. It is found in every case that the fault in the underburden unit does not substantially slip during the bulk of the injection, storage, or withdrawal periods. However, the fault slips significantly at the cross-over points between operation regimes (i.e., injection, storage, withdrawal) and at the very onset of injection at time $t = 0$, reflecting sudden changes in the stress field at these points. Only at these points, where slip is induced suddenly may the slip potentially be seismic. These findings are unsurprising, given that abrupt increases in injection rates tend to shortly preceed the occurrence of earthquakes [Alghannam and Juanes, 2020, Tang et al., 2018, Cuenot et al., 2008, Kim, 2013]. Alghannam and Juanes [2020] found that the likelihood of triggering earthquakes depends critically on the rate of increase in pore pressure, and that fluid injection at constant rate acts to trigger seismic rupture at early times, before transitioning to aseismic creep at late times. This supports the present findings, wherein the fault slips to a relatively large extent immediately following the onset of injection, due to the large injection volume of 40 m^3/s, and then slips very minimally for the remainder of the injection periods. For their case of injection at constant rate, it was observed that the critical stiffness increased at early times, potentially triggering earthquakes, and decreased at late times, potentially resulting in the cessation of earthquakes. Additionally, a dramatic drop in critical stiffness was observed upon stopping injection, showing that the propensity for seismicity rapidly follows changes in injection rate.

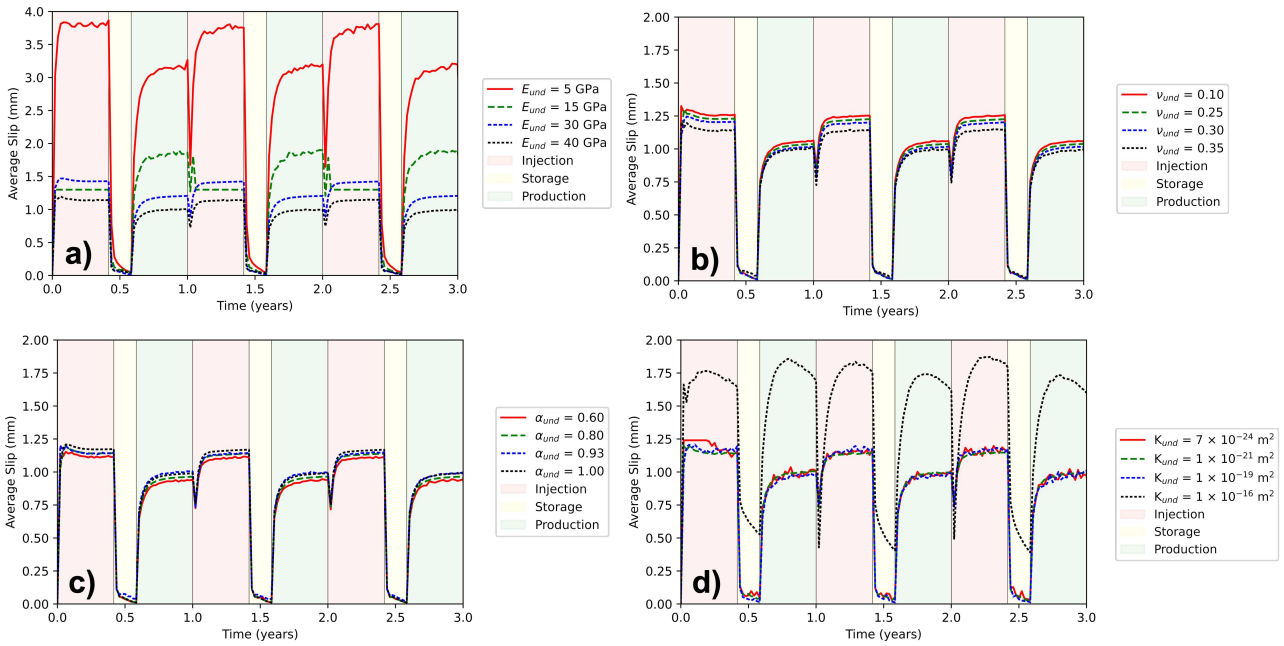


Figure 7.4: Average slip as a function of operation time for four cases of varying reservoir (a) Young's modulus, (b) Poisson's ratio, (c) Biot coefficient and (d) permeability.

7.4.1 Effect of Mechanical Properties

7.4.1.1 Young's modulus

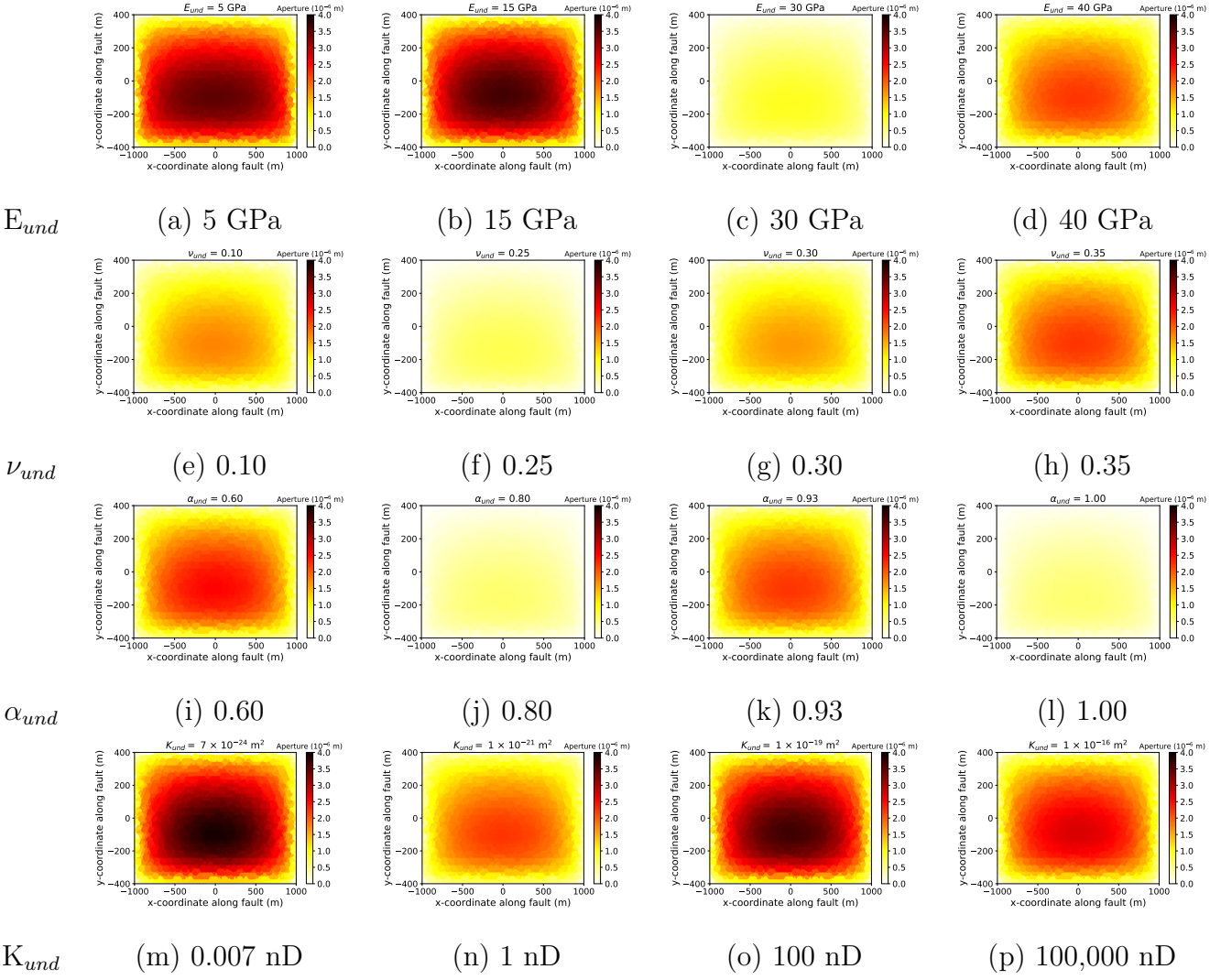
The Young's modulus of the shale underburden was varied between 5 GPa and 40 GPa, and the influence on average slip as a function of time is shown in Figure 7.4a. It is generally found that as Young's modulus increases, the fault slip decreases. The initial slip of the fault at $t = 0$, at the onset of injection, for the 5, 15, 30 and 40 GPa cases is approximately 3.83 mm, 1.31 mm, 1.48 mm, and 1.20 mm, respectively. For the slip period at approximately 1.58 years at the transition between storage and withdrawal regimes, the fault slip for the 5, 15, 30 and 40 GPa cases is approximately 2.61 mm, 1.61 mm, 1.05 mm, and 0.88 mm, respectively.

The fault aperture and the fault slip at each individual node on the fault surface at a time of 1.58 years is shown in Figures 7.5 and 7.6. No systematic change in aperture was found with increasing Young's modulus, although generally it is seen that larger apertures are observed for smaller Young's modulii. This broad change can be explained by the fact that a stiffer rock is less deformable and more resistant to changes in shape or size when subjected to stress. As a result, the rock adjacent to the fault experiences less deformation under the same stress conditions

compared to rock with lower Young's modulus, and this reduced displacement and contraction of the neighbouring rock restricts the ability of the fault to widen, leading to smaller fault apertures. The trend in aperture is not perfectly systematic, because a combination of other factors also influence the aperture. For example, the interaction between flow and mechanical deformation plays a crucial role in fault behaviour. Changes in Young's modulus can influence fluid flow patterns and pore pressure distribution, which in turn affect the mechanical response of the rock mass and ultimately the fault aperture.

Effective stress and strain are shown in Figures 7.7 and 7.13, respectively. It is found that as Young's modulus decreases, the strain in the underburden unit increases significantly. A rock with a lower Young's modulus is more compliant, meaning it is easier to deform and has less resistance to applied forces. As a result, when subjected to stress, such a rock exhibits greater strain because it is more willing to undergo deformation. Furthermore, the vertical stress profile through the model shows that at the depths of the upper underburden (2650 - 2950 m), the stress is the lowest in the 5 GPa case, where the most fault slip was observed and the stress is the highest in the 40 GPa case, where the least slip was observed, due to the fact that the high strain in the 5 GPa case results in larger stress relative to the very low strain in the 40 GPa case. The lower the effective normal stresses on the fault and the higher the strains in the vicinity of the fault, the greater the propensity the fault has to slip, which is observed here.

Taking into account Equations 3.11 and 3.12, and making the assumption that all the slip in one time step is released instantaneously, the upper bound for the moment magnitude of the potential induced seismicity at the onset of the initial injection is 2.73, 2.74, 2.98 and 3.00 for the 5, 15, 30 and 40 GPa cases, respectively. Therefore, despite fault slip increasing as Young's modulus decreases, the magnitude of the maximum potential induced seismicity decreases as Young's modulus decreases. This is because as Young's modulus decreases, the contribution of the smaller shear modulus, G, given by $E/2(1+\nu)$ in Equation 3.11 outweighs the increasing fault slip, d, and thus the seismic moment release is smaller as Young's modulus decreases. It is found that the Young's modulus of the underburden can have a strong influence on the magnitude of the induced seismicity.



E_{und} (a) 5 GPa (b) 15 GPa (c) 30 GPa (d) 40 GPa

ν_{und} (e) 0.10 (f) 0.25 (g) 0.30 (h) 0.35

α_{und} (i) 0.60 (j) 0.80 (k) 0.93 (l) 1.00

K_{und} (m) 0.007 nD (n) 1 nD (o) 100 nD (p) 100,000 nD

Figure 7.5: The apertures of the fault at a time of 1.58 years during the end of the second storage and beginning of the second withdrawal periods for cases of varying reservoir (a-d) Young's modulus, (e-h) Poisson's ratio, (i-l) Biot coefficient and (m-p) permeability.

7.4.1.2 Poisson's ratio

The Poisson's ratio of the shale underburden was varied between 0.10 and 0.35, and the influence on average slip as a function of time is shown in Figure 7.4b. It is found that as the underburden Poisson's ratio increases, the fault slip generally decreases. The initial slip of the fault at $t = 0$, at the onset of injection, for the 0.10, 0.25, 0.30 and 0.35 cases is approximately 1.33 mm, 1.16 mm, 1.15 mm and 1.20 mm, respectively. For the slip period at approximately 1.58 years at the transition between storage and withdrawal regimes, the fault slip for the 0.10, 0.25, 0.30, and 0.35 cases is approximately 0.92 mm, 0.91 mm, 0.90 mm and 0.88 mm, respectively. Thus, the Poisson's ratio of the underburden unit does not have a large influence on basement fault

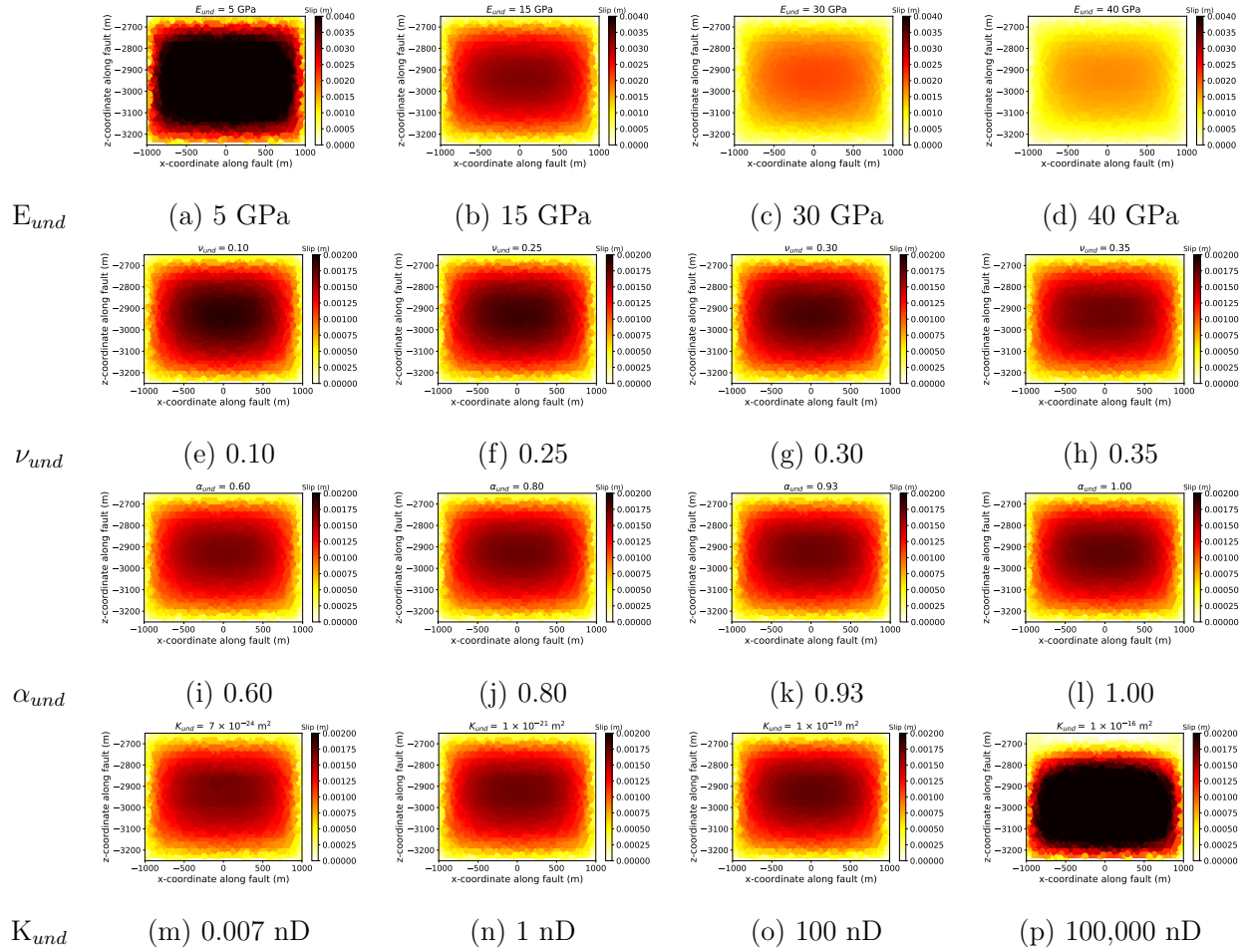


Figure 7.6: The individual slip at each node of the fault at a time of 1.58 years during the end of the second storage and beginning of the second withdrawal periods for cases of varying reservoir (a-d) Young's modulus, (e-h) Poisson's ratio, (i-l) Biot coefficient and (m-p) permeability. Note that the scales are not the same in each subfigure.

slip with the slip difference being a maximum of 125 microns between the cases.

The fault aperture and the fault slip at each individual node on the fault surface are shown in Figures 7.5 and 7.6. No systematic change in aperture is found with increasing Poisson's ratio. Poisson's ratio characterises the ratio of lateral contraction to longitudinal extension in a rock when it is subjected to stress. Changes in Poisson's ratio affect the distribution of stress within the rock, but it does not necessarily impact fault behaviour directly because the stress distribution around the fault remains relatively symmetrical with changes in Poisson's ratio. This results in relatively consistent fault apertures irrespective of Poisson's ratio.

Effective stress and strain are showed in Figures 7.7 and 7.13, respectively. The difference in underburden strain between the cases is minor, which is reflected in the near-identical fault

slip observed in the four cases. The vertical stress profile through the model shows that at the upper underburden (2650 - 3300 m), the stress is the highest in the highest Poisson's ratio case of 0.35, followed by the 0.30 case, with lower stresses seen in the 0.10 and 0.25 cases, implying a greater propensity for the fault to slip in the lower Poisson's ratio cases, which is what is observed. The broadly larger stress with increased Poisson's ratio occurs because a higher Poisson's ratio leads to greater lateral expansion of the underburden rock in response to the applied stress. This lateral expansion results in increased stress concentrations in the upper underburden because the underburden rock in these regions is trying to accommodate the lateral expansion while still being subjected to the compressive stress in the vertical direction and the opposing horizontal *in situ* stresses.

Taking into account Equations 3.11 and 3.12, and making the assumption that all the slip in one time step is released instantaneously, the upper bound for the moment magnitude of the potential induced seismicity at the onset of the initial injection is 3.09, 3.01, 3.00 and 3.00 for the 0.10, 0.25, 0.30 and 0.35 cases, respectively. Therefore, just as with the trend in fault slip, the magnitude of the maximum potential seismicity decreases as Poisson's ratio increases. The magnitude of the maximum potential seismicity is largely insensitive to changes in underburden Poisson's ratio, but is slightly larger when the Poisson's ratio was low (0.10).

7.4.1.3 Biot coefficient

The Biot coefficient of the shale underburden is varied between 0.60 and 1.00, and the influence on average slip as a function of time is shown in Figure 7.4c. It is found that the Biot coefficient is not a strong control on fault slip, but that a small trend is observed in which fault slip increases as Biot coefficient increases. The initial slip of the fault at $t = 0$, at the onset of injection, for the 0.60, 0.80, 0.93 and 1.00 cases is approximately 1.15 mm, 1.18 mm, 1.20 mm and 1.22 mm, respectively. For the slip period at approximately 1.58 years at the transition between storage and withdrawal regimes, the fault slip for the 0.60, 0.80, 0.93 and 1.00 cases is approximately 0.84 mm, 0.86 mm, 0.88 mm, and 0.89 mm, respectively. Thus, Biot coefficient does not have a strong influence on fault slip along basement faults for underburden rocks in the typical range

of 0.6 -1.0.

The fault aperture and the fault slip at each individual node on the fault surface at a time of 1.58 years is shown in Figures 7.5 and 7.6. No systematic change in aperture is found with increasing Biot coefficient. The Biot coefficient governs the extent to which changes in pore fluid pressure influence solid deformation and vice versa. Since the underburden has a very low permeability, fluid flow is somewhat decoupled from solid deformation in this unit because pore fluids are unable to move freely through the rock mass and exert significant pressure changes. In the absence of significant fluid flow and pressure changes, mechanical deformation processes become the dominant mechanism controlling fault slip behaviour. Variations in Biot coefficient therefore have minimal impact on fault behaviour in terms of slip and aperture because pressure change within and near the fault is inhibited.

Effective stress and strain are showed in Figures 7.7 and 7.13, respectively. The vertical stress profile through the model shows that throughout the upper underburden (2650 - 2950 m), the stress decreases with increasing Biot coefficient. This is because higher Biot coefficients lead to greater porosity changes and volume dilation, which can reduce stress within the rock mass. The lower the effective normal stresses on the fault, the greater propensity the fault has to slip which is observed here. The strains in the underburden unit are similar in each case, although in the region directly around the fault, the strain is slightly larger in the 0.60 and 0.93 cases, relative to the 0.80 and 1.00 cases. It is also seen that the aperture is larger in the 0.60 and 0.93 cases, relative to the 0.80 and 1.00 cases, showing that the aperture is a function of the strain.

Taking into account Equations 3.11 and 3.12, and making the assumption that all the slip in one time step is released instantaneously, the upper bound for the moment magnitude of the potential induced seismicity at the onset of the initial injection is 2.99, 3.00, 3.00 and 3.01 for the 0.60, 0.80, 0.93 and 1.00 cases, respectively. Therefore, the magnitude of the maximum potential seismicity is insensitive to changes in underburden Biot coefficient.

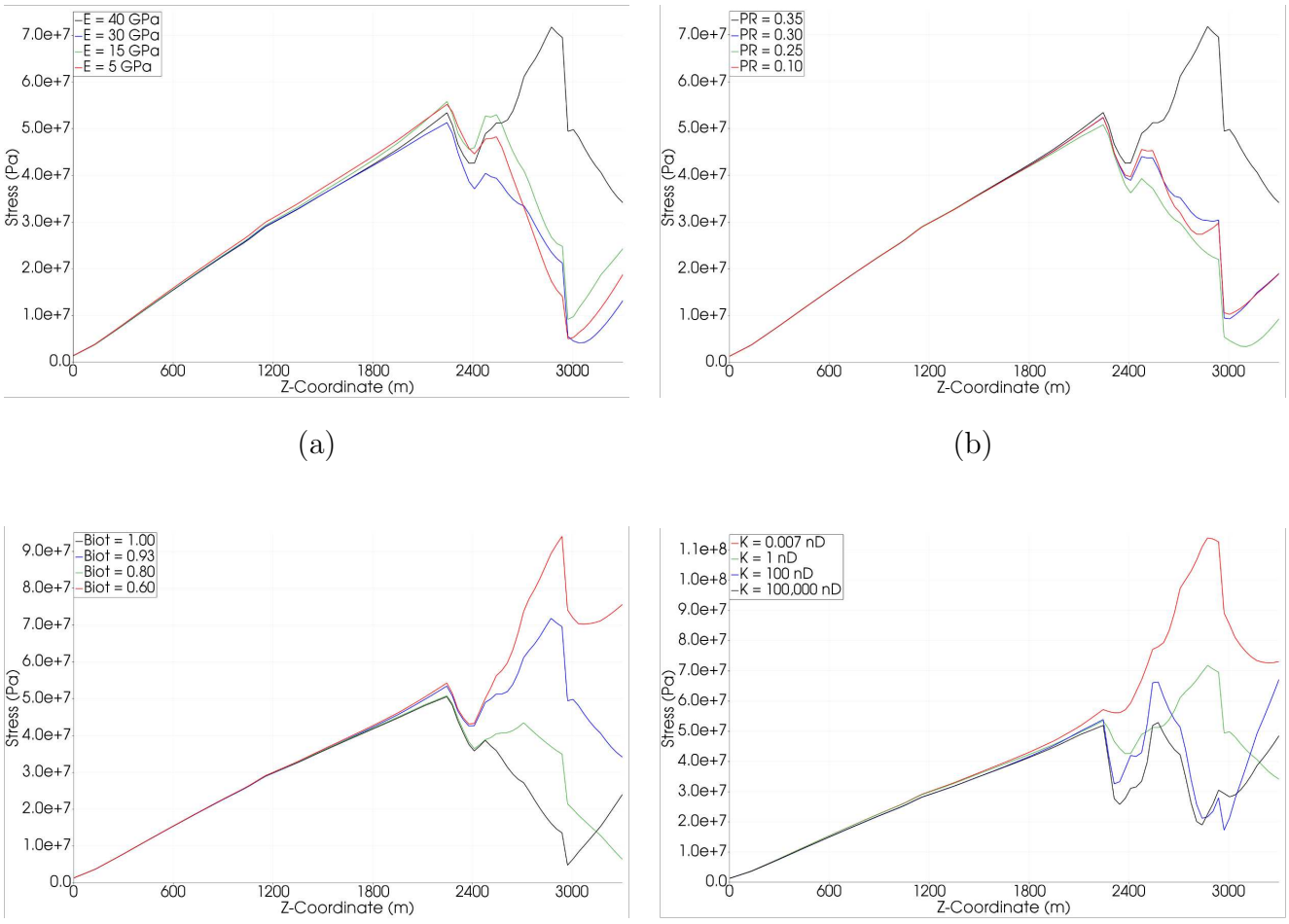


Figure 7.7: Plots of effective stress vertically through the center of the model in the z-direction for four cases of varying underburden (a) Young's modulus, (b) Poisson's ratio, (c) Biot coefficient and (d) permeability at a time of 1.58 years. z=0 refers to the centre point of the ground (top) surface.

7.4.1.4 Matrix permeability

The matrix permeability of the shale underburden is varied between 1×10^{-16} m^2 and 7×10^{-24} m^2, and the influence on average slip as a function of time is shown in Figure 7.4d. It is found that for permeabilities in the ranges 7×10^{-24} m^2 to 1×10^{-19} m^2, the fault slip is insensitive to changes in underburden permeability. However, when the permeability of the underburden unit is high (i.e., 1×10^{-16} m^2), the initial slip of the fault at t = 0 is considerably larger with 1.66 mm slip, compared to 1.25 mm, 1.20 mm and 1.06 mm in the 7×10^{-24} m^2, 1×10^{-21} m^2 and 1×10^{-19} m^2 cases. Thus, in particular early seismic hazard increases along underburden

faults when the underburden permeability is large. This is because with higher underburden permeability (1×10^{-16} m^2), the rock mass allows for more efficient fluid flow from the reservoir to the underburden. As a result, pore fluids can migrate more rapidly into and within the underburden, leading to a buildup of pore pressure within the fault zone. For the slip period at approximately 1.58 years at the transition between injection and storage regimes, the fault slip for the 7×10^{-24} m^2, 1×10^{-21} m^2, 1×10^{-19} m^{-21} and 1×10^{-16} m ^{2} cases is approximately 0.88 mm, 0.88 mm, 0.90 mm and 0.82 mm.

Effective stress and strain are showed in Figures 7.7 and 7.13, respectively. The average strain in the underburden unit increases as permeability decreases. Furthermore, the strain at the top of the underburden unit increases significantly as permeability decreases. Lower permeabilities are associated with higher pore pressures within the underburden unit that can exert additional support against the applied stresses, reducing the effective stress within the rock mass. This reduction in effective stress enhances the potential for mechanical deformation, resulting in increased strain within the underburden unit. However, in the region of the fault (centre of the underburden unit), the strain is very similar in all cases, supporting the fact that the permeability has no large effect on the induced fault slip after the initial slip at $t = 0$.

Taking into account Equations 3.11 and 3.12, and making the assumption that all the slip in one time step is released instantaneously, the upper bound for the moment magnitude of the potential induced seismicity at the onset of the initial injection is 3.01, 3.00, 2.96 and 3.09 for the 7×10^{-24} m^2, 1×10^{-21} m^2, 1×10^{-19} m^2 and 1×10^{-16} m^2 cases, respectively. Therefore, the magnitude of the maximum potential seismicity is largely insensitive to changes in underburden permeability when the permeability is between 10^{-24} and 10^{-19} m^2, but can increase for larger permeabilities.

7.4.2 Effect of Operational Properties

7.4.2.1 Injection Rate

The injection rate into the reservoir unit was varied between 5 m^3/s and 40 m^3/s, and the influence on average slip versus time is shown in Figure 7.8a. It was found that as the injection rate increased, the average fault slip increased. The initial slip of the underburden fault at t = 0, at the onset of injection, for the 5, 10, 30 and 40 m^3/s cases was approximately 0.15 mm, 0.30 mm, 0.87 mm and 1.20 mm, respectively. For the slip period at approximately 1.42 years at the transition between injection and storage regimes, the fault slip for the 5, 10, 30 and 40 m^3/s cases was approximately 0.14 mm, 0.28 mm, 0.81 mm and 1.07 mm, respectively. For the slip period at approximately 1.58 years at the transition between storage and withdrawal regimes, the fault slip for the 5, 10, 30 and 40 m^3/s cases was approximately 0.09 mm, 0.20 mm, 0.60 mm and 0.88 mm, respectively. Thus, the fault slip was strongly influenced by the injection rate, even though there is no direct hydraulic communication between the reservoir unit where the injection took place and the underburden unit which encapsulates the fault. This is possible because the poroelastic expansion of the reservoir, and thus the magnitude of the stresses transferred into the underburden, are still proportional to the injection rate. The fault slip was approximately linearly related to the injection rate.

The aperture and fault slip at each node across the fault surface are shown in Figures 7.10a and 7.11a. No systematic change in aperture was found as injection rate increased. In fact, the fault aperture was nearly identical in the 5, 10, and 40 m^3/s cases.

Effective stress and strain are shown in Figures 7.9a and 7.12a. The difference in strain between the cases was very minor. The vertical stress profile through the centre of the model shows that just below the reservoir-underburden interface, the stress was the smallest in the 40 m^3/s case, but throughout the remainder of the underburden, the total effective stress broadly decreased as the injection rate decreased. The stress profiles were almost identical in the 5 m^3/s and 10 m^3/s cases, implying that the stress in the underburden was only significantly disturbed for high injection rates (> 10 m^3/s).

Using the moment magnitude equation and making the assumption that all slip in one numerical time step is released instantaneously, the upper bound for the moment magnitude of the potential induced seismicity at the onset of the initial injection was 2.40, 2.60, 2.91 and 3.00 for the 5, 10, 30 and 40 m^3/s cases, respectively. Therefore, just as with the trend in fault slip, the magnitude of the maximum potential induced seismicity decreased significantly with decreasing injection rate.

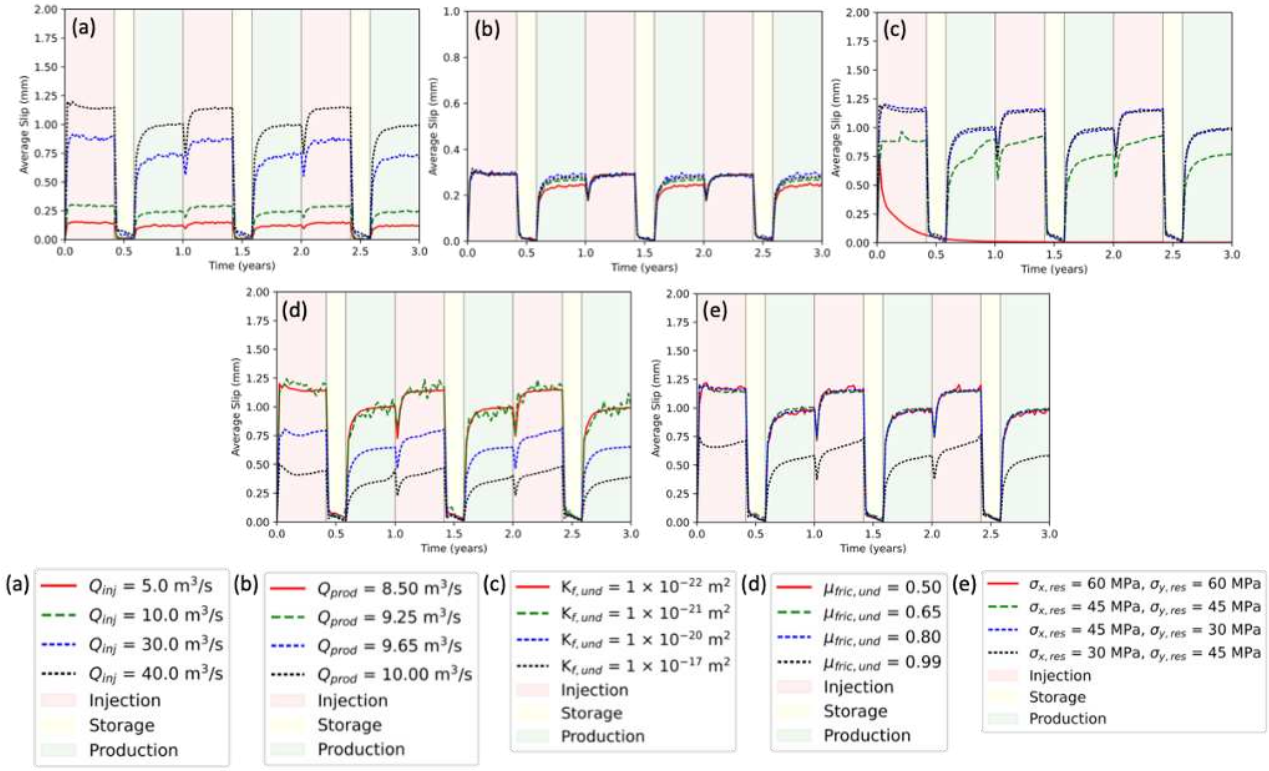


Figure 7.8: Fault slip versus time for four cases of varying (a) injection rate, (b) withdrawal rate, (c) fault permeability, (d) friction coefficient and (e) stresses.

7.4.2.2 Withdrawal Rate

In the withdrawal rate simulations in this section, the injection rate used was 10 m^3/s. The withdrawal rate from the reservoir unit was varied between 8.5 m^3/s and 10 m^3/s, representing recovery factors of between 85% and 100%. The influence on average slip versus time is shown in Figure 7.8b. It was found that underburden fault slip was essentially insensitive to changes in withdrawal rate. The initial slip of the underburden fault at t = 0, at the onset of injection, for the 8.50, 9.25, 9.65, and 10.00 m^3/s cases was approximately 0.30 mm, 0.30 mm, 0.29 mm, and

0.31 mm, respectively. For the slip period at approximately 1.42 years at the transition between injection and storage regimes, the fault slip for the 8.50, 9.25, 9.65, and 10.00 m^3/s cases was approximately 0.28 mm, 0.27 mm, 0.29 mm, and 0.27 mm, respectively. For the slip period at approximately 1.58 years at the transition between storage and withdrawal regimes, the fault slip for the 8.50, 9.25, 9.65 and 10.00 m^3/s cases was approximately 0.20 mm, 0.24 mm, 0.26 mm and 0.25 mm, respectively. Thus, a weak trend was found that suggests as withdrawal rate increased, the fault slip during the withdrawal periods broadly increased. However, in general, the withdrawal rate has little effect on fault slip.

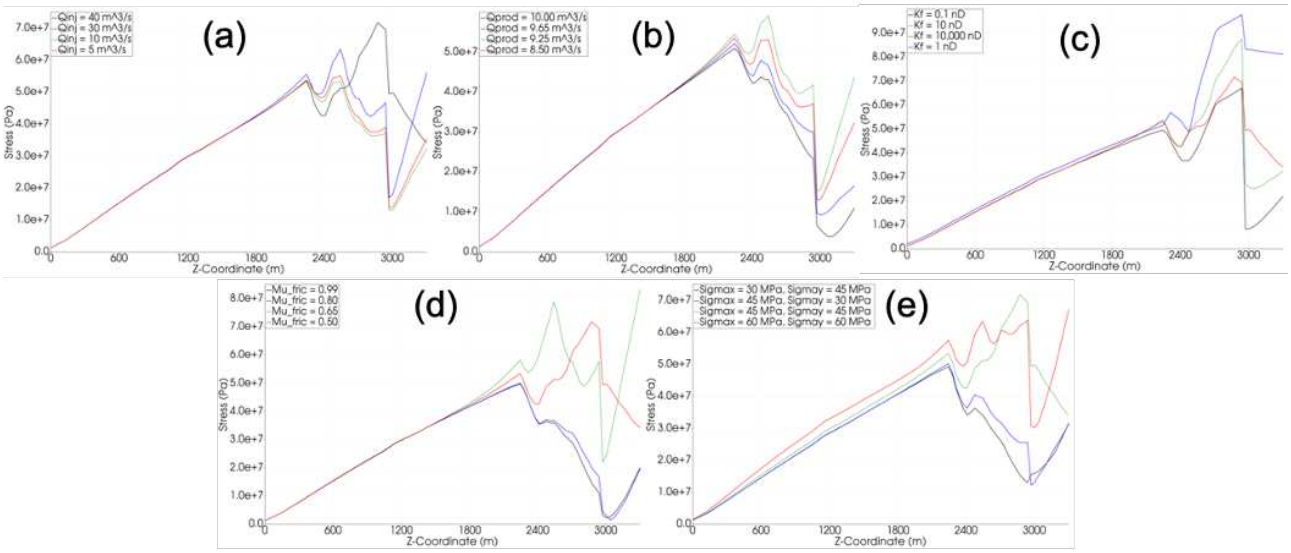


Figure 7.9: Plots of stress vertically through the center of the model in the z-direction for four cases of varying (a) injection rate, (b) withdrawal rate, (c) fault permeability, (d) friction coefficient and (e) stresses.

The aperture and fault slip at each node across the fault surface are shown in Figures 7.10b and 7.11b. No systematic change in aperture was found as injection rate increases. However, broadly it can be seen that as production rate increased, the fault aperture slightly decreased.

Effective stress and strain are shown in Figures 7.9b and 7.12b. The strain and stress fields show very little difference between the four cases, which supports the insensitivity of the slip to changes in production rate.

Using the moment magnitude equation and making the assumption that all slip in one numerical time step is released instantaneously, the upper bound for the moment magnitude of the potential induced seismicity at the onset of the initial injection was 2.60, 2.60, 2.59, and 2.61

for the 8.50, 9.25, 9.65, and 10.00 m^3/s cases, respectively. Therefore, just as with the trend in fault slip, the magnitude of the maximum potential induced seismicity was insensitive to changes in withdrawal rate.

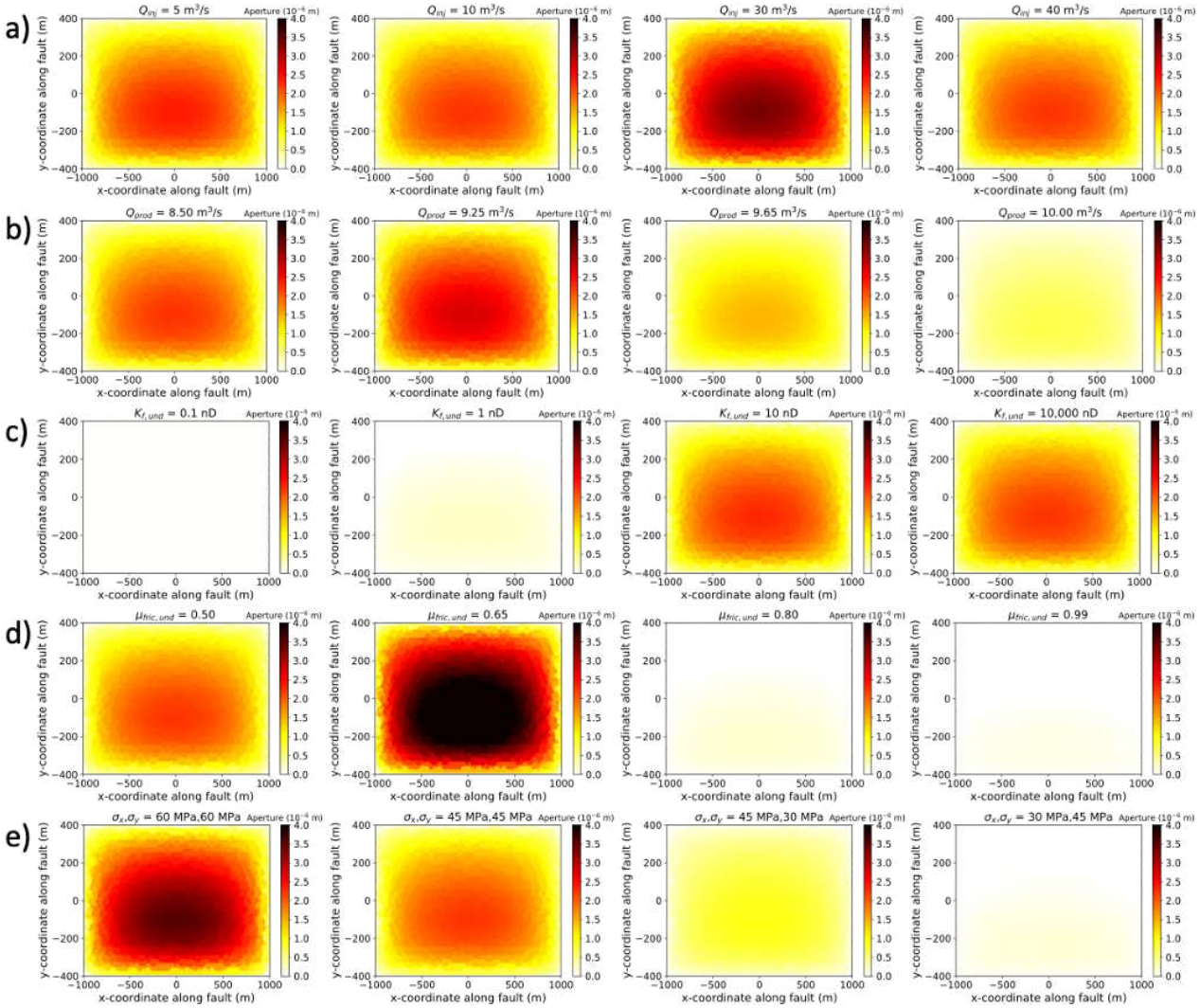


Figure 7.10: The apertures of the fault at a time of 1.58 years during the end of the second storage and beginning of the second withdrawal periods for cases of varying (a) injection rate, (b) withdrawal rate, (c) fault permeability, (d) friction coefficient and (e) stresses.

7.4.3 Effect of Fault Properties

7.4.3.1 Fault Permeability

The underburden fault permeability was varied between 0.1 nD and 10,000 nD, and the influence on average slip versus time is shown in Figure 7.8c. It was found that as fault permeability

increased, fault slip increased. The initial slip of the underburden fault at t = 0, at the onset of injection, for the 0.1, 1, 10 and 10,000 nD cases was approximately 0.74 mm, 0.88 mm, 1.17 mm, and 1.20 mm, respectively. For the slip period at approximately 1.42 years at the transition between injection and storage regimes, the fault slip for the 0.1, 1, 10, and 10,000 nD cases was approximately 0 mm, 0.88 mm, 1.09 mm, and 1.07 mm, respectively. For the slip period at approximately 1.58 years, at the transition between storage and withdrawal regimes, the fault slip for the 0.1, 1, 10, and 10,000 nD cases was approximately 0 mm, 0.65 mm, 0.89 mm, and 0.88 mm, respectively. Therefore, the fault slip was strongly influenced by the fault permeability in the range 0.1–10 nD. When the fault permeability was less than the underburden rock matrix permeability, as in the case of fault cementation or mineral precipitation, no slip occurred except some minor slip at the onset of the initial injection. For fault permeabilities between 10 nD and 10,000 nD, the fault slip was insensitive to changes in fault permeability.

The aperture and fault slip at each node across the fault surface are shown in Figures 7.10c and 7.11c. The increased. Furthermore, as fault permeability decreased, the proportion of the fault surface in stick increased and the proportion in slip decreased.

Effective stress and strain are shown in Figures 7.9c and 7.12c. The strain field shows that broadly as fault permeability decreased, the strain in the vicinity of the fault in the underburden unit decreased. Note that the strain around the fault in the underburden in the 0.1 nD case was very low, reflecting the zero slip observed.

Using the moment magnitude equation and making the assumption that all slip in one numerical time step is released instantaneously, the upper bound for the moment magnitude of the potential induced seismicity at the onset of the initial injection was 2.86, 2.91, 2.99, and 3.00 for the 0.1, 1, 10, and 10,000 nD cases, respectively. Thus, as fault permeability increased, the magnitude of the maximum potential induced seismicity increased.

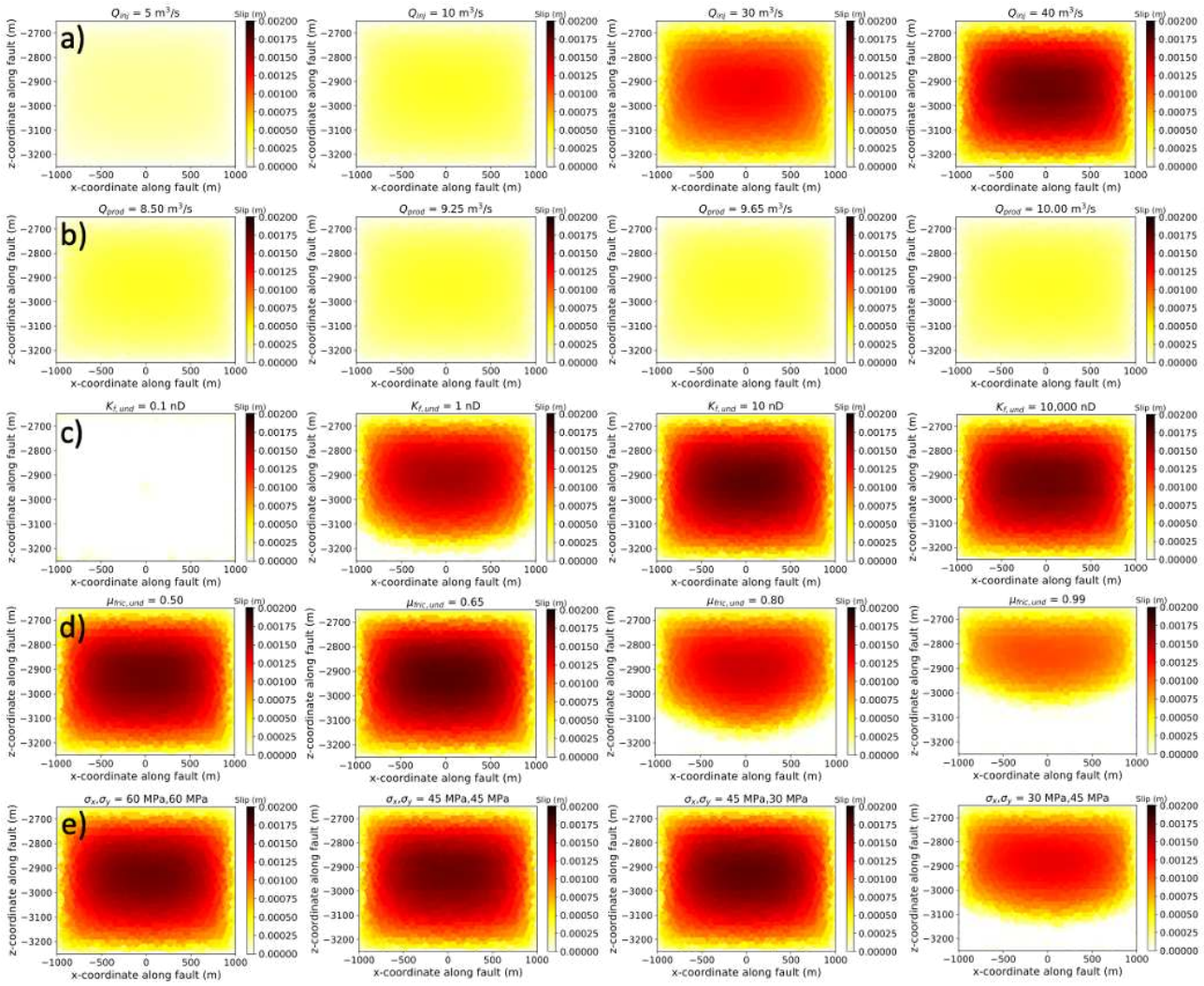


Figure 7.11: The individual slip at each node of the fault at a time of 1.58 years, during the end of the second storage and beginning of the second withdrawal periods, for cases of varying (a) injection rate, (b) withdrawal rate, (c) fault permeability, (d) friction coefficient and (e) stresses.

7.4.3.2 Friction Coefficient

The friction coefficient of the fault in the underburden unit was varied between 0.50 and 0.99, and the influence on average slip versus time is shown in Figure 7.8d. It was found that as the friction coefficient increased, the average fault slip decreased. The initial slip of the underburden fault at $t = 0$, at the onset of injection, for the 0.50, 0.65, 0.80 and 0.99 cases was approximately 1.20 mm, 1.15 mm, 0.75 mm, and 0.49 mm, respectively. For the slip period at approximately 1.42 years, at the transition between injection and storage regimes, the fault slip for the 0.50, 0.65, 0.80, and 0.99 cases was approximately 1.07 mm, 1.07 mm, 0.75 mm, and 0.44 mm, respectively. For the slip period at approximately 1.58 years at the transition between storage and withdrawal regimes, the fault slip for the 0.50, 0.65, 0.80, and 0.99 cases was approximately 0.88 mm, 0.89 mm, 0.39 mm, and 0.28 mm, respectively. Thus, the fault slip was strongly influenced by the underburden fault friction coefficient.

The aperture and fault slip at each node across the fault surface are shown in Figures 7.10d and 7.11d. No systematic change in aperture was found, although broadly, fault aperture decreased as the friction coefficient increased, with the fault being more closed in the high friction coefficient cases (> 0.80). The individual slip at each node shows that as the friction coefficient increased, the fault area in slip decreased significantly (approximately 100%, 100%, 80% and 61% in the 0.50, 0.65, 0.80, and 0.99 cases) and the fault area in stick increased, showing that the propensity of the fault to slip decreases as friction coefficient increases.

Effective stress and strain are shown in Figures 7.9d and 7.12d. It was found that the strain in the vicinity of the underburden fault was similar in the 0.50 and 0.65 cases, but in the same region, the strain was much smaller in the 0.80 and 0.99 cases, which correlates with the decreased slip in these two cases. The stress was much higher in the 0.50 and 0.65 cases, suggesting that the larger shear stress promoted fault slip.

Using the moment magnitude equation and making the assumption that all slip in one numerical time step is released instantaneously, the upper bound for the moment magnitude of the potential induced seismicity at the onset of the initial injection was 3.00, 2.99, 2.80, and 2.60

for the 0.50, 0.65, 0.80, and 0.99 cases, respectively. Thus, due to a combination of decreased fault slip and a decreased fault surface area in slip, the magnitude of the maximum potential induced seismicity strongly decreased as the friction coefficient increased.

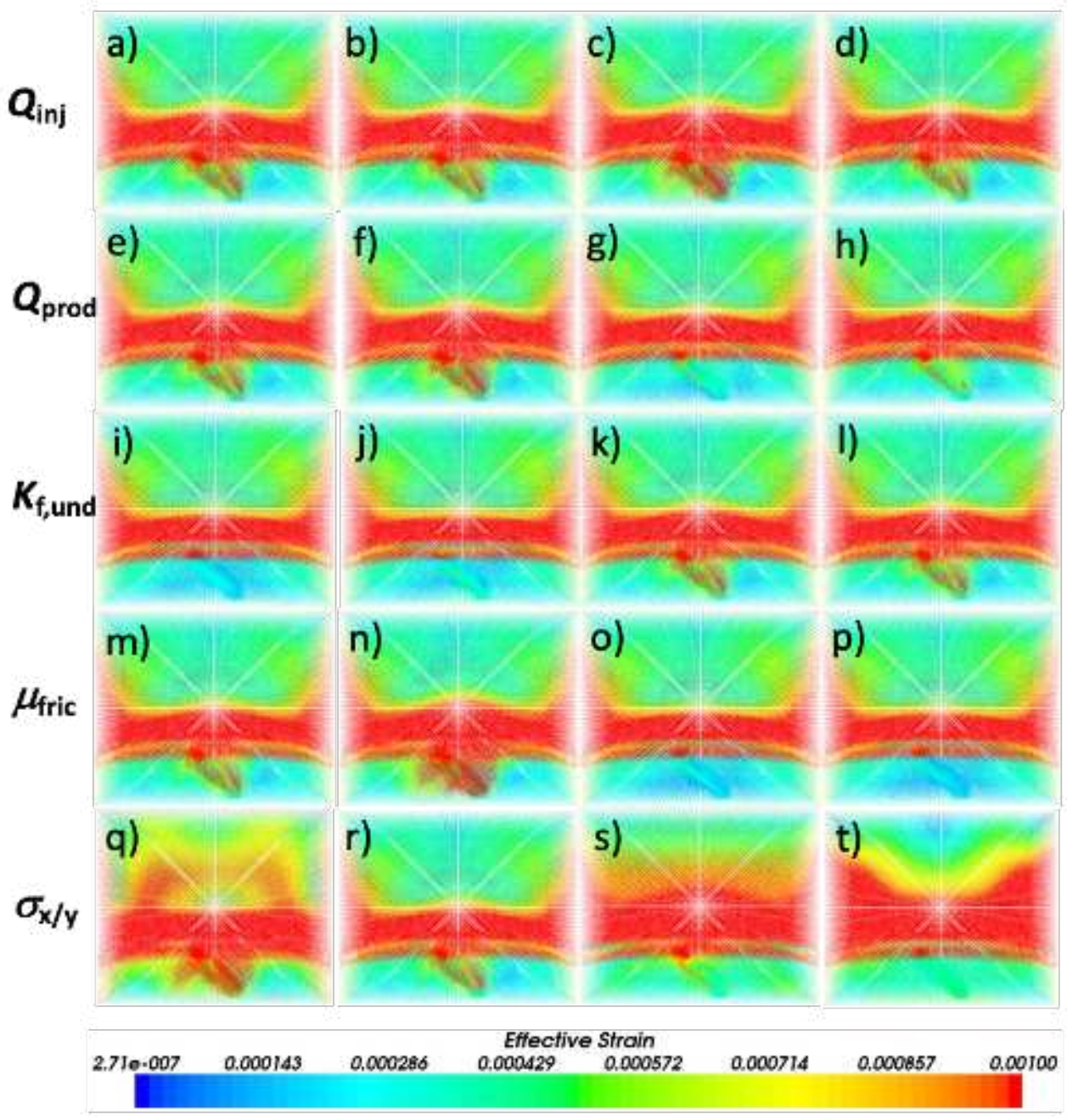


Figure 7.12: The effective strain over a vertical cut through the model at a time of 1.58 years, during the end of the second storage period and start of the second withdrawal period, for cases of (a-d) varying injection rate, (e-h) varying withdrawal rate, (i-l) varying fault permeability, (m-p) varying friction coefficient, and (q-t) varying stresses.

7.4.4 Stresses

The horizontal stresses at the mid-depth of the reservoir unit (in the x and y directions) was varied in four cases (σ_x, σ_y = 60 MPa, 60 MPa; σ_x, σ_y = 45 MPa, 45 MPa; σ_x, σ_y = 45 MPa, 30 MPa; σ_x, σ_y = 30 MPa, 45 MPa), and the influence on average slip versus time are shown in Figure 7.8e. Two cases represent an isotropic horizontal stress state (with different magnitudes in the two cases), and two cases represent an anisotropic stress state (with different orientations in the two cases). In the stress range studied, it was found that for isotropic stresses, the average fault slip was insensitive to the stress magnitude. However, for anisotropic stresses, when the horizontal stress in the plane of the fault strike was smaller, and the horizontal stress in the plane parallel to the dip direction of the fault was larger, the fault slip was smaller.

The initial slip of the underburden fault at $t = 0$, at the onset of injection, for the 60/60 MPa, 45/45 MPa, 45/30 MPa, and 30/45 MPa cases was approximately 1.22 mm, 1.20 mm, 1.21 mm, and 0.74 mm, respectively. For the slip period at approximately 1.42 years at the transition between injection and storage regimes, the fault slip for the 60/60 MPa, 45/45 MPa, 45/30 MPa, and 30/45 MPa cases was approximately 1.09 mm, 1.07 mm, 1.08 mm, and 0.68 mm, respectively. For the slip period at approximately 1.58 years, at the transition between injection and storage regimes, the fault slip for the 60/60 MPa, 45/45 MPa, 45/30 MPa, and 30/45 MPa cases was approximately 0.90 mm, 0.88 mm, 0.90 mm, and 0.43 mm, respectively. Thus, it was found that anisotropic horizontal stresses significantly impact fault slip.

The aperture and fault slip at each node across the fault surface are shown in Figures 7.10e and 7.11e. From both the isotropic and anisotropic stress cases, it was found that higher magnitude stresses resulted in slightly larger fault apertures. In the anisotropic stress cases, the orientation of $\sigma_{h,min}$ and $\sigma_{H,max}$ affected the fault aperture. When the horizontal stress in the plane of the fault strike was smaller, and the horizontal stress in the plane parallel to the dip direction of the fault was larger, the average aperture was smaller, and just under half the fault area had a closed fault aperture. The fault slip at each node shows that in the anisotropic cases, the orientation of $\sigma_{h,min}$ and $\sigma_{H,max}$ had an effect on the distribution of fault slip. When the horizontal stress in the plane of the fault strike was smaller, and the horizontal stress in the

plane parallel to the dip direction of the fault was larger, the location of the maximal slip was displaced away (upward) from the fault centroid and the portion of the fault in the lower underburden was in stick. Therefore, the propensity of the underburden fault to slip during the injection, storage, and withdrawal of hydrogen was strongly influenced by the orientation and the magnitude-ratio of the horizontal stresses.

Effective stress and strain are shown in Figures 7.9e and 7.12e. In the isotropic stress cases, the strain primarily differs in the overburden and reservoir units. The upper underburden had some minor variation, but the strain surrounding the fault was similar in both cases. In the anisotropic cases, the strain around the fault region was very low in the 30/45 MPa case, which had the smallest fault slip.

Using the moment magnitude equation and making the assumption that all slip in one time step is released instantaneously, the upper bound for the moment magnitude of the potential induced seismicity at the onset of the initial injection was 3.01, 3.00, 3.00, and 2.86 for the 60/60 MPa, 45/45 MPa, 45/30 MPa, and 30/45 MPa cases, respectively. Therefore, anisotropic stresses moderately influenced the magnitude of the maximum potential induced seismicity, with the magnitude increasing when the horizontal stress in the plane of the fault strike was smaller and the horizontal stress in the plane parallel to the dip direction of the fault was larger.

7.5 Discussion

By investigating the influence of the mechanical properties of the various lithological units within storage fields (during hydrogen injection, storage and withdrawal) on fault slip and potential induced seismicity, it is possible to understand ahead of the onset of hydrogen storage operations, which storage fields are most and least prone to triggering induced seismicity. Therefore, this work performed a thorough analysis of four underburden mechanical properties on fault slip and induced seismicity along a large-scale underburden fault that is hydraulically isolated from the overlying reservoir.

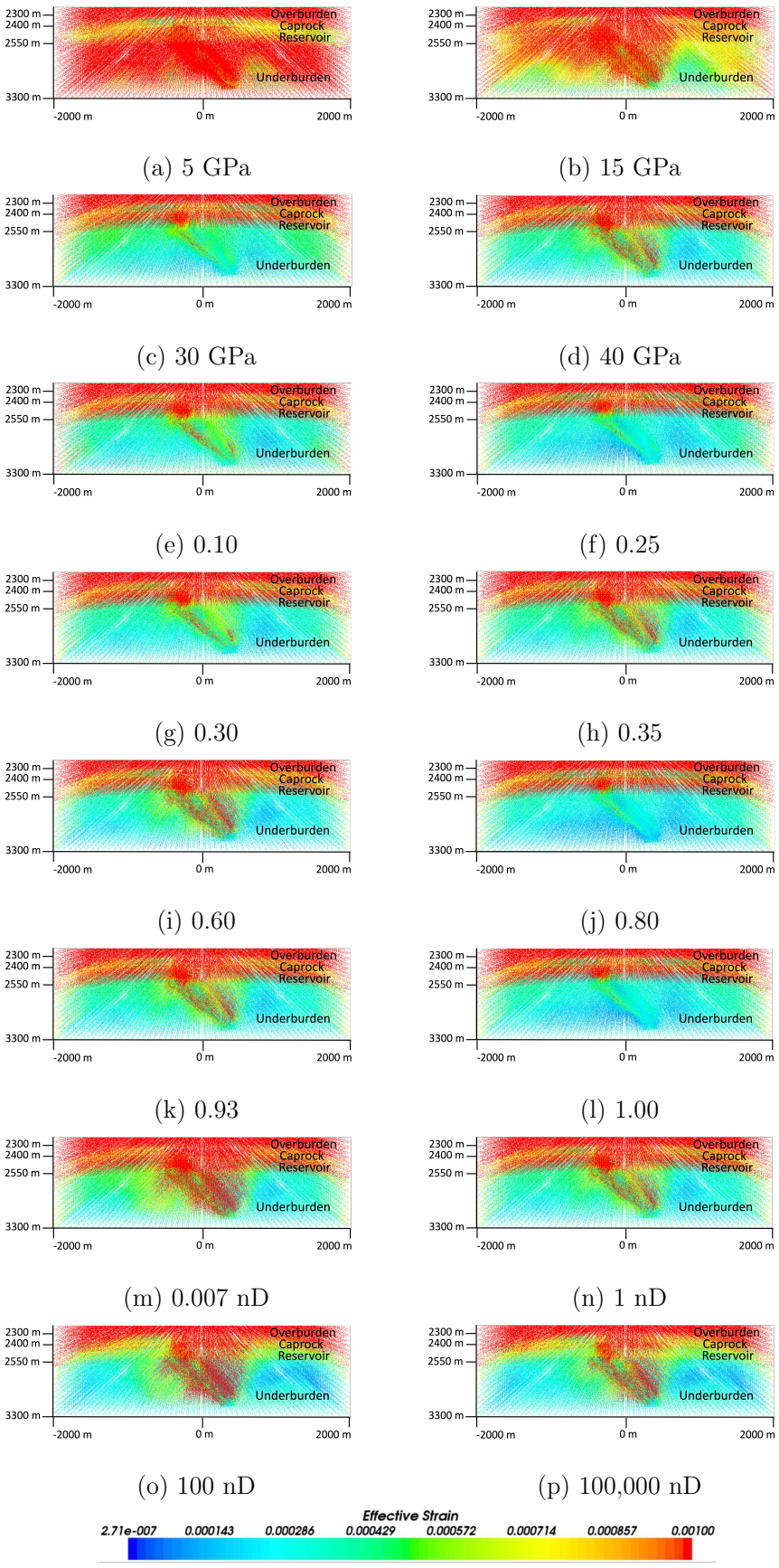


Figure 7.13: The strain over a vertical interval containing the anticlinal caprock, reservoir and underburden units at a time of 1.58 years during the end of the second storage and beginning of the second withdrawal periods for cases of varying reservoir (a-d) Young's modulus, (e-h) Poisson's ratio, (i-l) Biot coefficient and (m-p) permeability.

7.5.1 Young's Modulus

As underburden Young's modulus increases, the average fault slip generally decreases. For Young's modulii in the range 15 GPa - 40 GPa, the fault slips were similar, but the fault slip increased very significantly when the underburden Young's modulus was reduced to 5 GPa, with the 5 GPa case yielding over three times the fault slip of the 40 GPa case. However, the magnitude of the maximum potential induced seismicity does not correlate with the trend in fault slip. As Young's modulus decreased, the magnitude of the maximum potential induced seismicity decreased due to decreasing shear modulus with decreasing Young's modulus. The reduction in maximum magnitude was significant with a M_w 3.00 in the 40 GPa case decreasing to a M_w 2.73 in the 5 GPa case. The strain induced in the reservoir unit decreased with increasing Young's modulus.

No published results exist for comparison that study the influence of underburden Young's modulus on induced underburden fault slip. For a case of hydrogen storage, Burtonshaw et al. [2024a] varied the reservoir Young's modulus between 10 GPa and 60 GPa and found that as Young's modulus increased, the average reservoir fault slip decreased very significantly, with over 10 cm slip in the 10 GPa case and no slip when the reservoir Young's modulus was 40 GPa or more. However, they found that as Young's modulus increased, the magnitude of the maximum potential induced seismicity decreased because the increasing shear modulus as Young's modulus increased was not sufficient to outweigh the lack of any slip. In the hydraulic fracturing work of Meng et al. [2020], it was also found that reservoir fault slip decreased very significantly from 12 cm to 1-2 cm as Young's modulus was increased from 5 to 50 GPa. Therefore, as Young's modulus increases fault slip decreases for both reservoir and underburden faults. However, the trend with the maximum potential induced magnitude was different depending on whether the fault was in the underburden or reservoir unit, owing to the fact that the slip along the underburden fault is less sensitive to underburden Young's modulus than the slip along the reservoir fault is to reservoir Young's modulus, where absolutely no slip was observed for high Young's modulii (>40 GPa).

7.5.2 Poisson's Ratio

As underburden Poisson's ratio increases, the average fault slip decreases. However, the dependency of the underburden fault slip on Poisson's ratio is weak, with a maximum slip discrepancy between the Poisson's ratio cases of less than 0.2 mm (16% of the slip in the 0.10 case). The fault slip was very similar in the 0.10, 0.25 and 0.30 cases but decreased slightly more significantly when the Poisson's ratio was increased to 0.35, suggesting that the average fault slip might decrease more significantly for Poisson's ratio in the range 0.35 - 0.50. The magnitude of the maximum potential induced seismicity followed the same trend as the fault slip: as the Poisson's ratio increases, the magnitude of the potential seismicity decreases. The magnitude decreased from a maximum of 3.09 in the 0.10 case to 3.00 in the 0.35 case.

No prior results were found that examined the effect of underburden Poisson's ratio on induced underburden fault slip. Burtonshaw et al. [2024a] varied the reservoir Poisson's ratio between 0.00 and 0.30 and found that as Poisson's ratio increases, the average reservoir fault slip increases, with 4.53 cm of slip in the 0.00 case increasing to 10.43 cm in the 0.30 case. However, they found that for the highest Poisson's ratio case of 0.30, the magnitude of the maximum potential induced seismicity was the smallest, because a large proportion of the fault surface was now in stick. Therefore, as Poisson's ratio increases, the trend in fault slip is different for both underburden and reservoir faults. Furthermore, the reservoir Young's modulus exerts a much greater control on the average fault slip than the underburden Young's modulus. The trend in the maximum magnitude of the potential induced seismicity is the same for both underburden and reservoir faults: as Poisson's ratio increases, the magnitude decreases.

7.5.3 Biot Coefficient

As underburden Biot coefficient increases, the average fault slip increases. However, the strength of the dependence is very weak, with a maximum slip difference between the largest (1.00) and smallest (0.60) Biot coefficient cases of less than 0.1 mm. The moment magnitude of the maximum potential induced seismicity also increased as Biot coefficient increased, although

it was largely insensitive to changes in Biot coefficient, with a magnitude of 3.01 in the largest Biot coefficient case (1.00) and 2.99 in the smallest Biot coefficient case (0.60). The effective stress around the fault decreased as Biot coefficient increased, promoting fault slip.

Again, no published studies were found in the literature that analysed the effect of underburden Biot coefficient on underburden fault slip. However, for a case of wastewater injection, Fan et al. [2019] varied reservoir Biot coefficient in two cases (0.44 and 0.79) and computed the change in CFS. They found that as reservoir Biot coefficient decreased, the change in CFS became more positive and thus the likeliness of underburden fault slip increased. Although, just two test cases are likely insufficient to draw solid conclusions. Furthermore, the difference in changed CFS was between the two cases was less than 0.2 MPa, suggesting that the expected slip difference with differing Biot coefficient would be small. Burtonshaw et al. [2024a] varied the reservoir Biot coefficient between 0.25 and 0.90 and found that the relationship between reservoir fault slip and reservoir Biot coefficient was non-systematic, with the magnitude of the fault slip similar for values between 0.25 and 0.65 but no slip occurred when the Biot coefficient was as high as 0.90. Therefore, the fault slip along underbuden and reservoir faults responds differently to Biot coefficient depending on whether it is the reservoir or underburden Biot coefficient. The reservoir Biot coefficient has a much stronger influence on reservoir fault slip and event magnitude (varies between 3.56 and no event) than underburden Biot coefficient has on underburden fault slip and event magnitude (varies between 2.99 and 3.01).

7.5.4 Permeability

In the range 0.007 nD to 100 nD, the underburden fault slip is insensitive to changes in underburden permeability. Even when the underburden permeability increases to as much as 100,000 nD, the underburden fault slip remained insensitive to underburden permeability throughout the bulk of the three-year injection-storage-withdrawal period, only differing in places (i.e., at the onset of the initial injection where the fault slip was 33% higher in the 100,000 nD case relative to the 100 nD case). Therefore, it can be concluded that although underbuden fault slip is similar for most typical underburden permeabilities, the lower the underburden permeability,

the lower the risk of underburden seismicity.

As before, no previous studies have examined the influence on underburden permeability on underburden fault slip. Burtonshaw et al. [2024a] varied the intrinsic permeability of the reservoir between 5 mD and 800 mD and found broadly that as reservoir permeability decreased, the magnitude of the average fault slip increased. However, the strength of the dependence of the magnitude of the fault slip on the reservoir permeability was weak with only a 6% difference between the whole range of permeabilities. Additionally, they found that the reservoir permeability has an effect on the time in which the slip occurs. Slip was induced earlier for higher reservoir permeabilities due to the fact that the fault pressure at a given time varies depending on the permeability. For smaller permeabilities, the fluid front from the injection well takes longer to reach the fault, and subsequently leak-off into the fault or pressurise the surrounding area. Additionally, even though the magnitude of the average fault slip increased with decreasing permeability, the proportion of the fault area in stick increased as permeability decreased. As a result, it was found that the magnitude of the induced seismicity broadly decreased as reservoir permeability decreased. Therefore, for both underburden and reservoir faults, the magnitude of induced seismicity decreases as the underburden/reservoir permeability decreases. In this work, no temporal delay in the underburden fault slip was seen with changing permeability, like with the reservoir fault cases, because the underburden fault is hydraulically isolated from the injection unit where pore pressure is increasing. Thus, the seismicity is not a direct product of pore pressure change, since the underburden fault never comes into contact with the fluid pressure front and as such should not be temporally affected. In the case where the underburden permeability was extremely high (100,000 nD), some additional slip occurred at the onset because some of the injectant fluid front rapidly leaked into the upper underburden, allowing some minor pressurisation of the underburden fault.

7.5.5 Further Discussion

In order to assess the effect of the chosen fault orientation on the results, additional simulations were run varying the fault orientation (a 45° rotation and a 240° rotation from the direction

of the x-axis). It was found that the slip was maximal in the fault orientation case used in this Section (0° from the x-axis). When the fault was rotated by 240° from the direction of the x-axis, the fault slip was reduced by approximately 17% on average relative to the cases presented herein. Furthermore, when the fault was rotated by 45° from the direction of the x-axis, the fault slip was reduced by approximately 46% on average relative to the cases presented herein. This was because strain in the centre of the underburden was larger when the fault was oriented in the direction of the x-axis (in the plane of the maximum horizontal *in situ* stress). The strain at the centre of the underburden in the 45° orientation case was the lowest, reflecting the fact that the fault orientation is the furthest away from the maximum horizontal *in situ* principle stress in this case. Therefore, this further reinforces that our computed magnitudes in this work are upper bounds on the maximum potential magnitudes that may occur along basement faults of this size during geological hydrogen storage.

To minimise seismic risk during underground geological hydrogen storage, the depleted gas fields shortlisted as candidates fields that have low underburden Young's modulus (¡ 15 GPa), high underburden Poisson's ratio (> 0.25), low underburden Biot coefficient and low underburden intrinsic permeability ($< 1\times10^{-19}$ m^2) should be selected for storage. Equally, those with high reservoir Young's modulus (> 40 GPa), high reservoir Poisson's ratio (> 0.30), and high Biot coefficient (> 0.65).

Hydrogen storage differs from other geo-energy applications in that the adopted injection rates will need to be very high. The ultra-low density of hydrogen of less than 10 kg/m^3 (at typical reservoir temperatures and pressures) implies that very large volumes of fluid must be injected into the reservoir rock in order to store the masses necessary to successfully provide a reasonable percentage of the future energy mix. The injection rate used herein of 40 m^3/s corresponds to an injection volume of 525,600,000 m^3 over the five-month injection period, which itself corresponds to the period of time in which an energy excess from renewable energy will exist. Given the density of the hydrogen is 9 kg/m^3, this corresponds to an injected mass of 4,730,400,000 kg. One kg of hydrogen can produce 33.3 kWh of energy [Burtonshaw et al., 2024a, Ayodele et al., 2021], which means that in the present model 157,522,320,000 kWh of energy is stored (approximately 157 TWh). This corresponds to just less than 10% of the United Kingdom's

national annual energy demand today [Burtonshaw et al., 2024a]. Therefore, this injection rate was chosen to be a worst-case scenario, at the upper limit of the hydrogen volumes that may be stored in future geological hydrogen storage projects. This has enabled the maximum potential seismic magnitudes to be quantified.

7.5.6 Advantages and Limitations of the Modelling Procedure

7.5.6.1 1-D vs. 2-D Fault Representations

One of the benefits of the ICGT is that it has the capabilities of full hydromechanical coupling and friction, and can fully represent faults and fractures as negative volumes within a three-dimensional rock continuum. Due to this, fault slip can be fully resolved across the whole 2-D fault surface by directly computing node-to-node displacement comparisons of matching pairs of nodes on opposing fault surfaces. Other codes and commercial software used to investigate induced seismicity during a fluid injection, storage, or withdrawal process typically lack this capability, and thus, the literature is dominated by indirect evaluations of seismicity, such as via CFS [Hui et al., 2021b, Fan et al., 2019], as opposed to direct mechanical fault slips; or direct fault slip is indeed computed but along a 1-D fault within a 2-D model which results in the fault slip being computed at just a single point along the entire depth of the fault [Mortezaei and Vahedifard, 2015, Meng et al., 2020, Deng et al., 2021, Rutqvist et al., 2013, Zbinden et al., 2017, Mazzoldi et al., 2012].

7.5.6.2 Rock Homogeneity, Isotropy and Linear Elasticity

It is assumed in the work herein that each rock layer is homogeneous, but in reality, rock heterogeneities would likely have some influence on slip. Fault geometries and slip distributions across the fault surface are likely to be influenced by heterogeneities due to more complex fault zone architectures and fault thickness variations, as well as the presence of fault breccias and shear bands which impact localised permeability and thus the fault pressurisation and subsequently the induced slip. Furthermore, rock stiffness heterogeneities within the fault zone

may result in non-uniform stress distributions that alter the magnitude and distribution of stress accumulations during, and stress release after, slip events. It is also assumed that each strata is isotropic but non-isotropic rocks can have different horizontal and vertical permeabilities due to various rock fabrics that may exist within the rock that may enhance or limit fluid flow and pressure propagation in the vicinity of the fault relative to a homogeneous rock. These pore fluid pressure changes surrounding the fault may affect slip behaviour by influencing frictional resistance and altering effective stresses. Linear-elastic behaviour of the rock matrix is assumed but in reality some minor plastic deformation and damage accumulation may occur along the fault. The model does not include dynamic effects such as transient slip behaviour and seismic wave propagation which may lead to small inaccuracies in predicting the magnitude and timing of fault slip events.

7.5.6.3 Thermal Effects

Given the complexity of fully coupling thermal effects with hydromechanical processes in numerical simulations, excluding thermal effects can serve as an initial simplification to isolate the mechanical aspects of fault slip behaviour. This approach allows for a clearer and more focused analysis of the mechanical controls on fault behaviour, providing valuable insights that can later be integrated into more complex models. It is not expected that the temperature of the reservoir should change significantly during the injection and withdrawal of the hydrogen. However, there may be some minor thermal effects that influence fault slip. For example, hydrogen can exhibit a negative Joule-Thomson effect [Zhang et al., 2023], meaning that contrary to most gases, its temperature increases as it expands. Therefore, it would be expected that during periods of withdrawal the fault slip may be enhanced slightly relative to that predicted here. This is because as hydrogen is withdrawn, the reservoir pressure decreases, the hydrogen expands, and its temperature increases which can enhance pore fluid pressures due to increased fluid volumes within fault zones in a process known as thermal pressurisation and therefore reduce effective stress acting on the fault. Contrastingly, during periods of injection the fault slip may be reduced slightly relative to that predicted here due to the fact the hydrogen contracts as the reservoir pressure increases and its temperature decreases which minimises the effect

of thermal pressurisation. Even though hydrogen has a negative Joule-Thomson effect at certain temperatures and pressures more akin to surface conditions, at the conditions of a typical reservoir such as that used in this work (15 MPa and 90 °C), hydrogen has a Z-Factor of 1.04 showing that it essentially behaves as an ideal gas [Burtonshaw et al., 2024a]. Ideal gases have Joule-Thomson coefficients of zero under all conditions [Saygın and Şişman, 2001], meaning that ideal gases experience no change in temperature when undergoing an adiabatic expansion, regardless of the pressure or initial temperature. Therefore, the Joule-Thomson effect would not be expected to have any substantial influence on the fault slip behaviour. Furthermore, this effect would be expected to be more substantial if the fault was hydraulically connected to the injection interval. Given the fault is in the basement unit, this thermally-derived pore fluid pressure change should not disturb the fault. In some subsurface geo-energy activities, phase changes can result in significant increases in volume, which could lead to rapid rises in pore fluid pressure which would influence the fault slip behaviour. However, this is not the case for hydrogen as hydrogen remains in the gaseous state at all subsurface temperatures and pressures. Injecting the fluid at a temperature significantly different to the reservoir temperature may induce temperature changes and thermal stresses depending on the thermal conductivity and heat capacity of the reservoir that can influence fault apertures and thus fault permeability and pressurization [Salimzadeh et al., 2018]. However, these will occur distal from the basement fault. Ideally, the hydrogen should be injected at a temperature similar to the reservoir temperature as in this work to avoid potential additional thermal stresses.

7.5.6.4 Static Coulomb Friction vs. Rate-and-State Friction

The present study employs a static friction model based on the Coulomb criterion to characterize fault behaviour. The model delineates two distinct states according to Equation 3.8: stick and slip. In the stick state, the frictional traction is constrained to be less than or equal to the combined effect of cohesion and the product of the friction coefficient and normal traction. Conversely, in the slip state, the frictional traction exceeds this sum. While some might perceive this as a modelling constraint, adopting the rate-and-state model [Rice et al., 2001, Hosseini et al., 2023, Garagash, 2021] introduces additional uncertainties. Notably, the parameters a and

b required for the rate-and-state model exhibit significant variability across faults and geological formations, posing challenges for model calibration. Moreover, the availability of a and b values for the specific rock units studied here is limited. However, the present static friction model partly addresses the "evolution effect" [Liang et al., 2022] inherent in the rate-and-state model, as it considers changes in fault aperture over time due to geomechanical-fluid interactions. As fault apertures evolve over time, both tangential and normal tractions undergo changes, which dictate the occurrence of frictional stick-and-slip states on the fault. Consequently, the frictional resistance is subject to fluctuations due to mechanical and hydraulic variations over time. Although since the model does not account explicitly for phenomena such as fault gouge compaction [Proctor et al., 2020] and cementation of fault rocks [Williams and Fagereng, 2022, Romano et al., 2022] and the sealing and closure of the fault through mineral precipitation [Yehya and Rice, 2020], pressure solution [Bedford et al., 2023, Hunfeld et al., 2020], and stress-induced cementation [Ji et al., 2022], then full fault aging/healing is not accounted for which would be complex to model accurately numerically. Despite these limitations, the model still allows for speculation on post-slip fault behaviour if a rate-and-state model was employed. Additional simulations were run that examined the influence of the static friction coefficient between values of 0.50 and 1.00 on the fault slip. It was found that as the static friction coefficient increased, the fault slip decreased. For values between 0.50 and 0.65, the fault slip was nearly identical, but drastically reduced as the friction coefficient increased from 0.65 to 0.99. If the fault had an a - b value greater than zero, then the fault would be fault-strengthening post-slip and if it had an $a - b$ value less than zero, then the fault would be fault-weakening post-slip. If the fault was fault-strengthening, this would have a similar effect to a larger friction coefficient which from our results would suggest a reduction in the predicted fault slip. If the fault was fault-weakening, then this would have a similar effect to a smaller friction coefficient which from our results would suggest an increase in the predicted fault slip. It is worth noting that rate-and-state effects typically induce minimal changes in the effective friction coefficient (i.e., +/- 0.05. Therefore, the slip is not expected to differ significantly from our results herein. This assertion is supported by our observation from our additional simulations that slip profiles for different friction coefficients exhibit similarity within the range of 0.50-0.70 which most

faults in nature lie within, suggesting that temporal changes induced by a rate-and-state model would likely be insignificant.

7.5.6.5 Fault Geometry Simplifications

The fault is approximated as a smooth macrofracture, but in reality faults within the Mesozoic shales of the North Sea can be relatively mature and display complex internal and external structures. These complexities include fault gouge [Buijze et al., 2021], roughness [Wang et al., 2024b], damage zones [Thakur et al., 2020], and induced localized fracture networks. These features can influence fluid flow and stress distribution near the fault plane, affecting fault slip behaviour. Ignoring such internal heterogeneity in a smooth macrofracture representation may lead to small inaccuracies in estimating fault slip. Fluid flow along faults can induce the formation of secondary fractures and fracture networks. These features can influence fluid flow pathways, pressure distribution, and stress transfer near the fault. Smooth macrofracture representations neglect the presence of such induced fractures, leading to small inaccuracies in the timing and magnitude of fault slip.

7.5.6.6 Seismic vs. Aseismic Slip

Seismic slip occurs when movement along a fault line leads to an earthquake [Wallace, 2020], resulting in the sudden release of accumulated stress. This release causes surrounding rocks to fracture, generating seismic waves that propagate through the Earth, causing the ground to shake. In contrast, aseismic fault slip involves movement along a fault line without significant seismic wave generation or earthquake occurrence. This movement can be slow and continuous or episodic, allowing for gradual stress release over time. As this study does not model wave propagation, distinguishing between seismic and aseismic slip with certainty is not possible. However, seismic slip rates can range from fractions of a millimetre to several meters per event, while aseismic creep rates typically range from fractions of a millimetre to several centimetres per year [Wallace, 2020]. This annual aseismic creep rate range corresponds to a maximum of approximately 0.58 mm per week, which is the time step used in this work. Observations

indicate slip easily exceeding 3 mm within a single time step, which supports seismic activity. The moment magnitudes provided in this study represent the maximum potential moment magnitudes, assuming instantaneous occurrence of all slip within a given time step. They serve as constraints on the upper limits of potential magnitudes, rather than predictions of event magnitudes because the distribution of slip within a given time step is non-discernible.

7.5.6.7 Single Phase Flow vs. Multiphase Flow

A single-phase fluid model is used within the reservoir unit. The ICGT does not currently have capabilities for modelling multiphase. In order to assess the influence of the *in situ* reservoir fluid on fault slip, an additional simulation was performed in which the hydrogen was replaced by brine of density 1,040 kg/m^3. In this sense, the two end-member situations have been examined: (1) where the reservoir fluid is entirely hydrogen and (2) where the reservoir fluid is entirely brine. The real situation of brine and hydrogen coexisting within the reservoir system should therefore lie between these two end-member states. The case of brine in the reservoir showed that the fault slip was up to approximately 5% larger than in the case with hydrogen in the reservoir. This additional slip arises because brine has a higher density than gaseous hydrogen. As a result, when brine is injected into the reservoir, it exerts higher pressure on the surrounding rock matrix compared to hydrogen. This increased pressure gradient contributes to enhanced stress perturbations near the fault plane, promoting fault slip. The change in slip between the hydrogen and brine case is modestly small because the underburden fault and the reservoir fluid are not in direct hydraulic communication. Therefore, changes in pressure distribution in the reservoir associated with the *in situ* fluid can only impact fault slip via stress and strain transfer through the stiff underburden unit ($E = 40$ GPa) which does not facilitate much poroelastic deformation anyway. If the fault was in direct hydraulic communication with the reservoir fluid, it would be expected that the type of in situ fluid has a greater influence on the slip dynamics.

7.6 Conclusion

In this study, a 3-D, linear-elastic fracture mechanics simulator, with monolithic hydromechanical coupling was implemented to perform a parametric study aimed at assessing the influence of underburden mechanical properties on fault slip and induced seismicity along a basement fault during hydrogen storage into a depleted gas reservoir. The mechanical properties investigated were the Young's Modulus, the Poisson's ratio, the Biot coefficient and the intrinsic permeability. Gaseous hydrogen was injected for five months, stored for a further two months, and withdrawn for a further five months, with this three-stage cycle repreated three times. It was found that the underburden Young's modulus is the key parameter with the strongest control on basement fault slip: fault slip significantly decreased as Young's modulus increased. However, the increasing shear modulus of the underburden as the Young's modulus increases, outweighed the decreasing slip, such that higher Young's moduli resulted in larger magnitude seismicity. The Biot coefficient and Poisson's ratio of the underburden unit had little effect on induced fault slip. The fault slip was insensitive to changes in underburden permeability in the range 7×10^{-24} m^2 to 1×10^{-19} m^2, but increased significantly at times, when the underburden permeability was as high as 1×10^{-16} m^2. Although the magnitude of the fault slip was largely insensitive to changes in underburden Poisson's ratio, the maximum potential magnitude of the induced seismicity was most sensitive to the Poisson's ratio from the tested parameter space. The maximum potential magnitude of the induced seismicity was least sensitive to changes in Young's modulus. The underburden rock with low Young's modulus (< 15 GPa), high Poisson's ratio (> 0.25), low Biot coefficient and low matrix permeability ($< 1\times10^{-19}$ m^2) is found to minimise the magnitude of induced seismicity during the simulation of hydrogen storage in a depleted gas reservoir.

Chapter 8

Conclusion

This chapter outlines the main contributions of this thesis to the advancement of underground hydrogen storage (UHS) in depleted gas fields, which is a novel technology in the energy transition. It proposes future work that could be performed in order to improve, extend and refine the results and conclusions given. It also presents a summary risk table that highlights whether a certain property may be critical to either seismicity, caprock integrity or surface uplift/subsidence risks and whether increasing or decreasing that property exacerbates the risk.

8.1 Summary of Geomechanical Risks

Table 8.1 summarises all of the findings in this work. It presents what mechanical, operational, fluid, and fracture or fault properties can cause the greatest influence, and thus potential risk, on the three key geomechanical risks of underground hydrogen storage in depleted gas fields (uplift/subsidence, caprock integrity and induced seismicity). Risks are coloured either green, yellow or red, with red indicating high risk and green indicating low risk. High risk is assigned to properties in which a particular case triggered either high magnitude seismicity, extreme caprock integrity loss or large variations in ground surface level. Alternatively, properties were also assigned high risk if they had a strong influence on whether the geomechanical phenomenon under investigation would vary from safe to problematic dependent on its value. For example,

if varying the Biot coefficient from 0.3 to 1.0 induced little change in the caprock permeability, event magnitude or ground surface level it would be assigned green (low risk). Table 8.2 shows the quantitative variance in the parameter used to assess failure (effective permeability change in the caprock study, net uplift in the subsidence/uplift study and maximal induced earthquake magnitude in the seismicity studies) in each simulation set. Both tables reveal that across all simulations, for all three phenomena (seismicity, caprock integrity and surface uplift), the Young's modulus of the various rock units always plays a critical role in either ensuring geomechanically safe storage or inducing geomechanical issues. The safest storage fields will be those with as high reservoir Young's modulus and as low caprock, overburden and basement Young's moduli as possible.

The geomechanical parameters used throughout this thesis are directly measurable or inferable from standard subsurface characterization techniques, making them highly relevant to real-world underground hydrogen storage (UHS) operations. Fracture properties such as initial radius, spacing, and orientation can be assessed using core analysis, borehole image logs (i.e., Formation MicroImager), and high-resolution seismic data. Fracture propagation velocity, though difficult to measure directly, can be inferred from laboratory-scale hydraulic fracturing experiments or field-scale time-lapse microseismic monitoring. Fracture toughness and tensile strength are derived from mechanical testing of core samples, such as notched beam tests and Brazilian tensile tests, and are critical for evaluating caprock containment. Elastic properties like Young's modulus and Poisson's ratio are obtained either from static mechanical tests (i.e., uniaxial/triaxial compression) or from dynamic wireline logs (compressional and shear sonic velocity), while matrix permeability is routinely measured via core plug tests or formation pressure transient analysis (i.e., Drill Stem Test (DST) or Modular Formation Dynamics Tester (MDT)). The Biot coefficient can be determined from poroelastic laboratory testing under coupled stress and pore pressure conditions. In situ stress magnitudes are assessed using techniques like extended leak-off tests, hydraulic fracturing, or borehole breakout analysis. Fault-related properties, such as friction coefficient, dip, and length, are inferred from outcrop analogs, core, image logs, and structural interpretations from seismic surveys. Fault and formation permeabilities are measurable through pressure interference testing or tracer analysis.

Property	Caprock Integrity	Subsidence/Uplift	Reservoir Seismicity	Underburden Seismicity
Caprock Properties				
Initial Fracture Radius	Non-systematic	-	-	-
Initial Fracture Spacing	↑ with higher values		-	-
Fracture Orientation	Non-systematic	-	-	-
Crack Propagation Velocity	↑ with higher values	-	-	-
Vertical Fracture Spacing	Non-systematic	-	-	-
Fracture Toughness	↓ with higher values	-	-	-
Young's Modulus	↑ with higher values	Non-systematic	-	-
Poisson's Ratio	Non-systematic	↓ with higher values	-	-
Matrix Permeability	Non-systematic	↓ with higher values	-	-
Biot Coefficient	↑ with higher values	↑ with higher values	-	-
Tensile Strength	↓ with higher values	-	-	-
Reservoir Properties				
Permeability	-	↑ with higher values	↑ with higher values	-
Young's Modulus	-	↓ with higher values	Non-systematic	-
Biot Coefficient	-	↑ with higher values	Non-systematic	-
Poisson's Ratio	-	↑ with higher values	Non-systematic	-
Fault Friction Coefficient	-	-	Non-systematic	-
Fault Permeability	-	-	Insensitive	-
Fault Length	-	-	↑ with higher values	-
Fault Dip	-	-	Non-systematic	-
Fault Strike	-	-	Insensitive	-
In situ Stresses	↑ with higher values	-	Non-systematic	↓ with higher values
Injection Rate	-	↑ with higher values	↑ with higher values	↑ with higher values
Withdrawal Rate	-	-	Insensitive	Insensitive
Horizontal Well Length	-	-	Insensitive	-
Vertical Well Perforation Length	-	-	Insensitive	-
Hydrogen Viscosity	-	-	Non-systematic	-
Hydrogen Density	-	-	Insensitive	-
Hydrogen Compressibility	-	-	Non-systematic	-
Underburden Properties				
Permeability	-	-	-	Non-systematic
Young's Modulus	-	-	-	↑ with higher values
Biot Coefficient	-	-	-	Insensitive
Poisson's Ratio	-	-	-	↓ with higher values
Fault Permeability	-	-	-	↑ with higher values
Fault Friction Coefficient	-	-	-	↓ with higher values
Overburden Properties				
Permeability	-	↑ with higher values	-	-
Young's Modulus	-	↑ with higher values	-	-
Biot Coefficient	-	↓ with higher values	-	-
Poisson's Ratio	-	↓ with higher values	-	-

Table 8.1: Risk table for different geomechanical properties of the key geological units. Red indicates high risk and green indicates low risk. The arrows indicate an increasing or decreasing risk with higher values of that property.

Property	Range Tested	Variance in Failure Test	Max. Value in Failure Test
Caprock Integrity			
Cap. Initial Fracture Radius	0.2-5.0 m	0.595	197 mD
Cap. Initial Fracture Spacing	7.5-25.0 m	0.680	110 mD
Cap. Fracture Orientation	H/V/A	10.676	94,928 mD
Cap. Crack Propagation Velocity	0.05-1 μm/s	1.228	220 mD
Cap. Vertical Fracture Spacing	10-25 m	0.649	232 mD
Cap. Fracture Toughness	0.033-0.460 MPa $m^{1/2}$	7.740	110 mD
Cap. Young's Modulus	2-43 GPa	8.637	868 mD
Cap. Poisson's Ratio	0.11-0.35	0.125	110 mD
Cap. Matrix Permeability	0.01-100 nD	0.786	110 mD
Cap. Biot Coefficient	0.40-0.93	0.680	110 mD
In situ Stresses	15-75 MPa	2.673	330 mD
Subsidence/Uplift			
Cap. Young's Modulus	2-43 GPa	7.38 mm	8.63 mm
Cap. Poisson's Ratio	0.11-0.35	0.25 mm	1.46 mm
Cap. Matrix Permeability	0.01-100 nD	0.29 mm	1.21 mm
Cap. Biot Coefficient	0.65-1.00	0.24 mm	1.28 mm
Res. Young's Modulus	5-60 GPa	43.11 mm	44.30 mm
Res. Poisson's Ratio	0.00-0.30	1.43 mm	2.67 mm
Res. Matrix Permeability	0.1-1500 mD	0.91 mm	1.21 mm
Res. Biot Coefficient	0.35-1.00	0.58 mm	1.79 mm
Over. Young's Modulus	1-35 GPa	12.95 mm	14.20 mm
Over. Poisson's Ratio	0.20-0.42	3.71 mm	3.71 mm
Over. Matrix Permeability	0.1-100 mD	1.19 mm	1.97 mm
Over. Biot Coefficient	0.70-1.00	0.44 mm	1.48 mm
Injection Rate	0.01-40 m^3/s	4.84 mm	4.84 mm
Reservoir Seismicity			
Res. Young's Modulus	10-60 GPa	3.56 M_w	3.56 M_w
Res. Poisson's Ratio	0.00-0.30	0.18 M_w	3.56 M_w
Res. Matrix Permeability	5-800 mD	0.16 M_w	3.56 M_w
Res. Biot Coefficient	0.25-0.90	3.59 M_w	3.59 M_w
Res. Fault Friction Coefficient	0.20-0.99	0.71 M_w	3.72 M_w
Res. Fault Permeability	0.001-10,000 mD	3.56 M_w	3.56 M_w
Res. Fault Length	200-2000 m	0.94 M_w	3.56 M_w
Res. Fault Dip	30-80 °	0.68 M_w	3.75 M_w
Res. Fault Strike	0-135°	0.14 M_w	3.56 M_w
In situ Stresses	35-60 GPa	3.56 M_w	3.56 M_w
Injection Rate	2-30 m^3/s	3.64 M_w	3.64 M_w
Withdrawal Rate	14-20 m^3/s	0.14 M_w	3.56 M_w
Res. Horizontal Well Length	400-4000 m	0.09 M_w	3.56 M_w
Res. Vertical Well Perforation Length	20-80 m	0.07 M_w	3.55 M_w
Hydrogen Viscosity	7.0-17.5 μPa s	0.10 M_w	3.56 M_w
Hydrogen Density	5-40 kg/m^3	0.09 M_w	3.56 M_w
Hydrogen Compressibility	66.7-1000 GPa^{-1}	3.58 M_w	3.58 M_w
Underburden Seismicity			
In situ Stresses	30-60 MPa	0.15 M_w	3.01 M_w
Injection Rate	5-40 m^3/s	0.60 M_w	3.00 M_w
Withdrawal Rate	8.5-10 m^3/s	0.02 M_w	2.61 M_w
Und. Young's Modulus	5-40 GPa	0.27 M_w	3.00 M_w
Und. Poisson's Ratio	0.10-0.35	0.09 M_w	3.09 M_w
Und. Matrix Permeability	0.007-100,000 nD	0.13 M_w	3.09 M_w
Und. Biot Coefficient	0.60-1.00	0.02 M_w	3.01 M_w
Und. Fault Friction Coefficient	0.50-0.99	0.40 M_w	3.00 M_w
Und. Fault Permeability	0.1-10,000 nD	0.14 M_w	3.00 M_w

Table 8.2: Total variance in the chosen parameter used to assess failure or loss of integrity for each simulation set and maximal value of the chosen failure parameter in that simulation set. 'H', 'V' and 'A' denote horizontal, vertical and angled (non-horizontal or vertical) fractures, respectively. M_w refers to the moment magnitude. The quantities with units of mm and mD/nD are net surface uplifts and effective permeabilities, respectively. The dimensionless numbers are the logarithmic differences in the highest and lowest effective permeabilities: $\log_{10} k_{eff,max}$ - $\log_{10} k_{eff,min}$.

Operational variables, including injection and withdrawal rates, are controlled at the surface, while hydrogen-specific parameters like viscosity, density, and compressibility are temperature- and pressure-dependent and well-characterized via thermodynamic models. By identifying how each parameter can be empirically determined or constrained, we ensure that simulation insights directly inform both the screening of suitable fields and the design of operational strategies that manage geomechanical risks during UHS deployment.

8.2 Summary of Thesis

This thesis performed hydromechanical simulations to assess the likelihood of certain geomechanical risks occurring during the injection, storage and withdrawal of hydrogen from depleted gas fields. The mechanical, fluid and operational properties that exacerbate and reduce such risks were evaluated. It was generally found that for typical field properties and moderate injection rates, UHS in depleted gas fields is a geomechanically safe energy transition technology for mass energy storage.

In Chapter 2, a review of the existing physical, material and chemical storage methods for hydrogen was presented together with a comprehensive review of all challenges associated with underground hydrogen storage in porous media and the various different 'colour-scale' methods of hydrogen production. This set the scene for the importance of the work and where it fits in relation to the technology. The following conclusions were made: blue and turquoise hydrogen are likely to be the first forms of hydrogen stored commercially. Green hydrogen currently remains prohibitively expensive. Viscous fingers and gravity tongues are likely, thus leading to poor storage space utilisation. Therefore, WAG may be essential in UHS to mitigate such phenomena. Capillary fingers are also very likely to occur and therefore surfactant will most likely be required to ensure efficient storage space utilisation. Calcite presence in the reservoir could enhance storage capacity, injectivity and productivity via hydrogen-induced dissolution but equally can lead to the loss of a small proportion of hydrogen through chemical reactivity ($< 3\%$). However, high calcite presence in the caprock could lead to the loss of seal integrity.

Storage in reservoirs with temperature above 122°C ensures the reservoir is sterile, eliminating potential microbial-induced hydrogen losses. The key issue surrounding the feasibility of UHS in depleted gas fields is the embrittlement of wells and pipelines. This may limit the immediate re-use of existing natural gas pipelines. Hydrogen storage in depleted gas fields is superior to all other hydrogen storage methods for the purpose of national-scale/mass-scale energy storage.

In Chapter 3, a hydromechanical, linear-elastic, fracture nucleation and growth methodology was presented as a means of studying geomechanical phenomena such as induced seismicity, caprock integrity and surface subsidence and uplift during underground hydrogen storage. The fundamental equations of elasticity and linear-elastic fracture mechanics were discussed. Equations for the computation of coupled deformation, damage, contact and slip of fault surfaces, matrix and fracture fluid flow, stress-intensity factors, fracture growth, earthquake magnitude and effective and equivalent permeability were outlined.

In Chapter 4, a depleted gas field model with a shale caprock unit containing an array of small-scale natural fractures was used to study fracture growth and subsequent caprock permeability alteration through time in order to assess caprock integrity. Fracture properties such as initial size, orientation and spacing, caprock mechanical properties such as Young's modulus, Poisson's ratio and permeability and *in situ* stresses were varied to reveal the conditions under which caprock integrity may be lost or ensured. Furthermore, the predictions of the classical Snow effective permeability model was compared against the geomechanical equivalent permeability model of Lang. Caprock integrity was only lost when the caprock had a fracture toughnesses at the very lowest end of the range found in the literature ($< 1 \times 10^5$ Pa $m^{1/2}$). Even at very high injection rates of 5 m^3/s, the caprock remained a perfect seal outside of this condition. High Young's modulus caprocks (i.e., 43 GPa) encouraged extensive growth to the point that multiple caprock fractures coalesced into a single very large fracture inducing the total loss of caprock integrity. Storage in fields with caprocks of very low fracture toughness and high Young's modulus should be avoided. Otherwise, loss of caprock integrity is not at risk during UHS. The Snow effective permeability model yields a qualitatively accurate representation of how caprock permeability is influenced by various properties, but it is quantitatively inaccurate over short time-scales of a few years, relative to the geomechanical equivalent permeability model of Lang,

due to its inherent assumptions. Lang's model should be implemented to obtain temporally accurate quantitative predictions of caprock permeability.

In Chapter 5, a depleted gas field model with intact rock units was used to study surface uplift and subsidence during the injection, storage and withdrawal of gaseous hydrogen from a multi-purpose well in the reservoir. Compaction and surface subsidence were validated against the classical Geertsma's 'nulceus of strain' and 'nucleus of strain with free surface' models. Mechanical properties including permeability, Young's modulus, Poisson's ratio and Biot coefficient of the overburden, caprock and reservoir units were varied to understand which fields, from a geomechanical perspective, may excerbate or minimise surface deformation. For high injection rates such as 10 m^3/s, hydrogen should not be stored in reservoirs of very low Young's modulus (i.e., < 5 GPa). Biot coefficient had little influence on the observed uplift or subsidence. Subsidence and uplift are unlikely to pose a significant risk during UHS. The simulations were performed for a time of three years, but in reality, geological hydrogen storage will be required for tens to hundreds of years. The net uplift profiles show peaks that linearly increase with time and thus the uplift after one year can be multiplied by a given number of years to obtain a rough estimate of potential uplift values far into the future.

In Chapter 6, a depleted gas field model containing a fault isolated within the reservoir unit was implemented to examine the potential for induced seismicity during underground hydrogen storage in scenarios in which the injectant pressure front comes into direct contact with a fault. The ICGT's prediction of fault slip was validated against a numerical case study, implemented in the industry standard software COMSOL, in which CO_2 is stored into an aquifer. Operational properties (i.e., injection rate, well perforation length, withdrawal rate), reservoir mechanical properties (i.e., Young's modulus, Biot coefficient, permeability), hydrogen injectant fluid properties (i.e., viscosity, compressibility, density) and fault properties (i.e., fault length, fault friction coefficient, dip) were varied to reveal which reservoirs and which engineering conditions enhance or reduce fault slip and what maximal earthquake magnitudes will occur. Injection rates of over 5 m^3/s were required to induce any fault slip, showing that faults are likely to remain stable during UHS at normal injection rates. The injected hydrogen should have as high compressibility as possible ($> 5.00\times10^{-7}$ Pa^{-1}), so the injection temperature and

pressure should be carefully engineered to ensure this. At higher hydrogen compressibilities, the fault did not slip even at very high injection rates of 20 m^3/s. Storage in reservoir rocks with high Young's modulus (> 40 GPa) could eliminate any potential fault motion. The maximal magnitude event that was induced across all 72 simulations covering 16 material and operational properties was 3.75. Therefore, no induced earthquake above 'weak' to 'light' (according to the Modified Mercalli scale) is expected to occur during UHS. At such a magnitude, vehicles will be rocked noticeably. Serious damage and injury will not occur, but the rocking could be sufficient to anger local residents during onshore UHS, risking a social license to operate.

In Chapter 7, a depleted gas field model containing a fault isolated within the underburden unit was implemented to examine the potential for induced seismicity along faults that have no pressure communication with the injected hydrogen. The influence of four key mechanical properties of the underburden rock, Young's modulus, Poisson's ratio, Biot coefficient and permeability on the fault slip and maximum potential earthquake magnitudes were quantified. This highlights what fields, based on their mechanical properties, may pose a seismicity danger for underground hydrogen storage. Underburden Young's modulus was the only mechanical property examined that induced a moderate change in induced earthquake magnitude depending on its value and even then, this was only a difference of 0.27 from a magnitude 2.73 to 3.00 when Young's modulus was varied from 5 GPa to 40 GPa. The maximum induced event was 3.09 and this required a huge injection rate of 40 m^3/s, at the very upper limit of potential field injection rates. This is a 'weak' earthquake on the Modified Mercalli scale meaning many people do not notice that an earthquake has occurred, and only those on the upper floors of buildings are likely to feel anything substantial. Therefore, underburden induced seismicity is unlikely to be problematic for UHS deployment onshore. However, unlike reservoir seismicity that can be eliminated at low injection rates (< 5 m^3/s), magnitude 2 earthquakes can still occur at low rates (< 1 m^3/s) along underburden faults. Excluding injection rate, fault friction coefficient is the key parameter governing underburden earthquake magnitude. High fault friction coefficients (i.e., 0.99) reduced the maximal event magnitude to 2.60 from 3.00 when the friction coefficient was just 0.50. Ideally, hydrogen should be stored in fields where any present basement faults have as high friction coefficient as possible.

8.3 Future Work

The work presented in this thesis began the analysis of the geomechanical consequences of cyclically injecting, storing and withdrawing gaseous hydrogen from depleted gas fields over multi-year time scales. Given the chronic shortage of geomechanical literature in this topic, there are still many extensions, improvements and adaptions of this work that can be explored. Such extensions include:

- Varying reservoir mechanical properties and assessing their impact on the caprock natural fracture array and integrity.
- Conducting an analysis of how a suite of operational and mechanical properties impact the nucleation of new fractures within the caprock.
- Examine the impact of a vertical fracture array as fracture interaction may be different than in the horizontal array assessed in this work.
- Compute the Lang equivalent permeability versus time for all caprock integrity cases tested given the Snow and Lang models have now been shown to generate significantly different permeability values.
- Examine reservoir integrity by assessing the growth and nucleation of fractures within the reservoir unit under different injection rates and mechanical reservoir properties.
- Allow nucleation of fractures in the uplift and subsidence model in the overburden, caprock and reservoir to examine how their inclusion distorts pressure and stress distribution and ultimately the net uplift-time curves.
- In both induced seismicity models consider the impact of multiple faults and how their interaction may distort the slip along each one.
- Allow the fault the potential to grow and morph its geometry in response to injection, storage and withdrawal and examine if this alters the results.
- Perform longer term simulations over ten to fifty years.

- Examine the effect of reservoir mechanical properties on the underburden fault slip response.
- Perform the same simulations with a WAG-injection schedule instead of pure hydrogen to examine the impact on the results as this may be the more realistic hydrogen injection strategy.

Adaptations of this work and the numerical framework used that could enhance the analysis further include:

- **Plasticity**. Extend the ICGT simulator to include plasticity models to account for plastic deformation of rocks under extreme stress conditions, allowing irreversible deformation during high-pressure injection or withdrawal. Re-assess its impact on the same three phenomena: uplift/subsidence, caprock integrity and induced seismicity. The work herein assumes a clean, brittle sandstone reservoir, but there are some reservoirs that contain a large number of mudstone or claystone baffles that are more likely to deform plastically. This is because mudstones typically contain a significant proportion of clay minerals such as kaolinite, illite, and smectite, which have a platy or sheet-like structure that allows the sheets to slide past one another under stress. Thus, the reservoir stress state could be altered away from that observed in this work.
- **Chemical Reactions**. Add chemical reactions to the code to assess the impact of pressure and stress-induced mineral precipitation and dissolution and how this impacts the results through varying the mechanical behaviour and stiffness of the rock.
- **Material Heterogeneities**. Add permeability and material heterogeneity to the reservoir and caprock units to assess how this impacts the results. Run both directional heterogeneity as in rock fabrics (different permeability/Young's modulus in perpendicular directions) and also hundreds of realisations of randomly distributed properties across the whole reservoir which is useful for assessing rocks with no representative elementary volume, REV (vuggy carbonates).

- **Thermal effects**. Turn on thermal effects in the ICGT to assess the impact of the Joule-Thomson effect on the results. Hydrogen can exhibit a negative Joule-Thomson effect, meaning that in contrast to most gases, its temperature increases as it expands. Therefore, it would be expected that during periods of withdrawal, fault slip may be enhanced slightly relative to that predicted herein. This is because as hydrogen is withdrawn, the reservoir pressure decreases, the hydrogen expands, and its temperature increases which can enhance pore fluid pressures due to increased fluid volumes within fault zones resulting from thermal pressurisation and therefore reduce effective stress acting on the fault. Furthermore, heating the rock may induce expansion of the caprock which could alter the fracture aperture, connectivity, and propagation rate of the natural fracture array in the caprock study.

- **Real field data**. Acquiring a real exact geological model of a storage reservoir and field of interest, including the exact size and geometry (thickness, width, length, dip) of the units, the exact location and geometry of key geological structures such as faults, geomechanical data on the fracture intensity and aperture of fractures, the *in situ* stress conditions, the location of potential wellbores in relation to the key geological structures, and operational information such as injection rates or maximal and minimal bottomhole flowing pressures would enhance the value of the work further.

Bibliography

M. Abbas. Geomechanical characterization of shale caprock of the longyearbyen co2 storage pilot. Master's thesis, 2015.

S. Abdel-Azeim, A. Al-Yaseri, K. Norrman, P. Patil, A. Qasim, and A. Yousef. Wettability of caprock–h2–water: Insights from molecular dynamic simulations and sessile-drop experiment. *Energy & Fuels*, 37(23):19348–19356, 2023.

S. Abdulkareem, T. Ogedengbe, J. Aweda, T. Ajiboye, A. Khan, and M. Babatunde. Investigation on effect of material compositions on machinability of carbon steels. In *Journal of Physics: Conference Series*, volume 1378, page 022046. IOP Publishing, 2019.

D. Aberle and D. Agarwal. High performance corrosion resistant stainless steels and nickel alloys for oil & gas applications. In *NACE CORROSION*, pages NACE–08085. NACE, 2008.

A. Aftab, A. Hassanpouryouzband, H. Naderi, Q. Xie, and M. Sarmadivaleh. Quantifying onshore salt deposits and their potential for hydrogen energy storage in australia. *Journal of Energy Storage*, 65:107252, 2023.

H. Aghaei, A. Al-Yaseri, A. Toorajipour, B. Shahsavani, N. Yekeen, and K. Edlmann. Host-rock and caprock wettability during hydrogen drainage: Implications of hydrogen subsurface storage. *Fuel*, 351:129048, 2023.

N. Agofack, P. Cerasi, A. Stroisz, and S. Rørheim. Sorption of co2 and integrity of a caprock shale. In *ARMA US Rock Mechanics/Geomechanics Symposium*, pages ARMA–2019. ARMA, 2019.

R. K. Ahluwalia, J. K. Peng, and T. Q. Hua. *Cryo-compressed hydrogen storage*, pages 119–145. Compendium of Hydrogen Energy. Woodhead Publishing, 2016. ISBN 9781782423621. doi: https://doi.org/10.1016/B978-1-78242-362-1.00005-5. ID: 313075.

S. Akbayrak and S. Özkar. Ammonia borane as hydrogen storage materials. *International Journal of Hydrogen Energy*, 43(40):18592–18606, 2018.

M. Akhurst, T. Mallows, J. Pearce, and E. Mackay. Assessing interactions between multiple geological co2 storage sites to optimize capacity in regionally extensive storage sandstones. *Energy Procedia*, 114:4571–4582, 2017.

H. Al-Mukainah, A. Al-Yaseri, N. Yekeen, J. Al Hamad, and M. Mahmoud. Wettability of shale–brine–h2 system and h2-brine interfacial tension for assessment of the sealing capacities of shale formations during underground hydrogen storage. *Energy Reports*, 8:8830–8843, 2022.

A. Al-Yaseri, A. Amao, and A. Fatah. Experimental investigation of shale/hydrogen geochemical interactions. *Fuel*, 346:128272, 2023.

M. M. Alam, I. L. Fabricius, and H. F. Christensen. Static and dynamic effective stress coefficient of chalk. *Geophysics*, 77(2):L1–L11, 2012.

A. H. Alamri. Localized corrosion and mitigation approach of steel materials used in oil and gas pipelines–an overview. *Engineering failure analysis*, 116:104735, 2020.

A. Alanazi, N. Yekeen, M. Ali, M. Ali, I. S. Abu-Mahfouz, A. Keshavarz, S. Iglauer, and H. Hoteit. Influence of organics and gas mixing on hydrogen/brine and methane/brine wettability using jordanian oil shale rocks: Implications for hydrogen geological storage. *Journal of Energy Storage*, 62:106865, 2023.

H. T. Alassi. *Modeling reservoir geomechanics using discrete element method: application to reservoir monitoring*. PhD thesis, Norweigan University of Science and Technology (NTNU, 2008.

M. Alghannam and R. Juanes. Understanding rate effects in injection-induced earthquakes. *Nature communications*, 11(1):3053, 2020.

A. Ali and M. N. Shaikh. Recent developments in catalyst design for liquid organic hydrogen carriers: Bridging the gap to affordable hydrogen storage. *International Journal of Hydrogen Energy*, 78:1–21, 2024.

M. Ali, N. Yekeen, N. Pal, A. Keshavarz, S. Iglauer, and H. Hoteit. Influence of pressure, temperature and organic surface concentration on hydrogen wettability of caprock; implications for hydrogen geo-storage. *Energy Reports*, 7:5988–5996, 2021.

A. Alvarez, D. Mercado, and V. Salazar. Modeling caprock failure during injection in a co2 capture and storage project using a compositional/geochemical/geomechanical coupled numerical simulation. In *SPE Latin America and Caribbean Petroleum Engineering Conference*, page D021S011R003. SPE, 2023.

I. Amez, S. Gonzalez, L. Sanchez-Martin, M. F. Ortega, and B. Llamas. Underground methanation, a natural way to transform carbon dioxide into methane. In *Climate Change Science*, pages 81–106. Elsevier, 2021.

P. Amigavn, M. Greksak, J. Kozankova, F. Buzek, V. Onderka, and I. Wolf. Methanogenic bacteria as a key factor involved in changes of town gas stored in an underground reservoir. *FEMS Microbiology Ecology*, 6(3):221–224, 1990.

E. N. Aminaho, M. Hossain, N. H. Faisal, and R. Sanaee. Formation integrity evaluation for geosequestration of co2 in depleted petroleum reservoirs under cyclic stress conditions. *Geoenergy Science and Engineering*, page 212892, 2024.

M. Aminudin, S. Kamarudin, B. Lim, E. Majilan, M. Masdar, and N. Shaari. An overview: Current progress on hydrogen fuel cell vehicles. *International Journal of Hydrogen Energy*, 48(11):4371–4388, 2023.

A. Andiappan, M. Pichler, and S. Bauer. Investigation of subsurface integrity of depleted porous gas reservoirs for the purpose of hydrogen storage. In *SPE EuropEC-Europe Energy Conference featured at the 84th EAGE Annual Conference & Exhibition*. OnePetro, 2023.

M. Andreani, I. Daniel, and M. Pollet-Villard. Aluminum speeds up the hydrothermal alteration of olivine. *American Mineralogist*, 98(10):1738–1744, 2013.

J. Andrew. The embrittling of iron by caustic soda. *Transactions of the Faraday Society*, 9: 316–329, 1914.

A. Antropov, A. Lavrov, and B. Orlic. Effect of in-situ stress alterations on flow through faults and fractures in the cap rock. *Energy Procedia*, 114:3193–3201, 2017.

K. Anyim and Q. Gan. Fault zone exploitation in geothermal reservoirs: Production optimization, permeability evolution and induced seismicity. *Advances in Geo-Energy Research*, 4: 1–12, 2020.

A. Aobpaet, M. C. Cuenca, A. Hooper, and I. Trisirisatayawong. Insar time-series analysis of land subsidence in bangkok, thailand. *International Journal of Remote Sensing*, 34(8): 2969–2982, 2013.

S. N. Apak, H. T. Moors, and K. Ghori. *Basin development and petroleum exploration potential of the Yowalga area, Officer Basin, Western Australia*. Number 76. Geological Survey of Western Australia, 2000.

E. Arjomand, S. Salimzadeh, W. S. Mow, A. Movassagh, and J. Kear. Geomechanical modelling of ground surface deformation induced by co2 injection at in salah, algeria: Three wells, three responses. *International Journal of Greenhouse Gas Control*, 132:104034, 2024.

P. Armitage, D. Faulkner, R. Worden, A. Aplin, A. Butcher, and J. Iliffe. Experimental measurement of, and controls on, permeability and permeability anisotropy of caprocks from the co2 storage project at the krechba field, algeria. *Journal of Geophysical Research: Solid Earth*, 116(B12), 2011.

T. R. Ayodele, T. C. Mosetlhe, A. A. Yusuff, and A. Ogunjuyigbe. Off-grid hybrid renewable energy system with hydrogen storage for South African rural community health clinic. *International Journal of Hydrogen Energy*, 46(38):19871–19885, 2021.

C. Azzaro-Pantel. *Hydrogen Supply Chain: Design, Deployment and Operation*. Academic Press, 2018.

W. Badeghaish, M. Noui-Mehidi, and O. Salazar. The future of nonmetallic composite materials in upstream applications. In *SPE Gas & Oil Technology Showcase and Conference*, page D021S014R004. SPE, 2019.

P. Bai, Y. Liang, S. Zheng, and C. Chen. Effect of amorphous fes semiconductor on the corrosion behavior of pipe steel in h2s-containing environments. *Industrial & Engineering Chemistry Research*, 55(41):10932–10940, 2016.

T. Bai and P. Tahmasebi. Coupled hydro-mechanical analysis of seasonal underground hydrogen storage in a saline aquifer. *Journal of Energy Storage*, 50:104308, 2022.

T. Bai, Y. Yu, P. Li, Z. Jiao, M. Johnson, C. Nye, J. McLaughlin, and S. Quillinan. An integrated reservoir simulation and geomechanical modeling of co2 injection at the wyoming dry fork carbonsafe geologic storage complex. In *Carbon Capture, Utilization, and Storage Conference and Exhibition, 11–13 March 2024*, pages 183–197. Carbon Capture, Utilization, and Storage (CCUS) Conference and Exhibition, 2024.

Y. Bai, R. Zhou, and J. Wu. Hazard identification and analysis of urban utility tunnels in china. *Tunnelling and Underground Space Technology*, 106:103584, 2020.

S. Baisch, R. Weidler, R. Voros, D. Wyborn, and L. de Graaf. Induced seismicity during the stimulation of a geothermal hfr reservoir in the cooper basin, australia. *Bulletin of the Seismological Society of America*, 96(6):2242–2256, 2006.

S. Baisch, R. Vörös, E. Rothert, H. Stang, R. Jung, and R. Schellschmidt. A numerical model for fluid injection induced seismicity at soultz-sous-forêts. *International Journal of Rock Mechanics and Mining Sciences*, 47(3):405–413, 2010.

W. Balasooriya, C. Clute, B. Schrittesser, and G. Pinter. A review on applicability, limitations, and improvements of polymeric materials in high-pressure hydrogen gas atmospheres. *Polymer reviews*, 62(1):175–209, 2022.

X. Bao and D. W. Eaton. Fault activation by hydraulic fracturing in western canada. *Science*, 354(6318):1406–1409, 2016.

E. Baraj, K. Ciahotny, and T. Hlincík. The water gas shift reaction: Catalysts and reaction mechanism. *Fuel*, page 119817, 2020.

M. Barba-Sevilla, B. W. Baird, A. B. Liel, and K. F. Tiampo. Hazard implications of the 2016 mw 5.0 cushing, ok earthquake from a joint analysis of damage and insar data. *Remote Sensing*, 10(11):1715, 2018.

F. Barbir. *Fuel Cells and Hydrogen Economy*. Elsevier, 2021.

A. J. Barbour, J. H. Norbeck, and J. L. Rubinstein. The effects of varying injection rates in osage county, oklahoma, on the 2016 m w 5.8 pawnee earthquake. *Seismological Research Letters*, 88(4):1040–1053, 2017.

R. S. Barsoum. On the use of isoparametric finite elements in linear fracture mechanics. *International journal for numerical methods in engineering*, 10(1):25–37, 1976.

H. Barthélémy. Effects of pressure and purity on the hydrogen embrittlement of steels. *International Journal of Hydrogen Energy*, 36(3):2750–2758, 2011.

K. S. Basniev, R. J. Omelchenko, and F. A. Adzynova. Underground hydrogen storage problems in Russia. In *18th World Hydrogen Energy Conference 2010*, 2010.

D. Baú, M. Ferronato, G. Gambolati, and P. Teatini. Surface flow boundary conditions in modeling land subsidence due to fluid withdrawal. *Groundwater*, 42(4):516–525, 2004.

G. W. Bawden, W. Thatcher, R. S. Stein, K. W. Hudnut, and G. Peltzer. Tectonic contraction across los angeles after removal of groundwater pumping effects. *Nature*, 412(6849):812–815, 2001.

J. D. Bedford, T. Hirose, and Y. Hamada. Rapid fault healing after seismic slip. *Journal of Geophysical Research: Solid Earth*, 128(6):e2023JB026706, 2023.

F. G. Bell, D. C. Entwisle, and M. G. Culshaw. A geotechnical survey of some british coal measures mudstones, with particular emphasis on durability. *Engineering Geology*, 46(2): 115–129, 1997.

K. Benavides. *Exploring the Role of Hydrogen in Decarbonizing Heavy Industry*. PhD thesis, Massachusetts Institute of Technology, 2023.

J. P. Bensing, D. Misch, L. Skerbisch, and R. F. Sachsenhofer. Hydrogen-induced calcite dissolution in amaltheenton formation claystones: Implications for underground hydrogen storage caprock integrity. *International Journal of Hydrogen Energy*, 47(71):30621–30626, 2022.

V. Bhadariya, J. Kaur, P. Sapale, P. Rasane, and J. Singh. Hydrogen storage in porous media: Understanding and mitigating microbial risks for a sustainable future. *International Journal of Hydrogen Energy*, 67:681–693, 2024.

F. Birol. The future of hydrogen (iea). `https://www.iea.org/reports/the-future-of-hydrogen`, 2019. International Energy Agency.

M. Blunt. *Imperial College Lectures In Petroleum Engineering, The-Volume 2: Reservoir Engineering*, volume 2. World Scientific Publishing Company, 2017a.

M. J. Blunt. *Multiphase flow in permeable media: A pore-scale perspective*. Cambridge university press, 2017b.

Z. Bo, L. Zeng, Y. Chen, and Q. Xie. Geochemical reactions-induced hydrogen loss during underground hydrogen storage in sandstone reservoirs. *International Journal of Hydrogen Energy*, 46(38):19998–20009, 2021.

J. Boak. Patterns of induced seismicity in central and northwest oklahoma. In *SEG Technical Program Expanded Abstracts 2016*, pages 5039–5042. Society of Exploration Geophysicists, 2016.

B. Bogdanovic and M. Schwickardi. Ti-doped naalh4 as a hydrogen-storage material–preparation by ti-catalyzed hydrogenation of aluminum powder in conjunction with sodium hydride. *Applied Physics A*, 72:221–223, 2001.

B. Bohloli, T. I. Bjørnarå, J. Park, and A. Rucci. Can we use surface uplift data for reservoir

performance monitoring? a case study from in salah, algeria. *International Journal of Greenhouse Gas Control*, 76:200–207, 2018.

N. Boitz, C. Langenbruch, and S. A. Shapiro. Production-induced seismicity indicates a low risk of strong earthquakes in the groningen gas field. *Nature communications*, 15(1):329, 2024.

J. Bollmann, N. Schmidt, D. Beck, P. Preuster, L. Zigan, P. Wasserscheid, and S. Will. A path to a dynamic hydrogen storage system using a liquid organic hydrogen carrier (lohc): Burner-based direct heating of the dehydrogenation unit. *International Journal of Hydrogen Energy*, 48(3):1011–1023, 2023.

S. Bordiga, J. G. Vitillo, G. Ricchiardi, L. Regli, D. Cocina, A. Zecchina, B. Arstad, M. Bjørgen, J. Hafizovic, and K. P. Lillerud. Interaction of hydrogen with mof-5. *The Journal of Physical Chemistry B*, 109(39):18237–18242, 2005.

P. Bormann and D. Di Giacomo. The moment magnitude m w and the energy magnitude m e: common roots and differences. *Journal of Seismology*, 15:411–427, 2011.

P. Bormann, S. Wendt, and D. DiGiacomo. Seismic sources and source parameters. In *New manual of seismological observatory practice 2 (NMSOP2)*, pages 1–259. Deutsches GeoForschungsZentrum GFZ, 2013.

T. Boukharouba, M. Elboujdaini, and G. Pluvinage. *Damage and fracture mechanics: Failure analysis of engineering materials and structures*. Springer Science & Business Media, 2009.

J. Bourdet, C. Delle Piane, C. Wilske, D. Mallants, A. Suckow, D. Questiaux, C. Gerber, P. Crane, A. Deslandes, L. Martin, et al. Natural hydrogen in low temperature geofluids in a precambrian granite, south australia. implications for hydrogen generation and movement in the upper crust. *Chemical Geology*, 638:121698, 2023.

J. Bourgeois, N. Aupaix, R. Bloise, and J. Millet. Formation of hydrogen sulfide in underground storage reservoirs by reduction of sulfurous minerals in reservoir rocks. *Rev. Inst. Fr. Pet.;(France)*, 34, 1979.

J. Brauns and T. Turek. Alkaline water electrolysis powered by renewable energy: A review. *Processes*, 8(2):248, 2020.

J. Brauns, J. Schoenebeck, M. R. Kraglund, D. Aili, J. Hnat, J. Zitka, W. Mues, J. O. Jensen, K. Bouzek, and T. Turek. Evaluation of diaphragms and membranes as separators for alkaline water electrolysis. *Journal of the Electrochemical Society*, 168(1):014510, 2021.

N. Ø. Brevik. Experimental study of fracture toughness in sedimentary rocks. Master's thesis, NTNU, 2016.

G. Brown, V. Carvalho, A. Wray, D. Smith, M. Toombs, and S. Pennell. Monitoring alternating co2 and water injection and its effect on production in a carbonate reservoir using permanent fiber-optic distributed temperature systems. In *SPE Annual Technical Conference and Exhibition?*, pages SPE–90248. SPE, 2004.

G. Bru, G. Herrera, R. Tomás, J. Duro, R. De la Vega, and J. Mulas. Control of deformation of buildings affected by subsidence using persistent scatterer interferometry. *Structure and infrastructure engineering*, 9(2):188–200, 2013.

C. Brugier, A. Wayser-Langevin, and M. Rosen. USA: Air Liquide operates the world's largest hydrogen storage facility, 2017. `https://www.airliquide.com/sites/airliquide.com/files/2017/01/03/usa-air-liquide-operates-the_world-s-largest-hydrogen-storage-facility.pdf`.

J. Buckley and Y. Liu. Some mechanisms of crude oil/brine/solid interactions. *Journal of Petroleum Science and Engineering*, 20(3-4):155–160, 1998.

L. Buijze, L. van Bijsterveldt, H. Cremer, B. Jaarsma, B. Paap, H. Veldkamp, B. Wassing, J. van Wees, G. van Yperen, and J. Ter Heege. Induced seismicity in geothermal systems: Occurrences worldwide and implications for the netherlands. In *European Geothermal Congress*, pages 11–14, 2019.

L. Buijze, Y. Guo, A. Niemeijer, S. Ma, and C. Spiers. Effects of heterogeneous gouge segments on the slip behavior of experimental faults at dm scale. *Earth and Planetary Science Letters*, 554:116652, 2021.

S. Burgess. Settlement assessment of grey lynn tunnel and tawariki street shafts. Grey Lynn Tunnel Watercare Services Limited, 2019.

J. Burtonshaw, A. Paluszny, and R. W. Zimmerman. Numerical modelling of induced seismicity along a fault during co2 injection into a subsurface reservoir. *Proc. 15th Int. Congress of Rock Mechanics, 9-14 Oct 2023, pp. 2795-2800*, 2023a. `https://eposter.at/ISRM2023/data/PDF/1688.pdf`.

J. E. Burtonshaw, A. Paluszny, and R. W. Zimmerman. Numerical modelling of induced seismicity along a fault during co2 injection into a subsurface reservoir. In *Proceedings of the 15th ISRM Congress*, pages paper ISRM–2023–1688. ISRM, 2023b.

J. E. J. Burtonshaw, R. N. Thomas, A. Paluszny, and R. W. Zimmerman. Effect of viscosity and injection rate on the tensile and shear deformation experienced by interacting hydraulic and natural fractures. Proc. 55th U.S. Rock Mechanics Symposium, 18-25 June 2021, paper ARMA-2021-1865, 06 2021.

J. E. J. Burtonshaw, A. Paluszny, A. Mohammadpour, and R. W. Zimmerman. Effects of reservoir mechanical properties on induced seismicity during subsurface hydrogen storage. *Philosophical Transactions A*, 2024a. doi: 10.1098/rsta.2023.0187.

J. E. J. Burtonshaw, A. Paluszny, A. Mohammadpour, and R. W. Zimmerman. Effects of the underburden mechanical properties on induced seismicity along a basement fault during hydrogen storage in a depleted gas reservoir. *iScience*, 2024b.

T. A. Buscheck, A. Goodman, G. Lackey, J. D. T. Camargo, N. Huerta, F. Haeri, G. M. Freeman, and J. A. White. Underground storage of hydrogen and hydrogen/methane mixtures in porous reservoirs: Influence of reservoir factors and engineering choices on deliverability and storage operations. *International Journal of Hydrogen Energy*, 49:1088–1107, 2024.

F. Buzek, V. Onderka, P. Vanvcura, and I. Wolf. Carbon isotope study of methane production in a town gas storage reservoir. *Fuel*, 73(5):747–752, 1994.

T. Byrnes. Pipeline coatings. *Trends in Oil and Gas Corrosion Research and Technologies*, pages 563–591, 2017.

D. G. Caglayan, N. Weber, H. U. Heinrichs, J. Linßen, M. Robinius, P. A. Kukla, and D. Stolten. Technical potential of salt caverns for hydrogen storage in europe. *International Journal of Hydrogen Energy*, 45(11):6793–6805, 2020.

M. Camm, L. E. Armstrong, and A. Patel. The britannia field, blocks 15/29, 15/30, 16/26 and 16/27, uk north sea. *Geological Society, London, Memoirs*, 52(1):664–678, 2020.

W. Cao, J.-Q. Shi, S. Durucan, and A. Korre. Evaluation of shear slip stress transfer mechanism for induced microseismicity at in salah co2 storage site. *International Journal of Greenhouse Gas Control*, 107:103302, 2021.

W. Cao, J. P. Verdon, and M. Tao. Coupled poroelastic modeling of hydraulic fracturing-induced seismicity: Implications for understanding the post shut-in ml 2.9 earthquake at the preston new road, uk. *Journal of Geophysical Research: Solid Earth*, 127(3):e2021JB023376, 2022.

T. Capurso, M. Stefanizzi, M. Torresi, and S. Camporeale. Perspective of the role of hydrogen in the 21st century energy transition. *Energy Conversion and Management*, 251:114898, 2022.

P. Carden and L. Paterson. Physical, chemical and energy aspects of underground hydrogen storage. *International Journal of Hydrogen Energy*, 4(6):559–569, 1979.

E. S. Carlson and J. C. Mercer. Devonian shale gas production: mechanisms and simple models. *Journal of Petroleum technology*, 43(04):476–482, 1991.

M. R. Carlson. An analysis of the caprock failure at joslyn. In *SPE Canada Heavy Oil Conference*, pages SPE–156962. SPE, 2012.

P. Cavaliere. Safety issues and regulations. In *Water Electrolysis for Hydrogen Production*, pages 729–791. Springer, 2023.

P. Cerasi, M. Duda, L. Edvardsen, N. Agofack, and M. H. Bhuiyan. Effect of field caprock shale exposure to co2 on its mechanical properties—a comparison of experimental techniques. In *Physical Sciences Forum*, volume 4, page 33. MDPI, 2022.

S. Cerniauskas, A. J. C. Junco, T. Grube, M. Robinius, and D. Stolten. Options of natural gas pipeline reassignment for hydrogen: Cost assessment for a germany case study. *International Journal of Hydrogen Energy*, 45(21):12095–12107, 2020.

S.-S. Cha, K.-K. Lee, G.-O. Bae, D.-H. Lee, and N. Gatelier. Analysis of rock drainage and cooling experiments for underground cryogenic lng storage. *Engineering geology*, 93(3-4): 117–129, 2007.

M. J. Chadwick, N. H. Highton, and N. Lindman. *6 - Coal Conversion Technologies*, pages 105–155. Environmental Impacts of Coal Mining & Utilization. Pergamon, Amsterdam, 1987. ISBN 9780080314273. doi: https://doi.org/10.1016/B978-0-08-031427-3.50015-3. ID: 302250.

C. R. Chambers, M. R. M. Brown, S. M. Stokes, S. Ge, E. A. Menezes, K. F. Tiampo, and A. F. Sheehan. Surface deformation and seismicity linked to fluid injection in the raton basin. *Groundwater*, n/a(n/a), 2024. doi: https://doi.org/10.1111/gwat.13393. `https://ngwa.onlinelibrary.wiley.com/doi/abs/10.1111/gwat.13393`.

M. R. Chandler, A.-L. Fauchille, H. K. Kim, L. Ma, J. Mecklenburgh, R. Rizzo, M. Mostafavi, S. Marussi, R. Atwood, S. May, et al. Correlative optical and x-ray imaging of strain evolution during double-torsion fracture toughness measurements in shale. *Journal of Geophysical Research: Solid Earth*, 123(12):10–517, 2018.

K. W. Chang and P. Segall. Injection-induced seismicity on basement faults including poroelastic stressing. *Journal of Geophysical Research: Solid Earth*, 121(4):2708–2726, 2016a.

K. W. Chang and P. Segall. Seismicity on basement faults induced by simultaneous fluid injection–extraction. *Pure and Applied Geophysics*, 173:2621–2636, 2016b.

K. W. Chang, H. Yoon, and M. J. Martinez. Potential seismicity along basement faults induced by geological carbon sequestration. *Geophysical Research Letters*, 49(13):e2022GL098721, 2022.

K. R. Chaturvedi, S. Bajpai, J. Trivedi, and T. Sharma. Air foams for mobility control and

subsurface storage of hydrogen in porous media: an experimental study. *Energy & Fuels*, 36 (9):5036–5046, 2022.

L. Chen, Z. Qi, S. Zhang, J. Su, and G. A. Somorjai. Catalytic hydrogen production from methane: A review on recent progress and prospect. *Catalysts*, 10(8):858, 2020.

Y.-S. Chen, C. Huang, P.-Y. Liu, H.-W. Yen, R. Niu, P. Burr, K. L. Moore, E. Martínez-Paneda, A. Atrens, and J. M. Cairney. Hydrogen trapping and embrittlement in metals–a review. *International Journal of Hydrogen Energy*, 2024.

Y. Cheng, W. Liu, T. Xu, Y. Zhang, X. Zhang, Y. Xing, B. Feng, and Y. Xia. Seismicity induced by geological co2 storage: A review. *Earth-Science Reviews*, 239:104369, 2023.

A. C. Chien and S. S. Chuang. Static and dynamic hydrogen adsorption on pt/ac and mof-5. *International journal of hydrogen energy*, 36(10):6022–6030, 2011.

G. Chisholm and L. Cronin. *Hydrogen from water electrolysis*, pages 315–343. Storing Energy. Elsevier, 2016.

A. Christensen. Assessment of hydrogen production costs from electrolysis: United states and europe. *International Council on Clean Transportation: Washington, DC, USA*, pages 1–73, 2020.

K. Christenson. Lng-storage in insulated rock caverns. In *Storage in Excavated Rock Caverns: Rockstore 77*, pages 459–465. Elsevier, 1978.

A. Ciancimino, R. M. Cosentini, S. Foti, A. Messori, H. Ullah, G. Volonté, and G. Musso. A preliminary investigation on the mechanical behaviour of a stiff italian clay in the context of hydrogen storage. *Geomechanics for Energy and the Environment*, page 100562, 2024.

J. Cihlar, D. Mavins, and K. van der Leun. Picturing the value of underground gas storage to the european hydrogen system. *Guidehouse: Chicago, IL, USA*, 2021.

H. Clarke, L. Eisner, P. Styles, and P. Turner. Felt seismicity associated with shale gas hydraulic fracturing: The first documented example in europe. *Geophysical Research Letters*, 41(23): 8308–8314, 2014.

R. D. Cook. *Concepts and applications of finite element analysis*. John Wiley & sons, 2007.

A. H. Cooper. The classification, recording, databasing and use of information about building damage caused by subsidence and landslides. *Quarterly Journal of Engineering Geology and Hydrogeology*, 41(3):409–424, 2008.

C. Cornelio and M. Violay. Parametric analysis of the elastohydrodynamic lubrication efficiency on induced seismicity. *Geophysical Journal International*, 222(1):517–525, 2020a.

C. Cornelio and M. Violay. Effect of fluid viscosity on earthquake nucleation. *Geophysical Research Letters*, 47(12):e2020GL087854, 2020b.

C. Cornelio, E. Spagnuolo, G. Di Toro, S. Nielsen, and M. Violay. Mechanical behaviour of fluid-lubricated faults. *Nature Communications*, 10(1):1274, 2019.

P. Cotterill. The hydrogen embrittlement of metals. *Progress in Materials Science*, 9(4):205–301, 1961.

M. Cotton. Fair fracking? ethics and environmental justice in united kingdom shale gas policy and planning. *Local Environment*, 22(2):185–202, 2017.

C. Coutanceau, S. Baranton, and T. Audichon. *Hydrogen electrochemical production*. Academic Press, 2017.

A. Craig, S. Newman, P. Stephenson, C. Evans, S. Yancazos, and S. Barber. Hydrogen storage potential of depleted oil and gas fields in western australia. *The APPEA Journal*, 62(1): 185–195, 2022.

F. Crotogino, S. Donadei, U. Bünger, and H. Landinger. Large-scale hydrogen underground storage for securing future energy supplies. In *18th World hydrogen energy conference*, volume 78, pages 37–45, 2010.

F. Crotogino, G.-S. Schneider, and D. J. Evans. Renewable energy storage in geological formations. *Proceedings of the Institution of Mechanical Engineers, Part A: Journal of Power and Energy*, 232(1):100–114, 2018.

N. Cuenot, C. Dorbath, and L. Dorbath. Analysis of the microseismicity induced by fluid injections at the egs site of soultz-sous-forêts (alsace, france): implications for the characterization of the geothermal reservoir properties. *Pure and applied geophysics*, 165:797–828, 2008.

M. E. Curtis, C. H. Sondergeld, R. J. Ambrose, and C. S. Rai. Microstructural investigation of gas shales in two and three dimensions using nanometer-scale resolution imagingmicrostructure of gas shales. *AAPG Bulletin*, 96(4):665–677, 2012.

K. Cyran, T. Toboła, and P. Kamiński. Experimental study on mechanically driven migration of fluids in rock salt. *Engineering Geology*, 313:106975, 2023.

L. Dal Zilio, B. Hegyi, W. Behr, and T. Gerya. Hydro-mechanical earthquake cycles in a poro-visco-elasto-plastic fluid-bearing fault structure. *Tectonophysics*, 838:229516, 2022.

D. D'alessandro. Exploiting redox activity in metal–organic frameworks: concepts, trends and perspectives. *Chemical Communications*, 52(58):8957–8971, 2016.

D. R. Damasceno. *Modeling aspects of reliability-based design of lined rock caverns*. PhD thesis, KTH Royal Institute of Technology, 2022.

F. L. Darkrim, P. Malbrunot, and G. P. Tartaglia. Review of hydrogen storage by adsorption in carbon nanotubes. *International Journal of Hydrogen Energy*, 27(2):193–202, 2002.

M. David, C. Ocampo-Martinez, and R. Sanchez-Pena. Advances in alkaline water electrolyzers: A review. *Journal of Energy Storage*, 23:392–403, 2019.

F. Dawood, M. Anda, and G. M. Shafiullah. Hydrogen production for energy: An overview. *International Journal of Hydrogen Energy*, 45(7):3847–3869, 2020.

DBI GUT. The effects of hydrogen injection in natural gas networks for the dutch underground storages. Technical report, Ministry of Economic Affairs, Netherlands Enterprise Agency, 2017. `https://www.rvo.nl/sites/default/files/2017/07/The%20effects%20of%20hydrogen%20injection%20in%20natural%20gas%20networks%20for%20the%20Dutch%20underground%20storages.pdf`.

J. A. de Waal and M. W. Schouten. Regulating subsidence and its uncertainty in the dutch wadden sea. *Proceedings of the International Association of Hydrological Sciences*, 382:63–70, 2020.

R. Dehury, S. Chowdhury, and J. S. Sangwai. Dynamics of hydrogen storage in subsurface saline aquifers: A computational and experimental pore-scale displacement study. *International Journal of Hydrogen Energy*, 69:817–836, 2024.

R. M. Dell and N. J. Bridger. Hydrogen—the ultimate fuel. *Applied Energy*, 1(4):279–292, 1975.

U. Demirci, S. Bernard, R. Chiriac, F. Toche, and P. Miele. Hydrogen release by thermolysis of ammonia borane nh3bh3 and then hydrolysis of its by-product [bnhx]. *Journal of Power Sources*, 196(1):279–286, 2011.

F. Deng, T. H. Dixon, and S. Xie. Surface deformation and induced seismicity due to fluid injection and oil and gas extraction in western texas. *Journal of Geophysical Research: Solid Earth*, 125(5):e2019JB018962, 2020.

Q. Deng, G. Blöcher, M. Cacace, and J. Schmittbuhl. Modeling of fluid-induced seismicity during injection and after shut-in. *Computers and Geotechnics*, 140:104489, 2021.

F. Descamps, O. Faÿ-Gomord, S. Vandycke, C. Schroeder, R. Swennen, and J.-P. Tshibangu. Relationships between geomechanical properties and lithotypes in nw european chalks. *Geological Society, London, Special Publications*, 458(1):227–244, 2017.

D. N. Dewhurst, C. Delle Piane, L. Esteban, J. Sarout, M. Josh, M. Pervukhina, and M. B. Clennell. Microstructural, geomechanical, and petrophysical characterization of shale caprocks. *Geological Carbon Storage: Subsurface Seals and Caprock Integrity*, pages 1–30, 2018.

I. Dincer and C. Acar. Review and evaluation of hydrogen production methods for better sustainability. *International Journal of Hydrogen Energy*, 40(34):11094–11111, 2015.

I. Dincer and A. A. AlZahrani. *4.25 Electrolyzers*, pages 985–1025. Comprehensive Energy Systems. Elsevier, Oxford, 2018. ISBN 9780128149256. doi: https://doi.org/10.1016/B978-0-12-809597-3.00442-9. ID: 318626.

H. F. v. Dobben and P. A. Slim. Past and future plant diversity of a coastal wetland driven by soil subsidence and climate change. *Climatic Change*, 110:597–618, 2012.

E. C. Donaldson and W. Alam. *Wettability*. Elsevier, 2013.

J. Dong, M. Chen, Y. Jin, G. Hong, M. Zaman, and Y. Li. Study on micro-scale properties of cohesive zone in shale. *International Journal of Solids and Structures*, 163:178–193, 2019.

F.-V. Donze, L. Truche, P. Shekari Namin, N. Lefeuvre, and E. F. Bazarkina. Migration of natural hydrogen from deep-seated sources in the sao francisco basin, brazil. *Geosciences*, 10 (9):346, 2020.

N. Dopffel, S. Jansen, and J. Gerritse. Microbial side effects of underground hydrogen storage–knowledge gaps, risks and opportunities for successful implementation. *International Journal of Hydrogen Energy*, 46(12):8594–8606, 2021.

L. Dou, J. Chen, X. Zuo, Y. Liu, L. Sun, Y. Fang, X. Cheng, and T. Wang. Comparison of mechanical characteristics of different types of shales in the ordos basin. *Frontiers in Earth Science*, 11:1242567, 2023.

S. Dovletov. Effect of high temperature on physical and mechanical properties of clay shales (caprock). *University of Calgary*, 2022.

J. M. Dumore. Stability considerations in downward miscible displacements. *Society of Petroleum Engineers Journal*, 4(04):356–362, 1964.

D. J. Durbin and C. Malardier-Jugroot. Review of hydrogen storage techniques for on board vehicle applications. *International journal of hydrogen energy*, 38(34):14595–14617, 2013.

J. Dvorkin and A. Nur. Elasticity of high-porosity sandstones: Theory for two north sea data sets. *Geophysics*, 61(5):1363–1370, 1996.

N. Eddaoui, M. Panfilov, L. Ganzer, and B. Hagemann. Impact of pore clogging by bacteria on underground hydrogen storage. *Transport in Porous Media*, 139:89–108, 2021.

A. Einstein. Über die von der molekularkinetischen theorie der wärme geforderte bewegung von in ruhenden flüssigkeiten suspendierten teilchen. *Annalen der physik*, 4, 1905.

F. R. Eldridge. *Wind machines: report*, volume 75. The Foundation, 1975.

A. Elkhateeb, R. Rezaee, and A. Kadkhodaie. Prediction of high-resolution reservoir facies and permeability, an integrated approach in the irwin river coal measures formation, perth basin, western australia. *Journal of Petroleum Science and Engineering*, 181:106226, 2019.

W. L. Ellsworth. Injection-induced earthquakes. *Science*, 341(6142):1225942, 2013.

A. Elyasi, K. Goshtasbi, H. Hashemolhosseini, and S. Barati. Coupled solid and fluid mechanics simulation for estimating optimum injection pressure during reservoir co2-eor. *Struct. Eng. Mech*, 59(1):37–57, 2016.

B. O. Emerenini, B. A. Hense, C. Kuttler, and H. J. Eberl. A mathematical model of quorum sensing induced biofilm detachment. *PloS one*, 10(7):e0132385, 2015.

E. I. Epelle, W. Obande, G. A. Udourioh, I. C. Afolabi, K. S. Desongu, U. Orivri, B. Gunes, and J. A. Okolie. Perspectives and prospects of underground hydrogen storage and natural hydrogen. *Sustainable Energy & Fuels*, 6(14):3324–3343, 2022.

L. E. Erban, S. M. Gorelick, and H. A. Zebker. Groundwater extraction, land subsidence, and sea-level rise in the mekong delta, vietnam. *Environmental Research Letters*, 9(8):084010, 2014.

R. Ershadnia, M. Singh, S. Mahmoodpour, A. Meyal, F. Moeini, S. A. Hosseini, D. M. Sturmer, M. Rasoulzadeh, Z. Dai, and M. R. Soltanian. Impact of geological and operational conditions on underground hydrogen storage. *International Journal of Hydrogen Energy*, 48(4):1450–1471, 2023.

Z. Esmaeilzadeh and D. Eaton. Integrated reservoir study applied to induced seismicity analysis-case study of the montney formation, british columbia, canada. In *ARMA US Rock Mechanics/Geomechanics Symposium*, pages ARMA–2021. ARMA, 2021.

European Commission. Communication from the Commission to the European Parliament, the Council, the European Economic and Social Committee and the Committee of the Regions: A hydrogen strategy for a climate-neutral Europe. Technical report, European Commission, 2020.

D. M. Evans. The denver area earthquakes and the rocky mountain arsenal disposal well. *The Mountain Geologist*, 1966.

M. Ewing. Hydrogen on the path to net-zero emissions: Costs and climate benefits. Technical report, Pembina Institute, 2020. `https://www.pembina.org/reports/hydrogen-climate-primer-2020.pdf`.

Z. Fan, P. Eichhubl, and P. Newell. Basement fault reactivation by fluid injection into sedimentary reservoirs: Poroelastic effects. *Journal of Geophysical Research: Solid Earth*, 124 (7):7354–7369, 2019.

Z. Fan, E. Ochu, S. Braverman, Y. Lou, G. Smith, A. Bhardwaj, J. Brouwer, C. McCormick, and J. Friedmann. Green hydrogen in a circular carbon economy: Opportunities and limits. 2021.

A. M. Farahbod, H. Kao, J. F. Cassidy, and D. Walker. How did hydraulic-fracturing operations in the horn river basin change seismicity patterns in northeastern british columbia, canada? *The leading edge*, 34(6):658–663, 2015.

S. L. Fasola, M. R. Brudzinski, R. J. Skoumal, T. Langenkamp, B. S. Currie, and K. J. Smart. Hydraulic fracture injection strategy influences the probability of earthquakes in the eagle ford shale play of south texas. *Geophysical Research Letters*, 46(22):12958–12967, 2019.

F. J. Fayers and A. H. Muggeridge. Extensions to dietz theory and behavior of gravity tongues in slightly tilted reservoirs. *SPE Reservoir Engineering*, 5(04):487–494, 1990.

A. B. Featherston, R. G. Mirham, and A. Waters. Minimization of scale deposits in oil wells by placement of phosphates in producing zones. *Journal of Petroleum Technology*, 11(03): 29–32, 1959.

R. Fechte-Heinen, D. Fuhrländer, A. Mehner, H. Decho, M. Castens, K. Burkart, R. Tinscher, and T. Stührmann. The hydrogen challenge: Requirements for future materials. *HTM Journal of Heat Treatment and Materials*, 78(4):233–251, 2023.

F. Feldmann, B. Hagemann, L. Ganzer, and M. Panfilov. Numerical simulation of hydrodynamic and gas mixing processes in underground hydrogen storages. *Environmental Earth Sciences*, 75:1–15, 2016.

Q.-y. Feng, G.-J. Liu, M. Lei, E.-J. Fu, H.-R. Zhang, and K.-F. Zhang. Land subsidence induced by groundwater extraction and building damage level assessment—a case study of datun, china. *Journal of China University of Mining and Technology*, 18(4):556–560, 2008.

M. Ferronato, G. Gambolati, C. Janna, and P. Teatini. Numerical modelling of regional faults in land subsidence prediction above gas/oil reservoirs. *International journal for numerical and analytical methods in geomechanics*, 32(6):633–657, 2008.

A. Fick. Ueber diffusion. *Annalen der physik*, 170(1):59–86, 1855.

A. Finol and S. F. Ali. Numerical simulation of oil production with simultaneous ground subsidence. *Society of Petroleum Engineers Journal*, 15(05):411–424, 1975.

S. Fischer, A. Liebscher, M. De Lucia, L. Hecht, and K. Team. Reactivity of sandstone and siltstone samples from the ketzin pilot co 2 storage site-laboratory experiments and reactive geochemical modeling. *Environmental earth sciences*, 70:3687–3708, 2013.

E. Fjaer. *Petroleum related rock mechanics*, volume 491. Elsevier, 2008.

Ó. G. Flóvenz, K. Ágústsson, E. Á. Gunason, and S. Kristjánsdóttir. Reinjection and induced seismicity in geothermal fields in iceland. In *Proceedings world geothermal congress*, pages 19–25, 2015.

S. Flowers. The energy transition: Future energy from the edge. Technical report, Wood Mackenzie, 2020. https://www.woodmac.com/news/the-edge/future-energy-from-the-edge/.

S. Foh, M. Novil, E. Rockar, and P. Randolph. Underground hydrogen storage. final report.[salt caverns, excavated caverns, aquifers and depleted fields]. Technical report, Brookhaven National Lab.(BNL), Upton, NY (United States), 1979.

M. Fortin and F. Brezzi. *Mixed and hybrid finite element methods*, volume 2. New York: Springer-Verlag, 1991.

E. Fox and W. Jackson. Surfactants in fertilizer, sorption of surface active agents from aqueous solution by phosphate rock. *Journal of Agricultural and Food Chemistry*, 3(1):38–42, 1955.

H. Francke and M. Thorade. Density and viscosity of brine: An overview from a process engineers perspective. *Geochemistry*, 70:23–32, 2010.

K. Freeway. Advanced underground gas storage concepts refrigerated mined cavern storage. pittsburgh, pa, and morgantown, wv, 1998.

E. Frery, L. Langhi, and J. Markov. Natural hydrogen exploration in australia–state of knowledge and presentation of a case study. *The APPEA Journal*, 62(1):223–234, 2022.

C. Frohlich. Two-year survey comparing earthquake activity and injection-well locations in the barnett shale, texas. *Proceedings of the National Academy of Sciences*, 109(35):13934–13938, 2012.

C. Frohlich, C. Hayward, B. Stump, and E. Potter. The dallas–fort worth earthquake sequence: October 2008 through may 2009. *Bulletin of the Seismological Society of America*, 101(1): 327–340, 2011.

L. Fuentes, R. Palomo-Briones, J. de Jesús Montoya-Rosales, L. Braga, E. Castelló, A. Vesga, E. Tapia-Venegas, E. Razo-Flores, and C. Ecthebehere. Knowing the enemy: homoacetogens in hydrogen production reactors. *Applied Microbiology and Biotechnology*, 105:8989–9002, 2021.

G. Gambolati, M. Putti, and P. Teatini. Land subsidence. In *Hydrology of Disasters*, pages 231–268. Springer, 1996.

W. Gan and C. Frohlich. Gas injection may have triggered earthquakes in the cogdell oil field, texas. *Proceedings of the National Academy of Sciences*, 110(47):18786–18791, 2013.

K. K. Gangu, S. Maddila, and S. B. Jonnalagadda. The pioneering role of metal–organic framework-5 in ever-growing contemporary applications–a review. *RSC advances*, 12(22): 14282–14298, 2022.

D. I. Garagash. Fracture mechanics of rate-and-state faults and fluid injection induced slip. *Philosophical Transactions of the Royal Society A*, 379(2196):20200129, 2021.

W. E. Garner and E. Haycock. The thermal decomposition of lithium aluminium hydride. *Proceedings of the Royal Society of London. Series A. Mathematical and Physical Sciences*, 211(1106):335–351, 1952.

G. Gaus, A. Amann-Hildenbrand, B. M. Krooss, and R. Fink. Gas permeability tests on core plugs from unconventional reservoir rocks under controlled stress: A comparison of different transient methods. *Journal of Natural Gas Science and Engineering*, 65:224–236, 2019.

J. Geertsma. Land subsidence above compacting oil and gas reservoirs. *Journal of petroleum technology*, 25(06):734–744, 1973.

S. Gheibi, V. Vilarrasa, and R. M. Holt. Numerical analysis of mixed-mode rupture propagation of faults in reservoir-caprock system in co2 storage. *International Journal of Greenhouse Gas Control*, 71:46–61, 2018.

R. Gholami. Hydrogen storage in geological porous media: Solubility, mineral trapping, h2s generation and salt precipitation. *Journal of Energy Storage*, 59:106576, 2023.

G. Ghosh, P. Rostron, R. Garg, and A. Panday. Hydrogen induced cracking of pipeline and pressure vessel steels: A review. *Engineering Fracture Mechanics*, 199:609–618, 2018.

G. Giani, S. Orsatti, C. Peter, and V. Rocca. A coupled fluid flow—geomechanical approach for subsidence numerical simulation. *Energies*, 11(7):1804, 2018.

E. Gianni, P. Tyrologou, N. Couto, J. F. Carneiro, E. Scholtzová, and N. Koukouzas. Underground hydrogen storage: The techno-economic perspective. *Open Research Europe*, 4, 2024.

D. Gielen, E. Taibi, and R. Miranda. Hydrogen: A renewable energy perspective. Technical report, International Renewable Energy Agency (IRENA), 2019. `https://www.irena.org/publications/2019/Sep/Hydrogen-A-renewable-energy-perspective`.

R. Glamheden and U. Lindblom. Thermal and mechanical behaviour of refrigerated caverns in hard rock. *Tunnelling and Underground Space Technology*, 17(4):341–353, 2002.

M. Glasgow, B. Schmandt, R. Wang, M. Zhang, S. L. Bilek, and E. Kiser. Raton basin induced seismicity is hosted by networks of short basement faults and mimics tectonic earthquake statistics. *Journal of Geophysical Research: Solid Earth*, 126(11):e2021JB022839, 2021.

T. H. Goebel, S. M. Hosseini, F. Cappa, E. Hauksson, J.-P. Ampuero, F. Aminzadeh, and J. B. Saleeby. Wastewater disposal and earthquake swarm activity at the southern end of the central valley, california. *Geophysical Research Letters*, 43(3):1092–1099, 2016.

L. Gommesen, I. L. Fabricius, T. Mukerji, G. Mavko, and J. Pedersen. Elastic behaviour of north sea chalk: A well-log study. *Geophysical Prospecting*, 55(3):307–322, 2007.

G. Y. Gor and J. H. Prévost. Effect of co2 injection temperature on caprock stability. *Energy Procedia*, 37:3727–3732, 2013.

G. Y. Gor, T. R. Elliot, and J. H. Prevost. Effects of thermal stresses on caprock integrity during co2 storage. *International Journal of Greenhouse Gas Control*, 12:300–309, 2013a.

G. Y. Gor, H. A. Stone, and J. H. Prévost. Fracture propagation driven by fluid outflow from a low-permeability aquifer. *Transport in porous media*, 100:69–82, 2013b.

G. M. Graham, E. J. Mackay, S. J. Dyer, and H. Bourne. The challenges for scale control in deepwater production systems: chemical inhibition and placement. In *NACE CORROSION*, pages NACE–02316. NACE, 2002.

J.-R. Grasso, D. Amorese, and A. Karimov. Did wastewater disposal drive the longest seismic swarm triggered by fluid manipulations? lacq, france, 1969–2016. *Bulletin of the Seismological Society of America*, 111(5):2733–2752, 2021.

D. Gray and R. Rex. Formation damage in sandstones caused by dispersion and migration. *Clays Clay Miner*, 15:355, 1996.

S. P. Gregory, M. J. Barnett, L. P. Field, and A. E. Milodowski. Subsurface microbial hydrogen cycling: Natural occurrence and implications for industry. *Microorganisms*, 7(2):53, 2019.

S. Griffiths, B. K. Sovacool, J. Kim, M. Bazilian, and J. M. Uratani. Industrial decarbonization via hydrogen: A critical and systematic review of developments, socio-technical systems and policy options. *Energy Research & Social Science*, 80:102208, 2021.

J. Guélard, V. Beaumont, V. Rouchon, F. Guyot, D. Pillot, D. Jézéquel, M. Ader, K. Newell, and E. Deville. Natural h2 in k ansas: Deep or shallow origin? *Geochemistry, Geophysics, Geosystems*, 18(5):1841–1865, 2017.

Y. Guo, G. Li, J. Zhou, and Y. Liu. Comparison between hydrogen production by alkaline water electrolysis and hydrogen production by pem electrolysis. In *IOP Conference Series: Earth and Environmental Science*, volume 371, page 042022. IOP Publishing, 2019.

J. B. Haga, H. Osnes, and H. P. Langtangen. On the causes of pressure oscillations in low-permeable and low-compressible porous media. *International Journal for Numerical and Analytical Methods in Geomechanics*, 36(12):1507–1522, 2012.

S. Han, X. Hu, F. Zhou, Y. Qiu, M. Li, and G. Huang. Influence of temperature on the interaction of metal veins and hydraulic fractures in shale formations: Experiment and simulation. *Journal of Petroleum Science and Engineering*, 200:108372, 2021.

Y. Han, H. Liu, K. Alruwaili, and M. AlTammar. Wellbore and caprock integrity during co2 injection in saline aquifer. In *International Petroleum Technology Conference*, page D021S053R006. IPTC, 2024.

E. Hand. Hidden hydrogen. *Science (New York, NY)*, 379(6633):630–636, 2023.

J. Harman, P. Hjalmarsson, J. Mermelstein, J. Ryley, H. Sadler, and M. Selby. 1mw-class solid oxide electrolyser system prototype for low-cost green hydrogen. *ECS Transactions*, 103(1): 383, 2021. doi: 10.1149/10301.0383ecst.

L. Hashemi, W. Glerum, R. Farajzadeh, and H. Hajibeygi. Contact angle measurement for hydrogen/brine/sandstone system using captive-bubble method relevant for underground hydrogen storage. *Advances in Water Resources*, 154:103964, 2021.

Z. a. Hashin and S. Shtrikman. On some variational principles in anisotropic and nonhomogeneous elasticity. *Journal of the Mechanics and Physics of Solids*, 10(4):335–342, 1962.

A. Hassan, M. Mahmoud, B. S. Bageri, M. S. Aljawad, M. S. Kamal, A. A. Barri, and I. A. Hussein. Applications of chelating agents in the upstream oil and gas industry: a review. *Energy & Fuels*, 34(12):15593–15613, 2020.

A. Hassanpouryouzband, E. Joonaki, K. Edlmann, and R. S. Haszeldine. Offshore geological storage of hydrogen: is this our best option to achieve net-zero? *ACS Energy Letters*, 6(6): 2181–2186, 2021.

C. Haug, J.-A. Nüchter, and A. Henk. Assessment of geological factors potentially affecting production-induced seismicity in north german gas fields. *Geomechanics for Energy and the Environment*, 16:15–31, 2018.

D. Hawthorn. *An experimental study of the permeability of kimmeridge clay mudstone.* The University of Manchester (United Kingdom), 2004.

J. He, Z. Rui, and K. Ling. A new method to determine biot's coefficients of bakken samples. *Journal of Natural Gas Science and Engineering*, 35:259–264, 2016.

T. He, H. Cao, and P. Chen. Complex hydrides for energy storage, conversion, and utilization. *Advanced Materials*, 31(50):1902757, 2019.

E. H. Hearn, C. Koltermann, and J. L. Rubinstein. Numerical models of pore pressure and stress changes along basement faults due to wastewater injection: Applications to the 2014 milan, kansas earthquake. *Geochemistry, Geophysics, Geosystems*, 19(4):1178–1198, 2018.

C. Heimlich, N. Gourmelen, F. Masson, J. Schmittbuhl, S.-W. Kim, and J. Azzola. Uplift around the geothermal power plant of landau (germany) as observed by insar monitoring. *Geothermal Energy*, 3:1–12, 2015.

N. Heinemann, J. Alcalde, J. M. Miocic, S. J. Hangx, J. Kallmeyer, C. Ostertag-Henning, A. Hassanpouryouzband, E. M. Thaysen, G. J. Strobel, C. Schmidt-Hattenberger, et al. Enabling large-scale hydrogen storage in porous media–the scientific challenges. *Energy & Environmental Science*, 14(2):853–864, 2021.

B. Hemami, S. Feizi Masouleh, and A. Ghassemi. Basement fault reactivation in response to injection into overlying layers. In *ARMA US Rock Mechanics/Geomechanics Symposium*, pages ARMA–2021. ARMA, 2021.

R. Hemelsdael, O. Averbuch, L. Beccaletto, A. Izart, S. Marc, L. Capar, and R. Michels. A deformed wedge-top basin inverted during the collapse of the variscan belt: The permo-carboniferous lorraine basin (ne france). *Tectonics*, 42(11):e2022TC007668, 2023.

G. Herrera, R. Tomás, D. Monells, G. Centolanza, J. J. Mallorquí, F. Vicente, V. D. Navarro, J. M. Lopez-Sanchez, M. Sanabria, M. Cano, et al. Analysis of subsidence using terrasar-x data: Murcia case study. *Engineering Geology*, 116(3-4):284–295, 2010.

G. Hévin. Underground storage of hydrogen in salt caverns. In *European Workshop on Underground Energy Storage November 7th–8th*, 2019.

A. P. Hillier. The leman field, blocks 49/26, 49/27, 49/28, 53/1, 53/2, uk north sea. *Geological Society, London, Memoirs*, 20(1):761–770, 2003.

R. R. Hillis and E. J. Nelson. In situ stresses in the north sea and their applications: Petroleum geomechanics from exploration to development. In *Geological Society, London, Petroleum Geology Conference series*, volume 6, pages 551–564. Geological Society of London, 2005.

V. Hjörleifsdóttir, S. Ó. Snæbjörnsdóttir, G. Gunnarsson, B. R. Kristjánsson, K. Vogfjord, K. Jónsdóttir, S. Hjaltadóttir, K. Ágústsson, . Ágústsdóttir, M. McKenzie, et al. Induced earthquakes in the hellisheii geothermal field, iceland. In *Proceedings World Geothermal Congress*, volume 1, pages 1–6, 2020.

J. Holbrook, H. Cialone, E. Collings, E. Drauglis, P. Scott, and M. Mayfield. Control of hydrogen embrittlement of metals by chemical inhibitors and coatings. In *Gaseous hydrogen embrittlement of materials in energy technologies*, pages 129–153. Elsevier, 2012.

T. L. Holzer and D. L. Galloway. Impacts of land subsidence caused by withdrawal of underground fluids in the united states. 2005.

M. J. Hornbach, H. R. DeShon, W. L. Ellsworth, B. W. Stump, C. Hayward, C. Frohlich, H. R. Oldham, J. E. Olson, M. B. Magnani, C. Brokaw, et al. Causal factors for seismicity near azle, texas. *Nature communications*, 6(1):1–11, 2015.

B. E. Hornby. Experimental laboratory determination of the dynamic elastic properties of wet, drained shales. *Journal of Geophysical Research: Solid Earth*, 103(B12):29945–29964, 1998.

S. Horton. Disposal of hydrofracking waste fluid by injection into subsurface aquifers triggers earthquake swarm in central arkansas with potential for damaging earthquake. *Seismological Research Letters*, 83(2):250–260, 2012.

M. Hosseini, J. Fahimpour, M. Ali, A. Keshavarz, and S. Iglauer. H2- brine interfacial tension as a function of salinity, temperature, and pressure; implications for hydrogen geo-storage. *Journal of Petroleum Science and Engineering*, 213:110441, 2022.

N. Hosseini, J. A. Priest, and D. W. Eaton. Extended-fem analysis of injection-induced slip on a fault with rate-and-state friction: Insights into parameters that control induced seismicity. *Rock Mechanics and Rock Engineering*, 56(6):4229–4250, 2023.

R. W. Howarth and M. Z. Jacobson. How green is blue hydrogen? *Energy Science & Engineering*, 9(10):1676–1687, 2021.

Y.-T. Hsu, H.-Y. Jiang, H.-W. Yen, H.-C. Lin, and S. Hong. Hydrogen-induced embrittlement of nickel-chromium-molybdenum containing hsla steels. *Journal of the Chinese Institute of Engineers*, 43(1):58–66, 2020.

H. Huang, Y. Sun, X. Chang, Z. Wu, M. Li, and S. Qu. Experimental investigation of pore

characteristics and permeability in coal-measure sandstones in jixi basin, china. *Energies*, 15 (16):5898, 2022.

T. Huang, G. J. Moridis, T. A. Blasingame, A. M. Abdulkader, and B. Yan. Compositional reservoir simulation of underground hydrogen storage in depleted gas reservoirs. *International Journal of Hydrogen Energy*, 48(92):36035–36050, 2023.

G. Hui, S. Chen, Z. Chen, and F. Gu. An integrated approach to characterize hydraulic fracturing-induced seismicity in shale reservoirs. *Journal of Petroleum Science and Engineering*, 196:107624, 2021a.

G. Hui, S. Chen, F. Gu, Y. Pang, X. Yu, and L. Zhang. Insights on controlling factors of hydraulically induced seismicity in the duvernay east shale basin. *Geochemistry, Geophysics, Geosystems*, 22(2):e2020GC009563, 2021b.

L. B. Hunfeld, J. Chen, S. Hol, A. R. Niemeijer, and C. J. Spiers. Healing behavior of simulated fault gouges from the groningen gas field and implications for induced fault reactivation. *Journal of Geophysical Research: Solid Earth*, 125(7):e2019JB018790, 2020.

S. M. Hunt, E. M. Werner, B. Huang, M. A. Hamilton, and P. S. Stewart. Hypothesis for the role of nutrient starvation in biofilm detachment. *Applied and environmental microbiology*, 70(12):7418–7425, 2004.

Hydrogen Council. Hydrogen scaling up - a sustainable pathway for the global energy transition. Technical report, Hydrogen Council, 2017.

IAEA-PRIS. International atomic energy agency, power reactor information system: World nuclear association reactor database, 2021. `https://world-nuclear.org/information-library/facts-and-figures/nuclear-generation-by-country.aspx`.

A. Ibrahim, K. Hawboldt, C. Bottaro, and F. Khan. Review and analysis of microbiologically influenced corrosion: the chemical environment in oil and gas facilities. *Corrosion Engineering, Science and Technology*, 53(8):549–563, 2018.

M. Iding and P. Ringrose. Evaluating the impact of fractures on the performance of the in salah co2 storage site. *International Journal of Greenhouse Gas Control*, 4(2):242–248, 2010.

IEA. Hydrogen production costs by production source, 2018. https://www.iea.org/data-and-statistics/charts/hydrogen-production-costs-by-production-source-2018/, 2018.

S. Iglauer, H. Abid, A. Al-Yaseri, and A. Keshavarz. Hydrogen adsorption on sub-bituminous coal: Implications for hydrogen geo-storage. *Geophysical Research Letters*, 48 (10):e2021GL092976, 2021.

J. Incer-Valverde, A. Korayem, G. Tsatsaronis, and T. Morosuk. "colors" of hydrogen: Definitions and carbon intensity. *Energy conversion and management*, 291:117294, 2023.

IRENA. Hydrogen: A renewable energy perspective. Technical report, International Renewable Energy Agency (IRENA), 2019a. https://www.irena.org/-/media/Files/IRENA/Agency/Publication/2019/Sep/IRENA_Hydrogen_2019.pdf.

IRENA. Global energy transformation: A roadmap to 2050 (2019 edition). Technical report, International Renewable Energy Agency (IRENA), 2019b.

T. Ishida, Q. Chen, Y. Mizuta, and J.-C. Roegiers. Influence of fluid viscosity on the hydraulic fracturing mechanism. *J. Energy Resour. Technol.*, 126(3):190–200, 2004.

A. Izart, J. Barbarand, R. Michels, and V. Privalov. Modelling of the thermal history of the carboniferous lorraine coal basin: Consequences for coal bed methane. *international Journal of coal Geology*, 168:253–274, 2016.

U. Jacobsson. Storage for liquified gases in unlined, refrigerated rock caverns. In *Storage in Excavated Rock Caverns: Rockstore 77*, pages 449–458. Elsevier, 1978.

J. C. Jaeger, N. G. Cook, and R. Zimmerman. *Fundamentals of Rock Mechanics*. John Wiley & Sons, 2009.

A. Jahanbakhsh, A. L. Potapov-Crighton, A. Mosallanezhad, N. T. Kaloorazi, and M. M. Maroto-Valer. Underground hydrogen storage: A uk perspective. *Renewable and sustainable energy reviews*, 189:114001, 2024.

H. Jalalifar, M. Farrokhi, and S. Kariminasab. Effect of cyclic loading on anhydrite mechanical and petrophysical properties: an iranian underground gas storage caprock. *Journal of Oil, Gas and Petrochemical Technology*, 8(1):15–22, 2021.

P. Jalili, S. Saydam, and Y. Cinar. Co2 storage in abandoned coal mines. 2011.

P. Japsen. Regional velocity-depth anomalies, north sea chalk: a record of overpressure and neogene uplift and erosion. *AAPG Bulletin*, 82(11):2031–2074, 1998.

K. Jarrahian, O. Seiedi, M. Sheykhan, M. V. Sefti, and S. Ayatollahi. Wettability alteration of carbonate rocks by surfactants: a mechanistic study. *Colloids and Surfaces A: Physicochemical and Engineering Aspects*, 410:1–10, 2012.

L. Ji, Y. Zhang, Q. Wang, Y. Xin, and J. Li. Detecting land uplift associated with enhanced oil recovery using insar in the karamay oil field, xinjiang, china. *International Journal of Remote Sensing*, 37(7):1527–1540, 2016.

S. Ji, L. Li, H. B. Motra, F. Wuttke, S. Sun, K. Michibayashi, and M. H. Salisbury. Poisson's ratio and auxetic properties of natural rocks. *Journal of Geophysical Research: Solid Earth*, 123(2):1161–1185, 2018.

Y. Ji, H. Hofmann, E. H. Rutter, and A. Zang. Transition from slow to fast injection-induced slip of an experimental fault in granite promoted by elevated temperature. *Geophysical Research Letters*, 49(23):e2022GL101212, 2022.

Y. Ji, H. Hofmann, K. Duan, and A. Zang. Laboratory experiments on fault behavior towards better understanding of injection-induced seismicity in geoenergy systems. *Earth-Science Reviews*, 226:103916, 2022a.

Y. Ji, L. Wang, H. Hofmann, G. Kwiatek, and G. Dresen. High-rate fluid injection reduces the

nucleation length of laboratory earthquakes on critically stressed faults in granite. *Geophysical Research Letters*, page e2022GL100418, 2022b.

G. Ji-jiang, W. Yang, Z. Gui-cai, J. Ping, and S. Mingqin. Investigation of scale inhibition mechanisms based on the effect of hedp on surface charge of calcium carbonate. *Tenside Surfactants Detergents*, 53(1):29–36, 2016.

R. Jia, X. Fu, Y. Jin, T. Wu, S. Wang, and H. Cheng. Mechanical properties of mudstone caprock and influencing factors: implications for evaluation of caprock integrity. *Frontiers in Earth Science*, 11:1229851, 2023.

G. Jiang. Theoretical analysis of ground displacements induced by deep fluid injection based on fully-coupled poroelastic simulation. *Geodesy and Geodynamics*, 12(3):197–210, 2021.

H.-L. Jiang and Q. Xu. Catalytic hydrolysis of ammonia borane for chemical hydrogen storage. *Catalysis Today*, 170(1):56–63, 2011.

Z. Jin, W. Li, C. Jin, J. Hambleton, and G. Cusatis. Anisotropic elastic, strength, and fracture properties of marcellus shale. *International Journal of Rock Mechanics and Mining Sciences*, 109:124–137, 2018.

M. Jirasek. Damage and smeared crack models. In *Numerical modeling of concrete cracking*, pages 1–49. Springer, 2011.

M. C. Jo, J. Yoo, S. Kim, S. Kim, J. Oh, J. Bian, S. S. Sohn, and S. Lee. Effects of nb and mo alloying on resistance to hydrogen embrittlement in 1.9 gpa-grade hot-stamping steels. *Materials Science and Engineering: A*, 789:139656, 2020.

J. Johansson. *Cavern wall design principles*. PhD thesis, Byggvetenskap, 2003.

J.-M. Joubert, V. Paul-Boncour, F. Cuevas, J. Zhang, and M. Latroche. Lani5 related ab5 compounds: Structure, properties and applications. *Journal of Alloys and Compounds*, 862: 158163, 2021.

D. Juncu, T. Árnadóttir, H. Geirsson, G. Gumundsson, B. Lund, G. Gunnarsson, A. Hooper, S. Hreinsdottir, and K. Michalczewska. Injection-induced surface deformation and seismicity

at the hellisheidi geothermal field, iceland. *Journal of Volcanology and Geothermal Research*, 391:106337, 2020.

N. Kahraman, B. Gülenç, and F. Findik. Joining of titanium/stainless steel by explosive welding and effect on interface. *Journal of Materials Processing Technology*, 169(2):127–133, 2005.

A. Kampker, H. Heimes, M. Kehrer, S. Hagedorn, P. Euchner, and H. Butzer. Economic and ecological analysis of hydrogen storage systems. *ESSN: 2701-6277*, pages 503–516, 2024.

R. Kaplan and M. Kopacz. Economic conditions for developing hydrogen production based on coal gasification with carbon capture and storage in poland. *Energies*, 13(19):5074, 2020.

C. Karacan. Reservoir rock properties of coal measure strata of the lower monongahela group, greene county (southwestern pennsylvania), from methane control and production perspectives. *International Journal of Coal Geology*, 78(1):47–64, 2009.

S. Karahan, M. Zahmakıran, and S. Özkar. Catalytic hydrolysis of hydrazine borane for chemical hydrogen storage: highly efficient and fast hydrogen generation system at room temperature. *international journal of hydrogen energy*, 36(8):4958–4966, 2011.

V. Karu. *Potential Usage of Underground Mined Areas in Estonian Oil Shale Deposit*. TUT Press, 2012.

J. O. Kaven, S. H. Hickman, A. F. McGarr, and W. L. Ellsworth. Surface monitoring of microseismicity at the decatur, illinois, co2 sequestration demonstration site. *Seismological Research Letters*, 86(4):1096–1101, 2015.

A. Keith, C. Zlotea, and P. A. Szilagyi. Perspective of interstitial hydrides of high-entropy alloys for vehicular hydrogen storage. *International Journal of Hydrogen Energy*, 52:531–546, 2024.

K. M. Keranen, H. M. Savage, G. A. Abers, and E. S. Cochran. Potentially induced earthquakes in oklahoma, usa: Links between wastewater injection and the 2011 mw 5.7 earthquake sequence. *Geology*, 41(6):699–702, 2013.

D. Keszthelyi, D. K. Dysthe, and B. Jamtveit. Compaction of North-Sea chalk by pore-failure and pressure solution in a producing reservoir. *Frontiers in Physics*, 4:4, 2016.

T. Kettlety and J. P. Verdon. Fault triggering mechanisms for hydraulic fracturing-induced seismicity from the preston new road, uk case study. *Frontiers in Earth Science*, 9:670771, 2021.

S. Khan, Y. Khulief, and A. Al-Shuhail. Alleviation of pore pressure buildup and ground uplift during carbon dioxide injection into ghawar arab-d carbonate naturally fractured reservoir. *Environmental earth sciences*, 77:1–27, 2018.

M. Khandelwal and T. N. Singh. Correlating static properties of coal measures rocks with p-wave velocity. *International Journal of Coal Geology*, 79(1-2):55–60, 2009.

J.-H. Kihm, J.-M. Kim, S.-H. Song, and G.-S. Lee. Three-dimensional numerical simulation of fully coupled groundwater flow and land deformation due to groundwater pumping in an unsaturated fluvial aquifer system. *Journal of Hydrology*, 335(1-2):1–14, 2007.

E. Kim, H. W. Jang, and D. Shin. A methodology for evaluating structural and thermal performance of liquefied hydrogen tank. In *ISOPE International Ocean and Polar Engineering Conference*, pages ISOPE–I. ISOPE, 2023.

W.-Y. Kim. Induced seismicity associated with fluid injection into a deep well in youngstown, ohio. *Journal of Geophysical Research: Solid Earth*, 118(7):3506–3518, 2013.

M. King Hubbert and W. W. Rubey. Role of fluid pressure in mechanics of overthrust faulting: I. mechanics of fluid-filled porous solids and its application to overthrust faulting. *Geological Society of America Bulletin*, 70(2):115–166, 1959.

D. W. Kirkland. Cyclicity of katatectic layers within anhydrite caprocks, us gulf coastal region. *Journal of Sedimentary Research*, 2024.

A. Kiryukhin, J. Rutqvist, and M. Maguskin. Thermal-hydrodynamic-mechanical modeling of subsidence during exploitation of the mutnovsky geothermal field, kamchatka. In *Proceedings 39th Workshop on Geothermal Reservoir Engineering, edited by: Castro, JP*, pages 323–333, 2014.

I. R. Kivi, R. Makhnenko, and V. Vilarrasa. Two-phase flow mechanisms controlling co2 intrusion into shaly caprock. *Transport in Porous Media*, 141(3):771–798, 2022.

O. Kolawole, I. Ispas, M. Kumar, J. Weber, B. Zhao, and G. Zanoni. How can biogeomechanical alterations in shales impact caprock integrity and co2 storage? *Fuel*, 291:120149, 2021.

V. Kontogianni, S. Pytharouli, and S. Stiros. Ground subsidence, quaternary faults and vulnerability of utilities and transportation networks in thessaly, greece. *Environmental Geology*, 52:1085–1095, 2007.

D. Krieg. *Konzept und Kosten eines Pipelinesystems zur Versorgung des deutschen Straßenverkehrs mit Wasserstoff*, volume 144. Forschungszentrum Jülich, 2012.

O. Kruck, F. Crotogino, R. Prelicz, and T. Rudolph. Assessment of the potential, the actors and relevant business cases for large scale and seasonal storage of renewable electricity by hydrogen underground storage in europe. *KBB Undergr.Technol.GmbH*, 2013.

A. Kuchment. Drilling for earthquakes. *Scientific American*, 315(1):46–53, 2016.

K. R. Kumar, H. T. Honorio, and H. Hajibeygi. Simulation of the inelastic deformation of porous reservoirs under cyclic loading relevant for underground hydrogen storage. *Scientific reports*, 12(1):21404, 2022.

K. R. Kumar, H. Honorio, D. Chandra, M. Lesueur, and H. Hajibeygi. Comprehensive review of geomechanics of underground hydrogen storage in depleted reservoirs and salt caverns. *Journal of Energy Storage*, 73:108912, 2023.

L. Kumar and A. K. Sleiti. Modeling and analysis of effect of various tank geometries and relief pressure on liquid hydrogen (lh2) boil-off losses. 2024.

V. Kumar, C. H. Sondergeld, and C. S. Rai. Nano to macro mechanical characterization of shale. In *SPE annual technical conference and exhibition*. OnePetro, 2012.

I. Kunce, M. Polanski, and T. Czujko. Microstructures and hydrogen storage properties of lanifevmn alloys. *International Journal of Hydrogen Energy*, 42(44):27154–27164, 2017.

L. Küperkoch, K. Olbert, and T. Meier. Long-term monitoring of induced seismicity at the insheim geothermal site, germany. *Bulletin of the Seismological Society of America*, 108(6): 3668–3683, 2018.

A. Laalam, O. Tomomewo, and H. Chellal. A preliminary geomechanical study of underground hydrogen storage in the inyan kara saline aquifer in the williston basin. In *ARMA/DGS/SEG International Geomechanics Symposium*, pages ARMA–IGS. ARMA, 2023.

LABC Warranty. Technical manual. section 3: Foundations, 2021.

K. Labus and R. Tarkowski. Modeling hydrogen–rock–brine interactions for the jurassic reservoir and cap rocks from polish lowlands. *International Journal of Hydrogen Energy*, 47(20): 10947–10962, 2022.

P. Ladeveze, S. Sejourne, C. Rivard, D. Lavoie, R. Lefebvre, and A. Rouleau. Defining the natural fracture network in a shale gas play and its cover succession: the case of the utica shale in eastern canada. *Journal of Structural Geology*, 108:157–170, 2018.

R. Lai, Q. Li, C. Cheng, H. Shen, S. Liu, Y. Luo, Z. Zhang, and S. Sun. Bio-competitive exclusion of sulfate-reducing bacteria and its anticorrosion property. *Journal of Petroleum Science and Engineering*, 194:107480, 2020.

H. Lan, J. Chen, and R. Macciotta. Universal confined tensile strength of intact rock. *Scientific Reports*, 9(1):6170, 2019.

P. Lang, A. Paluszny, and R. Zimmerman. Permeability tensor of three-dimensional fractured porous rock and a comparison to trace map predictions. *Journal of Geophysical Research: Solid Earth*, 119(8):6288–6307, 2014.

C. Langenbruch, M. Weingarten, and M. D. Zoback. Physics-based forecasting of man-made earthquake hazards in oklahoma and kansas. *Nature communications*, 9(1):3946, 2018.

A. Lavrov. Dynamics of stresses and fractures in reservoir and cap rock under production and injection. *Energy Procedia*, 86:381–390, 2016.

S. T. Le, T. N. Nguyen, S. Linforth, and T. D. Ngo. Safety investigation of hydrogen energy storage systems using quantitative risk assessment. *International Journal of Hydrogen Energy*, 48(7):2861–2875, 2023.

A. Le Duigou, A.-G. Bader, J.-C. Lanoix, and L. Nadau. Relevance and costs of large scale underground hydrogen storage in france. *International Journal of Hydrogen Energy*, 42(36): 22987–23003, 2017. doi: 10.1016/j.ijhydene.2017.06.239.

C. Y. Lee and J. A. Tallmadge. Meniscus shapes in withdrawal of flat sheets from liquid baths. dynamic profile data at low capillary numbers. *Industrial & Engineering Chemistry Fundamentals*, 13(4):356–360, 1974.

K.-K. Lee, W. L. Ellsworth, D. Giardini, J. Townend, S. Ge, T. Shimamoto, I.-W. Yeo, T.-S. Kang, J. Rhie, D.-H. Sheen, et al. Managing injection-induced seismic risks. *Science*, 364 (6442):730–732, 2019.

A. Lemieux, K. Sharp, and A. Shkarupin. Preliminary assessment of underground hydrogen storage sites in ontario, canada. *International Journal of Hydrogen Energy*, 44(29):15193–15204, 2019.

R. Lenormand and C. Zarcone. Role of roughness and edges during imbibition in square capillaries. In *SPE Annual Technical Conference and Exhibition?*, pages SPE–13264. SPE, 1984.

C. Li and L. Laloui. Coupled multiphase thermo-hydro-mechanical analysis of supercritical co2 injection: Benchmark for the in salah surface uplift problem. *International Journal of Greenhouse Gas Control*, 51:394–408, 2016.

H. Li, D. Li, Q. He, Q. Sun, and X. Zhao. Controlling mechanism of shale palaeoenvironment on its tensile strength: A case study of banjiuguan formation in micangshan mountain. *Fuel*, 355:129505, 2024.

C. Liang, J.-P. Ampuero, and D. Pino Muñoz. The paucity of supershear earthquakes on large faults governed by rate and state friction. *Geophysical Research Letters*, 49(22): e2022GL099749, 2022.

Z. Liao, M. Wu, X. Chen, and H. Zou. Fracture mechanical properties of carbonate and evaporite caprocks in sichuan basin, china with implications for reservoir seal integrity. *Marine and Petroleum Geology*, 119:104468, 2020.

X. Lin, J. Jia, N. Champness, P. Hubberstey, and M. Schröder. Metal-organic framework materials for hydrogen storage. *Solid-State Hydrogen Storage*, pages 288–312, 2008.

V. S. Litvinenko, P. S. Tsvetkov, M. V. Dvoynikov, and G. V. Buslaev. Barriers to implementation of hydrogen initiatives in the context of global energy sustainable development. *Journal of Mining Institute*, 244, 2020.

M. Liu, L. Zhou, X. Luo, C. Wan, and L. Xu. Recent advances in noble metal catalysts for hydrogen production from ammonia borane. *Catalysts*, 10(7):788, 2020.

N. Liu, A. R. Kovscek, M. A. Fernø, and N. Dopffel. Pore-scale study of microbial hydrogen consumption and wettability alteration during underground hydrogen storage. *Frontiers in Energy Research*, 11:1124621, 2023.

Q. Liu, B. Liang, W. Sun, and H. Zhao. Experimental study on the difference of shale mechanical properties. *Advances in Civil Engineering*, 2021(1):6677992, 2021a.

W. Liu and P. Pei. Evaluation of the influencing factors of using underground space of abandoned coal mines to store hydrogen based on the improved anp method. *Advances in Materials Science and Engineering*, 2021(1):7506055, 2021.

W. Liu, H. Zuo, J. Wang, Q. Xue, B. Ren, and F. Yang. The production and application of hydrogen in steel industry. *International Journal of Hydrogen Energy*, 46(17):10548–10569, 2021b.

X. Liu, J. Hu, Q. Sun, Z. Li, and J. Zhu. Deriving 3-d time-series ground deformations induced by underground fluid flows with insar: Case study of sebei gas fields, china. *Remote Sensing*, 9(11):1129, 2017.

Y. Liu. Fracture toughness assessment of shales by nanoindentation. Masters's thesis, Department of Civil and Environmental Engineering. University of Massachusetts, Amherst, 2015.

L. F. Londe. Four ways to store large quantities of hydrogen. In *Abu Dhabi International Petroleum Exhibition & Conference*, 2021.

B. Looney. Statistical review of world energy, 2020. *BP*, 69, 2020.

A. S. Lord. Overview of geologic storage of natural gas with an emphasis on assessing the feasibility of storing hydrogen. Technical report, Sandia National Laboratories (SNL), Albuquerque, NM, and Livermore, CA ..., 2009.

A. S. Lord, P. H. Kobos, and D. J. Borns. Geologic storage of hydrogen: Scaling up to meet city transportation demands. *International journal of hydrogen energy*, 39(28):15570–15582, 2014.

T. Lu, Z. Li, and L. Du. Enhanced hydrogen sequestration through hydrogen foam generation with sds co-injection in subsurface formations. *Chemical Engineering Journal*, 481:148575, 2024.

W. Lu, H. Guo, I.-M. Chou, R. Burruss, and L. Li. Determination of diffusion coefficients of carbon dioxide in water between 268 and 473 k in a high-pressure capillary optical cell with in situ raman spectroscopic measurements. *Geochimica et Cosmochimica Acta*, 115:183–204, 2013.

W. Luo, P. G. Campbell, L. N. Zakharov, and S.-Y. Liu. A single-component liquid-phase hydrogen storage material. *Journal of the American Chemical Society*, 133(48):19326–19329, 2011.

X. Luo, P. Were, J. Liu, and Z. Hou. Estimation of biot's effective stress coefficient from well logs. *Environmental earth sciences*, 73:7019–7028, 2015.

J. Lykema, G. Fleer, J. Kleijn, F. Leermakers, W. Norde, and T. Van Vliet. Fundamentals of interface and colloid science, liquid–fluid interfaces, vol. 3, 2000.

M. Lysyy, N. Liu, D. Landa-Marbán, G. Ersland, and M. Fernø. Impact of gas type on microfluidic drainage experiments and pore network modeling relevant for underground hydrogen storage. *Journal of Energy Storage*, 87:111439, 2024.

S. Ma and M. Gutierrez. Determination of the poroelasticity of shale. *Acta Geotechnica*, 16: 581–594, 2021.

R. Magee. *Hydrogen Storage and Transfer: SECTION 1-INTRODUCTION & SCOPE*. PhD thesis, Stevens Institute of Technology, 1975.

Y. Maghsoudi, F. van der Meer, C. Hecker, D. Perissin, and A. Saepuloh. Using ps-insar to detect surface deformation in geothermal areas of west java in indonesia. *International journal of applied earth observation and geoinformation*, 64:386–396, 2018.

O. Maiga, E. Deville, J. Laval, A. Prinzhofer, and A. B. Diallo. Characterization of the spontaneously recharging natural hydrogen reservoirs of bourakebougou in mali. *Scientific Reports*, 13(1):11876, 2023.

E. L. Majer and J. E. Peterson. The impact of injection on seismicity at the geysers, california geothermal field. *International Journal of Rock Mechanics and Mining Sciences*, 44(8):1079–1090, 2007.

A. Malachowska, N. Lukasik, J. Mioduska, and J. Gkebicki. Hydrogen storage in geological formations—the potential of salt caverns. *Energies*, 15(14):5038, 2022.

V. Maruvanchery. Effects of extreme environmental conditions on the mesoscale and nanoscale properties of calcite-cemented sandstone. Phd thesis, Colorado School of Mines, 2019.

M. Masoudi, A. Hassanpouryouzband, H. Hellevang, and R. S. Haszeldine. Lined rock caverns: A hydrogen storage solution. *Journal of Energy Storage*, 84:110927, 2024.

Y. Mathur, V. Awosiji, T. Mukerji, A. H. Scheirer, and K. E. Peters. Soil geochemistry of hydrogen and other gases along the san andreas fault. *International Journal of Hydrogen Energy*, 50:411–419, 2024.

K. I. Matveev and J. W. Leachman. The effect of liquid hydrogen tank size on self-pressurization and constant-pressure venting. *Hydrogen*, 4(3):444–455, 2023.

A. Mayyas, M. Wei, and G. Levis. Hydrogen as a long-term, large-scale energy storage solution when coupled with renewable energy sources or grids with dynamic electricity pricing schemes. *International Journal of Hydrogen Energy*, 45(33):16311–16325, 2020. doi: 10.1016/j.ijhydene.2020.04.163.

J. Mazars. Application of continuous damage mechanic to non-linear behavior of concrete structures. *Doutorado em engenharia de estruturas, Paris VI University, Paris*, 1984.

A. Mazzoldi, A. P. Rinaldi, A. Borgia, and J. Rutqvist. Induced seismicity within geological carbon sequestration projects: Maximum earthquake magnitude and leakage potential from undetected faults. *International journal of greenhouse gas control*, 10:434–442, 2012.

C. McDermott, J. Williams, O. Tucker, M. Jin, E. Mackay, K. Edlmann, R. S. Haszeldine, W. Wang, O. Kolditz, and M. Akhurst. Screening the geomechanical stability (thermal and mechanical) of shared multi-user co2 storage assets: A simple effective tool applied to the captain sandstone aquifer. *International Journal of Greenhouse Gas Control*, 45:43–61, 2016.

A. McGarr. Maximum magnitude earthquakes induced by fluid injection. *Journal of Geophysical Research: solid earth*, 119(2):1008–1019, 2014.

A. McGarr, B. Bekins, N. Burkardt, J. Dewey, P. Earle, W. Ellsworth, S. Ge, S. Hickman, A. Holland, E. Majer, et al. Coping with earthquakes induced by fluid injection. *Science*, 347(6224):830–831, 2015.

R. McLellan and C. Harkins. Hydrogen interactions with metals. *Materials Science and Engineering*, 18(1):5–35, 1975.

C. J. McMahon, J. J. Roberts, G. Johnson, K. Edlmann, S. Flude, and Z. K. Shipton. Natural hydrogen seeps as analogues to inform monitoring of engineered geological hydrogen storage. 2023.

T. Megies and J. Wassermann. Microseismicity observed at a non-pressure-stimulated geothermal power plant. *Geothermics*, 52:36–49, 2014.

A. Mehrabian and Y. N. Abousleiman. Geertsma's subsidence solution extended to layered stratigraphy. *Journal of Petroleum Science and Engineering*, 130:68–76, 2015.

E. Meloni, M. Martino, and V. Palma. A short review on ni based catalysts and related engineering issues for methane steam reforming. *Catalysts*, 10(3):352, 2020.

H. Meng, H. Ge, D. Fu, X. Wang, Y. Shen, Z. Jiang, and J. Wang. Numerical investigation of casing shear deformation due to fracture/fault slip during hydraulic fracturing. *Energy Science Engineering*, 8(10):3588–3601, 2020.

A. Minardi, E. Stavropoulou, T. Kim, A. Ferrari, and L. Laloui. Experimental assessment of the hydro-mechanical behaviour of a shale caprock during co2 injection. *International Journal of Greenhouse Gas Control*, 106:103225, 2021.

J. D. Minougou, R. Gholami, and P. Andersen. Underground hydrogen storage in caverns: Challenges of impure salt structures. *Earth-Science Reviews*, page 104599, 2023.

V. Mirchi, M. Dejam, and V. Alvarado. Interfacial tension and contact angle measurements for hydrogen-methane mixtures/brine/oil-wet rocks at reservoir conditions. *International Journal of Hydrogen Energy*, 47(82):34963–34975, 2022.

S. K. Mital, J. Z. Gyekenyesi, S. M. Arnold, R. M. Sullivan, J. M. Manderscheid, and P. L. Murthy. Review of current state of the art and key design issues with potential solutions for liquid hydrogen cryogenic storage tank structures for aircraft applications. 2006.

M. J. Moein, C. Langenbruch, R. Schultz, F. Grigoli, W. L. Ellsworth, R. Wang, A. P. Rinaldi, and S. Shapiro. The physical mechanisms of induced earthquakes. *Nature Reviews Earth & Environment*, 4(12):847–863, 2023.

O. Mohr. Über die darstellung des spannungszustandes und des deformationszustandes eines körperelementes und über die anwendung derselben in der festigkeitslehre. *Der Civilingenieur*, 28(2):113–156, 1882.

O. Mohr. *Abhandlungen aus dem Gebiete der technischen Mechanik*. Ernst und Sohn, Berlin, 1914.

A. C. Monsees, S. F. Biebricher, B. Busch, M. Feinendegen, M. Ziegler, and C. Hilgers. Coupling of diagenetic alterations and mechanical properties of lower permian siliciclastic sandstones: a pilot study. *Environmental Earth Sciences*, 80:1–18, 2021.

N. Montesantos, M. N. Fini, J. Muff, and M. Maschietti. Proof of concept of hydrothermal oxidation for treatment of triazine-based spent and unspent h2s scavengers from offshore oil and gas production. *Chemical Engineering Journal*, 427:131020, 2022.

R. Moradi and K. M. Groth. Hydrogen storage and delivery: Review of the state of the art technologies and risk and reliability analysis. *International Journal of Hydrogen Energy*, 44 (23):12254–12269, 2019.

R. Morales-Ospino, A. Celzard, and V. Fierro. Strategies to recover and minimize boil-off losses during liquid hydrogen storage. *Renewable and Sustainable Energy Reviews*, 182:113360, 2023.

K. Morawa Eblagon, K. Tam, K. K. Yu, S.-L. Zhao, X.-Q. Gong, H. He, L. Ye, L.-C. Wang, A. J. Ramirez-Cuesta, and S. C. Tsang. Study of catalytic sites on ruthenium for hydrogenation of n-ethylcarbazole: implications of hydrogen storage via reversible catalytic hydrogenation. *The Journal of Physical Chemistry C*, 114(21):9720–9730, 2010.

K. Mortezaei and F. Vahedifard. Numerical simulation of induced seismicity in carbon capture and storage projects. *Geotechnical and Geological Engineering*, 33(2):411–424, 2015.

R. A. Morton, J. C. Bernier, J. A. Barras, N. F. Ferina, et al. Rapid subsidence and historical wetland loss in the mississippi delta plain: likely causes and future implications. Technical report, U. S. Geological Survey, 2005.

M. Motagh, R. Shamshiri, M. H. Haghighi, H.-U. Wetzel, B. Akbari, H. Nahavandchi, S. Roessner, and S. Arabi. Quantifying groundwater exploitation induced subsidence in the rafsanjan plain, southeastern iran, using insar time-series and in situ measurements. *Engineering geology*, 218:134–151, 2017.

Y. Mu, C. Zou, Z. Hu, S. Pan, X. Duan, Y. Gao, and Y. Tang. Hydrogen-water-rock interaction from the perspective of underground hydrogen storage: Micromechanical properties and mineral content of rock. *International Journal of Hydrogen Energy*, 70:79–90, 2024.

A. Muggeridge, S. Krevor, R. W. Zimmerman, D. Bond, and D. Waldren. *Imperial College Lectures In Petroleum Engineering, The-Volume 3: Topics In Reservoir Management*. World Scientific, 2017.

N. S. Muhammed, B. Haq, D. Al Shehri, A. Al-Ahmed, M. M. Rahman, and E. Zaman. A review on underground hydrogen storage: Insight into geological sites, influencing factors and future outlook. *Energy Reports*, 8:461–499, 2022.

N. S. Muhammed, B. Haq, and D. A. Al Shehri. Hydrogen storage in depleted gas reservoirs using nitrogen cushion gas: A contact angle and surface tension study. *International Journal of Hydrogen Energy*, 48(98):38782–38807, 2023a.

N. S. Muhammed, M. B. Haq, D. A. Al Shehri, A. Al-Ahmed, M. M. Rahman, E. Zaman, and S. Iglauer. Hydrogen storage in depleted gas reservoirs: A comprehensive review. *Fuel*, 337: 127032, 2023b.

S. S. Muir and X. Yao. Progress in sodium borohydride as a hydrogen storage material: Development of hydrolysis catalysts and reaction systems. *International Journal of Hydrogen Energy*, 36(10):5983–5997, 2011.

K. Muller, R. Aslam, A. Fischer, K. Stark, P. Wasserscheid, and W. Arlt. Experimental assessment of the degree of hydrogen loading for the dibenzyl toluene based lohc system. *international journal of hydrogen energy*, 41(47):22097–22103, 2016.

R. Muneer, M. R. Hashmet, and P. Pourafshary. Fine migration control in sandstones: Surface force analysis and application of dlvo theory. *ACS omega*, 5(49):31624–31639, 2020.

M. A. Murad and A. F. Loula. On stability and convergence of finite element approximations of biot's consolidation problem. *International Journal for Numerical Methods in Engineering*, 37(4):645–667, 1994.

Y. Nara, K. Morimoto, T. Yoneda, N. Hiroyoshi, and K. Kaneko. Effects of humidity and temperature on subcritical crack growth in sandstone. *International Journal of Solids and Structures*, 48(7-8):1130–1140, 2011.

F. Nath, E. Cabezudo, and N. Romero. Experimental investigations of caprock integrity for geological carbon storage using three-dimensional digital image correlation. In *SPE Western Regional Meeting*, page D031S014R002. SPE, 2024.

M. Nejati. *Finite element modeling of frictional contact and stress intensity factors in three-dimensional fractured media using unstructured tetrahedral meshes*. PhD thesis, Imperial College London, 2015.

M. Nejati, A. Paluszny, and R. W. Zimmerman. A disk-shaped domain integral method for the computation of stress intensity factors using tetrahedral meshes. *International Journal of Solids and Structures*, 69:230–251, 2015.

M. Nejati, A. Paluszny, and R. W. Zimmerman. A finite element framework for modeling internal frictional contact in three-dimensional fractured media using unstructured tetrahedral meshes. *Computer Methods in Applied Mechanics and Engineering*, 306:123–150, 2016.

J. N. Nelson. Overtone spectroscopy of hydrogen in mof-5. B.S. thesis, Oberlin College, 2014.

I. Nemes. Applications of automated petrel workflows in 3d reservoir geologic modelling–a case study. *Central European Geology*, 65(2):122–136, 2023.

M. Nepveu, K. van Thienen-Visser, and D. Sijacic. Statistics of seismic events at the groningen field. *Bulletin of Earthquake Engineering*, 14:3343–3362, 2016.

M. Neuwirth, T. Fleiter, P. Manz, and R. Hofmann. The future potential hydrogen demand in energy-intensive industries-a site-specific approach applied to germany. *Energy Conversion and Management*, 252:115052, 2022.

M. Newborough and G. Cooley. Developments in the global hydrogen market: The spectrum of hydrogen colours. *Fuel Cells Bulletin*, 2020(11):16–22, 2020.

P. Newell and M. J. Martinez. Numerical assessment of fault impact on caprock seals during co2 sequestration. *International Journal of Greenhouse Gas Control*, 94:102890, 2020.

D. T. Ngo. Numerical modeling of hydraulic stimulation and induced seismicity in deep geothermal reservoirs, 2019. PhD Thesis, Universite Paris sciences et lettres.

X. Nie, Z. Fan, Q. Zhou, Z. Yao, Z. Zhu, and L. Ren. Elasticity and characteristic stress thresholds of shale under deep in situ geological conditions. *Materials*, 16(19):6550, 2023.

A. Nikiforov, V. Kravchenko, E. Chesnokov, I. Nikiforov, and A. Popov. Optimization of metal-organic framework mof-5 synthesis for use in cryo-adsorption hydrogen storage. *Petroleum Chemistry*, 63(7):805–813, 2023.

B. Nilsen and J. Olsen. *Storage of Gases in Rock Caverns: Proceedings of the International Conference on Storage of Gases in Rock Caverns/Trondheim/26-28 June 1989*. Routledge, 2022.

Z. Niu, Q. Li, and X. Wei. Estimation of the surface uplift due to fluid injection into a reservoir with a clayey interbed. *Computers and Geotechnics*, 87:198–211, 2017.

V. A. Nivin. Occurrence forms, composition, distribution, origin and potential hazard of natural hydrogen–hydrocarbon gases in ore deposits of the khibiny and lovozero massifs: a review. *Minerals*, 9(9):535, 2019.

M. Noussan, P. P. Raimondi, R. Scita, and M. Hafner. The role of green and blue hydrogen in the energy transition—a technological and geopolitical perspective. *Sustainability*, 13(1): 298, 2021.

D. J. Noy, S. Holloway, R. A. Chadwick, J. Williams, S. A. Hannis, and R. W. Lahann. Modelling large-scale carbon dioxide injection into the bunter sandstone in the uk southern north sea. *International Journal of Greenhouse Gas Control*, 9:220–233, 2012.

P. O. Ogwari, H. R. DeShon, and M. J. Hornbach. The dallas-fort worth airport earthquake sequence: Seismicity beyond injection period. *Journal of Geophysical Research: Solid Earth*, 123(1):553–563, 2018.

L. Ohenhen and M. Shirzaei. Land subsidence hazard and building collapse risk in the coastal city of lagos, west africa. *Earth's Future*, 10(12):e2022EF003219, 2022.

A. A. Olajire. A review of oilfield scale management technology for oil and gas production. *Journal of petroleum science and engineering*, 135:723–737, 2015.

C. M. Oldenburg. Carbon dioxide as cushion gas for natural gas storage. *Energy & Fuels*, 17 (1):240–246, 2003.

C. Olsen. *Elastic and electric properties of North Sea Chalk*. Phd thesis, Technical University of Denmark, 2007.

C. Olsen, K. Hedegaard, I. L. Fabricius, and M. Prasad. Prediction of biot's coefficient from rock-physical modeling of north sea chalk. *Geophysics*, 73(2):E89–E96, 2008.

S.-i. Orimo, Y. Nakamori, J. R. Eliseo, A. Züttel, and C. M. Jensen. Complex hydrides for hydrogen storage. *Chemical reviews*, 107(10):4111–4132, 2007.

B. Orlic, J. ter Heege, and B. Wassing. Assessing the integrity of fault-and top seals at co2 storage sites. *Energy Procedia*, 4:4798–4805, 2011.

A. I. Osman, N. Mehta, A. M. Elgarahy, M. Hefny, A. Al-Hinai, A. H. Al-Muhtaseb, and D. W. Rooney. Hydrogen production, storage, utilisation and environmental impacts: a review. *Environmental Chemistry Letters*, pages 1–36, 2022.

F. Osselin, C. Soulaine, C. Fauguerolles, E. Gaucher, B. Scaillet, and M. Pichavant. Orange hydrogen is the new green. *Nature Geoscience*, 15(10):765–769, 2022.

O. S. Ovbije. State of study on the elastic and plastic behaviour of steel in contact with sour wellbore fluid. Master's thesis, University of Aberdeen, 2012.

B. Paap, A. Verdel, S. Meekes, P. Steeghs, V. Vandeweijer, and F. Neele. Four years of experience with a permanent seismic monitoring array at the ketzin co2 storage pilot site. *Energy Procedia*, 63:4043–4050, 2014.

A. Paluszny and S. Matthai. Impact of fracture development on the effective permeability of porous rocks as determined by 2-d discrete fracture growth modeling. *Journal of Geophysical Research: Solid Earth*, 115(B2), 2010.

A. Paluszny and R. W. Zimmerman. Numerical fracture growth modeling using smooth surface geometric deformation. *Engineering Fracture Mechanics*, 108:19–36, 2013.

A. Paluszny, S. Salimzadeh, P. Tempone, and R. Zimmerman. Evaluating natural fracture growth in shale caprocks during cold co2 injection at the heletz pilot site. In *ARMA US Rock Mechanics/Geomechanics Symposium*, pages ARMA–2017. ARMA, 2017.

A. Paluszny, C. C. Graham, K. A. Daniels, V. Tsaparli, D. Xenias, S. Salimzadeh, L. Whitmarsh, J. F. Harrington, and R. W. Zimmerman. Caprock integrity and public perception studies of carbon storage in depleted hydrocarbon reservoirs. *International Journal of Greenhouse Gas Control*, 98:103057, 2020a.

A. Paluszny, R. N. Thomas, M. C. Saceanu, and R. W. Zimmerman. Hydro-mechanical interaction effects and channelling in three-dimensional fracture networks undergoing growth and nucleation. *Journal of Rock Mechanics and Geotechnical Engineering*, 12(4):707–719, 2020b.

M. Panfilov. Underground storage of hydrogen: in situ self-organisation and methane generation. *Transport in porous media*, 85:841–865, 2010.

J. Pangborn and D. Gregory. Hydrogen energy technology—update 1976. *International Journal of Hydrogen Energy*, 1(3):331–340, 1976.

E.-S. Park, Y.-B. Jung, W.-K. Song, D.-H. Lee, and S.-K. Chung. Pilot study on the underground lined rock cavern for lng storage. *Engineering Geology*, 116(1-2):44–52, 2010.

Y. Park, S. M. Mousavi, W. Zhu, W. L. Ellsworth, and G. C. Beroza. Machine-learning-based analysis of the guy-greenbrier, arkansas earthquakes: A tale of two sequences. *Geophysical Research Letters*, 47(6):e2020GL087032, 2020.

L. Paterson. The implications of fingering in underground hydrogen storage. *International journal of hydrogen energy*, 8(1):53–59, 1983.

J. Pearse, V. Singhroy, S. Samsonov, and J. Li. Anomalous surface heave induced by enhanced oil recovery in northern alberta: Insar observations and numerical modeling. *Journal of Geophysical Research: Solid Earth*, 119(8):6630–6649, 2014.

A. M. P. Peedikakkal and I. H. Aljundi. Upgrading the hydrogen storage of mof-5 by post-synthetic exchange with divalent metal ions. *Applied Sciences*, 11(24):11687, 2021.

X. Pei, Y. Liu, L. Song, L. Mi, L. Xue, and G. Li. Subsidence above irregular-shaped reservoirs. *International Journal of Rock Mechanics and Mining Sciences*, 165:105367, 2023.

A. Peppas, S. Kottaridis, and C. Politi. Potential application of res and underground h2 storage in abandoned mines. *Materials Proceedings*, 15(1):30, 2023.

M. Perera. A review of underground hydrogen storage in depleted gas reservoirs: Insights into various rock-fluid interaction mechanisms and their impact on the process integrity. *Fuel*, 334:126677, 2023.

A. Pérez, E. Pérez, S. Dupraz, and J. Bolcich. Patagonia wind-hydrogen project: underground storage and methanation. In *21st World Hydrogen Energy Conference*, Zaragoza, Spain, 13th-16th June, 2016 2016.

W. Peters, M. Eypasch, T. Frank, J. Schwerdtfeger, C. Korner, A. Bosmann, and P. Wasserscheid. Efficient hydrogen release from perhydro-n-ethylcarbazole using catalyst-coated metallic structures produced by selective electron beam melting. *Energy & Environmental Science*, 8(2):641–649, 2015.

E. Petrie, J. Evans, and S. Bauer. Failure of cap-rock seals as determined from mechanical stratigraphy, stress history, and tensile-failure analysis of exhumed analogs. *AAPG Bulletin*, 98(11):2365–2389, 2014.

W. T. Pfeiffer and S. Bauer. Subsurface porous media hydrogen storage–scenario development and simulation. *Energy Procedia*, 76:565–572, 2015.

L. B. Pfeil. The effect of occluded hydrogen on the tensile strength of iron. *Proceedings of*

the Royal Society of London. Series A, Containing Papers of a Mathematical and Physical Character, 112(760):182–195, 1926.

H. T. Pham, W. Rühaak, V. Schuster, and I. Sass. Fully hydro-mechanical coupled plug-in (sub+) in feflow for analysis of land subsidence due to groundwater extraction. *SoftwareX*, 9:15–19, 2019.

M. Pichler. Underground sun storage results and outlook. In *EAGE/DGMK Joint Workshop on Underground Storage of Hydrogen*, volume 2019, pages 1–4. European Association of Geoscientists & Engineers, 2019.

J. Pickell, B. Swanson, and W. Hickman. Application of air-mercury and oil-air capillary pressure data in the study of pore structure and fluid distribution. *Society of Petroleum Engineers Journal*, 6(01):55–61, 1966.

R. Pinsky, P. Sabharwall, J. Hartvigsen, and J. O'Brien. Comparative review of hydrogen production technologies for nuclear hybrid energy systems. *Progress in Nuclear Energy*, 123: 103317, 2020.

B. G. Pollet, I. Staffell, J. L. Shang, and V. Molkov. *22 - Fuel-cell (hydrogen) electric hybrid vehicles*, pages 685–735. Alternative Fuels and Advanced Vehicle Technologies for Improved Environmental Performance. Woodhead Publishing, 2014. ISBN 9780857095220. doi: https://doi.org/10.1533/9780857097422.3.685. ID: 306647.

T. Postmes, N. Busscher, S. Hupkes, A. De Julio, and E. Vojvodic. The groningen gas field: The role of science in a slow-onset disaster. In *Climate Change and Safety in High-Risk Industries*, pages 63–75. Springer Nature Switzerland Cham, 2024.

D. Pourtoy, A. Onaisi, M. Lescanne, S. Thibeau, and C. Viaud. Seal integrity of the rousse depleted gas field impacted by co2 injection (lacq industrial ccs reference project france). *Energy Procedia*, 37:5480–5493, 2013.

D. Powell. Focus on blue hydrogen. `https://www.gaffneycline.com/sites/g/files/cozyhq681/files/2021-08/Focus_on_Blue_Hydrogen_Aug2020.pdf`, 08 2020. Gaffney Cline.

K. Pratikna, M. J. Rahman, and N. H. Mondol. Characterization of utsira formation around the sleipner co2 storage site, central north sea. In *SEG International Exposition and Annual Meeting*, page D011S030R003. SEG, 2022.

J. Prime and L. M. Martínez. Statistics report: Coal information - overview. Technical report, International Energy Agency (IEA), 2020. `https://iea.blob.core.windows.net/assets/a5f208e9-f66b-4d31-b5af-87d581b70c18/Coal_Information_Overview_2020_edition.pdf`.

B. Proctor, D. A. Lockner, B. D. Kilgore, T. M. Mitchell, and N. M. Beeler. Direct evidence for fluid pressure, dilatancy, and compaction affecting slip in isolated faults. *Geophysical Research Letters*, 47(16):e2019GL086767, 2020.

D. Pudlo, S. Flesch, D. Albrecht, and V. Reitenbach. The impact of hydrogen on potential underground energy reservoirs. In *EGU General Assembly Conference Abstracts*, page 8606, 2018.

N. Pugno, M. Ciavarella, P. Cornetti, and A. Carpinteri. A generalized paris' law for fatigue crack growth. *Journal of the Mechanics and Physics of Solids*, 54(7):1333–1349, 2006.

J. Purewal, D. Liu, J. Yang, A. Sudik, D. Siegel, S. Maurer, and U. Müller. Increased volumetric hydrogen uptake of mof-5 by powder densification. *international journal of hydrogen energy*, 37(3):2723–2727, 2012.

B. J. L. Pérez, J. A. M. Jiménez, R. Bhardwaj, E. Goetheer, M. van Sint Annaland, and F. Gallucci. Methane pyrolysis in a molten gallium bubble column reactor for sustainable hydrogen production: Proof of concept & techno-economic assessment. *International Journal of Hydrogen Energy*, 46(7):4917–4935, 2021.

M. A. Qyyum, R. Dickson, S. F. A. Shah, H. Niaz, A. Khan, J. J. Liu, and M. Lee. Availability, versatility, and viability of feedstocks for hydrogen production: Product space perspective. *Renewable and Sustainable Energy Reviews*, 145:110843, 2021.

M. J. Rahman, M. Fawad, and N. H. Mondol. Organic-rich shale caprock properties of potential

co2 storage sites in the northern north sea, offshore norway. *Marine and Petroleum Geology*, 122:104665, 2020.

K. Ramesh Kumar, A. Makhmutov, C. J. Spiers, and H. Hajibeygi. Geomechanical simulation of energy storage in salt formations. *Scientific Reports*, 11(1):19640, 2021.

Q.-h. Rao, Z. Wang, H.-f. Xie, and Q. Xie. Experimental study of mechanical properties of sandstone at high temperature. *Journal of Central South University of Technology*, 14(Suppl 1):478–483, 2007.

R. R. Ratnakar, N. Gupta, K. Zhang, C. van Doorne, J. Fesmire, B. Dindoruk, and V. Balakotaiah. Hydrogen supply chain and challenges in large-scale lh2 storage and transportation. *International Journal of Hydrogen Energy*, 46(47):24149–24168, 2021.

K. Ravi, V. Ramaswamy, and T. Namboodhiri. Effect of molybdenum on the resistance to h2s of high sulphur microalloyed steels. *Materials science and engineering: A*, 169(1-2):111–118, 1993.

V. Reitenbach, L. Ganzer, D. Albrecht, and B. Hagemann. Influence of added hydrogen on underground gas storage: a review of key issues. *Environmental Earth Sciences*, 73:6927–6937, 2015.

T. Ren, X. Shen, and F. Zhang. Numerical simulation of fingering in the underground hydrogen storage. In *IOP Conference Series: Earth and Environmental Science*, volume 1335, page 012049. IOP Publishing, 2024.

Z. Ren, X. Zhang, H.-W. Li, Z. Huang, J. Hu, M. Gao, H. Pan, and Y. Liu. Titanium hydride nanoplates enable 5 wt% of reversible hydrogen storage by sodium alanate below 80 c. *Research*, 2021, 2021.

C. E. Renshaw and D. D. Pollard. Numerical simulation of fracture set formation: A fracture mechanics model consistent with experimental observations. *Journal of Geophysical Research: Solid Earth*, 99(B5):9359–9372, 1994.

J. R. Rice, N. Lapusta, and K. Ranjith. Rate and state dependent friction and the stability of sliding between elastically deformable solids. *Journal of the Mechanics and Physics of Solids*, 49(9):1865–1898, 2001.

H. A. Richard, B. Schramm, and N.-H. Schirmeisen. Cracks on mixed mode loading–theories, experiments, simulations. *International Journal of Fatigue*, 62:93–103, 2014.

G. Richter, S. Hainzl, T. Dahm, and G. Zöller. Stress-based, statistical modeling of the induced seismicity at the groningen gas field, the netherlands. *Environmental Earth Sciences*, 79(11): 252, 2020.

A. P. Rinaldi, J. Rutqvist, S. Finsterle, and H.-H. Liu. Inverse modeling of ground surface uplift and pressure with itough-pest and tough-flac: The case of co2 injection at in salah, algeria. *Computers & Geosciences*, 108:98–109, 2017.

G. Rivolta, M. Maniglio, A. Elgendy, P. Panfili, and A. Cominelli. Evaluating the impact of biochemical reactions on h2 storage in depleted gas fields. *SPE Journal*, pages 1–16, 2024.

G. Rodríguez-Pradilla and J. P. Verdon. Quantifying the variability in fault density across the uk bowland shale with implications for induced seismicity hazard. *Geomechanics for Energy and the Environment*, 38:100534, 2024.

C. Romano, R. Williams, and F. Cheng. Evolution of fault-zone hydromechanical properties in response to different cementation processes. *Lithosphere*, 2022(1), 2022.

R. Rosenberg and D. Gregory. Hydrogen, an energy system concept. In *SPE Annual Technical Conference and Exhibition?*, pages SPE–4108. SPE, 1972.

J. T. Rutledge, T. D. Fairbanks, J. N. Albright, R. R. Boade, J. Dangerfield, and G. H. Landa. Reservoir microseismicity at the ekofisk oil field. In *SPE/ISRM Rock Mechanics in Petroleum Engineering*, pages SPE–28099. SPE, 1994.

J. Rutqvist. The geomechanics of co 2 storage in deep sedimentary formations. *Geotechnical and Geological Engineering*, 30:525–551, 2012.

J. Rutqvist and C.-F. Tsang. A study of caprock hydromechanical changes associated with co 2-injection into a brine formation. *Environmental Geology*, 42:296–305, 2002.

J. Rutqvist, D. W. Vasco, and L. Myer. Coupled reservoir-geomechanical analysis of co2 injection at in salah, algeria. *Energy Procedia*, 1(1):1847–1854, 2009.

J. Rutqvist, D. W. Vasco, and L. Myer. Coupled reservoir-geomechanical analysis of co2 injection and ground deformations at in salah, algeria. *International Journal of Greenhouse Gas Control*, 4(2):225–230, 2010.

J. Rutqvist, A. P. Rinaldi, F. Cappa, and G. J. Moridis. Modeling of fault reactivation and induced seismicity during hydraulic fracturing of shale-gas reservoirs. *Journal of Petroleum Science and Engineering*, 107:31–44, 2013.

E. Rybacki, A. Reinicke, T. Meier, M. Makasi, and G. Dresen. What controls the mechanical properties of shale rocks?–part i: Strength and young's modulus. *Journal of Petroleum Science and Engineering*, 135:702–722, 2015.

M. C. Saceanu, A. Paluszny, R. W. Zimmerman, and D. M. Ivars. Fracture growth leading to mechanical spalling around deposition boreholes of an underground nuclear waste repository. *International Journal of Rock Mechanics and Mining Sciences*, 152:105038, 2022.

M. Saeed and P. Jadhawar. Modelling underground hydrogen storage: A state-of-the-art review of fundamental approaches and findings. *Gas Science and Engineering*, page 205196, 2023.

P. Saffman. Viscous fingering in hele-shaw cells. *Journal of Fluid Mechanics*, 173:73–94, 1986.

P. G. Saffman and G. I. Taylor. The penetration of a fluid into a porous medium or hele-shaw cell containing a more viscous liquid. *Proceedings of the Royal Society of London. Series A. Mathematical and Physical Sciences*, 245(1242):312–329, 1958.

D. Saha and S. Deng. Synthesis, characterization and hydrogen adsorption in mixed crystals of mof-5 and mof-177. *International Journal of Hydrogen Energy*, 34(6):2670–2678, 2009.

C. Saigustia and S. Robak. Review of potential energy storage in abandoned mines in poland. *Energies*, 14(19):6272, 2021.

A. Salehabadi, M. I. Ahmad, N. Ismail, N. Morad, and M. Enhessari. *Solid-State Hydrogen Storage Materials*, pages 41–67. Energy, Society and the Environment. Springer, 2020.

S. Salimzadeh, A. Paluszny, and R. W. Zimmerman. Three-dimensional poroelastic effects during hydraulic fracturing in permeable rocks. *International Journal of Solids and Structures*, 108:153–163, 2017a.

S. Salimzadeh, T. Usui, A. Paluszny, and R. W. Zimmerman. Finite element simulations of interactions between multiple hydraulic fractures in a poroelastic rock. *International Journal of Rock Mechanics and Mining Sciences*, 99:9–20, 2017b.

S. Salimzadeh, A. Paluszny, and R. W. Zimmerman. Effect of cold co2 injection on fracture apertures and growth. *International Journal of Greenhouse Gas Control*, 74:130–141, 2018.

E. Salina Borello, S. Bocchini, A. Chiodoni, C. Coti, M. Fontana, F. Panini, C. Peter, C. F. Pirri, M. Tawil, A. Mantegazzi, et al. Underground hydrogen storage safety: Experimental study of hydrogen diffusion through caprocks. *Energies*, 17(2):394, 2024.

A. Salmachi, A. Seyfaee, R. J. Robert, T. Hosseini, G. Nathan, P. Ashman, A. Roberts, M. Jafarian, and C. Simon. Underground hydrogen storage: Integrated surface facilities and fluid flow modelling for depleted gas reservoirs. *International Journal of Hydrogen Energy*, 50: 1055–1069, 2024.

C. Sambo, A. Dudun, S. A. Samuel, P. Esenenjor, N. S. Muhammed, and B. Haq. A review on worldwide underground hydrogen storage operating and potential fields. *International Journal of Hydrogen Energy*, 47(54):22840–22880, 2022.

N. Sanchez-Bastardo, R. Schloegl, and H. Ruland. Methane pyrolysis for zero-emission hydrogen production: A potential bridge technology from fossil fuels to a renewable and sustainable hydrogen economy. *Industrial & Engineering Chemistry Research*, 60(32):11855–11881, 2021.

C. M. Sayers. The effect of anisotropy on the young's moduli and poisson's ratios of shales. *Geophysical Prospecting*, 61(2):416–426, 2013.

H. Saygın and A. Şişman. Joule–thomson coefficients of quantum ideal-gases. *Applied energy*, 70(1):49–57, 2001.

G. Scarascia, T. Wang, and P.-Y. Hong. Quorum sensing and the use of quorum quenchers as natural biocides to inhibit sulfate-reducing bacteria. *Antibiotics*, 5(4):39, 2016.

N. Schaaf, K. Senger, M. Mulrooney, K. Ogata, A. Braathen, and S. Olaussen. Towards characterization of natural fractures in a caprock shale: an integrated borehole-outcrop study of the agardhfjellet for-mation, svalbard, arctic norway. In *Norwegian Geological Society Winter Conference, Oslo, https://doi. org/10.13140/RG*, volume 2, page 1, 2017.

P. Schettler, C. Parmely, and W. Lee. Gas storage and transport in devonian shales. *SPE Formation Evaluation*, 4(03):371–376, 1989.

R. Schultz, R. Wang, Y. J. Gu, K. Haug, and G. Atkinson. A seismological overview of the induced earthquakes in the duvernay play near fox creek, alberta. *Journal of Geophysical Research: Solid Earth*, 122(1):492–505, 2017.

L. Schwab, L. Prinsen, G. Nowack, D. Popp, M. Noll, C. Vogt, and M. Wagner. Sulfate reduction and homoacetogenesis at various hypersaline conditions: Implications for h2 underground gas storage. *Frontiers in Energy Research*, 11:1125619, 2023.

M. Scuderi, C. Collettini, and C. Marone. Frictional stability and earthquake triggering during fluid pressure stimulation of an experimental fault. *Earth and Planetary Science Letters*, 477: 84–96, 2017.

T. A. Sebaey. Design of oil and gas composite pipes for energy production. *Energy Procedia*, 162:146–155, 2019.

G. S. Seck, E. Hache, J. Sabathier, F. Guedes, G. A. Reigstad, J. Straus, O. Wolfgang, J. A. Ouassou, M. Askeland, I. Hjorth, et al. Hydrogen and the decarbonization of the energy system in europe in 2050: A detailed model-based analysis. *Renewable and Sustainable Energy Reviews*, 167:112779, 2022.

L. Seeber, J. G. Armbruster, and W.-Y. Kim. A fluid-injection-triggered earthquake sequence in ashtabula, ohio: Implications for seismogenesis in stable continental regions. *Bulletin of the Seismological Society of America*, 94(1):76–87, 2004.

P. Segall and S. Lu. Injection-induced seismicity: Poroelastic and earthquake nucleation effects. *Journal of Geophysical Research: Solid Earth*, 120(7):5082–5103, 2015.

J. Senderens and P. Sabatier. Nouvelles syntheses du methane. *Comptes Rendus Acad. Sci*, 82: 514–516, 1902.

B. Shadidi, G. Najafi, and T. Yusaf. A review of hydrogen as a fuel in internal combustion engines. *Energies*, 14(19):6209, 2021.

S. Shapiro, R. Patzig, E. Rothert, and J. Rindschwentner. Triggering of seismicity by pore-pressure perturbations: Permeability-related signatures of the phenomenon. *Thermo-Hydro-Mechanical Coupling in Fractured Rock*, pages 1051–1066, 2003.

Shell. Peterhead ccs project - geomechanics report. Technical report, 2014. `https://assets.publishing.service.gov.uk/government/uploads/system/uploads/attachment_data/file/531054/Peterhead_11.115_-_Geomechanics_Report.pdf`.

Shell. Peterhead ccs project - storage development plan. Technical report, 2015a. `https://assets.publishing.service.gov.uk/government/uploads/system/uploads/attachment_data/file/531016/DECC_Ready_-_KKD_11.128_Storage_Development_Plan.pdf`.

Shell. Peterhead ccs project - petrophysical modelling report. Technical report, 2015b. `https://assets.publishing.service.gov.uk/government/uploads/system/uploads/attachment_data/file/433491/Petrophysical_Modelling_Report.pdf`.

C. Shen, Z. Li, Y. Chang, B. Zhang, and F. Zeng. Geomechanical modeling and minimum fracture pressure prediction of co2 storage reservoir caprock in the lloydminster area. In *SPE Canadian Energy Technology Conference*, page D011S015R004. SPE, 2024.

J. Shi, H. Yang, J. Peng, L. Wu, B. Xu, Y. Liu, and B. Zhao. Insar monitoring and analysis of ground deformation due to fluid or gas injection in fengcheng oil field, xinjiang, china. *Journal of the Indian Society of Remote Sensing*, 47:455–466, 2019.

X. Shi, D. Liu, W. Yao, Y. Shi, T. Tang, B. Wang, and W. Han. Investigation of the anisotropy of black shale in dynamic tensile strength. *Arabian Journal of Geosciences*, 11:1–11, 2018a.

Y.-J. Shi, M.-G. Li, J.-J. Chen, and J.-H. Wang. Long-term settlement behavior of a highway in land subsidence area. *Journal of Performance of Constructed Facilities*, 32(5):04018063, 2018b.

M. Shirzaei, W. L. Ellsworth, K. F. Tiampo, P. J. González, and M. Manga. Surface uplift and time-dependent seismic hazard due to fluid injection in eastern texas. *Science*, 353(6306): 1416–1419, 2016.

R. H. Sibson. A note on fault reactivation. *Journal of Structural Geology*, 7(6):751–754, 1985.

D. Sijacic, F. Pijpers, M. Nepveu, and K. van Thienen-Visser. Statistical evidence on the effect of production changes on induced seismicity. *Netherlands Journal of Geosciences*, 96(5): s27–s38, 2017.

A. K. Singh, S. Singh, and A. Kumar. Hydrogen energy future with formic acid: a renewable chemical hydrogen storage system. *Catalysis Science & Technology*, 6(1):12–40, 2016.

J. Singh. Synthetic fuels for ground transportation with special emphasis on hydrogen. Technical report, 1975.

M. K. Singla, P. Nijhawan, and A. S. Oberoi. Hydrogen fuel and fuel cell technology for cleaner future: a review. *Environmental Science and Pollution Research*, 28(13):15607–15626, 2021.

A. Skempton. Significance of terzaghi's concept of effective stress, 1960.

D. T. Snow. Anisotropie permeability of fractured media. *Water resources research*, 5(6): 1273–1289, 1969.

U. Sofregaz and C. Gustafsvag. Commercial potential of natural gas storage in lined rock caverns (lrc). *US Department of Energy*, 1999.

J. Song and D. Zhang. Comprehensive review of caprock-sealing mechanisms for geologic carbon sequestration. *Environmental science & technology*, 47(1):9–22, 2013.

B. Sorensen and G. Spazzafumo. *2 - Hydrogen*, pages 5–105. Hydrogen and Fuel Cells (Third Edition). Academic Press, 2018. ISBN 9780081007082. doi: https://doi.org/10.1016/B978-0-08-100708-2.00002-3. ID: 318858.

J. G. Speight. 5 - recovery, storage, and transportation. In J. G. Speight, editor, *Natural Gas (Second Edition)*, pages 149–186. Gulf Professional Publishing, Boston, second edition edition, 2019. ISBN 978-0-12-809570-6. doi: https://doi.org/10.1016/B978-0-12-809570-6.00005-9. https://www.sciencedirect.com/science/article/pii/B9780128095706000059.

P. Sridhar and N. S. Kaisare. A critical analysis of transport models for refueling of mof-5 based hydrogen adsorption system. *Journal of Industrial and Engineering Chemistry*, 85:170–180, 2020.

S. Stanchits, A. Surdi, P. Gathogo, E. Edelman, and R. Suarez-Rivera. Onset of hydraulic fracture initiation monitored by acoustic emission and volumetric deformation measurements. *Rock Mechanics and Rock Engineering*, 47(5):1521–1532, 2014.

S. Staniewicz, J. Chen, H. Lee, J. Olson, A. Savvaidis, R. Reedy, C. Breton, E. Rathje, and P. Hennings. Insar reveals complex surface deformation patterns over an 80,000 km2 oil-producing region in the permian basin. *Geophysical Research Letters*, 47(21):e2020GL090151, 2020.

Statista. Forecast of hydrogen demand as the share of total energy worldwide in 2050, by outlook scenario. https://www.statista.com/statistics/1292286/global-hydrogen-demand-estimates-as-share-of-total-energy/, April 2024.

R. Stevenson. Project hysecure phase 1 summary sept 2019. *His Majesty's Government UK*, 2019.

H. B. Stone, I. Veldhuis, and R. N. Richardson. An investigation into large-scale hydrogen storage in the uk. In *Proceedings International Hydrogen Energy Congress and Exhibition IHEC*, pages 13–15, 2005.

G. Suhett Helmer. Crack propagation in reservoir rocks in the co2 storage context. 2014.

M. Susan Gram. *Exploring the Energy Storage Capacity of Salt Caverns in the Netherlands*. PhD thesis, 2019.

D. Symons. Hydrogen embrittlement of ni-cr-fe alloys. *Metallurgical and Materials transactions A*, 28:655–663, 1997.

B. N. Tackie-Otoo and M. B. Haq. A comprehensive review on geo-storage of h2 in salt caverns: Prospect and research advances. *Fuel*, 356:129609, 2024.

E. Taibi, H. Blanco, R. Miranda, and M. Carmo. Green hydrogen cost reduction. 2020.

K. Takai, K. Nakamura, T. Toki, U. Tsunogai, M. Miyazaki, J. Miyazaki, H. Hirayama, S. Nakagawa, T. Nunoura, and K. Horikoshi. Cell proliferation at 122 c and isotopically heavy ch4 production by a hyperthermophilic methanogen under high-pressure cultivation. *Proceedings of the National Academy of Sciences*, 105(31):10949–10954, 2008.

C. Tan, I. Musa, and N. N. Kamaruddin. Geomechanical risk analysis for feasibility assessment and evaluation of co2 injection and long-term storage. In *Offshore Technology Conference Asia*, page D041S044R001. OTC, 2024.

L. Tang, Z. Lu, M. Zhang, L. Sun, and L. Wen. Seismicity induced by simultaneous abrupt changes of injection rate and well pressure in hutubi gas field. *Journal of Geophysical Research: Solid Earth*, 123(7):5929–5944, 2018.

R. Tarkowski. Underground hydrogen storage: Characteristics and prospects. *Renewable and Sustainable Energy Reviews*, 105:86–94, 2019.

M. Taube, D. Rippin, D. Cresswell, and W. Knecht. A system of hydrogen-powered vehicles with liquid organic hydrides. *International Journal of Hydrogen Energy*, 8(3):213–225, 1983.

P. Teatini, G. Gambolati, M. Ferronato, A. T. Settari, and D. Walters. Land uplift due to subsurface fluid injection. *Journal of Geodynamics*, 51(1):1–16, 2011.

K. Télessy, L. Barner, and F. Holz. Repurposing natural gas pipelines for hydrogen: Limits and options from a case study in germany. *International Journal of Hydrogen Energy*, 80: 821–831, 2024.

E. Tenthorey, W. M. Hsiao, R. Puspitasari, M. A. Giddins, Z. J. Pallikathekathil, R. Dandekar, O. Suriyanto, and A. J. Feitz. Geomechanics of hydrogen storage in a depleted gas field. *International Journal of Hydrogen Energy*, 60:636–649, 2024.

J. ter Heege. Experimental data on reactions between hydrogen and rock samples from reservoir and geological seals and effects on fluid flow and mechanical properties of reservoir and caprock. 2023.

R. E. Terry. Enhanced oil recovery. In R. A. Meyers, editor, *Encyclopedia of Physical Science and Technology (Third Edition)*, pages 503–518. Academic Press, New York, third edition edition, 2003. ISBN 978-0-12-227410-7. doi: https://doi.org/10.1016/B0-12-227410-5/00868-1. `https://www.sciencedirect.com/science/article/pii/B0122274105008681`.

P. Thakur, Y. Huang, and Y. Kaneko. Effects of low-velocity fault damage zones on long-term earthquake behaviors on mature strike-slip faults. *Journal of Geophysical Research: Solid Earth*, 125(8):e2020JB019587, 2020.

E. M. Thaysen, S. McMahon, G. J. Strobel, I. B. Butler, B. T. Ngwenya, N. Heinemann, M. Wilkinson, A. Hassanpouryouzband, C. I. McDermott, and K. Edlmann. Estimating microbial growth and hydrogen consumption in hydrogen storage in porous media. *Renewable and Sustainable Energy Reviews*, 151:111481, 2021.

R. Thomas and S. Churchill. Gas production over the last 200 years: Friend or foe. *A more sustainable energy future?*, page 8, 2014.

R. N. Thomas, A. Paluszny, and R. W. Zimmerman. Quantification of fracture interaction using stress intensity factor variation maps. *Journal of Geophysical Research: Solid Earth*, 122(10):7698–7717, 2017.

R. N. Thomas, A. Paluszny, and R. W. Zimmerman. Growth of three-dimensional fractures, arrays, and networks in brittle rocks under tension and compression. *Computers and Geotechnics*, 121:103447, 2020a.

R. N. Thomas, A. Paluszny, and R. W. Zimmerman. Permeability of three-dimensional numerically grown geomechanical discrete fracture networks with evolving geometry and mechanical apertures. *Journal of Geophysical Research: Solid Earth*, 125(4):e2019JB018899, 2020b.

N. Thompson, J. S. Andrews, and T. I. Bjørnarå. Assessing potential thermo-mechanical impacts on caprock due to co2 injection—a case study from northern lights ccs. *Energies*, 14 (16):5054, 2021.

Thunder Said Energy. Global energy demand: by region and through 2050? `https://thundersaidenergy.com/downloads/global-energy-demand-by-region-and-through-2050/`, 2024.

L. Tibane, H. Pöllmann, F. Ndongani, B. Landman, and W. Altermann. Evaluation of the lithofacies, petrography, mineralogy, and geochemistry of the onshore cretaceous zululand basin in south africa for geological co2 storage. *International Journal of Greenhouse Gas Control*, 109:103364, 2021.

S. Timmerberg, M. Kaltschmitt, and M. Finkbeiner. Hydrogen and hydrogen-derived fuels through methane decomposition of natural gas–ghg emissions and costs. *Energy Conversion and Management: X*, 7:100043, 2020.

G. Tiwari, A. Bose, J. Chakravartty, S. Wadekar, M. Totlani, R. Arya, and R. Fotedar. A study of internal hydrogen embrittlement of steels. *Materials Science and Engineering: A*, 286(2):269–281, 2000.

X. Tong, S. Ovtar, K. Brodersen, P. V. Hendriksen, and M. Chen. A 4× 4 cm2 nanoengineered solid oxide electrolysis cell for efficient and durable hydrogen production. *ACS applied materials & interfaces*, 11(29):25996–26004, 2019.

A. Trautmann, G. Mori, M. Oberndorfer, S. Bauer, C. Holzer, and C. Dittmann. Hydrogen

uptake and embrittlement of carbon steels in various environments. *Materials*, 13(16):3604, 2020.

L. Truche and E. F. Bazarkina. Natural hydrogen the fuel of the 21st century. In *E3S Web of Conferences*, volume 98, page 03006. EDP Sciences, 2019.

L. Truche, M.-C. Jodin-Caumon, C. Lerouge, G. Berger, R. Mosser-Ruck, E. Giffaut, and N. Michau. Sulphide mineral reactions in clay-rich rock induced by high hydrogen pressure. application to disturbed or natural settings up to 250 c and 30 bar. *Chemical Geology*, 351: 217–228, 2013.

N. Trujillo, D. Rose-Coss, J. E. Heath, T. A. Dewers, W. Ampomah, P. S. Mozley, and M. Cather. Multiscale assessment of caprock integrity for geologic carbon storage in the pennsylvanian farnsworth unit, texas, usa. *Energies*, 14(18):5824, 2021.

A. Turkiewicz, T. Steliga, D. Kluk, and Z. Gminski. Biomonitoring studies and preventing the formation of biogenic h2s in the wierzchowice underground gas storage facility. *Energies*, 14 (17):5463, 2021.

P. Tzampoglou and C. Loupasakis. Numerical simulation of the factors causing land subsidence due to overexploitation of the aquifer in the amyntaio open coal mine, greece. *HydroResearch*, 1:8–24, 2019.

H. Uchida and M. R. Harada. *Chapter 5.3.2 - Application of Hydrogen Combustion for Electrical and Motive Power Generation*, pages 259–278. Science and Engineering of Hydrogen-Based Energy Technologies. Academic Press, 2019. ISBN 9780128142516. doi: https://doi.org/10.1016/B978-0-12-814251-6.00005-8. ID: 318994.

J. Ukleja. Renovation of the historic building after damage connected with foundations subsidence-case study. In *MATEC Web of Conferences*, volume 174, page 03006. EDP Sciences, 2018.

E. Urban and J. F. Lermo. Local seismicity in the exploitation of los humeros geothermal field, mexico. In *Proceedings of thirtyeighth workshop on geothermal reservoir engineering*, 2013.

A. Ursua, L. M. Gandia, and P. Sanchis. Hydrogen production from water electrolysis: current status and future trends. *Proceedings of the IEEE*, 100(2):410–426, 2011.

U.S. Energy Information Administration. Natural gas weekly update: Groningen field natural gas production, September 2020. `https://www.eia.gov/naturalgas/weekly/archivenew_ngwu/2020/09_17/`.

U.S. Energy Information Administration. International Energy Outlook 2021 (IEO2021). Technical report, U.S. Energy Information Administration, 2021.

L. M. Valle-Falcones, C. Grima-Olmedo, L. F. Mazadiego-Martinez, A. Hurtado-Bezos, S. Eguilior-Diaz, and R. Rodriguez-Pons. Green hydrogen storage in an underground cavern: a case study in salt diapir of spain. *Applied Sciences*, 12(12):6081, 2022.

S. van Renssen. The hydrogen solution? *Nature Climate Change*, 10(9):799–801, 2020.

K. van Thienen-Visser and J. Breunese. Induced seismicity of the groningen gas field: History and recent developments. *The Leading Edge*, 34(6):664–671, 2015.

K. van Thienen-Visser, J. Pruiksma, and J. Breunese. Compaction and subsidence of the groningen gas field in the netherlands. *Proceedings of the International Association of Hydrological Sciences*, 372(372):367–373, 2015.

S. M. Vargas, R. Woollam, W. Durnie, M. Hodges, and D. Betancourt. Effect of nitrate on carbon steel corrosion. In *SPE International Conference on Oilfield Chemistry?*, page D011S001R006. SPE, 2017.

N. S. Venkataramanan, H. Mizuseki, and Y. Kawazoe. Hydrogen storage on nanofullerene cages. *Nano*, 4(05):253–263, 2009.

R. Venter and G. Pucher. Modelling of stationary bulk hydrogen storage systems. *International Journal of Hydrogen Energy*, 22(8):791–798, 1997.

J. P. Verdon. Significance for secure co2 storage of earthquakes induced by fluid injection. *Environmental Research Letters*, 9(6):064022, 2014.

J. P. Verdon. Using microseismic data recorded at the weyburn ccs-eor site to assess the likelihood of induced seismic activity. *International Journal of Greenhouse Gas Control*, 54: 421–428, 2016.

J. P. Verdon, A. L. Stork, R. C. Bissell, C. E. Bond, and M. J. Werner. Simulation of seismic events induced by co2 injection at in salah, algeria. *Earth and Planetary Science Letters*, 426:118–129, 2015.

M. J. Veshareh, E. M. Thaysen, and H. M. Nick. Feasibility of hydrogen storage in depleted hydrocarbon chalk reservoirs: Assessment of biochemical and chemical effects. *Applied Energy*, 323:119575, 2022.

V. Vilarrasa, O. Silva, J. Carrera, and S. Olivella. Liquid co2 injection for geological storage in deep saline aquifers. *International Journal of Greenhouse Gas Control*, 14:84–96, 2013.

V. Vilarrasa, J. Carrera, S. Olivella, J. Rutqvist, and L. Laloui. Induced seismicity in geologic carbon storage. *Solid Earth*, 10(3):871–892, 2019.

V. Vilarrasa, S. De Simone, J. Carrera, and A. Villaseñor. Unraveling the causes of the seismicity induced by underground gas storage at castor, spain. *Geophysical Research Letters*, 48(7): e2020GL092038, 2021.

V. Vishal, M. Rizwan, B. Mahanta, S. Pradhan, and T. Singh. Temperature effect on the mechanical behavior of shale: Implication for shale gas production. *Geosystems and Geoenvironment*, 1(4):100078, 2022.

G. Voordouw, M. Nemati, and G. Jenneman. Use of nitrate reducing, sulfide oxidizing bacteria to reduce souring in oil fields: interactions with srb and effects on corrosion. In *NACE CORROSION*, pages NACE–02034. NACE, 2002.

H. E. Wahls. Tolerable settlement of buildings. *Journal of the Geotechnical Engineering Division*, 107(11):1489–1504, 1981.

L. M. Wallace. Slow slip events in new zealand. *Annual Review of Earth and Planetary Sciences*, 48:175–203, 2020.

R. L. Wallace, Z. Cai, H. Zhang, K. Zhang, and C. Guo. Utility-scale subsurface hydrogen storage: Uk perspectives and technology. *International Journal of Hydrogen Energy*, 46(49): 25137–25159, 2021.

W. Wallace, R. Karlicek, and H. Imamura. Mechanism of hydrogen absorption by lanthanum-nickel (lani5). *Journal of Physical Chemistry*, 83(13):1708–1712, 1979.

I. Walton and J. McLennan. The role of natural fractures in shale gas production. In *ISRM International Conference for Effective and Sustainable Hydraulic Fracturing*, pages ISRM–ICHF. ISRM, 2013.

G. Wang, Y. Liu, Z. Hu, G. Zhang, J. Liu, Y. Lyu, Y. Gu, X. Huang, Q. Zhang, and L. Liu. Flood risk assessment of subway systems in metropolitan areas under land subsidence scenario: a case study of beijing. *Remote Sensing*, 13(4):637, 2021.

L. Wang, Y. Li, C. Li, and Z. Zhao. Cfd investigation of thermal and pressurization performance in lh2 tank during discharge. *Cryogenics*, 57:63–73, 2013.

L. Wang, M. Chen, R. Kuengas, T.-E. Lin, S. Diethelm, and F. Marechal. Power-to-fuels via solid-oxide electrolyzer: Operating window and techno-economics. *Renewable and Sustainable Energy Reviews*, 110:174–187, 2019.

L. Wang, G. Kwiatek, M. Bohnhoff, E. Rybacki, and G. Dresen. Injection-induced fault slip and associated seismicity in the lab: Insights from source mechanisms, local stress states and fault geometry. *Earth and Planetary Science Letters*, 626:118515, 2024a.

L. Wang, G. Kwiatek, F. Renard, S. Guérin-Marthe, E. Rybacki, M. Bohnhoff, M. Naumann, and G. Dresen. Fault roughness controls injection-induced seismicity. *Proceedings of the National Academy of Sciences*, 121(3):e2310039121, 2024b.

S. Wang, G. Jiang, M. Weingarten, and Y. Niu. Insar evidence indicates a link between fluid injection for salt mining and the 2019 changning (china) earthquake sequence. *Geophysical Research Letters*, 47(16):e2020GL087603, 2020.

S. Wang, H. Zhu, G. Zheng, F. Dong, and C. Liu. Dynamic changes in biofilm structures under dynamic flow conditions. *Applied and Environmental Microbiology*, 88(22):e01072–22, 2022.

Z. Wang and A. Krupnick. A retrospective review of shale gas development in the united states: What led to the boom? *Economics of Energy & Environmental Policy*, 4(1):5–18, 2015.

Z. Wang, X. Lyu, W. Shi, X.-t. Feng, L. Qiao, and R. Kong. Assessing the effect of intermediate principal geostress on the caprock integrity for underground gas storage. *Gas Science and Engineering*, page 205252, 2024c.

J. Wen, Y. Yin, and M. Zhang. Experimental study on fracture toughness of shale based on three-point bending semi-circular disk samples. *Processes*, 12(7):1368, 2024.

J. Whitcombe, N. McDonald, R. Cressey, B. H. Subrata, S. Falloon, N. Carr, and F. Glass. Ramsay 1 and ramsay 2, learnings from the first natural hydrogen exploration wells in australia. *Australian Energy Producers Journal*, 64(2):S453–S458, 2024.

D. White, L. Roach, B. Roberts, and T. Daley. Initial results from seismic monitoring at the aquistore co2 storage site, saskatchewan, canada. *Energy Procedia*, 63:4418–4423, 2014a.

D. White, K. Harris, L. Roach, B. Roberts, K. Worth, A. Stork, C. Nixon, D. Schmitt, T. Daley, and C. Samson. Monitoring results after 36 ktonnes of deep co2 injection at the aquistore co2 storage site, saskatchewan, canada. *Energy Procedia*, 114:4056–4061, 2017.

J. A. White, L. Chiaramonte, S. Ezzedine, W. Foxall, Y. Hao, A. Ramirez, and W. McNab. Geomechanical behavior of the reservoir and caprock system at the in salah co2 storage project. *Proceedings of the National Academy of Sciences*, 111(24):8747–8752, 2014b.

W. A. White and T. A. Tremblay. Submergence of wetlands as a result of human-induced subsidence and faulting along the upper texas gulf coast. *Journal of Coastal Research*, pages 788–807, 1995.

M. Whiteman and A. Troiano. Hydrogen embrittlement of austenitic stainless steel. *Corrosion*, 21(2):53–56, 1965.

J. Whitney. Resistance in the midst of the anthropocene: The rise and fall of artificial earthquakes at the rocky mountain arsenal, 1962–1966. *Arcadia*, 2019.

F. Widdel and F. Back. The genus desulfotomaculum. *The prokaryotes*, 4:787–794, 2006.

R. Wiebe and V. Gaddy. The solubility of hydrogen in water at 0, 50, 75 and 100 from 25 to 1000 atmospheres. *Journal of the American Chemical Society*, 56(1):76–79, 1934.

O. Wiener. Theorie des mischkorpers fur das feld der stationaren stromung. *Abhandl. Sachs. Ges. Wiss. Math. Phys. K1.*, pages 509–598, 1912.

J. Williams, S. Holloway, and G. A. Williams. Pressure constraints on the co2 storage capacity of the saline water-bearing parts of the bunter sandstone formation in the uk southern north sea. *Petroleum Geoscience*, 20(2):155–167, 2014.

R. T. Williams and Å. Fagereng. The role of quartz cementation in the seismic cycle: A critical review. *Reviews of Geophysics*, 60(1):e2021RG000768, 2022.

D. Wilson, L. Poindexter, and T. Nguyen. Role of surfactant structures on surfactant-rock adsorption in various rock types. In *SPE International Conference on Oilfield Chemistry?*, page D022S020R001. SPE, 2019.

R. A. Winschel. The relationship of carbon dioxide emissions with coal rank and sulfur content. *Journal of the Air & Waste Management Association*, 40(6):861–865, 1990.

D. L. Wise and G. Houghton. The diffusion coefficients of ten slightly soluble gases in water at 10–60 c. *Chemical Engineering Science*, 21(11):999–1010, 1966.

E. Wolf. *Large-scale hydrogen energy storage*, pages 129–142. Electrochemical energy storage for renewable sources and grid balancing. Elsevier, 2015.

B. L. Wood. Metamorphosed ultramafites and associated formations near milford sound, new zealand. *New Zealand Journal of Geology and Geophysics*, 15(1):88–128, 1972.

WoodMackenzie. The future for green hydrogen. `https://www.woodmac.com/news/editorial/the-future-for-green-hydrogen/`, 2019. Wood Mackenzie.

J. Wösten, A. Ismail, and A. Van Wijk. Peat subsidence and its practical implications: a case study in malaysia. *Geoderma*, 78(1-2):25–36, 1997.

F. Wu, Y. Liu, and R. Gao. Challenges and opportunities of energy storage technology in abandoned coal mines: A systematic review. *Journal of Energy Storage*, 83:110613, 2024.

H. Würdemann, G. Borm, and F. R. Schilling. CO2SINK Summary Technical Report. Technical report, CO2SINK (In-situ R&D Laboratory for Geological Storage of CO2), 2004. `https://cordis.europa.eu/docs/results/502/502599/123655671-6_en.pdf`.

D. Xu, L. Dong, and J. Ren. *Chapter 2 - Introduction of Hydrogen Routines*, pages 35–54. Hydrogen Economy. Academic Press, 2017. ISBN 9780128111321. doi: https://doi.org/10.1016/B978-0-12-811132-1.00002-X. ID: 316744.

Y. Xue, J. Liu, X. Liang, X. Li, S. Wang, Z. Ma, S. Zhang, and X. Jiao. Influence mechanism of brine-gas two-phase flow on sealing property of anisotropic caprock for hydrogen and carbon energy underground storage. *International Journal of Hydrogen Energy*, 48(30):11287–11302, 2023.

T. Yamamoto, H. Inui, and M. Yamaguchi. Deformation of lani5 by uniaxial compression and hydrogenation. *Intermetallics*, 9(10-11):987–991, 2001.

Q. Yang, W. Zhao, T. H. Dixon, F. Amelung, W. S. Han, and P. Li. Insar monitoring of ground deformation due to co2 injection at an enhanced oil recovery site, west texas. *International Journal of Greenhouse Gas Control*, 41:20–28, 2015.

Y. Yang, A. Zandanel, S. Liu, C. W. Neil, T. C. Germann, and M. R. Gross. Temperature dependence of hydrogen diffusion in reservoir rocks: implications for hydrogen geologic storage. *Energy Advances*, 3(8):2051–2065, 2024.

Z. Yanxing, G. Maoqiong, Z. Yuan, D. Xueqiang, and S. Jun. Thermodynamics analysis of hydrogen storage based on compressed gaseous hydrogen, liquid hydrogen and cryo-compressed hydrogen. *International Journal of Hydrogen Energy*, 44(31):16833–16840, 2019.

Y. Yao, S. Li, X. Jia, J. Song, D. Yue, Q. Zhang, and H. Xiang. Numerical simulation of ground subsidence response conditional on geothermal exploitation in a karst reservoir area of north china. *Sustainability*, 15(10):8089, 2023.

S. Ye, Y. Luo, J. Wu, X. Yan, H. Wang, X. Jiao, and P. Teatini. Three-dimensional numerical modeling of land subsidence in shanghai, china. *Hydrogeology Journal*, 3(24):695–709, 2016.

Y. Ye, Y. Yue, J. Lu, J. Ding, W. Wang, and J. Yan. Enhanced hydrogen storage of a lani5 based reactor by using phase change materials. *Renewable Energy*, 180:734–743, 2021.

W. L. Yeck, M. Weingarten, H. M. Benz, D. E. McNamara, E. Bergman, R. Herrmann, J. L. Rubinstein, and P. S. Earle. Far-field pressurization likely caused one of the largest injection induced earthquakes by reactivating a large preexisting basement fault structure. *Geophysical Research Letters*, 43(19):10–198, 2016.

W. L. Yeck, G. P. Hayes, D. E. McNamara, J. L. Rubinstein, W. D. Barnhart, P. S. Earle, and H. M. Benz. Oklahoma experiences largest earthquake during ongoing regional wastewater injection hazard mitigation efforts. *Geophysical Research Letters*, 44(2):711–717, 2017.

A. Yehya and J. R. Rice. Influence of fluid-assisted healing on fault permeability structure. *Journal of Geophysical Research: Solid Earth*, 125(10):e2020JB020553, 2020.

L. Yin, H. Yang, and Y. Ju. Review on the key technologies and future development of insulation structure for liquid hydrogen storage tanks. *International Journal of Hydrogen Energy*, 57: 1302–1315, 2024.

S. Yin, M. B. Dusseault, and L. Rothenburg. Fully coupled numerical modelling of ground surface uplift in steam injection. *Journal of Canadian Petroleum Technology*, 49(01):16–21, 2010.

T. Young. An essay on the cohesion of fluids. In *Abstracts of the Papers Printed in the Philosophical Transactions of the Royal Society of London*, number 1, pages 171–172. The Royal Society London, 1832.

Y. Yu, F. Xie, M. Zhu, S. Yu, and Y. Li. Design and optimization of the insulation performance of a 4000 m3 liquid hydrogen spherical tank. *Processes*, 11(6):1778, 2023.

T. Yusaf, M. Laimon, W. Alrefae, K. Kadirgama, H. A. Dhahad, D. Ramasamy, M. K. Kamarulzaman, and B. Yousif. Hydrogen energy demand growth prediction and assessment (2021–2050) using a system thinking and system dynamics approach. *Applied Sciences*, 12 (2):781, 2022.

J. Zabranska and D. Pokorna. Bioconversion of carbon dioxide to methane using hydrogen and hydrogenotrophic methanogens. *Biotechnology advances*, 36(3):707–720, 2018.

A. Zapantis. Blue hydrogen. `https://www.ourenergypolicy.org/resources/blue-hydrogen/`, 04 2021. Global CCS Institute.

D. Zbinden, A. P. Rinaldi, L. Urpi, and S. Wiemer. On the physics-based processes behind production-induced seismicity in natural gas fields. *Journal of Geophysical Research: Solid Earth*, 122(5):3792–3812, 2017.

D. Zbinden, A. P. Rinaldi, T. Diehl, and S. Wiemer. Potential influence of overpressurized gas on the induced seismicity in the st. gallen deep geothermal project (switzerland). *Solid Earth*, 11(3):909–933, 2020.

L. Zeng, S. Vialle, J. Ennis-King, L. Esteban, M. Sarmadivaleh, J. Sarout, J. Dautriat, A. Giwelli, and Q. Xie. Role of geochemical reactions on caprock integrity during underground hydrogen storage. *Journal of Energy Storage*, 65:107414, 2023.

L. Zeng, R. Sander, Y. Chen, and Q. Xie. Hydrogen storage performance during underground hydrogen storage in depleted gas reservoirs: A review. *Engineering*, 2024.

V. Zgonnik, V. Beaumont, N. Larin, D. Pillot, and E. Deville. Diffused flow of molecular hydrogen through the western hajar mountains, northern oman. *Arabian Journal of Geosciences*, 12:1–10, 2019.

L. Zhang, Y. Soong, and R. M. Dilmore. Numerical investigation of lower tuscaloosa sandstone

and selma chalk caprock under geological co2 sequestration conditions: mineral precipitation and permeability evolution. *Greenhouse Gases: Science and Technology*, 7(6):988–1007, 2017.

N. Zhang, X. Wang, J. Zhang, X. He, S. Kang, J. Pu, S. Fan, and X. Li. Experimental and statistical study on wellbore scaling mechanisms and characteristics for huanjiang oilfield. *Geofluids*, 2022(1):9068440, 2022.

S. Zhang, R. Zhong, and Y. Liu. Numerical modeling of land subsidence resulting from oil production. In *ARMA US Rock Mechanics/Geomechanics Symposium*, pages ARMA–2016. ARMA, 2016.

Y. Zhang, M. Person, J. Rupp, K. Ellett, M. A. Celia, C. W. Gable, B. Bowen, J. Evans, K. Bandilla, P. Mozley, et al. Hydrogeologic controls on induced seismicity in crystalline basement rocks due to fluid injection into basal reservoirs. *Groundwater*, 51(4):525–538, 2013.

Y. Zhang, S. Hao, Z. Yu, X. Li, and T. Xu. Land uplift induced by injection: a feasible method to evaluate the security of co 2 capture and sequestration projects. *Environmental Earth Sciences*, 77:1–11, 2018.

Z. Zhang, M. Gao, X. Chen, X. Wei, J. Liang, C. Wu, and L. Wang. The joule–thomson effect of (co2+ h2) binary system relevant to gas switching reforming with carbon capture and storage (ccs). *Chinese Journal of Chemical Engineering*, 54:215–231, 2023.

W. Zheng, J.-W. Kim, S. T. Ali, and Z. Lu. Wastewater leakage in west texas revealed by satellite radar imagery and numerical modeling. *Scientific reports*, 9(1):14601, 2019.

W. Zheng, Z. Lu, and J.-W. Kim. Bayesian monte carlo inversion of insar time series deformation induced by wastewater injection: A case study in west texas. *Geophysical Research Letters*, 50(10):e2023GL102991, 2023.

S. Zhirafar, A. Rezaeian, and M. Pugh. Effect of cryogenic treatment on the mechanical properties of 4340 steel. *Journal of Materials Processing Technology*, 186(1-3):298–303, 2007.

L. Zhou and Y. Zhou. Determination of compressibility factor and fugacity coefficient of hydrogen in studies of adsorptive storage. *International Journal of Hydrogen Energy*, 26(6): 597–601, 2001.

L. Zhou, X. Ren, J. Zhou, H. Li, and Q. Gan. Numerical study on the induced seismicity through hydraulic fracturing in the deep heat mining project in basel, switzerland using a pseudo dynamic model and considering fully hydro-mechanical coupling. *Geothermics*, 105: 102538, 2022.

S. Zhu, X. Shi, C. Yang, Y. Li, H. Li, K. Yang, X. Wei, W. Bai, and X. Liu. Hydrogen loss of salt cavern hydrogen storage. *Renewable Energy*, 218:119267, 2023.

X. Zhu, W. Li, T. Hsu, S. Zhou, L. Wang, and X. Jin. Improved resistance to hydrogen embrittlement in a high-strength steel by quenching–partitioning–tempering treatment. *Scripta Materialia*, 97:21–24, 2015.

R. W. Zimmerman. *The Imperial College Lectures in Petroleum Engineering: Volume 5: Fluid Flow in Porous Media*. World Scientific, 2018.

R. W. Zimmerman and G. S. Bodvarsson. Hydraulic conductivity of rock fractures. *Transport in porous media*, 23:1–30, 1996.

R. W. Zimmerman and A. Paluszny. *Fluid Flow in Fractured Rocks*. John Wiley & Sons, 2023.

D. Zivar, S. Kumar, and J. Foroozesh. Underground hydrogen storage: A comprehensive review. *International journal of hydrogen energy*, 46(45):23436–23462, 2021.

M. Zoback and D. Smit. Meeting the challenges of large-scale carbon storage and hydrogen production. *Proceedings of the National Academy of Sciences*, 120(11):e2202397120, 2023.